

## LA-UR-21-31605

Approved for public release; distribution is unlimited.

Title: Understanding Weld Formation and Microstructure Evolution in Laser  
Welded Stainless Steels and Ti-6Al-4V

Author(s): Patterson, Tate

Intended for: Report

Issued: 2021-11-23

---

**Disclaimer:**

Los Alamos National Laboratory, an affirmative action/equal opportunity employer, is operated by Triad National Security, LLC for the National Nuclear Security Administration of U.S. Department of Energy under contract 89233218CNA000001. By approving this article, the publisher recognizes that the U.S. Government retains nonexclusive, royalty-free license to publish or reproduce the published form of this contribution, or to allow others to do so, for U.S. Government purposes. Los Alamos National Laboratory requests that the publisher identify this article as work performed under the auspices of the U.S. Department of Energy. Los Alamos National Laboratory strongly supports academic freedom and a researcher's right to publish; as an institution, however, the Laboratory does not endorse the viewpoint of a publication or guarantee its technical correctness.

# **Understanding Weld Formation and Microstructure Evolution in Laser Welded Stainless Steels and Ti-6Al-4V**

Dissertation

Presented in Partial Fulfillment of the Requirements for the Degree Doctor of Philosophy  
in the Graduate School of The Ohio State University

By

Tate Patterson

Graduate Program in Welding Engineering

The Ohio State University

Fall 2021

Dissertation Committee

Dr. John C. Lippold, Advisor

Dr. Boyd Panton, Co-advisor

Dr. Carolin Fink

Dr. Xun Liu

Copyrighted by

Tate Patterson

2021

## **Abstract**

High energy density welding processes are used for many industrial applications, such as aerospace and defense, and certain joint configurations and welding situations render post-weld inspection techniques difficult. Due to the inability to confirm penetration, there is a continual industrial need to improve prediction capabilities to aid in parameter selection. It is also necessary to understand the microstructural evolution to modify phase fractions and mitigate weldability related concerns such as solidification cracking or reduced corrosion performance.

Using an ytterbium doped fiber laser, partial penetration laser beam welds were produced on a six stainless steel (SS) alloys and Ti-6Al-4V. The WRC-1992 Cr/Ni equivalencies for the SS alloys ranged from 1.7 to 2.8. These alloys included a commercially available 304L stainless steel (SS) and a commercially available 2205 duplex stainless steel. The other four SS alloys were experimental compositions.

From an industrial perspective regarding weld feature prediction, the two alloys of interest include 304L SS and Ti-6Al-4V. Therefore, analysis was performed to relate weld geometry characteristics to process parameters for these two alloys. The objective of the weld geometry analysis was to develop a neural network model that can predict weld geometry characteristics, most importantly penetration. The best results were

produced with individual neural networks developed for each weld feature and compiled into a comprehensive algorithm.

An inline coherent imaging (ICI) or depth measurement system was also incorporated during LBW to further understand keyhole evolution and weld pool development. Process parameters influenced the location of the keyhole relative to the process beam and the overall shape and width of the vapor capillary.

Transverse and longitudinal view sections were evaluated to determine solidification behavior, and electron backscatter diffraction (EBSD) patterns were used extensively to determine phase fractions and grain size. For SS alloys, relationships among penetration mode (conduction vs. keyhole), composition ( $Cr_{eq}/Ni_{eq}$ ), and microstructure (solidification mode and phase fraction) are presented. The results presented provide a more complete picture of rapid solidification phenomena associated with laser welds in SS alloys over a wide range of compositions.

For Ti-6Al-4V, the beta grain size and morphology were related to the welding conditions and weld pool shape. Prior-beta grains were reconstructed using EBSD analysis, and this information was used to determine the size, orientation, and growth of the beta grains at different travel speeds. Beta grain growth during solidification was strongly influenced by the weld pool shape and generally occurred by columnar growth from the fusion boundary to the weld surface and/or weld centerline. The average grain size decreased in the plan view orientation but showed minimal decrease in transverse and longitudinal sections.

## **Dedication**

This work is dedicated to the three most supportive and influential people in my life.

Bart Patterson (father)  
Kristi Patterson (mother)  
Brenda Peterson (aunt)

## **Acknowledgments**

I am extremely appreciative of my advisor, Dr. John C. Lippold, for keeping me on as a graduate student and allowing me to disrupt his golf schedule. In addition, his hands-off approach to advising and additional work facilitated a greater understanding of welding engineering and broadened my breadth of knowledge. I will be forever grateful for this opportunity.

From Los Alamos National Laboratory (LANL), I want to recognize and thank Dr. Matthew Johnson and Dr. David Tung who served as project mentors. Also, I want to acknowledge Dr. Paul Burgardt (retired) for his discussions and many e-mail conversations regarding the physics of high energy density welding.

I want to express gratitude to my co-advisor, Dr. Boyd Panton, and my committee members Dr. Carolin Fink and Dr. Xun Liu for their willingness to be on my committee and devotion of their time to reviewing manuscripts and performing examinations.

I thank Joris Hochanadel for his bizarre humor and all his help working with me on this project. I am also indebted to Samuel Casto for his willingness to learn and devote his time to generating additional weld results, and I apologize for not devoting multiple pages to his acknowledgement.

I am grateful to Dale Brush for providing me with a place to stay in Los Alamos and for his discussions and help with LabVIEW programming.

I would also like to thank my parents, Bart and Kristi; brothers, Tanner and Trevor; and aunt, Brenda, for their unwavering support and encouragement throughout my life and educational journey.

This research was supported through the National Science Foundation (NSF) sponsored Industry/University Cooperative Research Center (I/UCRC): Manufacturing and Materials Joining Innovation Center (Ma<sup>2</sup>JIC) under Grant No. 1822144, and I would like to thank LANL for providing the financial support through this cooperation. I would also like to thank IPG Photonics<sup>®</sup>, specifically the Midwest Operations group, for their support in implementing OSU's high-power laser lab.

## Vita

2012.....	Jerome High School Jerome, Idaho
2016.....	B.S. General Engineering, Montana Tech of the University of Montana
2018.....	M.S. Welding Engineering, The Ohio State University
2021.....	Ph.D. Welding Engineering, The Ohio State University

## Publications

T. Patterson and J. Lippold, “Effect of niobium on the microstructure and properties of submerged arc welds in HSLA steel,” *Weld. World*, vol. 64, no. 6, pp. 1089–1105, 2020.

J. Hochanadel, T. Patterson, J. Lippold, B. Panton, M. Johnson and D. Tung, “Influence of focus and deflection when comparing electron beam welds to laser welds at varying parameters in 304 SS,” *Weld. World*, vol. 65, no. 5, pp. 1007-1014, 2021.

T. Patterson, J. Hochanadel, S. Sutton, B. Panton, J. Lippold, “A Review of High Energy Density Beam Processes for Welding and Additive Manufacturing Applications,” *Weld. World*, vol. 65, no. 7, pp. 1235-1306, 2021.

T. Patterson, J. Lippold, B. Panton, “Laser Weld Formation and Microstructural Evolution in Stainless Steel Alloys,” Under review in *Weld. World*.

T. Patterson, J. Lippold, B. Panton, “Microstructure Evolution in Laser Welded Ti-6Al-4V,” Under review in *Weld. World*.

## Fields of Study

Major Field: Welding Engineering

## Table of Contents

Abstract .....	ii
Dedication .....	iv
Acknowledgments .....	v
Vita .....	vii
Table of Contents .....	viii
List of Tables .....	xiv
List of Figures .....	xv
Abbreviations and Symbols .....	xxx
1 Introduction .....	1
2 Background .....	6
2.1 Laser Fundamentals .....	6
2.1.1 Types of Lasers .....	8
2.1.2 Development and Operation of Fiber Lasers .....	9
2.1.3 History of Fiber Laser Development .....	10
2.1.4 Fiber Laser Operation .....	12
2.1.4.1 Beam Delivery .....	13
2.1.4.2 Reflective and Transmissive Optics .....	13
2.1.5 Beam Caustics .....	14
2.1.6 Inline Coherent Imaging .....	16
2.2 Weld Formation .....	21
2.2.1 Conduction Mode .....	22
2.2.2 Keyhole Mode .....	23
2.2.3 Transition Regime .....	24
2.3 Physical Process Interactions .....	25
2.3.1 Reflectivity .....	28

2.3.2	Vaporization.....	29
2.3.3	Plume Formation.....	32
2.3.4	Fluid Flow .....	39
2.4	Parameter Influences on Weld Pool Evolution .....	44
2.4.1	Beam Diameter .....	45
2.4.2	Power .....	46
2.4.3	Power Density .....	50
2.4.4	Travel Speed .....	52
2.4.5	Other Variables .....	55
2.4.6	Weld Defects.....	57
2.4.6.1	Porosity .....	57
2.4.6.2	Humping .....	58
2.5	Modeling and Weld Depth Prediction.....	59
2.5.1	Analytical Approaches.....	61
2.5.2	Dimensionless Approaches.....	65
2.5.3	Numerical Approaches.....	73
2.5.4	Artificial Neural Networks .....	74
2.5.4.1	ANN Overview.....	74
2.5.4.2	ANNs Relating to Weld Prediction .....	77
2.6	Microstructural Phenomena .....	78
2.6.1	Solidification Behavior, Thermal Gradients, and Growth Modes .....	78
2.6.1.1	Grain Orientation Related to HED Welds .....	84
2.6.1.2	Solidification Modes and Cell Size .....	86
2.6.2	Stainless Steel Microstructure.....	90
2.6.2.1	Duplex Stainless Steel .....	102
2.6.3	Ti-6Al-4V .....	104
3	Research Objectives.....	109
4	Experimental Procedures .....	110
4.1	Laser Welds.....	110

4.1.1	Inline Coherent Imaging .....	114
4.1.2	Weld Pool Decanting .....	116
4.2	Neural Network Modeling .....	117
4.3	Metallurgical Characterization .....	119
4.3.1	Chemical Analysis .....	119
4.3.2	Optical Metallography .....	120
4.3.3	Scanning Electron Microscopy .....	120
4.4	Material Compositions .....	121
4.5	Gas Tungsten Arc Welds.....	123
5	Results and Discussion .....	124
5.1	Weld Formation.....	124
5.1.1	Weld Geometry Analysis.....	124
5.1.2	Keyhole Formation .....	134
5.1.3	Weld Pool Decantation .....	144
5.1.4	Summary .....	149
5.2	Modeling .....	150
5.2.1	Artificial Neural Network.....	150
5.2.2	Summary .....	154
5.3	Microstructural Analysis .....	155
5.3.1	Stainless Steel Alloys.....	155
5.3.1.1	Weld Pool Profiles and Solidification Rates .....	156
5.3.1.2	Microstructure Analysis .....	160
5.3.1.3	Microstructure Maps.....	172
5.3.1.4	Summary.....	174
5.3.2	Ti-6Al-4V .....	175
5.3.2.1	Prior Beta Grain Analysis using EBSD.....	180
5.3.2.2	Beta Grain Size .....	186
5.3.2.3	Summary.....	191
6	Conclusions .....	192

6.1	Weld Formation.....	192
6.1.1	Weld Geometry .....	192
6.1.2	Keyhole Formation .....	193
6.2	Modeling .....	193
6.3	Microstructure .....	194
6.3.1	Stainless Steel Alloys.....	194
6.3.2	Ti-6Al-4V .....	195
7	Future Work .....	197
7.1	Weld Behavior Analysis.....	197
7.2	ANN Modeling.....	197
7.3	Microstructure .....	198
7.3.1	Stainless Steels.....	198
7.3.2	Titanium.....	199
	Bibliography .....	200
	Appendix A: Material Properties .....	228
	A.1 Stainless Steel .....	230
	A.1.1 Property Diagrams .....	232
	A.1.2 Scheil Computations .....	234
	A.2 Ti-6Al-4V .....	237
	A.2.1 Property Diagrams .....	240
	Appendix B: Weld Parameters.....	241
	Appendix C: Laser Beam Analysis.....	243
	Appendix D: Laser Weld Profiles – 304L .....	249
	D.1 Weld Surfaces – 304L.....	249
	D.2 Transverse Sections – 304L.....	255
	Appendix E: Weld Geometry Data – 304L.....	259
	Appendix F: Laser Weld Profiles – Ti-6Al-4V .....	261
	F.1 Weld Surfaces – Ti-6Al-4V.....	261
	F.2 Transverse Sections – Ti-6Al-4V .....	267

Appendix G: Weld Geometry Data – Ti-6Al-4V .....	271
Appendix H: Weld Geometry Data – All Stainless Steel Alloys .....	273
Appendix I: Neural Network GUI and Results .....	275
Appendix J: Ti-6Al-4V Prior Beta Grain Boundary Delineation Analysis .....	282
J.1 Etchant Attempts .....	282
J.2 Heat Treatment Attempts .....	291
J.3 SEM Analysis.....	295
J.4 Elevated Temperature EBSD .....	295
J.5 Pure Titanium Laser Weld PBGB Analysis .....	298
Appendix K: MATLAB® Script – Laser Beam Diagnostics .....	300
K.1 Beam Diameter Analysis Script.....	300
K.2 Spreadsheet Location Extraction Function .....	304
K.3 Power Density Calculation Function .....	306
K.4 Second Moment Calculation Function.....	307
K.5 D86 Calculation .....	309
K.6 Intensity Distribution Plot – 2D.....	312
K.7 Intensity Distribution Plot – 3D.....	314
K.8 Beam Caustic Plots .....	316
Appendix L: MATLAB® Script – Transverse Cross-Section Analysis.....	322
Appendix M: MATLAB® Script – Weld Surface Solidification Angle .....	337
Appendix N: MATLAB® Script – ICI Surface Fitting Algorithm .....	339
N.1 Keyhole Measurement Function .....	351
N.2 D86 Keyhole Diameter Calculation.....	353
N.3 Keyhole D2M Diameter Calculation .....	355
N.4 Keyhole FWHM Diameter Calculation .....	357
N.5 Keyhole Surface Visualization Script.....	360
Appendix O: MATLAB® Script – Neural Network .....	362
O.1 Graphical User Interface Script .....	362
O.2 Neural Network Training Script .....	381

O.3 Fusion Cross-Section Calculation Function.....	383
O.4 Feedforward Artificial Neural Network Function .....	389
O.5 Neural Network Data Combination Function .....	394
Appendix P: Gas Tungsten Arc Weld Micrographs .....	396

## List of Tables

Table 2.1. Dimensionless numbers used in fluid dynamics calculations.....	66
Table 4.1. Laser weld parameters evaluated at a 600 $\mu\text{m}$ beam diameter. ....	110
Table 4.2. Measured stainless steel alloy compositions (wt%) with Fe as the remainder. .....	122
Table 4.3. Ti-6Al-4V chemical composition (wt%). ....	122
Table 5.1. Measured features from decanting 304L SS at 1000 W. ....	148
Table 5.2. Decanted volume and calculated melting efficiency for 304L SS at 1000 W. .....	148
Table 5.3. Suutala, Hammar and Svensson (H&S), and WRC-1992 $\text{Cr}_{\text{eq}}/\text{Ni}_{\text{eq}}$ values. ...	155
Table A.1. Room temperature material properties for 304 SS and Ti-6Al-4V. All values were extracted from Mills [121]. ....	228
Table A.2. Liquid and vapor material properties for 304 SS and Ti-6Al-4V. ....	229
Table A.3. Temperature dependent material properties for solid 304L computed using Thermo-Calc <sup>®</sup> [236]. Thermal conductivity was extracted from Reference [121]. ....	230
Table A.4. Temperature dependent material properties for liquid 304L computed using Thermo-Calc <sup>®</sup> [236]. Thermal conductivity was computed using Reference [235]. ....	231
Table A.5. Scheil computation analysis results for temperature ranges relating to phase stability during solidification from the liquidus to the solidus temperatures.....	237
Table A.6. Temperature dependent material properties for solid Ti-6Al-4V computed using Thermo-Calc <sup>®</sup> [236]. Thermal conductivity was extracted from Reference [121]. .....	238
Table A.7. Temperature dependent material properties for liquid Ti-6Al-4V computed using Thermo-Calc <sup>®</sup> [236]. ....	239
Table B.1. Equipment and parameters used for all laser welding experiments. ....	241
Table C.1. IPG Photonics <sup>®</sup> YLS-6000 set power versus measured beam power. ....	244

## List of Figures

Figure 1.1. Laser weld geometries produced using different powers and travel speeds at a 500 $\mu\text{m}$ beam diameter on 304L SS.....	2
Figure 2.1. Fiber laser operation showing the active medium within a resonate cavity consisting of a Bragg grating and pumped via multi-mode diodes. ....	12
Figure 2.2. Beam profile comparison between Gaussian and multi-mode distributions at 800 W and a 500 $\mu\text{m}$ beam diameter (D86) [3]. ....	15
Figure 2.3. Schematic representation of inline coherent imaging system. Recreated from Ji et al. [59]. ....	18
Figure 2.4. Variation in ICI signal when welding different materials [64]. ....	20
Figure 2.5. Influence of keyhole geometry on ICI measurements. Recreated and modified from Boley et al. [68]. ....	21
Figure 2.6. Comparison of conduction, transition, and keyhole mode laser welds on 304 SS at a 500 $\mu\text{m}$ beam diameter [3]. ....	22
Figure 2.7. Laser beam conduction to keyhole mode transition for: 304L SS (a) and 2024-T3 aluminum (b) reported by Assunção and Williams [79]. ....	25
Figure 2.8. Schematic showing physical process considerations during keyhole LBW [3]. ....	26
Figure 2.9. Absorption at varying wavelengths and incident angles for s and p polarized light [91]. ....	29
Figure 2.10. Front wall angle versus heat input recreated from Gladush and Smurov [90]. ....	30
Figure 2.11. X-ray images of vapor capillary at varying shielding gas flow rates: 0 l/min (a), 36 l/min (b), 51 l/min (c), 81 l/min (d), 120 l/min (e). The welding direction is from left to right. The schematics were recreated based on the originals from Arata et al. [94]. ....	31
Figure 2.12. Penetration versus cross-jet height at 5 kW of power and a 33 mm/s travel speed [103]. ....	35
Figure 2.13. Laser attenuation versus atmospheric pressure for a 1070 nm wavelength at a 1 mm height for an aluminum alloy (squares) [109] and at a 3 mm height for a high-strength low-alloy steel (diamonds) [110]. ....	36
Figure 2.14. Steel welded at 16 kW and 0.3 m/min (5 mm/s). From left to right, LB weld at 100 kPa, LB weld at 0.01 kPa, and EB weld at 0.0001 kPa. Weld profiles were extracted from Reisgen et al. [108]. ....	37

Figure 2.15. Schematic of LB weld penetration versus pressure at a constant power and beam diameter for different travel speeds. Data interpreted from references [16], [106], [112], [116].	38
Figure 2.16. Change in surface tension versus sulfur content. Recreated from Mills [121].	41
Figure 2.17. Change in laser spot weld pool shape on 304L stainless steel at 40 ppm sulfur (a) and 140 ppm sulfur (b) [123].	41
Figure 2.18. Schematic of keyhole mode melt flow phenomena recreated from Kaplan [125].	42
Figure 2.19. Position of tungsten particle in weld pool showing the elapsed time in milliseconds from Matsunawa et al. [76].	42
Figure 2.20. Fluid flow velocity versus welding speed at different powers and beam diameters. Recreated from Gladush and Smurov [90].	44
Figure 2.21. Laser beam caustic showing the transition from multi-mode to a Gaussian distribution at the under and over-focused conditions [3].	46
Figure 2.22. Focal position relative to transverse section weld formation [71].	46
Figure 2.23. Penetration depth versus power or power density at constant beam diameters: X100 steel [134] (a) and S355 steel (b) [137].	47
Figure 2.24. Penetration depth versus power or power density at constant beam diameters: 304 SS (a), Ti-6Al-4V (b), and vanadium (c) [137].	49
Figure 2.25. Penetration versus power density for stainless steel, aluminum, and mild steel at a constant beam diameter (1.18 mm) and travel speed (58.3 mm/s). Data extracted from Assunção and Williams [79].	50
Figure 2.26. Fiber laser penetration versus power for steel alloys when welding in keyhole mode [79], [134], [137].	51
Figure 2.27. Stainless steel weld penetration using a fiber laser with a 200 $\mu\text{m}$ beam diameter [71].	52
Figure 2.28. Weld geometry on 304 SS using a multi-mode beam profile at sharp focus. An apparent change from keyhole mode to conduction mode occurs above 75 mm/s [3].	53
Figure 2.29. Change in LBW melting efficiency versus travel speed [90].	54
Figure 2.30. Average front wall angle versus welding speed (a) and Fresnel absorption versus welding speed (b) [88].	54
Figure 2.31. Weld metal porosity at: atmospheric pressure (a), $10^3$ Pa (b), $10^1$ Pa (c), $10^{-1}$ Pa (d), $10^{-3}$ Pa (e). Extracted from Cai et al. [150].	58

Figure 2.32. Schematic representing travel speed versus penetration at four different powers. Recreated from Smithells Metals Reference Book [155].	60
Figure 2.33. Schematic of moving line source to compute the angle of the keyhole wall based on energy balance [13].	65
Figure 2.34. Dimensionless plot of EB data for a range of alloys from Hablani [8].	68
Figure 2.35. Plot of CO <sub>2</sub> laser welding using dimensionless relationships from Locke and Hella [138].	69
Figure 2.36. Normalized depth as a function of nondimensional power [143].	72
Figure 2.37. Perceptron network with nodes or inputs (x) shown as circles and connected to a neuron with a weight (w). Without a bias (left) and with a bias (right) [172].	75
Figure 2.38. Schematic of a fully connected network where all inputs of one layer are connected to all the nodes of the following layer.	76
Figure 2.39. Illustration of columnar grain growth continually changing to maintain a <100> growth direction and perpendicular to the isotherm boundary. Recreated from Porter and Easterling [186].	80
Figure 2.40. Influence of thermal gradient versus solidification rate on crystal formation from Lippold [188].	81
Figure 2.41. Schematic representing the transition from cellular to columnar dendritic growth (left to right). Recreated from David and Vitek [187].	81
Figure 2.42. Influence of constitutional supercooling on solidification modes from Kou [123] where S, L, and M represent solid, liquid, and mushy zones respectively.	82
Figure 2.43. Schematic of constitutional supercooling based on heat input and weld pool geometry from Kou [123].	84
Figure 2.44. EB weld on a single crystal Fe-15Cr-15Ni alloy: pure (a) and with sulfur (b) from David and Vitek [187].	84
Figure 2.45. Illustration of crystal growth in an elliptical weld pool geometry (a) [192], [193]. Illustration of keyhole weld pool showing potential preferential growth directions (b) [193].	85
Figure 2.46. EB weld at 4.2 mm/s on an Fe-15Cr-15Ni single crystal alloy showing columnar dendritic growth in different orientations from Rappaz et al. [123], [193].	86
Figure 2.47. Primary austenite solidification showing dendritic solidification at a 6.5 mm/s travel speed (a) and cellular solidification at a 100 mm/s travel speed (b) [194].	87
Figure 2.48. Reduced cell size for an EB weld (top) cooled at $1.5 \times 10^6$ °C/s and a substrate cooled at $2 \times 10^3$ °C/s (bottom) [195].	88

Figure 2.49. Relationship between solidification time and secondary dendrite arm spacing for 310 stainless steel from Kou and Le [196].	89
Figure 2.50. Pseudo-binary Fe-Cr-Ni phase diagrams from Kou and Le [123], [196] at 55% Fe (a), 63% Fe (b), and 73% Fe (c).	91
Figure 2.51. Solidification growth modes: primary austenite (a), primary austenite with eutectic ferrite (b), a skeletal morphology of primary ferrite with austenite (c), and lathy morphology of primary ferrite with austenite (d) [190].	92
Figure 2.52. WRC-1992 constitution diagram from Kotecki and Siewert based on ferrite number (FN) [206].	94
Figure 2.53. Suutala diagram showing cracking susceptibility for sulfur and phosphorous versus $Cr_{eq}/Ni_{eq}$ contents [204].	95
Figure 2.54. Schematic of dendrite tip temperature versus solidification growth rate in stainless steels with varying $Cr_{eq}/Ni_{eq}$ from Lippold [190].	96
Figure 2.55. Weld solidification crack in the centerline of a SS EB weld [17].	97
Figure 2.56. Pseudo binary phase diagram for the SS alloy compositions analyzed by Elmer et al. [194]. WRC-1992 $Cr_{eq}/Ni_{eq}$ are as follows: Alloy 1–1.15, Alloy 2–1.39, Alloy 3–1.51, Alloy 4–1.60, Alloy 5–1.84, Alloy 6–2.01, and Alloy 7–2.18.	98
Figure 2.57. Electron beam weld microstructures at 25 mm/s for WRC-1992 $Cr_{eq}/Ni_{eq}$ of 1.39 (a) and 1.60 (b). Extracted from Elmer et al. [194].	98
Figure 2.58. Electron beam weld microstructures for a 2.01 WRC-1992 $Cr_{eq}/Ni_{eq}$ alloy welded at 500 mm/s (a) and 25 mm/s (b). Extracted from Elmer et al. [194].	99
Figure 2.59. Microstructural map produced from EBW stainless steel alloys from Elmer et al. [194]. Figure extracted from Kou [123].	99
Figure 2.60. Microstructural map for pulsed laser welded austenitic stainless steels. Extracted from Lippold [190].	100
Figure 2.61. Modified Suutala diagram (a) and a further modified Suutala diagram using Hammar and Svensson equivalencies (b) [190], [214]. Solid symbols indicating cracking and open symbols indicate no cracking.	102
Figure 2.62. Laser weld microstructures in a duplex stainless steel (a) and a super duplex stainless steel (b) from Taban and Kaluc [218].	103
Figure 2.63. Austenite phase fraction versus cooling rate from Sieurin and Sandström [217].	103
Figure 2.64. Ti-6Al-4V pulsed-LBW microstructures reported as increasing beta grain size with increasing average power: a) 474W, b) 543W, c) 555W [136].	105

Figure 2.65. Macrophotos for Ti-6Al-4V pulsed-LB welds in atmosphere with what appears to be adequate inert gas shielding (a) and inadequate shielding (b) [136]. .....	106
Figure 2.66. Optical micrographs of EB fusion zones in Ti-6Al-4V from Lu et al. [224]. .....	106
Figure 2.67. TEM images of Ti-6Al-4V laser weld microstructures from Kumar and Sinha [227]. A heat input of $\approx 55$ J (a) and a heat input of $\approx 105$ J (b). .....	108
Figure 2.68. TEM micrograph of laser weld microstructures (a) and optical micrograph (b). Extracted from Xu et al. [228] where they reported retained beta between $\alpha$ laths. ....	108
Figure 4.1. Measured intensity shown as power density ( $\text{kW}/\text{mm}^2$ ) for 1600 W of power. Beam waist or Plane 11 with a 608 $\mu\text{m}$ D2M beam diameter (a,b). Below beam waist by 1.47 mm or Plane 10 with a 614 $\mu\text{m}$ D2M beam diameter (c,d). .....	112
Figure 4.2. Three-dimensional beam caustic with solid arrow indicating the location of the beam axis projected onto the plate surface during welding and the dashed arrow representing the smallest measured D2M diameter: (a) 1400 W, (b) 1600 W. Note: The color scales are not the same between 1400 W (a) and 1600 W (b). .....	113
Figure 4.3. Schematic of ICI system scanning across the keyhole. ....	115
Figure 4.4. Schematic of the ICI beam scan progression from the start of the weld (left) to the end of the weld (right) across the keyhole. ....	115
Figure 4.5. Schematic (a) and photograph (b) showing the decanting nozzle (left) positioned in on the leading edge with the shielding nozzle (right) trailing the weld pool. ....	116
Figure 4.6. Schematic showing the architecture of the neural networks for penetration and transverse cross-section area predictions. ....	118
Figure 4.7. Schematic of FEI Apreo in-lens (T1 and T2) and in-column (T3) BSE detectors. ....	121
Figure 5.1. Measurements of transverse weld features showing a manually traced weld macrograph and the extracted features. ....	125
Figure 5.2. Constant power 304L laser weld macrosections at 1600 W and travel speeds of 25 mm/s (a), 50 mm/s (b), and 100 mm/s (c). ....	126
Figure 5.3. Constant travel speed 304L laser weld macrosections at 50 mm/s and powers of 1200 W (a), 2000 W (b), and 2400 W (c). ....	126
Figure 5.4. Constant power Ti-6Al-4V laser weld macrosections at 1600 W and travel speeds of 25 mm/s (a), 50 mm/s (b), and 100 mm/s (c). ....	126
Figure 5.5. Constant travel speed Ti-6Al-4V laser weld macrosections at 50 mm/s and powers of 1200 W (a), 2000 W (b), and 2400 W (c). ....	126

Figure 5.6. Penetration versus power at travel speeds ranging from 5 to 150 mm/s for 304L SS (a) and Ti-6Al-4V (b). The change between keyhole (deep penetration) and a transition into conduction mode welding is shown as the shaded region. ....	127
Figure 5.7. Macrophoto of the weld surface for Ti-6Al-4V (a) and the M58 SS alloy (b) welded at 800 W and 5 mm/s. A corresponding longitudinal section of Ti-6Al-4V showing the oscillation of root penetration and surface ripples (c). The dashed, red lines represent the weld surface (top) and fusion boundary (bottom). The dotted line is an estimation of the front wall angle. The travel direction is from left to right in all photos. ....	130
Figure 5.8. Weld toe width versus power at travel speeds ranging from 5 to 150 mm/s for 304L (a) and Ti-6Al-4V (b). ....	131
Figure 5.9. Weld centroid width versus power at travel speeds ranging from 5 to 150 mm/s for 304L (a) and Ti-6Al-4V (b). ....	132
Figure 5.10. Transverse cross-section area versus power at travel speeds ranging from 5 to 150 mm/s for 304L (a) and Ti-6Al-4V (b). ....	133
Figure 5.11. Melting efficiency [ $\text{mm}^3/\text{J}$ ] versus power at travel speeds ranging from 5 to 150 mm/s for 304L (a) and Ti-6Al-4V (b). ....	133
Figure 5.12. Schematic showing a potential utilization of the ICI system to capture the transition between conduction and keyhole mode welding. ....	135
Figure 5.13. ICI keyhole tracking scans on 304L SS at 1600 W and 25 mm/s (a) and 50 mm/s (b). The crosshairs represent the process beam center, the circle represents the process beam diameter, and the white represents no data. ....	136
Figure 5.14. ICI keyhole tracking scans at 1000 W and 10 mm/s (a), 25 mm/s (b), and 50 mm/s (c). The weld travel direction is left to right. The solid, black line represents the process beam center, and the dotted, red line (red) represents the process beam diameter. ....	136
Figure 5.15. Keyhole lag for 304L SS, 2205 DSS, and Ti-6Al-4V at a beam diameter of 600 $\mu\text{m}$ and a constant power of 1600 W. ....	137
Figure 5.16. Keyhole lag for 304L SS, 2205 DSS, and Ti-6Al-4V at a beam diameter of 600 $\mu\text{m}$ and a constant travel speed of 50 mm/s. ....	138
Figure 5.17. Surface fit ICI data from 304L SS at 1000 W and 10 mm/s (a), 25 mm/s (b), and 50 mm/s (c). ....	139
Figure 5.18. Change in keyhole volume for 304L SS, 2205 DSS, and Ti-6Al-4V at 1600 W and varying travel speeds (a) and 50 mm/s and varying power (b). ....	141
Figure 5.19. Change in keyhole diameter for 304L SS, 2205 DSS, and Ti-6Al-4V at 1600 W and varying travel speeds (a) and 50 mm/s and varying power (b). ....	142

Figure 5.20. Welds produced at 800 W showing low depth-to-width aspect ratios but maintaining keyholes as confirmed through ICI analysis: 5 mm/s (a) and 25 mm/s (b).	144
Figure 5.21. Schematic representation of weld pool decanting using an instantaneous jet of compressed gas to expel the liquid. ....	145
Figure 5.22. Surface photographs of the decanted weld pools for 304L SS at 1000 W and 5 mm/s (a), 10 mm/s (b), and 25 mm/s (c). The weld travel direction is from left-to-right, and the dashed line shows the approximate region of the decanted weld pool. The expelled and oxidized liquid covers the weld surface on the left. ....	146
Figure 5.23. Surface fit of the 304L SS decanted weld pools at 1000 W and 5 mm/s (a), 10 mm/s (b), and 25 mm/s (c). Travel is in the positive x-direction. Note: The images contain different z-axes and colorbar scales. ....	147
Figure 5.24. Neural network algorithm penetration results for 304L SS at 1600 W.....	152
Figure 5.25. Neural network algorithm penetration results for Ti-6Al-4V at 1600 W...	152
Figure 5.26. Illustration of overfitting penetration data using a single hidden layer with ten nodes for the feedforward ANN.....	153
Figure 5.27. Illustration of underfitting data using a single hidden layer with three nodes for the feedforward ANN.....	154
Figure 5.28. Previous microstructural map from Lippold [190] with vertical lines added showing the Cr/Ni equivalencies investigated in this study. The horizontal, dashed lines represent the range of travel speeds utilized. ....	156
Figure 5.29. 304L SS weld termination photographs, 1000 W of power at a) 5 mm/s, b) 50 mm/s.....	157
Figure 5.30. 304L SS weld end photographs. 1600 W of power at a) 50 mm/s, b) 100 mm/s.....	157
Figure 5.31. Longitudinal weld sections at 50 mm/s, a) 1000 W and b) 1600 W. Longitudinal micrographs are from stitched photos originally captured at 50X. ....	158
Figure 5.32. Schematic showing angles of the solid-liquid interface from a longitudinal weld termination cross-section. 1000 W, 5 mm/s (left) and 50 mm/s (right). The travel velocity is designated as $v_t$ , and the solidification velocity is designated as $v_s$ .....	159
Figure 5.33. Schematic showing angles of the solid-liquid interface from a longitudinal weld termination cross-section. 1600 W, 50 mm/s (left) and 100 mm/s (right). The travel velocity is designated as $v_t$ , and the solidification velocity is designated as $v_s$ .....	160
Figure 5.34. Schematic showing locations of optical micrographs and EBSD scans for each weld parameter. ....	161

Figure 5.35. Laser weld optical micrographs (left) and matching EBSD phase fractions (right) at 1000 W of power and a 5 mm/s travel speed: 304L (a), M58 (b), and M45 (c). For the EBSD images, red/dark is austenite and green/light is ferrite.....	162
Figure 5.36. Laser weld optical micrographs (left) and matching EBSD phase fractions (right) at 1000 W of power and a 5 mm/s travel speed: M53 (a), M54 (b), and 2205 DSS (c). For the EBSD images, red/dark is austenite and green/light is ferrite. ....	163
Figure 5.37. Laser weld optical micrographs (left) and matching EBSD phase fractions (right) at 1000 W of power and a 50 mm/s travel speed: 304L (a), M58 (b), and M45 (c). For the EBSD images, red/dark is austenite and green/light is ferrite.....	165
Figure 5.38. Laser weld optical micrographs (left) and matching EBSD phase fractions (right) at 1000 W of power and a 50 mm/s travel speed: M53 (a), M54 (b), and 2205 DSS (c). For the EBSD images, red/dark is austenite and green/light is ferrite. ....	166
Figure 5.39. Laser weld optical micrographs (left) and matching EBSD phase fractions (right) at 1600 W of power and a 50 mm/s travel speed: 304L (a), M58 (b), and M45 (c). For the EBSD images, red/dark is austenite and green/light is ferrite.....	168
Figure 5.40. Laser weld optical micrographs (left) and matching EBSD phase fractions (right) at 1600 W of power and a 50 mm/s travel speed: M53 (a), M54 (b), and 2205 DSS (c). For the EBSD images, red/dark is austenite and green/light is ferrite. ....	169
Figure 5.41. Laser weld optical micrographs (left) and matching EBSD phase fractions (right) at 1600 W of power and a 100 mm/s travel speed: 304L (a), M58 (b), and M45 (c). For the EBSD images, red/dark is austenite and green/light is ferrite.....	170
Figure 5.42. Laser weld optical micrographs (left) and matching EBSD phase fractions (right) at 1600 W of power and a 100 mm/s travel speed: M53 (a), M54 (b), and 2205 DSS (c). For the EBSD images, red/dark is austenite and green/light is ferrite. ....	171
Figure 5.43. Ferrite fractions versus WRC-1992 $Cr_{eq}/Ni_{eq}$ at 1000 W (a) and 1600 W (b). ....	173
Figure 5.44. Updated LBW SS microstructural map of travel speed versus WRC-1992 $Cr_{eq}/Ni_{eq}$ with data from References [190], [194].....	174
Figure 5.45. Laser beam weld transverse sections at 1600 W and 50 mm/s (a), 100 mm/s (b), and 150 mm/s (c).....	175
Figure 5.46. Ti-6Al-4V laser beam weld transverse micrographs. Weld parameters were 1600 W and 50 mm/s. Etched using Kroll's etchant for 2 minutes (a) and Keller's etchant for 2 minutes (b).....	176
Figure 5.47. Ti-6Al-4V laser beam weld transverse micrographs. Weld parameters were 1600 W and 50 mm/s. Etched using 2 mL HF, 50 mL HCl, 48 mL H <sub>2</sub> O for ≈20 seconds (a) and 20 mL HF, 40 mL HCl, 40 mL H <sub>2</sub> O for ≈1 minute (b). ....	177

Figure 5.48. Ti-6Al-4V longitudinal cross-sections at 1600 W etched with 20 mL HF, 40 mL HCl, 40 mL H <sub>2</sub> O for $\approx$ 1 minute: 50 mm/s (a), 100 mm/s (b), and 150 mm/s (c).....	178
Figure 5.49. SEM image of the etched fusion zone microstructure showing the fine morphology of the acicular $\alpha'$ martensite. Captured using the Everhart-Thornley detector (ETD) at 1,000X (a) and 10,000X (b).....	179
Figure 5.50. Ti-6Al-4V weld metal microstructure at an $\approx$ 18 mm working distance and 5,000X magnification using the T1 (BSE) detector. The structure appears to consist entirely of high aspect ratio, acicular $\alpha'$ . ....	179
Figure 5.51. EBSD scan locations for the transverse view (left), plan view (center), and longitudinal view (right) sections at each travel speed. ....	181
Figure 5.52. Transverse view of as-scanned EBSD IPF-IQ maps (left) and IPF-IQ maps of the reconstructed parent/beta grains (right), a) 50 mm/sec, b) 100 mm/sec, c) 150 mm/sec. Original magnification at 350X (a) and 500X (b,c). The dashed, white lines represent the fusion boundaries. ....	183
Figure 5.53. Longitudinal view of as-scanned EBSD IPF-IQ maps (left) and IPF-IQ maps of the reconstructed parent/beta grains (right). a) 50 mm/sec, b) 100 mm/sec, c) 150 mm/sec. The travel direction is from left to right. The dashed, white lines represent the fusion boundaries. ....	184
Figure 5.54. Plan view of as-scanned EBSD IPF-IQ maps (left) and IPF-IQ maps of the reconstructed parent/beta grains (right). The travel direction is from left to right. a) 50 mm/sec, b) 100 mm/sec, c) 150 mm/sec. The dashed, white lines represent the weld centerlines. ....	185
Figure 5.55. Transverse view of PBGS distribution at 1600 W with similar colors/shades representing a similar grain size at each condition: 50 mm/s (a), 100 mm/s (b), 150 mm/s (c). The dashed, black lines represent the fusion boundaries. ....	187
Figure 5.56. Longitudinal view of PBGS distribution at 1600 W with similar colors/shades representing a similar grain size at each condition: 50 mm/s (a), 100 mm/s (b), 150 mm/s (c). The grain size analysis at 50 mm/s was only evaluated below the continuous, black line for a closer comparison to 100 and 150 mm/s. The dashed, black line represents the fusion boundary. ....	187
Figure 5.57. PBGS versus travel speed at 1600 W showing the major axis (length) and minor axis (width) for the transverse view orientation (a) and the longitudinal view orientation (b).....	188
Figure 5.58. Plan view of PBGS distribution at 1600 W with similar colors/shades representing a similar grain size at each condition: 50 mm/s (a), 100 mm/s (b), 150 mm/s (c). The dashed, black lines represent the weld centerlines. ....	189
Figure 5.59. PBGS versus travel speed at 1600 W for the plan view orientation. ....	190

Figure A.1. Equilibrium property diagram for 304L SS.....	232
Figure A.2. Equilibrium property diagram for M58. ....	233
Figure A.3. Equilibrium property diagram for M45. ....	233
Figure A.4. Equilibrium property diagram for M53. ....	233
Figure A.5. Equilibrium property diagram for M54. ....	234
Figure A.6. Equilibrium property diagram for 2205 DSS. ....	234
Figure A.7. Scheil solidification simulation of 304L SS (a) and M58 (b).....	235
Figure A.8. Scheil solidification simulation of M53 (a) and M45 (b).....	235
Figure A.9. Scheil solidification simulation of M54 (a) and 2205 DSS (b). ....	236
Figure A.10. Scheil simulations showing solidification conditions for all SS alloys.....	236
Figure A.11. Equilibrium property diagram for Ti-6Al-4V. ....	240
Figure A.12. Equilibrium property diagram for the near commercially pure Ti alloy. ..	240
Figure B.1. Photographs showing the welding setup with the optics attached to a six-axis robot. ....	242
Figure C.1. Measured power reading for each set power. ....	243
Figure C.2. Beam profiles near sharp focus for 800 W (a), 1000 W (b), 1200 W (c), and 1600 W (d). Note: The scales are not comparable between powers. ....	246
Figure C.3. Beam profiles near sharp focus at 2000 W (a) and 2400 W (b). Note: The scales are not comparable between powers. ....	247
Figure C.4. Beam caustics with the color scale representing intensity distributions: 800 W (a) and 1000 W (b). Note: Color scales are not comparable between powers. ....	247
Figure C.5. Beam caustics with the color scale representing intensity distributions for 1200 W (a), 1600 W (b), 2000 W (c), and 2400 W (d). Note: Color scales are not comparable between powers. ....	248
Figure D.1. 304L laser weld surfaces at 800 W and travel speeds of 5 mm/s (a), 10 mm/s (b), 25 mm/s (c), and 50 mm/s (d). ....	249
Figure D.2. 304L laser weld surfaces at 1000 W and travel speeds of 5 mm/s (a), 10 mm/s (b), 25 mm/s (c), and 50 mm/s (d). ....	250
Figure D.3. 304L laser weld surfaces at 1200 W and travel speeds of 5 mm/s (a), 10 mm/s (b), 25 mm/s (c), and 50 mm/s (d). ....	250
Figure D.4. 304L laser weld surfaces at 1600 W and travel speeds of 25 mm/s (a), 50 mm/s (b), 100 mm/s (c), and 150 mm/s (d). ....	251

Figure D.5. 304L laser weld surfaces at 2000 W and travel speeds of 50 mm/s (a), 75 mm/s (b), 100 mm/s (c), and 150 mm/s (d). .....	251
Figure D.6. 304L laser weld surfaces at 2400 W and travel speeds of 50 mm/s (a), 75 mm/s (b), 100 mm/s (c), and 150 mm/s (d). .....	252
Figure D.7. 304L laser weld surface ends at 800 W and travel speeds of 5 mm/s (a), 10 mm/s (b), 25 mm/s (c), and 50 mm/s (d). .....	252
Figure D.8. 304L laser weld surface ends at 1000 W and travel speeds of 5 mm/s (a), 10 mm/s (b), 25 mm/s (c), and 50 mm/s (d). .....	253
Figure D.9. 304L laser weld surface ends at 1200 W and travel speeds of 5 mm/s (a), 10 mm/s (b), 25 mm/s (c), and 50 mm/s (d). .....	253
Figure D.10. 304L laser weld surface ends at 1600 W and travel speeds of 25 mm/s (a), 50 mm/s (b), 100 mm/s (c), and 150 mm/s (d). .....	254
Figure D.11. 304L laser weld surface ends at 2000 W and travel speeds of 50 mm/s (a), 75 mm/s (b), 100 mm/s (c), and 150 mm/s (d). .....	254
Figure D.12. 304L laser weld surface ends at 2400 W and travel speeds of 50 mm/s (a), 75 mm/s (b), 100 mm/s (c), and 150 mm/s (d). .....	255
Figure D.13. 304L laser weld macrosections at 800 W and travel speeds of 5 mm/s (a), 10 mm/s (b), 25 mm/s (c), and 50 mm/s (d). .....	256
Figure D.14. 304L laser weld macrosections at 1000 W and travel speeds of 5 mm/s (a), 10 mm/s (b), 25 mm/s (c), and 50 mm/s (d). .....	256
Figure D.15. 304L laser weld macrosections at 1200 W and travel speeds of 10 mm/s (a), 25 mm/s (b), 50 mm/s (c), and 100 mm/s (d). .....	257
Figure D.16. 304L laser weld macrosections at 1600 W and travel speeds of 25 mm/s (a), 50 mm/s (b), 100 mm/s (c), and 150 mm/s (d). .....	257
Figure D.17. 304L laser weld macrosections at 2000 W and travel speeds of 50 mm/s (a), 75 mm/s (b), 100 mm/s (c), and 150 mm/s (d). .....	258
Figure D.18. 304L laser weld macrosections at 2400 W and travel speeds of 50 mm/s (a), 75 mm/s (b), 100 mm/s (c), and 150 mm/s (d). .....	258
Figure E.1. Penetration (a) and transverse cross-sectional area (b) versus power for 304L. All data except 800 W is from two separate welds.....	259
Figure E.2. Weld toe width (a) and fusion boundary length (b) versus power for 304L stainless steel at varying travel speeds. Only data at 800 W is from a single weld.....	260
Figure E.3. Weld toe width (a) and fusion boundary length (b) versus power for 304L stainless steel at varying travel speeds. Only data at 800 W is from a single weld.....	260

Figure F.1. Ti-6Al-4V laser weld surfaces at 800 W and travel speeds of 5 mm/s (a), 10 mm/s (b), 25 mm/s (c), and 50 mm/s (d). .....	261
Figure F.2. Ti-6Al-4V laser weld surfaces at 1000 W and travel speeds of 5 mm/s (a), 10 mm/s (b), 25 mm/s (c), and 50 mm/s (d). .....	262
Figure F.3. Ti-6Al-4V laser weld surfaces at 1200 W and travel speeds of 25 mm/s (a), 50 mm/s (b), 75 mm/s (c), and 100 mm/s (d). .....	262
Figure F.4. Ti-6Al-4V laser weld surfaces at 1600 W and travel speeds of 25 mm/s (a), 50 mm/s (b), 100 mm/s (c), and 150 mm/s (d). .....	263
Figure F.5. Ti-6Al-4V laser weld surfaces at 2000 W and travel speeds of 50 mm/s (a), 75 mm/s (b), 100 mm/s (c), and 150 mm/s (d). .....	263
Figure F.6. Ti-6Al-4V laser weld surfaces at 2400 W and travel speeds of 50 mm/s (a), 75 mm/s (b), 100 mm/s (c), and 150 mm/s (d). .....	264
Figure F.7. Ti-6Al-4V laser weld surface ends at 800 W and travel speeds of 5 mm/s (a), 10 mm/s (b), 25 mm/s (c), and 50 mm/s (d). .....	264
Figure F.8. Ti-6Al-4V laser weld surface ends at 1000 W and travel speeds of 5 mm/s (a), 10 mm/s (b), 25 mm/s (c), and 50 mm/s (d). .....	265
Figure F.9. Ti-6Al-4V laser weld surface ends at 1200 W and travel speeds of 25 mm/s (a), 50 mm/s (b), 75 mm/s (c), and 100 mm/s (d). .....	265
Figure F.10. Ti-6Al-4V laser weld surface ends at 1600 W and travel speeds of 25 mm/s (a), 50 mm/s (b), 100 mm/s (c), and 150 mm/s (d). .....	266
Figure F.11. Ti-6Al-4V laser weld surface ends at 2000 W and travel speeds of 50 mm/s (a), 75 mm/s (b), 100 mm/s (c), and 150 mm/s (d). .....	266
Figure F.12. Ti-6Al-4V laser weld surface ends at 2400 W and travel speeds of 50 mm/s (a), 75 mm/s (b), 100 mm/s (c), and 150 mm/s (d). .....	267
Figure F.13. Ti-6Al-4V laser weld macrosections at 800 W and travel speeds of 5 mm/s (a), 10 mm/s (b), 25 mm/s (c), and 50 mm/s (d). .....	268
Figure F.14. Ti-6Al-4V laser weld macrosections at 1000 W and travel speeds of 5 mm/s (a), 10 mm/s (b), 25 mm/s (c), and 50 mm/s (d). .....	268
Figure F.15. Ti-6Al-4V laser weld macrosections at 1200 W and travel speeds of 25 mm/s (a), 50 mm/s (b), 75 mm/s (c), and 100 mm/s (d). .....	269
Figure F.16. Ti-6Al-4V laser weld macrosections at 1600 W and travel speeds of 25 mm/s (a), 50 mm/s (b), 75 mm/s (c), and 100 mm/s (d). .....	269
Figure F.17. Ti-6Al-4V laser weld macrosections at 2000 W and travel speeds of 50 mm/s (a), 75 mm/s (b), 100 mm/s (c), and 150 mm/s (d). .....	270

Figure F.18. Ti-6Al-4V laser weld macrosections at 2400 W and travel speeds of 50 mm/s (a), 75 mm/s (b), 100 mm/s (c), and 150 mm/s (d). .....	270
Figure G.1. Penetration (a) and transverse cross-sectional area (b) versus power for Ti-6Al-4V. All data except 800 W is from two separate welds. ....	271
Figure G.2. Weld toe width (a) and fusion boundary length (b) versus power for Ti-6Al-4V. All data except 800 W is from two separate welds. ....	272
Figure G.3. Full-width-half-maximum (FWHM) weld width (a) and centroid weld width (b) versus power for Ti-6Al-4V. All data except 800 W is from two separate welds. ....	272
Figure H.1. Penetration (a) and cross-sectional area (b) versus power at 50 mm/s for all SS alloys. ....	273
Figure H.2. Full-width-half-maximum (FWHM) weld width (a) and weld centroid width (b) versus power at 50 mm/s for all SS alloys. ....	274
Figure H.3. Weld toe width (a) and fusion boundary length (b) versus power at 50 mm/s for all SS alloys. ....	274
Figure I.1. Graphical user interface for the NN algorithm. ....	275
Figure I.2. ANN algorithm predicted penetration results for 304L SS at 1000 W (a), 1200 W (b), 1600 W (c), 2000 W (d), 2200 W (e), and 2400 W (f). ....	276
Figure I.3. ANN algorithm predicted penetration results for Ti-6Al-4V at 1000 W (a), 1200 W (b), 1600 W (c), 2000 W (d), 2200 W (e), and 2400 W (f). ....	277
Figure I.4. ANN algorithm predicted toe width results for 304L SS at 1000 W (a), 1200 W (b), 1600 W (c), 2000 W (d), 2200 W (e), and 2400 W (f). ....	278
Figure I.5. ANN algorithm predicted toe width results for Ti-6Al-4V at 1000 W (a), 1200 W (b), 1600 W (c), 2000 W (d), 2200 W (e), and 2400 W (f). ....	279
Figure I.6. ANN algorithm predicted centroid width results for 304L SS at 1000 W (a), 1200 W (b), 1600 W (c), 2000 W (d), 2200 W (e), and 2400 W (f). ....	280
Figure I.7. ANN algorithm predicted centroid width results for Ti-6Al-4V at 1000 W (a), 1200 W (b), 1600 W (c), 2000 W (d), and 2400 W (e). ....	281
Figure J.1. Ti-6Al-4V LB weld etched with Kroll's (2 mL HF, 4 mL HNO <sub>3</sub> , 94 mL H <sub>2</sub> O). Immersed for ≈20 seconds: a) 100X, b) 200X. ....	282
Figure J.2. Ti-6Al-4V LB weld etched with Kroll's Etch (2 mL HF, 4 mL HNO <sub>3</sub> , 94 mL H <sub>2</sub> O). Immersed for ≈2 minutes: a) 100X, b) 200X. ....	283
Figure J.3. Ti-6Al-4V LB weld etched with Keller's (2 mL HF, 3mL HCl, 5 mL HNO <sub>3</sub> , 190 mL H <sub>2</sub> O). Immersed for ≈1 minute: a) 100X, b) 200X. ....	283
Figure J.4. Ti-6Al-4V LB weld etched with Keller's Etch (2 mL HF, 3mL HCl, 5 mL HNO <sub>3</sub> , 190 mL H <sub>2</sub> O). Immersed for ≈2 minutes: a) 100X, b) 200X. ....	284

Figure J.5. Ti-6Al-4V LB weld etched with 2 mL HF – 10 mL 30% H <sub>2</sub> O <sub>2</sub> – 88 mL H <sub>2</sub> O. Immersed for ≈20 seconds: a) 100X, b) 200X.....	284
Figure J.6. Ti-6Al-4V LB weld etched with 2 mL HF – 10 mL 30% H <sub>2</sub> O <sub>2</sub> – 88 mL H <sub>2</sub> O. Immersed for ≈2 minutes: a) 100 X, b) 200X.....	285
Figure J.7. Ti-6Al-4V LB weld etched with 2 mL HF – 10 mL 30% H <sub>2</sub> O <sub>2</sub> – 10 mL HCl – 88 mL H <sub>2</sub> O. Immersed for ≈2 minutes: a) 100X, b) 200X. ....	285
Figure J.8. Ti-6Al-4V LB weld etched with 3 mL HF – 30 mL HNO <sub>3</sub> – 10 mL HCl – 88 mL H <sub>2</sub> O. Immersed for ≈20 seconds: a) 100X, b) 200X. ....	286
Figure J.9. Ti-6Al-4V LB weld etched with 10 mL HF – 15 mL HNO <sub>3</sub> – 75 mL H <sub>2</sub> O. Immersed for ≈20 seconds: a) 100X, b) 200X.....	286
Figure J.10. Ti-6Al-4V LB weld etched with 10 mL HF – 15 mL HNO <sub>3</sub> – 75 mL H <sub>2</sub> O. Immersed for ≈20 seconds. Darkfield photomicrographs: a) 100X, b) 200X. ....	287
Figure J.11. Ti-6Al-4V LB weld etched with 2 mL HF – 50 mL HCl – 48 mL H <sub>2</sub> O. Immersed for ≈20 seconds: a) 100X, b) 200X.....	287
Figure J.12. Ti-6Al-4V LB weld etched with 10 mL HF – 40 mL HCl – 50 mL H <sub>2</sub> O. Immersed for ≈1 minute: a) 100X, b) 200X. ....	288
Figure J.13. Ti-6Al-4V LB weld etched with 20 mL HF – 40 mL HCl – 50 mL H <sub>2</sub> O. Immersed for ≈1 minute: a) 100X, b) 200X. ....	288
Figure J.14. Ti-6Al-4V LB weld etched with 20 mL HF – 40 mL HCl – 40 mL H <sub>2</sub> O. Immersed for ≈5 minutes: a) 100X, b) 200X.....	289
Figure J.15. Ti-6Al-4V LB weld etched with 50 mL 10% oxalic – 2 mL HF – 48 mL H <sub>2</sub> O. Immersed for ≈20 seconds: a) 100X, b) 200X.....	289
Figure J.16. Ti-6Al-4V LB weld etched with 30 mL glycerin – 10 mL HF – 10 mL HNO <sub>3</sub> . Swabbed for ≈20 seconds: a) 100X, b) 200X. ....	290
Figure J.17. Ti-6Al-4V LB weld etched with boiling 4 mL HCl – 1 mL H <sub>2</sub> SO <sub>4</sub> – 95 mL H <sub>2</sub> O. Immersed for ≈2 minutes: a) 100X, b) 200X.....	290
Figure J.18. Ti-6Al-4V LB weld etched with boiling 50 mL 10% oxalic – 50 mL 40% KHO. Immersed for ≈1 minute: a) 100X, b) 200X.....	291
Figure J.19. Ti-6Al-4V LB weld heat treated by placing in 900°C furnace for 1 minute and free cooled. Kroll's etch. Immersed for ≈20 seconds: a) 100X, b) 200X .....	292
Figure J.20. Ti-6Al-4V LB weld heat treated by placing in 900°C furnace for 1 minute and free cooled. Kroll's etch. Immersed for ≈1 minute: a) 100X, b) 200X.....	292
Figure J.21. Ti-6Al-4V LB weld heat treated by placing in 900°C furnace for 5 minutes and free cooled. Kroll's etch. Immersed for ≈20 seconds: a) 100X, b) 200X .....	293

Figure J.22. Ti-6Al-4V LB weld heat treated by placing in 900°C furnace for 5 minutes and free cooled. Kroll's etch. Immersed for ≈1 minute: a) 100X, b) 200X.....	293
Figure J.23. Ti-6Al-4V LB weld heat treated by placing in 900°C furnace for 10 minutes and free cooled. Kroll's etch. Immersed for ≈20 seconds: a) 100X, b) 200X .....	294
Figure J.24. Ti-6Al-4V LB weld heat treated by placing in 900°C furnace for 10 minutes and free cooled. Kroll's etch. Immersed for ≈1 minute: a) 100X, b) 200X.....	294
Figure J.25. Ti-6Al-4V base metal microstructure. The larger alpha grains appear dark, and the beta grains appear light. ....	295
Figure J.26. Ti-6Al-4V laser weld fusion zone at 1600 W and 50 mm/s. EBSD scan performed at 20°C: a) IPF + IQ map and b) IPF + IQ map of reconstructed parent grains. ....	296
Figure J.27. Ti-6Al-4V laser weld FZ at 1600 W and 50 mm/s. EBSD scan performed at 900°C: a) IPF + IQ map and b) IPF + IQ map of reconstructed parent grains. ....	297
Figure J.28. Ti-6Al-4V laser weld metal at 1600 W and 50 mm/s. EBSD scan performed at 900°C: a) Image from ETD detector using SE imaging mode after cooling from 900°C, b) IPF + IQ map and c) IPF + IQ map of reconstructed parent grains. ....	298
Figure J.29. Pure titanium base material (a). Commercially pure titanium laser weld (b). Kroll's etch. Immersed for ≈10 seconds: a) 200X, b) 100X.....	299
Figure J.30. Pure titanium laser weld microstructure. Kroll's etch. Immersed for ≈10 seconds: a) 100X, b) 200X.....	299
Figure P.1. Laser (left) and gas tungsten arc weld (right) comparison micrographs at 1000 W of power and a 5 mm/s travel speed: 304L (a) and M58 (b).....	396
Figure P.2. Laser (left) and gas tungsten arc weld (right) comparison micrographs at 1000 W of power and a 5 mm/s travel speed: M45 (a), M53 (b), and M54 (c).....	397
Figure P.3. Laser (left) and gas tungsten arc weld (right) comparison micrographs at 1000 W of power and a 5 mm/s travel speed for 2205 DSS.....	398

## Abbreviations and Symbols

ANN – artificial neural network  
BSE – backscattered electrons  
BCC – body centered cubic  
CTE – coefficient of thermal expansion  
CW – continuous wave  
DIC – differential image contrast  
DCEN – direct current electrode negative  
D2M – second moment beam diameter measurement  
D86 – eighty six percent beam diameter measurement  
EB – electron beam  
ED – energy density  
EBW – electron beam welding  
EBSD – electron backscattered diffraction  
eSEM – environmental scanning electron microscope  
ETD – Everhart-Thornley detector  
FCC – face centered cubic  
FFT – fast Fourier transform  
FN – ferrite number  
FZ – fusion zone  
GTA – gas tungsten arc  
GTAW – gas tungsten arc welding  
HAZ – heat affected zone  
HCP – hexagonal close packed  
HI – heat input  
ICI – inline coherent imaging  
IPF – inverse pole figure  
IQ – image quality  
LB – laser beam  
LBW – laser beam welding  
LDD<sup>TM</sup> – Laser Depth Dynamics<sup>TM</sup>  
NN – neural network  
NPAR<sup>TM</sup> – Neighbor Pattern Averaging & Reindexing  
OIM – orientation imaging microscopy  
OCT – optical coherence tomography  
PBG – prior beta grain  
PBGs – prior beta grains  
PBGB – prior beta grain boundary  
PBGBs – prior beta grain boundaries  
PBGS – prior beta grain size

PBGSs – prior beta grain sizes  
 P-LBW – pulsed laser beam welding  
 SE – secondary electron  
 SEM – scanning electron microscope  
 SLD – superluminescent diode  
 SPE – specific point energy  
 SS – stainless steel  
 STR – solidification temperature range  
 TEM – transmission electron microscope  
 TEM<sub>xy</sub> – transverse electromagnetic mode of a propagating laser beam  
 T1 – in-lens SEM BSE detector  
 WRC – Welding Research Council  
 1D – one-dimensional  
 2D – two-dimensional  
 3D – three-dimensional

### ***Variable/Material Properties***

$A_w$  = transverse cross-sectional area of weld – [mm<sup>2</sup>]  
 $b$  = bias for neural network – [unitless]  
 $C_0$  = nominal solute composition – [wt%]  
 $C_L$  = nominal solute composition – [wt%]  
 $C_p$  = specific heat – [J · kg<sup>-1</sup>K<sup>-1</sup>]  
 $C_s$  = nominal solute composition – [wt%]  
 $CTE$  = coefficient of thermal expansion – [°C<sup>-1</sup>]  
 $CTE_L$  = coefficient of thermal expansion of liquid – [°C<sup>-1</sup>]  
 $CTE_s$  = coefficient of thermal expansion of solid – [°C<sup>-1</sup>]  
 $d_b$  = diameter of laser or electron beam – [μm]  
 $d_p$  = depth of penetration – [mm]  
 $D_L$  = diffusion coefficient of solute in liquid – [mm<sup>2</sup> · s<sup>-1</sup>]  
 $D_s$  = diffusion coefficient of solute in solid – [mm<sup>2</sup> · s<sup>-1</sup>]  
 $E_d$  = energy density – [J · mm<sup>-2</sup>]  
 $G$  = Gibbs free energy – [J · mm<sup>-1</sup>]  
 $G_L$  = thermal gradient – [°C · mm<sup>-1</sup>]  
 $H$  = enthalpy – [J · kg<sup>-1</sup>]  
 $H_m$  = enthalpy at melting – [J · kg<sup>-1</sup>]  
 $H_v$  = enthalpy at vaporization – [J · kg<sup>-1</sup>]  
 $I_t$  = transmitted intensity – [W · mm<sup>-2</sup>]  
 $I_0$  = incident intensity – [W · mm<sup>-2</sup>]  
 $k$  = partition coefficient – [unitless]

$L$  = characteristic length – [mm]  
 $L_m$  = latent heat of melting – [ $J \cdot kg^{-1}$ ]  
 $L_v$  = latent heat of vaporization – [ $J \cdot kg^{-1}$ ]  
 $m_L$  = slope of liquids line – [ $^{\circ}C \cdot wt\%^{-1}$ ]  
 $n$  = index of refraction – [unitless]  
 $P$  = total power – [W]  
 $P_i$  = power absorbed – [W]  
 $P_d$  = power density – [ $W \cdot mm^{-2}$ ]  
 $P_e$  = Peclet number – [unitless]  
 $P_r$  = Prandtl number – [unitless]  
 $R$  = Reynolds number – [unitless]  
 $R_L$  = solidification rate of liquid – [ $mm \cdot s^{-1}$ ]  
 $S$  = entropy – [ $J \cdot kg^{-1}$ ]  
 $T_0$  = initial temperature – [K or  $^{\circ}C$ ]  
 $t_i$  = interaction time – [s]  
 $T_L$  = liquidus temperature – [K or  $^{\circ}C$ ]  
 $T_m$  = melting temperature – [K or  $^{\circ}C$ ]  
 $T_s$  = solidus temperature – [K or  $^{\circ}C$ ]  
 $T_v$  = vaporization temperature – [K or  $^{\circ}C$ ]  
 $v_b$  = weld (beam) velocity – [ $mm \cdot s^{-1}$ ]  
 $w$  = weight for neural network – [unitless]  
 $w_w$  = weld width – [mm]  
 $x$  = length or position – [mm]  
 $\alpha$  = thermal diffusivity – [ $m^2 \cdot s^{-1}$ ]  
 $\alpha_{ext}$  = attenuation coefficient – [ $mm^{-1}$ ]  
 $\kappa$  = thermal conductivity – [ $W \cdot m^{-1}K^{-1}$ ]  
 $\kappa_L$  = thermal conductivity of liquid – [ $W \cdot m^{-1}K^{-1}$ ]  
 $\kappa_s$  = thermal conductivity of solid – [ $W \cdot m^{-1}K^{-1}$ ]  
 $\lambda_1$  = primary dendrite arm spacing – [ $\mu m$ ]  
 $\lambda_2$  = secondary dendrite arm spacing – [ $\mu m$ ]  
 $\rho$  = density – [ $kg \cdot m^{-3}$ ]  
 $\rho_L$  = density of liquid – [ $kg \cdot m^{-3}$ ]  
 $\rho_s$  = density of solid – [ $kg \cdot m^{-3}$ ]  
 $\sigma$  = half-width of Gaussian beam (radius) – [ $\mu m$ ]  
 $\eta$  = heat transfer efficiency – [unitless]  
 $\eta_m$  = melting efficiency – [unitless]  
 $\mu$  = dynamic viscosity – [ $Pa \cdot s, kg \cdot m^{-1}s^{-1}$ ]  
 $\nu$  = kinematic viscosity – [ $St, m^2 \cdot s^{-1}$ ]

### ***Unit Abbreviations***

*A* = amps  
*C* = celcius  
*cP* = centiPoise  
*cSt* = centiStokes  
*cm* = centimeter  
*ft* = feet  
*in* = inch  
*J* = Joule  
*K* = kelvin  
*kg* = kilogram  
*kPa* = kiloPascal  
*ksi* = thousand pounds per square inch  
*lb* = pound  
*l* = liter  
*l/min* = liter per minute  
*m* = meter  
*min* = minute  
*mm* = millimeter  
*mPa* = milliPascal  
*MPa* = megaPascal  
*N* = Newton  
*Pa* = Pascal  
*P* = Poise  
*ppm* = parts per million  
*psi* = pounds per square inch  
*s* = second  
*St* = Stokes  
*V* = volts  
*W* = watts

### ***Microstructure***

*A* = primary austenite solidification  
*AF* = primary austenite, secondary ferrite solidification  
*FA* = primary ferrite, secondary austenite solidification  
*F* = primary ferrite solidification  
*A<sub>m</sub>* = solid state massive austenite transformation microstructure  
*Cr<sub>eq</sub>* = chromium equivalency

$Cr_{eq}/Ni_{eq}$  = chromium equivalency to nickel equivalency ratio

$Ni_{eq}$  = nickel equivalency

$\alpha$  = alpha (hcp) microstructural phase in titanium

$\alpha$  = ferrite (bcc) formed in the solid state in stainless steels

$\alpha'$  = martensitic (distorted hcp) microstructural phase in titanium

$\beta$  = beta (bcc) microstructural phase in titanium

$\delta$  = ferrite (bcc) formed during solidification in stainless steels

$\gamma$  = austenite (fcc) phase in stainless steels

## 1 Introduction

Laser beam welding (LBW) is a fusion welding process that enables high energy to be constricted over a small area to efficiently melt and coalesce materials. Along with electron beam welding (EBW), LBW is a form of high energy density (HED) welding. HED processes are viable for many applications (defense systems, aerospace, medical, automotive, etc.) due to deep penetration, high welding speed, low heat input, narrow heat affected zone (HAZ), and ease of precise control [1]. HED welding can produce penetration depths ( $>60$  mm [2]) at travel speeds higher than most fusion welding processes, thus substantially improving manufacturing productivity and reducing costs [1], [3]. As compared to EBW, LBW has less capital expense and is easily performed under atmospheric conditions with or without shielding gas.

HED welds are commonly performed autogenously and can be altered to have fusion zone geometries that conform to drastically different shapes and aspect ratios as shown in Figure 1.1. Welds are categorized as conduction or “keyhole” mode; keyhole refers to the shape of a transverse section of the fusion zone. Relatively low power densities and/or short interaction times produce conduction mode welds that are loosely recognized as having depth-to-width aspect ratios less than one [1], [4]. Keyhole mode welds have aspect ratios greater than one caused by high power densities and/or long interaction times, which produces vaporization and the ability to transfer energy deeper

into the workpiece. As with the heat source characteristics, the material properties contribute to the variation in weld pool formation and the distinction between conduction mode and keyhole mode.

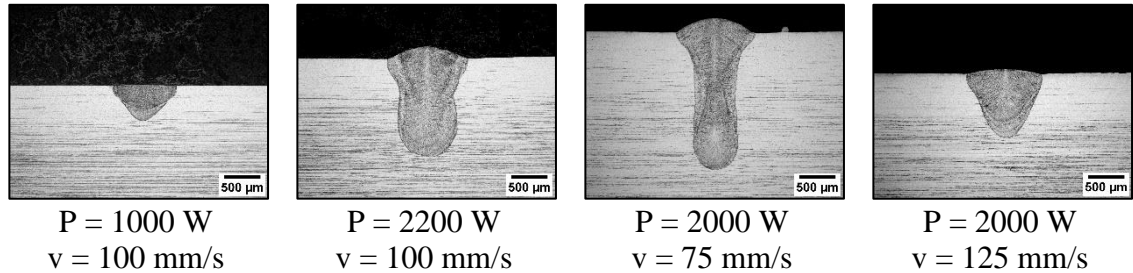


*Figure 1.1. Laser weld geometries produced using different powers and travel speeds at a 500 μm beam diameter on 304L SS.*

The nature of HED processes escalates weldability related concerns regarding process stability, weld penetration, and microstructure formation. During manufacturing processes, it becomes critical to understand how HED weld parameters influence weld formation, particularly in joints that are difficult to evaluate through post-weld inspection techniques. Therefore, the industry has a continuous need to predict resultant weld penetrations based on input parameters and material properties, and this study has a specific interest in laser welding stainless steel alloys and Ti-6Al-4V.

Type 304L stainless steel (SS) and Ti-6Al-4V are two alloys commonly used in aerospace and defense industries. Type 304L SS has intermediate strength, high ductility, high corrosion resistance, and typically good weldability [5]. Ti-6Al-4V has a high strength-to-weight ratio, good toughness, good ductility, good weldability, and high corrosion resistance up to 400°C [6], [7]. These two alloys have different material

properties including crystal structure, melting temperature, vaporization temperature, thermal conductivity, and coefficient of thermal expansion (CTE). The material property variations influence beam-material interactions and alter the resultant weld profile.

Material properties for 304L and Ti-6Al-4V are provided in Appendix A:.

Attempts at predicting HED weld penetration date back to at least 1963 [8], which is nearly as old as HED welding processes. The inability to generate fast and adequate predictions warrants continued interest to better understand how input parameters and material properties function together to create a respective penetration or three-dimensional weld pool geometry. There is considerable information in the open literature explaining beam interactions and weld pool development [9]–[16]; however, the actual physics of the HED processes are extremely complex. The physical properties are temperature dependent, and available databases often only list room temperature values. Using erroneous property values leads to highly inaccurate models. Because of the complexity and inaccuracies, it is difficult to successfully produce an accurate, fully predictive model that determines penetration depth and geometric features.

Microstructure evolution is directly coupled to the fusion zone formation and temperature gradients. Therefore, understanding the shape of the weld pool is imperative to recognizing the microstructural relationships developed from solidification. As previously shown in Figure 1.1, LBW can generate distinct weld cross-sections, with large variability depending on the parameter – material relationships. This is caused by high power density and low linear heat input as compared to other fusion welding

processes [3]. However, the low heat input may result in metallurgical issues through rapid solidification and fast cooling rates. Some of these issues include solidification cracking [17]; martensite formation [7], [18]; low toughness [19]; precipitate formation [5], [20], [21]; and elemental loss [22], [23].

Partial penetration, bead-on-plate laser beam (LB) welds were performed utilizing the latest real-time process monitoring technology, known as inline coherent imaging (ICI). All welds were sectioned to analyze the penetration and transverse section width characteristics. The parameter trends were analyzed and used for model development and penetration prediction analysis. The ICI technique was used to construct profiles of the vapor cavity or weld pool depression. The ICI data obtained from 304L and Ti-6Al-4V was compared for an enhanced understanding of vaporization and keyhole formation.

Due to the difficulty in developing suitable empirical relationships, artificial neural network models were produced to fit the experimental data measured from the transverse cross-section weld profiles. These models predicted penetration, weld widths, and cross-sectional area based on power and travel speed for 304L SS and Ti-6Al-4V.

To augment the microstructural analysis for 304L, welds were performed on SS alloys with chromium equivalent to nickel equivalent ( $Cr_{eq}/Ni_{eq}$ ) compositions varying from 304L SS to a 2205 duplex stainless steel (DSS). Light optical microscopy (LOM) and scanning electron microscopy with electron backscattered diffraction (EBSD) were utilized to determine solidification structures, grain size, and/or resultant phase fractions resulting at different powers and travel speeds. This information aided in both expanding

and “fine-tuning” existing SS microstructural “maps” for better prediction of microstructure development and resultant phase fractions.

This document addresses the background and review of prior literature on fiber lasers, inline coherent imaging, laser welding, physical process interactions, parameter influences pertaining to LBW, metallurgical phenomena associated with SS and Ti-6Al-4V alloys, and modeling efforts to predict LB weld penetration. This is followed by the experimental procedures and discussion of results. The results include weld geometry/penetration analysis, keyhole analysis using inline coherent imaging, predictive modeling, and microstructural analysis.

## **2 Background**

This section contains the necessary background information and literature review pertaining to laser operation, fiber laser development, physics associated with laser/material interaction, ICI, weld formation, and microstructural phenomenon relating to LBW.

### **2.1 Laser Fundamentals**

Light amplification by stimulated emission of radiation (laser) is the process of generating light consisting of photons that have the same phase and wavelength. There are many mechanistic variations to generate a laser beam, but all lasers are an energy conversion device. The transformation can occur from sources of electrical, optical, thermal, chemical, or nuclear energy [1]. The light is generated from the incident energy by exciting the electrons of atoms or molecules. Electrons falling between specific energy levels emit photons with a very narrow band of electromagnetic frequencies (ideally monochromatic) with an in-phase electric field (coherent). A simplified version of laser operation can be disseminated into three components: an active/gain/lasing medium, a pumping source, and an optical cavity/resonator.

The active medium is what generates stimulated emission and contains the elements or ions responsible for producing the desired emission wavelength. Energizing

the atoms increases the energy state of the outer electrons. Under standard conditions, a natural reduction in energy would cause the electron to fall to a lower energy state.

Assuming this electron is excited to a random energy level, this is known as spontaneous emission and produces a photon uncharacteristic of other photons. However, stimulated emission is when atoms or molecules are selectively elevated to specific, higher energy levels. Then, an incoming photon interacts with the excited electron to reduce its energy. This causes emission of a photon that matches the phase, frequency, direction, and polarization of the incident photon [1], [4], [24].

Energizing or “pumping” the lasing medium is necessary to elevate the atoms or molecules of the lasing medium to the higher energy state. For welding, most lasers are pumped via electrical or light energy. For welding sources, light energy is generally produced with flash lamps or laser diodes, and there are advantages of different pumping sources to improve the useable lifetime and optimize absorption of pump light frequencies [24].

Simply pumping the active medium is not sufficient to produce a useful level of output. This requires housing the active medium within some form of optical cavity. The purpose of the optical cavity is to reflect (resonate) laser light across the active medium. This amplifies the laser light based on a positive feedback mechanism to effectively gain the output power. Many variations in optical cavities exist, but the premise for operation is to continually reflect the photons. This is performed using different configurations of parallelly aligned mirrors or Bragg gratings in fiber cavities [25], [26]. Eventually, the

light reflection reaches a threshold where light amplification surpasses losses. Thus, a higher fraction of atoms remain in an excited state for continued emission (net gain  $>1$ ). This higher percentage of atoms in the excited state leads to what is known as population inversion [4] and is a result of the nearly instantaneous process of spontaneous emission, stimulated emission, and amplification [4].

It is the monochromatic, coherent nature of the emitted electromagnetic waves that makes laser beam welding or cutting applications possible. Without these attributes, eliminating chromatic aberration, which is the inability to focus light composed of multiple wavelengths, would not be possible. Therefore, it would not be viable to focus a high-power beam to small diameter spot sizes. With a single wavelength, low beam divergence can be achieved, and power densities greater than  $10^6 \text{ W/cm}^2$  can be produced for LBW and cutting applications [24].

### ***2.1.1 Types of Lasers***

Lasers are traditionally characterized according to the type of active medium. For welding, this is largely limited to high-power gas, “solid-state”, and diode lasers. The most common gas laser utilizes carbon dioxide ( $\text{CO}_2$ ) and has a frequency of  $10.6 \mu\text{m}$ . Solid-state mostly refers to lasers that utilize optical pumping and host an active ion within a crystal or glass [27]. These generally operate near wavelengths of  $1.06 \mu\text{m}$ . Common solid-state lasers include a neodymium doped glass (Nd:glass) or a neodymium doped yttrium aluminum garnet (Nd:YAG). Although, disk and fiber lasers also consist of an ion doped, solid phase active medium but are mechanistically different according to

the host material geometries. Lastly, diode lasers operate based on doped semi-conductor electron-hole pairs; the use of these types of lasers are increasing as technology advancements continue to improve the output beam characteristics.

Various forms of laser beam outputs are possible such as continuous, quasi-continuous, or pulsed mode operation. Continuous wave (CW) operation is via a constant output power, and pulsed operation enables outputs of various energy waveforms defined by a peak power, pulse width, and pulse repetition rate or frequency. For more information on pulsed mode operation, the reader is referred to References [3], [27]. Pulsed laser beam welding (P-LBW) can be advantageous for welding highly reflective, thin, and/or heat sensitive components. This is through minimizing the heat input as compared to continuous wave (CW) LBW, which can also improve mechanical properties through reduced grain growth [28]. However, with a reduced heat input, extreme solidification rates may exacerbate the propensity to undergo solidification cracking [4].

### ***2.1.2 Development and Operation of Fiber Lasers***

An advantage of fiber lasers as opposed to other solid-state or gas lasers is the ability to generate a beam of exceptionally high quality (low beam parameter product) [1]. This allows for high power densities that are conducive for welding processes. Fiber lasers can also be Q-switched and mode locked for ultrashort laser pulse applications [29]; however, this work will only analyze weld results using CW power output. Because this research is

specifically related to fiber lasers, all proceeding laser information is regarding the development and function of fiber laser systems.

### ***2.1.3 History of Fiber Laser Development***

Albert Einstein originally proposed the concept of stimulated emission and absorption of radiation in 1916 [30]. It was not until the 1950s that the theory was converted to application with the development of the MASER or microwave amplification by stimulated emission of radiation [31]. The laser soon followed, and it has been debated as to whether it was originally designed by Charles Townes or Gordon Gould. Townes filed the first patent in 1958 describing the production of infrared radiation [32], [33], and Gould's initial patent application was in 1959 [34]. The late 1950s and 1960s was a significant era for producing fundamental laser technology. The laser technologies developed included gas, crystal, glass rod, diode, and fiber active mediums.

In 1961, Snitzer [35] theorized using a thin glass fiber to transmit a single electromagnetic mode. The first amplification within a fiber lasing medium was originally developed by Snitzer and Koester circa 1964 [36]. This fiber laser was doped with neodymium ( $\text{Nd}^{3+}$ ) ions. Although, excessive beam attenuation within the fiber proved impractical for application. Optical waveguides with acceptable (low) levels of attenuation were eventually developed in 1973 by Keck and Schultz [37]. The rapid evolution of the telecommunications industry boosted the development of optical fibers. A major achievement in fiber lasers was the introduction of double-clad fiber technology

such as that introduced by Snitzer et al. [38], which contained an offset, single mode core contained within a multi-mode pumping fiber. The benefits of this technology included improved coupling efficiency of the pump light and the ability to produce a high intensity, single mode beam [39]. Variations in dopants and pumping methods were continually being developed for fiber lasers, and in 1989 Wyatt [40] reported on an Er-doped fiber laser with over 250 mW of power output.

An improvement in solid-state laser development is attributed to advancements in diode technologies [41], [42]. Diodes selectively pump the dopant near its specific absorption frequencies. This narrow band of light improved solid-state laser efficiency by minimizing wasted heat from chromatic flash lamps. Eventually, diode pumping enabled high-power solid-state lasers to become competitive with high-power CO<sub>2</sub> lasers used in manufacturing processes [42]. The lifetime expectancies of diodes are reported as high as 100,000 hours of operation [43], which is a substantial improvement compared to other pumping sources such as flash lamps.

Gapontsev and Samartsev [44], in 1994, patented side pumping a single mode fiber with multi-mode pump light. By injecting numerous locations along the doped fiber with pump light, substantial power scaling was produced. In 2004, Gapontsev [43] had produced fiber lasers with total powers up to 10 kW. Power was effectively scaled by combining individual, lower power laser modules into a single output fiber, and the first commercially available single mode, 10 kW laser was available in 2009 [45]. Essentially, this is the fundamental design of laser used in this study.

### 2.1.4 Fiber Laser Operation

Fiber laser generation occurs in a flexible, glass silica fiber that is doped with rare earth elements. Rare earth elements ytterbium, erbium, and thorium have minimal attenuation within silica and are suitable dopants in fibers [29], and the ytterbium ion ( $\text{Yb}^{3+}$ ) is a common dopant because it enables efficient energy conversion [4]. The operational wavelength of the  $\text{Yb}^{3+}$  doped fiber is near 1070 nm. Diodes emitting multi-mode beams are a common pumping source and couple the energy into the fiber core or cladding [46].  $\text{Yb}^{3+}$  doped fiber lasers are reported to produce wall-plug efficiencies upwards of 40% or 50% [4], [47]. Figure 2.1 shows a schematic of fiber laser generation with diode side pumping.

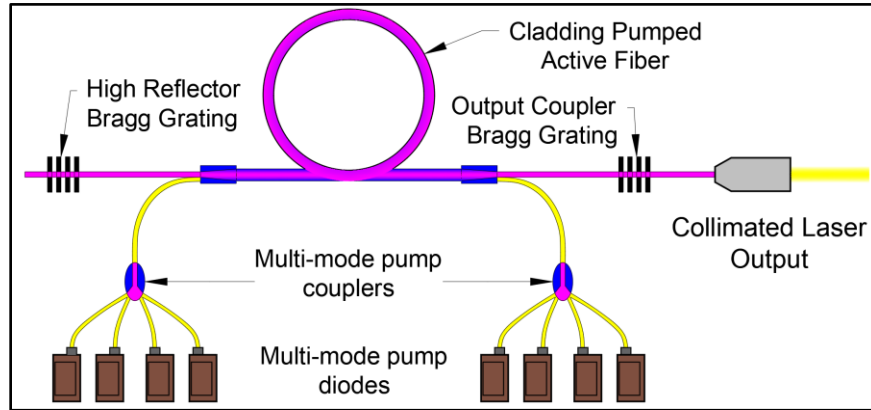


Figure 2.1. Fiber laser operation showing the active medium within a resonator cavity consisting of a Bragg grating and pumped via multi-mode diodes.

Efficiently coupling light into the core is influenced by the core location and geometry, and variations in core geometries and clad layers are used to enhance pump light coupling efficiencies [46]. The resonator consists of a fiber Bragg grating (FBG)

that acts as full or partial reflector [4]. The FBG grating is physically etched into the fiber in a periodic sequence and alters the refractive index. This allows for passing and reflecting specific wavelengths. A single laser module, as previously shown in Figure 2.1, can be combined with other identical modules to continually increase the overall laser output power. This has produced fiber lasers with powers in excess of 100 kW [2].

#### ***2.1.4.1 Beam Delivery***

The transmission fibers and focusing optics influence beam distribution and focus diameter as well as influence process consistency. A silica, fiber optic cable is commonly used to transport the beam from the laser source to the focusing optics. These fibers range in core diameter sizes from approximately 10-1000  $\mu\text{m}$  [4], and are a flexible means of transporting the beam. Small fiber diameters ( $< \approx 50 \mu\text{m}$ ) are used to restrict beam outputs to a single mode operation, which is the fundamental transverse electromagnetic mode ( $\text{TEM}_{00}$ ) or Gaussian intensity distribution.

#### ***2.1.4.2 Reflective and Transmissive Optics***

Transporting, guiding, and focusing a laser requires optics that either transmit or reflect the beam and can be configured in a variety of ways. Transmissive optics must be transparent to the wavelength utilized, and the lenses consist of fused silica or  $\text{CaF}_2$ . Other features include antireflective coatings to mitigate photons from reflecting back into the laser cavity. Reflective optics are composed of mirrors of highly polished copper, molybdenum, or gold to maximize reflectivity and aid in decreased beam attenuation [1].

Reflective optics may be advantageous by mitigating what is commonly referred to as thermal lensing. Thermal lensing [1], [24], [48], [49] is caused by a temperature rise when some fraction of the beam is absorbed into the lens. This results in thermal expansion and distortion, which can cause a shift in the focal position and spot size. A shift in the focal position may result in process instability through a change in the beam diameter. High power and/or long illumination times exacerbate thermal lensing and a focal position shift [48]–[50]. Blecher et al. [49] reported substantial changes to the focal length and beam diameter when welding at 12 kW using transmissive optics. Other research showed beam diameters increasing by over 100  $\mu\text{m}$  at 7 kW of power after 50 seconds of illumination [50]. Utilizing reflective optics allows for easy heat extraction through water cooling and effectively mitigates issues relating to thermal lensing.

### ***2.1.5 Beam Caustics***

The combination of the laser generation, transport fiber, and focusing optics dictate the laser intensity distribution and spot size. Understanding resultant weld formation is not possible without a high degree of certainty regarding the beam distribution at the workpiece surface. Many methods are utilized to determine a beam diameter, but this study utilized a commercially available pinhole device [24], [51]. This device samples a portion of the beam by rotating a copper tip with a small hole ( $\approx 20\ \mu\text{m}$ ) through the beam [51]. The light that enters the hole is reflected to a detector (photodiode) that generates a voltage output and relates it to light intensity.

The optical cavity can produce various transverse electromagnetic modes ( $TEM_{xy}$ ) or standing wave patterns that can be output through the delivery fiber, assuming the delivery fiber has a large enough diameter to propagate multiple modes. If the delivery fiber has a small enough diameter, only a single mode can be transported. This single mode is a Gaussian intensity distribution. Selectively designing this combination of optical cavities, fibers, and optics allows for manipulating the  $TEM_{xy}$  patterns. A common distribution for LBW is “multi-mode” or a “top-hat” distribution. This higher order  $TEM_{xy}$  mode is colloquially known as a “top-hat” distribution because the uniform intensity sharply drops to zero. A comparison of a Gaussian distribution and multi-mode profile is shown in Figure 2.2a and Figure 2.2b respectively.

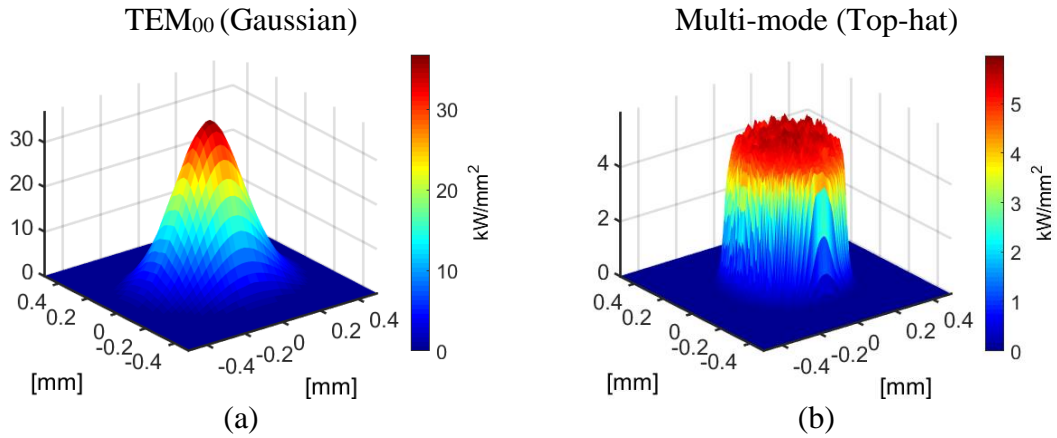


*Figure 2.2. Beam profile comparison between Gaussian and multi-mode distributions at 800 W and a 500  $\mu\text{m}$  beam diameter (D86) [3].*

Both distributions in Figure 2.2 contain nearly the same total power and calculated 86% beam diameter (D86), but the peak intensity varies considerably. Common

computations to quantify beam diameter include full-width-at-half maximum (FWHM),  $1/e^2$ , D86, and second moment (D2M or  $4\sigma$ ) [52], [53]. FWHM is beam diameter measured at half the peak intensity, and the  $1/e^2$  diameter is the distance measured between two points where the intensity reduces by 0.135 ( $1/e^2$ ). D86 is the diameter centered above the centroid where 86% of the total power is contained, and D2M is the second-moment diameter. The D2M diameter is the International Standard Organization (ISO) definition of laser beam diameter [53]. The D2M calculation is an integral of the intensity weighted according to the square of the distance from the centroid. For an ideal Gaussian beam, the  $1/e^2$ , D86, and D2M methods will compute an identical beam diameter. However, complex, non-ideal shapes of propagating beams are not conducive to defining an absolute beam diameter. Variations in TEM modes or beam shapes with nonsymmetrical profiles will produce results that are specific to the computational method utilized. This is evident in the ISO 11146-1 [53] D2M calculation. The square of the radius for a measured point heavily weights the intensity outside of the beam center defined by the centroid. Burgardt and Pierce [52] reported how a non-ideal EB caustic skewed the diameter results for a D2M computation as compared to a D86 computation.

### ***2.1.6 Inline Coherent Imaging***

Numerous methods have been incorporated to provide real-time process analysis during LBW [3]. However, the most practical of those approaches is inline coherent imaging (ICI) based on optical coherence tomography (OCT) and initially developed for monitoring laser processes used in medical applications [54]–[59]. Optical coherence

tomography (OCT) is a measurement technique that utilizes low-coherence interferometry and a broad-band light source. The broad-band light source for the system of interest is produced from a superluminescent diode (SLD). The broad-band light is split into two paths of equal intensity, one referred to as a “sample arm” and the other as the “measurement arm”. The sample arm light is directed towards the measurement object, and the measurement arm directs light through a specific path length. The back scattered light from the sample arm is then recombined with the measurement beam. These superimposed beams are projected onto an interferometer to produce an interferogram, an image of an interference pattern, to determine variations in path lengths based on phase shifts and destructive/constructive interference. This technique is based on Michelson interferometry [59]. Figure 2.3 shows a schematic representation of a system composed of an SLD illumination source, measurement (reference) arm, sample arm, and spectrometer.

Two types of measurement methods exist that include time-domain and spectral-domain, also known as Fourier domain. For time-domain, the reference arm is mechanically positioned during scanning. This leads to slow scan speeds and low sensitivity. In the spectral domain, the reference arm is stationary, and the pattern forming the interferogram is spectrally resolved [60]. This technique is derived from spectral domain optical coherence tomography (SD-OCT) [61].

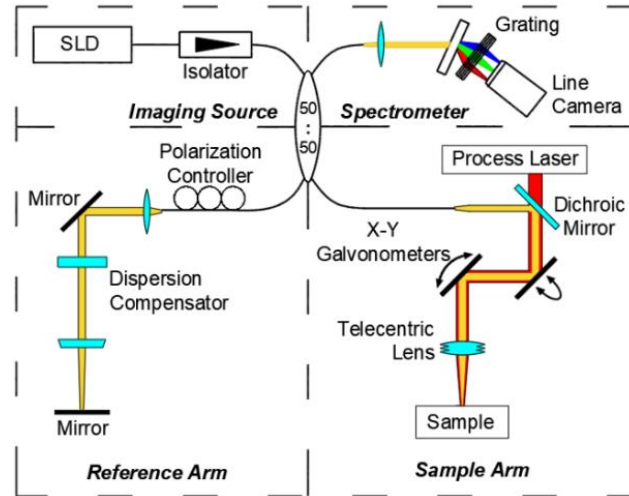


Figure 2.3. Schematic representation of inline coherent imaging system. Recreated from Ji et al. [59].

The inline coherent imaging (ICI) terminology originated from using the OCT technique and projecting the beam coaxially or “inline” with the laser process beam as shown with the dichroic mirror in Figure 2.3. The constructive/destructive interference patterns create “fringes” in the frequency domain, and the spectrometer processes these fringe patterns at nearly real-time. Following Fourier transformation or filtering, data is output as an amplitude or A-line plot comparable to an A-line in ultrasonic testing. A-line plots correspond to amplitude versus position. If time is used instead of position, the plots are referred to as M-mode [56] and were reported as being useful for observing rapidly changing depth profiles. Webster et al. [56], [59], [62] utilized a technique known as homodyne filtering to eliminate the computationally intensive fast Fourier transform (FFT). Bandwidth determines the resolution with resolutions reported as low as 5-10  $\mu\text{m}$

[63], and acquisition rates were reported as high as 300 kHz using CMOS camera technology [56].

The term tomography in OCT suggests that the technique can represent a cross-section through a solid object such as in ultrasonic or x-ray imaging. This is possible in biological tissues where OCT was implemented but is not the case in welding applications where the photons are not transparent to the material. Therefore, it should not be confused with internal imaging. Perhaps this is why Dorsch et al. [64] defined it as optical coherence “topography” in their weld monitoring research. However, ICI imaging has practical potential for monitoring workpiece heights, joint gaps, and weld penetration during deep penetration welding when a vapor depression exists. One aspect of ICI capability is to incorporate feedback control with the LBW process [56], [60], [65], [66].

The ICI system was shown to be successful in monitoring weld penetration when the welding regime is within keyhole mode, but different alloys showed variability in the quality of signals produced. Dorsch et al. [64] evaluated two steel alloys and an aluminum alloy, and Figure 2.4 shows the ICI data points overlayed on longitudinal weld cross-sections. The aluminum alloy showed the greatest noise for detected depth followed by the high-alloyed steel. Yun et al. [67] reported that noise was most likely a result of high fluctuations of the vapor capillary and weld pool dynamics.

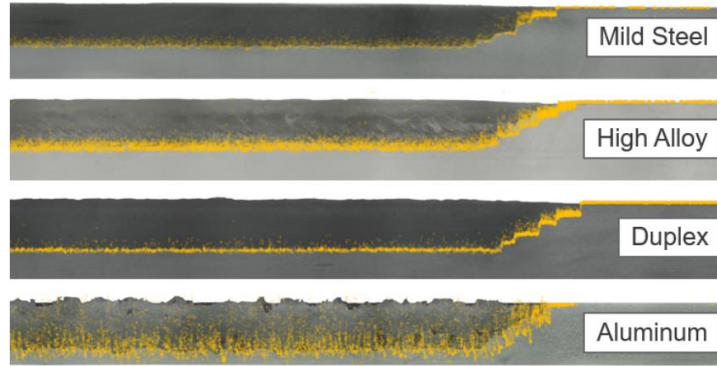


*Figure 2.4. Variation in ICI signal when welding different materials [64].*

Because the ICI system works by reflecting light back from the keyhole wall and measuring optical path length, only conditions producing ideal, straight-line reflections generate a correct depth measurement. Figure 2.5 shows a schematic with ray tracing demonstrating how different keyhole geometries influence the light reflection back to the detector [68]. The first condition (Figure 2.5a) produces a correct measurement based on a direct “line of sight”. However, an incident beam reflecting off the keyhole wall multiple times before returning to the detector would result in a length measurement that is a sum of those reflections. This is shown in Figure 2.5b. Similarly, features on the keyhole wall caused by abnormal geometries or fluctuations during the process will reflect the photons back to the detector and provide false indications of keyhole depth, as in Figure 2.5c. It is also likely that a photon will never return to the detector and become absorbed within the keyhole or exit the keyhole at an angle uncondusive to detection, as shown in Figure 2.5d.

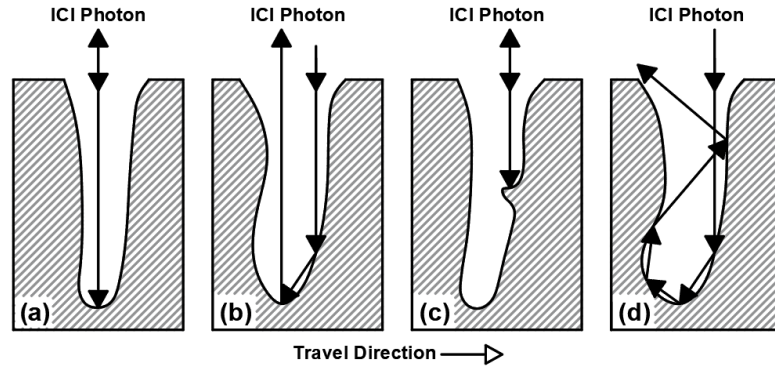


*Figure 2.5. Influence of keyhole geometry on ICI measurements. Recreated and modified from Boley et al. [68].*

Webster et al. [57] reported that ICI was capable of detecting pore formation. Although, this relied on varying power and transitioning between two drastically different penetration depths. However, Boley et al. [68], [69] reported that the region that contained greater noise may coincide with locations of porosity, but ICI is not necessarily sensitive enough to distinguishing pore locations. The issue is mostly represented by the fundamental mechanism depicted in Figure 2.5, and most likely, pore formation may only be indirectly monitored through the detection of keyhole instability.

## 2.2 Weld Formation

HED processes generally operate in what are distinguished as conduction and keyhole mode welding. These two modes determine the depth of penetration and resultant weld profile. Although generally defined as a distinct transition in depth-to-width aspect ratios, such as 1 or 1.5 [1], [4], the actual transition is much more complex and has resulted in researchers reporting a “transition” region with characteristics of both

modes. Figure 2.6 shows a schematic comparing transverse fusion zone sections of conduction, transition, and keyhole mode welds. These welds were produced from autogenous LB welds at a 500  $\mu\text{m}$  beam diameter on 304 SS [3].

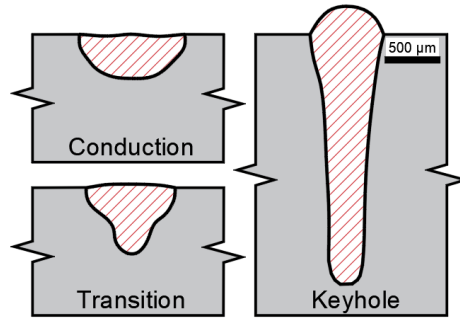


*Figure 2.6. Comparison of conduction, transition, and keyhole mode laser welds on 304 SS at a 500  $\mu\text{m}$  beam diameter [3].*

### **2.2.1 Conduction Mode**

Welds produced in conduction mode are a result of low power density and/or short interaction times (i.e., high travel speed). These welds maintain a transverse shape characteristic of arc welding processes and result in a fusion zone with a low depth-to-width aspect ratio ( $< 1$ ). The heat input to the material surface results in thermal diffusion or conductive heat transfer into the underlying material. The combination of conductive heat loss and fluid flow (weld pool convection) results in the characteristic weld size and shape [70]. It is common to define the shape of the weld based on the Prandtl number ( $P_r$ ) of the material [71]. The equation defining the Prandtl number is provided in Equation 2.1 and is a ratio of the kinematic viscosity over the thermal diffusivity. When the Prandtl

number is low, pool shape becomes dominated by heat conduction and conforms to a spherical geometry. High Prandtl numbers, such as in steel ( $\approx 0.1$ ), generate shallower weld pools that are dominated by surface tension driven fluid flow [71], [72].

$$\text{Equation 2.1: } Pr = \frac{v}{\alpha} = \frac{\mu C_p}{k} \quad [\text{unitless}]$$

Where:  $Pr$  = Prandtl number,  $v$  = kinematic viscosity,  $\alpha$  = thermal diffusivity,  $\mu$  = dynamic viscosity,  $\rho$  = density,  $k$  = thermal conductivity,  $C_p$  = specific heat

Conduction mode welding is advantageous due to a higher probability of producing welds free of defects by avoiding instabilities associated with vaporization. However, penetration is limited in conduction mode welding, and failure to induce a weld pool depression results in low laser coupling and melting efficiencies.

### **2.2.2 Keyhole Mode**

Deep penetration welding, known as keyhole mode, requires simultaneous melting and vaporization. The benefits to keyhole mode include deep penetration, low heat input, higher coupling efficiencies, and narrow heat affected zones [1], [71]. The formation of a vapor capillary requires rapid vaporization that imparts a recoil force to depress the molten weld pool [73], [74]. The power density is high enough that conduction, convection, and radiation heat loss is not adequate at removing heat from the incident beam. The complexity of the solid–fluid–vapor–beam interaction phenomena governing keyhole formation induces transient events [75], [76] between the beam and the weld pool. Instability of the keyhole can be a major issue and lead to root spiking

defects and/or keyhole collapse. The collapse of the vapor cavity then induces pore formation through entrainment of atmospheric air and/or shielding gas that cannot float out prior to solidification. The transient nature also increases the difficulty in fully understanding the mechanisms involved during keyhole mode welding.

### ***2.2.3 Transition Regime***

Ambiguity exists when the weld parameters are such that neither full conduction nor full keyhole mode is exhibited in the resultant weld cross-section. The power density and interaction time is such that conduction mode is present with the onset of vaporization and weld pool depression. Although power densities and aspect ratios are reported to distinguish between keyhole and conduction [77], these numbers are approximations, and the actual weld region is dependent on power, travel speed, beam diameter, and the material under investigation [78]. Figure 2.7 shows results reported by Assunção and Williams [79] with a large range of power densities between their classification of conduction and keyhole mode welding. For 304L (Figure 2.7a), the transition region switched to keyhole mode just above  $3 \text{ kW/mm}^2$ , but the transition to keyhole for aluminum (Figure 2.7b) was not until  $5 \text{ kW/mm}^2$ . The comparison of two materials containing drastically different material properties indicates the necessity in fundamentally understanding the relation of the beam on material properties such as reflectivity, thermal conductivity, melting point, vaporization temperature, enthalpy, etc.

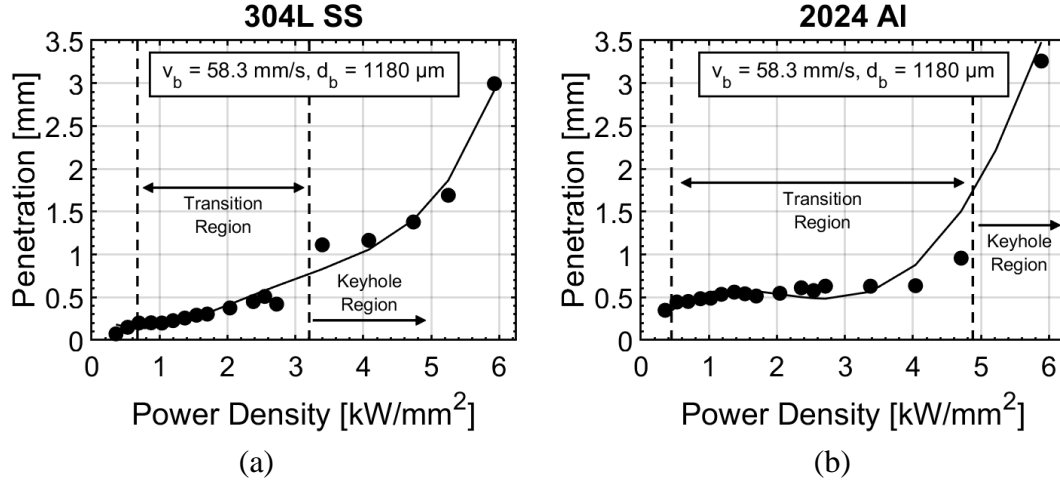


Figure 2.7. Laser beam conduction to keyhole mode transition for: 304L SS (a) and 2024-T3 aluminum (b) reported by Assunção and Williams [79].

An issue regarding LBW is the ability for the workpiece to absorb the light energy, and this drastically changes depending on material, surface preparation, and input parameters. As compared to EBW, the poor energy absorption during LBW requires higher threshold power densities, as large as two orders of magnitude [77], to produce similar weld penetration.

### 2.3 Physical Process Interactions

Weld formation and variability in the welding process can be attributed to the beam interacting with the solid workpiece, liquid, particles within the plume, and if it exists, a plasma. In the steady-state welding condition, the beam first interacts with the vapor plume and then becomes partially absorbed and reflected by the solid and/or liquid where it produces more liquid and/or vaporization. Once the energy is absorbed, convective weld pool currents, heat conduction, vapor pressures, phase transformations, and

metallurgical changes all combine to influence the resultant weld [3]. Figure 2.8 shows an illustration containing the majority of physical phenomenon associated with keyhole LBW.

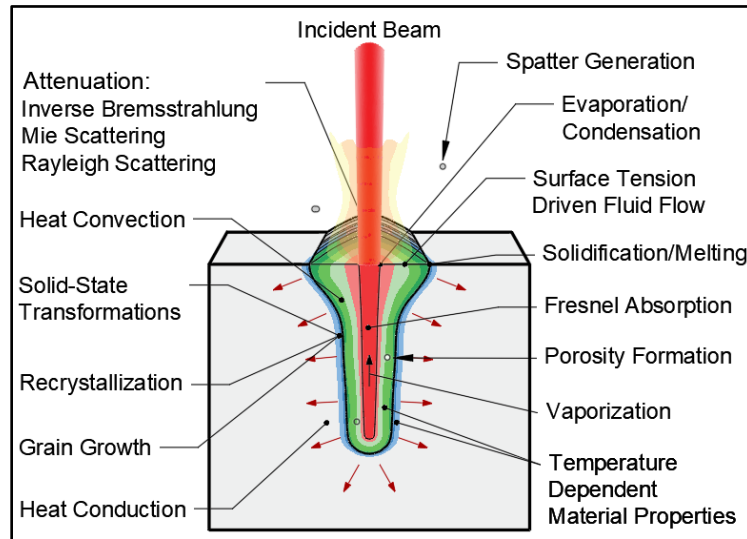


Figure 2.8. Schematic showing physical process considerations during keyhole LBW [3].

The laser beam potentially interacts with all four states of matter (solid, liquid, gas, and plasma). The proportion of the interaction is largely dependent on the process parameters because these parameters influence the fraction of each phase developed. The nature of photon interactions with metals can pose an issue associated with coupling the energy into metallic workpieces. Metal surfaces are inherently reflective, and the reflectivity (absorptivity) can fluctuate greatly depending on the photon wavelength, angle of incident radiation, and surface roughness. Incorporating the incident power into the workpiece is represented by the energy transfer efficiency [80], [81]. The energy

transfer efficiency is represented by the total power absorbed into the material divided by the laser power projected on the material surface as shown in Equation 2.2.

$$\text{Equation 2.2: } \eta = \frac{P_i}{P} \quad [\text{unitless}]$$

Where:  $\eta$  = heat transfer efficiency,  $P_i$  = power absorbed,  $P$  = total power input

The energy transfer efficiency is based on reflection and/or beam attenuation and is different than the melting efficiency (or ratio) [80]. This accounts for the power to melt a volume of material relative to the input power. Ream [82] defined a “melting efficiency” based on the weld cross-sectional area, travel speed, and power as shown in Equation 2.3. However, solely analyzing the transverse cross-section does not consider a variation in three-dimensional weld pool growth.

$$\text{Equation 2.3: } \eta_m = \frac{A_w v_b}{P} \quad [\text{mm}^3/\text{J}]$$

Where:  $\eta_m$  = melting efficiency,  $A_w$  = weld transverse cross-sectional area,  $v_b$  = weld velocity, and  $P$  = total power input

The following subsections review the fundamental physics associated with material interactions and is provided as an overview to understand the complexity of LBW physics that are necessary to produce a truly predictive weld model based on physical properties.

### 2.3.1 Reflectivity

Although reflectivity is wavelength dependent and increases for longer wavelengths [1], [24], [83], Webb et al. [71] reported that absorptivity for 304 SS is <15% and Ti-6Al-4V is  $\approx$ 15%. Absorptivity (reflectivity) is proportional to the square root of electrical resistivity [71], [84], and as with electrical or thermal conductivity, the reflectivity decreases as temperature increases. The relatively large photon wavelength (0.5-10  $\mu\text{m}$  for welding related lasers) and lower energy results in reflection off metallic, close packed atomic surfaces, and it is believed that photons only interact with atoms or the free electrons near depths of approximately 10-100 nm below the metal surface [71], [77], [84].

Reducing the laser wavelength [85], [86] can improve beam coupling but is not always a viable option. Higher absorption can be achieved through generation of a deep-penetrating weld. The ensuing high aspect vapor cavity within the weld pool acts like a black body by “trapping” the incident photons. The photons then become reflected and absorbed along the wall of the vapor cavity. The partial absorption and partial reflection at the vapor-liquid interface is characterized as Fresnel absorption [24], [87]–[89] and is independent of the intensity [87]. Fresnel absorption is dependent on polarization, refractive indices of the interface, and angle of incidence [87].

Gladush and Smurov [90] reported the absorption versus angle of incidence for s and p polarization on iron as shown in Figure 2.9. Although it is for CO<sub>2</sub> LBW (10.6  $\mu\text{m}$

wavelength), at some relatively high travel velocity the absorption coefficient (beam coupling) reduced at high travel speeds.

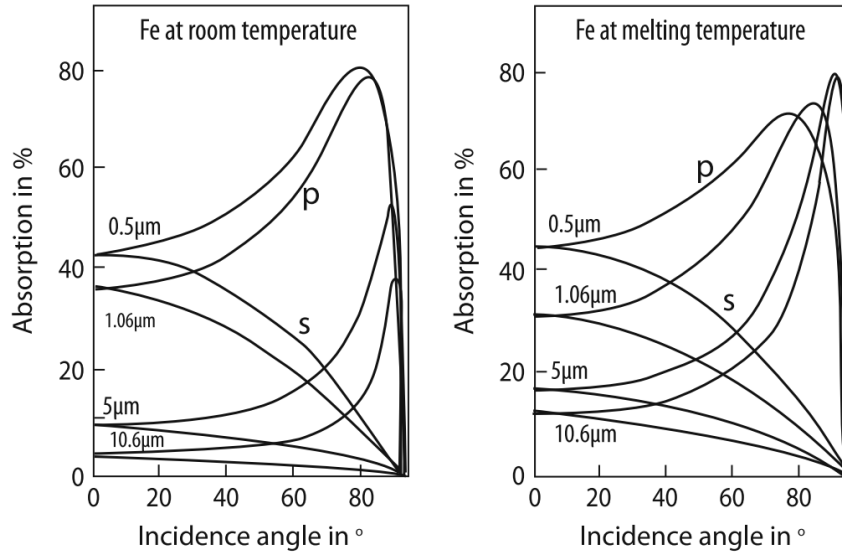


Figure 2.9. Absorption at varying wavelengths and incident angles for *s* and *p* polarized light [91].

### 2.3.2 Vaporization

Fluid flow, surface temperature, and diffusivities of elements in the gas phase all influence vaporization. The generated vapor plume imparts a recoil pressure on the liquid to maintain a compressive force against the keyhole wall [92], and the vapor motion induces shear stress on the liquid, which results in additional fluid flow. This recoil pressure is necessary for keyhole formation and stabilization, and the back pressure from the vapor plume must exceed the surface tension and hydrostatic forces attempting to close the keyhole [90], [93].

X-ray imaging performed by Miyagi and Wang [11] revealed inclination of the keyhole front relative to the plate surface. The front wall angle changed from nearly 90° at a 17 mm/s travel speed to 77° at a 167 mm/s travel speed. This is important regarding process stability as well as better understanding the transitions between conduction and keyhole mode. Similarly, Figure 2.10 shows a variation in front wall angle relative to what was defined as a power-to-travel speed ratio by Gladush and Smurov [90]. This ratio or heat input (HI) is defined in Equation 2.4. At heat inputs producing a keyhole wall angle above 80°, deep penetration, high aspect ratio welds are reported to remain stabilized. This indicated complete transition into keyhole mode welding.

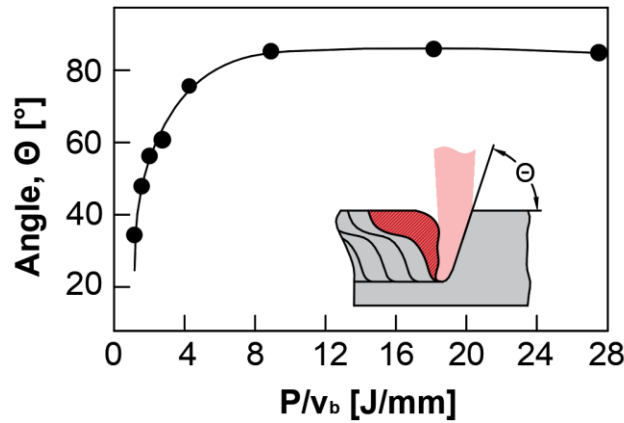


Figure 2.10. Front wall angle versus heat input recreated from Gladush and Smurov [90].

$$\text{Equation 2.4: } HI = \frac{P}{v_b} \quad [J/mm]$$

Where:  $HI$  = heat input,  $P$  = power,  $v_b$  = beam velocity

Some of the extreme complexity in understanding keyhole dynamics was further shown by Arata [94] using CO<sub>2</sub> LBW and x-ray imaging. Keyhole dynamics were heavily influenced by increasing the shielding gas flow rate as shown in Figure 2.11. At flow rates below 36 l/min, there was minimal distinction of keyhole formation. Increased flow at 51 l/min showed a distinctive keyhole appearance (Figure 2.11c), and higher flow rates of 81 and 120 l/min elongated the vapor depression. However, there appeared to be minimal influence on penetration behavior. Although, not reported, the x-ray images appear to indicate that the flow rate influenced the keyhole front wall angle.

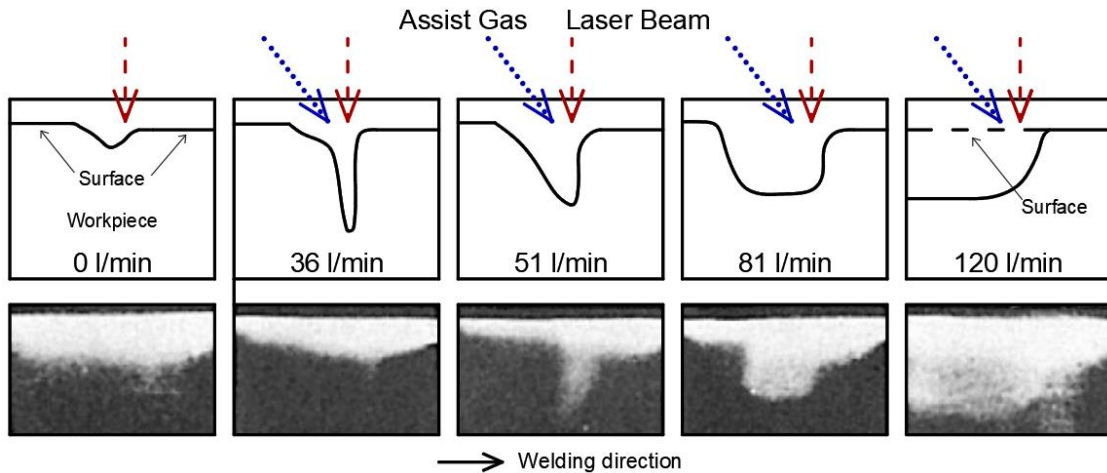


Figure 2.11. X-ray images of vapor capillary at varying shielding gas flow rates: 0 l/min (a), 36 l/min (b), 51 l/min (c), 81 l/min (d), 120 l/min (e). The welding direction is from left to right. The schematics were recreated based on the originals from Arata et al. [94].

Although, vaporization is largely attributed to keyhole formation, it is also relevant in conduction mode welding and can influence the pool depression, fluid flow, and process stability [70]. In addition, vaporization during conduction mode welding may

cause variations in weld metal composition due to preferential vaporization of alloying elements [22], [23]. Elemental loss can negatively influence microstructural formation and is particularly important when as-welded phase fractions are easily altered with minimal changes in alloy contents, such as in DSS [95].

### **2.3.3 Plume Formation**

Plume formation can pose an issue by interacting with the incident beam. The plume causes attenuation (reduction in intensity) through absorption and scattering mechanisms. By absorbing or scattering the laser beam, the incident energy is not transferred into the workpiece and/or is dispersed to an enlarged diameter. The absorption is influenced by plume temperature and particle size for a given wavelength, and an increasing plume temperature increases absorption. The amount of intensity lost as a result of the plume is commonly described by the Beer–Lambert Law [96] as presented in Equation 2.5. This shows the exponential relationship that is dependent on the initial intensity, length of particles within the beam, and an attenuation coefficient. The attenuation coefficient is dependent on the particle size, particle densities, and photon wavelength. For more information, the reader is referred to References [96], [97].

$$\text{Equation 2.5: } I_t(x) = I_0 e^{-\alpha x} \quad [W/mm^2]$$

*Where:  $I_t$  = transmitted intensity,  $I_0$  = incident intensity,  $x$  = length of laser interaction with the plume, and  $\alpha$  = attenuation coefficient*

Originally, the plume was considered a plasma. Hence, the common reference to it as a “plasma plume”. This original definition of ions and free electrons was based on plume studies using CO<sub>2</sub> lasers [98]. These studies reported temperatures as high as 17,000 K [99] and within a temperature range in agreement with plasma stabilization. Because plume formation is largely influenced by wavelength, it is believed that wavelengths near 1070 nm mostly generate a thermally excited, high temperature gas [100], [101]. Maximum plume temperature measurements were reported at approximately 4000-6000 K [102]–[105], and a plasma would only exist at ionization potentials of a few percent. However, beam scattering and attenuation is also associated with other physical phenomenon such as Rayleigh and/or Mie scattering.

Plasma formation is believed to be caused by inverse bremsstrahlung where bremsstrahlung means “braking” radiation. Inverse bremsstrahlung occurs when the molecules or atoms are heated above the ionization temperature and free electrons absorb the incident photons. Therefore, the plasma above the weld absorbs the incident energy, which is no longer transferred into the base material. Fabbro et al. [106] reported that the inverse bremsstrahlung effect scales with a square of the laser wavelength. Because the shorter wavelengths of solid-state lasers are less affected by inverse bremsstrahlung, it is believed that beam attenuation is mostly influenced by Rayleigh and/or Mie scattering, and inverse bremsstrahlung influences can be neglected [106].

Rayleigh and Mie scattering depend on the size of particles within the plume and the wavelength. Rayleigh scattering happens when condensed particles are much smaller

than the wavelength of incident light, and Mie scattering occurs when the plume particles are comparable in size to the wavelength of light. Scholz et al. [96] analyzed plume particle formation on 304 SS using a fiber laser and showed that power, travel speed, and shielding gas influenced the particle size. An increase in power from 0.8 kW to 1.6 kW increased the average particle size from 8 nm to 15 nm respectively. Also, higher welding speeds showed a reduction in particle size [96]. Therefore, by altering the process parameters, particle formation and scattering mechanisms will influence the fractions of incident energy imparted into the weld. This inability to appropriately account for attenuation and scattering influences the ability to sufficiently predict weld formation.

The open literature reports contradictory information on the degree that weld plume attenuates fiber lasers operating at 1070 nm wavelengths. On austenitic stainless steel, Kawahito et al. [101] reported a maximum attenuation of 4% measured at 3 mm above the plate surface. These results used a 10 kW fiber laser at atmospheric pressure. Likewise, Zou et al. [103] reported a maximum attenuation of 5% when welding on mild steel in atmosphere. Contrary to these low attenuations, Greses et al. [107] reported attenuations of nearly 40% at 3 mm above the weld. As with Zou et al. [103], these welds were performed on steel under atmospheric conditions.

Minimizing plume interaction during LBW is a useful mechanism for improving process efficiency [98] and increasing penetration [98], [108]. Two methods to reduce the plume interaction are to remove it via a high-pressure gas applied above the weld or perform welds under reduced atmospheric pressure.

An easy and universal plume suppression technique incorporates a “cross-jet” or “air knife” of high-pressure gas to blow the plume out of the beam path. Chiang and Albright [98] and Zou et al. [103] reported that minimizing the amount of plume available to interact with the beam improved penetration. Thus, attenuation was decreased enabling an increased heat transfer efficiency. Chiang and Albright [98] and Zou et al. [103] showed that locating the cross-jet closer to the material surface aided in greater plume removal and increased penetration. The results from Zou et al. [103] are shown in Figure 2.12.

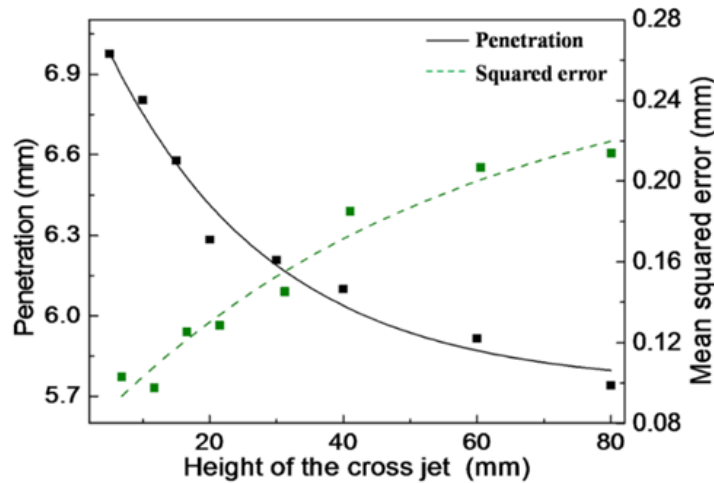


*Figure 2.12. Penetration versus cross-jet height at 5 kW of power and a 33 mm/s travel speed [103].*

Although not always practical, LBW under vacuum nearly eliminates detrimental beam–plume interactions and improves penetration. Figure 2.13 shows measured beam attenuation relative to atmospheric pressure for an aluminum alloy [109] and a high-strength low-alloy steel [110]. These results showed a reduction in attenuation at

increasing vacuum levels from atmospheric pressure ( $\sim 100$  kPa). It is believed that the vapor particles are swiftly removed from the beam path at lower pressures due to an increase in the pressure differential.

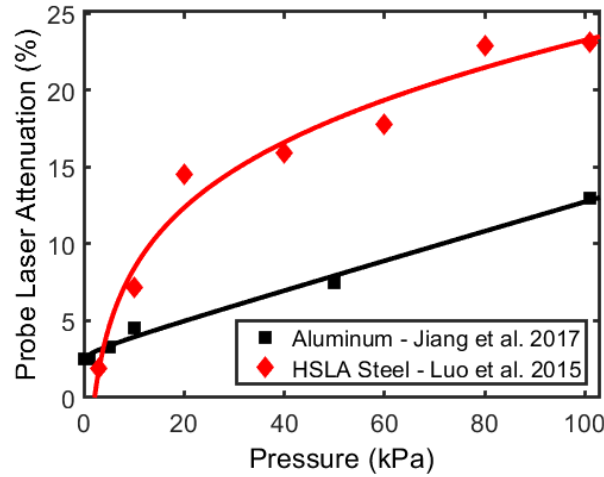


*Figure 2.13. Laser attenuation versus atmospheric pressure for a 1070 nm wavelength at a 1 mm height for an aluminum alloy (squares) [109] and at a 3 mm height for a high-strength low-alloy steel (diamonds) [110].*

At decreased pressure, the length of beam interaction with the plume continually decreased (Figure 2.13). Higher pressures compress the vaporized atoms/molecules, which is attributed to condensation and greater particle agglomeration directly above the weld. Not only does the pressure increase the local plume density, but the dense plume alters the heat distribution as the high temperature gas interacts with the material surface. Then, the plume redistributes heat further from the region of direct beam irradiation.

Results from Reisgen et al. [108] showed the usefulness of reduced pressure for increasing LB weld penetration. Figure 2.14 shows a schematic representing laser welds

produced at identical parameters for atmospheric pressure and 0.01 kPa. The low-pressure weld significantly increased in penetration while reducing the weld toe width. For comparison, penetration is nearly identical to an EB weld produced under high vacuum conditions using the same power [106], [108], [111].

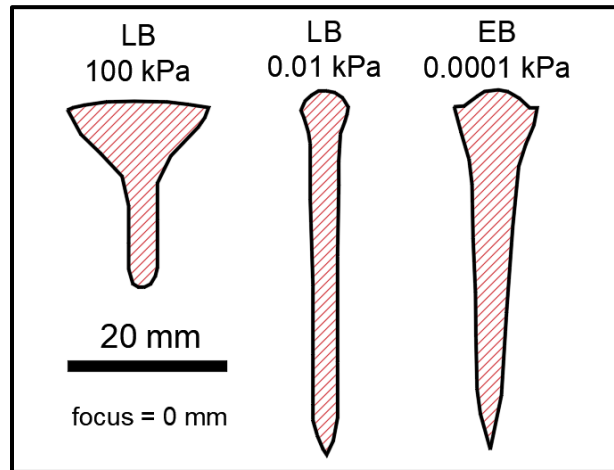


*Figure 2.14. Steel welded at 16 kW and 0.3 m/min (5 mm/s). From left to right, LB weld at 100 kPa, LB weld at 0.01 kPa, and EB weld at 0.0001 kPa. Weld profiles were extracted from Reisgen et al. [108].*

The trends for penetration characteristics with decreasing vacuum levels are consistent among researchers using various laser types and alloys [16], [106], [108], [112]–[114]. Reported literature has stated that vacuum LBW can improve penetration by a factor of two to four [115]–[117] compared to atmospheric conditions. The trend of penetration and welding speed at reducing atmospheric pressure is shown in Figure 2.15. Higher travel speeds showed a reduced influence regarding pressure. This is believed to be due to a reduction in plume formation at higher interaction times and the ability for the beam to effectively “out run” the plume. Gladush and Smurov [90] reported that the

penetration depth in a vacuum linearly depends on the recoil vapor pressure on the keyhole wall, which linearly depends on the radiation intensity. The equation for recoil vapor pressure under vacuum is shown in Equation 2.6. Gladush and Smurov [90] also showed a penetration depth calculation for laser welding under vacuum as presented in Equation 2.7.

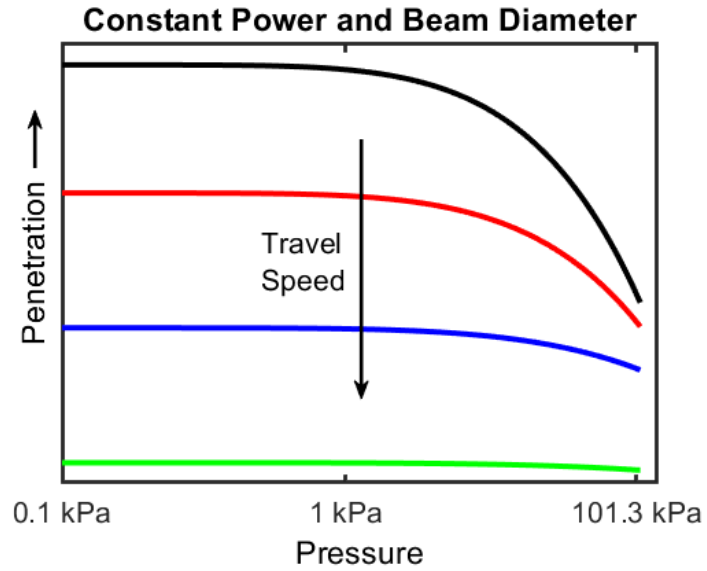


Figure 2.15. Schematic of LB weld penetration versus pressure at a constant power and beam diameter for different travel speeds. Data interpreted from references [16], [106], [112], [116].

$$\text{Equation 2.6: } P_v = q \frac{c_s}{H_f} \cos \theta \quad [J]$$

Where:  $P_v$  = vapor pressure,  $q$  = power density,  $c_s$  = speed of metal vapor moving away from the surface,  $\theta$  = angle of incident beam normal to the surface,  $H_f$  = latent heat of vaporization

$$\text{Equation 2.7: } d_p = \left( \frac{qc_s r_b}{H_v \rho g} \right)^{1/2} \left[ 1 + \ln \left( \frac{w_{1/2}}{r_b} \right) \right] \quad [J]$$

Where:  $d_p$  = depth of penetration,  $q$  = power density,  $c_s$  = speed of metal vapor moving away from the surface,  $r_b$  = beam radius at waist,  $H_v$  = enthalpy at vaporization temperature,  $\rho$  = density,  $g$  = gravitational acceleration,  $w_{1/2}$  = half width of the fusion zone

There appears to be a vacuum level where increasing the vacuum does not produce a further increase in penetration (Figure 2.15). This region is known as a critical threshold and is reported as occurring at pressures as high as 10 kPa (75 torr). However, it is largely influenced by the alloy, wavelength, power density, and travel speed. High travel speeds in excess of 3 m/min (66.7 mm/s) are reported to exhibit critical thresholds at or near atmospheric pressures [112], [113].

A benefit of LBW with reduced pressure in comparison to EBW is the ability to substantially increase penetration at moderately low vacuum levels, such as 1 kPa (7.5 torr). In contrast, EBW requires much lower vacuum pressures (<0.1 torr) to minimize electron-molecule interaction that results in extensive beam attenuation [108], [117]. Thus, LBW with small reductions in atmospheric pressure can provide penetration improvement with faster vacuum pumping times and decreased vacuum system complexity as compared to EBW.

#### **2.3.4 Fluid Flow**

Convective weld pool fluid flow contributes to the resultant geometry. These flows are largely influenced by the vapor interaction, thermal gradients, and chemical composition. These active forces include Marangoni (temperature dependent surface

tension), buoyancy, and vapor pressure, and the combination and relative magnitudes of each force dictates the resultant weld shape. Although vaporization is generally regarded as the contributing factor to the keyhole formation, there is still debate on the impact of surface tension and weld pool convection relative to vaporization [118].

For conduction mode welding, fluid flow is largely dependent on the surface tension gradient as shown by Heiple et al. [119] and Kou et al. [120], and the surface tension can be highly influenced by alloy compositions or impurity contents. Mills [121] presented the variation in surface tension versus sulfur content in 304L SS as recreated in Figure 2.16. Initially, there is a decrease in surface tension with increasing sulfur, but at contents greater than  $\approx 250$  ppm, further increases in sulfur marginally influenced the surface tension. This is shown through the exponential decay in Figure 2.16. Figure 2.17 shows cross-sections of laser spot welds on stainless steel at two sulfur contents. Sulfur levels increased to 140 ppm (0.014 %) increased the weld penetration. The mechanism, as reported by Heiple and Roper [122], is via a reversal of the surface tension gradient caused by surface active elements, which generated downward fluid flow along the weld centerline [123]. However, during keyhole mode welding, Heiple et al. [124] showed no influence of surface active elements modifying fluid flow behavior.

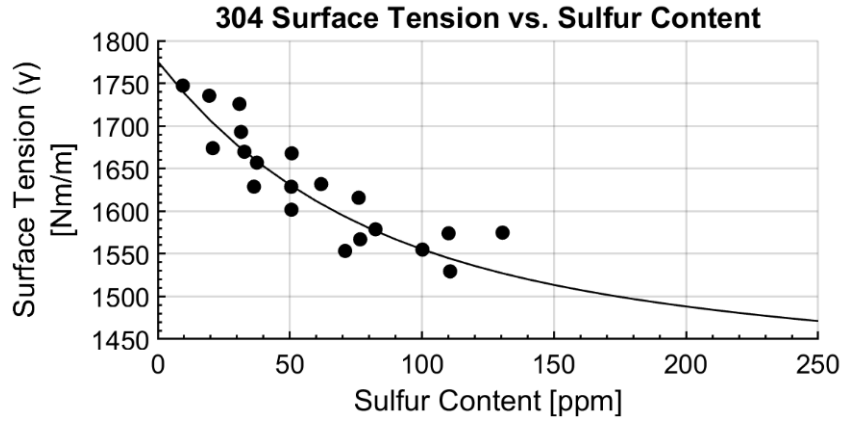


Figure 2.16. Change in surface tension versus sulfur content. Recreated from Mills [121].

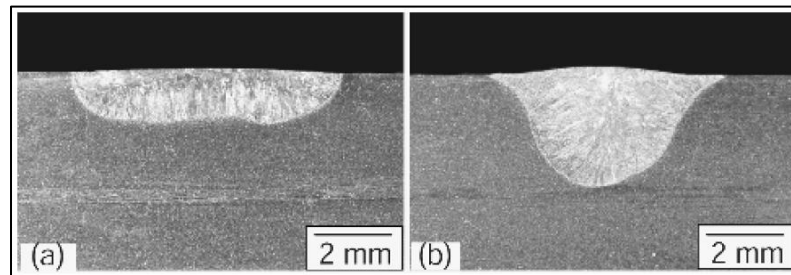


Figure 2.17. Change in laser spot weld pool shape on 304L stainless steel at 40 ppm sulfur (a) and 140 ppm sulfur (b) [123].

Melt flows during keyhole mode become increasingly complicated due to additional interaction of the vapor capillary with the molten metal. Figure 2.18 shows a schematic of weld pool flow directions during keyhole mode welding as reported by Kaplan [125]. Along the keyhole front wall, liquid must be vaporized or diverted around the vapor capillary. For this to happen, the fluid must accelerate rapidly, which was reported to be caused by the evaporative recoil forces [92].

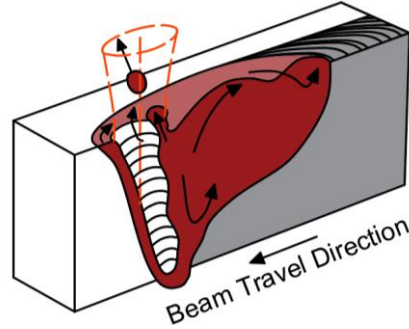


Figure 2.18. Schematic of keyhole mode melt flow phenomena recreated from Kaplan [125].

Katayama et al. [10] and Matsunawa et al. [76] confirmed how dynamic the keyhole fluctuation actually is by using *in situ* x-ray imaging. Their observations indicated that the vapor capillary constantly changed, and vaporization was not uniform. The introduction of tungsten particles to the weld along with x-ray observation allowed for tracing fluid flow patterns as shown in Figure 2.19 [76].

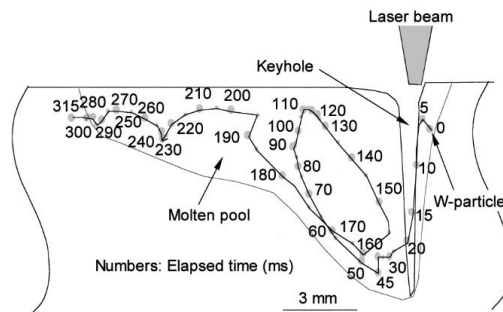


Figure 2.19. Position of tungsten particle in weld pool showing the elapsed time in milliseconds from Matsunawa et al. [76].

It was reported that fluid flow velocity increases with travel speed based on changes to the recoil pressure or evaporation at the keyhole wall front [9], [126] and temperature dependent changes in surface tension [126]. Dowden [87] reported that the

liquid is extremely turbulent as confirmed by instability issues and x-ray imaging [10], [76], [127]. However, Dowden [87] reported that the vapor maintains a laminar like flow caused by a reduction in the density, which reduced the Reynolds number. The Reynolds number is a dimensionless number used in fluid dynamics to differentiate turbulent versus laminar flow as show in Equation 2.8.

$$\text{Equation 2.8: } R_e = \frac{uL}{\nu} = \frac{\rho uL}{\mu} \quad [\text{unitless}]$$

Where:  $R_e$  = Reynolds number,  $u$  = fluid velocity,  $L$  = characteristic length of flow,  $\nu$  = kinematic viscosity,  $\rho$  = density,  $\mu$  = dynamic viscosity

Gladush and Smurov [90] reported that melt flow velocities can exceed travel speeds by orders of magnitude and showed weld pool velocity versus travel speed at varying parameters. These results are replotted as shown in Figure 2.20. The critical melt flow velocity line is reported as the distinction between humping, where higher flow velocities result in humping. The exact mechanism driving fluid flow is difficult to quantify due to the transient nature of the process and inability to sufficiently measure the flow. Therefore, many models have attempted to account for fluid motion to accurately reproduce weld geometries. These models typically make assumptions regarding dimensionless fluid dynamics numbers, such as the Prandtl number defined in Equation 2.1, in an attempt to improve the current understanding of weld formation [14], [15], [92], [128].

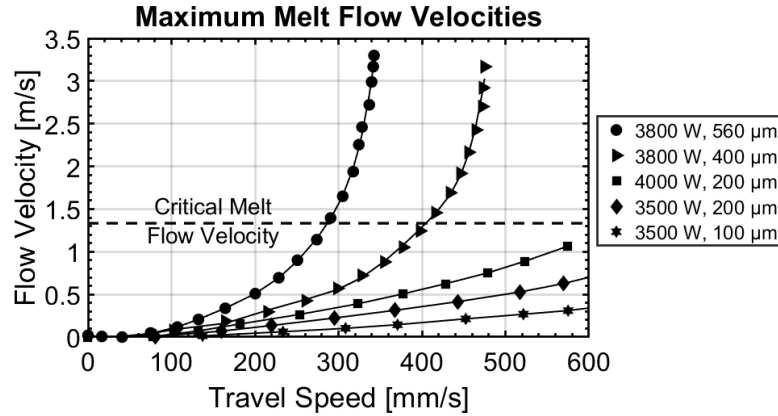


Figure 2.20. Fluid flow velocity versus welding speed at different powers and beam diameters. Recreated from Gladush and Smurov [90].

## 2.4 Parameter Influences on Weld Pool Evolution

The parameters or independent variables influencing LB fusion zone characteristics include power, beam diameter/distribution, and travel speed. This assumes that all other variables are held constant such as wavelength, beam quality, atmospheric conditions, shielding gas, etc. Then, the dependent variables include the measurable aspects of the weld geometry. For this study, all evaluated LBW data was from partial penetration welds unless explicitly specified. The purpose of limiting the weld analysis to bead-on-plate, partial penetration welds was to better understand fundamental reasons for altering penetration depth. The following subsections address the influence of the three fundamental laser parameters: beam diameter, power, and travel speed. Decoupling the analysis of beam power and beam diameter is difficult, and this often leads to weld analysis based on power per unit area or power density.

### **2.4.1 Beam Diameter**

The beam diameter is a complex variable caused by different intensity distributions. As previous discussed, diameters are not always directly comparable. This is due to non-ideal outputs, different TEM modes [129], beam diameter measurement techniques, and computation methods [52]. Although, reducing the beam diameter at a constant power and travel speed will increase the intensity and result in deeper weld penetration [78], [130], [131].

For the majority of LBW systems, the sharp focused beam diameter is a fixed variable and altering this would require physically changing the process fiber or focusing optics. An easy method of altering the beam diameter is to change the focal condition relative to the work piece surface. However, this results in a drastic change in the intensity distribution relative to the workpiece surface. This is especially true for multi-mode distributions. Figure 2.21 shows a representative beam caustic with the multi-mode distribution at sharp focus changing into a Gaussian distribution at the under and over-focused conditions [3].

Welding in the over-focused condition (focal position above the plate surface) increases the beam diameter resulting in reduced weld penetration, but welding in the under-focused condition (focal point below the plate surface) can improve weld penetration [71], [112]. Figure 2.22 shows a schematic representing the change in transverse cross-sections at varying focal points, where negative values reference an under-focused condition [3].

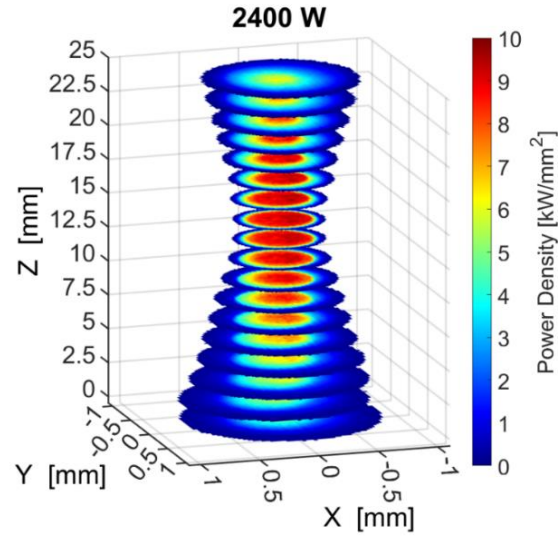


Figure 2.21. Laser beam caustic showing the transition from multi-mode to a Gaussian distribution at the under and over-focused conditions [3].

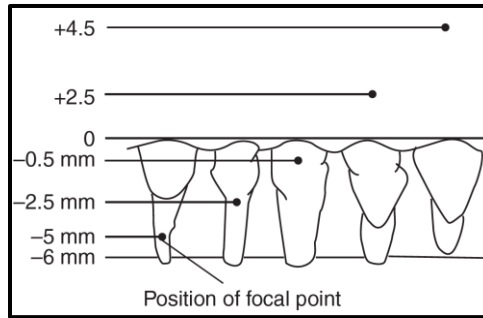


Figure 2.22. Focal position relative to transverse section weld formation [71].

#### 2.4.2 Power

For keyhole mode welding, a considerable amount of literature showed that the depth of penetration increased nearly linearly with increased beam power at a constant travel speed. These penetration results are consistent with results from numerous researchers [14], [73], [132]–[135] but most likely are only valid for a finite range of

power variation [136]. Other research suggests that LBW penetration depth increases proportional to two-thirds the power ( $d_p \propto P^{2/3}$ ) at low welding speeds and directly proportional to power at high welding speeds ( $> 100$  mm/s). Figure 2.23a shows results from Quintino et al. [134] for penetration depth versus power at different travel speeds on a steel alloy. Similarly, results extracted from Suder and Williams [137] for a steel alloy are shown in Figure 2.23b.

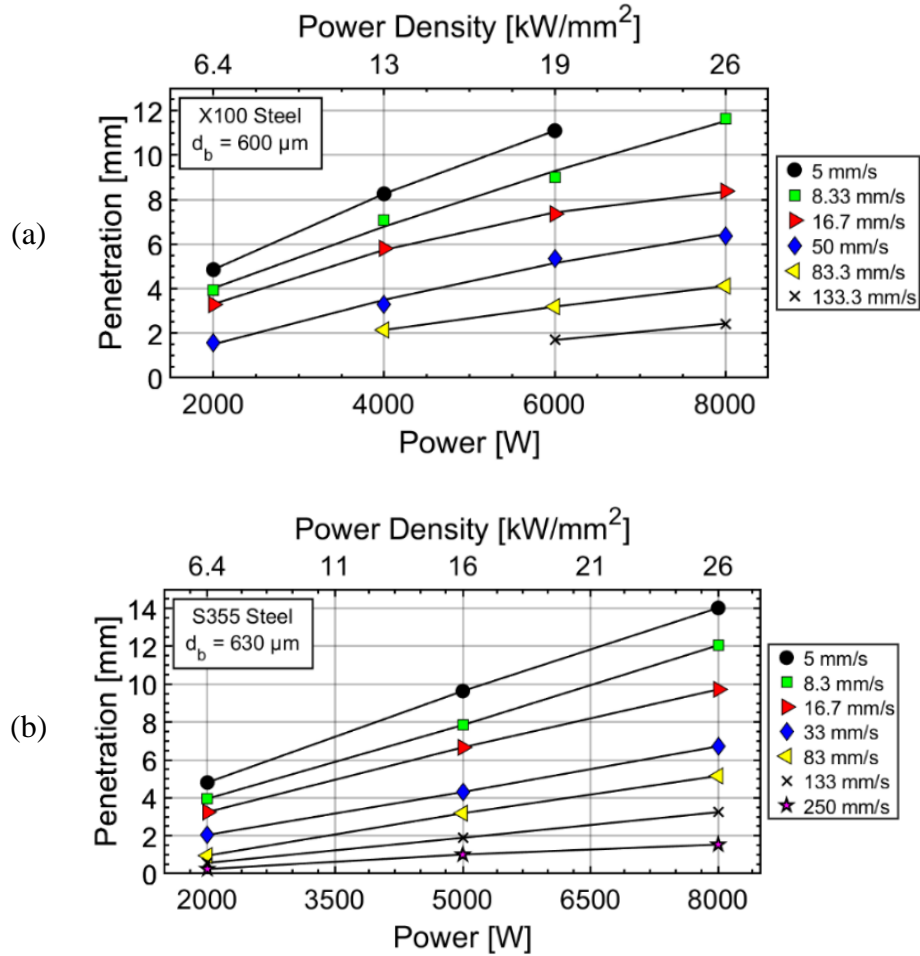


Figure 2.23. Penetration depth versus power or power density at constant beam diameters: X100 steel [134] (a) and S355 steel (b) [137].

Although reported as power density, the data in Figure 2.23b was produced at a constant beam diameter and showed a linear-like penetration rise. Suder and Williams [137] emphasized the linear nature of increased penetration while also stating that the slope is dependent on the interaction time, and longer interaction times showed increasingly steeper penetration versus power slopes. Figure 2.24 also shows nearly linear penetration on 304 SS (Figure 2.24a), Ti-6Al-4V (Figure 2.24b), and vanadium (Figure 2.24c) at the same beam diameter but different travel speeds [14].

The data in Figure 2.23 and Figure 2.24 shows nearly linear behavior, this is likely attributed to a limited amount of data and relatively high powers, and Figure 2.23a indicates nonlinear behavior at 16.7 and 50 mm/s travel speeds. Akman et al. [136] reported a linear increase in penetration depth up to a threshold power. Further increase in power decreased the rate of increasing penetration, which lead to nonlinearity. This was reported to be caused by greater plume interaction at higher power densities [136] and may explain the reduced penetration rate in Figure 2.23a.

Data that showed a linear rise in penetration with increasing power was restricted to parameters within a keyhole regime, so changes to the weld penetration were not introduced via a transition from conduction to keyhole mode. Welding in regimes far outside of keyhole mode (lower power density or high travel speed) may substantially alter penetration behavior [79], [138]. These transitions and ambiguous regions between fully conduction and keyhole mode are represented in Figure 2.25 [79].

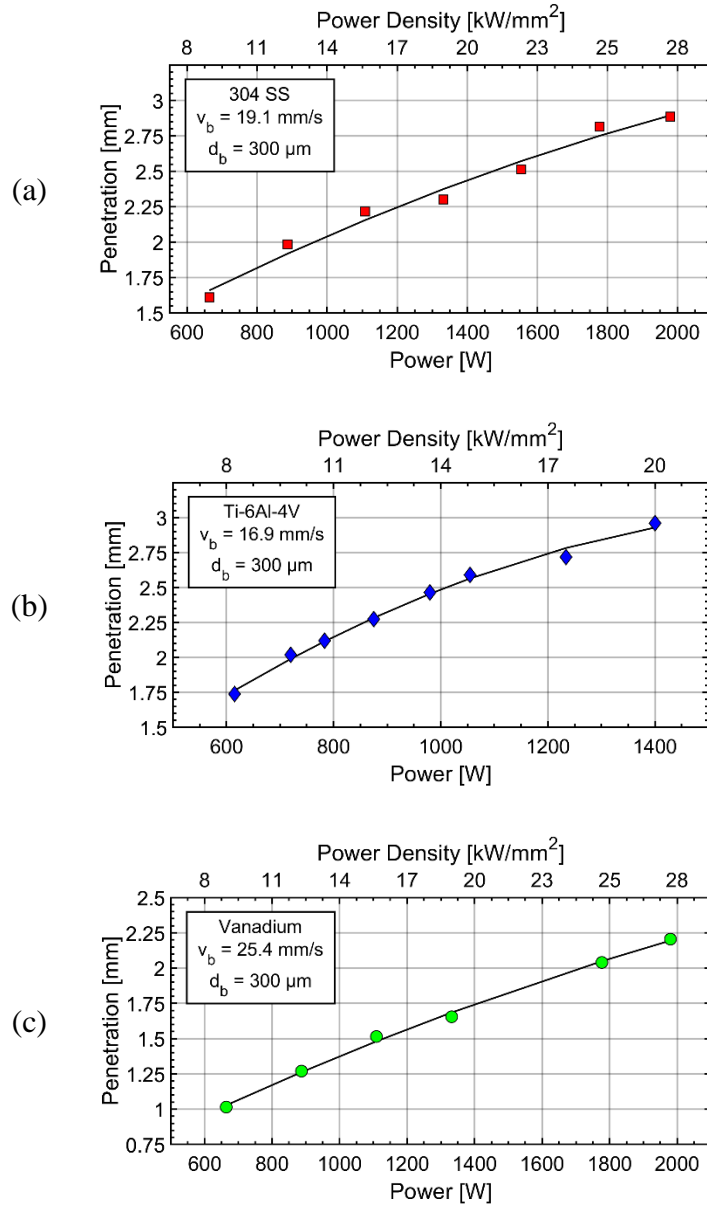


Figure 2.24. Penetration depth versus power or power density at constant beam diameters: 304 SS (a), Ti-6Al-4V (b), and vanadium (c) [137].

The CW LB welds in Figure 2.25 were produced using a travel speed of 3.5 m/min (58.3 mm/s) and a 1.18 mm beam diameter. Assunção [78] argued that there was

not a clear transition between conduction and keyhole mode welding. The relatively large beam diameter expanded the degree at which a transition occurred, and the complexity in vaporization and surface tension driven fluid flows are drastically different depending on the alloys and parameters under investigation [120], [139]. Therefore, to effectively model weld pool development, it becomes necessary to fully understand how the combination of power and beam diameter influence the material dependent properties.

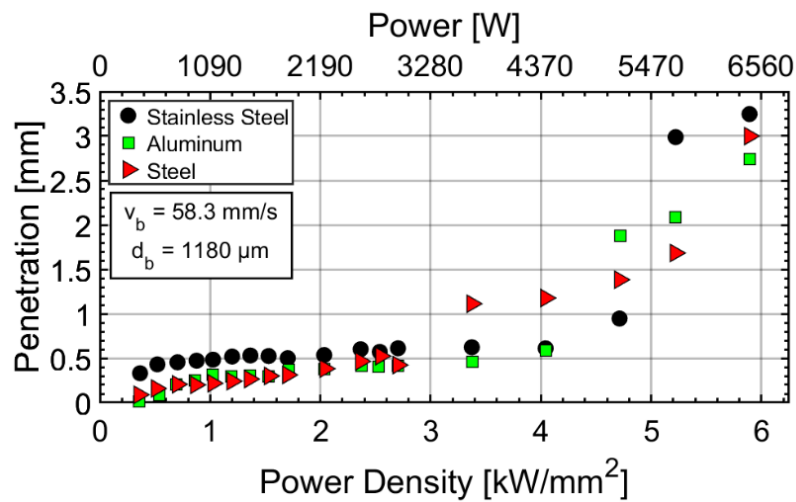


Figure 2.25. Penetration versus power density for stainless steel, aluminum, and mild steel at a constant beam diameter (1.18 mm) and travel speed (58.3 mm/s). Data extracted from Assunção and Williams [79].

### 2.4.3 Power Density

Power density combines the computed or believed beam diameter with the total beam power. Variation in the actual power density is largely dependent on the intensity distribution and focal position, but Equation 2.9 shows the calculation assuming a known beam diameter. If power is increased under a constant beam diameter, the power density

proportionally scales accordingly. Although, an issue arises when attempting to compare similar power densities at different beam diameters. Figure 2.26 shows results from fiber laser welds performed using multi-mode, or uniform, beam distributions [79], [134], [137].

$$\text{Equation 2.9: } P_d = \frac{P}{A_b} = \frac{P}{\pi d_b^2/4} \quad [W/m^2]$$

Where:  $P_d$  = power density,  $P$  = power,  $A_b$  = beam area,  $d_b$  = beam diameter

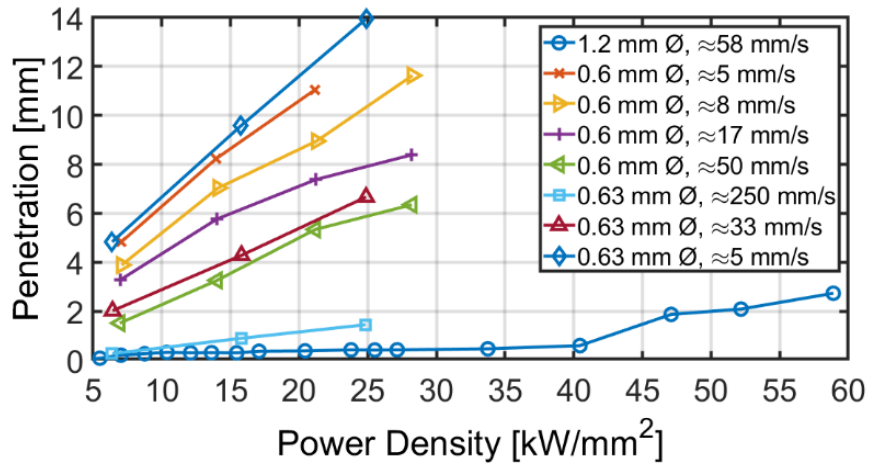


Figure 2.26. Fiber laser penetration versus power for steel alloys when welding in keyhole mode [79], [134], [137].

The circles (lowest penetration) in Figure 2.26 represent twice the beam diameter (1.18 mm) as the other welds (0.6 mm) and were performed at a similar travel speed as the left facing (green) triangles. At double the power density compared to the weld made using a 0.6 mm beam diameter, the penetration remained substantially lower using the 1.18 mm diameter beam. The large difference in penetration shows the significance in

understanding the distribution of heat projected onto the material and the ability to produce an extreme penetration variation at equivalent power densities through varying beam diameter.

#### 2.4.4 Travel Speed

Penetration exhibits an exponential decrease at an increasing travel speed [24], [135], and there is a substantial amount of literature published that plots the LBW relationship between penetration and travel speed [73], [78], [98], [134], [135], [138], [140]. Figure 2.27 shows penetration versus travel speed for fiber LBW of SS. Travel speed changes the shape of the weld profile with higher travel speeds resulting in reduced penetration and a narrower weld toe [1].

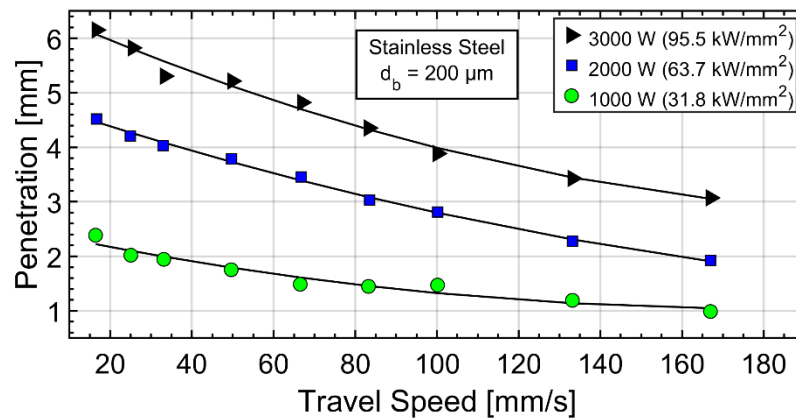
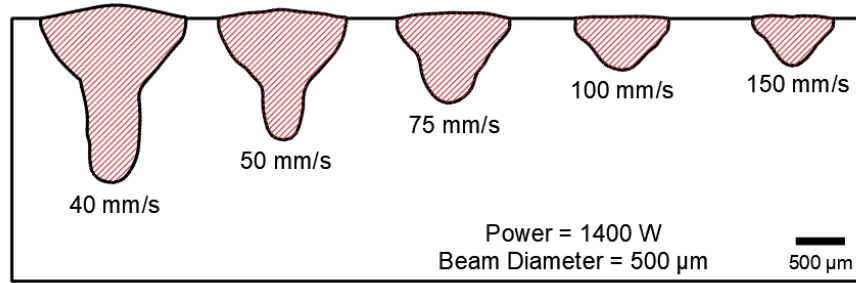


Figure 2.27. Stainless steel weld penetration using a fiber laser with a 200  $\mu\text{m}$  beam diameter [71].

Slower travel speeds increase the overall energy and heat deposited into the workpiece. This causes the weld pool to widen and reduces the weld aspect ratio [1].

Figure 2.28 shows transverse cross-section results from welds performed using a fiber laser on 304L SS. The change in weld penetration was much more pronounced than the change in weld width under these welding conditions, and a transition likely occurred between keyhole to conduction mode between 75 and 100 mm/s.



*Figure 2.28. Weld geometry on 304 SS using a multi-mode beam profile at sharp focus. An apparent change from keyhole mode to conduction mode occurs above 75 mm/s [3].*

Baardsen et al. [135] reported that LB weld penetration depths did not show a corresponding relationship between penetration and travel speed. This was based on the idea that higher travel speeds require some amount of “illumination time” to form a weld pool. Therefore, reflectivity was reported to be greater at higher speed which caused less energy to be “captured” within the keyhole [135]. The complexity of the travel speed is exacerbated by laser plume interactions [108], [111], [114], [141], [142], which is also travel speed dependent [98]. Gladush and Smurov [90] presented results which showed the change in melting efficiency relative to weld velocity. It was reported that an optimal travel speed (14 mm/s) provided the highest efficiency [90]. These results are shown in Figure 2.29.

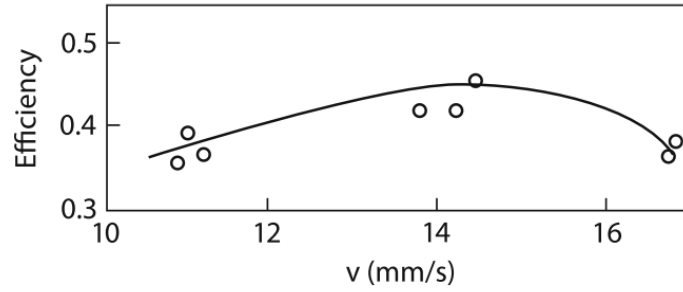


Figure 2.29. Change in LBW melting efficiency versus travel speed [90].

Altering the welding speed within a keyhole region influences the vapor capillary. As Baardsen et al. [135] reported, reflectivity changes with travel speed, and this change is related to Fresnel absorption along the keyhole wall. Figure 2.30 shows results of the front wall angle versus welding speed from Kaplan [88]. Kaplan's [88] data showed that a higher welding speed increased the front wall angle, which resulted in higher Fresnel absorption at a 1  $\mu\text{m}$  wavelength (Figure 2.30a). However, it was reported that there was minimal influence on the average absorption (Figure 2.30b).

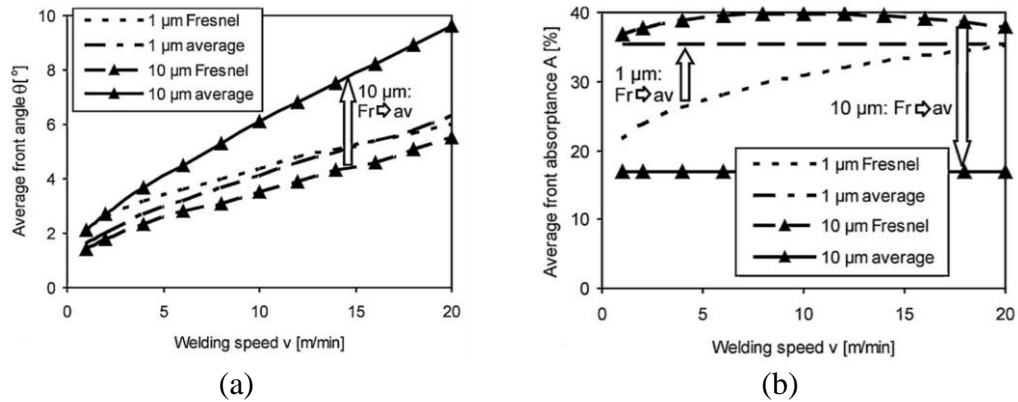


Figure 2.30. Average front wall angle versus welding speed (a) and Fresnel absorption versus welding speed (b) [88].

#### 2.4.5 Other Variables

Literature reported modification of the three fundamental parameters that attempted to better quantify weld formation. The modified variables include interaction time [78], [143]–[145], specific point energy [131], [144], [146], and energy density [131], [144]. Interaction time incorporates diameter and travel speed to calculate the unit of time a finite point in the center of the beam path is exposed to radiation, and Equation 2.10 shows the calculation.

$$\text{Equation 2.10: } t_i = d_b / v_b \quad [s]$$

Where:  $t_i$  = interaction time,  $v_b$  = beam velocity,  $d_b$  = beam diameter

Fundamentally, interaction time is only accurate along the beam centerline. Assuming a circular beam profile and moving away from the beam center parallel to the travel direction, the length of the beam exposed to a specific point would decrease. However, Suder and Williams [78], [137] assumed that the effect of beam radius was negligible for the small spot sizes used in LBW. Multiple researchers incorporated interaction time into weld width and penetration analysis [78], [131], [146], [147], and Suder and Williams [137] related the interaction time for CW LBW to a pulse duration or period of radiation during pulsed-LBW.

Specific point energy (SPE) is the energy equivalence of interaction time. Equation 2.11 shows this calculation, which multiplies interaction time with beam power.

SPE represents how much energy is exposed to an infinitesimally small point, and literature expanded the SPE to include an energy density as shown in Equation 2.12. The energy density is the SPE divided by the beam area or power density multiplied by the interaction time.

$$\text{Equation 2.11: } SPE = \frac{Pd_b}{v_b} = Pt_i \quad [J]$$

Where:  $SPE$  = specific point energy,  $P$  = power,  $d_d$  = beam diameter,  $v_b$  = beam velocity,  $t_i$  = interaction time

$$\text{Equation 2.12: } ED = \frac{Pd_b}{A_b v_b} = \frac{SPE}{A_b} = P_d t_i \quad \left[ \frac{J}{m^2} \right]$$

Where:  $ED$  = energy density,  $P$  = power,  $d_d$  = beam diameter,  $v_b$  = beam velocity,  $A_b$  = beam area,  $SPE$  = specific point energy,  $t_i$  = interaction time,  $P_d$  = power density

Suder and Williams [137] analyzed the influence of a constant interaction time for bead-on-plate welds using a fiber laser. The keyhole penetration depth increased linearly with an increasing power density when a constant interaction time was maintained. It was reported that some length of interaction time was required to establish a keyhole for a given power density. Similarly, Suder and Williams reported a need for a threshold energy density to elevate the material to its boiling point and transition to a keyhole [130], [137], [144].

### **2.4.6 Weld Defects**

Porosity and solidification cracking are issues inherent to HED processes. Porosity defects are associated with substantial vaporization, rapid solidification, and vigorous weld pool mixing. Porosity is greater in deep penetration welding (higher power densities and/or long interaction times) and certain alloy systems are prone to pore formation, such as aluminum [75]. Solidification cracking is an issue caused by lower heat inputs, rapid solidification rates, alloy compositions, and internal shrinkage stress. Because microstructural transformations are an important part of weld discontinuities such as cracking related issues, the microstructural phenomenon important to HED welding of SS alloys and Ti-6Al-4V is covered in detail in Section 2.6.

#### **2.4.6.1 Porosity**

Porosity can be classified into root porosity (keyhole collapse) and uniform porosity (gas entrapment). Norris et al. [148] and Blecher et al. [149] reported that an increased weld volume/area increased the amount of porosity during CW LBW. Cai et al. [150] reported that liquid flow along the keyhole wall influenced pore formation with fewer pores attributed to greater keyhole stability. Elmer et al. [151] reported that using nitrogen shielding gas as compared to argon improved and nearly eliminated porosity in 304L SS during LBW. Similar results were achieved in A36 steel, but welds on nickel exhibited high amounts of porosity regardless of shielding gas. They attributed the improvement in porosity to the solubility of nitrogen in liquid as compared to argon. It

was also reported that the higher fractions of manganese, which contains a low vapor pressure, stabilized the keyhole in a steel alloy as compared to nickel 201 [151].

Reduced pressure has not only shown increased penetration but also the ability to reduce porosity [115], [141], [150]. Figure 2.31 shows x-ray images of longitudinal weld sections starting at atmospheric pressure (top left) and reducing until pore formation was eliminated (right) [150]. Elmer et al. [115] also reported differences in the morphology of the pores under vacuum conditions. Reduced pressure reduced the size of the pores but increased the number of pores present.



Figure 2.31. Weld metal porosity at: atmospheric pressure (a),  $10^3$  Pa (b),  $10^1$  Pa (c),  $10^{-1}$  Pa (d),  $10^{-3}$  Pa (e). Extracted from Cai et al. [150].

#### 2.4.6.2 Humping

Welding at extreme travel speeds may cause “humping” where the weld surface experiences insufficient wetting and discontinuous droplets [110], [112], [152], [153]. Humping is usually prefaced by “ropy” beads and undercut [153], and is most likely a result of surface tension and Marangoni flows. Therefore, material composition may also influence the formation of a high and discontinuous weld crown. Kawahito et al. [152] showed that humping is exacerbated at smaller beam diameters (130-200  $\mu$ m) and travel

speeds in excess of 75 mm/s. Vacuum conditions were reported to exacerbate the tendency for humping at pressures less than 1 kPa by Luo et al. [154] and Katayama et al. [112]. Although, Katayama et al. [112] and Börner et al. [113] were able to eliminate humping at reduced pressures by welding in an under-focused condition (i.e., with the beam waist below the plate surface).

## **2.5 Modeling and Weld Depth Prediction**

The term modeling is often used to describe any form of predictive efforts spanning simple solutions to complex numerical simulations. The open literature contains a substantial amount of information for predicting weld formation. These predictions are via mathematical formulas generated from empirical data or computationally evaluated based on material properties, constants, and equations. Although generally contrary to reported success, there is great difficulty in producing accurate and/or computationally efficient models for HED processes. This drives a continued need to further investigate and incorporate solutions to solve an industrial need for weld prediction. An idealized model output for this investigation would include an accurate prediction of weld penetration as shown with a “map” in Figure 2.32.

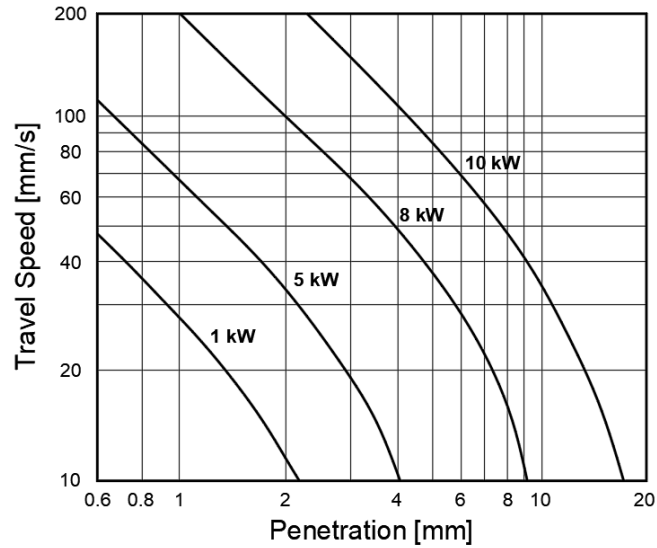


*Figure 2.32. Schematic representing travel speed versus penetration at four different powers. Recreated from Smithells Metals Reference Book [155].*

This map recreated from the Smithells Metals Reference Book [155] shows what are reported to be the penetration trends for iron, nickel, and titanium alloys relative to power and travel speed. However, diagrams such as in Figure 2.32 are subjected to severe prediction limitations. These limitations are caused by the inability to incorporate all the necessary variables such as material properties, composition variations, beam diameter/distribution, incident beam angle, cross-jet height, shielding gas composition, shielding gas flow rates, shielding gas angles, pressure, etc.

This section reviews some of the dimensionless relationships, analytical equations, numerical models, and artificial neural networks historically used to predict weld penetration and/or geometries. For the reported modeling approaches, the assumptions or

specific issues that hinder the model from being truly predictive and universal across variations in laser welding setups is also discussed.

### ***2.5.1 Analytical Approaches***

Analytical approaches generally consist of relatively simple equations that attempt to incorporate the fundamental input parameters (i.e., power, travel speed, and beam diameter) and material properties such as thermal conductivity, melting temperature, and vaporization temperatures. Assumptions are made to allow the computations to be tractable, and these solutions generally have limited success in prediction efforts caused by the necessity to make gross assumptions [123]. Generally, the only process considerations are power and/or diameter, and the analytical approaches do not incorporate time or temperature dependent iterative analysis as in numerical simulations.

Chiang and Albright [98] utilized the formula shown in Equation 2.13 to estimate the power needed to produce a weld pool for a known cross-sectional area. By rearranging the formula, the area of the weld metal is calculated based on melting related material properties and incident power. However, the energy to reach the boiling point of the material is not incorporated, and this approximation only provides an estimation of the melted area and disregards penetration depth or weld shape.

$$\text{Equation 2.13: } P_m = A_w \rho C_p [(T_m - T_0) + L_m/C_p] \quad [J]$$

Where:  $P_m$  = power to melt,  $A_w$  = weld cross-sectional area,  $\rho$  = density,  
 $C_p$  = specific heat,  $T_m$  = melting temperature,  $T_0$  = plate (room) temperature,  
 $L_m$  = latent heat of melting

Although not directly applicable, a modeling technique utilized in laser cutting is referred to as the “lumped heat capacity model” as reported by Steen and Mazumder [24]. The approximation is shown in Equation 2.14 and attempts to compute the volume of material removed per second if vaporization occurs at such a rate that conduction is not possible. This model expands on Equation 2.13 to include a vaporization dependency and beam area via power density. The depth of material removed per second, or penetration rate ( $d_{pr}$ ), is based on the beam cross-sectional area. Thus, the beam is assumed to have a uniform intensity distribution [24].

$$\text{Equation 2.14: } d_{pr} = \frac{P_d}{\rho[L_v + L_m + C_p(T_v - T_0)]}$$

Where:  $d_{pr}$  = penetration rate,  $P_d$  = absorbed power density,  $\rho$  = density,  
 $L_m$  = latent heat of melting,  $L_v$  = latent heat of vaporization,  $C_p$  = specific heat capacity,  
 $T_v$  = vaporization temperature,  $T_0$  = initial temperature

Steen and Mazumder [24] reported that the time for vaporization can be estimated by rearranging the one dimensional (1D) heat conduction equation and assuming the temperature at the surface is equivalent to the vaporization temperature. This calculation is shown in Equation 2.15. However, Gladush and Smurov [90] reported that time for vaporization is determined by the vaporization wave velocity as shown in Equation 2.16.

The importance in computing the time for vaporization is relatable to the interaction time of the beam and the quantity of material that can be vaporized at varying travel speeds.

$$\text{Equation 2.15: } t_v = \left(\frac{\pi}{\alpha}\right) \left[\frac{T_v \kappa}{2P_d}\right]^2$$

Where:  $t_v$  = time for vaporization,  $\kappa$  = thermal conductivity,  $\alpha$  = thermal diffusivity,  
 $T_v$  = vaporization temperature,  $P_d$  = power density

$$\text{Equation 2.16: } v_v = \frac{P}{\pi r_b^2 H_v \rho}$$

Where:  $P$  = absorbed power,  $r_b$  = beam radius,  $H_v$  = enthalpy of vaporization,  $\rho$  = density

Many of these techniques are based on the solution to the 1D heat flow equation or Fourier's second law [24], [78], [90]. The major assumptions for this form of analysis includes: no convection, no heat generation, constant thermal properties, and no radiant heat loss. An analytical solution to the 1D heat conduction equation is shown in Equation 2.17.

$$\text{Equation 2.17: } T_{z,t} = \frac{2P_d}{\kappa} \left[ \sqrt{\alpha t} \cdot \text{ierfc} \left( \frac{z}{2\sqrt{\alpha t}} \right) \right] \quad [^{\circ}\text{C}]$$

Where:  $T$  = temperature,  $P_d$  = power density,  $\kappa$  = thermal conductivity,  
 $\alpha$  = thermal diffusivity,  $z$  = position,  $t$  = time,  
 $\text{ierfc}$  = integral of the complimentary error function

Other analytical solutions include calculations of thermal gradients based on a stationary point, a line, or a Gaussian source with more detailed explanations discussed in

References [24], [90]. Incorporating travel or moving heat sources into these equations was originally derived by Rosenthal c. 1940 [24], [123], [156], [157]. The equation for a moving point source is presented in Equation 2.18. The primary issue with the point source solution is singularity at the origin, which is not respective of actual conditions and has no representation of melting or vaporization.

$$\text{Equation 2.18: } T - T_0 = \left( \frac{Q}{2\pi\kappa} \right) \left[ \frac{e^{-v \left( x - \sqrt{x^2 + y^2 + z^2} \right) / 2\alpha}}{\sqrt{x^2 + y^2 + z^2}} \right] \quad [^{\circ}\text{C}]$$

Where:  $T$  = temperature,  $T_0$  = initial temperature,  $Q$  = heat transferred to work piece,  $v$  = travel speed,  $\kappa$  = thermal conductivity,  $\alpha$  = thermal diffusivity,  $x$  = position,  $y$  = position,  $z$  = position

Rosenthal [156], [157] also derived the line source solution. This line source assumes that heat is uniformly absorbed along a line of some depth commonly used to simulate full penetration fusion welding of thin plate [123] or full penetration keyhole mode HED welds [24], [80], [158]. This solution is shown in Equation 2.19, and the line source has been extended to many models [13], [80], [158], [159], including that introduced by Kaplan [160] in 1994.

$$\text{Equation 2.19: } T - T_0 = \left( \frac{Q}{2\pi\kappa g} \right) e^{\left( \frac{vx}{2\alpha} \right)} K_0 \left( \frac{v\sqrt{x^2 + y^2 + z^2}}{2\alpha} \right) \quad [^{\circ}\text{C}]$$

Where:  $T$  = temperature,  $T_0$  = initial temperature,  $Q$  = heat transferred to work piece,  $v$  = travel speed,  $\kappa$  = thermal conductivity,  $\alpha$  = thermal diffusivity,  $x$  = position,  $y$  = position,  $z$  = position,  $K_0$  = modified Bessel function of the second kind and zeroth order

Kaplan [13] used a modified version of the moving line source equation to calculate the angle of the keyhole wall based on the incident beam intensity and the heat flow conditions that satisfy evaporation. A schematic of this analysis is shown in Figure 2.33. This procedure was further incorporated by Rai et al. [14], [15], [161] to predict the keyhole geometry. The authors then expanded the analysis to include numerical solutions to determine the fusion zone shape and heat flow conditions.

Figure 2.33. Schematic of moving line source to compute the angle of the keyhole wall based on energy balance [13].

### 2.5.2 Dimensionless Approaches

*Table 2.1. Dimensionless numbers used in fluid dynamics calculations.*

Dimensionless Number	Equation	Description
Fourier Number	$F = \frac{\alpha t}{L^2}$	Dimensionless time
Péclet Number (heat transfer)	$P_e = \frac{Lv}{\alpha} = R_e P_r$	Ratio of advective heat transfer to conductive heat transfer
Prandlt Number	$P_r = \frac{\nu}{\alpha} = \frac{\mu/\rho}{k/(C_p \rho)} = \frac{\mu C_p}{k}$	Ratio of momentum diffusivity to thermal diffusivity
Reynolds Number	$R_e = \frac{\rho v L}{\mu} = \frac{v L}{\nu}$	Ratio of internal forces to viscous forces of a fluid (laminar to turbulent flow)

These dimensionless numbers are utilized in some form of dimensionless or “normalized” penetration analysis [13], [24], [80], [143], [147]. The Péclet number is a ratio of convection to conduction within a fluid and is largely dependent on the fluid flow velocity. Therefore, the Péclet number varies throughout the weld pool based on varying fluid flow velocities and is an approximation at best. The Fourier number is a dimensionless time and can be derived from Fourier’s law of heat conduction. Essentially, the numbers shown in Table 2.1 represent material dependent properties and scale calculations accordingly. However, these numbers are not strictly a subset of analysis and are commonly used in all categories of modeling, including analytical [13] and/or numerical solutions [14], [15], [161]–[163].

One of the earliest reports of HED weld prediction using dimensionless analysis is from Hablanian [8] c.1960. The total energy to melt is expressed as shown in Equation

2.20, which includes the temperature rise to the melting point added to a “temperature” increase based on the heat of fusion. Note that this is similar as previously presented in Equation 2.13. Habalanian [8] utilized the following dimensionless relationship as shown in Equation 2.21 where the right-hand side of the equation is reported to be a function of the velocity, beam diameter, and thermal conductivity. An issue with this approach is incorporation of a constant “C” reported to be 0.09 and added solely based on the empirical data. A log-based plot of the EB weld penetration data and fit line is shown in Figure 2.34. Because of the addition of the constant, the prediction capabilities of this technique are largely limited.

$$\text{Equation 2.20: } T_{mm} = (T_m - T_0) + L_m/C_p \quad [^{\circ}\text{C}]$$

Where:  $T_{mm}$  = modified melting temperature,  $T_m$  = melting temperature,  $T_0$  = initial temperature,  $L_m$  = latent heat of melting,  $C_p$  = specific heat

$$\text{Equation 2.21: } \frac{d_p T_{mm}}{P} = C \sqrt{\left(\frac{\kappa}{v_b d_b}\right)} \quad [\text{unitless}]$$

Where:  $T_{mm}$  = modified melting temperature,  $d_p$  = penetration depth,  $P$  = power,  $v_b$  = beam velocity,  $d_b$  = beam diameter,  $\kappa$  = thermal conductivity,  $C$  = constant

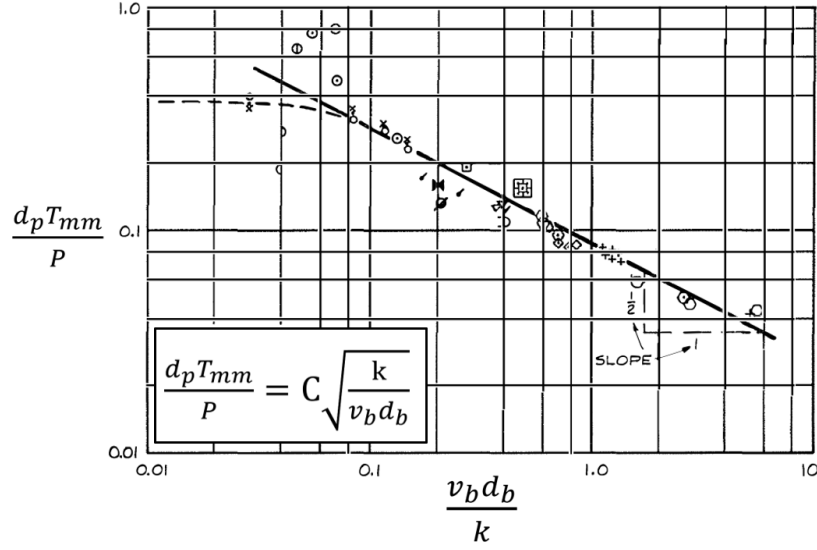


Figure 2.34. Dimensionless plot of EB data for a range of alloys from Hablanian [8].

Locke et al. [138], [164] extracted and manipulated the parameter relationships introduced by Hablanian in an attempt to further correlate the travel speed, beam diameter, and thermal diffusivity versus power, thickness, melting temperature, and thermal conductivity. Locke et al.'s [164] similar relationship is shown in Equation 2.22. Also, using a log-based scale, Locke and Hella [138] plotted the relationships for their CO<sub>2</sub> LBW data along with EB data from Hablanian [8]. The data for these stainless steel welds is shown in Figure 2.35.

$$\text{Equation 2.22: } \frac{v_b d_b}{\alpha} = \frac{P}{d_p T_m k} \quad [\text{unitless}]$$

Where:  $v_b$  = beam velocity,  $d_b$  = beam diameter,  $\alpha$  = thermal diffusivity,  $T_m$  = melting temperature,  $d_p$  = penetration depth,  $P$  = power,  $k$  = thermal conductivity

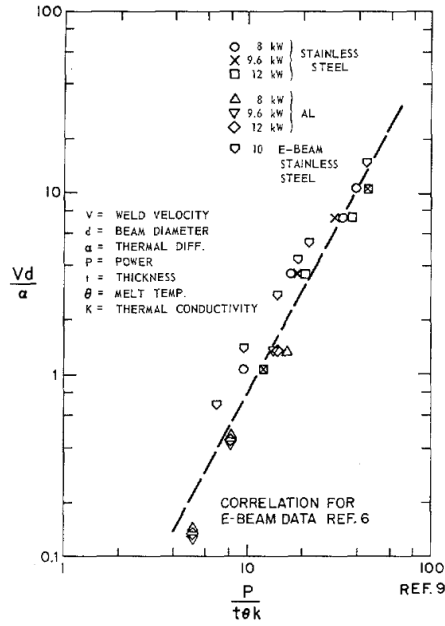


Figure 2.35. Plot of CO<sub>2</sub> laser welding using dimensionless relationships from Locke and Hella [138].

Elmer et. al [159] plotted EB weld data with dimensionless depth, width, and length against a dimensionless parameter including power and travel speed. These parameters were previously developed by Christensen [165] for arc welding conditions. EB welds on 2024 aluminum at lower power (300 W) were reported to maintain close correlation to the dimensionless depth, but higher power deviated from the prediction. Further analysis from Elmer et. al [159] concluded that the keyhole weld shape was dependent on energy density and power density, and relationships were developed to include enthalpy of melting. But data fitting coefficients were necessary to fit the analytical solution to the generated data, therefore eliminating truly predictive capabilities.

Steen and Mazumder [24] reported on dimensionless relationships used to plot normalized speed versus normalized power based on derivations originally from Swift-Hook and Gick [80]. The normalized velocity can be defined by a modification of the Péclet number utilizing the beam radius. Utilization of the modified Péclet number was previously performed by Locke and Hella [138] by employing the weld width rather than the beam radius. An issue can arise with weld width analysis based on drastic differences attributed to parameters, properties, and the HED weld regimes. Also, the assumption must be made that the welding speeds are sufficiently high, so the Péclet number is much greater than one (i.e., convection  $\gg$  conduction).

Quintino et al. [134] attempted a similar approach utilizing a relationship between what is referred to as the welding speed parameter and laser power parameter as shown in Equation 2.23 and Equation 2.24, respectively. They defined a linear relationship between these parameters with a slope of approximately 0.66 between normalized speed and normalized power for the y-axis and x-axis respectively. This produced the relationship shown in Equation 2.25. Quintino et al. [134] reported that the slope is the difference in the process melting efficiency. It should be noted that Steen and Mazumder [24], based on the Swift-Hook and Gick [80] relations, reported a slope of approximately 0.48 [129].

$$\text{Equation 2.23: Normalized Speed} = \frac{vw}{\alpha} \quad [\text{unitless}]$$

$$\text{Equation 2.24: Normalized Power} = \frac{P}{d_p K \left( T_m - T_0 + \frac{H}{C_p} \right)} \quad [\text{unitless}]$$

$$\text{Equation 2.25: } Y = 0.66X$$

Where:  $v$  = welding velocity,  $w$  = weld width,  $\alpha$  = thermal diffusivity,  $Q$  = absorbed power,  $d_p$  = penetration depth,  $T_m$  = melting temperature,  $T_0$  = initial temperature,  $H_f$  = latent heat of fusion,  $C_p$  = specific heat,  $Y$  = normalized speed, and  $X$  = normalized power

Hann et al. [143], [147] incorporated both input parameters and material properties for weld penetration prediction. They fit a function to data through what they deemed as “optimized data reduction techniques” and came up with a function incorporating a “normalization” constant [143]. In addition, Hann et al. [147], [166] reported and used interaction time, “characteristic thermodynamic” time, and dimensionless depth. Whereas, the characteristic thermodynamic time was reported as the beam diameter squared divided by the material thermal diffusivity as shown in Equation 2.26 [143]. The normalized depth calculation is presented in Equation 2.27 and is based on a measured penetration depth.

$$\text{Equation 2.26: } t_c = \frac{4r_b^2}{\alpha} \quad [s]$$

Where:  $t_c$  = characteristic thermodynamic time,  $r_b$  = beam radius,  $\alpha$  = thermal diffusivity

$$\text{Equation 2.27: } d_p^* = \frac{d_p}{2r_b} \quad [\text{unitless}]$$

Where:  $d_p^*$  = dimensionless penetration depth,  $d_p$  = penetration depth,  $r_b$  = beam radius

A plot of dimensionless depth versus normalized power was recreated from Hann et al. [147] and is shown in Figure 2.36 with the equations represented on the respective axes. Continued analysis incorporated material properties based on what Hann et al. [147], [166] considered to be normalized enthalpies. The issues with this approach are based on a necessary constant and the requirement of experimentally determined values to establish the dimensionless depth.

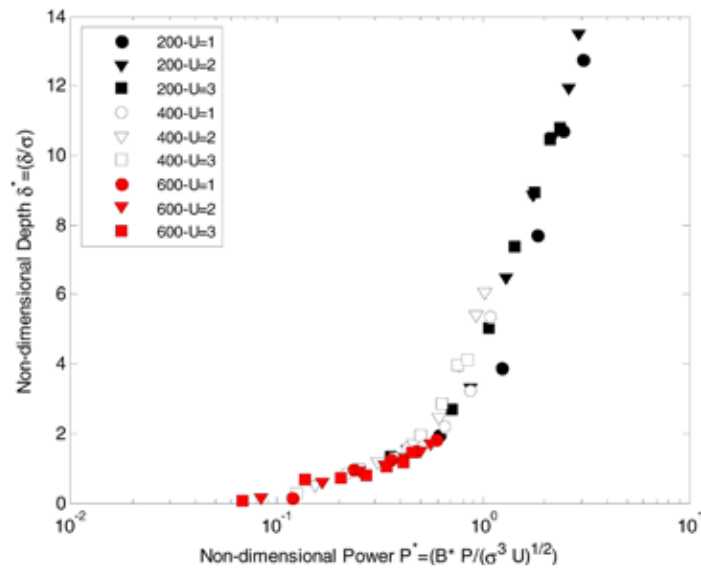


Figure 2.36. Normalized depth as a function of nondimensional power [143].

The approach of normalized enthalpy from Hann et al. [143], [147] was extended to compute the distinction between conduction and keyhole mode welding for additive manufacturing by Rubenchik et al. [167] and King et al. [168]. King et al. [168] reported that their experimental data showed that values of normalized enthalpy ( $\Delta H/H_m$ ) of  $\approx 30$

indicated the transition from conduction to keyhole mode welding regardless of the beam diameter. The calculation for normalized enthalpy is shown in Equation 2.28.

$$\text{Equation 2.28: } \frac{\Delta H}{H_m} = \frac{\eta P}{H_m \sqrt{\pi \alpha \nu r_b^3}} \quad [\text{unitless}]$$

Where:  $\Delta H$  = change in enthalpy,  $H_m$  = enthalpy at melting,  $\eta$  = absorptivity,  $P$  = power,  $\alpha$  = thermal diffusivity,  $\nu$  = travel speed,  $r_b$  = beam radius

### 2.5.3 Numerical Approaches

Numerical models utilize techniques such as the finite difference or finite element methods to solve conservation equations of mass, momentum, and/or energy [15], [133], [161], [162], [169], [170]. Although iterative solvers are more complex, these models are also subjected to highly influential assumptions regarding physical properties and beam interactions. An advantage to numerical solutions is the ability to define the heat source shape, such as a cylinder or complex geometries, rather than a line or point source, and perform complex computations to better understand the physics associated with the process. Typically, numerical solutions are solved with commercial software packages [24], [171]. The disadvantages to numerical simulations are long computational times and limited ability to fundamentally solve weld penetration. Because of this, these approaches were determined outside the scope of this investigation.

#### **2.5.4 Artificial Neural Networks**

An artificial neural network (ANN) is a complex algorithm that combines directional flow of mathematical operations in an attempt to emulate the neurological thought process of living animals [172]–[175]. Using neural network techniques is a major deviation from analytical/numerical modeling because physical interactions associated with the incident beam and the workpiece are not directly considered. ANN models fit solutions solely based on trends of the experimental data but can be extremely useful given that adequate amounts of quality, experimental data is available. Neural networks have been applied to all sectors of industry from aerospace to financial analysis [176]. In theory, ANNs could be used to predict the physical equations governing weld penetration.

##### **2.5.4.1 ANN Overview**

One type of network is referred to as a feedforward neural network, which is the most fundamental and widely used network [175]. The structure of this network includes three main components: input layer, hidden layer, and output layer [172]. The input layer contains simple units called neurons that pass the input data to the subsequent layers. For HED welding, the inputs may include power, beam diameter, and travel speed. A schematic example of the simplest neural network, called a perceptron, is shown on the left in Figure 2.37. A weight ( $w$ ) is multiplied to each value of an input vector and summed within what is referred to as a node. Biases are also used and summed to the scaled inputs ( $x$ ) after the inputs are multiplied by the weight ( $w$ ) as shown on the right in

Figure 2.37. The summed value from the inputs, weights, and bias are then passed through an activation function (sign function shown in Figure 2.37) to produce the output (y) as zero or one [172], [176]. The mathematical calculations for a single node with a bias relating to Figure 2.37 is shown in Equation 2.29 [173].

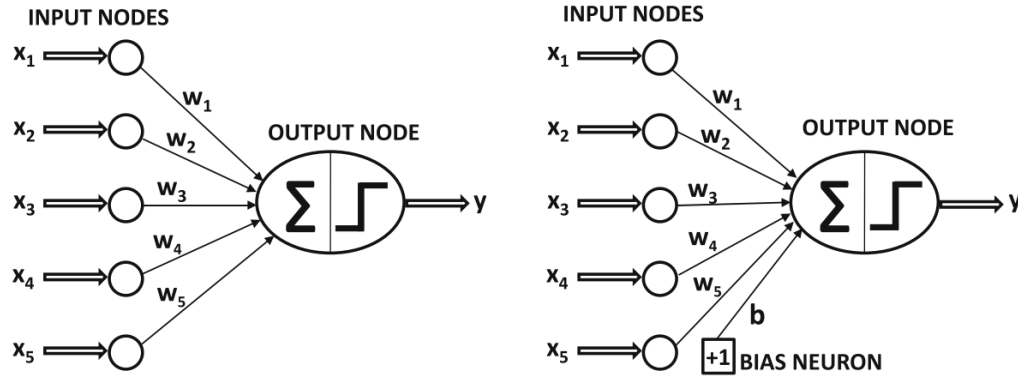


Figure 2.37. Perceptron network with nodes or inputs ( $x$ ) shown as circles and connected to a neuron with a weight ( $w$ ). Without a bias (left) and with a bias (right) [172].

$$\text{Equation 2.29: } y = \text{sign}\{\sum_{j=1}^j w_j x_j + b\}$$

Where:  $y$  = output,  $x_j$  = inputs,  $w_j$  = weights,  $b$  = bias

The initial layer containing the activation function is a mathematical operation to normalize the values. Many activation functions exist, but the activation function used in this study was a sigmoid function where values can range between zero and one as shown in Equation 2.30 [175]–[177]. This node(s) containing the weights, biases, and activation function(s) is referred to as the hidden layer.

$$\text{Equation 2.30: } f(x) = \frac{1}{1+e^{-x}}$$

To scale the network up for improved fitting performance, similar to higher orders for a polynomial fit, nodes are added and used in a method defined as a fully connected network. A schematic of this is shown in Figure 2.38. Every value from the input is passed to each node within the first layer of the network (fully connected). Similarly, the number of layers may be increased to improve the model performance, where each layer acts as an input to the next layer. All the nodes between the inputs and output layers are referred to as hidden layers because they are not available to the user.

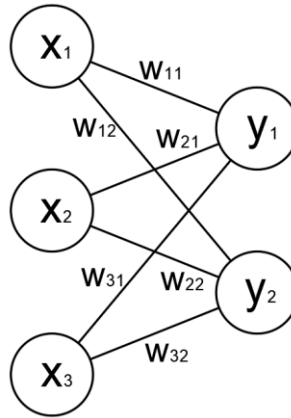


*Figure 2.38. Schematic of a fully connected network where all inputs of one layer are connected to all the nodes of the following layer.*

The last layer or output layer converts the normalized values from the activation functions in the hidden layer to the desired results. Different transfer functions may be used in the output layer, but for the purpose of this study only linear scaling was used [172]. At this point, nothing has mentioned the values of weights and biases used in

producing the desired output. For this to happen, the desired outputs must be known, and there are many techniques for initializing values for weights and biases. The simplest of techniques is to randomly assign a value to the weight and set the biases to zero.

After the first set of outputs are determined, the ANN calculated values are compared to the empirical values and an error is determined. This error is continually fed back into the model to reassign new weights and biases until sufficient model outputs are achieved. “Backpropagation” is one technique used to compare the predicted output to the empirical values, and many variations of the algorithms exist [175], [176]. A single round of evaluating a network for the output relative to the inputs is referred to as an “epoch”. In instances where training cannot be performed, the algorithms are programmed to exit training after a defined number of epochs.

Issues with neural networks stem from the need to be trained on extraordinarily large data sets that are not always practical to experimentally obtain [172]. This is particularly an issue in welding where modeling is generally warranted based on not wanting to undergo time consuming and costly experimental trials. However, with enough quality, experimental data ANN models can be practical tools to aid in weld prediction.

#### ***2.5.4.2 ANNs Relating to Weld Prediction***

Neural networks (NN) have been used in many welding related scenarios such as arc weld penetration prediction [177]–[180] and ferrite prediction in stainless steel arc

welds [174], [181]. Vitek et al. [174] reported the ability to improve prediction accuracy compared to other ferrite number prediction models.

Most neural network modeling results from prior literature are based on data from weld monitoring devices and/or are not specific to LBW. These are attempts to monitor the process in real-time [182]–[184] and couple this information to a NN to predict weld characteristics. However, these monitoring techniques are highly sensitive to process variations and have limited use in production environments. Other models have predicted weld bead geometries based on experimental data [177]–[179], [185], but the information is limited regarding LBW [180].

## **2.6 Microstructural Phenomena**

The following section will summarize the results from previous literature regarding microstructure evolution relating to HED fusion welding. This starts with weld solidification and transitions to the specific behavior and associated issues involving SS alloys and Ti-6Al-4V.

### ***2.6.1 Solidification Behavior, Thermal Gradients, and Growth Modes***

Understanding the fundamentals of solidification is necessary to understand the liquid–solid transformation behavior. The nature of HED processes can result in variations in solidification rates based on process parameters, and these solidification rates influence weldability related issues such as phase fractions, solidification cracking, and precipitation.

Growth of a crystalline solid in welding applications occurs heterogeneously, or with preferential nucleation off a solid substrate. The heterogenous nucleation occurs because the activation barrier is smaller than for homogenous nucleation within the weld pool (i.e., energetically more favorable) [186]. Most often, this substrate/interface is the fusion boundary where growth initiates epitaxially or with the same structure and orientation as the grain at the solid–liquid interface. The crystal then continues to grow in preferential growth directions, parallel to and in the opposite direction of the thermal gradient [186], [187]. For the materials of interest, nucleation and growth occurs as either BCC, FCC, or competitive BCC/FCC structures. These cubic structures attempt to maintain preferential growth in the  $\langle 100 \rangle$  crystallographic or “easy growth” directions [123], [186].

However, the thermal gradient constantly changes depending on the location along the solid–liquid interface. These grains may need to alter the growth direction to maintain perpendicular growth relative to the heat source isotherms. An illustration of this is shown in Figure 2.39. The schematic in Figure 2.39a shows a teardrop shaped weld pool where the fusion boundary or isotherms maintain the same angle from the fusion boundary to the weld centerline. In this condition, there is no driving force for the grains to alter direction, but when the weld pool is round or takes on non-uniform shapes, the grains must alter direction to follow the maximum temperature gradient and maintain a  $\langle 100 \rangle$  direction [186]. This is shown in Figure 2.39b. The grains that cannot effectively change direction become extinguished by surrounding grains that are favorably oriented

to both, the thermal gradient and easy growth direction. This mechanism is referred to as “competitive” growth [123], [188].

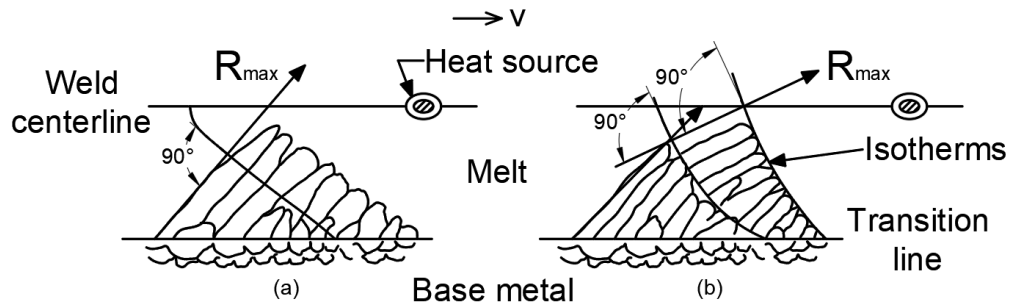


*Figure 2.39. Illustration of columnar grain growth continually changing to maintain a  $\langle 100 \rangle$  growth direction and perpendicular to the isotherm boundary. Recreated from Porter and Easterling [186].*

A solid crystal forming by growth into a liquid is often described as a dendrite. The term dendrite is derived from the Greek work “dendros” meaning tree and in reference to the tree-shaped morphology [189]. The morphology of the crystalline growth is dependent on the thermal gradient ( $G_L$ ) and the solidification rate ( $R_L$ ) at the solid–liquid interface [187], [190]. A schematic showing how the thermal gradient and solidification rate influence crystal formation is shown in Figure 2.40 with the morphologies represented in Figure 2.41. The HED processes are capable of substantially increasing the temperature gradients and solidification rates as compared to arc-based processes. The product of the thermal gradient and the solidification rate ( $G_L \cdot R_L$ ) determines the scale of the solidification structure, while the ratio of the thermal gradient to the solidification rate ( $G_L/R_L$ ) determines the mode of solidification shown in Figure

2.40 and Figure 2.41 [14], [123], [187]. Generally, LB weld structures range from cellular to columnar dendritic morphologies.

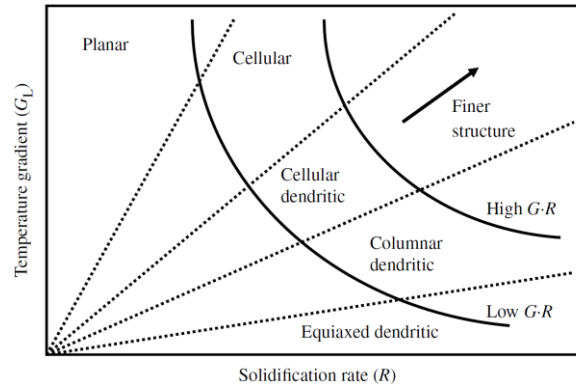


Figure 2.40. Influence of thermal gradient versus solidification rate on crystal formation from Lippold [188].

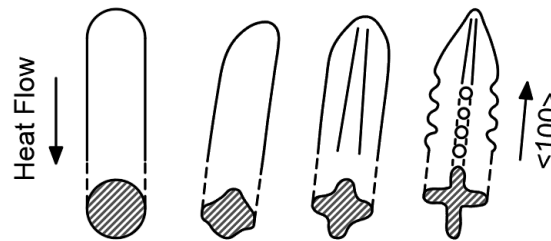


Figure 2.41. Schematic representing the transition from cellular to columnar dendritic growth (left to right). Recreated from David and Vitek [187].

Alloyed systems melt over a range of temperatures where solid and liquid can coexist due to elemental partitioning. This range of temperature defined by the equilibrium phase diagram solidus and liquidus lines is referred to as the solidification temperature range (STR). In addition to the thermal gradient and solidification rate, the STR will influence the solidification behavior by promoting constitutional supercooling as reported by David and Vitek [187]. These modes are shown in Figure 2.42. Higher

constitutional supercooling occurs when the actual temperature gradient is shallower than the equilibrium profile (i.e., where the remaining liquid during cooling is below the liquidus temperature). This region or “mushy zone” is composed of both solid and liquid [123]. At high constitutional supercooling, equiaxed dendritic formation may be possible where it becomes energetically favorable to nucleate within the liquid. Suppressing constitutional supercooling to produce planar growth requires steep temperature gradients and low solidification rates that typically only occur at the fusion boundary. David and Vitek [187] defined the criterion for supercooling and planar front instability as shown in Equation 2.31 [123], [187], [191]. This is based on the slope of the solidus and liquidus line and partition coefficient,  $k$ , which is the composition of the solid divided by the composition of the liquid as shown in Equation 2.32. Therefore, to avoid the breakdown at the interface and create planar solidification, the thermal gradient must be equal to or greater than  $(R_L \cdot \Delta T)/D_L$ . For a more detailed explanation, the reader is referred to References [123], [187]–[189], [191].

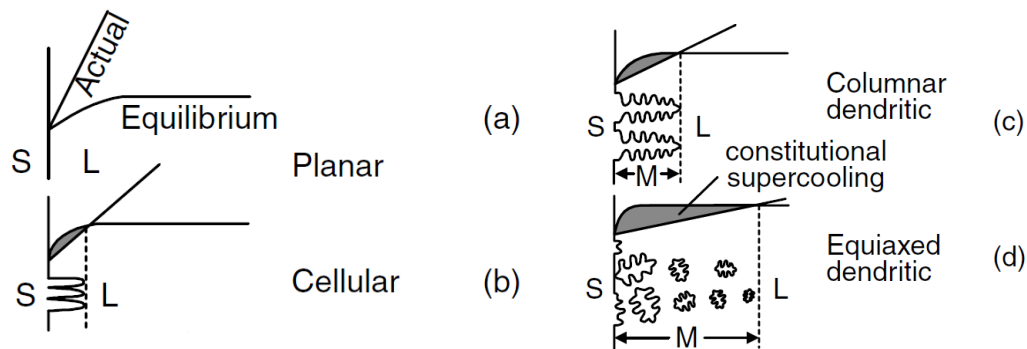


Figure 2.42. Influence of constitutional supercooling on solidification modes from Kou [123] where S, L, and M represent solid, liquid, and mushy zones respectively.

$$\text{Equation 2.31: } \frac{G_L}{R_L} < \frac{m_L C_o (k-1)}{k D_L} \quad \text{or} \quad \frac{G_L}{R_L} < \frac{\Delta T_o}{D_L} \quad \left[ \frac{\text{mm}^2}{\text{s}} \right]$$

Where:  $G_L$  = thermal gradient in the liquid,  $R_L$  = solidification rate,  $m_L$  slope of equilibrium liquidus line,  $C_o$  = nominal alloy composition,  $D_L$  = diffusion coefficient of solute in the liquid,  $k$  = partition coefficient,  $\Delta T_o$  = temperature between the liquidus and solidus

$$\text{Equation 2.32: } k = \frac{C_S}{C_L} \quad [\text{unitless}]$$

Where:  $k$  = partition coefficient,  $C_S$  = composition of the solid,  $C_L$  = composition of the liquid

Kou presented a schematic of varying pool shapes based on heat input and welding speed as shown in Figure 2.43. At low heat inputs or travel speed, elliptical weld pools result in low constitutional supercooling and promote columnar and cellular growth. At high heat input and high welding speeds, constitutional supercooling increases with potential for nucleation of equiaxed dendritic grains along the weld centerline. This was demonstrated by David and Vitek [187] via EB welding on an Fe-15Cr-15Ni alloy with and without sulfur as shown in Figure 2.44. At high purity, only a columnar dendritic mode was reported to be present, but when the alloy was doped with sulfur, equiaxed dendrites formed along the weld centerline. Although it is likely that surface tension and weld pool currents varied with the addition of sulfur, constitutional supercooling was also increased through solute partitioning during solidification [187]. Therefore, there was a substantial increase in the STR.

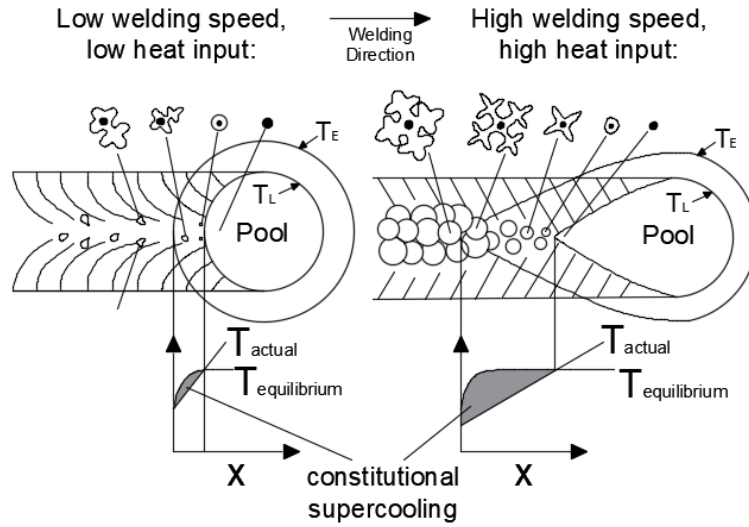


Figure 2.43. Schematic of constitutional supercooling based on heat input and weld pool geometry from Kou [123].

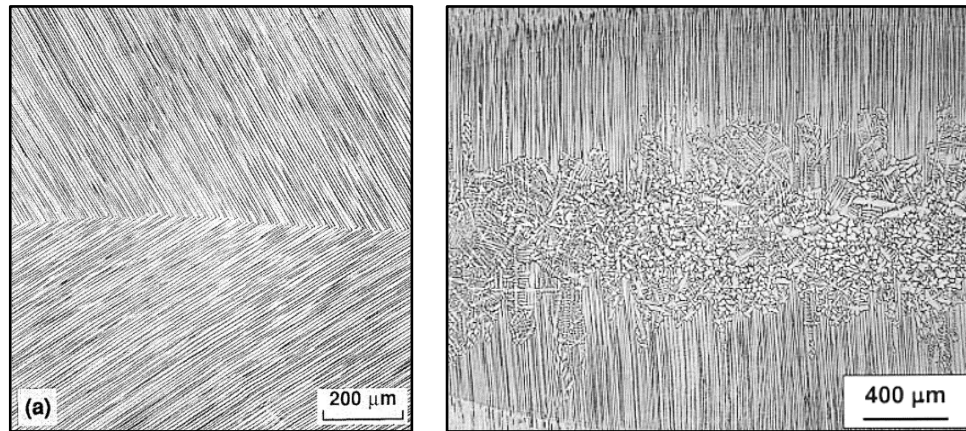


Figure 2.44. EB weld on a single crystal Fe-15Cr-15Ni alloy: pure (a) and with sulfur (b) from David and Vitek [187].

#### 2.6.1.1 Grain Orientation Related to HED Welds

Conduction mode welds with elliptical pools behave similar to arc welds at relatively low travel speeds. Figure 2.45a represents a conduction mode pool geometry and crystal growth from Rappaz et al. [192], [193]. They reported that grains grow

gradually from the weld toe towards the weld centerline. However, transition region and deep penetration HED welds generate distinct weld pool geometries that can drastically vary relative to power to travel speed ratios. Due to the geometric variation of the solid-liquid interface with respect to the travel direction, it is possible to develop abrupt changes in the crystal growth direction. A schematic representing a high aspect ratio weld pool and the changing growth directions is shown in Figure 2.45b. The schematics in Figure 2.45 were based on experimentally observed growth directions for EB welds on an Fe-15Cr-15Ni single crystal alloy [193]. A keyhole mode weld produced by welding in the  $\langle 100 \rangle$  direction is shown in Figure 2.46.

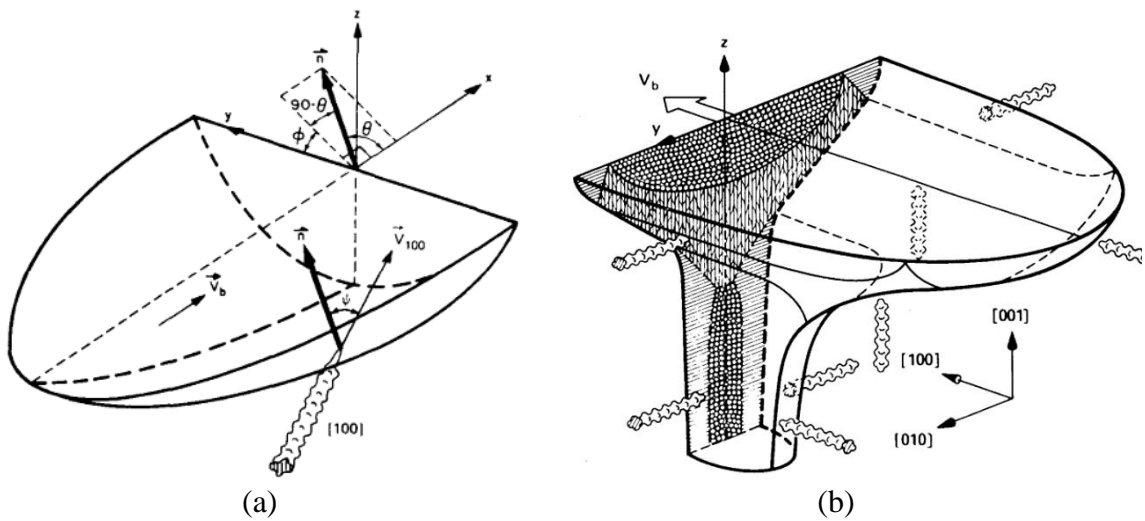


Figure 2.45. Illustration of crystal growth in an elliptical weld pool geometry (a) [192], [193]. Illustration of keyhole weld pool showing potential preferential growth directions (b) [193].

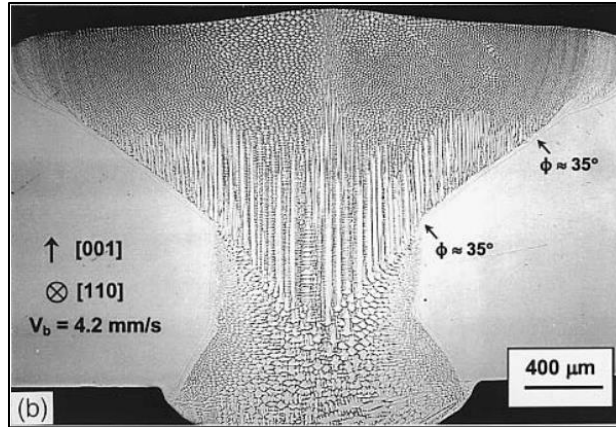


Figure 2.46. EB weld at 4.2 mm/s on an Fe-15Cr-15Ni single crystal alloy showing columnar dendritic growth in different orientations from Rappaz et al. [123], [193].

The dendrites growing normal to the interface ( $\vec{n}$ ) grow at the slowest velocity and require the lowest degree of undercooling. Thus, the crystals conform to the shape of the weld pool until impinged upon by more favorably oriented dendrites. Along the keyhole portion of the weld, grains grew inward from the outer edge of the fusion boundary and trailed the back, center while remaining normal to the weld/material surface. At the transition from the keyhole to the “nail head”, grains grew vertically toward the surface until meeting grains trailing the top of the weld pool and growing with the direction of travel. It is important to note that the welds presented and discussed regarding Figure 2.44-Figure 2.46 were produced on a single crystal alloy and do not directly reflect the behavior of polycrystalline materials, as evaluated in this study.

### 2.6.1.2 Solidification Modes and Cell Size

Elmer et al. [194] reported a transition between dendritic solidification to cellular solidification as shown in Figure 2.47. These were EB welds at travel speeds of 6.5 mm/s

(Figure 2.47a) and 100 mm/s (Figure 2.47b) on a SS alloy near a 58Fe-22Cr-19Ni composition in weight percent (wt%) [194]. Not only did these results show the change in structure, but they also showed the difference in scale of the structure from a larger, cellular dendritic morphology to a finer, cellular structure.

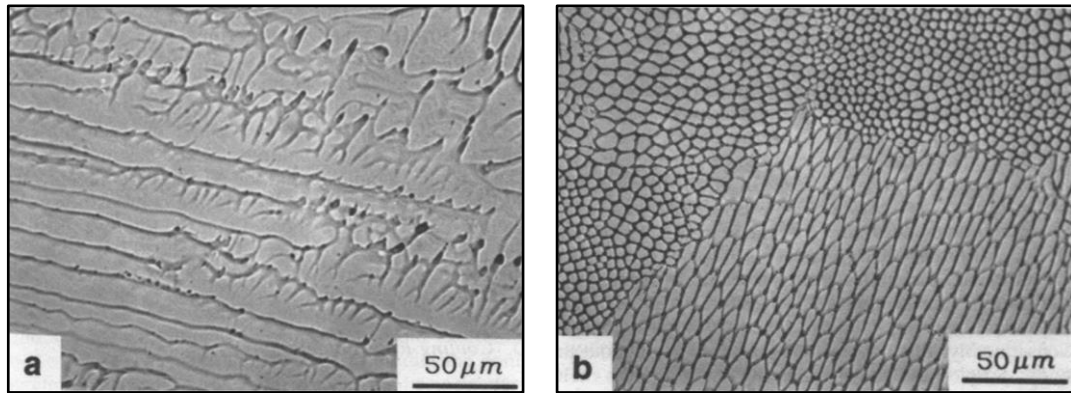


*Figure 2.47. Primary austenite solidification showing dendritic solidification at a 6.5 mm/s travel speed (a) and cellular solidification at a 100 mm/s travel speed (b) [194].*

Directional growth of dendrites into the weld pool, as previously depicted in Figure 2.39 and Figure 2.43, results in parallelly aligned crystals with distinct spacings relating to the thermal gradient and solidification rate. The spacing between the cores or “trunks” of the dendrites is comparable to the grain diameter. This is referred to as the primary dendrite arm spacing ( $\lambda_1$ ). Similarly, a secondary dendrite arm spacing can be defined for columnar and equiaxed dendrites ( $\lambda_2$ ). The growth of the cell or dendrite occurs due to the breakdown of planar solidification and via a perturbation advancing into the liquid. As this perturbation tip advances, solute is rejected laterally outward and

accumulates during continued growth or ripening [186], [189]. The solute partitioning allows for distinguishing the individual cells and characterizing the dendrite arm spacing.

The combination of high solidification rates and steep thermal gradients achievable with EBW and LBW can reduce cell sizes as compared to other fusion processes. Figure 2.48 shows cell size reduction results produced by Elmer et al. [195]. This micrograph was produced with an electron beam weld on a 58.5Fe-25Cr-16.5Ni alloy with a reported cooling rate of  $1.5 \times 10^6$  °C/s (top in Figure 2.48) versus the substrate cooled at three orders of magnitude slower (bottom in Figure 2.48).

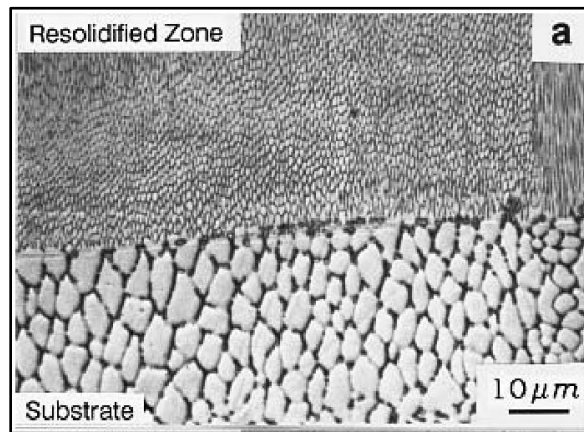


*Figure 2.48. Reduced cell size for an EB weld (top) cooled at  $1.5 \times 10^6$  °C/s and a substrate cooled at  $2 \times 10^3$  °C/s (bottom) [195].*

Prior literature has shown correlations between dendrite arm spacing and cooling rates. Kou [123] reported that the cell or dendrite arm spacing is based on a heat input–travel speed ratio and expressed a secondary dendrite arm spacing relationship as shown in Equation 2.33. This relationship is dependent on solidification time or cooling rate. Using an approximation of solidification time, Kou and Le [196] plotted a logarithmic

relationship between secondary dendrite arm spacing and solidification time for 310 stainless steel as shown in Figure 2.49.

$$\text{Equation 2.33: } \lambda_2 = at_s^n = b(\varepsilon)^{-n} \quad [\mu\text{m}]$$

Where:  $\lambda_2$  = secondary dendrite arm spacing,  $t_s$  local solidification time,  $a$  = constant,  $b$  = constant,  $n$  = constant,  $\varepsilon$ =cooling rate

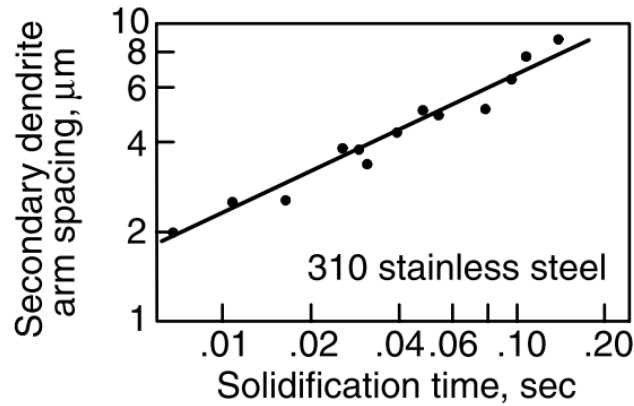


Figure 2.49. Relationship between solidification time and secondary dendrite arm spacing for 310 stainless steel from Kou and Le [196].

Katayama and Matsunawa [197] experimentally determined the constants for a Type 310 SS as presented in Equation 2.34. These equations were used by Elmer et al. [194] to approximate solidification rates in other SS alloys as previously represented in Figure 2.48. Contrary to Equation 2.34, Kurz and Fisher [189] stated that primary dendrites do not obey these simplified relationships. Based on the results of Trivedi [198], [199], Kurz and Fisher [189] reported that the primary arm spacing is proportional

to the difference in temperatures from the dendrite tip and root divided by the mean thermal gradient. The calculation is shown in Equation 2.35 [189].

$$\text{Equation 2.34: } \lambda_1 = 80(\Delta T)^{-0.33}, \quad \lambda_2 = 25(\Delta T)^{-0.28}, \quad [\mu m]$$

Where:  $\lambda_1$  = primary dendrite arm spacing,  $\lambda_2$  = secondary dendrite arm spacing,  $\Delta T$  = composition of the liquid

$$\text{Equation 2.35: } \lambda_1 = \sqrt{\frac{3(T^* - T_s')R_L}{G_L}} \quad [\mu m]$$

Where:  $\lambda_1$  = primary dendrite arm spacing,  $T^*$  = dendrite tip temperature,  $T_s'$  = eutectic or solidus temperature,  $R_L$  = solidification rate,  $G_L$  = thermal gradient

The influential factor regarding crystallographic growth into the liquid is based on the dendrite tip temperature [191], and this localized undercooling not only dictates the stability and growth modes but the size of cells or dendrites. This is particularly important in SS alloys that may solidify through a region where competitive growth between  $\delta$ -ferrite and austenite exists [190].

## 2.6.2 Stainless Steel Microstructure

Varying proportions of ferrite and austenite can drastically influence weldability, mechanical properties, and corrosion resistance in SS welds. The ability to form primary ferrite is advantageous when welding austenitic stainless steels by reducing the susceptibility to solidification cracking [5], [17], [200], [201], and maintaining equivalent

phase fractions is crucial for mechanical properties and corrosion behavior in DSS [5], [19], [202].

The transformation into ferrite or austenite for a given set of process conditions is based on the proportions of elements added to the alloy. Applicable elements that thermodynamically stabilize ferrite include Cr, Mo, Nb, Ti, and Si, and applicable elements that stabilize austenite include Ni, C, N, Mn, and Cu. Assuming a ternary alloy that only contains Fe, Cr, and Ni, pseudo binary phase diagrams were developed by Lippold and Savage [200]. These represent the phase formations at varying SS compositions under equilibrium cooling conditions. Figure 2.50 shows similar diagrams from Kou and Le [196].

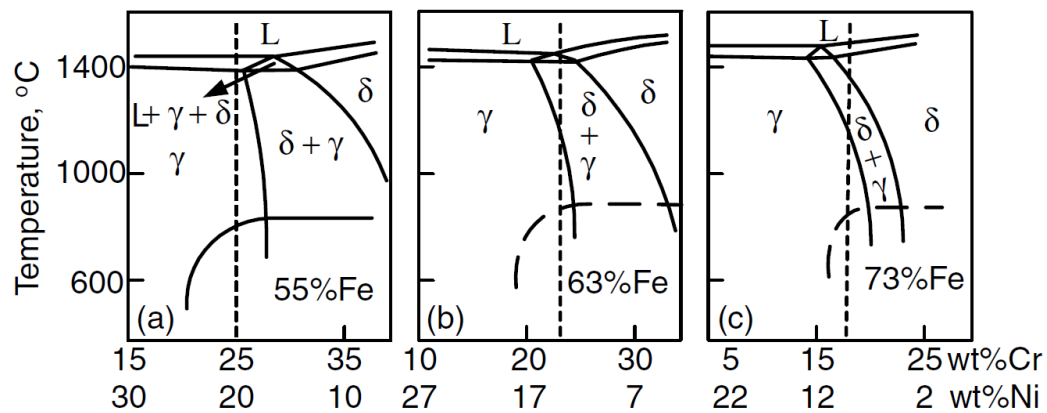
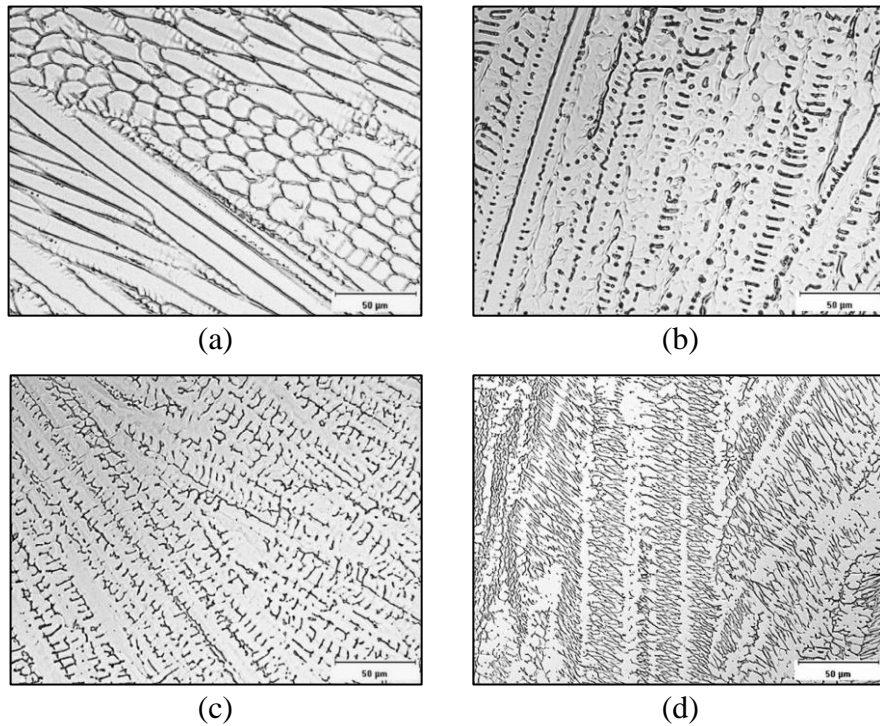


Figure 2.50. Pseudo-binary Fe-Cr-Ni phase diagrams from Kou and Le [123], [196] at 55% Fe (a), 63% Fe (b), and 73% Fe (c).

The pseudo-binary diagrams show the differences in phase formations by altering the Cr/Ni contents while iron remains constant. A triangular region exists showing the coexistence of ferrite, austenite, and liquid. Compositions left of this triangle stabilize

primary austenite (Type A) solidification, while compositions right of this triangle stabilize primary ferrite (Type F) solidification. Within this three-phase region, solidification can occur as primary austenite with secondary ferrite (Type AF) or primary ferrite with secondary austenite (Type FA). Microstructure morphologies produced under varying solidification modes are shown in Figure 2.51 [5].



*Figure 2.51. Solidification growth modes: primary austenite (a), primary austenite with eutectic ferrite (b), a skeletal morphology of primary ferrite with austenite (c), and lathy morphology of primary ferrite with austenite (d) [190].*

Type A solidification is shown in Figure 2.51a where the cells and dendrites are distinctly visible based on solute partitioning and limited back diffusion in the solid-state. In Figure 2.51b, eutectic ferrite is present in the interdendritic regions of austenite

indicative of Type AF solidification. Due to the enrichment of ferrite stabilizing elements such as Cr and Mo into the liquid and slow solid-state diffusion, the ferrite at the grain and subgrain boundaries remains stable to room temperature. At higher Cr/Ni contents, primary ferrite and secondary austenite, or Type FA, results through ferrite initially nucleating and austenite forming via a peritectic–eutectic reaction that is composition dependent [200], [203]. The resulting microstructure from a slower cooling rate or lower Cr/Ni content is characterized as skeletal, or vermicular, as shown in Figure 2.51c. Increasing the cooling rate or Cr/Ni contents decreases time for diffusion and results in a refined morphology described as lathy ferrite as shown in Figure 2.51d [5], [204].

However, the complexity associated with alloys containing a variety of elemental compositions skews the distinct boundaries depicted through these ternary diagrams. In an effort to predict ferrite content in SS weld metal, numerous diagrams were developed from experimental, arc welding data [205]–[207]. These diagrams weight the percentages of alloying elements in the analysis. Using this data, “maps” of solidification modes were produced according to relationships based on chromium-to-nickel equivalencies ( $Cr_{eq}/Ni_{eq}$ ) relating to ferrite and austenite promoting elements, respectively. A common diagram is the WRC-1992 diagram from Kotecki and Siewert [206] and is shown in Figure 2.52. Other equivalency relationships exist, but this is reported to be the most accurate and reliable predictive diagram for austenitic and duplex stainless steel weld metal [5]. The formulas for three equivalency relationships utilized in this study are

shown in Equation 2.36-Equation 2.38 from Kotecki and Siewert (WRC-1992) [206], Kujanpää et al. [204], and Hammar and Svernnson [208], respectively.

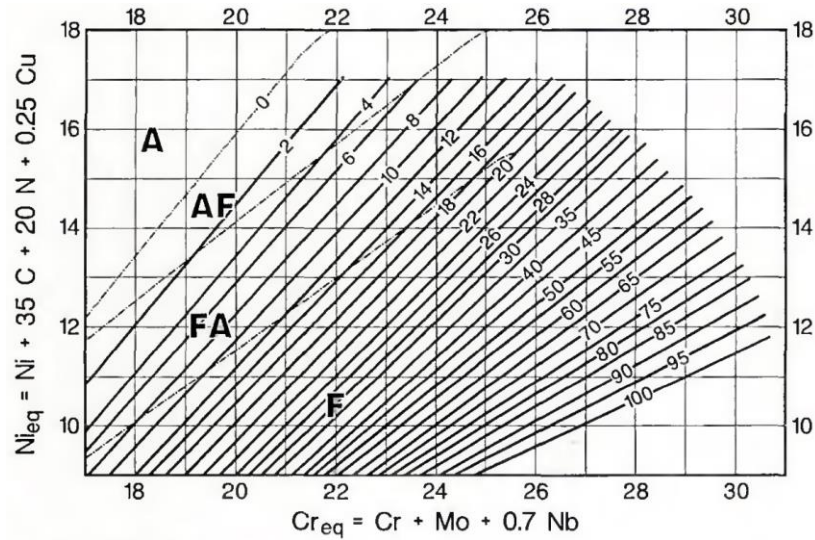


Figure 2.52. WRC-1992 constitution diagram from Kotecki and Siewert based on ferrite number (FN) [206].

Equation 2.36: WRC-1992  $Cr_{eq}$  and  $Ni_{eq}$  Formulas [206]

$$Cr_{Eq.} = Cr + Mo + 0.7Nb$$

$$Ni_{Eq.} = Ni + 35C + 20N + 0.25Cu$$

Equation 2.37: Suutala  $Cr_{eq}$  and  $Ni_{eq}$  Formulas [204]

$$Cr_{Eq.} = Cr + 1.37Mo + 1.5Si + 2Nb + 3Ti$$

$$Ni_{Eq.} = Ni + 0.31Mn + 22C + 14.2N + Cu$$

Equation 2.38: Hammar and Svernnson  $Cr_{eq}$  and  $Ni_{eq}$  Formulas [208]

$$Cr_{Eq.} = Cr + 1.37Mo$$

$$Ni_{Eq.} = Ni + 0.31Mn + 22C + 14.2N$$

In addition to the ratios of ferrite and austenite promoting elements, impurity elements, such as sulfur, phosphorus, and boron, further increase solidification cracking susceptibility. The original Suutala diagram developed by Kujanpää et al. [204] showed

crack susceptibility of phosphorus and sulfur contents relative to a  $Cr_{eq}/Ni_{eq}$ . This diagram is shown in Figure 2.53. Although very low phosphorus and sulfur contents can reduce cracking susceptibility, cracking is best controlled via a  $Cr_{eq}/Ni_{eq}$  above 1.48.

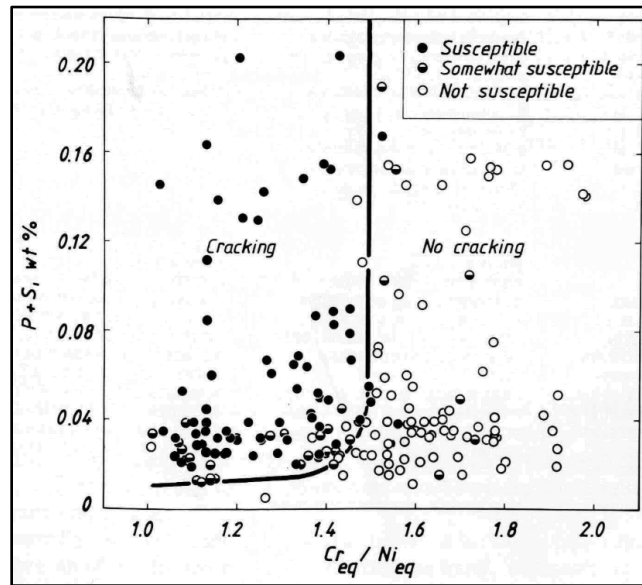
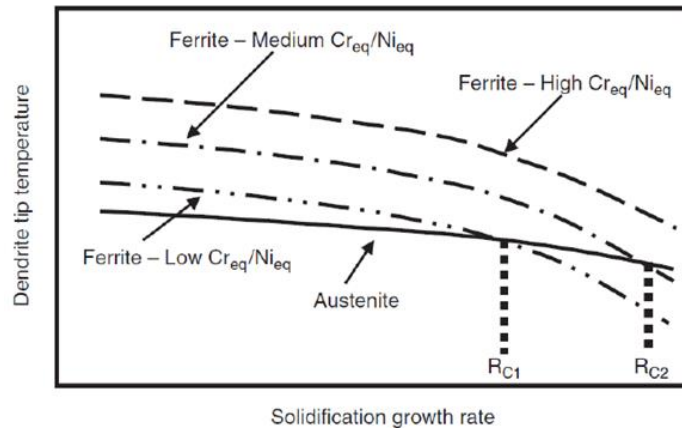


Figure 2.53. Suutala diagram showing cracking susceptibility for sulfur and phosphorous versus  $Cr_{eq}/Ni_{eq}$  contents [204].

Because HED welding produces rapid solidification and cooling rates, the previously mentioned diagrams are not directly applicable. In arc-based processes, maintaining a ferrite content above  $\approx 3\text{--}5\%$  or a ferrite number (FN) of 3-5 is known to successfully mitigate solidification cracking susceptibility. However, high solidification rates in HED processes support a transition from primary ferrite to primary austenite solidification [17], [190], [209], [210]. This is believed to be based on the dendrite tip undercooling and stability of ferrite versus austenite [189], [190], [211]–[213]. Lippold

[190] produced a schematic showing the relative differences between dendrite tip temperatures versus solidification growth rates. This is shown in Figure 2.54. It was proposed by Suutala [213] that the ferrite dendrite tip temperatures reduce at a greater rate than austenite tip temperatures relative to increasing solidification rates. Thus, a critical growth rate exists where austenite growth becomes more stable than ferrite, and increasing the  $Cr_{eq}/Ni_{eq}$  shifts the critical point to higher solidification growth rates [190], [213].



*Figure 2.54. Schematic of dendrite tip temperature versus solidification growth rate in stainless steels with varying  $Cr_{eq}/Ni_{eq}$  from Lippold [190].*

The change in solidification mode along with restraint, grain orientation, and impurity levels can lead to increased cracking susceptibility during HED welding.

Lippold [17] reported crack formation in a deep penetration EB weld as shown in Figure 2.55. A transition from primary ferrite to primary austenite solidification was caused by an increased solidification rate at the weld centerline and resulted in solidification cracking.

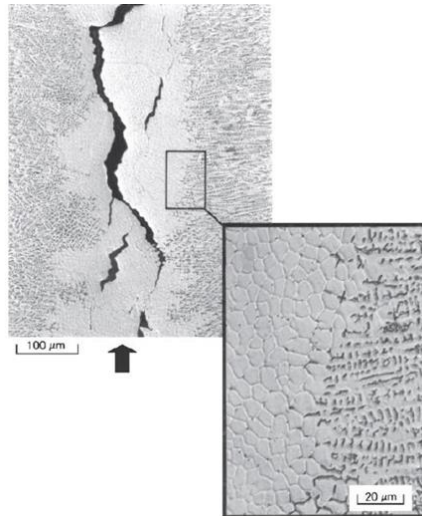


*Figure 2.55. Weld solidification crack in the centerline of a SS EB weld [17].*

Elmer et al. [194] studied solidification modes and solid-state phase transformations in Fe-Cr-Ni alloys with a 59 wt% Fe content. The chromium and nickel contents of these alloys ranged from the left of the eutectic triangle with Type A solidification to the right with Type F solidification. The pseudo binary phase diagram representing these compositions is shown in Figure 2.56. EB welds were deposited on these alloys, and the microstructural formation was analyzed relative to travel speed. Results for WRC  $Cr_{eq}/Ni_{eq}$  at 1.15 were previously shown in Figure 2.47. Microstructure results for two alloys with compositions through the three-phase region are shown in Figure 2.57. These structures were produced at the same travel speed on materials with WRC-1992  $Cr_{eq}/Ni_{eq}$  of 1.39 (Figure 2.57a) and 1.60 (Figure 2.57b) respectively. Although similar in appearance, it was reported that Figure 2.57a shows Type AF solidification. This is based on the morphology of the ferrite appearing restricted to the

cell boundaries. Whereas, Figure 2.57b contains the skeletal morphology and shows the interconnected dendrite cores from ferrite solidification [194].

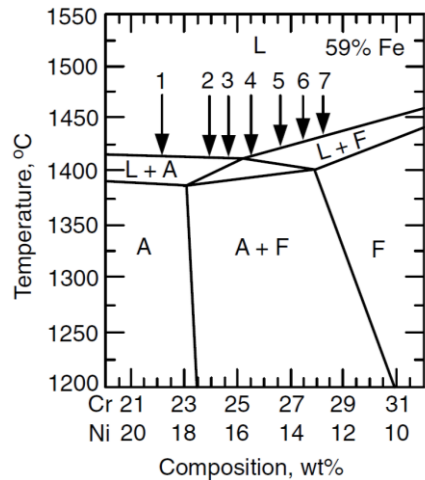


Figure 2.56. Pseudo binary phase diagram for the SS alloy compositions analyzed by Elmer et al. [194]. WRC-1992  $Cr_{eq}/Ni_{eq}$  are as follows: Alloy 1–1.15, Alloy 2–1.39, Alloy 3–1.51, Alloy 4–1.60, Alloy 5–1.84, Alloy 6–2.01, and Alloy 7–2.18.

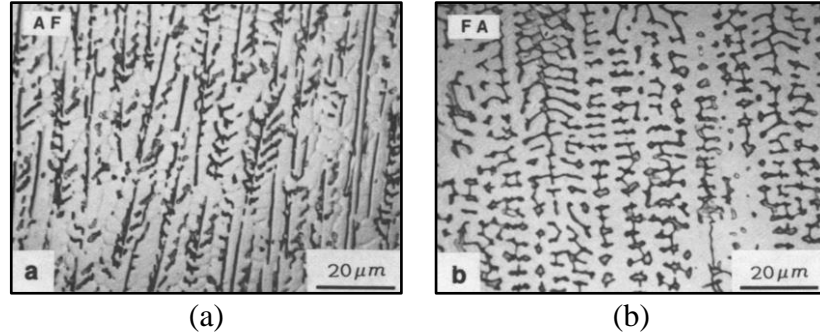


Figure 2.57. Electron beam weld microstructures at 25 mm/s for WRC-1992  $Cr_{eq}/Ni_{eq}$  of 1.39 (a) and 1.60 (b). Extracted from Elmer et al. [194].

Figure 2.58 shows the results on the alloy with a WRC-1992  $Cr_{eq}/Ni_{eq}$  of 2.01 at travel speeds of 500 mm/s and 25 mm/s. At the extreme travel speed (Figure 2.58a), the structure is entirely ferrite, but at a reasonable travel speed of 25 mm/s (Figure 2.58b)

primary ferrite solidification occurred with Widmanstätten austenite formation along the ferrite grain boundaries. Elmer et al. [194] used these results to produce a microstructural “map” containing solidification modes and microstructure morphologies based on travel speed and chromium and nickel content as shown in Figure 2.59.

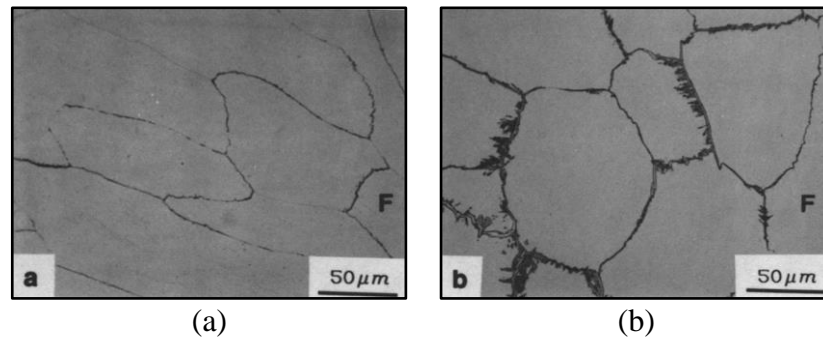


Figure 2.58. Electron beam weld microstructures for a 2.01 WRC-1992  $Cr_{eq}/Ni_{eq}$  alloy welded at 500 mm/s (a) and 25 mm/s (b). Extracted from Elmer et al. [194].

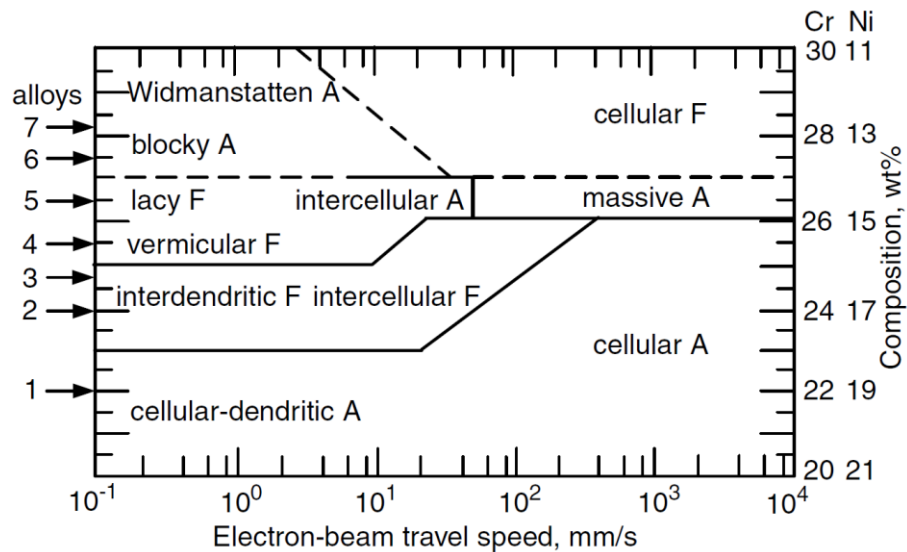
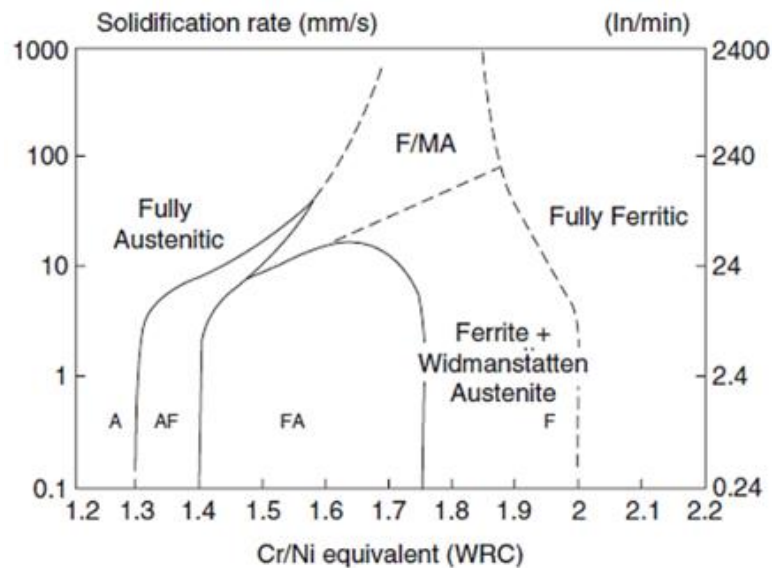


Figure 2.59. Microstructural map produced from EBW stainless steel alloys from Elmer et al. [194]. Figure extracted from Kou [123].

Lippold [190] expanded the analysis of solidification modes and microstructural formations based on the solidification rates for pulsed-LBW. Along with prior data, a microstructural map was developed for 300-series (austenitic) stainless steel alloys as shown in Figure 2.60. The 304L alloys investigated contained WRC-1992  $Cr_{eq}/Ni_{eq}$  ranging from 1.49-1.67, and the welds were fully austenitic with observed solidification modes of Type A, F, and mixed modes of Type A and Type F. Type F solidification further transformed to massive austenite (MA) upon cooling, eliminating the solidification microstructure. Lippold [190] reported that weld energy input showed minimal variation to the solidification conditions and was justified based on the observation of nearly consistent dendrite arm spacing. Although, the increased energy was reported to influence the penetration depth and weld pool geometry.



*Figure 2.60. Microstructural map for pulsed laser welded austenitic stainless steels. Extracted from Lippold [190].*

Vitek et al. [201] analyzed the results of rapid solidification on Type 308 stainless steel using CW CO<sub>2</sub> LBW. At an  $\approx 1.5$  WRC-1992  $Cr_{eq}/Ni_{eq}$ , it was reported that the microstructures consisted of fully austenite at travel speeds above 25 mm/s. While a 13 mm/s travel speed exhibited a range of microstructures from fully austenitic to austenite plus ferrite (Type AF). It was reported that the cooling rate necessary to promote the transition from primary ferrite to primary austenite was in the range of  $10^5$ - $10^6$  K/s [201].

The Suutala diagram is no longer effective for crack prediction during HED welding, and further analysis extended the Suutala diagram to include rapid solidification. Evaluation of rapid solidification developed into the modified Suutala diagram [5] with the latest modification reported by Lienert and Lippold [190], [214]. Lippold [190] included boron as an impurity element in addition to phosphorus and sulfur, and this diagram is shown in Figure 2.61a. The results of the modified Suutala diagram shifted the  $Cr_{eq}/Ni_{eq}$  ratio up to approximately 1.65 [190] versus the previous 1.49 [204]. Additional analysis of LBW on austenitic stainless steels was performed by Lienert and Lippold [214] using the Hammar and Svenson (H&S) [208] equivalencies. The diagram is shown in Figure 2.61b and only contained analysis based on phosphorus and sulfur. Lienert and Lippold's [214] results showed Type A solidification occurring below 1.59 and mixed mode austenite and ferrite microstructures up to 1.69 H&S  $Cr_{eq}/Ni_{eq}$ . Above a 1.69 H&S  $Cr_{eq}/Ni_{eq}$ , the microstructures exhibited primary ferrite solidification, and no cracks were observed [214].

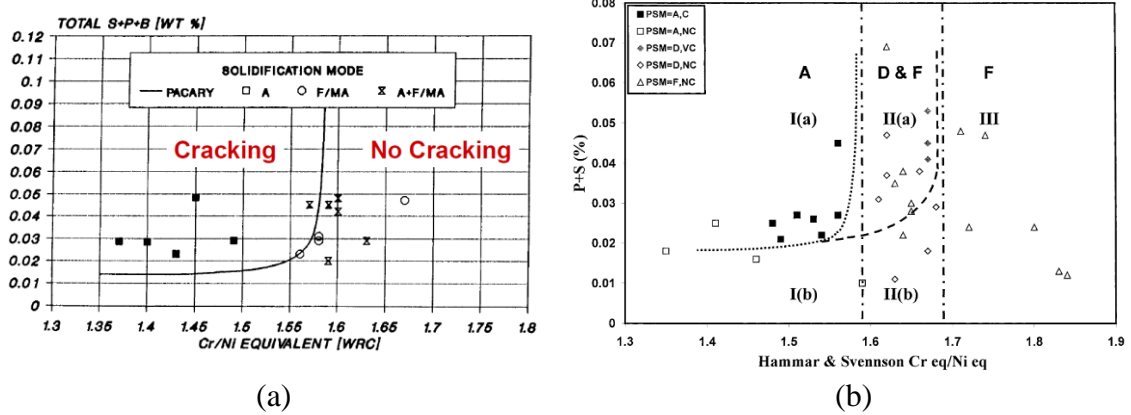


Figure 2.61. Modified Suutala diagram (a) and a further modified Suutala diagram using Hammar and Svensson equivalencies (b) [190], [214]. Solid symbols indicating cracking and open symbols indicate no cracking.

### 2.6.2.1 Duplex Stainless Steel

Some of the experimental alloys analyzed by Elmer et al. [194] have  $Cr_{eq}/Ni_{eq}$  comparable to DSS and produced solidification structures of cellular ferrite and ferrite with Widmanstätten austenite. The ability to maintain ideal ferrite/austenite ratios is a concern when welding DSS ( $Cr_{eq}/Ni_{eq} > 2.25$ ) with HED processes because the extreme cooling rates promote excessive fractions of ferrite [22], [215]–[217]. Taban and Kaluc reported laser weld results in duplex and super duplex stainless steel (SDSS) as shown in Figure 2.62a and Figure 2.62b respectively. The respective WRC-1992  $Cr_{eq}/Ni_{eq}$  between these alloys are 4.0 for the DSS and 2.1 for the SDSS. The DSS was reported to contain ferrite fractions as high as 74%, while the SDSS decreased the as-welded ferrite fraction to as high as 61%. The increased austenite in the SDSS is likely a result of nearly double the nitrogen content and indicated by nearly half the  $Cr_{eq}/Ni_{eq}$  value.

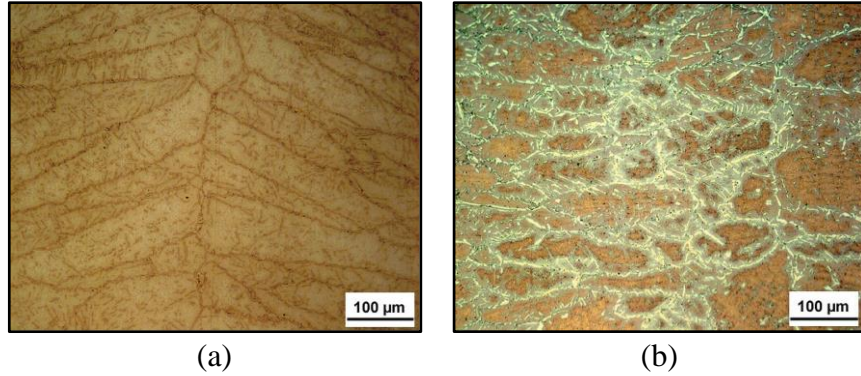


Figure 2.62. Laser weld microstructures in a duplex stainless steel (a) and a super duplex stainless steel (b) from Taban and Kaluc [218].

Prior literature has analyzed microstructural evolution of DSS and showed that faster travel speeds (lower heat input and higher cooling rates) led to higher fractions of ferrite [219]. Sieurin and Sandström [217] showed the need to maintain cooling rates well below 50°C/s to maintain phase fractions near ideal austenite/ferrite ratios. This data is represented in Figure 2.63 [217].

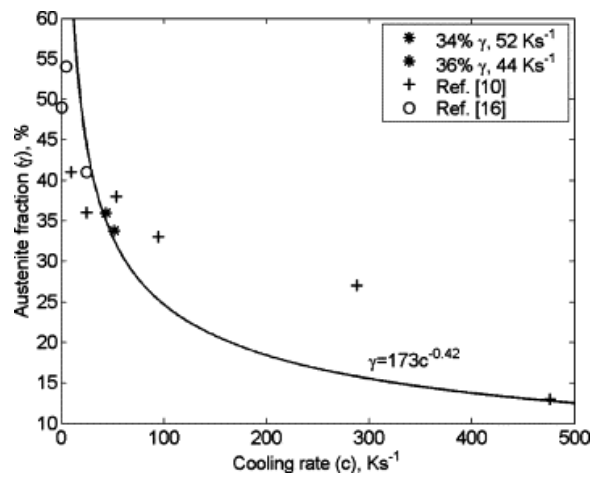


Figure 2.63. Austenite phase fraction versus cooling rate from Sieurin and Sandström [217].

It was also shown that rapid cooling can lead to a saturation of nitrogen [216]. Within the ferrite, nitrogen readily forms  $\text{Cr}_2\text{N}$  precipitates and influences corrosion properties [5], [22], [202]. It is generally not recommended to weld DSS with an HED process [22]; however, research has attempted to utilize alternative methods such as filler metal (alloying) additions, nitrogen shielding gas, preheating or post weld heat treating, and/or laser hybrid processes to facilitate austenite formation [202], [218].

### **2.6.3 *Ti-6Al-4V***

Titanium alloys are widely used in aerospace, nuclear power, and defense applications due to their relatively high strength, low density, excellent corrosion resistance, and high temperature creep resistance [6], [18], [220]–[222]. One of the most common structural alloys is Ti-6Al-4V [6]. Welding  $\alpha$ - $\beta$  alloys may result in changes to mechanical properties relative to the base material. This alloy is often used in relatively thin sections where low heat input may be advantageous relative to arc welding processes with the goal of optimizing mechanical properties and reducing distortion.

High heat inputs promote epitaxial nucleation and growth of coarse, columnar-shaped beta grains in the fusion zone, which has been shown to be detrimental to mechanical properties [223]. Baeslack et al. [18] reported that large prior beta grain size (PBGS) may result in poor ductility due to easy crack propagation along prior beta grain boundaries (PBGBs).

Results from Akman et al. [136] showed an increase in PBGS with increasing average power (constant peak power) for pulsed-LBW. Microstructures showing these

results are shown in Figure 2.64. The average grain size was reported to increase by approximately 250  $\mu\text{m}$  for each 100 W of increasing average power [136]. It is not clear as to how the grain boundaries were delineated by Akman et al. [136]. These welds were performed in atmosphere using a leading shielding nozzle, and it is suspected that excessive oxidation allowed for oxygen to penetrate the beta boundaries, which accentuated the PBGBs once etched. To further illustrate this point, two different macrophotos were extracted from Akman et al. [136] as shown in Figure 2.65. The left photomicrograph (Figure 2.65a) appears to be a weld where adequate shielding was present, but the right macrograph indicates heavy oxidation due to the dark etching response of the fusion zone.

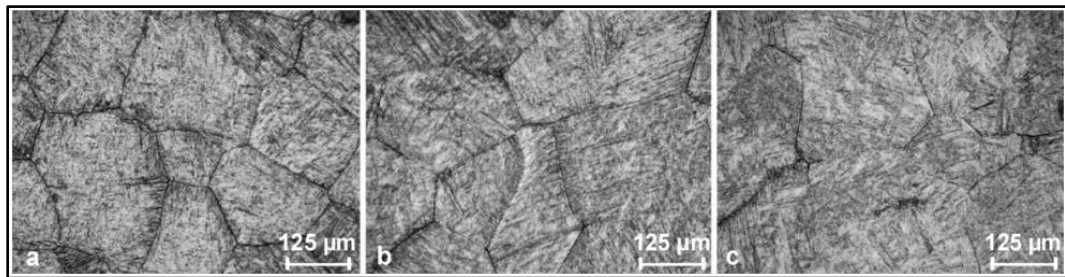


*Figure 2.64. Ti-6Al-4V pulsed-LBW microstructures reported as increasing beta grain size with increasing average power: a) 474W, b) 543W, c) 555W [136].*

Lu et. al [224] analyzed EB weld microstructures on low impurity Ti-6Al-4V and reported a fusion zone microstructure consisting of large PBGs entirely transformed to  $\alpha'$ . Lu et. al [224] also quantified the length and width of the PBGs. A fusion zone microstructure is shown in Figure 2.66 at two different magnifications. The reported results from Lu et. al [224] showed that the beta grain size slightly decreased (length and

width) from the top of the weld to the root along with a 50% reduction in the length of the acicular,  $\alpha'$  grains [224]. This is as expected based on the geometry of the keyhole weld, but it is unknown as to how they interpreted grain size based on the information and micrographs presented.

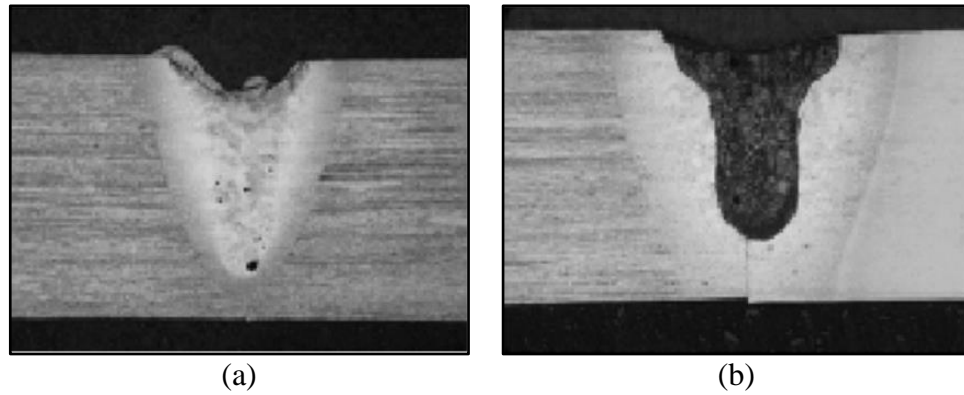


*Figure 2.65. Macrophotos for Ti-6Al-4V pulsed-LB welds in atmosphere with what appears to be adequate inert gas shielding (a) and inadequate shielding (b) [136].*

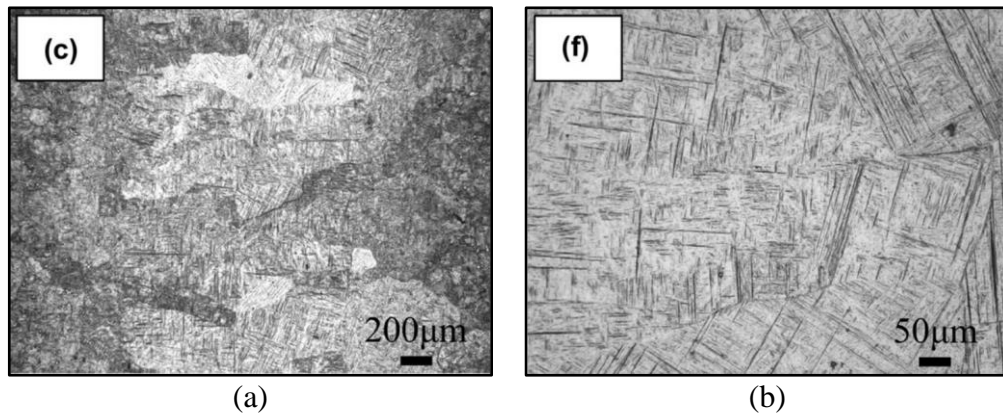


*Figure 2.66. Optical micrographs of EB fusion zones in Ti-6Al-4V from Lu et al. [224].*

Delineating the PBGBs to quantify beta grain size has been a challenge using optical microscopy or scanning electron microscopy techniques. This is particularly

evident when the microstructure appears to fully consist of martensite without grain boundary allotriomorphs. Fully understanding as-welded microstructure evolution also results from a difficulty in distinguishing between the  $\alpha$  and  $\alpha'$  structures [223] as well as detecting the presence of retained  $\beta$ .

The solid-state microstructural changes are a consequence of the allotropic nature of Ti-6Al-4V, and the transformation of the high temperature beta phase to  $\alpha$  or  $\alpha'$  martensite may further embrittle the weld metal [220], [223], [225], [226]. Kohyama et al. [226] characterized EB weld fusion zones in Ti-6Al-4V as “columnar” dendritic solidification structures that transformed into fine acicular alpha and “planar” alpha along the PBGBs [226]. Based on the published micrograph, it appears as though these weld metal structures were largely  $\alpha'$  martensite. Full penetration, pulse-LBW of Ti-6Al-4V at high heat inputs ( $>75$  J/mm) were reported to form  $\alpha'$ ,  $\alpha$  along the prior  $\beta$  grain boundaries, and massive  $\alpha$  by Kumar and Sinha [227]. The massive  $\alpha$  transformation was believed to be caused by the reduced cooling rate associated with higher heat inputs.

However, Kumar and Sinha [227] reported that transmission electron microscopy analysis revealed regions of  $\beta$  between  $\alpha'$  laths that were not observable with optical or scanning electron microscopy. The TEM images from Kumar and Sinha are shown in Figure 2.67. Similarly, Xu et al. [228] also reported retained  $\beta$  between  $\alpha$  laths as shown in Figure 2.68 with the arrows pointing to what was reported as retained  $\beta$  between the acicular  $\alpha$  laths (Figure 2.68a). For comparison purposes, an optical micrograph is presented in Figure 2.68b.

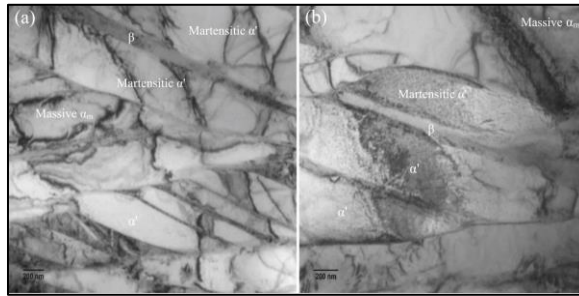


Figure 2.67. TEM images of Ti-6Al-4V laser weld microstructures from Kumar and Sinha [227]. A heat input of  $\approx 55$  J (a) and a heat input of  $\approx 105$  J (b).

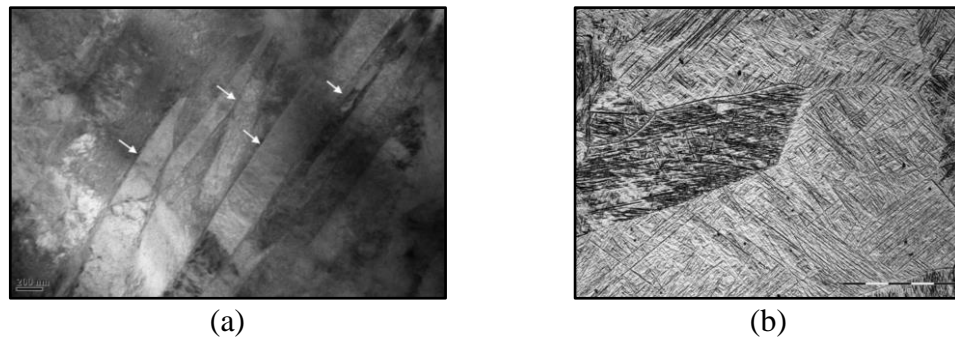


Figure 2.68. TEM micrograph of laser weld microstructures (a) and optical micrograph (b). Extracted from Xu et al. [228] where they reported retained beta between  $\alpha$  laths.

Based on the literature, it is believed that the HED weld analysis of Ti-6Al-4V will result primarily in  $\alpha'$  unless advanced characterization is performed utilizing transmission electron microscopy to identify  $\beta$  at sub-micron scales. Potentially, it is not possible to alter the solid-state transformations with the LBW parameter range used in this study. Therefore, it was believed to be of greater interest to only quantify the beta grain size response in Ti-6Al-4V.

### 3 Research Objectives

The overall objective of this research was to perform an in-depth experimental analysis of LBW to expand the current understanding of the parameter relationships relating to weld geometry formation. The goal was to utilize the experimentally produced LB weld data to develop a useful modeling tool that can conveniently predict weld width and penetration. Because it is necessary to predict penetration over a large range of parameters, a neural network modeling approach was utilized. In addition, the keyhole vapor capillary is not well understood, and an approach to reconstruct the vapor capillary was incorporated using an ICI system. This novel approach was to further the scientific understanding of weld formation as it relates to vaporization, weld pool depressions, and the transition from conduction to keyhole mode welding.

Because microstructure formation is directly related to the fusion zone formation, it was deemed necessary to correlate the microstructure evolution to process parameters. For SS alloys, compositions with varying  $Cr_{eq.}/Ni_{eq.}$  values between 304L SS to 2205 DSS were evaluated. These alloys were introduced to further the knowledge of SS microstructure transformations and based on the inability to reasonably alter solidification modes in the 304L SS. The objective of Ti-6Al-4V microstructural analysis was to quantify how beta grain size changed relative to travel speed because the open literature reported a potential for reduced ductility and toughness with increasing prior beta grain size. To perform a beta grain size analysis, an initial objective became suitability revealing the beta grain boundaries for quantitative measurements.

## 4 Experimental Procedures

### 4.1 Laser Welds

All welds were performed using an ytterbium-doped ( $\text{Yb}^{3+}$ ) fiber laser and transmissive optics with an  $\approx 600\text{ }\mu\text{m}$  beam diameter and a uniform or “top-hat” intensity distribution. The optics were manipulated using a six-axis robot programmed to maintain the determined working distance throughout three points along the weld length. The optics were positioned perpendicular to the workpiece surface along and transverse to the travel direction ( $0^\circ$  beam angle). Argon shielding was applied across and trailing the weld pool. The specific information for laser type, optics, flow rates, etc. are provided in Appendix C:. For all alloys, the main laser welding parameters used in this study are listed in Table 4.1. An “x” distinguishes the corresponding powers and travel speeds analyzed.

*Table 4.1. Laser weld parameters evaluated at a  $600\text{ }\mu\text{m}$  beam diameter.*

Power [W]	Travel Speed [mm/s]								
	5	10	25	35	50	60	75	100	150
800	x	x	x	-	x				
1000	x	x	x	x	x	x	-	-	-
1200	x	x	x	x	x	x	x	x	-
1600	-	x	x	x	x	x	x	x	x
2000	-	-	x	x	x	x	x	x	x
2400	-	-	x	x	x	x	x	x	x

The nominal laser power was measured using a thermopile type power sensor with the average data collected for 30 seconds of illumination time. All weld power settings were adjusted to match the difference in the measured power versus the set power as provided in Table C.1 in Appendix C:. The measured output power was consistently lower for all measurements, and the laser set values were adjusted accordingly. For instance, all welds reported at 1600 W utilized a 1750 W set value to compensate according to the power sensor/meter reading. More detail on the power sensor, meter, and data collection is provided in Appendix C:.

Beam diameters were confirmed utilizing a commercially available rotating pinhole device [51] with data collected and exported as “raw” analog-to-digital values. More information on the beam diagnostics device is provided in Appendix C:.

MATLAB<sup>®</sup> script was developed to compute the second moment (D2M) and 86% (D86) beam diameters at each height scanned along the beam axis. This entire script, including user defined functions, is provided in Appendix K:. A 3D representation of the 1600 W beam profile at the beam waist is shown in Figure 4.1a with the pseudo-2D representation with color scale shown in Figure 4.1b. Figure 4.1c and Figure 4.1d show the same respective beam profiles at a plane scanned 1.47 mm below what was determined to be the beam waist (Figure 4.1a and Figure 4.1d).

The positive x-direction in all beam profiles corresponds to the positive travel direction during welding. Relative to welding, Figure 4.1a and Figure 4.1b show the intensity distribution focused on the plate surface, while Figure 4.1c and Figure 4.1d are

1.47 mm below the plate surface. Three-dimensional beam caustics were produced by incorporating each scan into a single plot as shown in Figure 4.2.

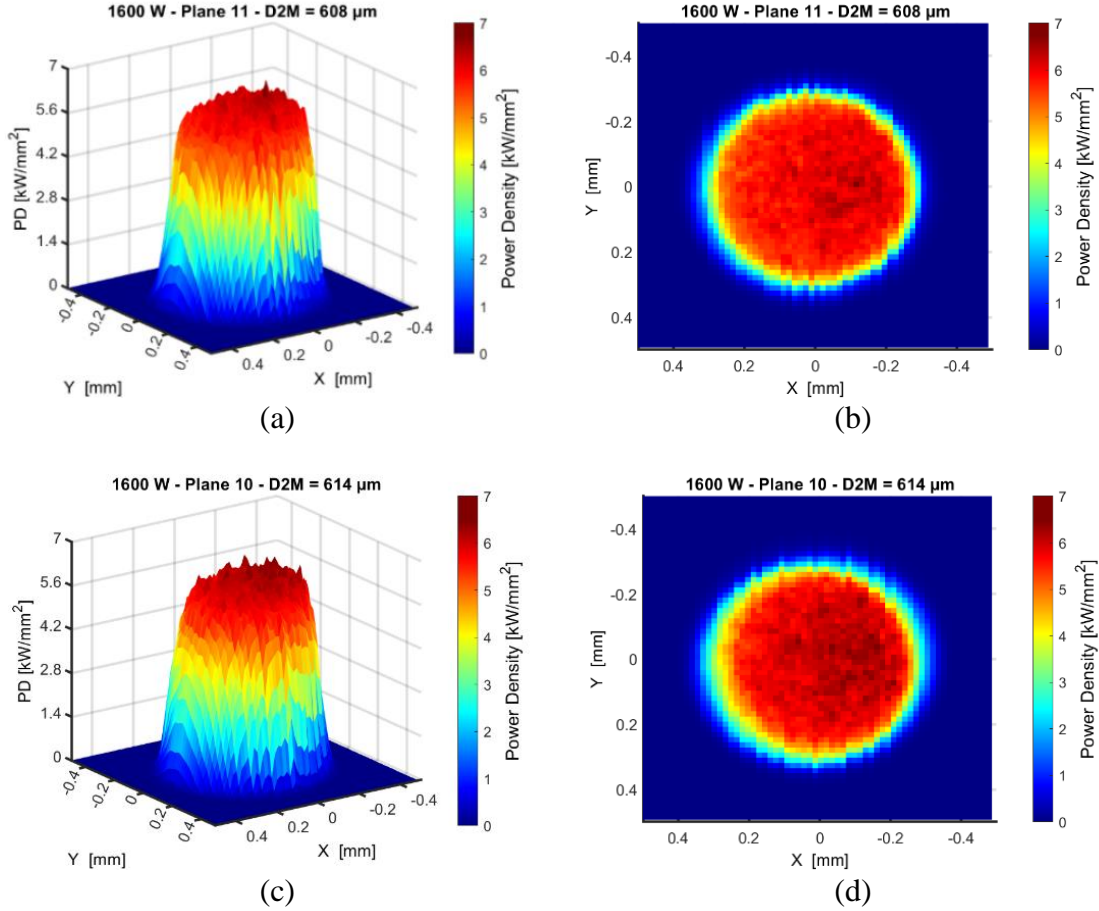
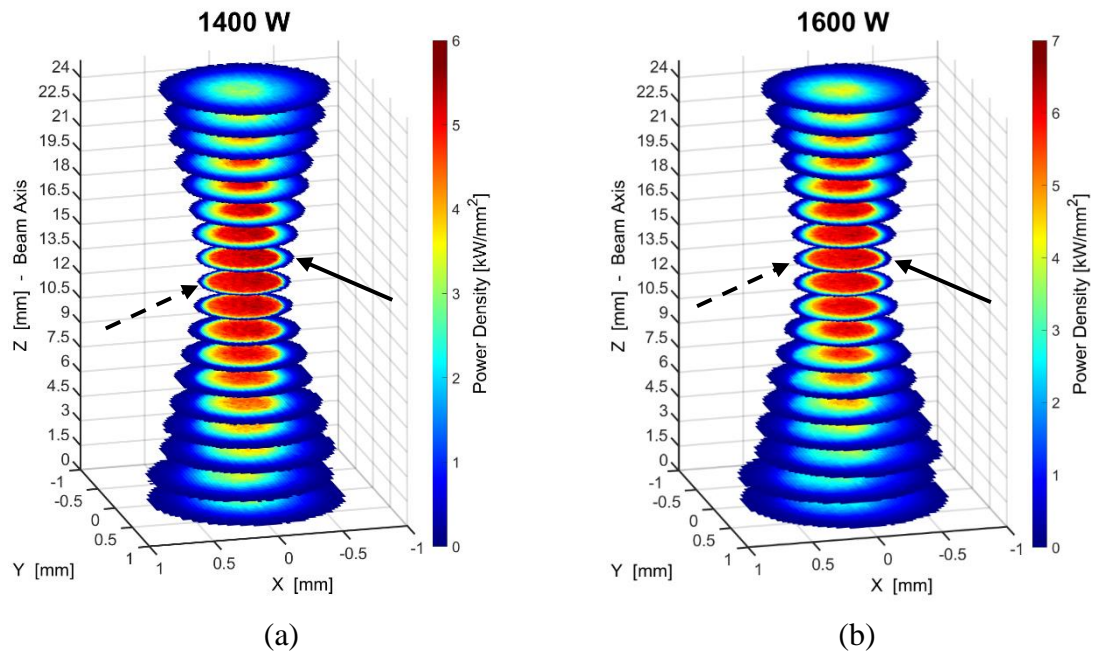


Figure 4.1. Measured intensity shown as power density ( $\text{kW/mm}^2$ ) for 1600 W of power. Beam waist or Plane 11 with a  $608 \mu\text{m}$  D2M beam diameter (a,b). Below beam waist by 1.47 mm or Plane 10 with a  $614 \mu\text{m}$  D2M beam diameter (c,d).

Figure 4.2a shows the beam caustic at 1400 W and Figure 4.2b shows the beam caustic at 1600 W. The computed Rayleigh lengths for all powers analyzed are  $\approx 8$  mm with a BPP of  $\approx 10 \text{ mm} \cdot \text{mrad}$  and a  $M^2$  value of  $\approx 30$ . The solid arrows represent the intensity distribution applied on the workpiece surface during welding, and the dashed

arrows represent the smallest D2M beam diameter in Figure 4.2. There was a shift in the focal position between 1400 W and 1600 W. This is believed to be attributed to thermal lensing at higher powers. All powers below 1400 W maintained the smallest measured diameter at Plane 10, whereas all powers above 1600 W maintained the smallest measured diameter at Plane 11. All welds were performed with the working distance set to Plane 11 to match the smallest beam diameter produced at 1600 W. However, this is considered to have negligible influence on the welds below 1600 W due to the 8 mm Rayleigh length. Within  $\pm 1.5$  mm of the focal position, the measured 600  $\mu\text{m}$  diameter was maintained within  $\approx \pm 20$   $\mu\text{m}$ . Additional beam data is provided in Appendix C:.



*Figure 4.2. Three-dimensional beam caustic with solid arrow indicating the location of the beam axis projected onto the plate surface during welding and the dashed arrow representing the smallest measured D2M diameter: (a) 1400 W, (b) 1600 W. Note: The color scales are not the same between 1400 W (a) and 1600 W (b).*

All welds were produced by immediately extinguishing the process beam while maintaining the travel velocity and argon gas shielding through the end of the weld. It was assumed that this technique allowed rapid enough solidification that the geometry of the progressing pool remained. This does not apply to the keyhole, which was backfilled with fluid. Using this assumption, longitudinal sections and macro photos of the weld-end surfaces were used to approximate weld pool shapes.

#### ***4.1.1 Inline Coherent Imaging***

The ICI system utilized a Laser Depth Dynamics™ 700 (LDD-700™) system with a 6 mm field of view, and the optics module consisted of the LD-700-OM1M-2 with a 3DM3R module to couple the ICI beam into the welding optics. The software was IPG OmniWeld™ v2.5.2.5 [229]. It is believed that the ICI beam size is  $\approx 30 \mu\text{m}$  as reported by Ji et al. [59], but the ICI beam size was not quantified. The SLD broad-band wavelength was around  $\approx 840 \text{ nm}$  [229]. Further information about the ICI system setup is provided in Appendix B:.

The ICI system was only used in the manufacturer's keyhole tracking mode. This feature is designed for detecting the keyhole locations relative to the process beam. But to better understand keyhole formation from a fundamental perspective, the data was extracted from the system and further processed. Figure 4.3 represents a longitudinal view of the ICI beam. The ICI beam is believed to be much smaller than the process beam but manipulated to scan larger areas defined by the user. The system tracks each x-y location and outputs a depth measurement assuming that a reflection was able to

return to the detector. Similarly, Figure 4.4 shows a schematic to illustrate how the beam is rastered with a predefined width and acquired data points based on the set resolution. As the weld progressed, the ICI beam was traversed across the keyhole based on a predefined scan size and resolution.

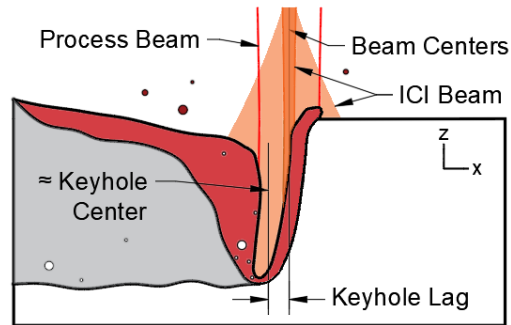


Figure 4.3. Schematic of ICI system scanning across the keyhole.

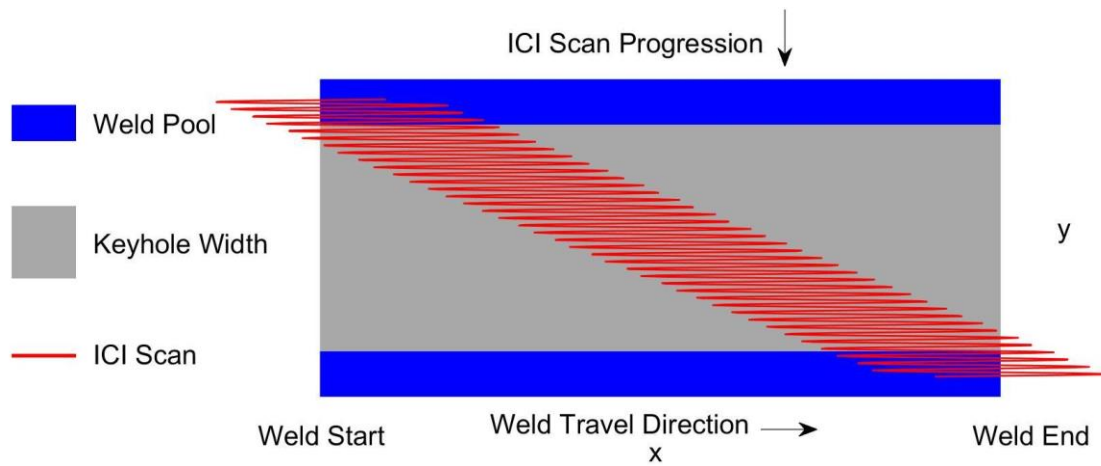
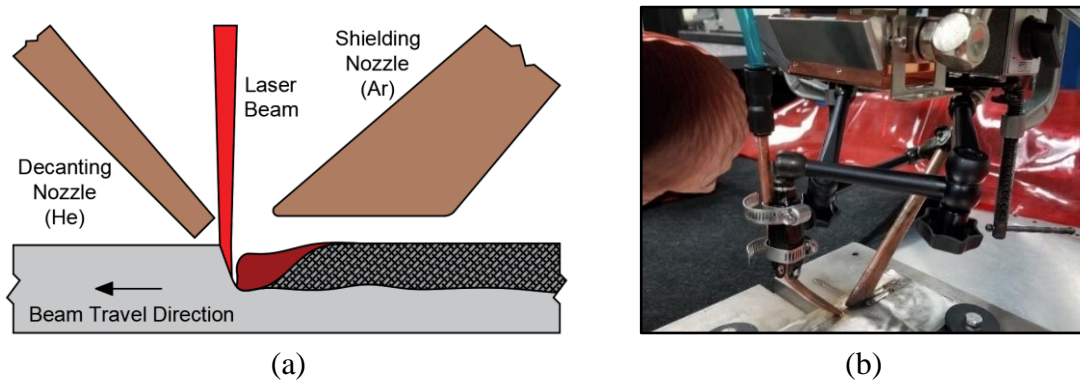


Figure 4.4. Schematic of the ICI beam scan progression from the start of the weld (left) to the end of the weld (right) across the keyhole.

#### 4.1.2 Weld Pool Decanting

Attempts were made to “decant” the weld pool to measure the profile and volume of molten material for a given process parameter. This was performed by blowing a jet of compressed helium into a steady-state weld pool as the beam traversed the work piece surface. Helium was used as the decanting medium to mitigate oxidation and has higher cooling potential than other gases. The decantation nozzle was oriented at an  $\approx 45^\circ$  angle, and attempts were made with the nozzle leading and trailing the weld pool. The best results were produced with the decanting nozzle on the leading side of the weld. The nozzle was a 0.19-inch (4.83 mm) internal diameter copper nozzle swaged to an opening of  $\approx 0.0625$ -inches (1.59 mm) in height and  $\approx 0.25$ -inches (6.35 mm) wide. A schematic of the setup showing the decanting nozzle leading the laser beam with a trailing shielding nozzle is shown in Figure 4.5a, and a photograph of the actual setup relative to the optics and plate surface is shown in Figure 4.5b.



*Figure 4.5. Schematic (a) and photograph (b) showing the decanting nozzle (left) positioned in on the leading edge with the shielding nozzle (right) trailing the weld pool.*

Once the weld was initiated and in a steady-state condition, a valve was instantaneously opened to allow the high-pressure gas to blow the liquid weld pool out from the solid material. Following decantation, the profile region of extracted liquid was measured using a static scan with the ICI system. The scans were captured with a length and width of 5000x5000  $\mu\text{m}$  and a step size of 800x800 pixels (6.25x6.25 $\mu\text{m}$ ). The height data from the ICI software was extracted for further processing and analysis. The analysis fit a surface profile to calculate the volume of each condition as in the ICI keyhole analysis.

## **4.2 Neural Network Modeling**

An algorithm consisting of neural network models was developed using MATLAB<sup>®</sup> software, and the code producing these results is provided in Appendix O:. The model is based on a feedforward artificial neural network using a built-in MATLAB<sup>®</sup> function ‘fitnet’. The networks consisted of a single input, which was travel speed, and used a single hidden layer and output layer as shown in Figure 4.6.

The hidden layer used a sigmoid fit function, as previously presented in Equation 2.30. Training was accomplished using three nodes for the weld penetration and the transverse section area and six nodes for all weld widths. The variations in nodes were based on trial and error and overfitting of penetration and cross-sectional area data. Increasing the number of nodes for the width measurements reduced underfitting issues. Training the model was performed via a Bayesian Regularization algorithm and MATLAB<sup>®</sup> function ‘trainbr’.

Only 304L SS and Ti-6Al-4V data was modeled using the neural network. This information was compiled into an algorithm and output through a stand-alone graphical user interface (GUI) that can be distributed and download for further use. By providing the code, the goal is to allow for continued improvement of the model to further increase the prediction methodologies, capabilities, and accuracy.

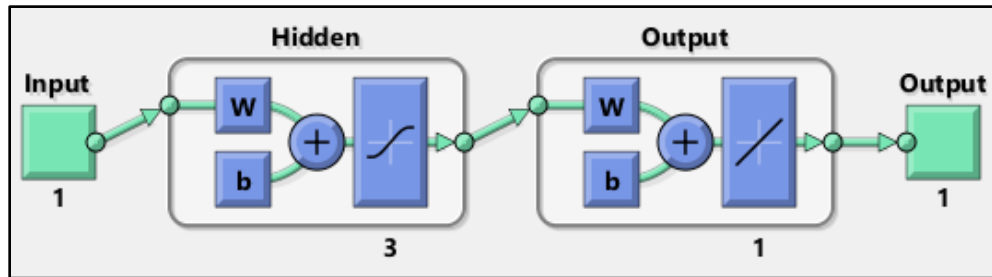


Figure 4.6. Schematic showing the architecture of the neural networks for penetration and transverse cross-section area predictions.

Data extraction to programmatically retrain the model is via the *Fusion Zone Cross-Section Calculation Function* provided in Appendix O:. This function allows a user to select a captured macrophoto of the fusion zone and trace the entire transverse section boundary. The function outputs a binary image file that can be moved to a specific folder for automatic detection of all transverse weld features analyzed in this study. During retraining of the model, these programmatically measured features are automatically populated into training the new network(s). This functionality was incorporated to provide a relatively simple method of continuous improvement through additional empirical data.

## **4.3 Metallurgical Characterization**

### **4.3.1 Chemical Analysis**

The chemical compositions, except carbon, hydrogen, nitrogen, oxygen, and sulfur, were measured using optical emission spectroscopy (OES). The OES instrument was an AMETEK SPECTROMAXx using 99.999% purity argon. OES sample preparation involved grinding with 60 grit aluminum oxide abrasive paper. All SS samples were measured with compositions corrected based on a manufacturer (AMETEK) provided 304L reference standard. Likewise, the Ti-6Al-4V measurements were corrected based on a manufacturer provided Ti-6Al-4V reference standard. All elemental values measured via OES are an average of three measurements.

For stainless steel, carbon (C) and sulfur (S) were measured via combustion analysis. Nitrogen (N) and oxygen (O) were measured using inert gas fusion. These measurements were performed according to ASTM E1019-18 [230].

For Ti-6Al-4V, carbon was measured via combustion analysis according to ASTM E1941 [231]. Oxygen and nitrogen were measured via inert gas fusion according to ASTM E1409 [232], and hydrogen was measured via inert gas fusion thermal conductivity/infrared detection according to ASTM E1447 [233]. All other elements were reported based on the OES measurement.

#### **4.3.2 *Optical Metallography***

All macro view optical images at 50X magnification were captured using an Olympus® GX51 inverted microscope using Olympus DP2-BSW software. An Olympus® GX53 inverted microscope with PAX-it!™ 2 v1.5.1.0 was used for magnifications at or greater than 100X. For Ti-6Al-4V welds, differential interference contrast (DIC) was used for all micrographs at or greater than 100X unless otherwise noted. Also, all photomicrographs are captured using bright field imaging unless otherwise specified.

#### **4.3.3 *Scanning Electron Microscopy***

Scanning electron microscope (SEM) images were captured using a ThermoFisher Scientific Inc. Apreo microscope equipped with a field emission gun (FEG). The detector type, accelerating voltage, and beam current were adjusted for each situation and is provided with the data. Images were captured using the ETD (Everhart-Thornley detector) or T1 detector. The T1 detector is an in-line backscattered electron (BSE) detector with a schematic representation shown in Figure 4.7.

For stainless steel welds, EBSD was performed in the Apreo as previously described using an EDAX high-speed Hikari camera utilizing a charged-coupled device (CCD) sensor. The samples were positioned at a 70° tilt from horizontal and relative to the EBSD camera. Data collection was performed using EDAX OIM DCv7.3.1 software, and data analysis was performed using OIM Analysis™ v8.6.0028 software, where OIM stands for orientation imaging microscopy.

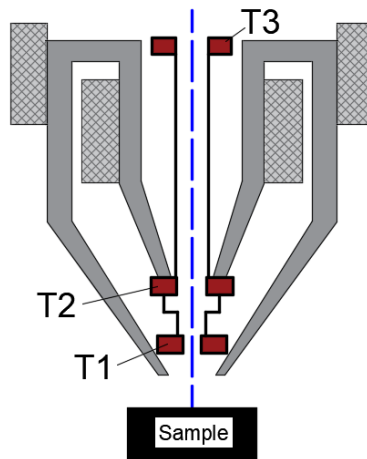


*Figure 4.7. Schematic of FEI Apreo in-lens (T1 and T2) and in-column (T3) BSE detectors.*

For Ti-6Al-4V EBSD, a Thermo Scientific Inc. Quattro environmental scanning electron microscope (eSEM) was used. The EBSD camera was an EDAX Velocity™ using a complementary metal oxide semiconductor (CMOS) sensor. The samples were positioned at a 70° tilt from horizontal and relative to the EBSD camera. Data collection utilized APEX™ EBSD software. Post collection analysis utilized OIM Analysis™ software (v8.6.0028). The individual Kikuchi patterns were saved for reprocessing by performing additional background subtraction and pattern reindexing. After reindexing, OIM Analysis™ software was used to produce the PBG reconstruction [234].

#### **4.4 Material Compositions**

The measured chemical compositions for all the SS alloys are shown in Table 4.2, and the measured chemical composition for Ti-6Al-4V is shown in Table 4.3. The elements designated with an asterisk were measured via combustion or infrared analysis,

as opposed to OES. All alloys evaluated in this study were from a single heat to minimize heat-to-heat variations that may influence weld results. The alloys designated with an “M” are experimental alloys added to the analysis to vary the microstructural morphologies and phase fractions relative to the 304L. The experimental alloys span a  $Cr_{eq}/Ni_{eq}$  up to a commercially available 2205 DSS. The property differences between 304L SS and Ti-6Al-4V is a higher melting temperature and nearly half the thermal conductivity and density for Ti-6Al-4V. The specific property values are shown in Table A.1 in Appendix A:.

*Table 4.2. Measured stainless steel alloy compositions (wt%) with Fe as the remainder.*

Alloys		Cr	Mo	Si	Nb	Ni	Mn	Cu	C*	N*	S*	P*
304L	◆	18.2	0.30	0.28	0.020	8.14	1.23	0.50	0.030	0.065	0.001	0.027
M58	▲	20.2	0.003	0.45	0.004	9.99	1.76	0.002	0.019	0.005	0.008	<0.001
M45	■	21.1	0.004	0.13	0.004	9.70	0.13	0.002	0.005	0.006	0.004	<0.001
M53	●	21.1	0.003	0.45	0.004	9.02	1.77	0.003	0.012	0.008	0.010	<0.001
M54	★	22.7	0.002	0.49	0.004	7.09	1.86	0.005	0.021	0.007	0.011	<0.001
2205	⬠	22.3	3.02	0.32	0.010	5.40	1.76	0.31	0.025	0.15	0.001	0.032

*Table 4.3. Ti-6Al-4V chemical composition (wt%).*

Alloy	Ti	Al	O*	N*	C*	V	Nb	Fe	Cr	H*
Ti-6Al-4V	89.4	6.27	0.18	0.0083	0.021	4.00	0.033	0.18	0.08	0.0051

## **4.5 Gas Tungsten Arc Welds**

Solely for microstructural comparison purposes, gas tungsten arc (GTA) welds were deposited on the SS alloys using a Lincoln Electric Aspect<sup>®</sup> 375 power supply and WeldCraft<sup>®</sup> water cooled torch. The motion system used a carriage control Jetline<sup>®</sup> Model 9627 with Model 9690 arc length control. Welds were performed autogenously using direct current electrode negative (DCEN) at 100 A and feedback voltage control to maintain the arc at 10 V. A 0.125 inch, 2% thoriated tungsten electrode was prepared with a 30° included angle and truncated tip. The travel speed was 5 mm/s. Argon shielding was applied at 45 CFH (21.2 l/min) using a Linde size 10 gas cup. The current, voltage, and travel speed parameters were utilized to match laser welds at 1000 W for a direct microstructural comparison between LBW and GTAW.

## **5 Results and Discussion**

The following results contain weld geometry behavior, keyhole formation, and weld pool analysis. This is followed by modeling results using the empirical data from the weld behavior incorporated into prior literature models and the developed neural network algorithm. Lastly, the microstructural results are discussed independently for SS alloys and Ti-6Al-4V. All laser welds were performed with the setup as described in the experimental procedures and Appendices B-D. This approach attempted to fix as many variables as possible and only changed the power and travel speed, while the beam diameter was constant. For referencing variations in material properties, the values for 304L and Ti-6Al-4V are provided in Appendix A:. The material property values were either extracted from literature [14], [121], [235] or computed using ThermoCalc<sup>®</sup> software [236].

### **5.1 Weld Formation**

To understand the relationships between fusion zone formation and laser parameters, transverse macro-sections, ICI keyhole analysis, and weld pool decanting were analyzed as presented in the following subsections.

#### ***5.1.1 Weld Geometry Analysis***

For each weld on 304L SS and Ti-6Al-4V, the results for the geometric analysis of weld profiles relating to process parameters were evaluated based on macrophotos of the

weld ends and transverse cross-sections. Weld surface, weld end, and cross-section macrophotos are provided in Appendix D: for 304L and Appendix F: for Ti-6Al-4V. Code was written in MATLAB® software to improve the transverse section analysis and output measurable features other than weld penetration and weld toe width. The code for the transverse section analysis is provided in Appendix L:, and Figure 5.1 shows the method of analysis and features analyzed in this study.

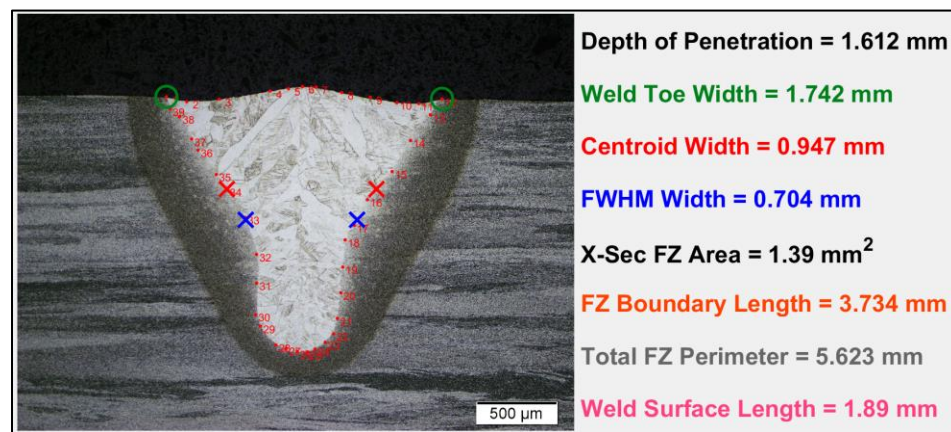


*Figure 5.1. Measurements of transverse weld features showing a manually traced weld macrograph and the extracted features.*

The most important feature is weld penetration, and the necessity for adequate and consistent penetration is to satisfy strict, internal weld quality requirements. The cross-sections of 304L welds at a constant 1600 W of power and varying travel speeds are shown in Figure 5.2, and 304L welds at a constant 50 mm/s travel speed and varying power are shown in Figure 5.3. The identical parameters for Ti-6Al-4V are shown in Figure 5.4 and Figure 5.5 for constant power (1600 W) and constant travel speed (50 mm/s), respectively.

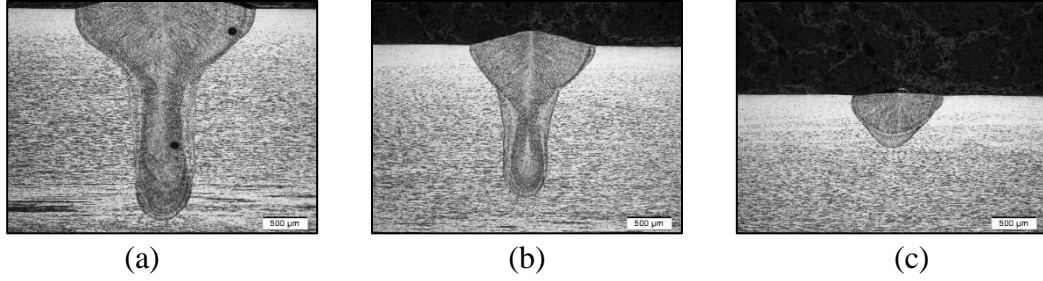


*Figure 5.2. Constant power 304L laser weld macrosections at 1600 W and travel speeds of 25 mm/s (a), 50 mm/s (b), and 100 mm/s (c).*

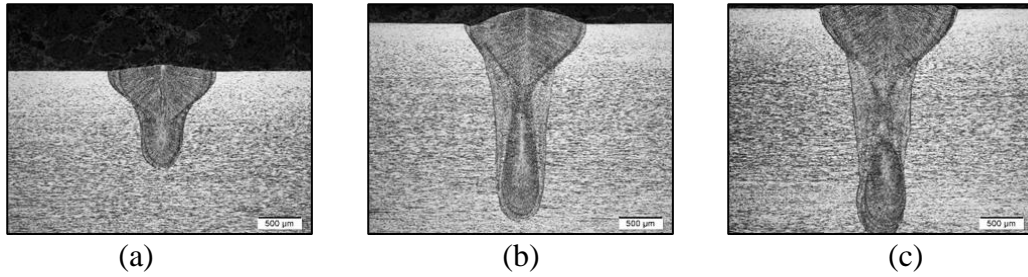


*Figure 5.3. Constant travel speed 304L laser weld macrosections at 50 mm/s and powers of 1200 W (a), 2000 W (b), and 2400 W (c).*

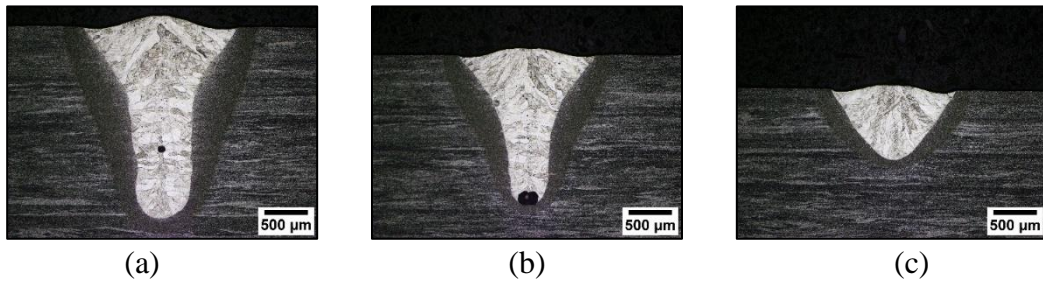


*Figure 5.4. Constant power Ti-6Al-4V laser weld macrosections at 1600 W and travel speeds of 25 mm/s (a), 50 mm/s (b), and 100 mm/s (c).*

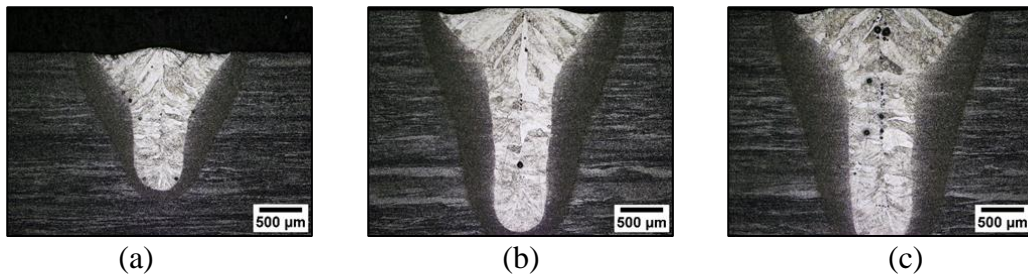


*Figure 5.5. Constant travel speed Ti-6Al-4V laser weld macrosections at 50 mm/s and powers of 1200 W (a), 2000 W (b), and 2400 W (c).*

The penetration data over a large range of process parameters is shown in Figure 5.6a for 304L SS and Figure 5.6b for Ti-6Al-4V. The plots for both alloys are presented with the same scales for comparison purposes. Except for 800 W, the data is an average of a single cross-section from two separate welds. For all welds, there was negligible scatter for penetration and cross-sectional area. However, the welds at 800 W showed inconsistency, so duplicate welds were not produced. The measured weld geometry results for 2205 DSS were consistent with 304L. For comparison, the results at a constant travel speed of 50 mm/s are provided in Appendix H: Appendix H: also includes the comparable weld measurements from the experimental SS alloys, but because the experimental alloys were intended for microstructural analysis, they are not included in the weld behavior analysis.

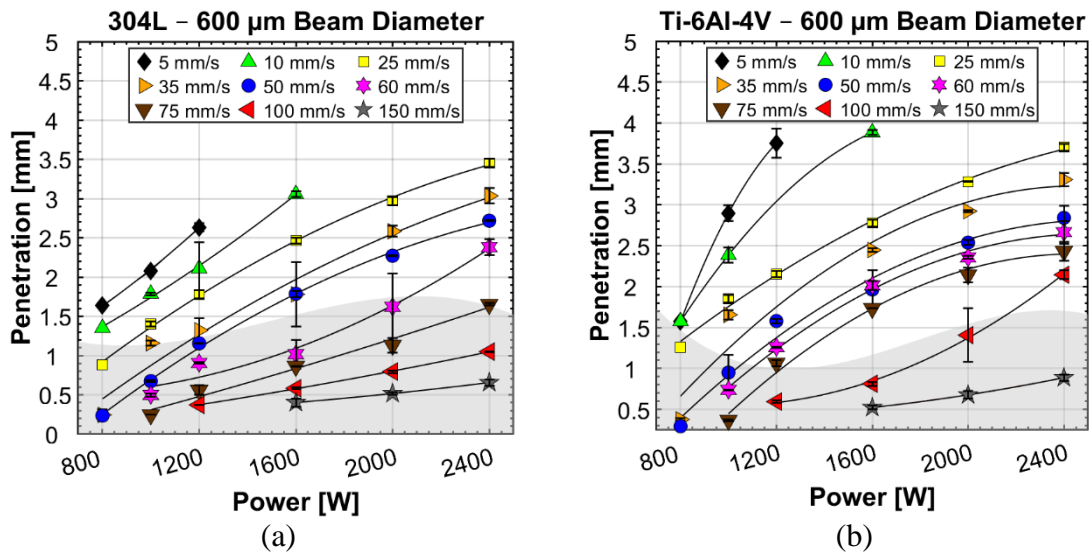


Figure 5.6. Penetration versus power at travel speeds ranging from 5 to 150 mm/s for 304L SS (a) and Ti-6Al-4V (b). The change between keyhole (deep penetration) and a transition into conduction mode welding is shown as the shaded region.

The weld penetration showed nonlinearity for 304L and Ti-6Al-4V. This was expected because the goal was to traverse a range of welding conditions from conduction to keyhole mode. However, even for high aspect ratio welds, or keyhole mode, the rate of increased penetration decreased with increased power. For 304L, the reduced rate of increasing penetration was below a 50 mm/s travel speed. At a 60 mm/s travel speed, a change in penetration occurred at a power above 2000 W. This change is based on the transition from conduction to keyhole mode welding. The approximate region distinguishing keyhole (deep penetration) versus the transition into conduction mode is shown by the shaded area in Figure 5.6a and Figure 5.6b. Ti-6Al-4V showed similar trends but was more pronounced than 304L, and the transition between decreasing to increasing penetration rates occurred at higher travel speeds (i.e., between 75 mm/s and 100 mm/s). Ti-6Al-4V transitioned into a high aspect ratio at lower powers and/or higher travel speeds, and the earlier transition is likely attributed to half the thermal conductivity relative to 304L. Thus, more incident energy is retained for melting and vaporization.

A potential explanation for decreasing penetration rate at lower travel speeds is related to beam attenuation caused by the vapor plume. At higher travel speeds there is potential that the beam can effectively “out-run” the plume. It was noted that Ti-6Al-4V showed inconsistency in the weld behavior at 800 W and a 5 mm/s travel speed. This was not specific to Ti-6Al-4V and was also produced in varying degrees on all alloys investigated. This is speculated to be either keyhole instability relating to beam attenuation and/or collapse of the molten pool into the vapor capillary.

To substantiate the claim of beam attenuation and keyhole instability, a macrophoto of the weld surface for Ti-6Al-4V at 800 W and 5 mm/s is shown in Figure 5.7a with a corresponding longitudinal metallographic section shown in Figure 5.7c. The CW laser weld shows a periodic change in the weld surface that has the appearance of a pulsed laser weld. The pulsed characteristic was not exclusive to Ti-6Al-4V and was also produced in the SS alloys. The M58 SS alloy weld surface produced at the same parameters is shown in Figure 5.7b. However, the transitions were not always periodic and varied depending on the power, travel speed, and material. The pulsed behavior of the weld surface appeared to correspond to the oscillating penetration in the weld root (Figure 5.7c). The root showed a pronounced “root spiking” behavior that related to the peaks and troughs of the weld surface. The line in Figure 5.7c represents an estimation of the front wall angle with the travel direction from left to right. The surface depression corresponds to the location where the keyhole penetrated the workpiece.

A possible explanation is that a keyhole formed and produced vaporization leading to plume formation. The incident energy was quickly reduced through beam attenuation via the generated vapor and/or losses to the surroundings. The reduced incident energy resulted in a transition to conduction mode and reduced vaporization. With reduced plume interaction and beam attenuation, the keyhole reformed starting the process over. This explanation is only a speculation and further analysis is required for confirmation.

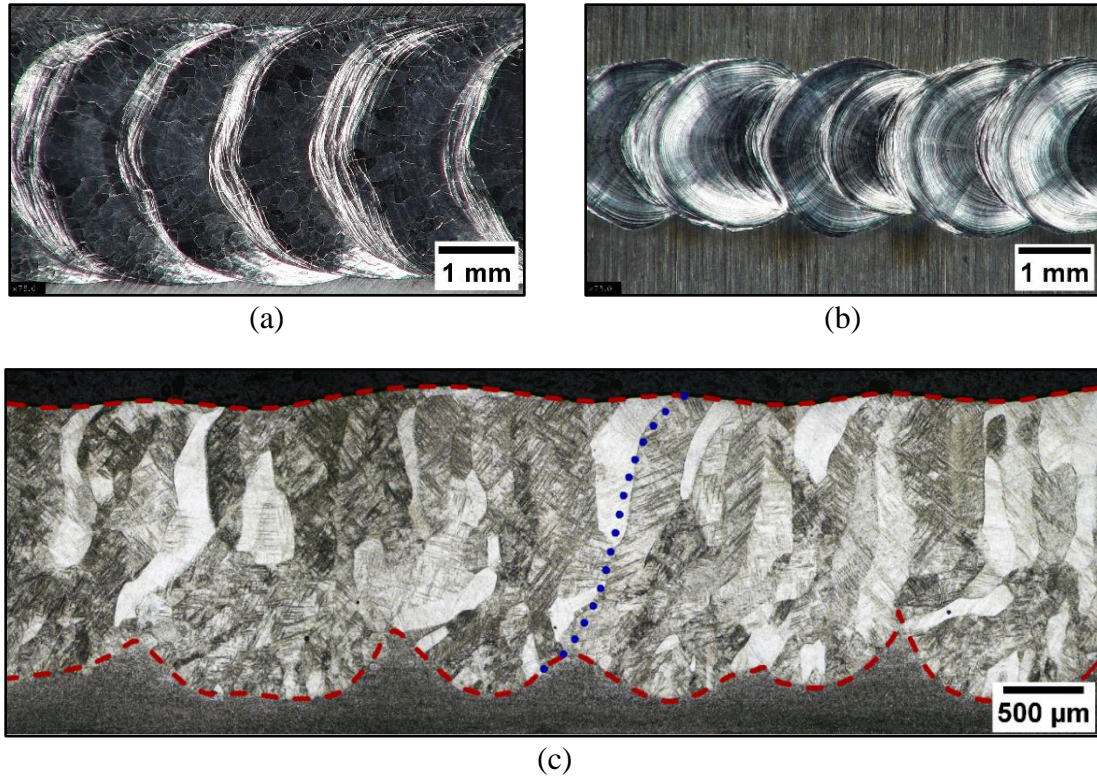


*Figure 5.7. Macrophoto of the weld surface for Ti-6Al-4V (a) and the M58 SS alloy (b) welded at 800 W and 5 mm/s. A corresponding longitudinal section of Ti-6Al-4V showing the oscillation of root penetration and surface ripples (c). The dashed, red lines represent the weld surface (top) and fusion boundary (bottom). The dotted line is an estimation of the front wall angle. The travel direction is from left to right in all photos.*

Another important weld feature includes the weld width, especially where joint fit-up tolerance is a concern. An issue with HED welds is the large variation in transverse weld profiles relative to process parameters. The weld toe width can undergo a major change and is not representative of the widths below the plate surface in deep penetration welding as previously shown in Figure 5.2-Figure 5.5. It was hypothesized that measuring weld width other than horizontally across the weld toes may lead to greater consistency and aid in information regarding keyhole formation.

Width measurements were taken at the weld toe, full-width-half-maximum (FWHM), and the centroid of the transverse section as previously shown in Figure 5.1. The weld toe widths for 304L and Ti-6Al-4V are shown in Figure 5.8a and Figure 5.8b, respectively. The weld toe widths are consistently wider for Ti-6Al-4V compared to 304L but showed similar trends. Further analysis of weld width based on the two-dimensional (2D) centroid of the fusion zone cross-section is shown in Figure 5.9a and Figure 5.9b for 304L and Ti-6Al-4V, respectively. The FWHM approach was adapted from beam diameter analysis but was taken halfway between the plate surface and deepest location of the weld root. The FWHM width followed the same trend as the centroid width but was consistently lower.

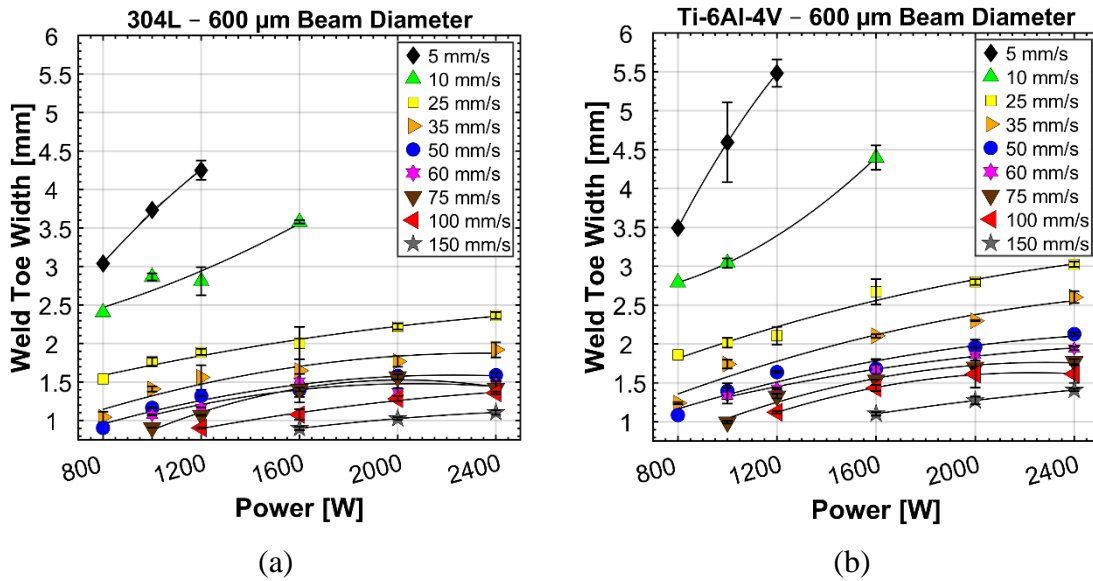


Figure 5.8. Weld toe width versus power at travel speeds ranging from 5 to 150 mm/s for 304L (a) and Ti-6Al-4V (b).

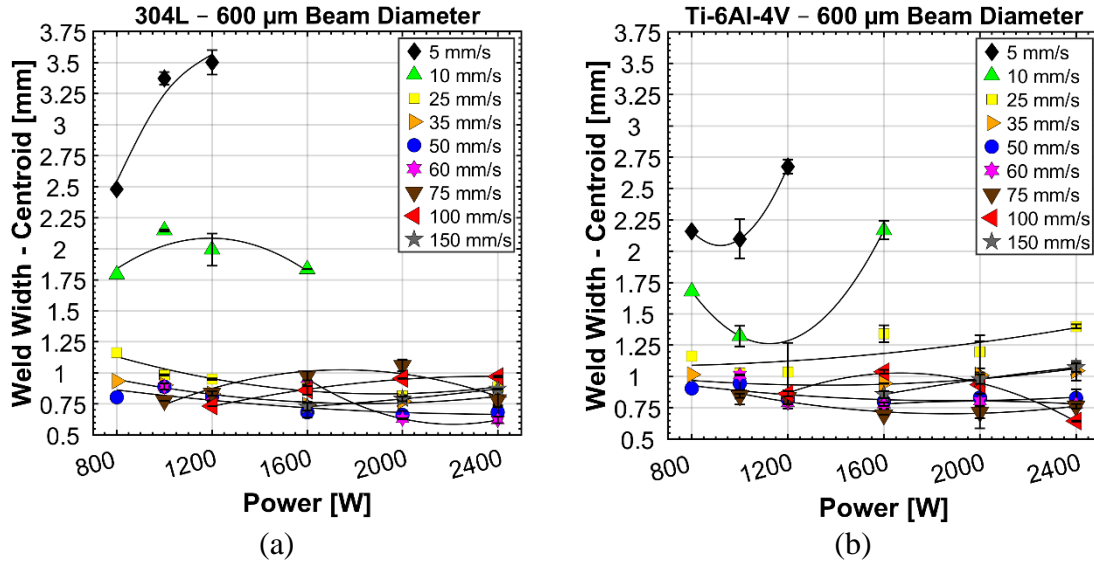


Figure 5.9. Weld centroid width versus power at travel speeds ranging from 5 to 150 mm/s for 304L (a) and Ti-6Al-4V (b).

Other measurements included the fusion boundary length and cross-section area.

The fusion boundary length only includes the fusion boundary within the material (excludes the weld crown). The fusion boundary length followed the same trends as penetration. Cross-section area is a common measurement used to compute melting efficiency [80], [82]. The plot of cross-section versus power for 304L and Ti-6Al-4V is respectively shown in Figure 5.10a and Figure 5.10b, and the change in cross-section area versus power showed nearly linear relationships.

Using the cross-section area to compute the “efficiency” based on the equation reported by Ream [82], the efficiencies are compared in Figure 5.11a for 304L and Figure 5.11b for Ti-6Al-4V. This calculation was previously shown in Equation 2.3 and does not include an energy transfer efficiency, which incorporates losses from reflection or beam

attenuation. Thus, this melting efficiency calculation encompasses the heat transfer efficiency.

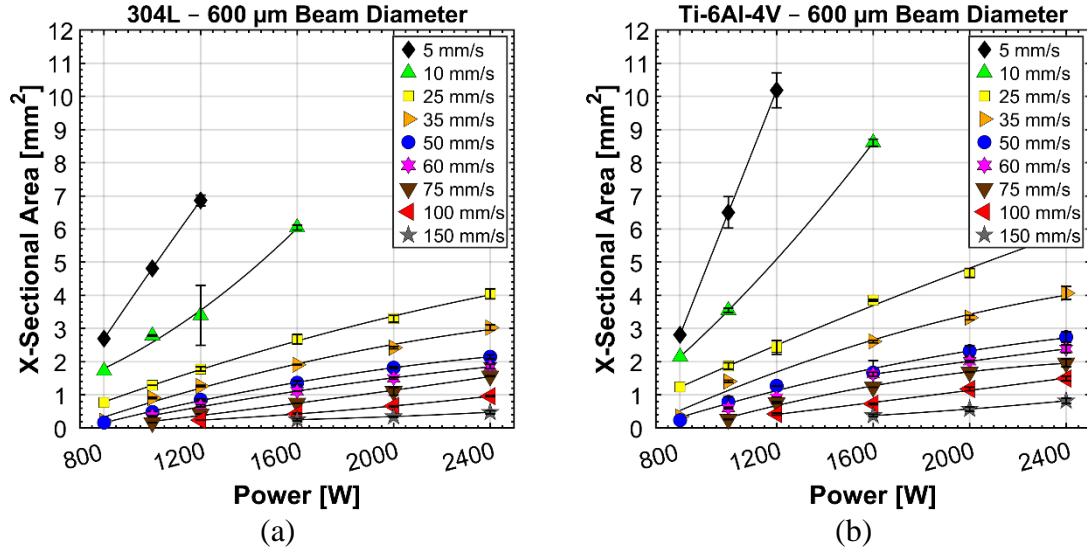


Figure 5.10. Transverse cross-section area versus power at travel speeds ranging from 5 to 150 mm/s for 304L (a) and Ti-6Al-4V (b).

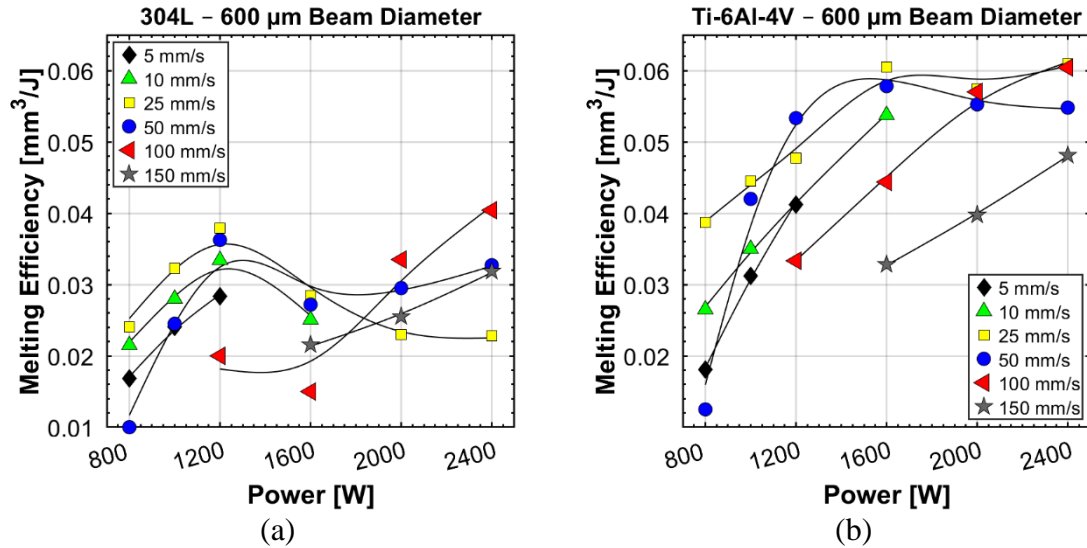


Figure 5.11. Melting efficiency  $[\text{mm}^3/\text{J}]$  versus power at travel speeds ranging from 5 to 150 mm/s for 304L (a) and Ti-6Al-4V (b).

Under the assumption that the same fraction of beam power is absorbed into the workpiece, the greater efficiency for Ti-6Al-4V is attributed to the lower thermal conductivity. This was also manifested in the penetration results with a transition out of a conduction or transition region into keyhole mode welding at lower powers and/or higher travel speeds.

The results presented in this section are solely a presentation of the process-parameter relationships and do not aid in the physical understanding of the welding process. To fundamentally understand and further the current understanding of the physics behind keyhole formation, the ICI system was used to acquire 3D profiles of the vapor capillary, and attempts were made to decant the liquid weld pool to provide an actual measurement of melting efficiency. The following subsections present and discuss these results.

### ***5.1.2 Keyhole Formation***

The previous understanding of keyhole formation through experimental observation was solely through 1D x-ray imaging [11], [68] or 1D surface views from high-speed, optical imaging [237]. The usefulness of the ICI data is to support the underlying mechanisms behind keyhole formation and shape relative to the influences of weld pool convection [118]. It was postulated that this information can show the variation between the vapor depression and the weld pool depth. Figure 5.12 shows a schematic representation of the weld pool depression due to the onset of vaporization and the potential for measuring the depression using the ICI system.

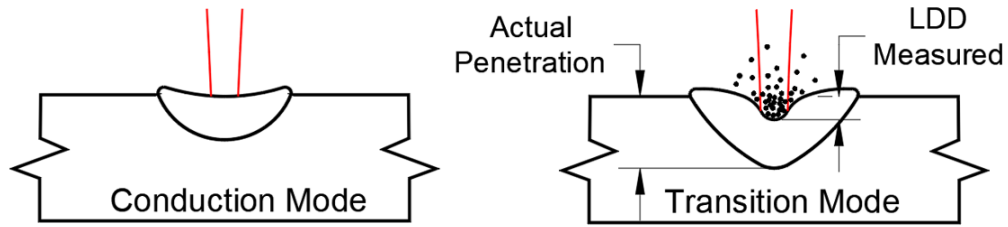


*Figure 5.12. Schematic showing a potential utilization of the ICI system to capture the transition between conduction and keyhole mode welding.*

Fundamentally, the purpose of the ICI system is to quantify the shape, position, and volume of the keyhole or vapor capillary as it relates to process parameters. It is also of interest to characterize the region where a vapor depression/vapor capillary initially forms and relate this to the metallographic section. By post processing a compilation of depth measurements scanned across the weld length, the 3D data was evaluated at different orientations. Welds for 304L SS at 1600 W for 25 mm/s and 50 mm/s are shown in Figure 5.13a and Figure 5.13b, respectively.

In Figure 5.13, the entire region mapped via the ICI system does not contain data relative to the original scan resolution. Due to the nature of the measurement [68], signal is lost or cannot be processed to generate a depth measurement. The regions where the data does not exist are shown as white. However, the region of lost signal distinctly shows the weld pool depression shifted further behind the process beam center at the higher travel speed (50 mm/s). A distinct representation of the keyhole shift is shown in Figure 5.14 for 304L SS at 1000 W. The images are a depiction of a longitudinal orientation through the keyhole center with the travel direction from left to right.

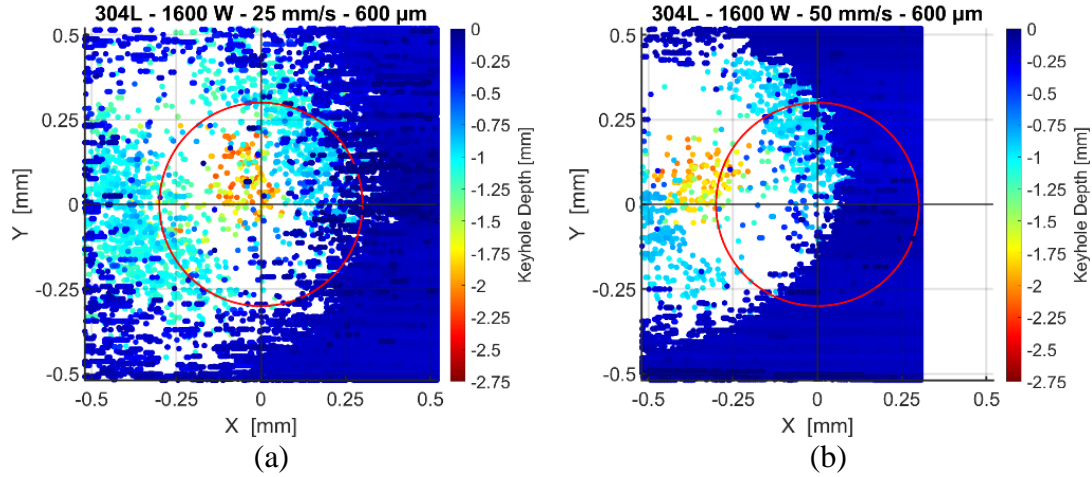


Figure 5.13. ICI keyhole tracking scans on 304L SS at 1600 W and 25 mm/s (a) and 50 mm/s (b). The crosshairs represent the process beam center, the circle represents the process beam diameter, and the white represents no data.

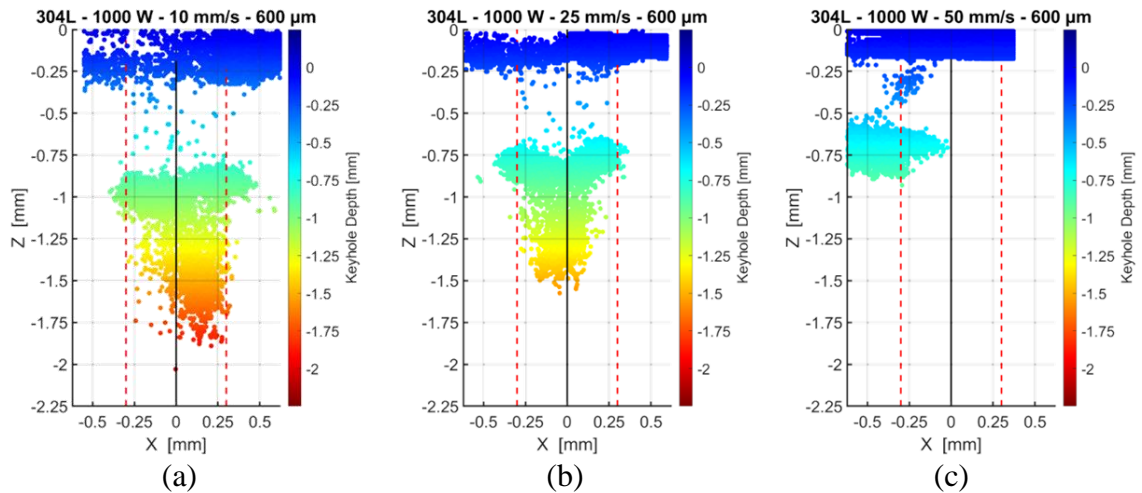


Figure 5.14. ICI keyhole tracking scans at 1000 W and 10 mm/s (a), 25 mm/s (b), and 50 mm/s (c). The weld travel direction is left to right. The solid, black line represents the process beam center, and the dotted, red line (red) represents the process beam diameter.

As the travel speed increased from 10 mm/s (Figure 5.14a) to 25 mm/s (Figure 5.14b), there was a reduction in the depth and a shift of the keyhole root (i.e., bottom) back from the front edge of the process beam. The shift or lag was exacerbated at 50

mm/s (Figure 5.14c) with the bulk of the keyhole behind the process beam. By measuring the deepest location of the keyhole relative to the process beam center, the lag of the keyhole relative to the process beam was plotted for 304L SS, 2205 DSS, and Ti-6Al-4V. Figure 5.15 shows a constant power of 1600 W with increasing travel speed, and Figure 5.16 shows a constant travel speed of 50 mm/s with increasing power.

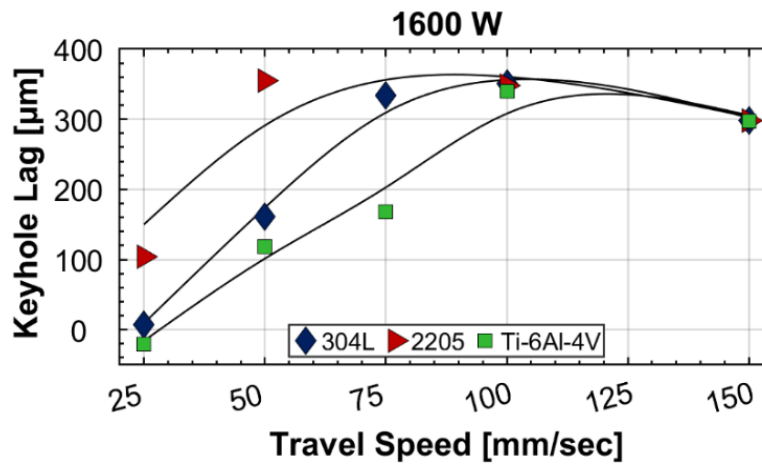


Figure 5.15. Keyhole lag for 304L SS, 2205 DSS, and Ti-6Al-4V at a beam diameter of 600  $\mu\text{m}$  and a constant power of 1600 W.

It is assumed that the high nitrogen content of the 2205 DSS resulted in considerable keyhole lag in regions of deep penetration welding. The assumption is based on similar keyhole behavior for all the SS alloys, except 2205 DSS. Contrary to this, Ti-6Al-4V had the least amount of keyhole lag. At the high travel speeds ( $\geq 100$  mm/s) or low powers ( $\leq 1200$  W), the measured “keyhole” lag became relatively similar between the three alloys. This was likely a result of the ICI system detecting a weld pool depression in the transition/conduction regimes, regardless of the material. Fully

characterizing regions within limited weld pool depression was skewed by excessive noise in the data, particularly at higher travel speeds. Due to this, the transition regions versus conduction mode were not fully characterized.

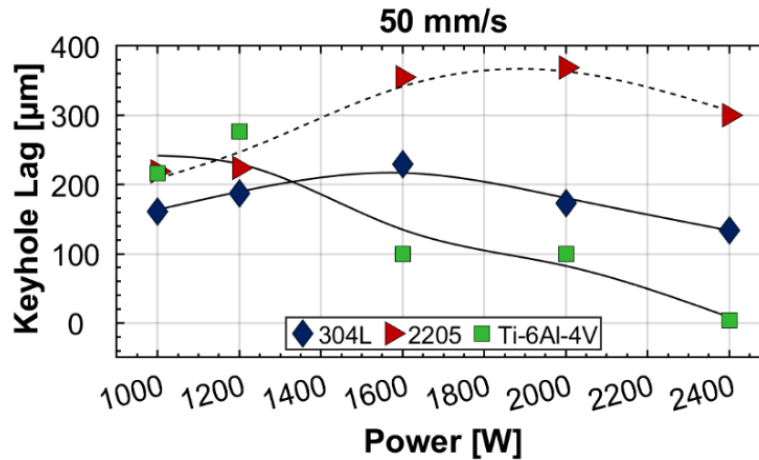


Figure 5.16. Keyhole lag for 304L SS, 2205 DSS, and Ti-6Al-4V at a beam diameter of 600  $\mu\text{m}$  and a constant travel speed of 50 mm/s.

The keyhole position results are crucial for better understanding the beam interaction with the workpiece. If the lag of the keyhole increases behind the process beam, the incident laser energy cannot propagate into the depths of the cavity and be fully absorbed into the workpiece. Thus, the energy may become projected onto material in front of the weld that is assumed to be solid and oriented normal to the incident beam. This can be visualized in Figure 5.14 between the slower travel speeds and 50 mm/s (Figure 5.14c). If this assumption is valid, the process efficiency would be greatly influenced. Another influential factor is the absorption of beam energy along the keyhole wall. Changing the wall angle will alter absorption and the heat flow into the interface

[13]–[15]. Also, the beam will become distributed across an angled surface that is no longer representative of the beam diameter of 600  $\mu\text{m}$  normal to the beam axis.

To further understand the keyhole, a surface fitting algorithm was developed in MATLAB<sup>®</sup> and is provided in Appendix N:. The difficulty in performing this operation was attributed to the variation in signal between process parameters and materials. In addition to regions of data absent from the measurement matrix, there was substantial noise in the data. It is assumed that a source of noise was caused by acceleration and deceleration, which introduced vibrations into the optics [67]. The lack of data and noise necessitated compounding numerous fitting operations such as finding peak locations and performing running averages. Figure 5.17 shows the surface fits for 304L at the same parameters shown in Figure 5.14.

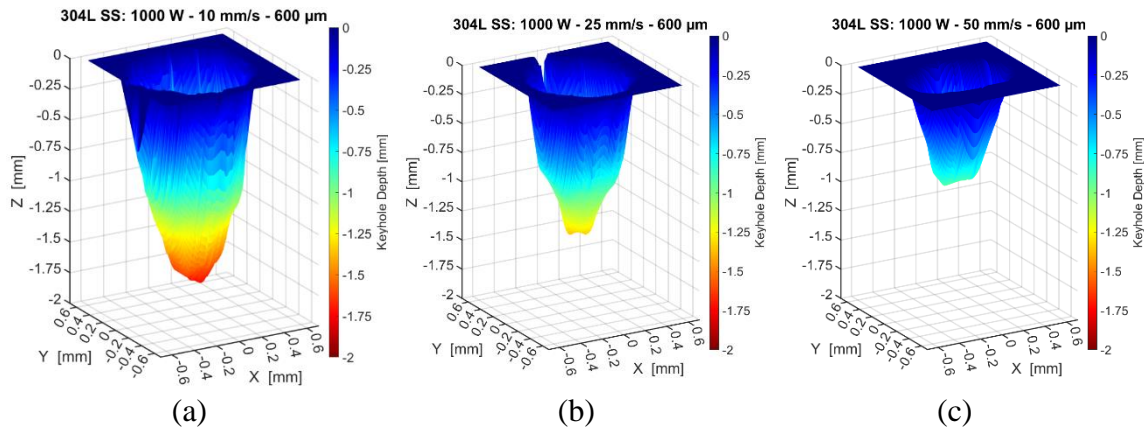


Figure 5.17. Surface fit ICI data from 304L SS at 1000 W and 10 mm/s (a), 25 mm/s (b), and 50 mm/s (c).

Analysis of the results in Figure 5.14 and Figure 5.17 shows that there are two distinct regions within a keyhole. The upper region of the vapor cavity that connects to the weld pool surface maintains a wider diameter and is consistent across keyhole to conduction transition conditions. At long interaction time and/or high power sufficient to generate a deep penetration weld, a second region forms that contains a smaller radius than the initial weld pool depression. Based on these results, it is argued that conduction mode, or low aspect ratio, welds may maintain a considerable amount of vaporization, which imparts a back pressure to sufficiently depress the weld pool surface. At some interaction time or power, the recoil forces from vaporization can sufficiently overcome the surface tension and penetrate deeper into the workpiece. The difference in weld pool depression shown between Figure 5.17b and Figure 5.17c is believed to be the distinction between keyhole and conduction mode welding. The 304L macrosections in Figure D.14 in Appendix D: support this analysis.

It should be noted that the wall angle between the detected transition and the pool surface may have a drastically different appearance than produced by the fitting algorithm and results presented in Figure 5.17. If the vapor cavity were to bulge outward in a spherical or elliptical shape or taper behind the beam and underneath the weld pool, the geometry would not be detectable via the ICI system.

Using the surface fitting results, the keyhole volumes and diameters were estimated for 304L SS, 2205 DSS, and Ti-6Al-4V. The volume results at a constant power of 1600 W and varying travel speed are shown in Figure 5.18. The measured

keyhole diameters at the same parameters are shown in Figure 5.19. The volume computation was performed through a summation of the pixel volumes computed from each pixel value (height). The diameter computation was adapted from the second moment (D2M) beam diameter calculation and applied to measure the surface fitting results.

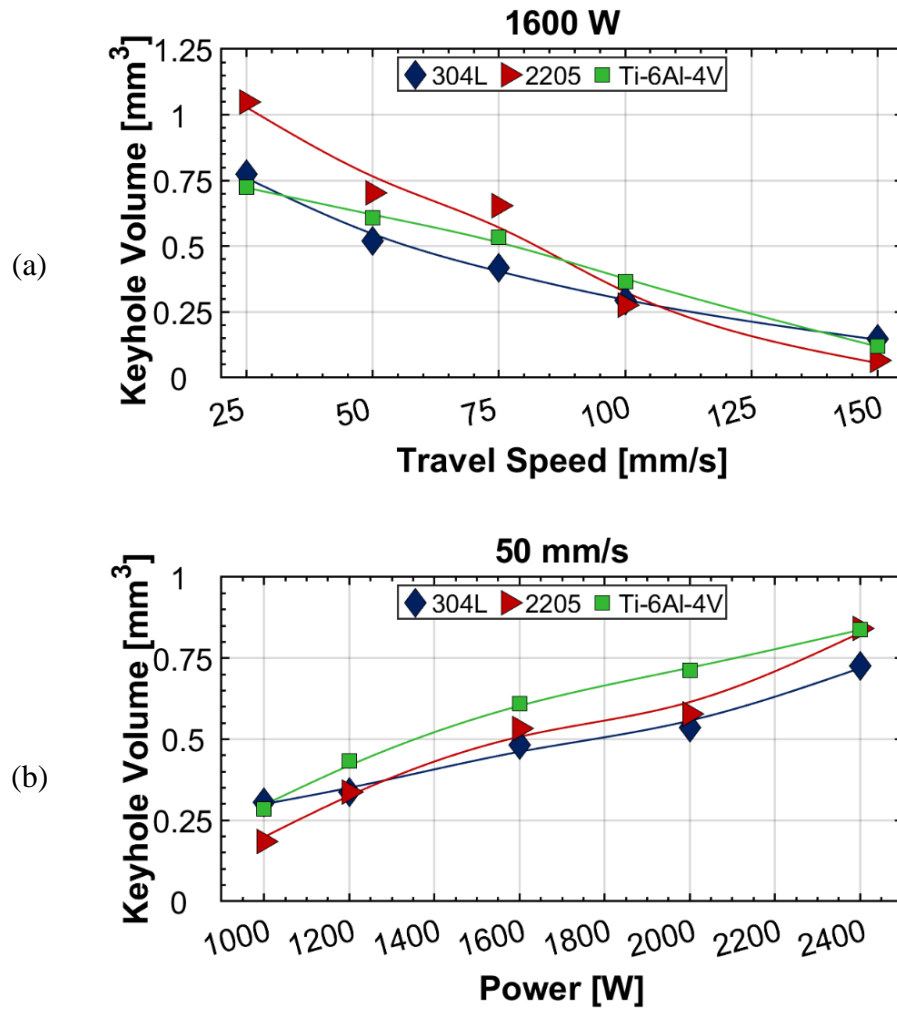


Figure 5.18. Change in keyhole volume for 304L SS, 2205 DSS, and Ti-6Al-4V at 1600 W and varying travel speeds (a) and 50 mm/s and varying power (b).

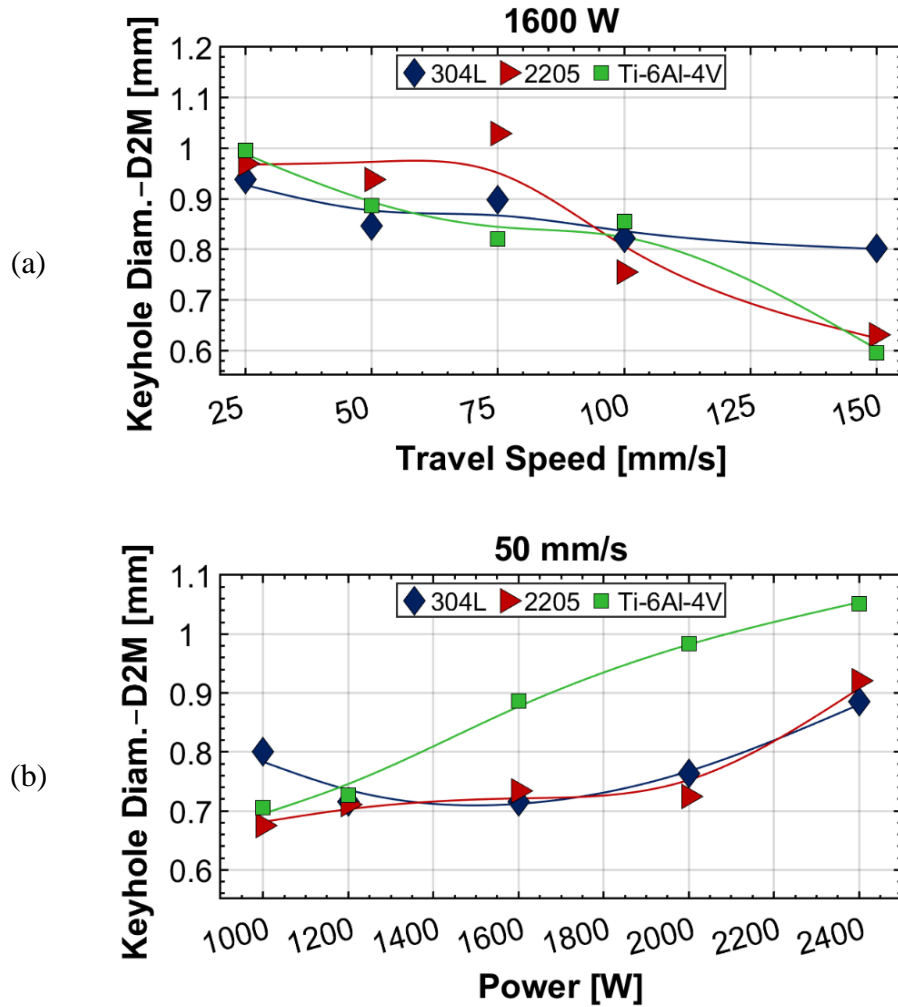


Figure 5.19. Change in keyhole diameter for 304L SS, 2205 DSS, and Ti-6Al-4V at 1600 W and varying travel speeds (a) and 50 mm/s and varying power (b).

Increased travel speed (Figure 5.18a) reduced the volume with a similar relationship as penetration versus travel speed. At a constant travel speed (Figure 5.18b), the keyhole volume nearly showed a linearly increasing relationship with increasing power. For constant power, the keyhole diameter appeared to maintain a relatively consistent size until a transition occurred into conduction mode at speeds greater than 75

mm/s (Figure 5.19a). The diameters were  $\approx 0.7$ -1 mm and  $\approx 0.35$  mm larger than the beam diameter, but at constant travel speed, the diameters significantly varied. At 2400 W, all alloys showed an increase in the keyhole diameter, and Ti-6Al-4V maintained a larger diameter from 1600 W to 2400 W than 304L SS and 2205 DSS. It should be noted that Figure 5.18 and Figure 5.19 only contain data assessed from a single keyhole scan, so in-depth comparisons and relationships cannot be drawn due to the scatter and the overlap in the data for each alloy.

Historically, depth-to-width aspect ratios greater than 1-1.5 [1], [4] are used to distinguish the transition from conduction to keyhole mode welding. This is under the assumption that weld toe was/is used as the location for determining the weld width. However, the indication of keyhole formation related to a weld toe-based aspect ratio is not a reliable distinction between conduction and keyhole mode, assuming keyhole is in fact referring to the creation of a vapor capillary within the liquid pool. ICI results along with macrophotos are shown in Figure 5.20 to illustrate the comparison between a detected vapor cavity and low aspect ratio weld.

There is a clear indication of a keyhole from the ICI results at 800 W and travel speeds of 5 mm/s (Figure 5.20a) and 25 mm/s (Figure 5.20b). Analysis of the weld macrophotos showed measured depth-to-width aspect ratios around 0.5 and lower than the generalized value near 1-1.5. If the depth-to-width analysis is performed using the centroid width or FWHM weld width, the 800 W and 25 mm/s weld has an aspect ratio

near 1.0, and therefore, indicates the cusp for keyhole formation, which is confirmed based on the macrophoto and ICI data.

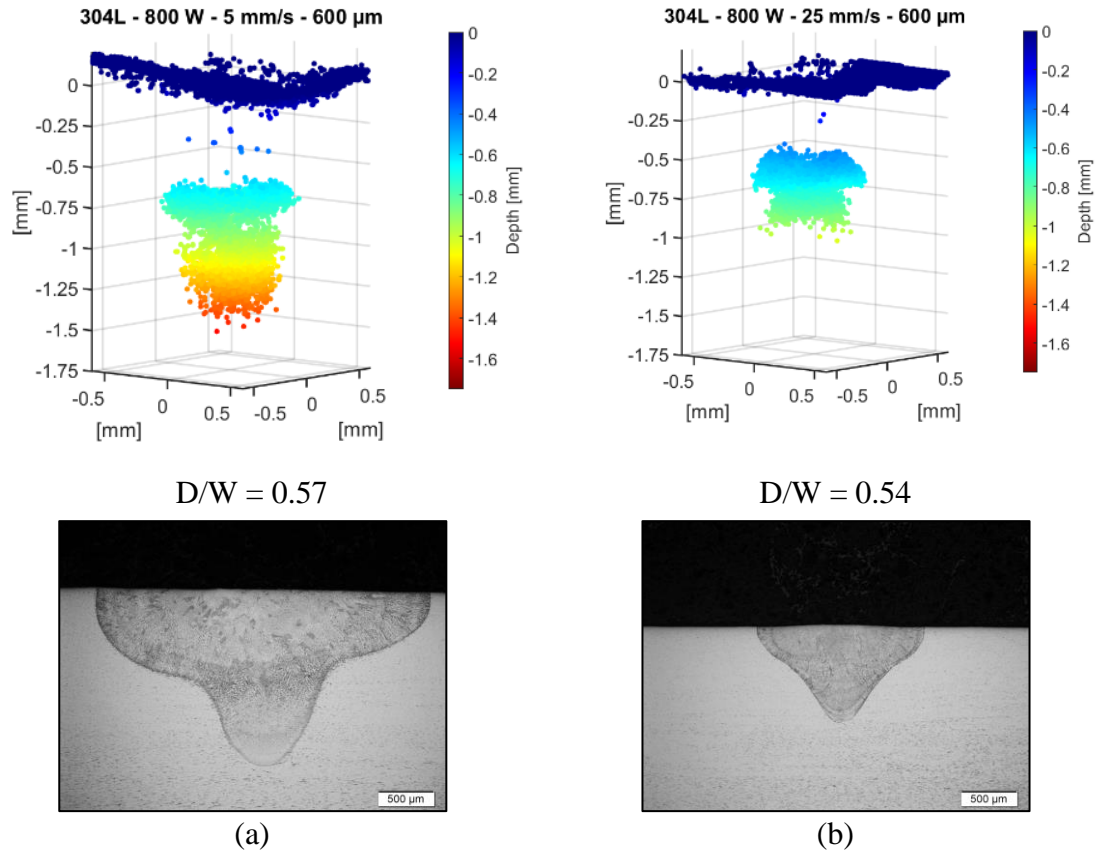
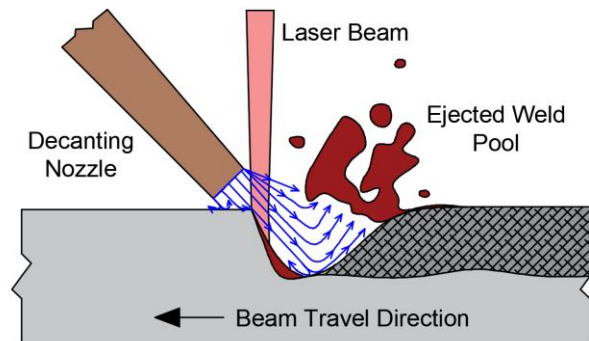


Figure 5.20. Welds produced at 800 W showing low depth-to-width aspect ratios but maintaining keyholes as confirmed through ICI analysis: 5 mm/s (a) and 25 mm/s (b).

### 5.1.3 Weld Pool Decantation

Weld pool decantation was an attempt to instantaneously remove the liquid pool during the welding process. This was performed by blowing a jet of compressed helium into the pool on the leading edge of the weld. An idealized liquid pool removal is shown

schematically in Figure 5.21. The purpose of this experiment was to measure the region where liquid exists and quantify welding efficiency through a volume of extracted liquid. This volume measurement was performed using a stationary scan with the ICI system over the region of extracted liquid.



*Figure 5.21. Schematic representation of weld pool decanting using an instantaneous jet of compressed gas to expel the liquid.*

An important parameter is the angle of the decanting nozzle relative to the front wall angle of the weld. It was necessary to force the liquid along the front wall of the weld and out the back where the trailing edge of the pool has solidified. The steeper the front wall slope relative to the plate surface, the easier it was to force the molten pool deeper into the material, and when the front wall angle approached vertical, as in deep penetration welds, sufficiently expelling the liquid away became increasingly difficult.

Photographic results from pool decanting of 304L SS at 1000 W and 5 mm/s, 10 mm/s, and 25 mm/s are shown in Figure 5.22. The topographical ICI profiles are shown in Figure 5.23. The travel direction is from left to right in the photographs and measured topography results.

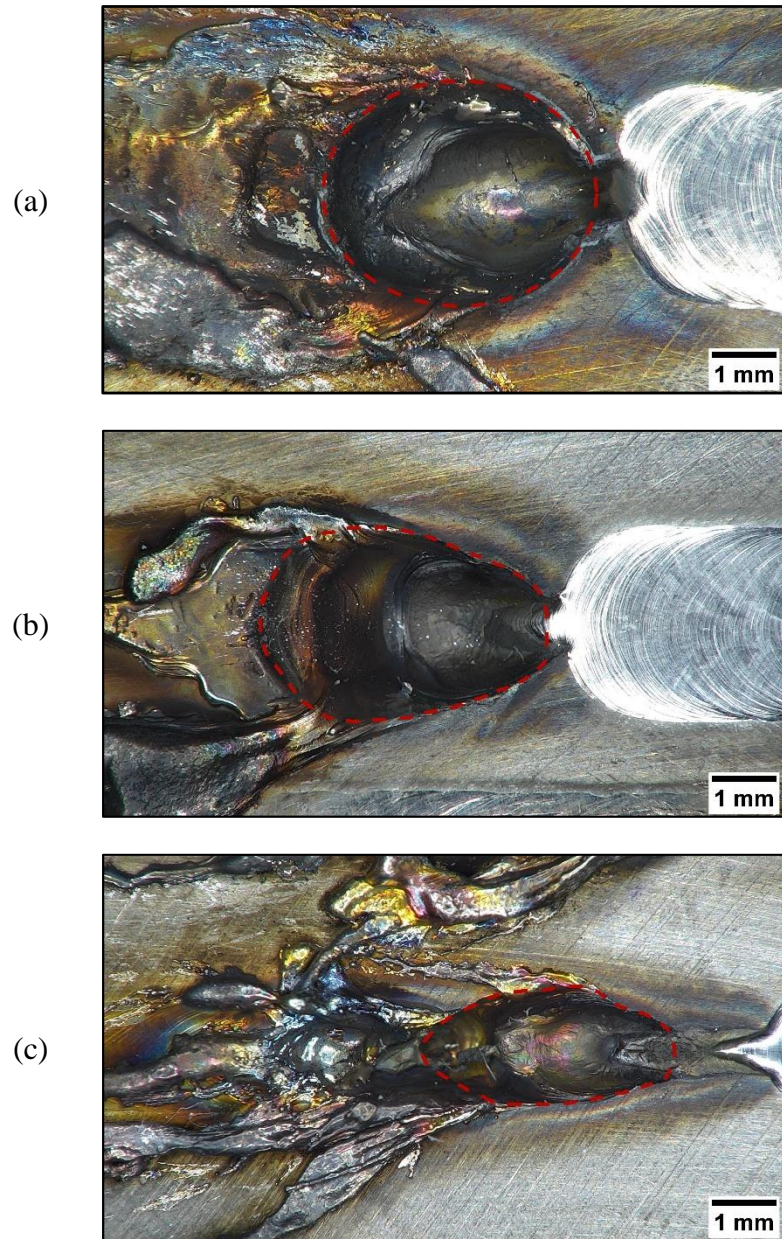


*Figure 5.22. Surface photographs of the decanted weld pools for 304L SS at 1000 W and 5 mm/s (a), 10 mm/s (b), and 25 mm/s (c). The weld travel direction is from left-to-right, and the dashed line shows the approximate region of the decanted weld pool. The expelled and oxidized liquid covers the weld surface on the left.*

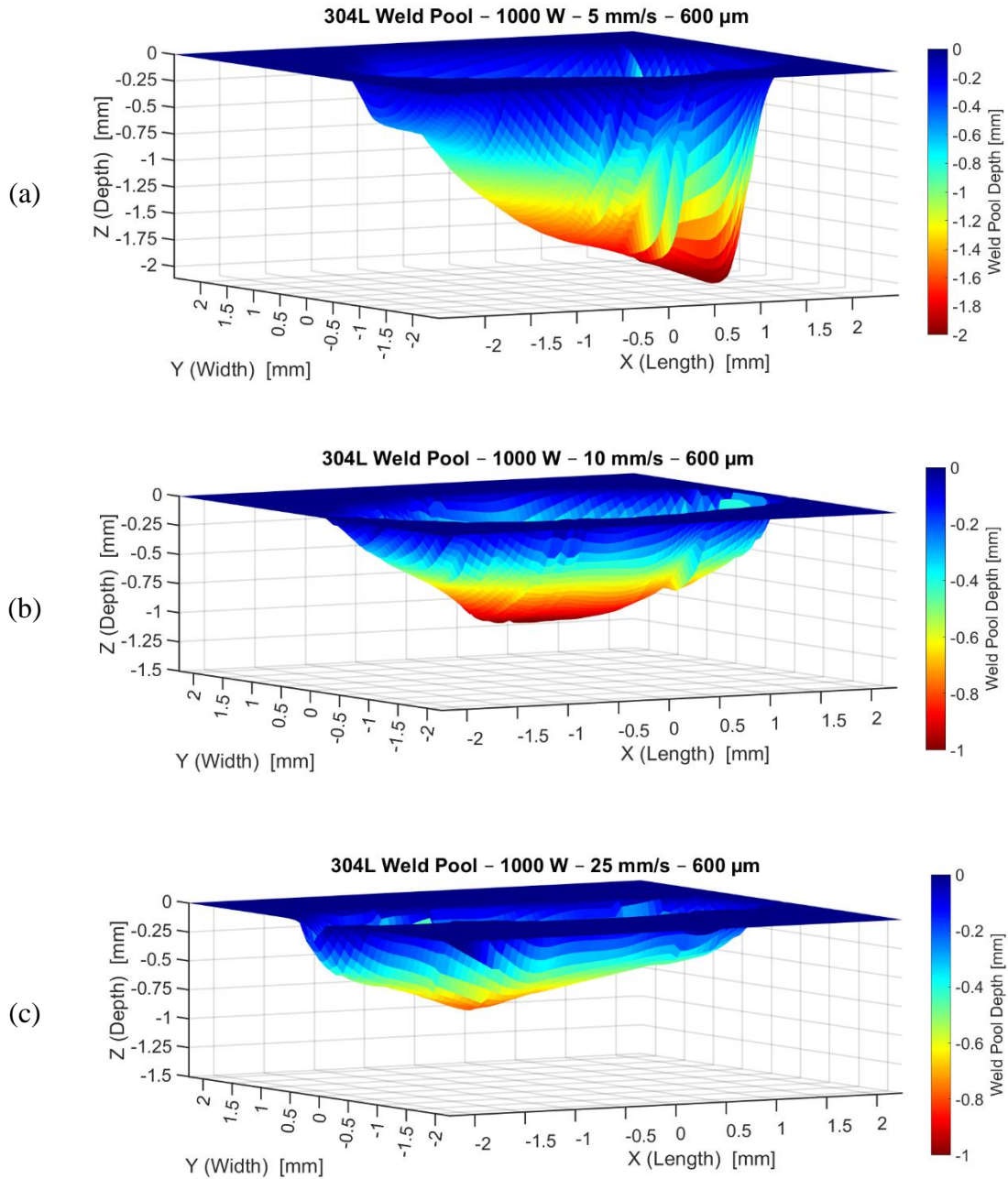


Figure 5.23. Surface fit of the 304L SS decanted weld pools at 1000 W and 5 mm/s (a), 10 mm/s (b), and 25 mm/s (c). Travel is in the positive x-direction. Note: The images contain different z-axes and colorbar scales.

The decanting procedure was only performed on 304L SS using 1000 W due to issues related to sufficiently removing the molten pool. Other attempts were performed at 1600 W, but the high-pressure helium further deepened the weld. The high-pressure gas caused the keyhole to deepen with a transition similar to laser beam cutting systems and coaxial gas flow. However, exhaustive trial and error to optimize the decanting procedures for different laser parameters was not performed.

Using the information from surface fitting the point cloud ICI data, parameters were extracted to include the maximum depth, volume, and D2M diameter. These results are presented in Table 5.1 and Table 5.2. The measured weld depth from decanting was similar to the transverse section penetration at 5 mm/s but was less than the measured depth at 10 mm/s and 25 mm/s.

*Table 5.1. Measured features from decanting 304L SS at 1000 W.*

Travel Speed [mm/s]	Measured Weld Depth [mm]	Maximum Decanted Depth [mm]	Depth Percent Difference [%]	Measured FWHM Diameter [mm]	Decanted FWHM Diameter [mm]
5	2.2	2.1	3.1	0.7	2.2
10	1.8	1.1	24	1	2.4
25	1.4	0.8	14	2.4	2.3

*Table 5.2. Decanted volume and calculated melting efficiency for 304L SS at 1000 W.*

Travel Speed [mm/s]	Measured Volume [mm <sup>3</sup> ]	Theoretical Melt Volume [mm <sup>3</sup> ]	Measured Melting Efficiency ( $\eta_{\text{melt}}$ ) [%]
5	11.1	15.1	73
10	4.5	7.6	60
25	2.3	3.0	76

Further analysis of the volume measurement was performed by relating the total energy input to the interaction time. The calculation for this theoretical volume assuming no heat loss is shown in Equation 5.1. With the theoretical melting efficiency calculation, a measured melting efficiency was determined by dividing the measured liquid volume by the theoretical volume as shown in Equation 5.2. The efficiency results presented in Table 5.2 and show that the LBW process on 304L SS at 1000 W is nearly 70% efficient at transferring the incident beam energy into weld pool melting.

$$\text{Equation 5.1: } Q = mC_p\Delta T + mL_m = \rho VC_p(T_m - T_0) + \rho VL_m$$

$$Q = Pt_i \rightarrow V_{100\%} = \frac{Pt_i}{\rho[C_p(T_m - T_0) + L_m]} \quad [\text{mm}^3]$$

Where:  $Q$  = energy input,  $m$  = mass,  $C_p$  = specific heat,  $V$  = volume,  $T_m$  = melting temperature,  $T_0$  = initial temperature,  $\rho$  = density,  $P$  = power,  $t_i$  = interaction time,  $L_m$  = latent heat of melting

$$\text{Equation 5.2: } \eta_{\text{melt}} = \frac{V_{\text{decant}}}{V_{100\%}} \quad [\%]$$

Where:  $\eta_{\text{melt}}$  = measured melting efficiency,  $V_{\text{decant}}$  = measured volume from weld pool decantation,  $V_{100\%}$  = calculated volume

#### 5.1.4 Summary

The results presented in this section showed a transition to deep penetration welding at lower powers and higher travel speeds for Ti-6Al-4V as compared to 304L SS. At 800 W of power, periodic surface ripples were produced at low travel speeds

(5 mm/s) and are speculated to relate to a transition in and out of keyhole mode. Weld pool decanting indicated that the melting efficiency for LBW 304L SS at 1000 W of power is nearly 70%.

The ICI analysis showed that the keyhole can lag the process beam position, and the lag was greatest with 2205 DSS followed by 304L and Ti-6Al-4V. The ICI system also detected a weld pool depression or vapor cavity in welds appearing as conduction mode based on the metallographic section. In addition, the ICI system was used to estimate the 3D geometry of the vapor capillary, and there was a negligible difference in the keyhole volume between 2205, 304L, and Ti-6Al-4V.

## **5.2 Modeling**

The error associated with the analytical/dimensionless solutions, as reviewed in Section 2.5, and the inability to satisfactorily improve these models led to neural network analysis for an adequate predictive tool. The results from the developed neural network algorithm are presented in this section.

### **5.2.1 *Artificial Neural Network***

Based on the procedures defined in the experimental section, a feedforward neural network algorithm was developed using MATLAB<sup>®</sup> software. The empirical weld data was used to train the models with the features explained in Section 4.2 and presented in Section 5.1.1. Each power and feature were trained using a separate model, and these

individual models were compiled together to generate a complete, predictive algorithm. This algorithm was implemented into a graphical user interface (GUI) that can be easily deployed to a desktop or laptop computer for quickly analyzing process parameters and weld outputs for 304L and Ti-6Al-4V.

The models currently have severe limitations, and these limitations are based on the lack of data available for training. The greatest limitation is the beam diameter restriction of 600  $\mu\text{m}$ . Because this was the only diameter the models were trained on, predictions cannot be made for any other beam diameter. Also, other restrictions include the bounds of powers and travel speeds used to train the data. Although it is possible that the models may be predictive outside these ranges, validation was not performed.

The layout of the neural network GUI is presented in Appendix I: in Figure I.1. The functionality of the interface was developed for continually populating the models with new LBW data. The main user selections include material, power, and travel speed. Three other selection dropdowns include beam diameter, beam angle, and shielding gas. At the time of this writing, these cannot be changed and were consistent throughout this investigation. Figure 5.24 shows modeled penetration results for 304L SS at 1600 W, and Figure 5.25 shows the same results for Ti-6Al-4V. The distinct penetration changes for Ti-6Al-4V between 35 mm/s and 100 mm/s is relatively easy for the neural network to fit. However, sharp transitions created overfitting issues.

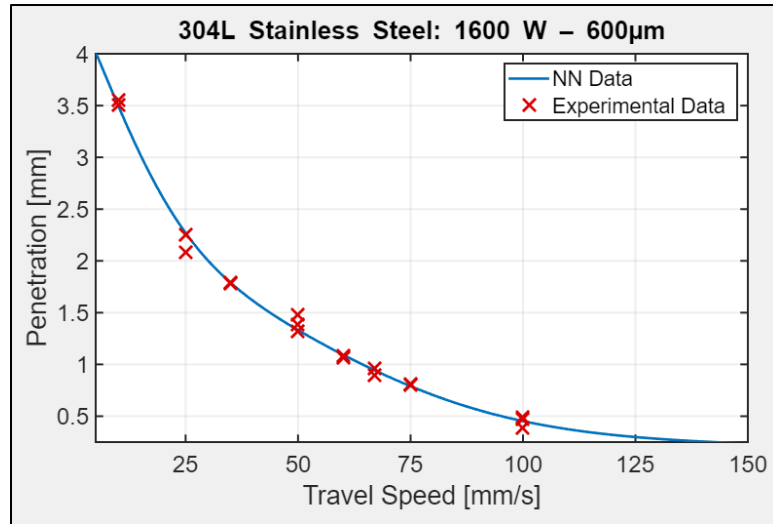


Figure 5.24. Neural network algorithm penetration results for 304L SS at 1600 W.

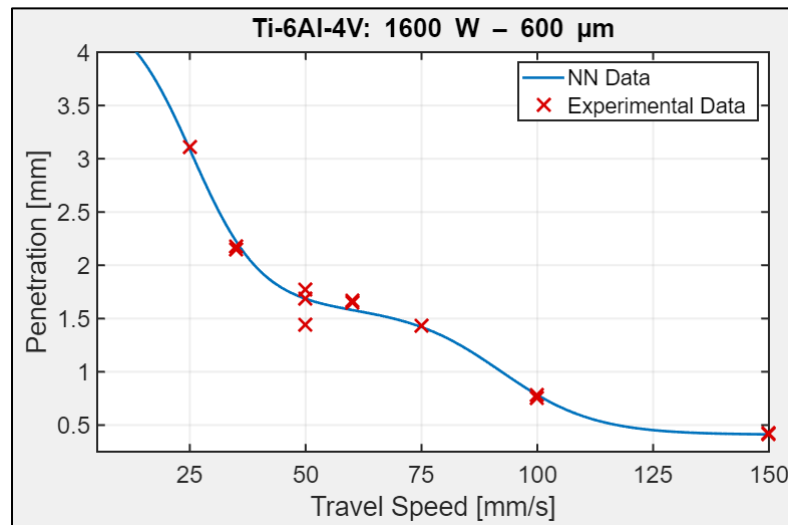
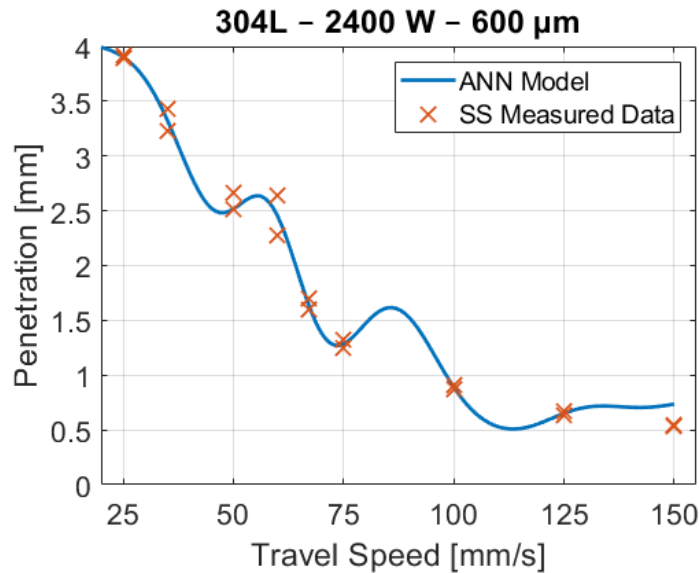


Figure 5.25. Neural network algorithm penetration results for Ti-6Al-4V at 1600 W.

An extreme example of overfitting data is presented in Figure 5.26 using a model trained with ten nodes. The data is from penetration measurements on 304L SS at 2400 W. Conversely, underfitting data can also be an issue with too few nodes. Figure

5.27 shows NN results that underfit the centroid weld width data. This model (Figure 5.27) was trained using three nodes. As stated in the experimental procedures section, the final models deployed to the GUI were trained with four nodes for the penetration and the cross-sectional area and six nodes for the three width measurements. The algorithm results for 304L and Ti-6Al-4V published to the GUI are presented in Appendix I:.

Reports of computed error are not provided because most of the data was used to train the models. Thus, the limited amount of data was biased towards training the models to produce the best fits possible. Also, the algorithm was developed for continuous improvement with the ability to add data, retrain the models, and redeploy the application.



*Figure 5.26. Illustration of overfitting penetration data using a single hidden layer with ten nodes for the feedforward ANN.*

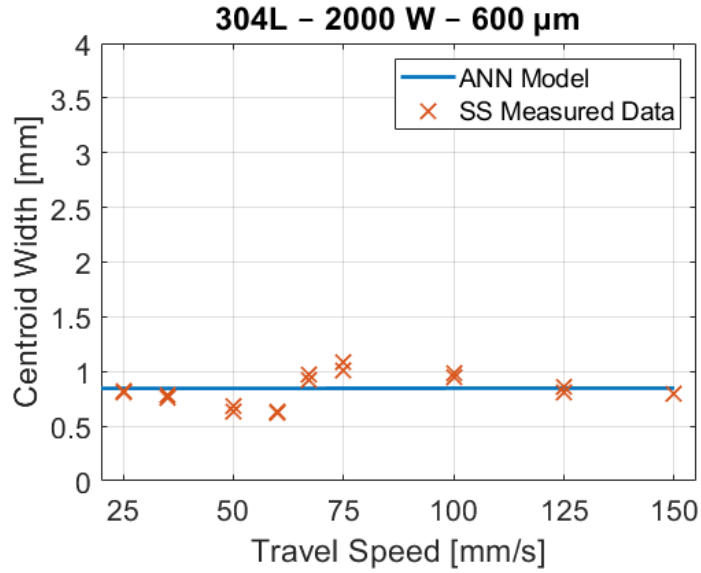


*Figure 5.27. Illustration of underfitting data using a single hidden layer with three nodes for the feedforward ANN.*

### 5.2.2 Summary

A feedforward artificial neural network was produced for each weld feature analyzed, and the individual models were compiled into a comprehensive algorithm. The best fitting results were achieved with a single hidden layer composed of three nodes for predicting penetration and cross-section area and six nodes for fitting all weld width measurements. The respective number of nodes produced results with the least overfitting or underfitting for all the weld parameters incorporated into the model.

### 5.3 Microstructural Analysis

This section analyzes the microstructural results observed from optical microscopy, scanning electron microscopy, and EBSD analysis and evaluates the variations in microstructures at transverse, longitudinal, and plan view weld sections. The results are analyzed separately for stainless steels and Ti-6Al-4V.

#### 5.3.1 Stainless Steel Alloys

Table 5.3 contains the calculated  $Cr_{eq}/Ni_{eq}$  relationships developed by Kujanpää et al. (Suutala) [204], Hammar and Svensson [208], and Kotecki and Siewert (WRC-1992) [206]. Figure 5.28 shows the locations where the SS compositions analyzed in this study are represented on the prior microstructural map developed by Lippold [190]. Based on the microstructural map, the alloys with WRC-1992  $Cr_{eq}/Ni_{eq}$  of 2.1 or greater were anticipated to solidify as  $\delta$ -ferrite and maintain a fully ferritic structure at room temperature regardless of the solidification velocity.

Table 5.3. Suutala, Hammar and Svensson (H&S), and WRC-1992  $Cr_{eq}/Ni_{eq}$  values.

Alloys		Suutala	H&S	WRC-1992
304L	◆	2.0	1.8	1.7
M58	▲	1.8	1.8	1.9
M45	■	2.1	2.1	2.1
M53	●	2.1	2.1	2.2
M54	★	2.8	2.8	2.8
2205	⬢	3.1	3.1	2.7

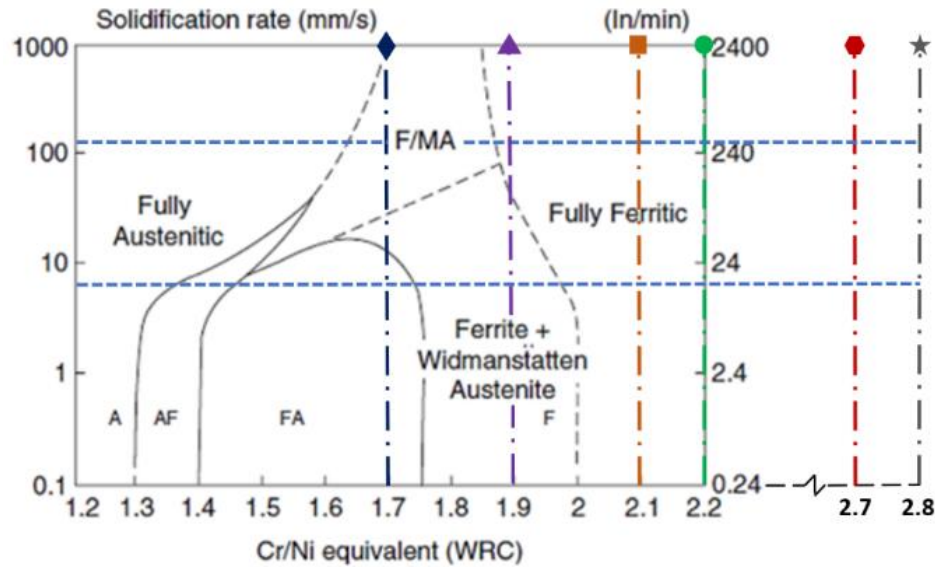
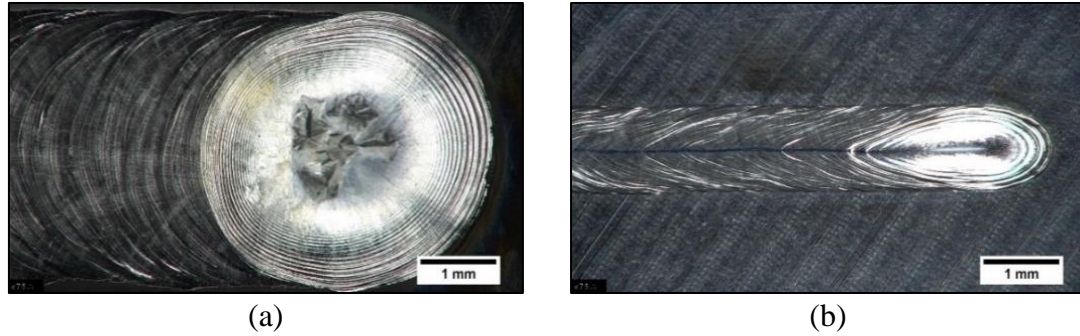


Figure 5.28. Previous microstructural map from Lippold [190] with vertical lines added showing the Cr/Ni equivalencies investigated in this study. The horizontal, dashed lines represent the range of travel speeds utilized.

### 5.3.1.1 Weld Pool Profiles and Solidification Rates

It was assumed that by maintaining the travel velocity and abruptly extinguishing the laser beam, the weld pool depression solidified without considerable backfilling and effectively quenched in the geometry of the progressing pool. With this assumption, longitudinal sections and macro photos of the weld-end surfaces were used to construct approximate weld pool shapes. Macro photos of the weld termination at 1000 W and a travel speed of 5 mm/s and 50 mm/s are provided in the Figure 5.29a and Figure 5.29b, respectively. Weld termination macro photos at 1600 W and travel speeds of 50 mm/s and 100 mm/s are shown in Figure 5.30a and Figure 5.30b, respectively.



*Figure 5.29. 304L SS weld termination photographs, 1000 W of power at a) 5 mm/s, b) 50 mm/s.*

The slow travel speed and high heat input at 1000 W and 5 mm/s (Figure 5.29a) created a circular weld pool comparable to low travel speeds in GTAW. The high energy density at 1600 W developed pools that maintained a “tear-drop” shape throughout the travel speeds analyzed. Beneath the weld surface, these elongated profiles developed drastically different shapes depending on the input parameters. Transverse and longitudinal cross-sections at 50 mm/s for 1000 W and 1600 W are shown in Figure 5.31a and Figure 5.31b, respectively.

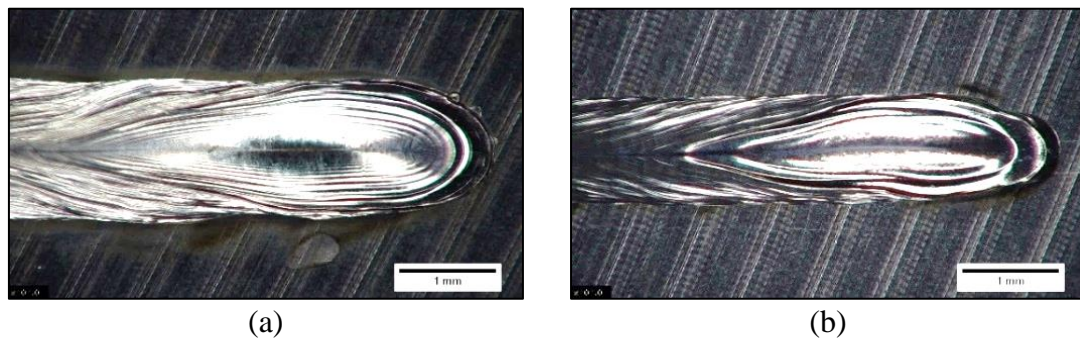
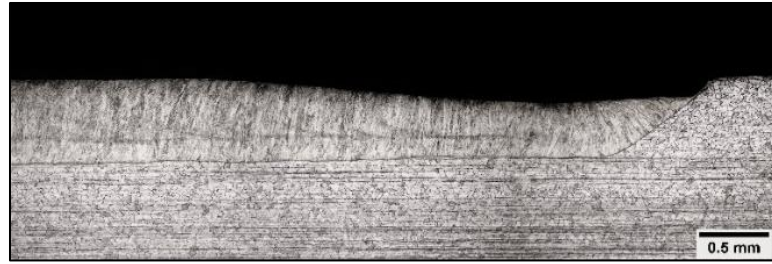


*Figure 5.30. 304L SS weld end photographs. 1600 W of power at a) 50 mm/s, b) 100 mm/s.*



(a)



(b)

*Figure 5.31. Longitudinal weld sections at 50 mm/s, a) 1000 W and b) 1600 W. Longitudinal micrographs are from stitched photos originally captured at 50X.*

Figure 5.31a shows the nearly vertical grain growth from the root to the surface. The etching response in Figure 5.31b indicated that the transition into keyhole mode welding generated grain growth nucleating from the root that became impeded by grain growth orthogonal to the welding direction.

At 1000 W and 5 mm/s, a sharp transition in velocity vectors was created from the root to the weld surface as shown in Figure 5.32. This resulted in solidification rates slowing from nearly 4 mm/s ( $30^\circ$ ) to 0.7 mm/s ( $82^\circ$ ). Increasing the travel speed to 50 mm/s and eliminating a high aspect ratio produced uniform weld pool elongation and solidification rates of  $\approx 17$ -20 mm/s ( $67$ - $70^\circ$ ).

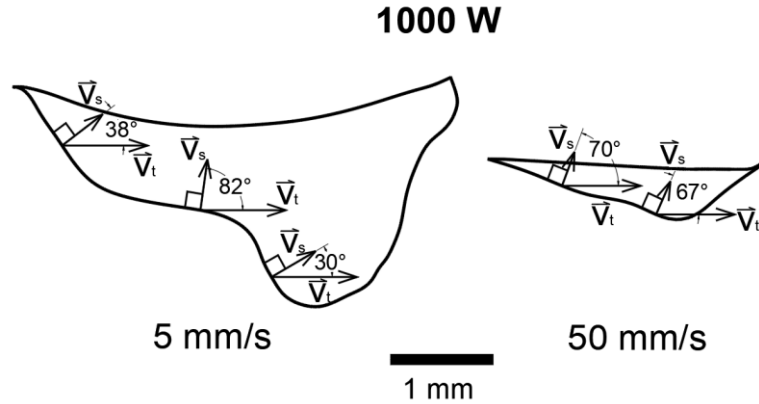
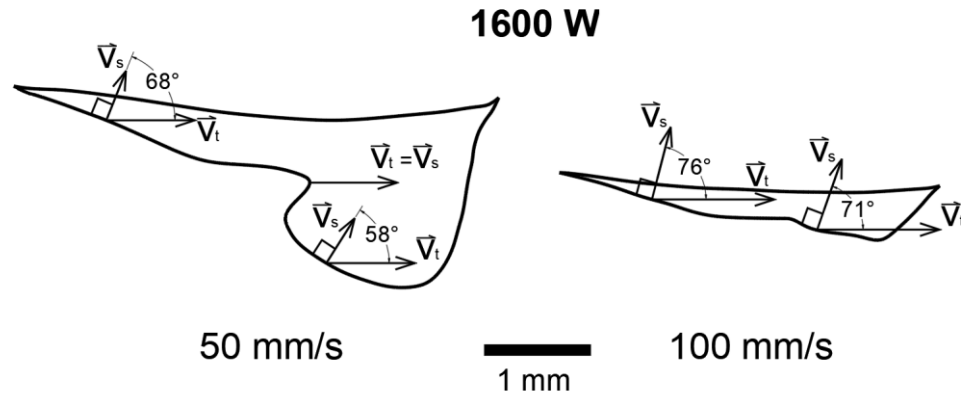


Figure 5.32. Schematic showing angles of the solid-liquid interface from a longitudinal weld termination cross-section. 1000 W, 5 mm/s (left) and 50 mm/s (right). The travel velocity is designated as  $v_t$ , and the solidification velocity is designated as  $v_s$ .

At 1600 W and 50 mm/s, a region developed where the solidification rate approached the travel velocity. In Figure 5.33, the longitudinal sections showed the difference in solidification rate based on weld parameters and the location within the weld pool. The 100 mm/s travel speed showed minimal change in solidification rate based on weld pool location. The solidification rate was  $\approx 12$ -16 mm/s. However, at 50 mm/s travel speed, the solidification rate varied from 18 mm/s ( $68^\circ$ ) near the weld surface up to the travel speed of 50 mm/s. Further towards the root, the solidification rate decreased to  $\approx 26$  mm/s due to a decreased angle ( $58^\circ$ ).

For the welds produced at 1600 W, the maximum solidification rate along the weld centerline was greatest for the slower travel speed (50 mm/s). This was solely attributed to the large variation in weld pool geometry because the solidification rate became equivalent to the travel speed at 50 mm/s. This is shown in the left of Figure 5.33. However, the highest solidification rate at 100 mm/s and along the weld centerline was

$\approx 30$  mm/s. Although slower travel speeds are generally regarded as mitigating metallurgical issues such as solidification cracking, a substantial change in pool shape may alleviate metallurgical issues through a reduction in solidification rate.



*Figure 5.33. Schematic showing angles of the solid-liquid interface from a longitudinal weld termination cross-section. 1600 W, 50 mm/s (left) and 100 mm/s (right). The travel velocity is designated as  $v_t$ , and the solidification velocity is designated as  $v_s$ .*

### 5.3.1.2 Microstructure Analysis

Figure 5.34 shows a schematic of traced, transverse fusion zone sections and the approximate locations where the following optical micrographs and EBSD scans were captured. Analysis was performed at the weld centerline because the centerline has the highest solidification rate and is most likely to contain a transition between primary ferrite and austenite solidification modes. The keyhole area in deep penetration welds was analyzed based on the assumption that the region contained the highest cooling rate and greatest propensity to generate or suppress phase transformations, such as the suppression of austenite nucleation and growth in 2205 DSS.

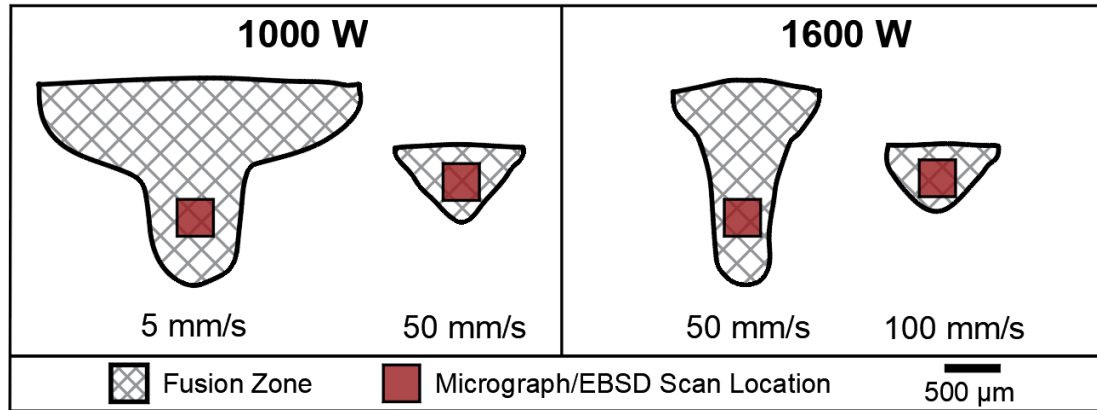
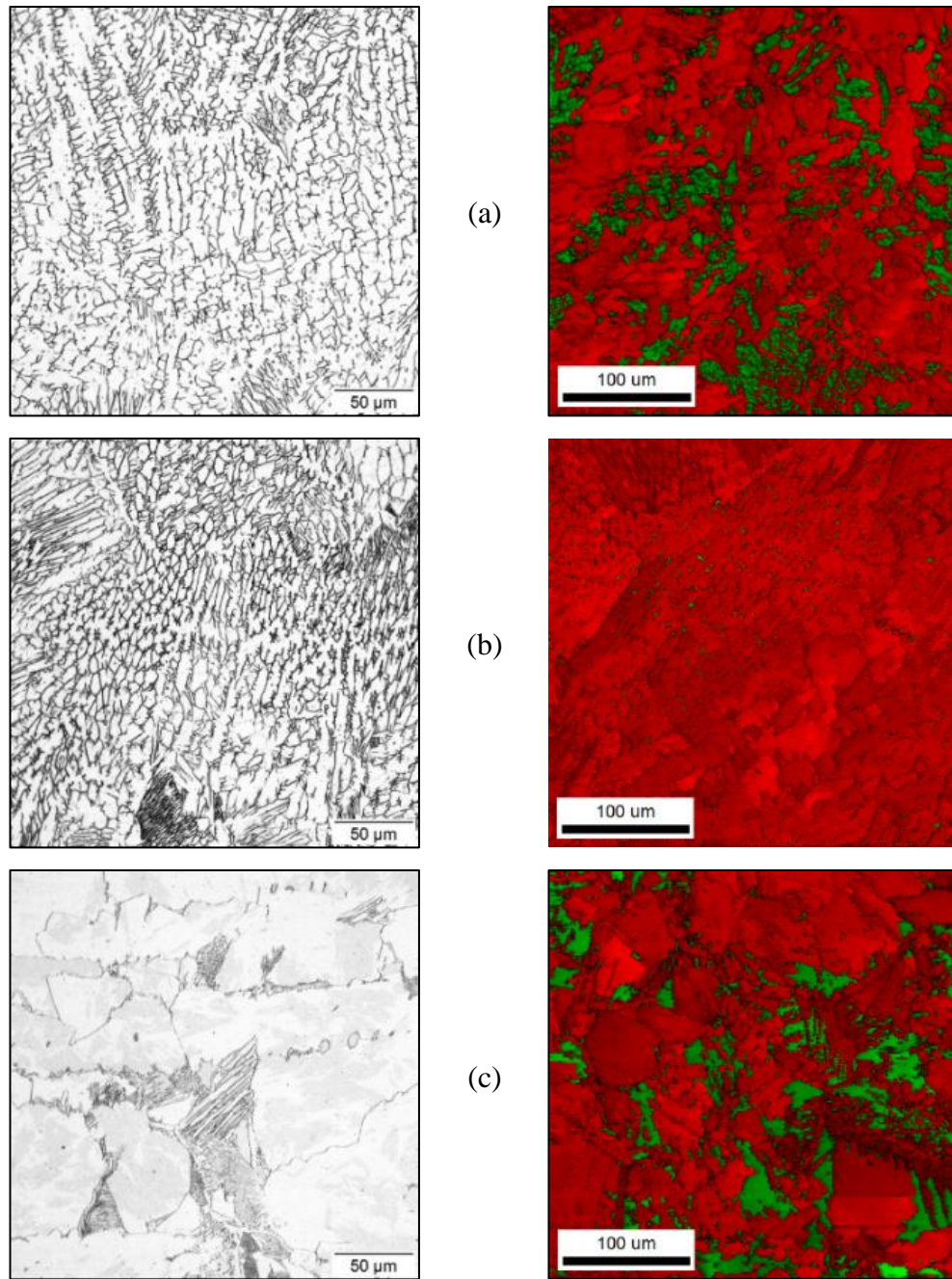
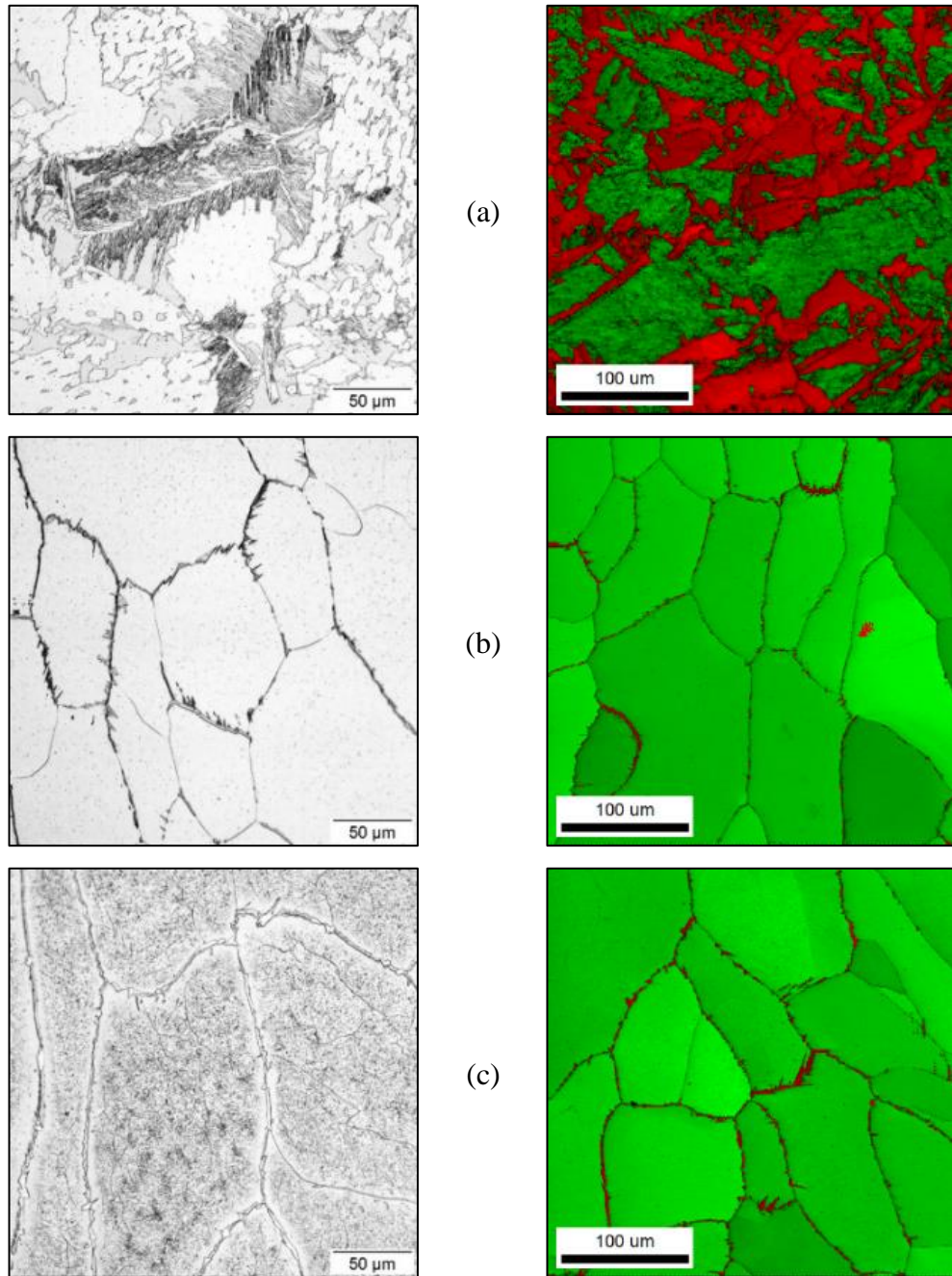


Figure 5.34. Schematic showing locations of optical micrographs and EBSD scans for each weld parameter.

Figure 5.35 and Figure 5.36 show transverse, optical micrographs and EBSD phase maps from the laser welds produced on all the SS alloys at 1000 W and a 5 mm/s travel speed. The phase maps include an overlay of the EBSD image quality map to visually accentuate the phase boundaries. The optical micrograph in Figure 5.35a shows a primary ferrite (FA-type) solidification mode in 304L SS based on the skeletal ferrite morphology. The EBSD phase map of 304L revealed a relatively large fraction of ferrite, which does not reflect the skeletal morphology shown in the optical micrograph. Likewise, the M58 alloy solidified in FA-mode and showed a similar skeletal morphology as 304L. However, the EBSD phase analysis consisted of negligible amounts of ferrite. The fine regions of detected ferrite appear as a morphology consistent with  $\delta$ -ferrite formation from solidification.



*Figure 5.35. Laser weld optical micrographs (left) and matching EBSD phase fractions (right) at 1000 W of power and a 5 mm/s travel speed: 304L (a), M58 (b), and M45 (c). For the EBSD images, red/dark is austenite and green/light is ferrite.*



*Figure 5.36. Laser weld optical micrographs (left) and matching EBSD phase fractions (right) at 1000 W of power and a 5 mm/s travel speed: M53 (a), M54 (b), and 2205 DSS (c). For the EBSD images, red/dark is austenite and green/light is ferrite.*

Increasing the WRC-1992  $Cr_{eq}/Ni_{eq}$  to 2.1 (M45) produced a transition to what is believed to be a primary ferrite (F-mode) solidification followed by a solid-state austenite transformation and relatively equiaxed austenite grains (Figure 5.35c). The 2.2  $Cr_{eq}/Ni_{eq}$  alloy (M53) also showed F-mode solidification and solid-state austenite transformation at the ferrite grain boundaries, and extensive Widmanstätten austenite ( $A_w$ ) nucleating at the ferrite grain boundaries. The near-ternary alloy at a 2.8  $Cr_{eq}/Ni_{eq}$  (M54) also showed F-mode solidification with small amounts of  $A_w$  nucleating at the ferrite grain boundaries (Figure 5.35b). The 2205 DSS at a 2.7  $Cr_{eq}/Ni_{eq}$  also exhibited F-type solidification and minimal amounts of  $A_w$  at the grain boundaries but also formed intragranular chromium nitrides ( $CrN/CrN_2$ ) [238]. This is evident in the optical micrograph by the speckled appearance and chromium nitride denuded regions near the grain boundaries where austenite transformation occurred allowing for a higher solid solubility of nitrogen.

The transverse optical micrographs and EBSD data at 1000 W and 50 mm/s is shown in Figure 5.37 and Figure 5.38. The 304L weld (Figure 5.37a) contained a relatively large fraction of retained ferrite as compared to M58 (Figure 5.37b). No ferrite was present in the M58 alloy at a 1.8  $Cr_{eq}/Ni_{eq}$ . This higher travel speed decreased the  $A_w$  structures present in the M45 and M53 alloys. M45 showed a decrease in ferrite (Figure 5.37c), but the ferrite content increased in M53 (Figure 5.38a). Both are believed to represent FA-type solidification with a massive transformation to austenite. The higher travel speed eliminated the solid-state  $A_w$  transformation for M54 (Figure 5.38b) and the 2205 DSS (Figure 5.38c). A noticeable grain size reduction is also observed in the 2.7

and 2.8 Cr/Ni equivalent alloys. Figure 5.38c also shows chromium nitrides, particularly around the pore in the upper left.

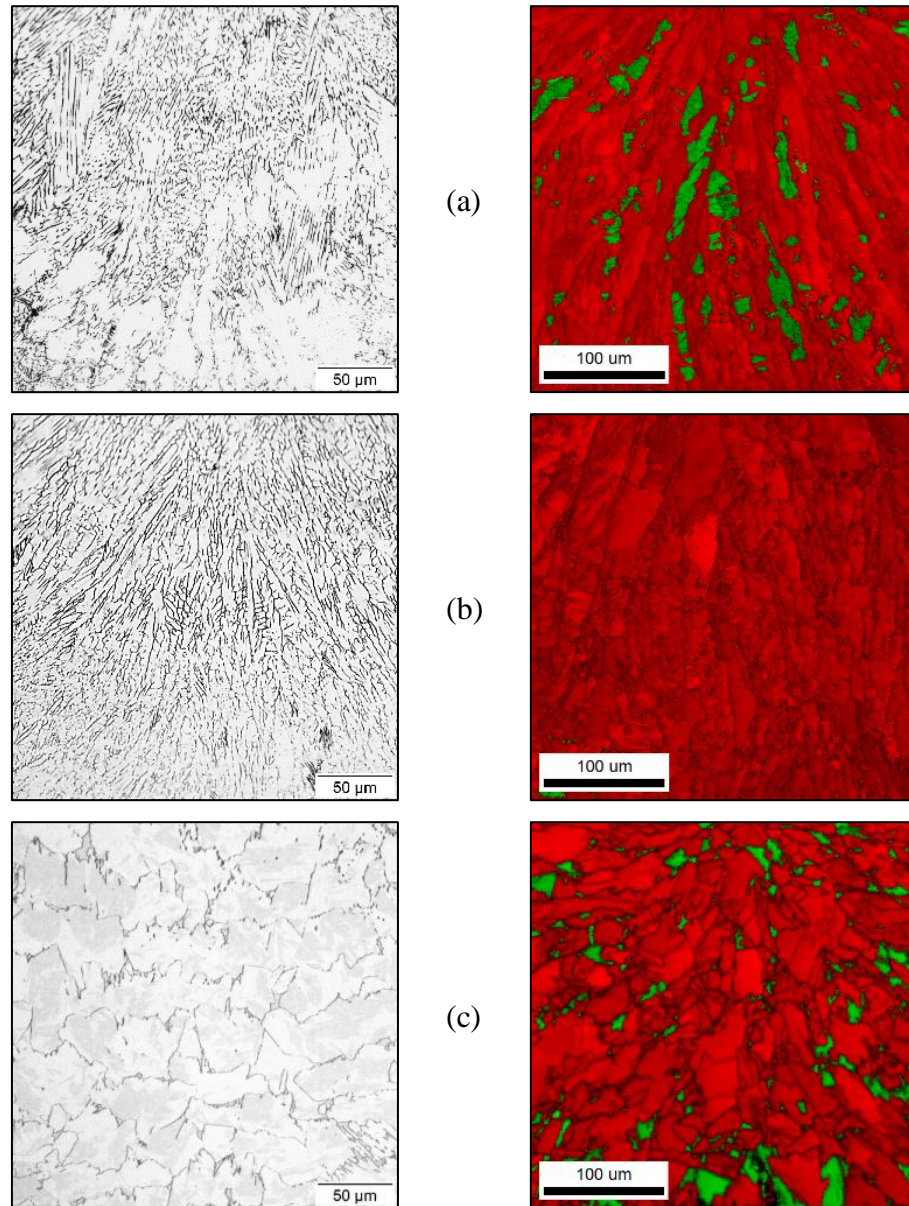


*Figure 5.37. Laser weld optical micrographs (left) and matching EBSD phase fractions (right) at 1000 W of power and a 50 mm/s travel speed: 304L (a), M58 (b), and M45 (c). For the EBSD images, red/dark is austenite and green/light is ferrite.*

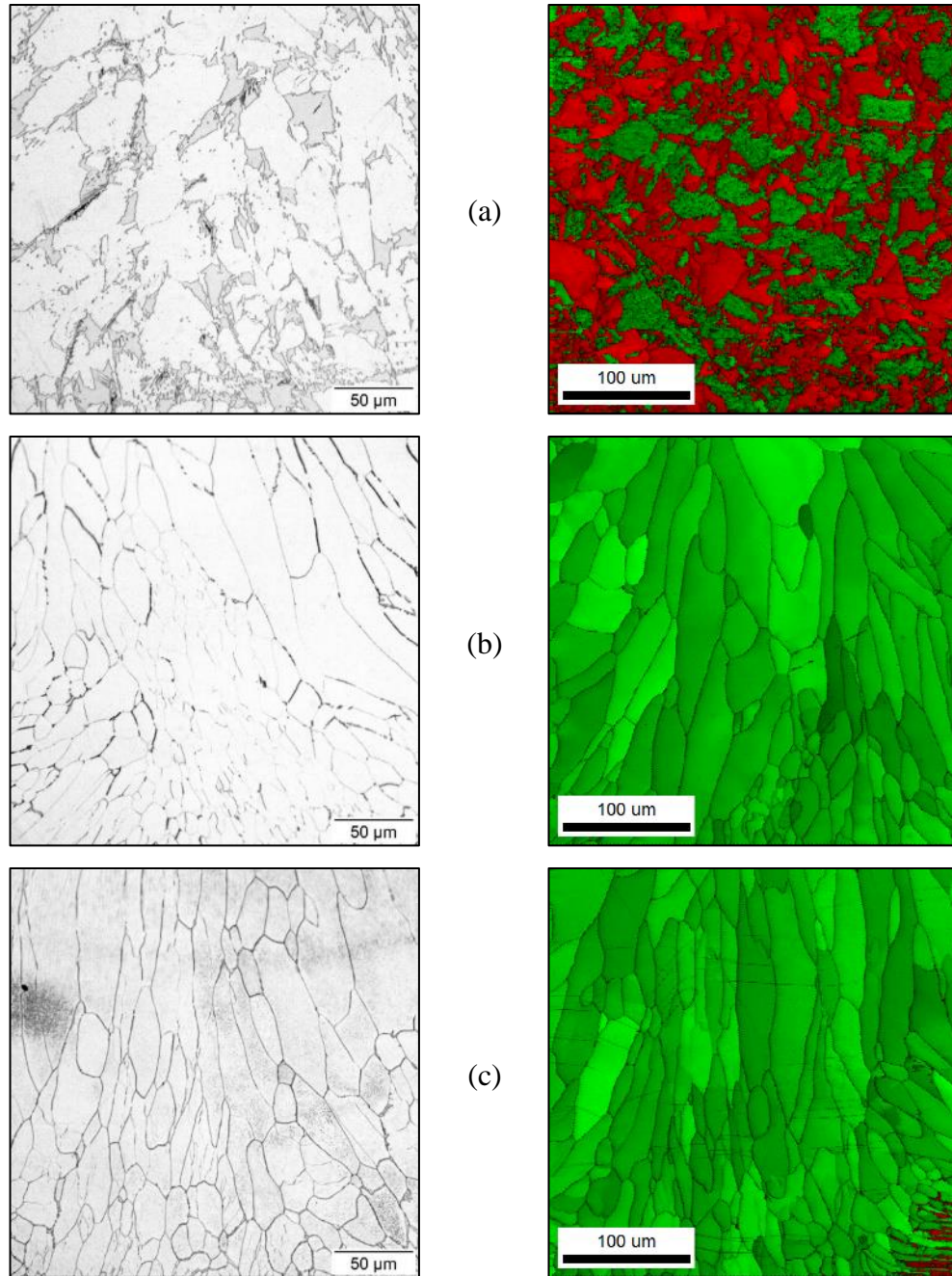


*Figure 5.38. Laser weld optical micrographs (left) and matching EBSD phase fractions (right) at 1000 W of power and a 50 mm/s travel speed: M53 (a), M54 (b), and 2205 DSS (c). For the EBSD images, red/dark is austenite and green/light is ferrite.*

At 1600 W and 50 mm/s, a distinguishable weld centerline developed in the keyhole mode welds as shown in Figure 5.39 and Figure 5.40. At these weld centerlines, it is expected that the solidification rate approached that of the travel speed as previously illustrated in Figure 5.33. Within the keyhole, solidification largely occurs with grains growing from the fusion boundary horizontally to the weld centerline. The 304L and M58 alloys contained nearly 100% austenite appearing as an FA solidification morphology based on the chemically etched microstructure. However, the M58 alloy weld centerline contained a distinct, lightly etched region denuded of compositional segregation, which indicates a possibility of primary austenite (A-type) solidification (Figure 5.39b). Through the retention of ferrite, solidification structures were present in the M45 and M53 alloys as shown in Figure 5.39c and Figure 5.40a, respectively. Although austenite is present along the grain boundaries in M54 and 2205 DSS, each alloy contains over 98% ferrite.

Increasing the travel speed to 100 mm/s at 1600 W showed a slight increase in ferrite for 304L (Figure 5.41a) but a negligible change for the M58 (Figure 5.41b) and M45 (Figure 5.41c) welds. However, the M53 ferrite fraction decreased as shown in Figure 5.42a. Nearly all the austenite formation was suppressed in M54 (Figure 5.42b) and 2205 (Figure 5.42c). The grains grew with minimal width ( $\approx 20 \mu\text{m}$ ) but with lengths spanning a substantial fraction of the weld pool.

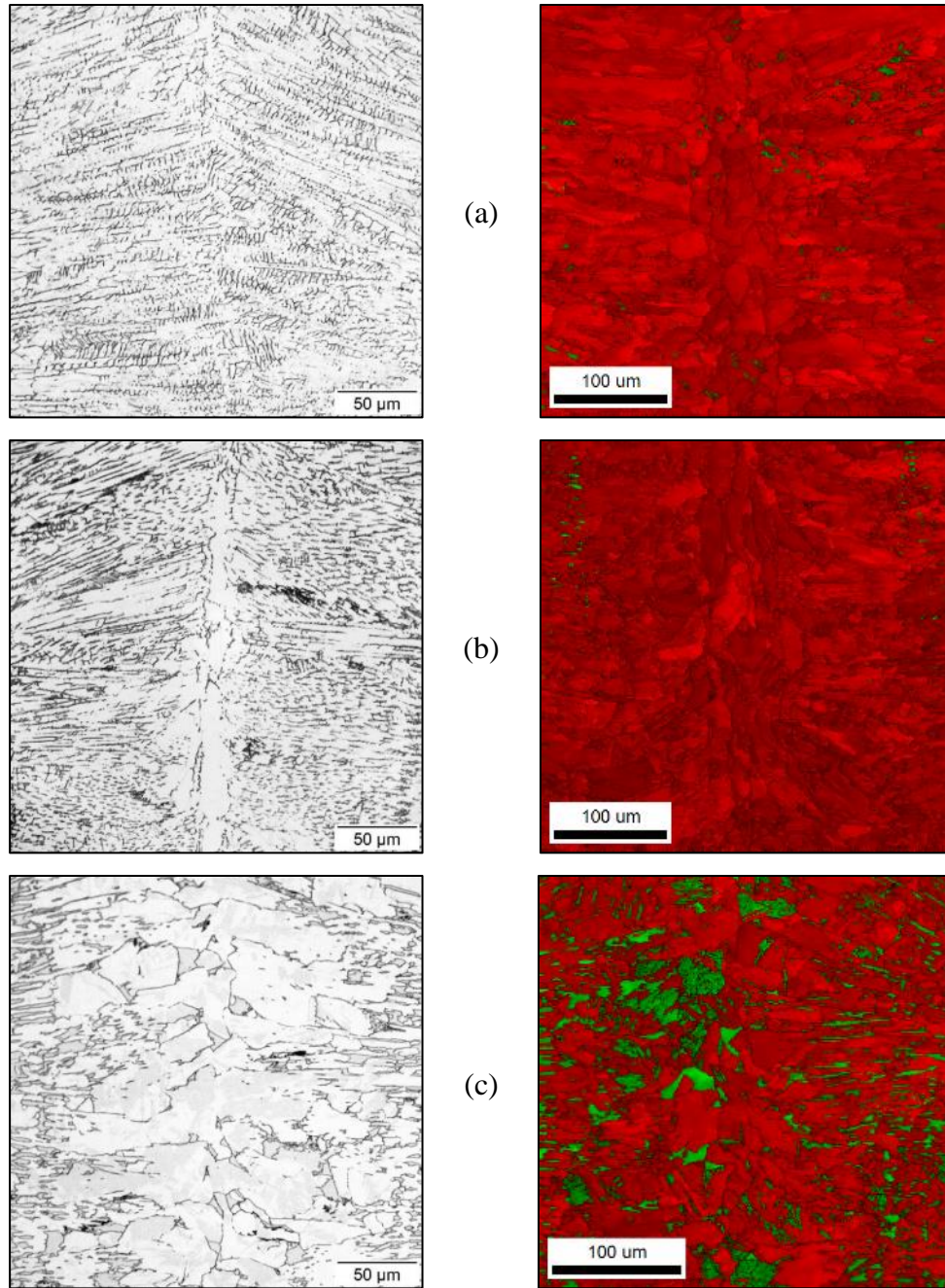


*Figure 5.39. Laser weld optical micrographs (left) and matching EBSD phase fractions (right) at 1600 W of power and a 50 mm/s travel speed: 304L (a), M58 (b), and M45 (c). For the EBSD images, red/dark is austenite and green/light is ferrite.*

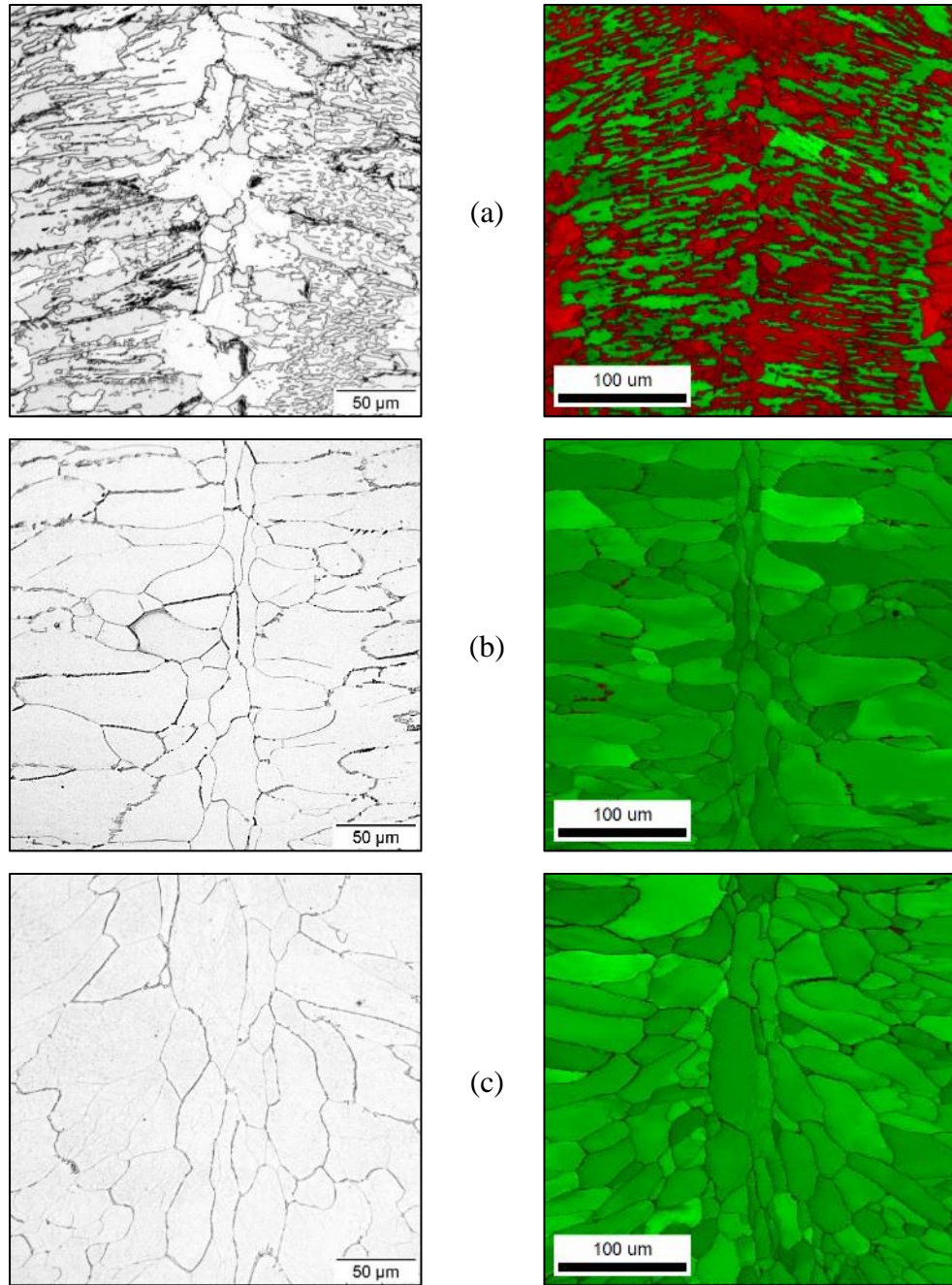


*Figure 5.40. Laser weld optical micrographs (left) and matching EBSD phase fractions (right) at 1600 W of power and a 50 mm/s travel speed: M53 (a), M54 (b), and 2205 DSS (c). For the EBSD images, red/dark is austenite and green/light is ferrite.*

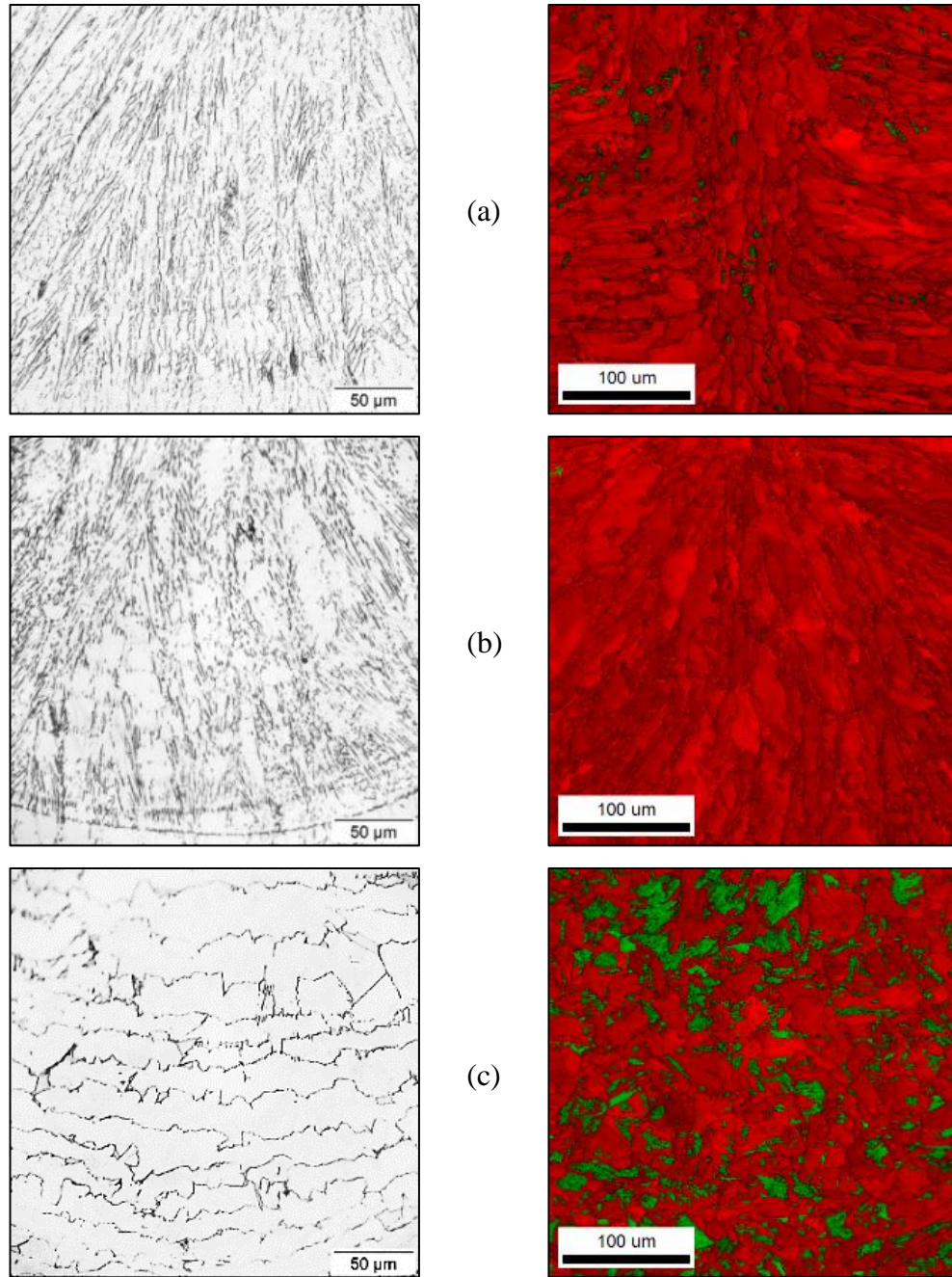


*Figure 5.41. Laser weld optical micrographs (left) and matching EBSD phase fractions (right) at 1600 W of power and a 100 mm/s travel speed: 304L (a), M58 (b), and M45 (c). For the EBSD images, red/dark is austenite and green/light is ferrite.*

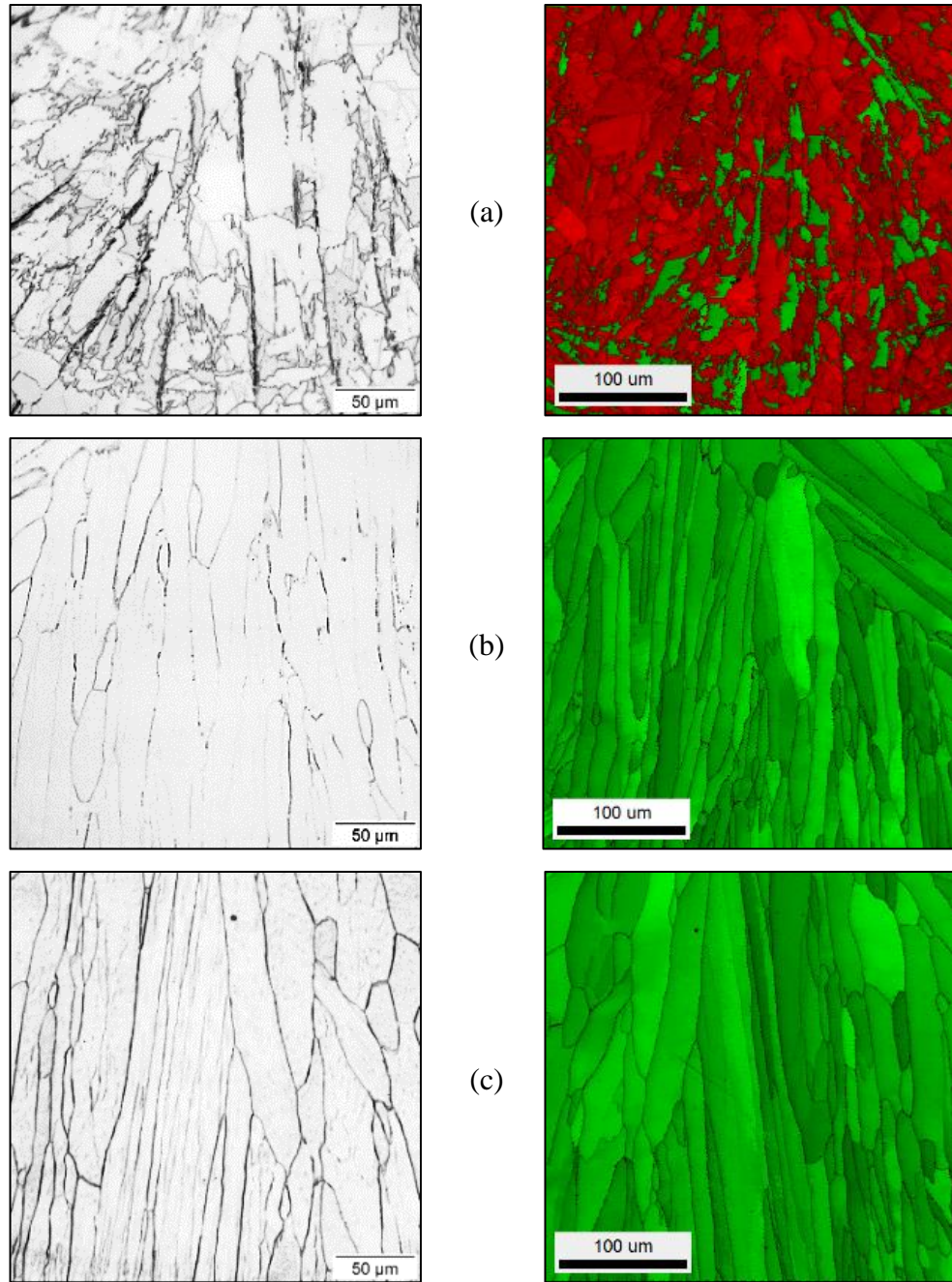


*Figure 5.42. Laser weld optical micrographs (left) and matching EBSD phase fractions (right) at 1600 W of power and a 100 mm/s travel speed: M53 (a), M54 (b), and 2205 DSS (c). For the EBSD images, red/dark is austenite and green/light is ferrite.*

The low aspect ratio (conduction mode) welds exhibited nearly unimpeded columnar grain growth from the root towards the weld surface. This was evident in the transverse optical micrograph, EBSD results, and the centerline, longitudinal sections. Although higher travel speeds are generally related to greater susceptibility to solidification cracking, the drastic change in HED weld profiles indicated that shallower weld pools caused by conduction mode can maintain solidification rates below that of keyhole mode welds at higher travel speeds. Therefore, a higher potential for solidification cracking is possible with high aspect ratio welds.

#### **5.3.1.3 Microstructure Maps**

Plots of the EBSD phase fractions relative to WRC-1992  $Cr_{eq}/Ni_{eq}$  ratio for welds made at 1000 W and 1600 W are shown in Figure 5.43a and Figure 5.43b, respectively. The higher travel speed, lower heat input welds at 1600 W shifted the projected 50%-50% austenite-to-ferrite transition from a 2.2 to a 2.3 WRC-1992  $Cr_{eq}/Ni_{eq}$ . Most importantly, the 2205 DSS formed only small amounts of austenite at the LBW parameters evaluated.

Figure 5.44 shows an updated microstructural map utilizing preexisting data from Elmer [194] and Lippold [190] in addition to the microstructural data generated in this study. A significant contribution from this study showed that a fully ferritic microstructure was shifted to relatively high  $Cr_{eq}/Ni_{eq}$  values and at travel speeds exceeding 50 mm/s. This approximation further aids in predicting future LBW microstructural transformation behavior at higher  $Cr_{eq}/Ni_{eq}$  values. However, information

is still needed to definitively identify the boundaries between the different microstructure regimes.

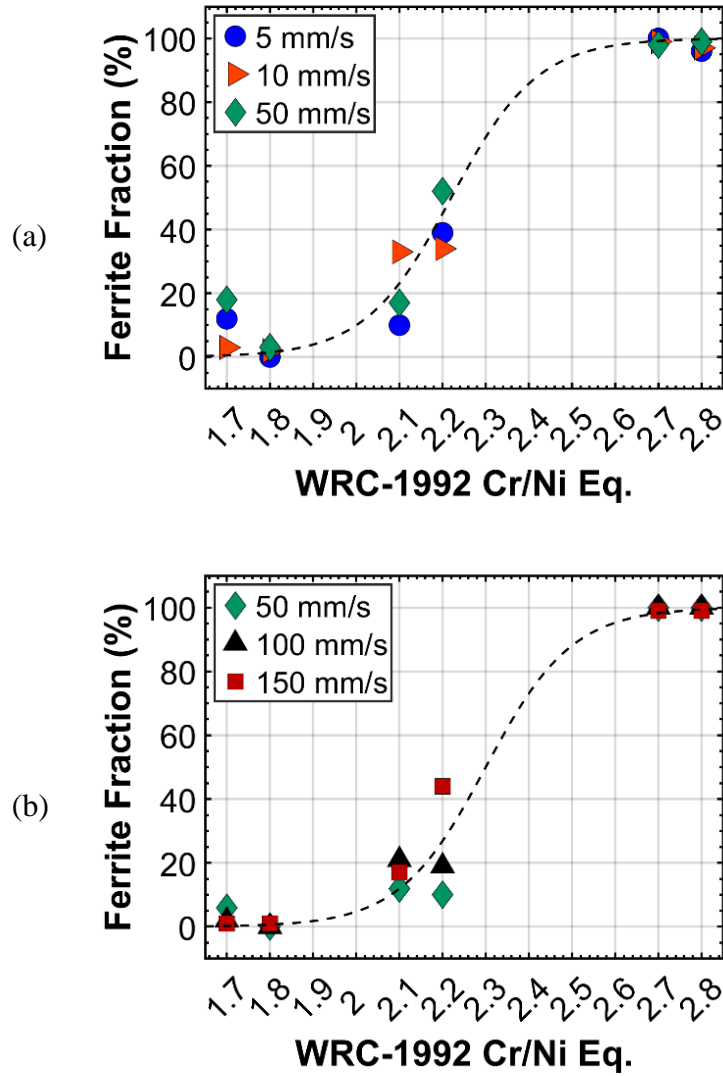


Figure 5.43. Ferrite fractions versus WRC-1992  $Cr_{eq}/Ni_{eq}$  at 1000 W (a) and 1600 W (b).

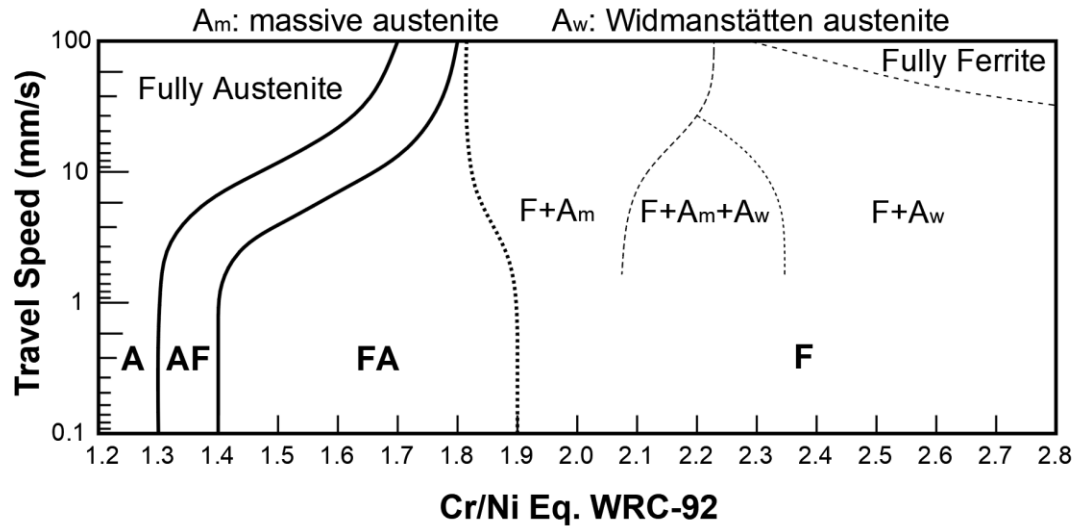


Figure 5.44. Updated LBW SS microstructural map of travel speed versus WRC-1992  $Cr_{eq}/Ni_{eq}$  with data from References [190], [194].

Finally, while this study involved only laser beam welding, it is expected that the results presented here will also apply to other rapid solidification processes including electron beam welding and additive manufacturing processes that use HED processes. Validation of the data presented in Figure 5.43 and the microstructure map in Figure 5.44 is needed to fully understand the effects of rapid solidification rates and high cooling rates on microstructure prediction in stainless steels which solidify as delta ferrite.

#### 5.3.1.4 Summary

Grains grew vertically in conduction mode welds and maintained uniform solidification rates across the weld pool. High aspect ratio welds altered the angle of the solid-liquid interface and created locations with solidification rates nearly equal to the travel speed. At 1600 W, the high aspect ratio weld generated a solidification rate of  $\approx 20$

mm/s higher than a low aspect ratio weld produced at twice the travel speed. Producing as-welded 50/50 ferrite-to-austenite fractions with LBW would require WRC-1992  $Cr_{eq}/Ni_{eq}$  around 2.2-2.3 as shown through the extensive use of EBSD phase analysis. The LOM analysis combined with EBSD allowed for generating a new LBW microstructural map with more information at WRC  $Cr_{eq}/Ni_{eq}$  values exceeding 1.8.

### 5.3.2 Ti-6Al-4V

Transverse section profiles for welds produced at 1600 W are shown in Figure 5.45. These macrographs were captured after etching in Kroll's reagent [239] (2 mL HF, 4 mL HNO<sub>3</sub>, 94 mL H<sub>2</sub>O) for  $\approx 20$  seconds. At 50 mm/s (Figure 5.45a), the weld exhibits keyhole mode penetration with an aspect ratio of  $\approx 1.2$ . Increasing the travel speeds to 100 mm/s and 150 mm/s resulted in conduction mode penetration with aspect ratios below 0.6 as shown in Figure 5.45b and Figure 5.45c, respectively.

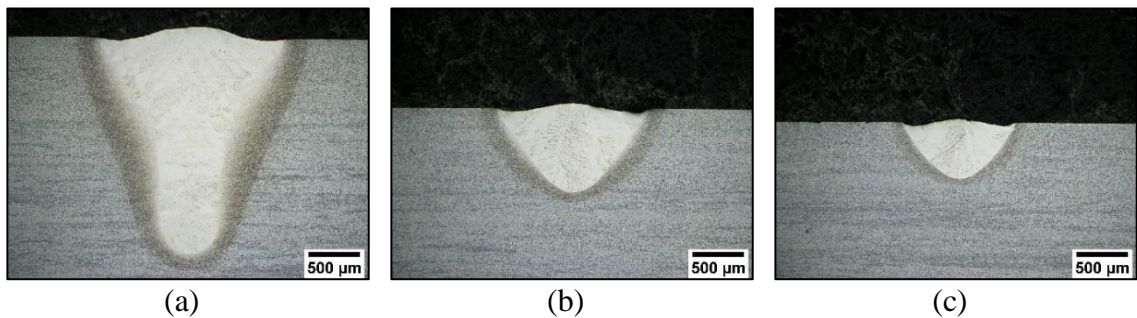
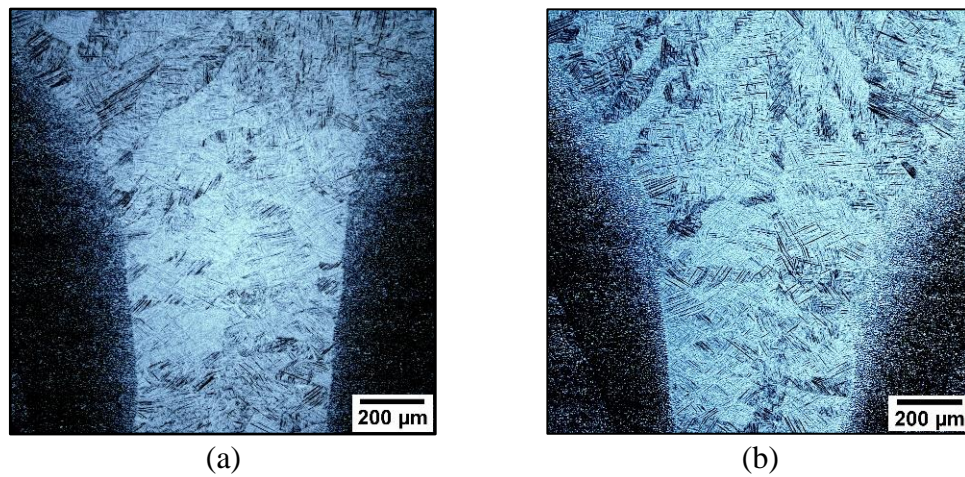


Figure 5.45. Laser beam weld transverse sections at 1600 W and 50 mm/s (a), 100 mm/s (b), and 150 mm/s (c).

Further evaluation of the fusion zone microstructures at high magnification was complicated due to difficulties in distinguishing prior beta grain boundaries (PBGBs). To remedy this, numerous etching attempts and variations in acids and/or fractions of acids were analyzed. Microstructural results for a 2-minute etching time with Kroll's and Keller's etchants [240] (2 mL HF, 3 mL HCl, 5 mL HNO<sub>3</sub>, 190 mL H<sub>2</sub>O) are shown in Figure 5.46a and Figure 5.46b, respectively.



*Figure 5.46. Ti-6Al-4V laser beam weld transverse micrographs. Weld parameters were 1600 W and 50 mm/s. Etched using Kroll's etchant for 2 minutes (a) and Keller's etchant for 2 minutes (b).*

Although some of the PBGBs could be identified, most of the grain boundaries are not sufficiently distinguishable to determine a quantitative measurement of grain size. Using HF acid with a high fraction of HCl (Figure 5.47a) resulted in a different appearance than Kroll's or Keller's but had limited success in delineating PBGBs. The best etching approach for revealing grain boundaries used a high concentration of HF and HCl for a long etch time ( $\approx 1$  min) as shown in Figure 5.47b. It is believed that the high

concentrations and/or long reaction times produced higher amounts of topography that became accentuated when imaging using DIC. More microstructural examples using different etchants, etch times, and imaging techniques are provided in Appendix J:.

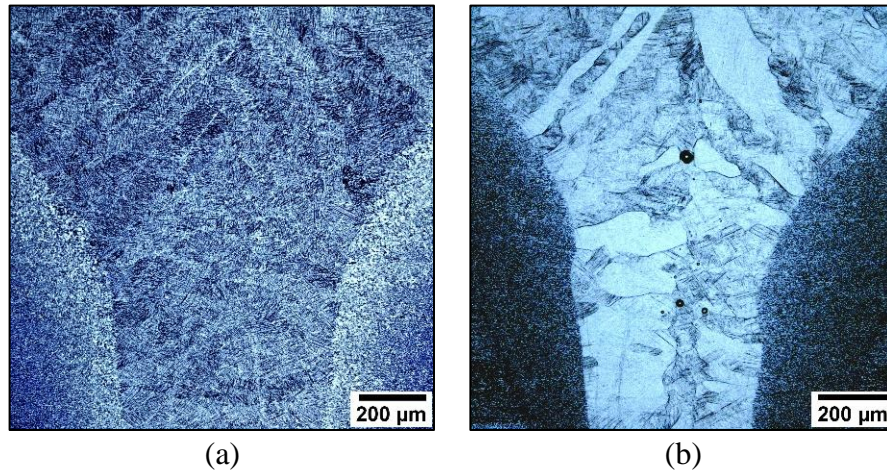


*Figure 5.47. Ti-6Al-4V laser beam weld transverse micrographs. Weld parameters were 1600 W and 50 mm/s. Etched using 2 mL HF, 50 mL HCl, 48 mL H<sub>2</sub>O for  $\approx$ 20 seconds (a) and 20 mL HF, 40 mL HCl, 40 mL H<sub>2</sub>O for  $\approx$ 1 minute (b).*

Figure 5.48 shows longitudinal section micrographs etched with the same high concentration of HF and HCl as used for Figure 5.47b. The faint images of PBGBs showed the difference in grain growth between the conduction and keyhole mode welds. At 50 mm/s (Figure 5.48a), grains epitaxially nucleated from the fusion boundary at the root of the weld and grew vertically where they were impeded by grains appearing equiaxed due to grow in a different direction. This location is represented with the dashed line in Figure 5.48a. In the low aspect ratio weld at 100 mm/s (Figure 5.48b), PBGs grew vertically at nearly 90° from the root to the weld surface. This continuous, vertical grain growth was also present in the 150 mm/s weld as shown in Figure 5.48c.

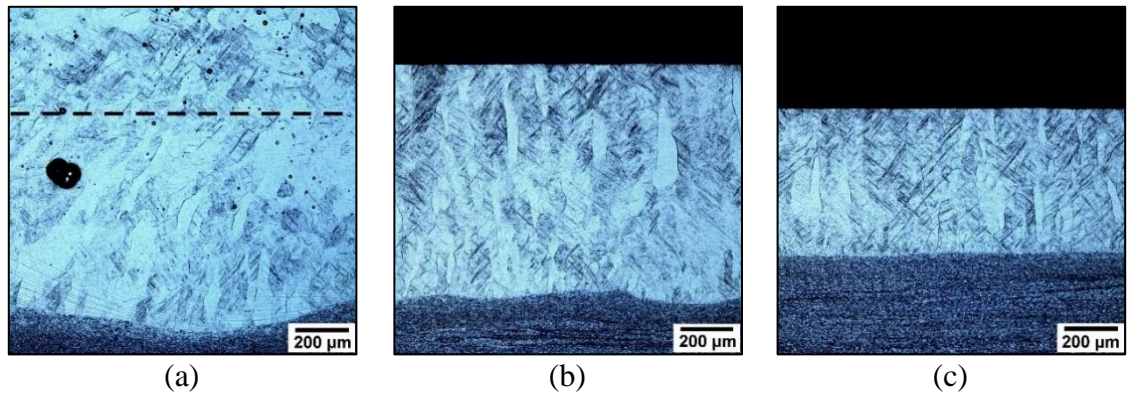


*Figure 5.48. Ti-6Al-4V longitudinal cross-sections at 1600 W etched with 20 mL HF, 40 mL HCl, 40 mL H<sub>2</sub>O for  $\approx 1$  minute: 50 mm/s (a), 100 mm/s (b), and 150 mm/s (c).*

Solidification substructure (cells and dendrites) is not observed in the Ti-6Al-4V laser welds due to the low solid-liquid partition coefficient ( $k$ ) of Al or V within Ti [18], resulting in minimal solute redistribution during solidification. In addition, solid-state diffusion of the segregating elements is high in the BCC beta phase [5]. The combination of these factors minimizes any solute redistribution that occurred during solidification. This homogenous beta phase is then believed to completely transform to martensite upon cooling with negligible amounts of retained beta. The fine, martensitic structure is shown in Figure 5.49, which is an SEM image in the etched condition. A BSE SEM image captured using the T1 detector with the sample preparation in the unetched condition is shown in Figure 5.50. The unetched, BSE image provides a clearer representation of the martensitic laths but does not facilitate a clear distinction of PBGBs. Therefore, PBGBs remained relatively indistinguishable whether analyzed in the etched or unetched condition. Also, the fine martensitic lath size proved difficult to achieve quality EBSD

patterns at reasonable scan times [241]. These difficulties resulted in transitioning to the Quattro SEM with a faster EBSD camera as discussed in the experimental procedures.

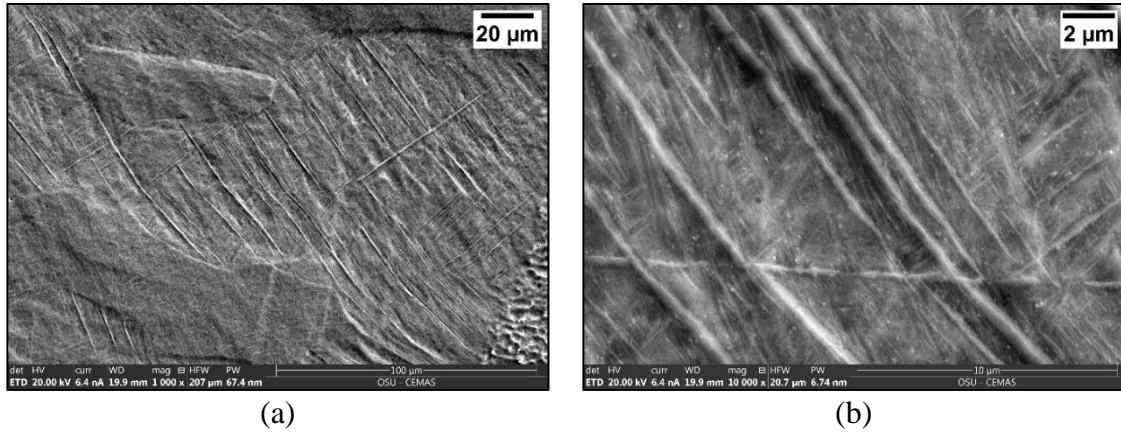


*Figure 5.49. SEM image of the etched fusion zone microstructure showing the fine morphology of the acicular  $\alpha'$  martensite. Captured using the Everhart-Thornley detector (ETD) at 1,000X (a) and 10,000X (b).*

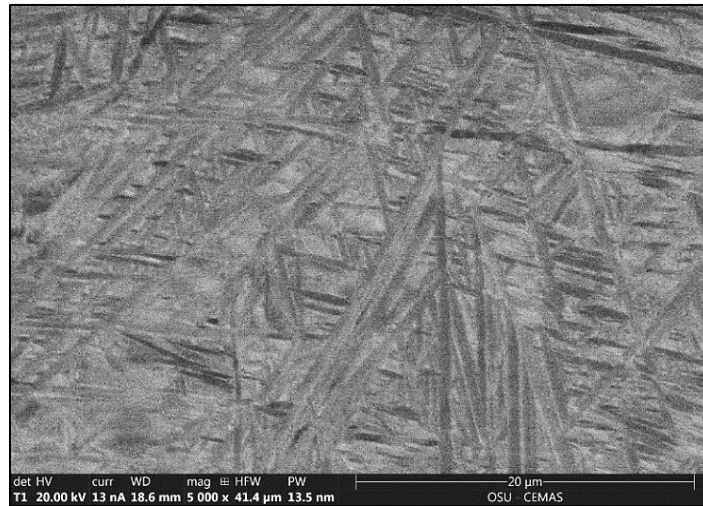


*Figure 5.50. Ti-6Al-4V weld metal microstructure at an  $\approx 18$  mm working distance and 5,000X magnification using the T1 (BSE) detector. The structure appears to consist entirely of high aspect ratio, acicular  $\alpha'$ .*

### 5.3.2.1 *Prior Beta Grain Analysis using EBSD*

Acquiring high resolution EBSD maps while indexing  $\alpha$  and  $\beta$  phases is shown here to successfully perform prior grain reconstruction utilizing the algorithms within the OIM Analysis<sup>TM</sup> software. For successful parent grain reconstruction, NPAR<sup>TM</sup>, a dynamic background correction, dataset background correction, and auto brightness and contrast was utilized after exporting the discrete Kikuchi patterns. The NPAR<sup>TM</sup> algorithm averaged the Kikuchi patterns from the four nearest neighbors as reported by Wright *et al.* [241] and improved the average confidence index (CI) above 0.2. This processing was followed with a grain dilation algorithm, which assigned non-indexed or mis-indexed points to a neighboring point that belongs to a grain with the highest confidence index [242]. Figure 5.51 shows the locations and size of EBSD patterns for tranverse, plan, and longitudinal view weld sections. A schematic of the weld pool regarding the plan and longitudinal views (center and right in Figure 5.51, respectively) is presented for better reference relative to each orientation.

Images of the EBSD scans at 1600 W of power and 50, 100, and 150 mm/s from a transverse cross-section are shown in Figure 5.52. These images consist of the inverse pole figure (IPF) and image quality (IQ) map following NPAR<sup>TM</sup> processing and grain dilation. The right-side images in Figure 5.52 contain the IPF map of the reconstructed parent ( $\beta$ ) grains along with the IQ map from the original scan.

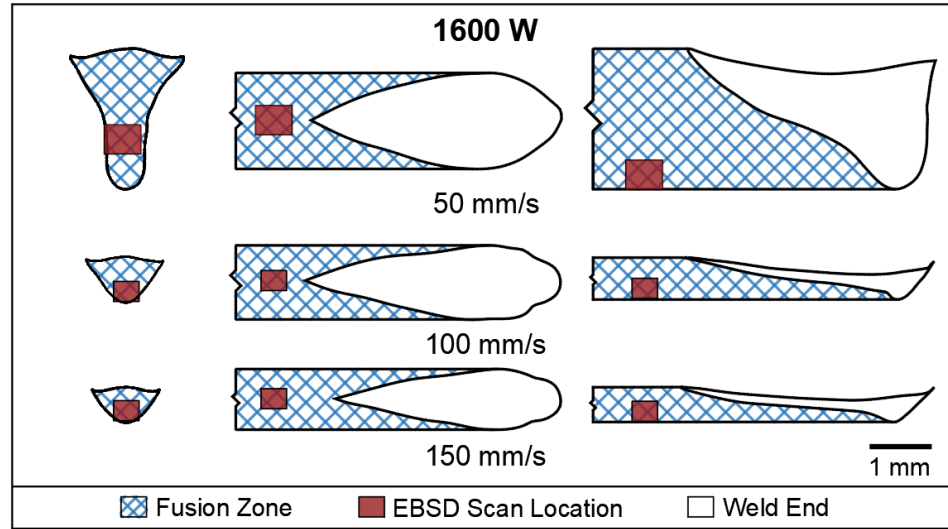


*Figure 5.51. EBSD scan locations for the transverse view (left), plan view (center), and longitudinal view (right) sections at each travel speed.*

The 50 mm/s weld scanned within the keyhole region is shown in Figure 5.52a. The left side in Figure 5.52a shows the epitaxial nucleation with grains growing horizontally into the weld center until terminating at the centerline by competitive growth. At higher travel speeds of 100 and 150 mm/s, beta grain growth is nearly normal to the fusion boundary and proceeds vertically towards the weld surface as shown in Figure 5.52b and Figure 5.52c. At 50 mm/s the weld is made under keyhole mode conditions and exhibits a distinct weld centerline and a grain size of  $\approx 50 \mu\text{m}$ . These centerline grains appeared equiaxed but only relative to the transverse view orientation. This distinct centerline is eliminated when the weld transitions into low aspect ratio or conduction mode at higher travel speeds (see Figure 5.52). It should be noted that the top of the keyhole weld, commonly referred to as the “nail-head”, shows grain growth similar to the conduction mode welds as evaluated via optical microscopy.

Figure 5.53 shows the results of the same weld parameters from a longitudinal cross-section. The epitaxial nucleation along the weld root at 50 mm/s showed grains growing nearly vertically for  $\approx 200\text{ }\mu\text{m}$ . Above this, grains appeared equiaxed due to the orthogonal growth direction inwards towards the weld centerline and from the side wall of the fusion boundary. As in the transverse view, the longitudinal view for the conduction mode welds showed grain growth perpendicular to the weld root and travel direction (left to right).

Figure 5.54 shows the processed and parent grain reconstruction results for the plan view at the same parameters as Figure 5.52 and Figure 5.53. These EBSD scans were taken slightly below the plate surface after grinding through the weld crown. An equiaxed grain size based on the upwards grain growth towards the weld crown was present in the plan view orientation at all travel speeds. However, there was an apparent grain size reduction with increasing travel speed.

The welds made at 100 mm/s and 150 mm/s showed a distinct texture on each side of the weld centerline. At the time of this writing, it is unknown as to what is the mechanism creating the texture present in Figure 5.54b and Figure 5.54c. The weld centerline is approximately centered vertically within each image in Figure 5.54. At these travel speeds (Figure 5.54b and Figure 5.54c), the top appears heavily biased towards a [001] direction, while the bottom mostly contained [101] and [111] directions.

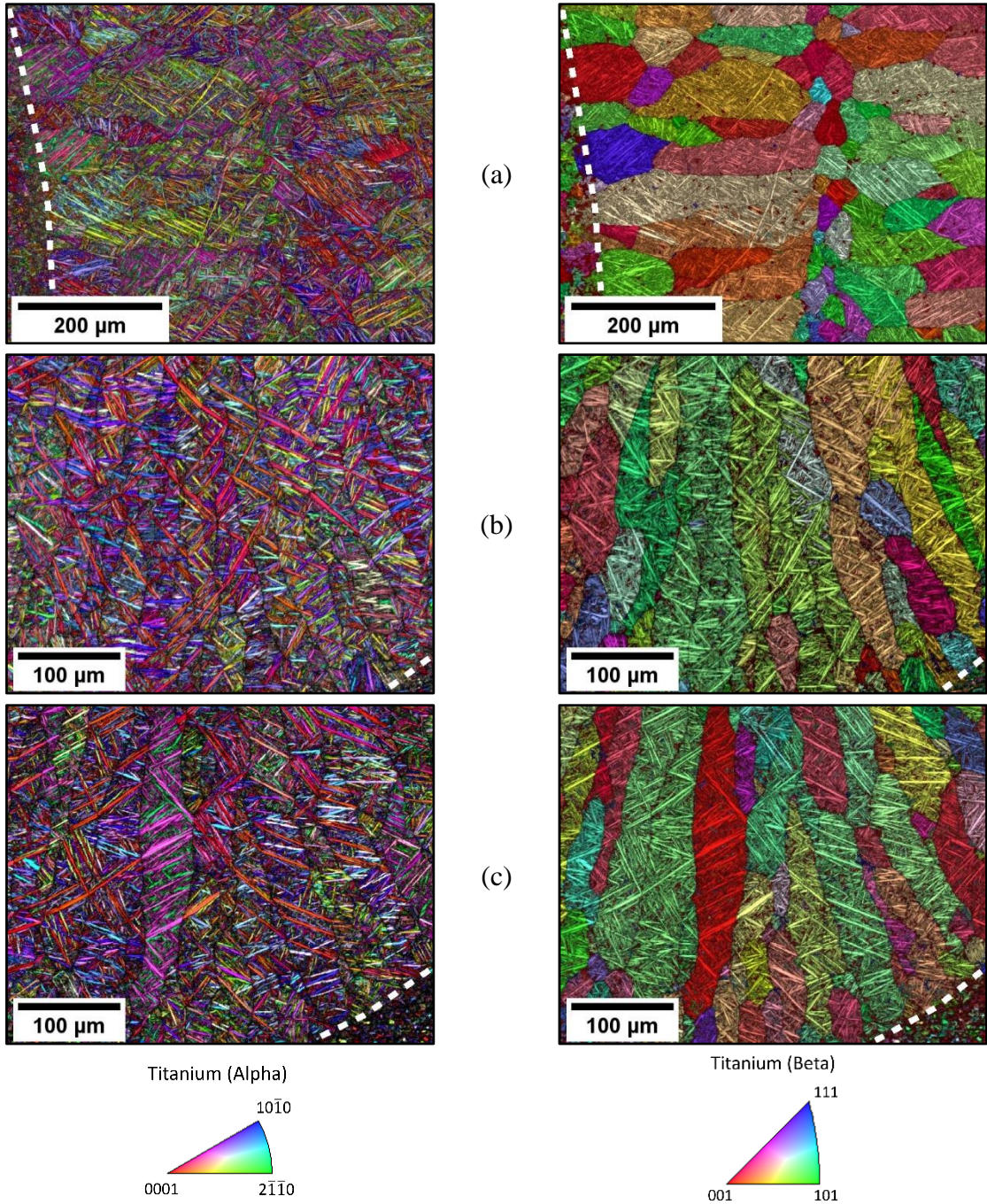


*Figure 5.52. Transverse view of as-scanned EBSD IPF-IQ maps (left) and IPF-IQ maps of the reconstructed parent/beta grains (right), a) 50 mm/sec, b) 100 mm/sec, c) 150 mm/sec. Original magnification at 350X (a) and 500X (b,c). The dashed, white lines represent the fusion boundaries.*

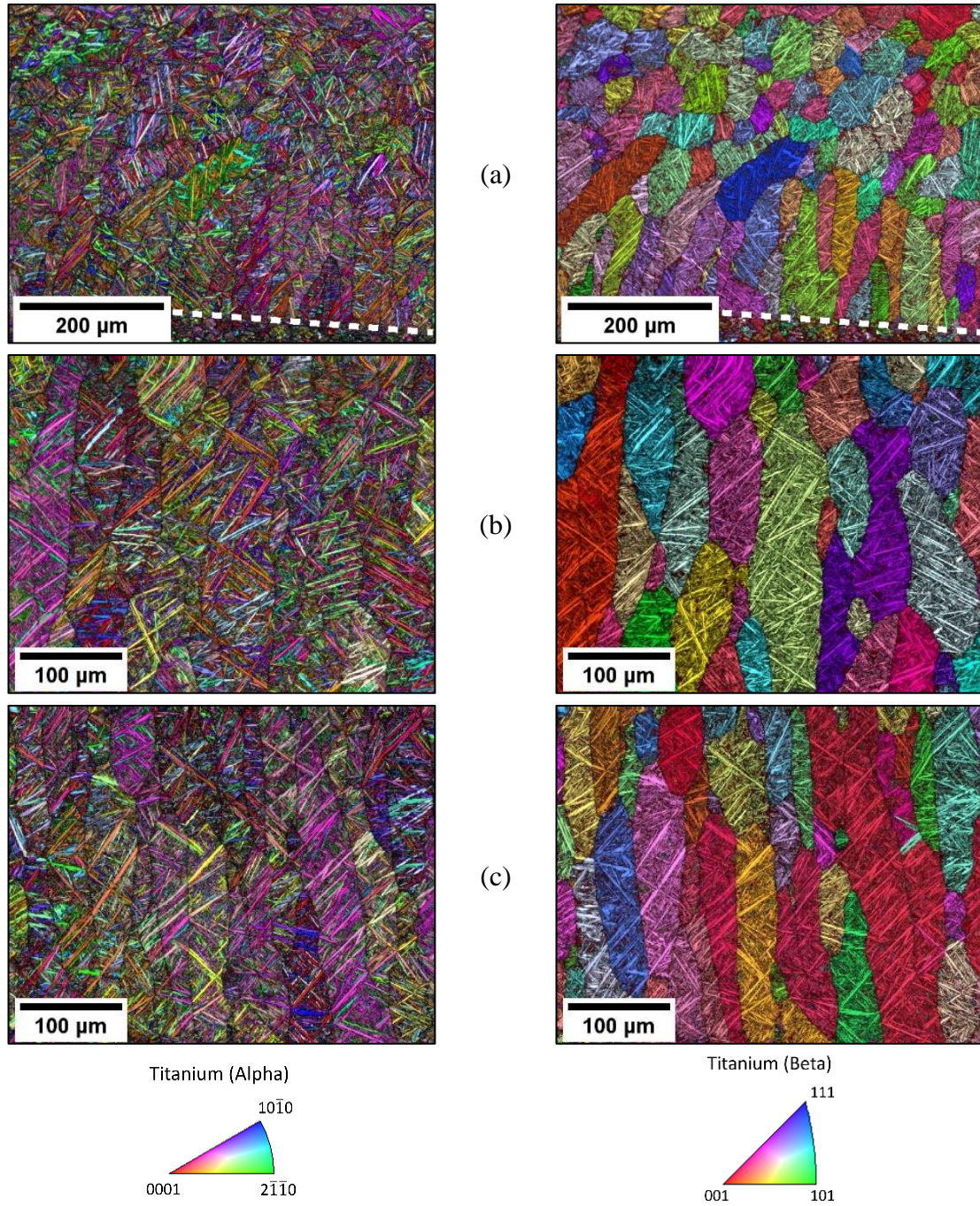


Figure 5.53. Longitudinal view of as-scanned EBSD IPF-IQ maps (left) and IPF-IQ maps of the reconstructed parent/beta grains (right). a) 50 mm/sec, b) 100 mm/sec, c) 150 mm/sec. The travel direction is from left to right. The dashed, white lines represent the fusion boundaries.

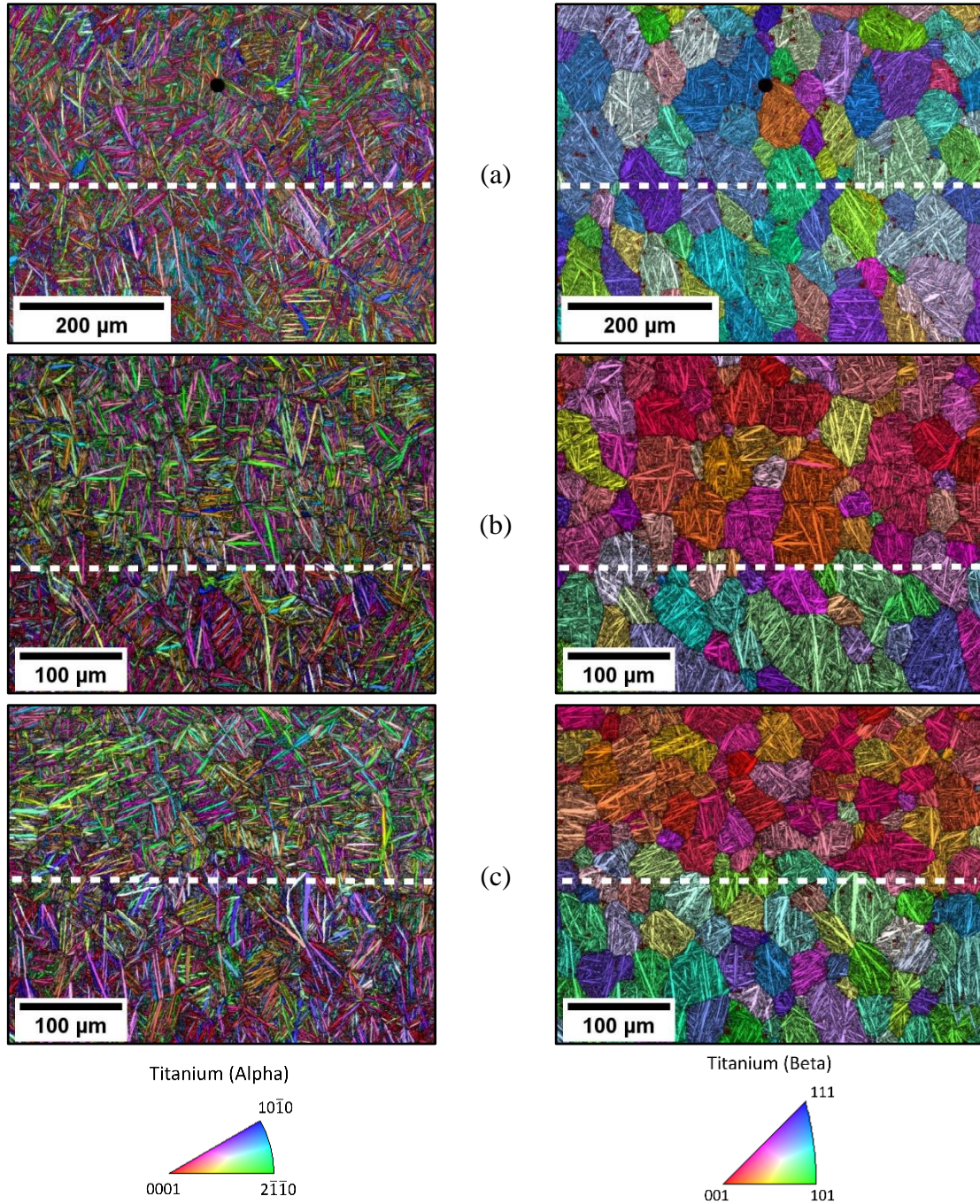


Figure 5.54. Plan view of as-scanned EBSD IPF-IQ maps (left) and IPF-IQ maps of the reconstructed parent/beta grains (right). The travel direction is from left to right. a) 50 mm/sec, b) 100 mm/sec, c) 150 mm/sec. The dashed, white lines represent the weld centerlines.

#### **5.3.2.2 *Beta Grain Size***

Grain size analysis was performed using the reconstructed beta grain data from Figure 5.52-Figure 5.54 and are the same locations as previously presented in Figure 5.51. The grain size figures for the transverse and longitudinal views are shown in Figure 5.55 and Figure 5.56, respectively. The EBSD data that was improperly indexed or not indexed was excluded from the analysis. This excluded data is the fine, white speckled regions. Also, the areas within the EBSD map consisting of the heat-affected zone, such as the left edge in Figure 5.55a or bottom in Figure 5.56a, was excluded during grain size analysis. The small grains within the fusion zone in each image in Figure 5.55 and Figure 5.56 are either an artifact of sectioning through a small portion of a three-dimensional grain or a result of competitive growth mechanisms and suppressed by favorable growth of adjacent grains. Figure 5.56a contains a horizontal, dashed line depicting the location representing a distinct difference in nucleation direction and competitive growth. At the root, the grains nucleate off the fusion boundary and grow vertically until terminated by grains growing directly inward toward the weld centerline. Although the grains above the dashed line appear equiaxed in the longitudinal section (Figure 5.56a), these grains grow with a high aspect ratio directly inward toward the fusion boundary as shown in Figure 5.55a.

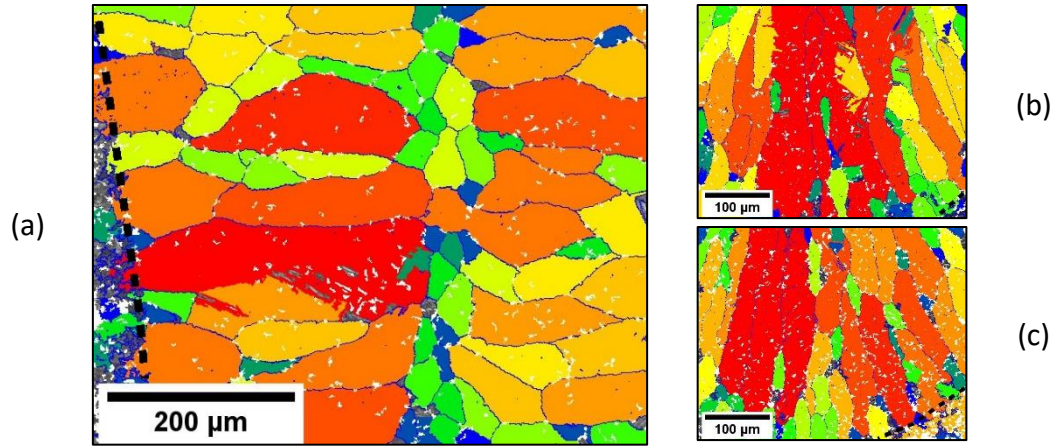


Figure 5.55. Transverse view of PBGS distribution at 1600 W with similar colors/shades representing a similar grain size at each condition: 50 mm/s (a), 100 mm/s (b), 150 mm/s (c). The dashed, black lines represent the fusion boundaries.

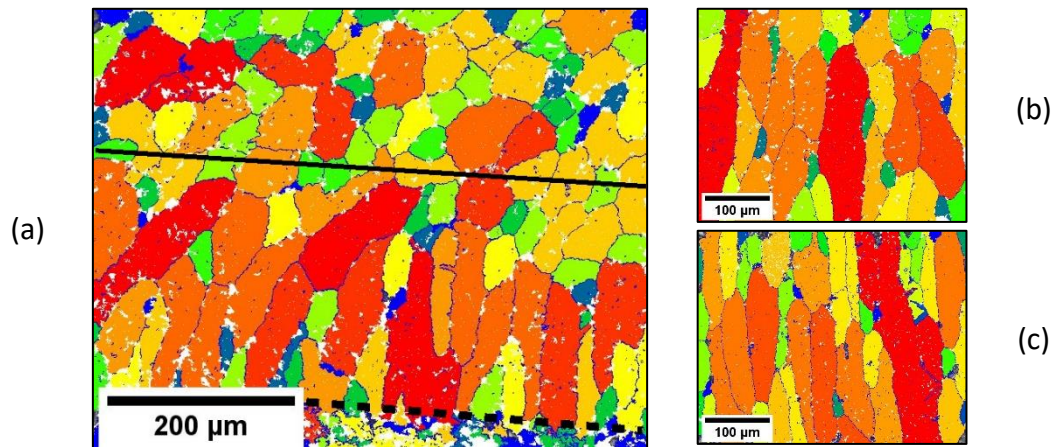


Figure 5.56. Longitudinal view of PBGS distribution at 1600 W with similar colors/shades representing a similar grain size at each condition: 50 mm/s (a), 100 mm/s (b), 150 mm/s (c). The grain size analysis at 50 mm/s was only evaluated below the continuous, black line for a closer comparison to 100 and 150 mm/s. The dashed, black line represents the fusion boundary.

Using this information, an approximation of the PBG lengths and widths were computed as shown in the plots in Figure 5.57a and Figure 5.57b. The lengths are based

on the major axis, and the widths are based on the minor axis using an ellipsoid fitted to each grain from Figure 5.55 and Figure 5.56. The lengths and widths were analyzed separately due to the high aspect ratios. Also, the grain size for the longitudinal view at 50 mm/s was only evaluated below the horizontal, dashed line shown in Figure 5.56a. This was to eliminate the bias of the variation in growth direction and better compare to the conduction mode welds.

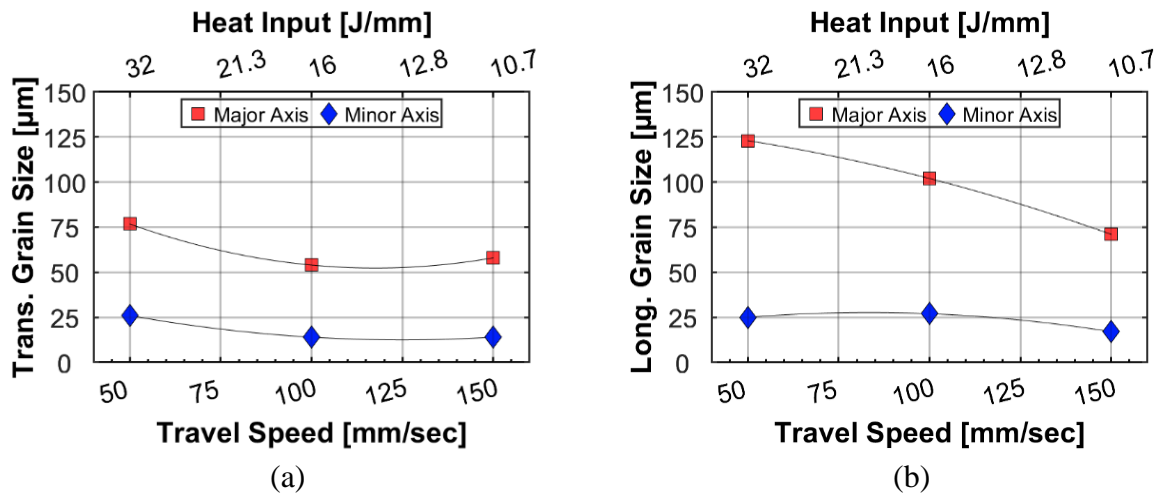
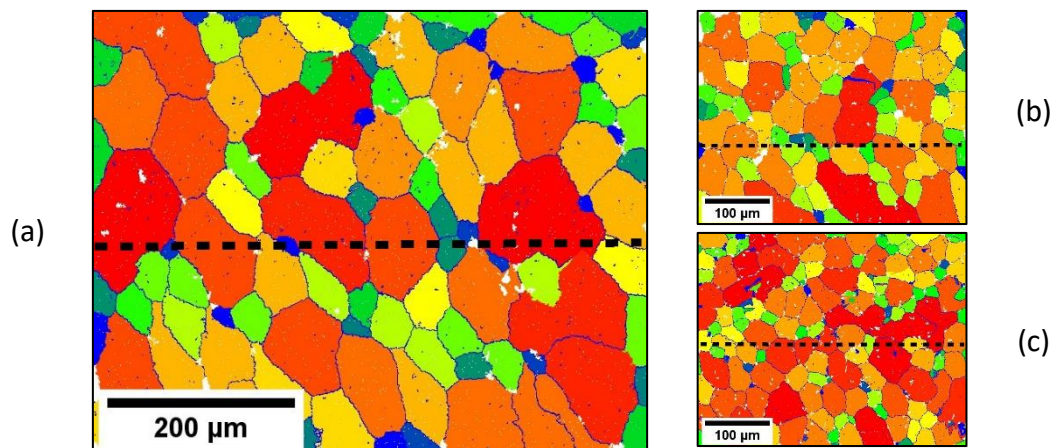


Figure 5.57. PBGS versus travel speed at 1600 W showing the major axis (length) and minor axis (width) for the transverse view orientation (a) and the longitudinal view orientation (b).

The transverse sections showed a reduced PBGS from the keyhole to the conduction mode welds and a negligible change in grain size between the two conduction mode welds (Figure 5.57a). The longitudinal view showed a decrease in the major axis with a minimal change in the minor axis for increasing travel speed (Figure 5.57b). This result is based on computing the grain size only using the high aspect ratio grains

nucleating from the root. The directional beta grain growth at the root is due to the preferential nucleation/growth resulting from the local weld pool geometry. At 50 mm/s, in Figure 5.56a, the average grain size above the dashed line was  $\approx 50 \mu\text{m}$ .

Due to the equiaxed nature of the beta grains in the plan view, a grain size (diameter) was estimated instead of distinctly characterizing the widths and lengths. The grain size color maps for each travel speed are shown in Figure 5.58. There is a clear reduction in the grain size with increasing weld speed, as shown in Figure 5.59. With an increase in travel speed from 50 mm/s to 150 mm/s, the PBGS decreased by nearly half the diameter from  $\approx 50 \mu\text{m}$  to  $\approx 25 \mu\text{m}$ . The plan view (z-direction) orientation provides a better comparison of the grain size in similar locations of the weld pool. Because the data in Figure 5.58a is from the weld pool surface, it is not related and comparable to grains represented in the maps previously presented in Figure 5.55a and Figure 5.56a.



*Figure 5.58. Plan view of PBGS distribution at 1600 W with similar colors/shades representing a similar grain size at each condition: 50 mm/s (a), 100 mm/s (b), 150 mm/s (c). The dashed, black lines represent the weld centerlines.*

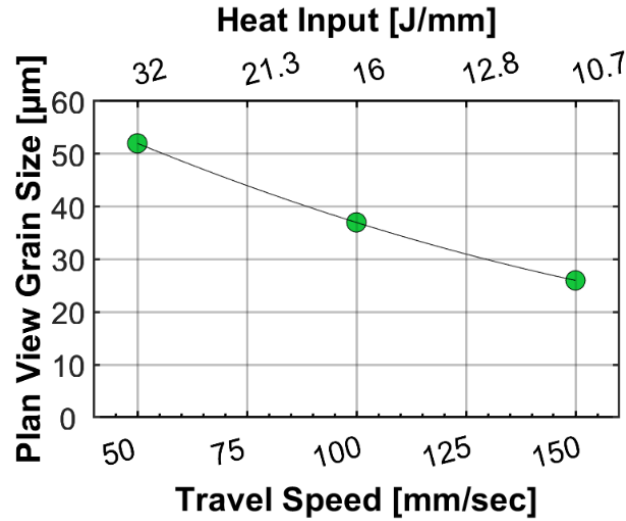


Figure 5.59. PBGS versus travel speed at 1600 W for the plan view orientation.

It should be noted that this data is single EBSD scans from a single metallographic section and does not represent a statistically significant analysis. However, a trend relating to grain size evolution is still apparent.

Finally, it can be seen in the longitudinal and transverse views (Figure 5.52 and Figure 5.53) that the  $\alpha'$  laths nucleate and terminate at PBGBs with directions approximately  $45^\circ$  relative to the PBG boundary interface. Using this approximation and the width of the beta grains, the  $\alpha'$  lath lengths can be roughly defined as a width from the transverse and longitudinal cross-sections. Therefore,  $\alpha'$  lengths were loosely considered as 1.4 times ( $1/\cos 45^\circ$ ) the beta grain widths. This approximation would produce  $\alpha'$  lengths reducing from  $\approx 28 \mu\text{m}$  to  $\approx 20 \mu\text{m}$  between 50 mm/s and 150 mm/s, respectively. This suggests that by controlling the weld pool solidification behavior to

reduce the PBGS and length of the  $\alpha'$  martensite laths, it may be possible to promote improved as-welded toughness.

Beta grain size may be influenced by the size of the base metal grains. As shown in the SEM image in Appendix J:, the base metal grains are  $\approx 5 \mu\text{m}$  in diameter. It is assumed that finer grains tend to promote smaller grain size within the weld metal. This is caused by epitaxial nucleation from grains at the fusion boundary in polycrystalline materials. However, the influence of base metal grain size was not evaluated in this study, and the PBGs are an order of magnitude larger than the base metal grains.

#### **5.3.2.3 Summary**

In conduction mode welds, beta grains grew vertically from the weld root to the weld surface with lengths nearly equivalent to the weld pool depth, but an increase in travel speed (decreased heat input) caused grain widths to narrow. High aspect ratio/keyhole welds showed a variation in growth direction within the keyhole. The beta grain growth terminated at the weld centerline. Analysis of the plan view orientation showed nearly equiaxed beta grains near the weld surface that increased in size as the travel speed decreased (heat input increased) for both conduction and keyhole mode.

## **6 Conclusions**

The following conclusions detail the major findings and advancement of this study regarding LBW on stainless steel alloys and Ti-6Al-4V.

### **6.1 Weld Formation**

The weld formation analysis showed the ability to influence the pool geometry during LBW and the difficulty in generating a model to predict features over a large range of process parameters. The ICI analysis showed new insight to the 3D geometry associated with the vapor capillary and how this geometry changes between alloys and weld parameters. The results specific to each analysis are summarized as follows:

#### ***6.1.1 Weld Geometry***

1. A transition to deep penetration welding occurred at lower powers and higher travel speeds for Ti-6Al-4V as compared to 304L SS. This indicated a difference in melting efficiency between the two alloys.
2. Periodic surface ripples were produced at 800 W of power and a 5 mm/s travel speed for stainless steels and Ti-6Al-4V. The frequency of these transitions varied with material.
3. Weld pool decanting was demonstrated at low powers and travel speeds (1000 W and 5-25 mm/s). The results indicated that the melting efficiency for LBW 304L SS at 1000 W of power is nearly 70%.

### **6.1.2 Keyhole Formation**

1. The vapor capillary was shown to lag the process beam at higher travel speeds and/or lower powers. The 2205 DSS showed the greatest keyhole lag followed by 304L and Ti-6Al-4V.
2. The ICI system detected a weld pool depression or vapor cavity in low aspect ratio welds appearing as conduction mode in the metallographic section.
3. There was a negligible difference in the vapor capillary volume between 2205, 304L, and Ti-6Al-4V across all parameters investigated.
4. At a constant power of 1600 W and travel speeds generating deep penetration welds, keyhole diameters were slightly larger than the beam diameter and approximately 0.8 mm for 304L, 2205, and Ti-6Al-4V.
5. Distinguishing conduction versus keyhole mode welding based on a depth-to-width aspect ratio of 1-1.5 is insufficient unless the width is measured with the keyhole portion of the weld.

## **6.2 Modeling**

HED weld modeling using analytical solutions with or without dimensionless relationships were insufficient for accurately predicting weld penetration in this investigation. Because these solutions could not be further advanced in an appreciable manner, a model for weld feature prediction was developed using a neural network algorithm. It was shown that the NN algorithm is a useful tool to successfully predict

weld geometries over the range of process parameters evaluated. However, this is directly dependent on the quantity and quality of data produced.

1. Overfitting data was exacerbated when sharp changes occurred in the weld features and/or an insufficient quantity of data was present.
2. Fitting a model to each weld feature instead of using a single model with numerous outputs produced acceptable results with the least error.

### **6.3 Microstructure**

#### **6.3.1 *Stainless Steel Alloys***

Large variations in LBW process parameters can strongly influence the weld metal microstructure in stainless steels that may solidify with or as delta ferrite. Over a large range of powers and travel speeds, it was shown that weld pool development can alter weld pool geometries, grain orientation, and solidification rates. The important findings regarding SS microstructures are as follows:

1. Grain growth was nearly vertical in low ( $<1$ ) depth-to-width aspect ratio welds made in a conduction mode. Therefore, it can be assumed that a relatively uniform solidification rate was maintained throughout the weld pool.
2. Keyhole or high aspect ratio welds created a large range of solidification rates, and the keyhole region created a location with solidification rates nearly equal to the travel speed.

3. At 1600 W, the high aspect ratio weld generated a solidification rate  $\approx 20$  mm/s higher than a low aspect ratio weld produced at twice the travel speed.
4. The as-welded 50/50 ferrite-to-austenite fractions in SS alloys would require WRC  $Cr_{eq}/Ni_{eq}$  near  $\approx 2.2$ -2.3.
5. Extensive use of electron backscattered diffraction (EBSD) provided new insight into weld metal phase fractions and provides better correlations between the WRC  $Cr_{eq}/Ni_{eq}$  value and ferrite content in SS laser welds.
6. A new microstructural map for LBW is proposed that defines microstructure regions at WRC  $Cr_{eq}/Ni_{eq}$  values exceeding 1.8.

### **6.3.2 Ti-6Al-4V**

Rapid grain growth in titanium alloys has historically created an issue regarding the mechanical performance of welded joints. In this study, the prior beta grain size was characterized as a function of travel speed during laser welding of Ti-6Al-4V. By altering the weld travel speed to transition from keyhole to conduction mode welding, a variation in beta grain size and growth direction was produced and quantified. The main conclusions are as follows:

1. Low aspect ratio welds ( $<1$ ) showed vertical prior beta grain (PBG) growth with PBG lengths nearly equivalent to the weld pool depth. Increasing the travel speed (decreased heat input) caused grain widths to narrow but maintained lengths largely restricted to the weld pool depth.

2. High aspect ratio/keyhole welds showed a variation in growth direction based on the weld pool profile. Within the keyhole region, grain growth proceeded orthogonally from the weld pool wall and along the travel direction. Growth terminated along the weld centerline by grains nucleated from the opposite boundary, which created a distinct weld centerline.
3. The plan view EBSD data showed nearly equiaxed beta grains near the weld surface that increased in size as the heat input increased (decrease in welding speed).
4. The length of the  $\alpha'$  martensite laths was restricted to the width of the PBGs, and therefore, a reduction in beta grain size resulted in a restricted lath structure.

## **7 Future Work**

The proposed future work is summarized in the following subsections for weld behavior, neural network modeling, and microstructural analysis.

### **7.1 Weld Behavior Analysis**

1. It is proposed to further analyze the pulsed-like nature of the 800 W, 5 mm/s welds. High speed photography of the weld pool and plume may be able to determine if a relation exists.
2. Determine the front wall angle of the keyhole using the ICI scans and project the beam distribution across the front wall angle to determine how the angle influences the intensity distribution.
3. Examine the influence of welded joints in comparison to the bead-on-plate welds analyzed in this investigation. Specifically, analyze how variations in joint fit-up may influence weld formation. A proposed experiment is to utilize stationary optics and a power sensor below a butt joint with an increasing joint gap. Analysis of the transmitted power will aid in understanding how joint gaps influence laser power absorption.

### **7.2 ANN Modeling**

1. Add measured features to the NN algorithm including crown height, undercut, and porosity information.

3. Continue to incorporate parameters to the ANN to evolve the model to be better suited for large variations. This would include beam diameter, incident angle, materials, etc.
4. Eventually, it may be desirable to replace specific material selections with chemical compositions. The envisioned long-range goal would be to continually upload new data via a measured beam caustic, power measurement, travel speed, material composition (or properties), weld cross-section, and weld defect formation. This would require an enormous quantity of data [172], but may prove worthwhile for a wide range of prediction capabilities.

### **7.3 Microstructure**

#### **7.3.1 *Stainless Steels***

1. It is necessary to further characterize SS microstructural morphologies between a 2.2 and 2.8 WRC-1992  $Cr_{eq}/Ni_{eq}$  using LOM and EBSD. The information from characterizing microstructure morphologies and phase fractions along with data extracted from prior literature [174], [181], [190], [194] is necessary to better fit process parameters and  $Cr_{eq}/Ni_{eq}$  relationships.
2. For confirmation of deformation induced martensite skewing EBSD phase fraction results, it is necessary to perform electropolishing on the alloys at and below a 2.2  $Cr_{eq}/Ni_{eq}$ . Then, perform EBSD on the electropolished weld sections to directly measured phase fractions relative to a mechanical polishing procedure.

### **7.3.2 *Titanium***

1. Capture a statistically number of EBSD scans for a given weld parameter to provide a statistical analysis and confirmation of grain size and/or orientation. In addition, characterize grain growth in Ti-6Al-4V LB welds at different beam powers using the EBSD PBGB delineation technique. Incorporate these results into a comprehensive map of grain size relative to power and travel speed for Ti-6Al-4V.
2. Analyze heat treatment methods to reveal PBGBs using controlled heating rates, hold times, and cooling rates near the beta transus temperature. It is believed that this will result in a transformation to beta at the PBGB. Cooling at a rate to maintain this microstructure will allow for optically measuring grain size.

## Bibliography

- [1] American Welding Society, “Laser Beam Welding, Cutting, and Associated Processes,” in *Welding Handbook Volume 3 Welding Processes, Part 2*, 9th ed., D. Kautz, V. E. Merchant, J. O. Milewski, and D. E. Powers, Eds. Miami, Florida, USA: American Welding Society, 2007, pp. 503–560.
- [2] Y. Kawahito, H. Wang, S. Katayama, and D. Sumimori, “Ultra High Power (100 kW) Fiber Laser Welding of Steel,” *Opt. Lett.*, vol. 43, no. 19, pp. 4667–4670, 2018, doi: 10.1364/ol.43.004667.
- [3] T. Patterson, J. Hochanadel, S. Sutton, B. Panton, and J. Lippold, “A Review of High Energy Density Beam Processes for Welding and Additive Manufacturing Applications,” *Weld. World*, vol. 65, no. 7, pp. 1235–1306, 2021, doi: 10.1007/s40194-021-01116-0.
- [4] I. Amada Miyachi America, “Laser Welding Fundamentals.” Amada Miyachi America, INC., Monrovia, CA, 2016, [Online]. Available: [http://www.amadamiyachi.com/servlet/servlet.FileDownload?retURL=%2Fapex%2Feducationalresources\\_articles&file=01580000001Jz8A](http://www.amadamiyachi.com/servlet/servlet.FileDownload?retURL=%2Fapex%2Feducationalresources_articles&file=01580000001Jz8A).
- [5] J. C. Lippold and D. J. Kotecki, *Welding Metallurgy and Weldability of Stainless Steels*. John Wiley & Sons, Inc., 2005.
- [6] RMI Titanium, “Titanium Alloy Guide.” RMI Titanium Company, 2000, [Online]. Available: [www.RMITitanium.com](http://www.RMITitanium.com).
- [7] W. A. Baeslack, J. R. Davis, and C. E. Cross, “Selection and Weldability of Conventional Titanium Alloys,” in *ASM Handbook, Volume 6: Welding, Brazing, and Soldering*, vol. 6, D. L. Olson, T. A. Siewert, S. Liu, and G. R. Edwards, Eds.

ASM International, 1993, pp. 507–523.

- [8] Hablani, “A Correlation of Welding Variables,” in *Proceedings of the Electron Beam Symposium Fifth Annual Meeting*, 1963, pp. 262–268.
- [9] I. Eriksson, J. Powell, and A. F. H. Kaplan, “Melt Behavior on the Keyhole Front during High Speed Laser Welding,” *Opt. Lasers Eng.*, vol. 51, no. 6, pp. 735–740, 2013, doi: 10.1016/j.optlaseng.2013.01.008.
- [10] S. Katayama, N. Seto, J. Do Kim, and A. Matsunawa, “Formation Mechanism and Reduction Method of Porosity in Laser Welding of Stainless Steel,” *Laser Inst. Am. Proc.*, vol. 83, no. 2, 1997, doi: 10.2351/1.5059741.
- [11] M. Miyagi and J. Wang, “Keyhole Dynamics and Morphology Visualized by in-situ X-ray Imaging in Laser Melting of Austenitic Stainless Steel,” *J. Mater. Process. Technol.*, vol. 282, 2020, doi: 10.1016/j.jmatprotec.2020.116673.
- [12] J. Dowden, M. Davis, and P. Kapadia, “The Flow of Heat and the Motion of the Weld Pool in Penetration Welding with a Laser,” *J. Appl. Phys.*, vol. 57, no. 9, pp. 4474–4479, 1985, doi: 10.1063/1.334571.
- [13] A. F. H. Kaplan, “A Model of Deep Penetration Laser Welding Based on Calculation of the Keyhole Profile,” *J. Phys. D. Appl. Phys.*, vol. 27, no. 9, pp. 1805–1814, 1994, doi: 10.1088/0022-3727/27/9/002.
- [14] R. Rai, J. W. Elmer, T. A. Palmer, and T. Debroy, “Heat Transfer and Fluid Flow during Keyhole Mode Laser Welding of Tantalum, Ti-6Al-4V, 304L Stainless Steel and Vanadium,” *J. Phys. D. Appl. Phys.*, vol. 40, no. 18, pp. 5753–5766, 2007, doi: 10.1109/JQE.1974.1145810.
- [15] R. Rai, P. Burgardt, J. O. Milewski, T. J. Lienert, and T. Debroy, “Heat Transfer and Fluid Flow during Electron Beam Welding of 21Cr-6Ni-9Mn Steel and Ti-6Al-4V Alloy,” *J. Phys. D. Appl. Phys.*, vol. 42, no. 2, 2009, doi: 10.1088/0022-3727/42/2/025503.

- [16] M. Jiang, Y. B. Chen, X. Chen, W. Toa, and T. Debroy, “Enhanced Penetration Depth during Reduced Pressure Keyhole-Mode Laser Welding,” *Weld. J.*, vol. 99, no. 4, pp. 110–124, 2020, doi: 10.29391/2020.99.011.
- [17] J. C. Lippold, “Centerline Cracking in Deep Penetration Electron Beam Welds in Type 304L Stainless Steel,” *Weld. J.*, no. 5, pp. 127s-136s, 1985.
- [18] W. A. Baeslack III, D. W. Becker, and F. H. Froes, “Advances in Titanium Alloy Welding Metallurgy,” *J. Met.*, vol. 36, no. 5, pp. 46–58, 1984, doi: 10.1039/c2ay25041a.
- [19] I. Varol, J. C. Lippold, and W. A. Baeslack, “Welding of Duplex Stainless Steels,” *Key Eng. Mater.*, vol. 69 and 70, pp. 217–252, 1992.
- [20] A. Baghdadchi, V. A. Hosseini, K. Hurtig, and L. Karlsson, “Promoting Austenite Formation in Laser Welding of Duplex Stainless Steel—Impact of Shielding Gas and Laser Reheating,” *Weld. World*, vol. 65, no. 3, pp. 499–511, 2021, doi: 10.1007/s40194-020-01026-7.
- [21] T. Omura, T. Kushida, and Y. Komizo, “Microstructural Features and Corrosion Properties in Laser Welded Duplex Stainless Steels,” *Weld. Int.*, vol. 14, no. 4, pp. 257–260, 2000, doi: 10.1080/09507110009549176.
- [22] L. Karlsson, “Welding Duplex Stainless Steels - A Review of Current Recommendations,” *Weld. World*, vol. 56, no. 5–6, pp. 65–76, 2012, doi: 10.5937/zzk1802065k.
- [23] J. Berger, “Effect of Preferential Vaporization during Laser Rewelding on the Solidification and Cracking Response of Type 304L Stainless Steel Alloys with Systematically Varied Manganese Contents Thesis,” The Ohio State University, 2018.
- [24] W. Steen and J. Mazumder, *Laser Material Processing*, 4th ed. Springer, 2010.
- [25] W. L. Stellwag, “Fiber Laser Welding of 304 Stainless Steel and the Effects of

Various Parameters on Material Coupling and Back-Reflection,” The Ohio State University, 2012.

- [26] B. C. Gahan and B. Shiner, “New High-Power Fiber Laser,” *Laser Technol.*, pp. 29–31, 2004.
- [27] W. Koechner, “Optical Sciences,” in *Solid-State Laser Engineering*, Sixth., W. T. Rhodes, Ed. Springer, 2006.
- [28] K. Richter, W. Behr, and U. Reisgen, “Low Heat Welding of Titanium Materials with a Pulsed Nd:YAG Laser,” *Materwiss. Werksttech.*, vol. 38, no. 1, pp. 51–56, 2007, doi: 10.1002/mawe.200600095.
- [29] L. Dong and M. E. Fermann, “Introduction to Optical Fiber Lasers,” in *High-Power Laser Handbook*, H. Injeyan and G. D. Goodno, Eds. McGraw-Hill Companies, Inc., 2011, pp. 413–462.
- [30] A. Einstein, “Emission and Absorption of Radiation in Quantum Theory,” in *The Collected Papers of Albert Einstein The Berlin Years: Writings, 1914-1917*, A. J. Kox, M. J. Klein, and R. Schulmann, Eds. 1996, pp. 212–216.
- [31] J. Hecht, “A Short History of Laser Development,” *Opt. Eng.*, vol. 49, no. 49, pp. 99–122, 2010, doi: 10.1117/1.3483597.
- [32] A. L. Schawlow and C. H. Townes, “Masers and Maser Communications System,” US 2,929,922, 1960.
- [33] A. L. Schawlow and C. H. Townes, “Infrared and Optical Masers,” *Phys. Rev.*, vol. 112, no. 6, pp. 1940–1949, 1958, doi: 10.1103/PhysRev.112.1940.
- [34] G. Gould, “Apparatus for Generating Radiation of Frequencies Higher than those of Light,” 3388314, 1968.
- [35] E. Snitzer, “Proposed Fiber Cavities for Optical Masers,” *J. Appl. Phys.*, vol. 32, no. 1, pp. 36–39, 1961, doi: 10.1063/1.1735955.

- [36] C. J. Koester and E. Snitzer, "Amplification in a Fiber Laser," *Appl. Opt.*, vol. 3, no. 10, pp. 1182–1186, 1964, doi: 10.1364/oaa.1997.rp1.
- [37] D. B. Keck, P. Schlutz, and P. C. Schultz, "Method of Producing Optical Waveguide Fibers," 3711262, 1973.
- [38] E. Snitzer, H. Po, F. Hakimi, R. Tumminelli, and B. C. McCollum, "Double Clad, Offset Core Nd Fiber Laser," in *Optical Fiber Communication Conference*, 1988, pp. PD5-1-PD5-3, doi: 10.1364/ofs.1988.pd5.
- [39] H. Po *et al.*, "Double Clad High Brightness Nd Fiber Laser Pumped by GaAlAs Phaser Array," in *Optical Fiber Communication Conference*, 1989, pp. 1–4, doi: 10.1364/ofc.1989.pd7.
- [40] R. Wyatt, "High Power Broadly Tunable Erbium-Doped Silica Fibre Laser," *Electrons Lett.*, vol. 25, no. 22, pp. 1498–1499, 1989.
- [41] R. B. Allen and S. J. Scalise, "Continuous Operation of a YAlG: Nd Laser by Injection Luminescent Pumping," *Appl. Phys. Lett.*, vol. 14, no. 6, pp. 188–190, 1969, doi: 10.1063/1.1652768.
- [42] D. F. Welch, "A Brief History of High-Power Semiconductor Lasers," *IEEE J. Sel. Top. Quantum Electron.*, vol. 6, no. 6, pp. 1470–1477, 2000, doi: 10.1109/2944.902203.
- [43] V. Gapontsev, "Ultra High Power Ytterbium Fiber Lasers," 2004.
- [44] P. V. Gapontsev and I. Samartsev, "Coupling Arrangement Between a Multi-mode Light Source and an Optical Fiber through an Intermediate Optical Fiber Length," US5999673, 1999.
- [45] "IPG Photonics Successfully Tests World's First 10 Kilowatt Single-Mode Production Laser," 2009.  
<https://www.laserfocusworld.com/home/article/16559922/ipg-photonics-successfully-tests-worlds-first-10-kilowatt-singlemode-production-laser> (accessed

Jun. 23, 2020).

- [46] M. N. Zervas and C. A. Codemard, “High Power Fiber Lasers: A Review,” *IEEE J. Sel. Top. Quantum Electron.*, vol. 20, no. 5, 2014, doi: 10.1109/JSTQE.2014.2321279.
- [47] IPG Photonics Inc., “YLS, 1-120+ kW,” 2019.  
<https://www.ipgphotonics.com/en/products/lasers/high-power-cw-fiber-lasers/1-micron/yls-1-120-kw> (accessed Jan. 02, 2019).
- [48] C. A. Klein, “Materials for High-energy Laser Windows: How Thermal Lensing and Thermal Stresses Control the Performance,” *Opt. Mater. Struct. Technol. III*, vol. 6666, no. May, p. 66660Z, 2007, doi: 10.1117/12.732946.
- [49] J. Blecher, T. A. Palmer, S. M. Kelly, and R. P. Martukanitz, “Identifying Performance Differences in Transmissive and Reflective Laser Optics using Beam Diagnostic Tools,” *Weld. J.*, vol. 91, no. 7, 2012.
- [50] D. Reitemeyer, T. Seefeld, and F. Vollertsen, “Online Focus Shift Measurement in High Power Fiber Laser Welding,” *Phys. Procedia*, vol. 5, no. PART 2, pp. 455–463, 2010, doi: 10.1016/j.phpro.2010.08.073.
- [51] PRIMES GmbH, “FocusMonitor FM+,” pp. 1–7.
- [52] P. Burgardt, S. W. Pierce, and M. J. Dvornak, “Definition of Beam Diameter for Electron Beam Welding,” Los Alamos, NM, 2016.
- [53] International Standards Organization, “ISO 11146-1:2005 Lasers and laser-related equipment – Test methods for laser beam widths, divergence angles and beam propagation ratios – Part1: Stigmatic and simple astigmatic beams.” International Standards Organization, 2005.
- [54] B. Y. C. Leung, P. J. L. Webster, J. M. Fraser, and V. X. D. Yang, “Real-time Guidance of Thermal and Ultrashort Pulsed Laser Ablation in Hard Tissue using Inline Coherent Imaging,” *Lasers Surg. Med.*, vol. 44, no. 3, pp. 249–256, 2012, 205

doi: 10.1002/lsm.21162.

- [55] J. J. Blecher *et al.*, “Real Time Monitoring of Laser Beam Welding Keyhole Depth by Laser Interferometry,” *Sci. Technol. Weld. Join.*, vol. 19, no. 7, pp. 560–564, Oct. 2014, doi: 10.1179/1362171814Y.00000000225.
- [56] P. J. L. L. Webster, L. G. Wright, K. D. Mortimer, B. Y. Leung, J. X. Z. Z. Yu, and J. M. Fraser, “Automatic Real-time Guidance of Laser Machining with Inline Coherent Imaging,” in *29th International Congress on Applications of Lasers and Electro-Optics, ICALEO 2010 - Congress Proceedings*, 2010, vol. 103, pp. 1386–1393, doi: 10.2351/1.3567955.
- [57] P. J. L. Webster *et al.*, “Automatic Laser Welding and Milling with in situ Inline Coherent Imaging,” *Opt. Lett.*, vol. 39, no. 21, pp. 6217–6220, 2014, doi: 10.1364/ol.39.006217.
- [58] P. J. L. Webster, M. S. Muller, and J. M. Fraser, “High Speed in situ Depth Profiling of Ultrafast Micromachining,” *Opt. Express*, vol. 15, no. 23, p. 14967, 2007, doi: 10.1364/OE.15.014967.
- [59] Y. Ji, A. W. Grindal, P. J. L. L. Webster, and J. M. Fraser, “Real-time Depth Monitoring and Control of Laser Machining through Scanning Beam Delivery System,” *J. Phys. D. Appl. Phys.*, vol. 48, no. 15, Apr. 2015, doi: 10.1088/0022-3727/48/15/155301.
- [60] J. M. Fraser, “Inline Coherent Imaging of Laser Processing,” *Front. Ultrafast Opt. Biomed. Sci. Ind. Appl. XI*, vol. 7925, no. February 2011, p. 792516, Feb. 2011, doi: 10.1117/12.877745.
- [61] F. Altal, T. R. Allen, S. G. L. Nestor, T. G. Fleming, and J. M. Fraser, “Dual-channel Inline Coherent Imaging,” *Appl. Opt.*, vol. 58, no. 7, pp. 1614–1620, 2019, doi: 10.1364/ao.58.001614.
- [62] P. J. L. Webster, J. X. Z. Yu, B. Y. C. Leung, L. G. Wright, K. D. Mortimer, and J.

- M. Fraser, "Inline Coherent Imaging of Laser Micromachining," Oct. 2010, doi: 10.1109/ISOT.2010.5687305.
- [63] J. M. Fraser, "Laser Process Monitoring and Automatic Control at kHz Rates through Inline Coherent Imaging," *AIP Conf. Proc.*, vol. 1464, no. July 2012, pp. 492–496, 2012, doi: 10.1063/1.4739903.
- [64] F. Dorsch *et al.*, "Controlling Laser Processing via Optical Coherence Topography," in *High-Power Laser Materials Processing: Applications, Diagnostics, and Systems VIII*, Feb. 2019, doi: 10.1117/12.2509630.
- [65] T. G. Fleming, S. G. L. Nestor, T. R. Allen, M. A. Boukhaled, N. J. Smith, and J. M. Fraser, "Tracking and Controlling the Morphology Evolution of 3D Powder-bed Fusion in situ using Inline Coherent Imaging," *Addit. Manuf.*, vol. 32, Mar. 2020, doi: 10.1016/j.addma.2019.100978.
- [66] P. J. L. L. Webster, J. M. Fraser, and V. X. D. D. Yang, "Methods and Systems for Coherent Imaging and Feedback Control for Modification of Materials," US 8,822,875 B2, 2014.
- [67] S. H. Yun, G. J. Tearney, J. F. de Boer, and B. E. Bouma, "Motion Artifacts in Optical Coherence Tomography with Frequency-domain Ranging," *Opt. Express*, vol. 12, no. 13, p. 2977, 2004, doi: 10.1364/OPEX.12.002977.
- [68] M. Boley, P. Webster, A. Heider, R. Weber, and T. Graf, "Investigating the Keyhole Behavior by using X-ray and Optical Depth Measurement Techniques," pp. 426–430, 2014, doi: 10.2351/1.5063091.
- [69] M. Boley, F. Fetzner, R. Weber, and T. Graf, "Statistical Evaluation Method to Determine the Laser Welding Depth by Optical Coherence Tomography," *Opt. Lasers Eng.*, vol. 119, pp. 56–64, Aug. 2019, doi: 10.1016/j.optlaseng.2019.03.014.
- [70] A. J. Russo, R. L. Akau, and J. L. Jellison, "Thermocapillary Flow in Pulsed Laser

- Beam Weld Pools,” *Weld. J.*, vol. 69, no. 1, pp. 23–29, 1990.
- [71] T. Webber, T. Lieb, and J. Mazumder, “Laser Beam Welding,” in *ASM Handbook, Volume 6A, Welding Fundamentals and Processes*, vol. 6A, T. Lienert, T. Siewert, S. Babu, and V. Acoff, Eds. ASM International, 2011, pp. 556–569.
  - [72] C. L. Chan, J. Mazumder, and M. M. Chen, “Effect of Surface Tension Gradient Driven Convection in a Laser Melt Pool: Three-dimensional Perturbation Model,” *J. Appl. Phys.*, vol. 64, no. 11, pp. 6166–6174, 1988.
  - [73] J. H. Cho, D. F. Farson, and M. J. Reiter, “Analysis of Penetration Depth Fluctuations in Single-mode Fibre Laser Welds,” *J. Phys. D. Appl. Phys.*, vol. 42, no. 11, 2009, doi: 10.1088/0022-3727/42/11/115501.
  - [74] J. Y. Lee, S. H. Ko, D. F. Farson, and C. D. Yoo, “Mechanism of Keyhole Formation and Stability in Stationary Laser Welding,” *J. Phys. D. Appl. Phys.*, vol. 35, no. 13, pp. 1570–1576, 2002, doi: 10.1088/0022-3727/35/13/320.
  - [75] A. Matsunawa, “Science of Laser Welding - Mechanisms of Keyhole and Pool Dynamics,” in *ICALEO 2002 - 21st International Congress on Applications of Laser and Electro-Optics, Congress Proceedings*, 2002, vol. 290, no. 2002, doi: 10.2351/1.5065734.
  - [76] A. Matsunawa, J. Kim, S. Katayama, N. Seto, M. Mizutani, and S. Katayama, “Dynamics of Keyhole and Molten Pool in Laser Welding,” *J. Laser Appl.*, vol. 10, no. 6, pp. 247–254, 1998, doi: 10.2351/1.521858.
  - [77] J. W. Elmer, P. W. Hochanadel, K. Lachenberg, and T. Webber, “Introduction to High Energy Density Electron and Laser Beam Welding,” in *ASM Handbook, Volume 6A, Welding Fundamentals and Processes*, vol. 6A, T. Lienert, T. Siewert, S. Babu, and V. Acoff, Eds. ASM International, 2011, pp. 507–513.
  - [78] E. G. Assunção, “Investigation of Conduction to Keyhole Mode Transition,” Cranfield University, 2012.

- [79] E. G. Assunção and S. Williams, “Effect of Material Properties on the Laser Welding Mode Limits,” *J. Laser Appl.*, vol. 26, no. 1, 2014, doi: 10.2351/1.4826153.
- [80] D. T. Swift-Hook and A. E. F. Gick, “Penetration Welding with Lasers,” *Weld. J.*, no. 11, pp. 492s-499s, 1973, [Online]. Available: <https://unicorn.dmz.cranfield.ac.uk/uhtbin/cgiisirs/?ps=MHwR2FMU8e/CRANFIELD/141340320/9>.
- [81] P. W. Fuerschbach, “Measurement and Prediction of Energy Transfer Efficiency in Laser Beam Welding,” *Weld. J.*, vol. 75, no. 1, pp. 24s-34s, 1996.
- [82] S. L. Ream, “Laser Welding Efficiency and Cost: CO<sub>2</sub>, YAG, fiber, and Disc,” 2004, doi: 10.2351/1.5060242.
- [83] J. Xie, A. Kar, J. A. Rothenflue, and W. P. Latham, “Temperature-dependent Absorptivity and Cutting Capability of CO<sub>2</sub>, Nd:YAG and Chemical Oxygen–Iodine Lasers,” *J. Laser Appl.*, vol. 9, no. 2, pp. 77–85, 1997, doi: 10.2351/1.4745447.
- [84] J. Mazumder, “Laser Welding: State of the Art Review,” *JOM J. Miner. Met. Mater. Soc.*, vol. 34, no. 7, pp. 16–24, 1982, doi: 10.1007/BF03338045.
- [85] A. Hess, R. Schuster, A. Heider, R. Weber, and T. Graf, “Continuous Wave Laser Welding of Copper with Combined Beams at Wavelengths of 1030 nm and of 515 nm,” *Phys. Procedia*, vol. 12, pp. 88–94, 2011, doi: 10.1016/j.phpro.2011.03.012.
- [86] J. P. Bergmann, M. Bielenin, and T. Feustel, “Aluminum Welding by Combining a Diode Laser with a Pulsed Nd:YAG Laser,” *Weld. World*, vol. 59, no. 2, pp. 307–315, 2015, doi: 10.1007/s40194-014-0218-8.
- [87] J. Dowden, “Laser Keyhole Welding: The Vapour Phase,” in *The Theory of Laser Materials Processing: Heat and Mass Transfer in Modern Technology*, J. Dowden, Ed. Springer, 2009, pp. 113–151.

- [88] A. F. H. Kaplan, “Fresnel Absorption of 1  $\mu\text{m}$ - and 10  $\mu\text{m}$ -Laser Beams at the Keyhole Wall during Laser Beam Welding: Comparison between Smooth and Wavy Surfaces,” *Appl. Surf. Sci.*, vol. 258, no. 8, pp. 3354–3363, 2012, doi: 10.1016/j.apsusc.2011.08.086.
- [89] M. Schneider, L. Berthe, R. Fabbro, and M. Muller, “Measurement of Laser Absorptivity for Operating Parameters Characteristic of Laser Drilling Regime,” *J. Phys. D. Appl. Phys.*, vol. 41, no. 15, 2008, doi: 10.1088/0022-3727/41/15/155502.
- [90] G. G. Gladush and I. Smurov, *Physics Of Laser Materials Processing Theory and Experiment*. Springer, 2011.
- [91] J. Mazumder, O. Conde, R. Villar, and W. Steen, Eds., *Laser Processing: Surface Treatment and Film Deposition*. Kluwer Academic Publishers, 1996.
- [92] V. Semak and A. Matsunawa, “The Role of Recoil Pressure in Energy Balance during Laser Materials Processing,” *J. Phys. D Appl. Phys.*, vol. 30, pp. 2541–2552, 1997.
- [93] A. Matsunawa and V. Semak, “The Simulation of Front Keyhole Wall Dynamics during Laser Welding,” *J. Phys. D. Appl. Phys.*, vol. 30, no. 5, pp. 798–809, 1997, doi: 10.1088/0022-3727/30/5/013.
- [94] V. Arata, “Fundamental Characteristics of High Energy Density Beams in Material Processing,” in *International Congress on Applications of Lasers & Electro-Optics*, 1986, vol. 73, pp. 73–79, doi: 10.2351/1.5057871.
- [95] M. Keskitalo, K. Mäntyjärvi, J. Sundqvist, J. Powell, and A. F. H. Kaplan, “Laser Welding of Duplex Stainless Steel with Nitrogen as Shielding Gas,” *J. Mater. Process. Technol.*, vol. 216, pp. 381–384, 2015, doi: 10.1016/j.jmatprotec.2014.10.004.
- [96] T. Scholz, K. Dickmann, A. Ostendorf, H. Uphoff, and M. Michalewicz, “Effect of Process Parameters on the Formation of Laser-induced Nanoparticles during

- Material Processing with Continuous Solid-state Lasers,” *J. Laser Appl.*, vol. 27, no. 3, p. 032001, 2015, doi: 10.2351/1.4916081.
- [97] F. Hansen and W. W. Duley, “Attenuation of Laser Radiation by Particles during Laser Materials Processing,” *J. Laser Appl.*, vol. 6, no. 137, pp. 137–143, 2016, doi: <https://doi.org/10.2351/1.4745348>.
- [98] S. Chiang and C. E. Albright, “CO<sub>2</sub> Laser Beam - Materials Interactions in the Welding of Mild Steel Part 2: Effects of Plume Suppression on Heat Transfer Efficiencies in Argon - Shielded Laser Beam Welding,” *Laser Inst. Am.*, vol. 75, pp. 491–522, 1992, doi: 10.2351/1.5058522.
- [99] T. J. Rockstroh and J. Mazumder, “Spectroscopic Studies of Plasma during CW Laser Materials Interaction,” *J. Appl. Phys.*, vol. 61, no. 3, pp. 917–923, 1987, doi: 10.1063/1.338142.
- [100] Y. Kawahito, K. Kinoshita, N. Matsumoto, M. Mizutani, and S. Katayama, “Effect of Weakly Ionised Plasma on Penetration of Stainless Steel Weld Produced with Ultra High Power Density Fibre Laser,” *Sci. Technol. Weld. Join.*, vol. 13, no. 8, pp. 749–753, 2008, doi: 10.1179/136217108X356971.
- [101] Y. Kawahito, N. Matsumoto, M. Mizutani, and S. Katayama, “Characterisation of Plasma Induced during High Power Fibre Laser Welding of Stainless Steel,” *Sci. Technol. Weld. Join.*, vol. 13, no. 8, pp. 744–748, 2008, doi: 10.1179/136217108X329313.
- [102] P. Y. Shcheglov, A. V. Gumenyuk, I. B. Gornushkin, M. Rethmeier, and V. N. Petrovskiy, “Vapor-plasma Plume Investigation during High-power Fiber Laser Welding,” *Laser Phys.*, vol. 23, no. 1, 2013, doi: 10.1088/1054-660X/23/1/016001.
- [103] J. Zou, W. Yang, S. Wu, Y. He, and R. Xiao, “Effect of Plume on Weld Penetration during High-power Fiber Laser Welding,” *J. Laser Appl.*, vol. 28, no.

- 2, p. 022003, 2016, doi: 10.2351/1.4940148.
- [104] Y. Cai, H. Heng, F. Li, and M. Wang, “The Influences of Welding Parameters on the Metal Vapor Plume in Fiber Laser Welding Based on 3D Reconstruction,” *Opt. Laser Technol.*, vol. 107, pp. 1–7, 2018, doi: 10.1016/j.optlastec.2018.05.016.
- [105] J. Katayama, J. Kruse, and S. Katayama, “Introduction: Fundamentals of Laser Welding,” in *Handbook of Laser Welding Technologies*, no. July, S. Katayama, Ed. Woodhead Publishing, 2013, pp. 3–16.
- [106] R. Fabbro, K. Hirano, and S. Pang, “Analysis of the Physical Processes occurring during Deep Penetration Laser Welding under Reduced Pressure,” *J. Laser Appl.*, vol. 28, no. 2, 2016, doi: 10.2351/1.4944002.
- [107] J. Greses, P. A. Hilton, C. Y. Barlow, and W. M. Steen, “Plume Attenuation under High Power Nd : Yttrium–Aluminum–Garnet Laser Welding,” *J. Laser Appl.*, vol. 16, no. 1, 2004.
- [108] U. Reisgen, S. Olschok, S. Jakobs, and C. Turner, “Laser Beam Welding under Vacuum of High Grade Materials,” *Weld. World*, vol. 60, no. 3, pp. 403–413, 2016, doi: 10.1007/s40194-016-0302-3.
- [109] M. Jiang, W. Tao, S. Wang, L. Li, and Y. Chen, “Effect of Ambient Pressure on Interaction between Laser Radiation and Plasma Plume in Fiber Laser Welding,” *Vacuum*, vol. 138, pp. 70–79, 2017, doi: 10.1016/j.vacuum.2017.01.012.
- [110] Y. Luo, X. Tang, F. Lu, Q. Chen, and H. Cui, “Effect of Subatmospheric Pressure on Plasma Plume in Fiber Laser Welding,” *J. Mater. Process. Technol.*, vol. 215, no. 1, pp. 219–224, 2015, doi: 10.1016/j.jmatprotec.2014.08.011.
- [111] C. Börner, T. Krüssel, and K. Dilger, “Process Characteristics of Laser Beam Welding at Reduced Ambient Pressure,” in *High-Power Laser Materials Processing: Lasers, Beam Delivery, Diagnostics, and Applications II*, 2013, vol. 8603, doi: 10.1117/12.2003858.

- [112] S. Katayama, A. Yohei, M. Mizutani, and Y. Kawahito, “Development of Deep Penetration Welding Technology with High Brightness Laser under Vacuum,” *Phys. Procedia*, vol. 12, no. PART 1, pp. 75–80, 2011, doi: 10.1016/j.phpro.2011.03.010.
- [113] C. Börner, K. Dilger, V. Rominger, T. Harrer, T. Krüssel, and T. Löwer, “Influence of Ambient Pressure on Spattering and Weld Seam Quality in Laser Beam Welding with the Solid-state Laser,” in *30th International Congress on Applications of Lasers and Electro-Optics, ICALEO*, 2011, pp. 621–629, doi: 10.2351/1.5062302.
- [114] M. Jiang, X. Chen, Y. Chen, and W. Tao, “Increasing Keyhole Stability of Fiber Laser Welding under Reduced Ambient Pressure,” *J. Mater. Process. Technol.*, no. January, pp. 213–222, 2019, doi: 10.1016/j.jmatprotec.2019.01.026.
- [115] J. W. Elmer, J. Vaja, and H. D. Carlton, “The Effect of Reduced Pressure on Laser Keyhole Weld Porosity and Weld Geometry in Commercially Pure Titanium and Nickel,” *Weld. J.*, vol. 95, no. 11, pp. 419s-430s, 2016.
- [116] Y. Arata, N. Abe, and T. Oda, “Fundamental Phenomena in High Power CO<sub>2</sub> Laser (Report II) : Vacuum Laser Welding,” *Trans. JWRI*, 1985.
- [117] M. Jiang, W. Tao, and Y. Chen, “Laser Welding under Vacuum: A Review,” *Appl. Sci.*, vol. 7, no. 9, 2017, doi: 10.3390/app7090909.
- [118] R. D. Seidgazov, “Thermocapillary Mechanism of Melt Displacement during Keyhole Formation by the Laser Beam,” *J. Phys. D. Appl. Phys.*, vol. 42, no. 17, 2009, doi: 10.1088/0022-3727/42/17/175501.
- [119] C. R. Heiple, J. R. Rope, R. T. Stagner, and R. J. Aden, “Surface Active Element Effects on the Shape of GTA, Laser, and Electron Beam Welds.,” *Weld. J.*, vol. 62, no. 3, pp. 72–77, 1983.
- [120] S. Kou, C. Limmaneevichitr, and P. S. Wei, “Oscillatory Marangoni Flow: A

- Fundamental Study by Conduction-mode Laser Spot Welding,” *Weld. J.*, vol. 90, no. 12, pp. 229s-240s, 2011.
- [121] K. C. Mills, *Recommended Values of Thermophysical Properties for Selected Commercial Alloys*. Woodhead Publishing, 2002.
- [122] C. R. Heiple and J. R. Roper, “Mechanism for Minor Element Effect on Gta Fusion Zone Geometry.,” *Weld. J.*, vol. 61, no. 4, 1982.
- [123] Sindo Kou, *Welding Metallurgy*, Second. Hoboken: John Wiley & Sons, Inc., 2003.
- [124] C. R. Heiple, J. R. Rope, R. T. Stagner, and R. J. Aden, “Surface Active Element Effects on the Shape of Gta, Laser, and Electron Beam Welds.,” *Weld. J.*, vol. 62, no. 3, pp. 72–77, 1983.
- [125] A. Kaplan, “Keyhole Welding: The Solid and Liquid Phases,” in *The Theory of Laser Materials Processing: Heat and Mass Transfer in Modern Technology*, J. Dowden, Ed. Springer, 2009, pp. 71–93.
- [126] F. Tenner, B. Berg, C. Brock, F. Klämpfl, and M. Schmidt, “Experimental Approach for Quantification of Fluid Dynamics in Laser Metal Welding,” *J. Laser Appl.*, vol. 27, no. S2, p. S29003, 2015, doi: 10.2351/1.4906302.
- [127] S. Fujinaga, H. Takenaka, T. Narikiyo, S. Katayama, and A. Matsunawa, “Direct Observation of Keyhole Behaviour during Pulse Modulated High-power Nd:YAG Laser Irradiation,” *J. Phys. D. Appl. Phys.*, vol. 33, no. 5, pp. 492–497, 2000, doi: 10.1088/0022-3727/33/5/304.
- [128] A. De and T. DebRoy, “A Smart Model to Estimate Effective Thermal Conductivity and Viscosity in the Weld Pool,” *J. Appl. Phys.*, vol. 95, no. 9, pp. 5230–5240, 2004, doi: 10.1063/1.1695593.
- [129] C. A. Walsh, “Laser Welding - Literature Review,” Cambridge, England, 2002.

- [130] W. Suder and S. Williams, "Parameter Selection in Laser Welding using the Power Factor Concept," *29th Int. Congr. Appl. Lasers Electro-Optics, ICALEO 2010 - Congr. Proc.*, vol. 103, 2010, doi: 10.2351/1.5062095.
- [131] W.A. Ayoola, W. J. Suder, and S. W. Williams, "Parameters controlling weld bead profile in conduction laser welding," *J. Mater. Process. Technol.*, vol. 249, no. 17, pp. 522–530, 2017, doi: 10.1016/j.jmatprotec.2017.06.026.
- [132] Y. Ai *et al.*, "The Prediction of the Whole Weld in Fiber Laser Keyhole Welding based on Numerical Simulation," *Appl. Therm. Eng.*, vol. 113, pp. 980–993, 2016, doi: 10.1016/j.applthermaleng.2016.11.050.
- [133] X. He *et al.*, "Understanding Metal Vaporization from Laser Welding," *J. Phys. D. Appl. Phys.*, vol. 39, no. 6, pp. 1–2, 2010, doi: 10.1016/j.ijheatmasstransfer.2018.05.031.
- [134] L. Quintino, A. Costa, R. Miranda, D. Yapp, V. Kumar, and C. J. Kong, "Welding with high power fiber lasers - A preliminary study," *Mater. Des.*, vol. 28, no. 4, pp. 1231–1237, 2007, doi: 10.1016/j.matdes.2006.01.009.
- [135] E. L. Baardsen, D. J. Schmatz, and R. E. Bisaro, "High Speed Welding of Sheet Steel with a CO<sub>2</sub> Laser," *Weld. J.*, no. 4, pp. 226–228, 1973.
- [136] E. Akman, A. Demir, T. Canel, and T. Sinmazçelik, "Laser welding of Ti6Al4V titanium alloys," *J. Mater. Process. Technol.*, vol. 209, no. 8, pp. 3705–3713, 2009, doi: 10.1016/j.jmatprotec.2008.08.026.
- [137] W. J. Suder and S. W. Williams, "Investigation of the effects of basic laser material interaction parameters in laser welding," *J. Laser Appl.*, vol. 24, no. 3, 2012, doi: 10.2351/1.4728136.
- [138] E. V. Locke and R. A. Hella, "Metal Processing with a High-Power CO<sub>2</sub> Laser," *IEEE J. Quantum Electron.*, vol. QE-10, no. 2, pp. 179–185, 1974, doi: 10.1109/JQE.1974.1145810.

- [139] C. Limmaneevichitr and S. Kou, “Visualization of Marangoni Convection in Simulated Weld Pools Containing a Surface-Active Agent,” *Weld. J.*, no. 11, pp. 324s-330s, 2000.
- [140] W. J. Suder and S. Williams, “Power Factor Model for Selection of Welding Parameters in CW Laser Welding,” *Opt. Laser Technol.*, vol. 56, pp. 223–229, 2014, doi: 10.1016/j.optlastec.2013.08.016.
- [141] S. Katayama, Y. Kobayashi, N. Seto, M. Mizutani, and A. Matsunawa, “Effect of Vacuum on Penetration and Defects in Laser Welding,” *J. Laser Appl.*, vol. 13, no. 5, pp. 187–192, 2001, doi: 10.2351/1.5059435.
- [142] H. Nakamura, Y. Kawahito, K. Nishimoto, and S. Katayama, “Elucidation of melt flows and spatter formation mechanisms during high power laser welding of pure titanium,” *J. Laser Appl.*, vol. 27, no. 3, p. 032012, 2015, doi: 10.2351/1.4922383.
- [143] D. B. Hann, J. Iammi, and J. Folkes, “Keyholing or Conduction - Prediction of Laser Penetration Depth,” *Lasers Eng.*, vol. 22, pp. 309–317, 2011.
- [144] S. Williams and W. Suder, “Use of Fundamental Laser Material Interaction Parameters in Laser Welding,” *J. Laser Appl.*, vol. 24, no. 8, 2012.
- [145] M. Courtois, M. Carin, P. Le Masson, S. Gaied, and M. Balabane, “A New Approach to Compute Multi-reflections of Laser Beam in a Keyhole for Heat Transfer and Fluid Flow Modelling in Laser Welding,” *J. Phys. D. Appl. Phys.*, vol. 46, no. 50, 2013, doi: 10.1088/0022-3727/46/50/505305.
- [146] J. Corrado *et al.*, “Fundamental Understanding of the Interaction of Continuous Wave Laser with Aluminium,” *Int. J. Adv. Manuf. Technol.*, vol. 93, pp. 3165–3174, 2017, doi: 10.1007/s00170-017-0702-6.
- [147] D. B. Hann, J. Iammi, and J. Folkes, “A Simple Methodology for Predicting Laser-weld Properties from Material and Laser Parameters,” *J. Phys. D. Appl. Phys.*, vol. 44, 2011, doi: 10.1088/0022-3727/44/44/445401.

- [148] J. T. Norris, C. V. Robino, D. A. Hirschfeld, and M. J. Perricone, “Effects of Laser Parameters on Porosity Formation: Investigating Millimeter Scale Continuous Wave Nd:YAG Laser Welds,” *Weld. J.*, vol. 90, no. 10, pp. 198–204, 2011.
- [149] J. J. Blecher, T. A. Palmer, and T. Debroy, “Porosity in Thick Section Alloy 690 Welds - Experiments, Modeling, Mechanism, and Remedy,” *Weld. J.*, vol. 95, no. 1, pp. 17s-26s, 2016.
- [150] C. Cai, G. C. Peng, L. Q. Li, Y. B. Chen, and L. Qiao, “Comparative Study on Laser Welding Characteristics of Aluminium Alloy Under Atmospheric and Subatmospheric Pressures,” *Sci. Technol. Weld. Join.*, vol. 19, no. 7, pp. 547–553, 2014, doi: 10.1179/1362171814Y.00000000223.
- [151] J. W. Elmer, J. Vaja, H. D. Carlton, and R. Pong, “The Effect of Ar and N<sub>2</sub> Shielding Gas on Laser Weld Porosity in Steel, Stainless Steels, and Nickel,” *Weld. J.*, vol. 94, no. 10, pp. 313s-325s, 2015.
- [152] Y. Kawahito, M. Mizutani, and S. Katayama, “Elucidation of High-power Fibre Laser Welding Phenomena of Stainless Steel and Effect of Factors on Weld Geometry,” *J. Phys. D. Appl. Phys.*, vol. 40, pp. 5854–5859, 2007, doi: 10.1088/0022-3727/40/19/009.
- [153] C. E. Albright and S. Chiang, “High-Speed Laser Welding Discontinuities,” *J. Laser Appl.*, vol. 1, no. 1, pp. 18–24, 1988, doi: 10.2351/1.4745217.
- [154] J. Xie, “Weld Morphology and Thermal Modeling in Dual-Beam Laser Welding,” *Weld. J.*, no. 12, pp. 283s-290s, 2002, doi: 10.1177/1533210108324847.
- [155] E. A. Brandes and G. B. Brook, Eds., *Smithells Metals Reference Book*, Seventh Ed. Butterworth-Heinemann, 1992.
- [156] D. Rosenthal, “Mathematical Theory of Heat Distribution During Welding and Cutting,” *Weld. J. (Miami, Fla)*, vol. 20, no. 5, pp. 220s-234s, 1941, doi: 10.1039/c2ay25041a.

- [157] D. Rosenthal, “The Theory of Moving Sources of Heat and Its Application to Metal Treatments,” *Trans. ASME*, vol. 68, pp. 848–866, 1946.
- [158] W. M. Steen, J. Dowden, M. Davis, and P. Kapadia, “A Point and Line Source Model of Laser Keyhole Welding,” *J. Phys. D. Appl. Phys.*, vol. 21, pp. 1255–1260, 1988.
- [159] J.W. Elmer *et al.*, “The Transition from Shallow to Deep Penetration during Electron Beam Welding,” *Weld. J.*, no. 5, pp. 167s-176s, 1990.
- [160] A. F. H. Kaplan, “Absorptivity Modulation on Wavy Molten Steel Surfaces: The Influence of Laser Wavelength and Angle of Incidence,” *Appl. Phys. Lett.*, vol. 101, no. 15, 2012, doi: 10.1063/1.4759126.
- [161] R. Rai, “Modeling of Heat Transfer and Fluid Flow in Keyhole Mode Welding,” Pennsylvania State University, 2008.
- [162] R. Rai, G. G. Roy, and T. Debroy, “A Computationally Efficient Model of Convective Heat Transfer and Solidification Characteristics during Keyhole Mode Laser Welding,” *J. Appl. Phys.*, vol. 101, no. 5, 2007, doi: 10.1063/1.2537587.
- [163] R. Rai, S. M. Kelly, R. P. Martukanitz, and T. DebRoy, “Experimental and Computational Investigation of Fusion Zone Geometries during Autogenous Keyhole Mode Laser Welds,” in *ICALEO 2006 -Laser Materials Processing Conference*, 2006, vol. 805, pp. 515–524, doi: 10.2351/1.5060852.
- [164] E. V. Locke, E. D. Hoag, and R. A. Hella, “Deep Penetration Welding With High-Power CO<sub>2</sub> Lasers,” *IEEE J. Quantum Electron.*, vol. QE-8, no. 2, pp. 135–138, 1972.
- [165] N. Christensen, V. Davies, and K. Gjermundsen, “The Distribution of Temperatures in Arc Welding,” *Br. Weld. J.*, vol. 12, no. 2, pp. 54–75, 1965, [Online]. Available: <http://info.lib.uh.edu/p/ill>.
- [166] D. B. Hann, J. Iammi, and J. Folkes, “Keyholing or Conduction – Prediction of

- Laser Penetration Depth,” *Proc. 36th Int. MATADOR Conf.*, pp. 309–317, 2010, doi: 10.1007/978-1-84996-432-6\_63.
- [167] A. M. Rubenchik, W. E. King, and S. S. Wu, “Scaling Laws for the Additive Manufacturing,” *J. Mater. Process. Technol.*, vol. 257, pp. 234–243, 2018, doi: 10.1016/j.jmatprotec.2018.02.034.
- [168] W. E. King *et al.*, “Observation of Keyhole-mode Laser Melting in Laser Powder-bed Fusion Additive Manufacturing,” 2013. doi: 10.1016/j.jmatprotec.2014.06.005.
- [169] X. He, P. W. Fuerschbach, and T. DebRoy, “Heat Transfer and Fluid Flow during Laser Spot Welding of 304 Stainless Steel,” *J. Phys. D. Appl. Phys.*, vol. 36, no. 12, pp. 1388–1398, 2003, doi: 10.1088/0022-3727/36/12/306.
- [170] S. V. Patankar, *Numerical Heat Transfer and Fluid Flow*. Hemisphere Publishing Corporation, 1980.
- [171] A. Ottoa and M. Schmidta, “Towards a Universal Numerical Simulation Model for Laser Material Processing,” *Phys. Procedia*, vol. 5, pp. 35–46, 2010, doi: 10.1016/j.phpro.2010.08.120.
- [172] C. C. Aggarwal, *Neural Networks and Deep Learning*. Springer, 2018.
- [173] H. Abdi, D. Valentin, and B. Edelman, *Neural Networks*. SAGE Publications, Inc., 1999.
- [174] J. M. Vitek, Y. S. Iskander, and E. M. Oblow, “Improved Ferrite Number Prediction in Stainless Steel Arc Welds Using Artificial Neural Networks Part 1: Neural Network Development,” *Weld. J.*, no. 2, pp. 33s-40s, 2000.
- [175] G. Yagawa and A. Oishi, *Computational Mechanics with Neural Networks*. Springer, 2021.
- [176] H. Demuth and M. Beale, “Neural Network Toolbox.” The MathWorks, 2004.

- [177] D. S. Nagesh and G. L. Datta, "Prediction of Weld Bead Geometry and Penetration in Shielded Metal-arc Welding using Artificial Neural Networks," *J. Mater. Process. Technol.*, vol. 123, no. 2, pp. 303–312, 2002, doi: 10.1016/S0924-0136(02)00101-2.
- [178] S. W. Campbell, A. M. Galloway, and N. A. McPherson, "Artificial Neural Network Prediction of Weld Geometry Performed using GMAW with Alternating Shielding Gases," *Weld. J.*, vol. 91, no. 6, pp. 174s-182s, 2012.
- [179] K. Manikya Kanti and P. Srinivasa Rao, "Prediction of Bead Geometry in Pulsed GMA Welding using Back Propagation Neural Network," *J. Mater. Process. Technol.*, vol. 200, pp. 300–305, 2008, doi: 10.1016/j.jmatprotec.2007.09.034.
- [180] G. Casalino, F. Facchini, M. Mortello, and G. Mummolo, "ANN Modelling to Optimize Manufacturing Processes: The Case of Laser Welding," *IFAC-PapersOnLine*, vol. 49, no. 12, pp. 378–383, 2016, doi: 10.1016/j.ifacol.2016.07.634.
- [181] J. M. Vitek, S. A. David, and C. R. Hinman, "Improved Ferrite Number Prediction Model that Accounts for Cooling Rate Effects-Part 2: Model Results," *Weld. J.*, no. 2, pp. 43s-50s, 2003.
- [182] P. Ghanty *et al.*, "Artificial Neural Network Approach for Estimating Weld Bead Width and Depth of Penetration from Infrared Thermal Image of Weld Pool," *Sci. Technol. Weld. Join.*, vol. 13, no. 4, pp. 395–401, 2008, doi: 10.1179/174329308X300118.
- [183] Y. M. Zhang, R. Kovacevic, and L. Li, "Characterization and Real-time Measurement of Geometrical Appearance of the Weld Pool," *Int. J. Mach. Tools Manuf.*, vol. 36, no. 7, pp. 799–816, 1996, doi: 10.1016/0890-6955(95)00083-6.
- [184] Y. Huang, S. Xu, L. Yang, S. Zhao, Y. Liu, and Y. Shi, "Defect Eetection during Laser Welding using Electrical Signals and High-speed Photography," *J. Mater.*

*Process. Technol.*, vol. 271, pp. 394–403, Sep. 2019, doi:  
10.1016/j.jmatprotec.2019.04.022.

- [185] P. Ghanty, S. Paul, D. P. Mukherjee, M. Vasudevan, N. R. Pal, and A. K. Bhaduri, “Modelling Weld Bead Geometry using Neural Networks for GTAW of Austenitic Stainless Steel,” *Sci. Technol. Weld. Join.*, vol. 12, no. 7, pp. 649–658, 2007, doi: 10.1179/174329307X238399.
- [186] D. A. Porter and K. E. Easterling, *Phase Transformations in Metals and Alloys*, 2nd ed. London: Nelson Thornes Ltd, 1992.
- [187] S. A. David and J. M. Vitek, “Correlation between Solidification Parameters and Weld Microstructures,” *Int. Mater. Rev.*, vol. 34, no. 1, pp. 213–245, 1989, doi: 10.1179/imr.1989.34.1.213.
- [188] J. C. Lippold, *Welding Metallurgy and Weldability*. Hoboken, New Jersey, U.S.A.: John Wiley & Sons, Inc., 2015.
- [189] W. Kurz and D. J. Fisher, *Fundamentals of Solidification*. Trans Tech Publications, 1986.
- [190] J. C. Lippold, “Solidification Behavior and Cracking Susceptibility of Pulsed-Laser Welds in Austenitic Stainless Steels,” *Weld. J.*, vol. 73, no. 6, pp. 129s-139s, 1994.
- [191] R. Trivedi *et al.*, “In situ Observations of Weld Pool Solidification using Transparent Metal-analog Systems,” *J. Appl. Phys.*, vol. 93, no. 8, pp. 4885–4895, 2003, doi: 10.1063/1.1559934.
- [192] M. Rappaz, S. A. David, J. M. Vitek, and L. A. Boatner, “Analysis of Solidification Microstructures in Fe-Ni-Cr Single-crystal Welds,” *Metall. Trans. A*, vol. 21, no. 6, pp. 1767–1782, 1990, doi: 10.1007/BF02672593.
- [193] M. Rappaz, S. A. David, J. M. Vitek, and L. A. Boatner, “Development of Microstructures in Fe-15Ni-15Cr Single Crystal Electron Beam Welds,” *Metall.*

*Trans. A*, vol. 20, no. 6, pp. 1125–1138, 1989, doi: 10.1007/BF02650147.

- [194] J. W. Elmer, S. M. Allen, and T. W. Eagar, “Microstructural Development during Solidification of Stainless Steel Alloys,” *Metall. Trans. A*, vol. 20A, no. October, pp. 2117–2131, 1989.
- [195] J. W. Elmer, T. W. Eagar, and S. M. Allen, “Single-Phase Solidification During Rapid-Resolidification of Stainless Steel Alloys,” *Proc. Mater. Weldability Symp. Mater. Week, Detroit, MI*, vol. 3, no. July, pp. 143–150, 1990.
- [196] S. Kou and Y. Le, “The Effect of Quenching on the Solidification Structure and Transformation Behavior of Stainless Steel Welds,” *Metall. Trans. A*, vol. 13A, no. 7, pp. 1141–1152, 1982.
- [197] S. Katayama and A. Matsunawa, “Solidification Microstructure of Laser Welded Stainless Steels,” in *International Congress on Applications of Lasers & Electro-Optics*, 1984, vol. 44, pp. 60–67.
- [198] R. Trivedi, “Growth of Dendritic Needles from a Supercooled Melt,” *Acta Metall.*, no. 3, pp. 287–296, 1970.
- [199] R. Trivedi, “Theory of Dendritic Growth during the Directional Solidification of Binary Alloys,” *J. Cryst. Growth*, vol. 49, pp. 219–232, 1980.
- [200] J. C. Lippold and W. F. Savage, “Solidification of Austenitic Stainless Steel Weldments : Part I — A Proposed Mechanism,” *Weld. J.*, no. 12, pp. 362s–374s, 1979.
- [201] J. M. Vitek, A. Dasgupta, and S. A. David, “Microstructural Modification of Austenitic Stainless Steels By Rapid Solidification.,” *Metall. Trans. A, Phys. Metall. Mater. Sci.*, vol. 14 A, no. 9, pp. 1833–1841, 1983, doi: 10.1007/BF02645553.
- [202] F. Kolenič, L. Kovac, and D. Drimal, “Effect of Laser Welding Conditions on Austenite/Ferrite Ratio in Duplex Stainless Steel 2507 Welds,” *Weld. World*, vol. 222

55, no. 5–6, 2011, doi: 10.1007/BF03321292.

- [203] J. C. Lippold and W. F. Savage, “Solidification of Austenitic Stainless Steel Weldments : Part 2 — The Effect of Alloy Composition on Ferrite Morphology,” *Weld. J.*, no. 2, pp. 48s-58s, 1980.
- [204] V. Kujanpää, N. Suutala, T. Takalo, and T. Moisio, “Correlation between Solidification Cracking and Microstructure in Austenitic and Austenitic-ferritic Stainless Steel Welds,” *Weld. Res. Int.*, vol. 9, no. 2, pp. 55–75, 1979.
- [205] A. L. Schaeffler, “Constitution Diagram for Stainless Steel Weld Metal,” *Met. Prog.*, vol. 56, no. 11, pp. 680, 680B, 1949.
- [206] D. J. Kotecki and T. A. Siewert, “WRC-1992 Constitution Diagram for Stainless Steel Weld Metals: A Modification of the WRC-1988 Diagram,” *Weld. J.*, no. 5, pp. 171s-178s, 1992.
- [207] C. J. Long and W. T. Delong, “The Ferrite Content of Austenitic Stainless Steel Weld Metal,” *Weld. J.*, no. 7, pp. 281s-297s, 1973.
- [208] O. Hammar and U. Svennson, “Influence of Steel Composition on Segregation and Microstructure during Solidification of Austenitic Stainless Steels,” *Solidif. Cast. Met.*, vol. 192, pp. 401–410, 1979, [Online]. Available: <http://info.lib.uh.edu/p/ill>.
- [209] J. A. Brooks, M. I. Baskes, and F. A. Greulich, “Solidification Modeling and Solid-State Transformations in High-Energy Density Stainless Steel Welds,” *Metall. Trans. A*, vol. 22A, no. 4, pp. 915–926, 1991.
- [210] J. A. Brooks and A. W. Thompson, “Microstructural Development and Solidification Cracking Susceptibility of Austenitic Stainless Steel welds,” *Int. Mater. Rev.*, vol. 36, no. 1, pp. 16–44, 1991, doi: 10.1179/imr.1991.36.1.16.
- [211] S. A. David, J. M. Vitek, and T. L. Hebble, “Effect of Rapid Solidification on Stainless Steel Weld Metal Microstructures and Its Implications on the Schaeffler Diagram,” *Weld. J.*, no. 8, pp. 289s-300s, 1987.

- [212] W. Kurz and D. J. Fisher, “Dendrite Growth at the Limit of Stability: Tip Radius and Spacing,” *Acta Metall.*, vol. 29, pp. 11–20, 1981.
- [213] N. Suutala, “Effect of Solidification Conditions on the Solidification Mode in Austenitic Stainless Steels,” *Metall. Trans. A*, vol. 14, no. 1, pp. 191–197, 1983, doi: 10.1007/BF02651615.
- [214] T. J. Lienert and J. C. Lippold, “Improved Weldability Diagram for Pulsed Laser Welded Austenitic Stainless Steels,” *Sci. Technol. Weld. Join.*, vol. 8, no. 1, pp. 1–9, 2003, doi: 10.1179/136217103225008847.
- [215] J. Verma and R. V. Taiwade, “Effect of Welding Processes and Conditions on the Microstructure, Mechanical Properties and Corrosion Resistance of Duplex Stainless Steel Weldments—A Review,” *J. Manuf. Process.*, vol. 25, pp. 134–152, 2017, doi: 10.1016/j.jmapro.2016.11.003.
- [216] V. Muthupandi, P. Bala Srinivasan, S. K. Seshadri, and S. Sundaresan, “Effect of Weld Metal Chemistry and Heat Input on the Structure and Properties of Duplex Stainless Steel Welds,” *Mater. Sci. Eng. A*, vol. 358, no. 1–2, pp. 9–16, 2003, doi: 10.1016/S0921-5093(03)00077-7.
- [217] H. Sieurin and R. Sandström, “Austenite Reformation in the Heat-affected Zone of Duplex Stainless Steel 2205,” *Mater. Sci. Eng. A*, vol. 418, no. 1–2, pp. 250–256, 2006, doi: 10.1016/j.msea.2005.11.025.
- [218] E. Taban and E. Kaluc, “Welding Behaviour of Duplex and Superduplex Stainless Steels using Laser and Plasma Arc Welding Processes,” *Weld. World*, vol. 55, no. 7–8, pp. 48–57, 2011, doi: 10.1007/BF03321307.
- [219] M. Bolut, C. Y. Kong, J. Blackburn, K. A. Cashell, and P. R. Hobson, “Yb-fibre Laser Welding of 6 mm Duplex Stainless Steel 2205,” *Phys. Procedia*, vol. 83, pp. 417–425, 2016, doi: 10.1016/j.phpro.2016.08.043.
- [220] L. W. Tsay and C. Y. Tsay, “The Effect of Microstructures on the Fatigue Crack

- Growth in Ti-6Al-4V Laser Welds,” *Int. J. Fatigue*, vol. 19, no. 10, pp. 713–720, 1997, doi: 10.1016/S0142-1123(97)00113-8.
- [221] N. Kherrouba, M. Bouabdallah, R. Badji, D. Carron, and M. Amir, “Beta to Alpha Transformation Kinetics and Microstructure of Ti-6Al-4V Alloy during Continuous Cooling,” *Mater. Chem. Phys.*, vol. 181, pp. 462–469, 2016, doi: 10.1016/j.matchemphys.2016.06.082.
- [222] S. T. Auwal, S. Ramesh, F. Yusof, and S. M. Manladan, “A Review on Laser Beam Welding of Titanium Alloys,” *Int. J. Adv. Manuf. Technol.*, vol. 97, no. 1–4, pp. 1071–1098, 2018, doi: 10.1007/s00170-018-2030-x.
- [223] W. A. Baeslack III and C. M. Banas, “Comparative Evaluation of Laser and Gas Tungsten Arc Weldments in High-Temperature Titanium Alloys,” *Weld. J.*, no. 7, pp. 121s-130s, 1981.
- [224] W. Lu, Y. Shi, Y. Lei, and X. Li, “Effect of Electron Beam Welding on the Microstructures and Mechanical Properties of Thick TC4-DT Alloy,” *Mater. Des.*, vol. 34, pp. 509–515, 2012, doi: 10.1016/j.matdes.2011.09.004.
- [225] N. Sareesh, M. G. Pillai, and J. Mathew, “Investigations into the Effects of Electron Beam Welding on Thick Ti-6Al-4V Titanium Alloy,” *J. Mater. Process. Technol.*, vol. 192–193, pp. 83–88, 2007, doi: 10.1016/j.jmatprotec.2007.04.048.
- [226] A. Kohyamaa, Y. Arata, M. Tomie, and N. Igata, “Electron Beam Welding of Titanium and Ti-6Al-4V Thick Plates,” *J. Nucl. Mater.*, vol. 122, no. 1–3, pp. 772–776, 1984.
- [227] P. Kumar and A. N. Sinha, “Effect of Heat Input in Pulsed Nd:YAG Laser Welding of Titanium Alloy (Ti6Al4V) on Microstructure and Mechanical Properties,” *Weld. World*, vol. 63, no. 3, pp. 673–689, 2019, doi: 10.1007/s40194-018-00694-w.
- [228] P. Q. Xu, L. Li, and C. Zhang, “Microstructure Characterization of Laser Welded

- Ti-6Al-4V Fusion Zones,” *Mater. Charact.*, vol. 87, pp. 179–185, 2014, doi: 10.1016/j.matchar.2013.11.005.
- [229] IPG Photonics, “Inline Coherent Imaging System Software Manual.” IPG Photonics, Oxford, MA, USA, 2018.
- [230] *ASTM E1019-11: Standard Test Methods for Determination of Carbon, Sulfur, Nitrogen, and Oxygen in Steel and in Steel, Iron, Nickel, and Cobalt Alloys by Various Combustion and Fusion Techniques*. West Conshohocken, PA, United States: ASTM International, 2011.
- [231] *ASTM E1941-10: Standard Test Method for Determination of Carbon in Refractory and Reactive Metals and Their Alloys by Combustion Analysis*. West Conshohocken, PA, United States: ASTM International, 2016.
- [232] *ASTM E1409-13: Standard Test Method for Determination of Oxygen and Nitrogen in Titanium and Titanium Alloys by Inert Gas Fusion*. West Conshohocken, PA, United States: ASTM International, 2013.
- [233] *ASTM E1447-09: Standard Test Method for Determination of Hydrogen in Titanium and Titanium Alloys by Inert Gas Fusion Thermal Conductivity / Infrared Detection*. West Conshohocken, PA, United States: ASTM International, 2016.
- [234] S. Wright, “How to Reconstruct Microstructures in OIM.” Ametek Materials Analysis Division: EDAX, 2021.
- [235] J. J. Valencia and P. N. Quested, “Thermophysical Properties,” in *ASM Handbook, Volume 22B, Metals Process Simulation*, vol. 22B, D. U. Furrer and S. L. Semiatin, Eds. 2010.
- [236] J. O. Andersson, T. Helander, L. Höglund, P. Shi, and B. Sundman, “Thermo-Calc & DICTRA, Computational Tools for Materials Science,” *Calphad Comput. Coupling Phase Diagrams Thermochem.*, vol. 26, no. 2, pp. 273–312, 2002, doi:

10.1016/S0364-5916(02)00037-8.

- [237] M. Boley, F. Abt, R. Weber, and T. Graf, “X-ray and Optical Videography for 3D Measurement of Capillary and Melt Pool Geometry in Laser Welding,” *Phys. Procedia*, vol. 41, pp. 488–495, 2013, doi: 10.1016/j.phpro.2013.03.105.
- [238] M. Knyazeva and M. Pohl, “Duplex Steels. Part II: Carbides and Nitrides,” *Metallogr. Microstruct. Anal.*, vol. 2, no. 5, pp. 343–351, 2013, doi: 10.1007/s13632-013-0088-2.
- [239] ASM International, “ASM Handbook. Volume 9, Metallography and Microstructures, Metallography and Microstructures of Carbon and Low Alloy Steels,” in *ASM Handbook*, Metals Park, OH: ASM International, 2004, pp. 608–626.
- [240] “ASTM E407-07: Standard Practice for Microetching Metals and Alloys.” ASTM International, West Conshohocken, PA, United States, 2015, doi: 10.1520/E0407-07R15E01.2.
- [241] S. I. Wright, M. M. Nowell, S. P. Lindeman, P. P. Camus, M. De Graef, and M. A. Jackson, “Introduction and Comparison of New EBSD Post-processing Methodologies,” *Ultramicroscopy*, vol. 159, no. P1, pp. 81–94, 2015, doi: 10.1016/j.ultramic.2015.08.001.
- [242] S. I. Wright, “Random Thoughts on Non-random Misorientation Distributions,” *Mater. Sci. Technol.*, vol. 22, no. 11, pp. 1287–1296, 2006, doi: 10.1179/174328406X130876.

## Appendix A: Material Properties

Table A.1 contains the material properties for 304L SS and Ti-6Al-4V near room temperature, and Table A.2 contains the material property values for the liquid and vapor phases. An issue when attempting to utilize material properties for predictive analysis is attributed to the temperature dependency of properties, and simply using a room temperature value or average value is insufficient for fundamentally computing the physical interactions. Thus, iterative analysis throughout discrete temperature ranges is necessary to better account for the physical phenomena. Also, measuring material properties in liquid and vapor phases is increasingly difficult, and literature values may vary between sources. Some of the discrepancies between two sources are presented in Table A.2.

*Table A.1. Room temperature material properties for 304 SS and Ti-6Al-4V. All values were extracted from Mills [121].*

Properties	Units	304L	Ti-6Al-4V
Density ( $\rho_s$ ) of Solid	kg/m <sup>3</sup>	8020	4420
Specific Heat ( $C_p$ ) of Solid	J/kgK	480	546
Thermal Conductivity ( $\kappa_s$ ) of Solid	W/mK	14.8	7.0
Coefficient of Thermal Expansion ( $CTE_s$ )	1/K	$14.2 \times 10^{-6}$	$11 \times 10^{-6}$

Table A.2. Liquid and vapor material properties for 304 SS and Ti-6Al-4V.

Properties	Units	304	Ti-6Al-4V	References	
				304L	Ti-6Al-4V
Solidus Temperature (T <sub>s</sub> )	°C	1400	—	[121], [235]	—
Liquidus Temperature (T <sub>L</sub> )	°C	1454, 1434	1928, 1923	[121], [235]	[121], [235]
Density ( $\rho$ ) of Liquid at Liquidus Temperature	kg/m <sup>3</sup>	6900	3920	[121]	[121]
Latent Heat of Fusion (L <sub>m</sub> )	kJ/kg	290, 328	286	[121], [235]	[121], [235]
Thermal Conductivity ( $\kappa_L$ ) of Liquid	W/mK	28	33.4-34.6	[121]	[121], [235]
Specific Heat (C <sub>p</sub> ) of Liquid	J/kgK	800	700, 830	[121], [235]	[121], [235]
Dynamic Viscosity ( $\mu$ ) at Liquidus Temperature	Pas	0.0080	0.00325	[121], [235]	[121], [235]
Vaporization Temperature (T <sub>v</sub> )	°C	2827	3042	[14]	[14]
Density ( $\rho$ ) at Boiling Point	kg/m <sup>3</sup>	5800	3780	[14]	[14]
Latent Heat of Vaporization (L <sub>v</sub> )	J/kg	6.52x10 <sup>6</sup> (Fe)	1.03x10 <sup>6</sup> (Ti)	[14]	[14]
Absorption Coefficient	[unitless]	0.30	0.30	[14]	[14]
Plasma Attenuation	[1/m]	100	100	[14]	[14]

*The Ti-6Al-4V beta transus, as reported by Mills [121], is 995±15°C with a transition enthalpy of 48±10 J/g.*

## A.1 Stainless Steel

Table A.3 contains the computed temperature dependent values for 304L SS in the solid state. Table A.4 contains the 304L temperature dependent properties for liquid 304L. This data was computed using Thermo-Calc<sup>®</sup> [236] software.

*Table A.3. Temperature dependent material properties for solid 304L computed using Thermo-Calc<sup>®</sup> [236]. Thermal conductivity was extracted from Reference [121].*

Temperature [°C]	Density [kg/m <sup>3</sup> ]	Enthalpy [J/g]	Entropy [J/gK]	Gibbs Energy [J/g]	Thermal Conductivity [W/mK]
25	7781	-39.7	0.50	-188	14.8
100	7758	0	0.61	-234	15.8
200	7724	55.5	0.74	-302	17.7
300	7683	123	0.87	-383	18.8
400	7643	217	1.02	-478	20.7
500	7620	306	1.14	-578	21.4
600	7626	404	1.26	-698	23.5
700	7637	493	1.36	-830	24.5
800	7591	552	1.42	-969	25.8
900	7544	613	1.47	-1113	27.5
1000	7498	676	1.52	-1263	28.8
1100	7452	740	1.57	-1418	29.9
1200	7406	807	1.62	-1577	31.6
1300	7354	879	1.67	-1742	32.8
1400	7283	961	1.72	-1911	33.5

*Table A.4. Temperature dependent material properties for liquid 304L computed using Thermo-Calc<sup>®</sup> [236]. Thermal conductivity was computed using Reference [235].*

<b>Temperature [°C]</b>	<b>Density [kg/m<sup>3</sup>]</b>	<b>Enthalpy [J/g]</b>	<b>Entropy [J/gK]</b>	<b>Gibbs Energy [J/g]</b>	<b>Dynamic Viscosity [Pas]</b>	<b>Kinematic Viscosity [m<sup>2</sup>/s]</b>	<b>Surface Tension [J/m<sup>2</sup>]</b>	<b>Thermal Conductivity [W/mK]</b>
1500	6941	1221	1.87	-2091	6.4105e <sup>-3</sup>	9.2362e <sup>-7</sup>	1.73	8.8
1600	6853	1303	1.91	-2280	5.3598e <sup>-3</sup>	7.8210e <sup>-7</sup>	1.72	8.6
1700	6767	1386	1.96	-2473	4.5634e <sup>-3</sup>	6.7439e <sup>-7</sup>	1.69	24.3
1800	6681	1469	2.00	-2671	3.9461e <sup>-3</sup>	5.9061e <sup>-7</sup>	1.66	28.5
1900	6597	1553	2.04	-2873	3.4582e <sup>-3</sup>	5.2420e <sup>-7</sup>	1.63	29.7
2000	6514	1637	2.07	-3078	3.0661e <sup>-3</sup>	4.7070e <sup>-7</sup>	1.60	30.8
2100	6432	1721	2.11	-3287	2.7461e <sup>-3</sup>	4.2696e <sup>-7</sup>	1.56	32.1
2200	6351	1805	2.15	-3500	2.4815e <sup>-3</sup>	3.9075e <sup>-7</sup>	1.52	33.3
2300	6271	1889	2.18	-3716	2.2602e <sup>-3</sup>	3.6045e <sup>-7</sup>	1.48	34.5
2400	6191	1973	2.21	-3936	2.0731e <sup>-3</sup>	3.3482e <sup>-7</sup>	1.44	35.7
2500	6113	2057	2.24	-4159	1.9133e <sup>-3</sup>	3.1296e <sup>-7</sup>	1.40	37.0
2600	6036	2142	2.27	-4384	1.7757e <sup>-3</sup>	2.9442e <sup>-7</sup>	1.36	38.2
2700	5960	2226	2.30	-4613	1.6563e <sup>-3</sup>	2.7790e <sup>-7</sup>	1.31	39.4
2800	5885	2310	2.33	-4844	1.5519e <sup>-3</sup>	2.6371e <sup>-7</sup>	1.27	40.6

### A.1.1 Property Diagrams

Stainless steel property diagrams were computed using Thermo-Calc<sup>®</sup> [236] software and the TCFE11: Steels/Fe-Alloys v11.0 database. The elements used in the 304L computation include Fe, Cr, Mo, Nb, Si, Ni, Mn, Cu, C, and N, and the percentages were input as weight percent according to the values reported in Table 4.2 in Section 4.4. For the other SS alloys, only the elements previously listed with measurable compositions were included in the analysis. The computation was restricted to only the following phases: BCC\_A2, FCC\_A1, and LIQUID, which is ferrite, austenite, and liquid, respectively. The property diagrams for each SS alloy are shown in Figure A.1- Figure A.6 and are normalized relative to mass.

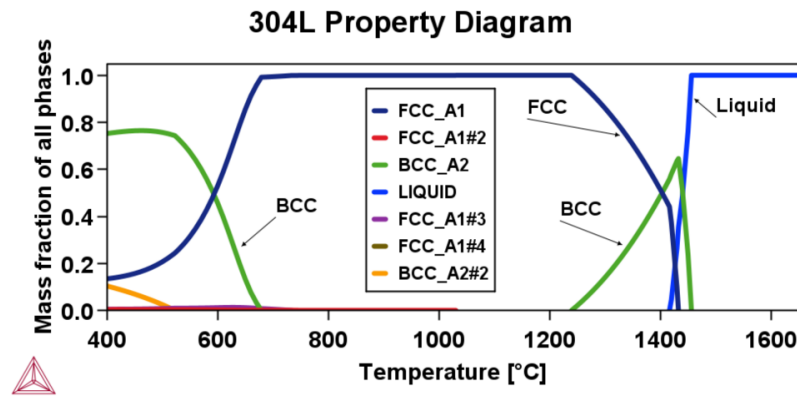


Figure A.1. Equilibrium property diagram for 304L SS.

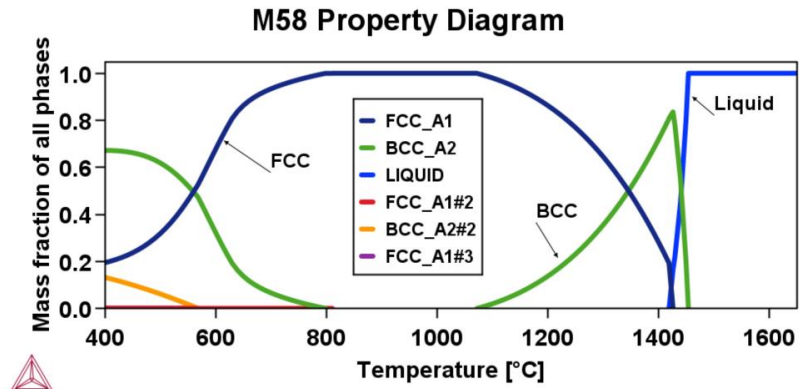


Figure A.2. Equilibrium property diagram for M58.

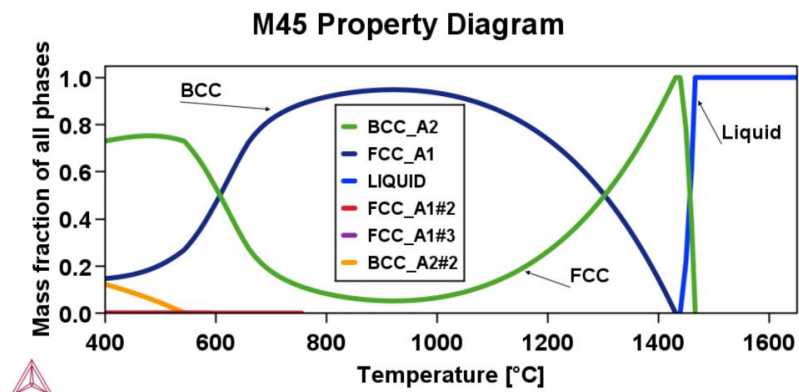


Figure A.3. Equilibrium property diagram for M45.

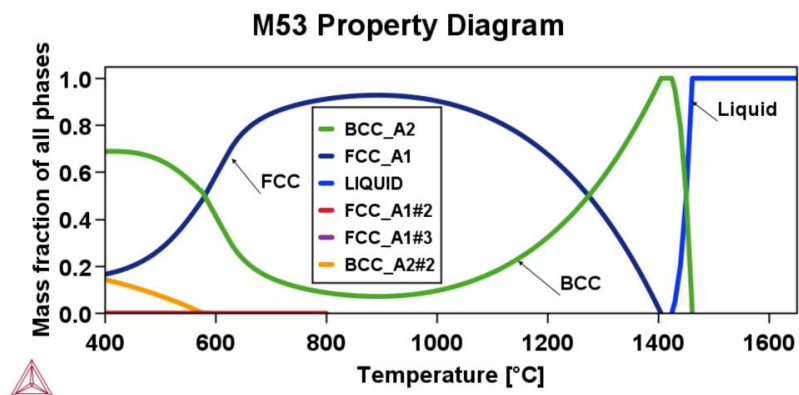


Figure A.4. Equilibrium property diagram for M53.

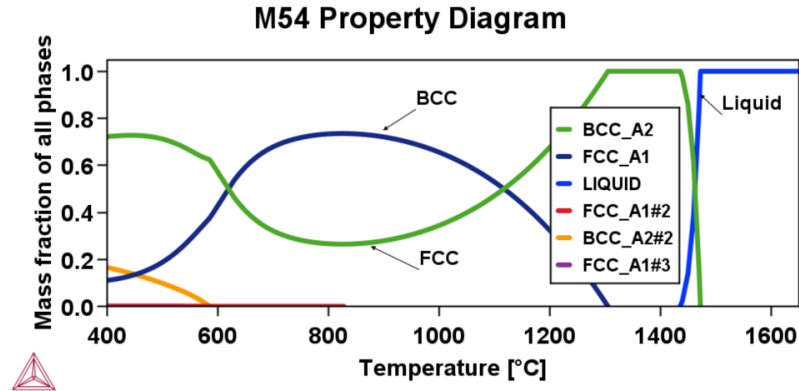


Figure A.5. Equilibrium property diagram for M54.

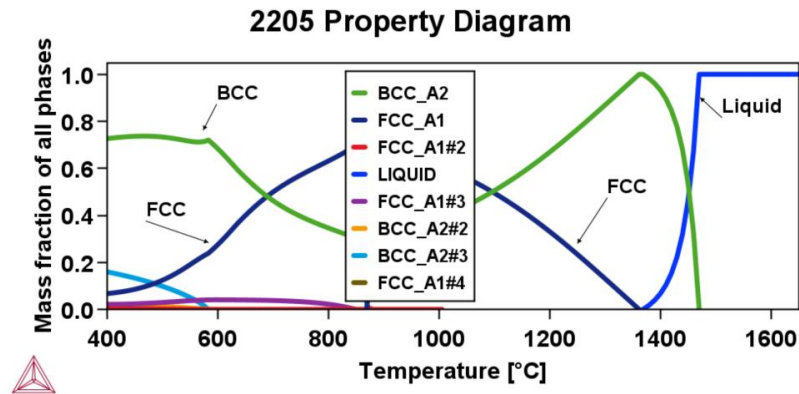


Figure A.6. Equilibrium property diagram for 2205 DSS.

### A.1.2 Scheil Computations

Scheil solidification predictions were performed using Thermo-Calc<sup>®</sup> under the same conditions as the property diagrams except C and N were selected as fast diffusing (interstitial) elements for all computations. These results are provided in Figure A.7- Figure A.9.

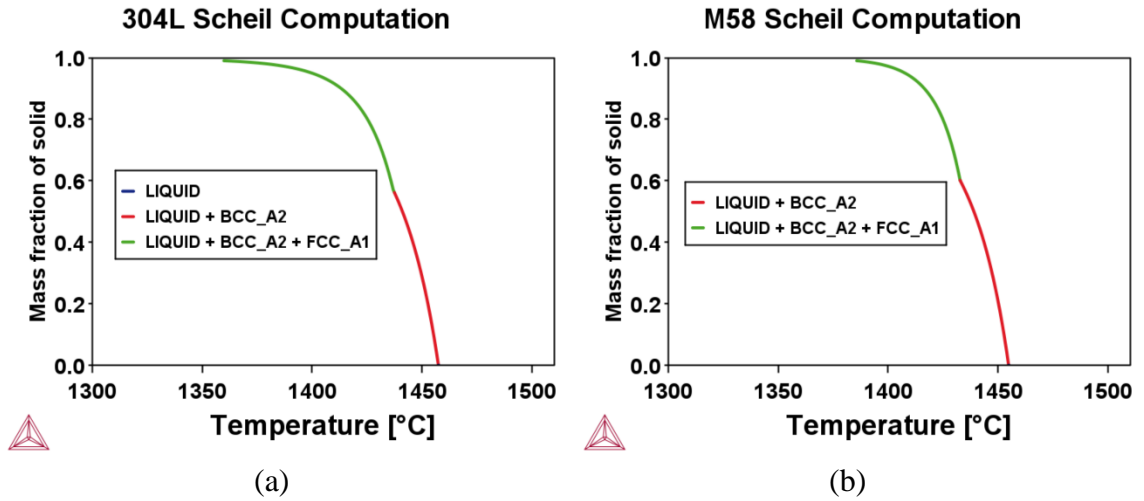


Figure A.7. Scheil solidification simulation of 304L SS (a) and M58 (b).

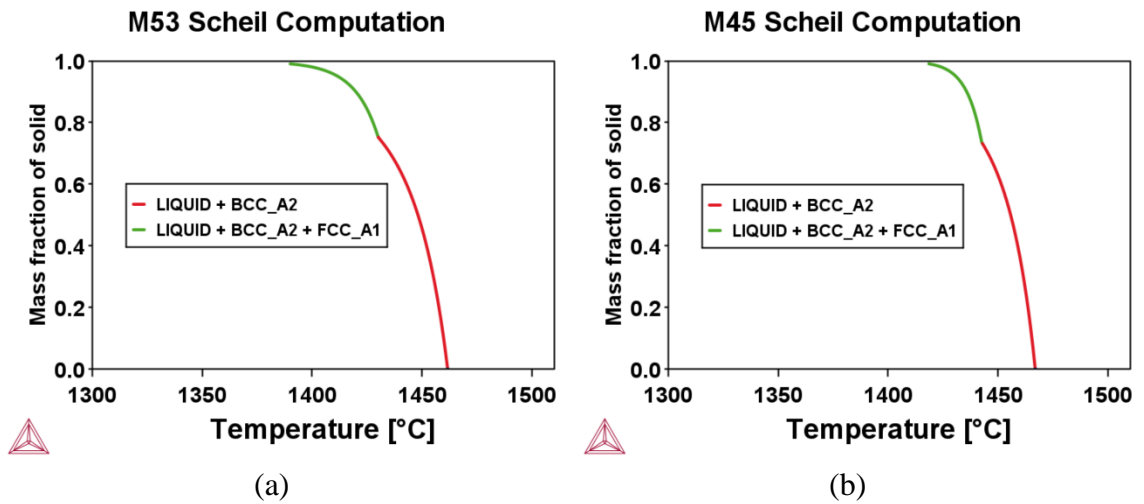


Figure A.8. Scheil solidification simulation of M53 (a) and M45 (b).

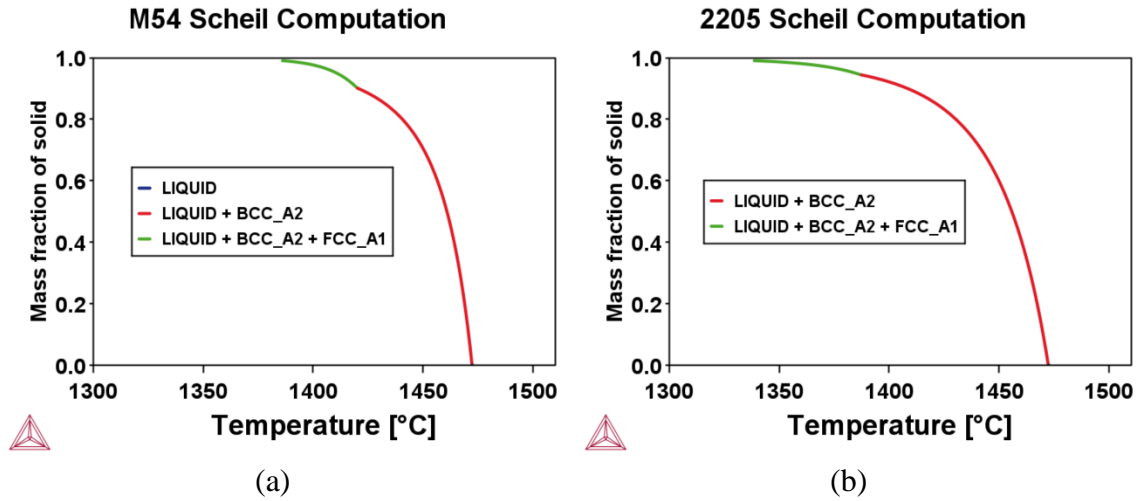


Figure A.9. Scheil solidification simulation of M54 (a) and 2205 DSS (b).

Further analysis of the Scheil computations is shown in Figure A.10 and Table A.5. The temperature variation relative to  $\delta$ -ferrite and austenite is an indication of phase stability on solidification (Table A.5).

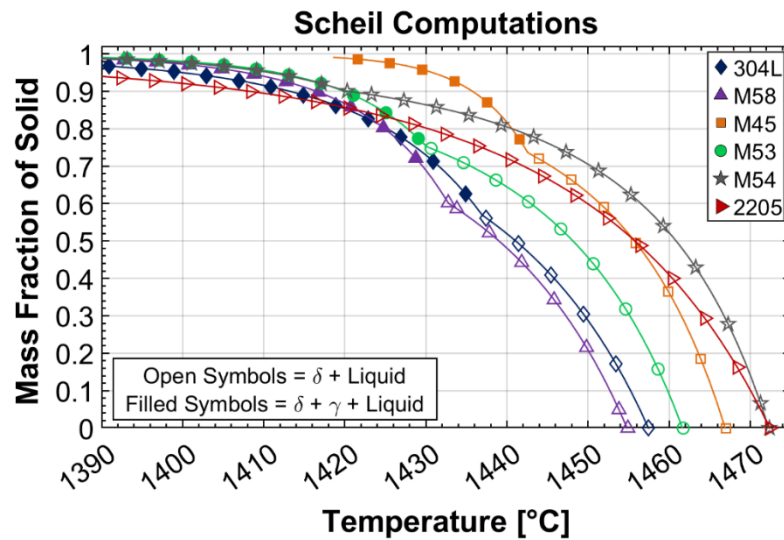


Figure A.10. Scheil simulations showing solidification conditions for all SS alloys.

*Table A.5. Scheil computation analysis results for temperature ranges relating to phase stability during solidification from the liquidus to the solidus temperatures.*

Temperature Change ( $\Delta T$ )			
Alloys	Liquid + BCC [°C]	Liquid + BCC + FCC [°C]	$T_L - T_s$ [°C]
304L	21	76	97
M58	23	47	70
M45	24	24	48
M53	31	40	71
M54	52	34	86
2205	85	48	133

## A.2 Ti-6Al-4V

For Ti-6Al-4V, the temperature dependent properties were extracted from Thermo-Calc® 2021a software using the TCTI3: Ti-Alloys v3.0 database. The elements used in computation include Ti, Al, V, O, N, C, Nb, Fe, Cr, Ni, Si, and H, and the percentages were input as weight percent according to the values reported in Table 4.3 in Section 4.4. The computation was restricted to only computing: BCC\_B2, HCP\_A3, and LIQUID, which is beta, alpha, and liquid phases, respectively.

Table A.6 contains the computed temperature dependent values for Ti-6Al-4V in the solid state. Table A.7 contains the temperature dependent properties for liquid Ti-6Al-4V. This data was computed using Thermo-Calc® [236] software.

*Table A.6. Temperature dependent material properties for solid Ti-6Al-4V computed using Thermo-Calc® [236]. Thermal conductivity was extracted from Reference [121].*

<b>Temperature (T) [°C]</b>	<b>Density (<math>\rho</math>) [kg/m<sup>3</sup>]</b>	<b>Enthalpy (H) [J/g]</b>	<b>Entropy (S) [J/gK]</b>	<b>Gibbs Energy (G) [J/g]</b>	<b>Thermal Conductivity (<math>\kappa</math>) [W/mK]</b>
25	4427	-273	0.645	-465	7.0
100	4416	-230	0.773	-518	7.45
200	4401	-169	0.917	-603	8.75
300	4386	-102	1.058	-701	10.15
400	4373	-33.4	1.156	-812	11.35
500	4360	37.3	1.254	-932	12.6
600	4345	110	1.343	-1062	14.2
700	4328	185	1.424	-1201	15.5
800	4310	259	1.497	-1347	17.8
900	4297	339	1.568	-1500	20.2
1000	4303	475	1.678	-1662	19.3
1100	4289	541	1.728	-1832	21.0
1200	4275	610	1.776	-2007	22.9
1300	4259	680	1.823	-2187	23.7
1400	4244	753	1.868	-2372	24.6
1500	4227	828	1.911	-2561	25.8
1600	4210	906	1.954	-2754	27.0
1700	4090	1372	2.198	-2964	34.6
1800	4067	1470	2.246	-3186	-
1900	4043	1568	2.292	-3413	-

Table A.7. Temperature dependent material properties for liquid Ti-6Al-4V computed using Thermo-Calc<sup>®</sup> [236].

Temperature [°C]	Density [kg/m <sup>3</sup> ]	Enthalpy [J/g]	Entropy [J/gK]	Gibbs Energy [J/g]	Dynamic Viscosity [Pas]	Kinematic Viscosity [m <sup>2</sup> /s]	Surface Tension [J/m <sup>2</sup> ]
2000	4021	1665	2.336	-3645	2.3324e <sup>-3</sup>	5.8013e <sup>-7</sup>	1.05
2100	3999	1763	2.378	-3880	2.1951e <sup>-3</sup>	5.4898e <sup>-7</sup>	1.06
2200	3967	1861	2.418	-4120	2.0758e <sup>-3</sup>	5.2207e <sup>-7</sup>	1.07
2300	3954	1959	2.457	-4364	1.9715e <sup>-3</sup>	4.9863e <sup>-7</sup>	1.08
2400	3931	2057	2.4946	-4611	1.8797e <sup>-3</sup>	4.7809e <sup>-7</sup>	1.08
2500	3910	2155	2.531	-4863	1.7984e <sup>-3</sup>	4.5997e <sup>-7</sup>	1.08
2600	3888	2253	2.565	-5117	1.7258e <sup>-3</sup>	4.4391e <sup>-7</sup>	1.08
2700	3866	2350	2.599	-5376	1.6608e <sup>-3</sup>	4.2960e <sup>-7</sup>	1.08
2800	3844	2448	2.631	-5637	1.6022e <sup>-3</sup>	4.1679e <sup>-7</sup>	1.08
2900	3823	2546	2.662	-5902	1.5492e <sup>-3</sup>	4.0527e <sup>-7</sup>	1.07
3000	3801	2644	2.693	-6170	1.5011e <sup>-3</sup>	3.9488e <sup>-7</sup>	1.06

### A.2.1 Property Diagrams

The computed property diagram for Ti-6Al-4V is shown in Figure A.11. For reference, a property diagram for a Ti alloy near commercially pure is shown in Figure A.12.

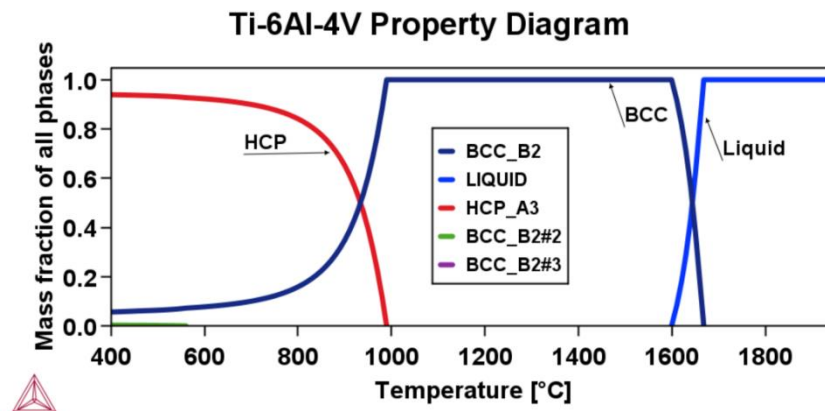


Figure A.11. Equilibrium property diagram for Ti-6Al-4V.

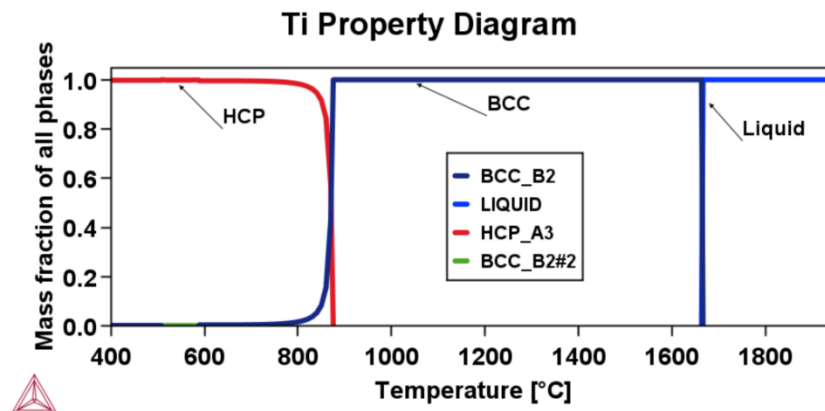


Figure A.12. Equilibrium property diagram for the near commercially pure Ti alloy.

## Appendix B: Weld Parameters

Table B.1 contains the information pertaining to the laser welding setup, and Figure B.1 shows the setup with the optics attached to a six-axis robotic positioner.

*Table B.1. Equipment and parameters used for all laser welding experiments.*

Equipment/Parameter	Specifics/Quantity
Power Supply	IPG Photonics® YLS-6000-S4T (ytterbium fiber laser)
Optics	IPG Photonics® D50 Wobble Head (P/N: P30-010595-V4D1)
Focusing Lens	300 mm
Collimating Lens	150 mm
Working Distance	247 mm
Fiber Diameter	300 $\mu\text{m}$
Ideal Spot Size at Sharp Focus	600 $\mu\text{m}$
Inline Coherent Imaging (ICI) System	Laser Depth Dynamics™ (LDD™) LDD-700 with 6 mm field of view
LDD-700™ Optics Module	LD-700-OM1M-2 with 3DM3R Module
ICI Software	© IPG OmniWELD™ v2.5.2.5
Manipulator/Robot	Yaskawa Motoman MC2000 Robot with DX100 Controller
Manipulator/Robot Capacity	50 kg
Manipulator/Robot Repeatability	$\pm 0.7$ mm
Shielding Gas	argon, trailing
Shielding Gas Flow Rate	45 cubic feet per hour (CFH)
Cross Jet	compressed air ( $\approx 95$ CFH)
Beam Angle (x and y)	0°

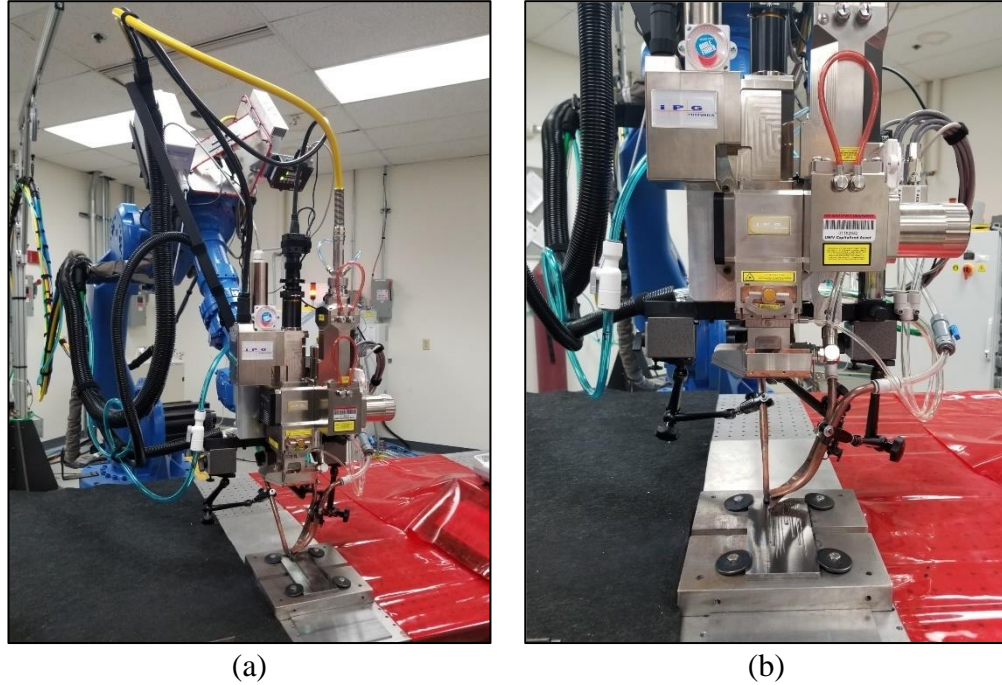


*Figure B.1. Photographs showing the welding setup with the optics attached to a six-axis robot.*

The Laser Depth Dynamics™ (LDD™) inline coherent imaging system is coupled into the D50 Wobble Head optics on the upper, left (Figure B.1b) via the 3DMR module. The IPG Photonics® D50 Wobble Controller and LDD™ optics module is affixed to the robot between axes three and four or Yaskawa defined axes “U” and “R”. Argon shielding gas was applied via two separate supplies for trailing and leading/side shielding. For plume suppression, a “cross-jet” or “air knife” consisting of compressed air was applied  $\approx 10$  mm above the workpiece/weld surface. Argon shielding and the cross-jet were projected onto the workpiece via formed, copper tube adjusted until optimal shielding was achieved based on visual surface oxidation.

## Appendix C: Laser Beam Analysis

All welds were performed based on the measured beam power using an Ophir<sup>®</sup> 10K-W-BB-45-V3 power sensor connected to an Ophir<sup>®</sup> Juno power meter and the Ophir<sup>®</sup> StarLab software. Power values were recorded in the StarLab software and output to a text file. The beam was focused onto the power sensor in the over-focused condition at a working distance of  $\approx 18$  inches (457 mm) with a diameter estimated to be  $\approx 18$  mm. A plot of the power measurements for  $\approx 35$  seconds of sensor illumination time is shown in Figure C.1.

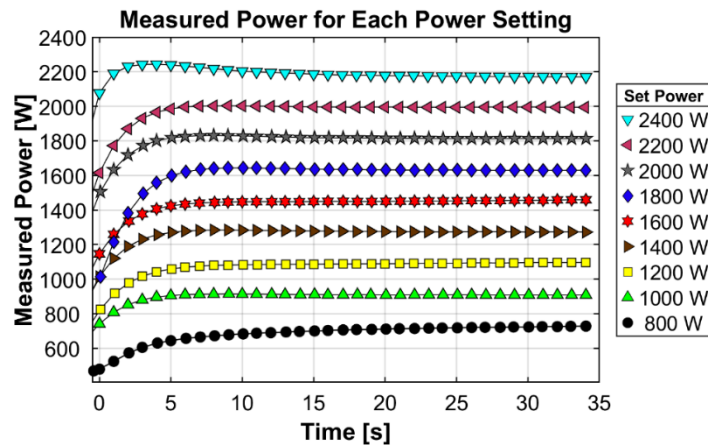


Figure C.1. Measured power reading for each set power.

Flowrate and temperature of the water through the flowmeter were monitored and recorded using an Omega<sup>™</sup> FP1402-RTD flowmeter containing a resistance temperature detector (RTD). The flowmeter measurement range is 0.04-5 gal/min (0.15-18.9 l/min) with an accuracy of  $\pm 1\%$ . The flowmeter was connected to a National Instruments<sup>™</sup> NI USB-6001 data acquisition device (DAQ) for analog-to-digital (ADC) conversion of a 0-

5V output. Flowrate and temperature were recorded using a program written in LabVIEW software. The average flow rate was maintained at  $\approx 12$  l/min with water temperature ranging from  $\approx 14.5$ - $15^\circ\text{C}$  for all power measurements. Based on the power measurements shown in Figure C.1, a linear equation was fit to the data to determine the needed set power to achieve the correct nominal powers. This equation is shown in Equation C.1. Table C.1 contains set values, measured values, and adjusted output powers based on Equation C.1. The adjusted output power is the power set in all welding experiments but referred to as the nominal power.

$$\text{Equation C.1: } P_{nom} = P_{set} + [(0.0945 * P_{set}) - 1.2637 \text{ W}] \quad [\text{W}]$$

Where:  $P_{nom}$  = nominal power,  $P_{set}$  = nominal power

*Table C.1. IPG Photonics® YLS-6000 set power versus measured beam power.*

Set Laser Power (W)	Average Measured Power (W)	Percent Difference (%)	Adjusted Power (W)
800	740	2.1	870
1000	910	2.4	1090
1200	1100	2.2	1310
1400	1270	2.4	1530
1600	1450	2.5	1750
1800	1630	2.5	1970
2000	1820	2.4	2190
2200	2000	2.4	2410
2400	2170	2.6	2630

The laser beam caustics at each power were analyzed using the following focus monitor: PRIMES GmbH Type FM35 with a DFY-PS detector for wavelengths ranging from 0.4-1.1  $\mu\text{m}$ . The “raw” data was extracted from the PRIMES GmbH LaserDiagnoseSoftware v2.98.91 as analog-to-digital converted (ADC) values via spreadsheet (.xls) format in matrix form. Script was written in MATLAB<sup>®</sup> software to compute the beam diameters and plot the intensity distributions and beam caustics. The MATLAB<sup>®</sup> code is provided in Appendix K:. The second moment beam diameter (D2M) was computed according to ISO 11146-1 “*Lasers and laser-related equipment – Test methods for laser beam widths, divergence angles and beam propagation ratios – Part1: Stigmatic and simple astigmatic beams*” [53]. This standard defines the diameter as a computation of the first and second moments as shown in *Equation C.2* and *Equation C.3* respectively. *Equation C.4* shows the calculation of the overall standard deviation, and *Equation C.5* shows the final computation of the overall diameter.

$$\text{Equation C.2: First Moment: } X = \frac{\sum E(x,y)x}{\sum E(x,y)}, Y = \frac{\sum E(x,y)y}{\sum E(x,y)}$$

$$\text{Equation C.3: Second Moment: } \sigma_x^2 = \frac{\sum E(x,y)(x-X)^2}{\sum E(x,y)}, \sigma_y^2 = \frac{\sum E(x,y)(y-Y)^2}{\sum E(x,y)}$$

$$\text{Equation C.4: Overall Standard Deviation: } \sigma^2 = \sigma_x^2 + \sigma_y^2$$

$$\text{Equation C.5: Overall Diameter: } D2M = 2\sqrt{2}\sigma$$

The D2M calculation assumes that the data is in a pixel form. This is output by the PRIMES GmbH rotating pinhole device with a predefined x-y grid along a single plane in the beam axis. Figure C.2 and Figure C.3 show the beam distributions near sharp focus at each power used for welding. The intensity is plotted based on the power density in  $\text{kW}/\text{mm}^2$ , and the positive x-direction corresponds to the welding travel direction. Similarly, the beam caustics are provided in Figure C.4 and Figure C.5 with the power density represented via a color scale that only correlates to the given power.

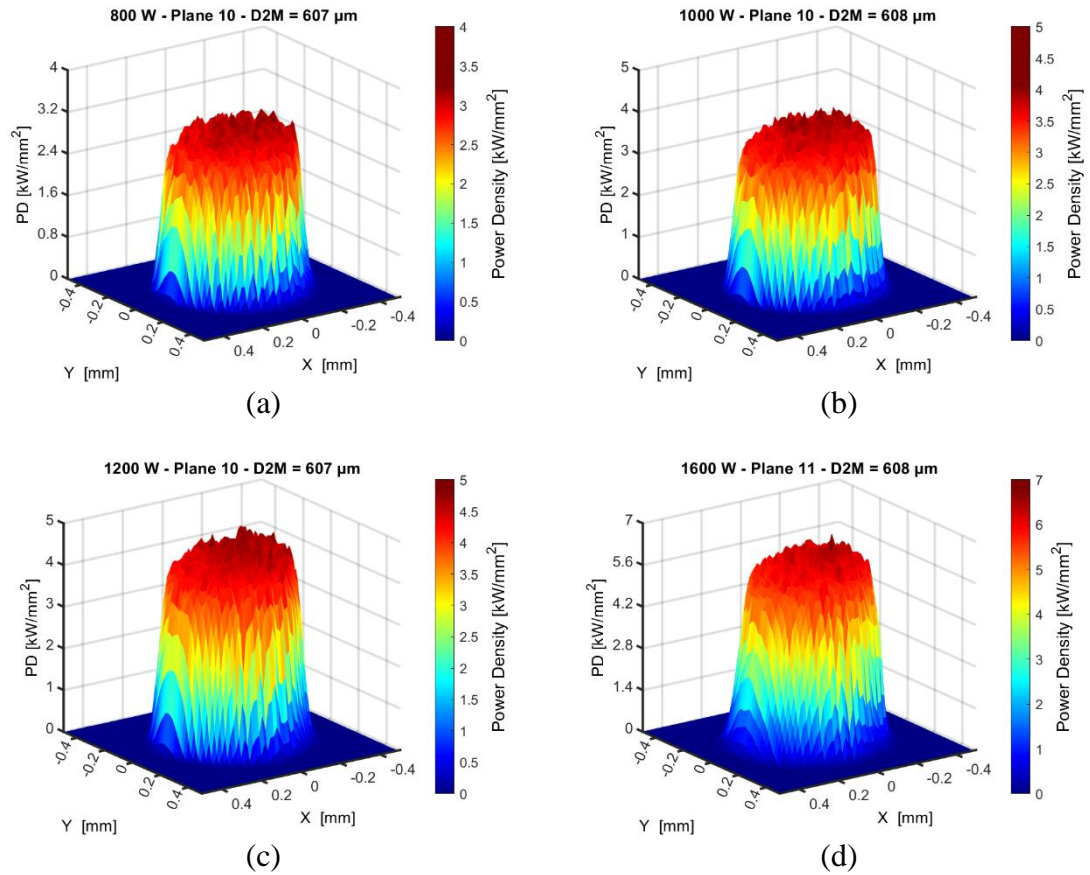


Figure C.2. Beam profiles near sharp focus for 800 W (a), 1000 W (b), 1200 W (c), and 1600 W (d). Note: The scales are not comparable between powers.

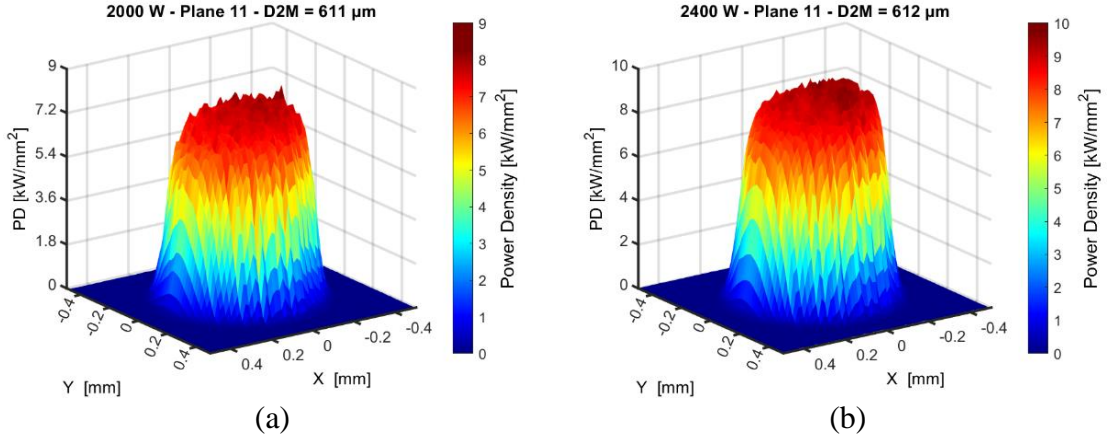


Figure C.3. Beam profiles near sharp focus at 2000 W (a) and 2400 W (b). Note: The scales are not comparable between powers.

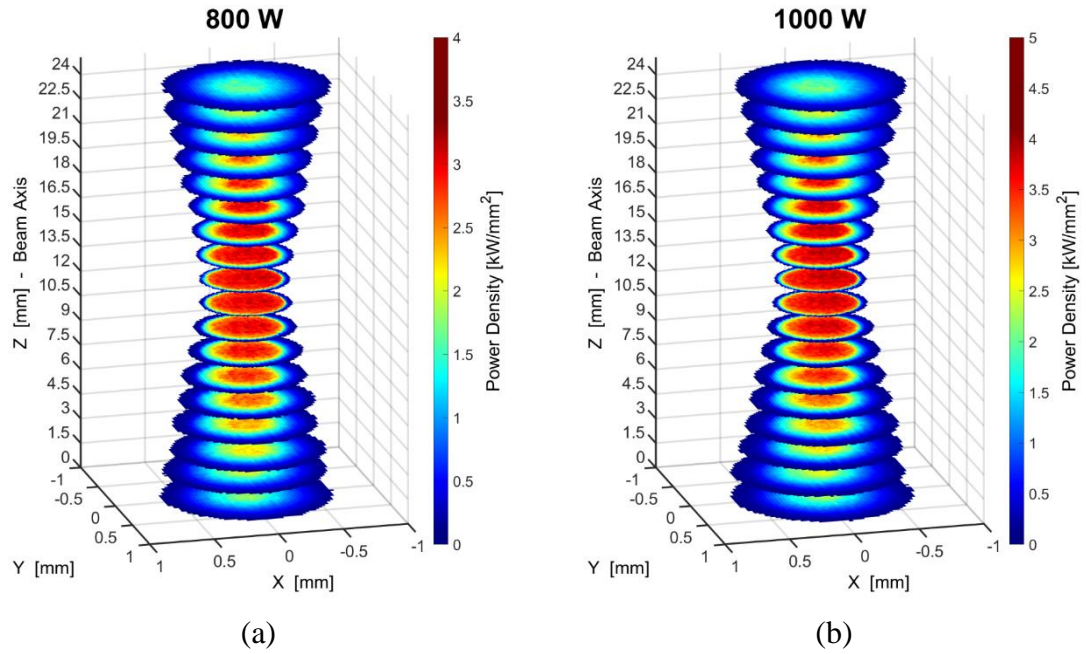


Figure C.4. Beam caustics with the color scale representing intensity distributions: 800 W (a) and 1000 W (b). Note: Color scales are not comparable between powers.

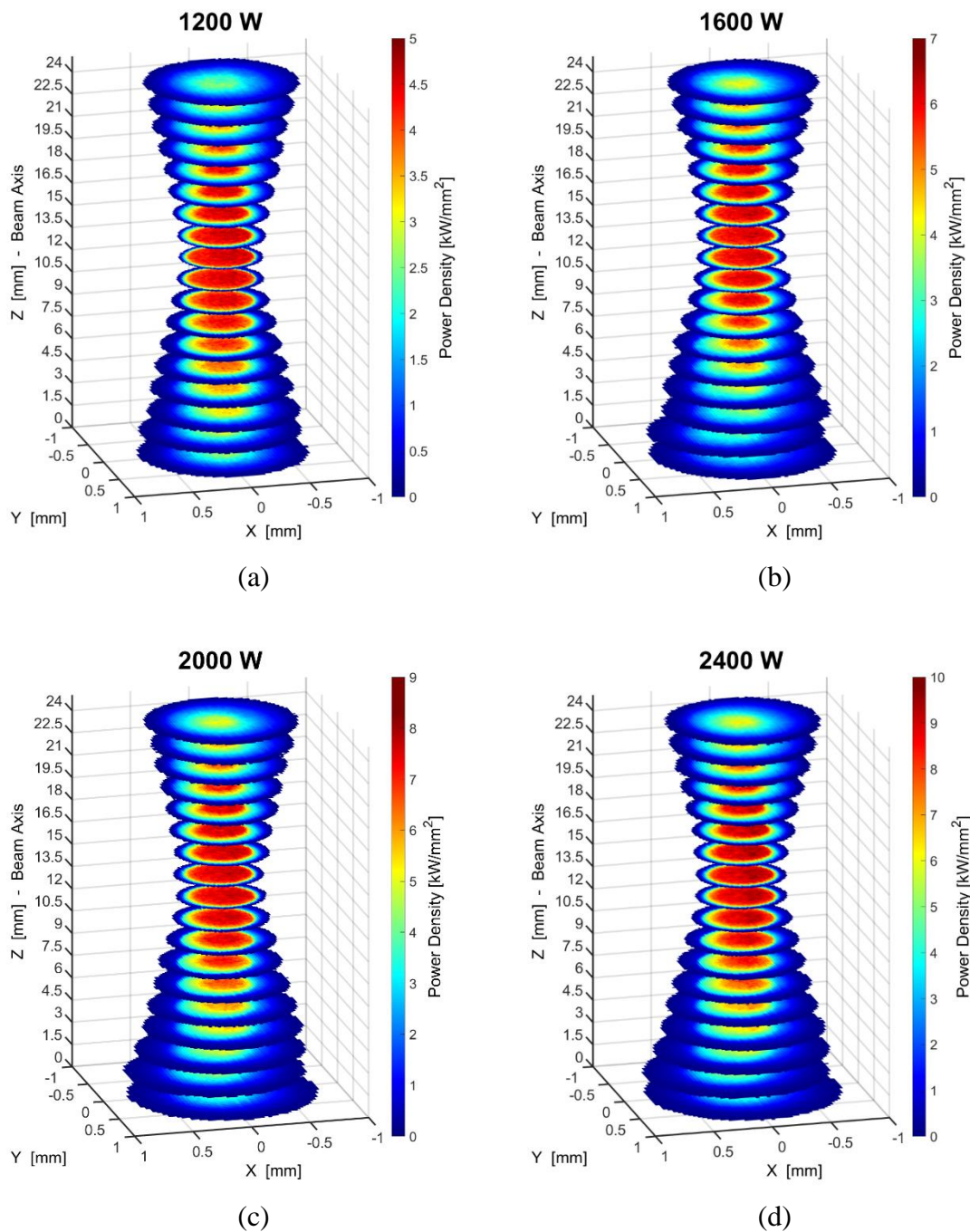


Figure C.5. Beam caustics with the color scale representing intensity distributions for 1200 W (a), 1600 W (b), 2000 W (c), and 2400 W (d). Note: Color scales are not comparable between powers.

## Appendix D: Laser Weld Profiles – 304L

The following subsections contain surface photographs and transverse section macrographs for the 304L welds.

### D.1 Weld Surfaces – 304L

Figure D.1-Figure D.6 show photographs of the weld surfaces at respective powers of 800W, 1000 W, 1200 W, 1600 W, 2000 W, and 2400 W for 304L. Four travel speeds at each power are represented. Figure D.7-Figure D.12 show photographs of the weld ends that were used to approximate the weld pool geometries. These were produced by maintaining the beam travel velocity and instantly extinguishing the laser beam.

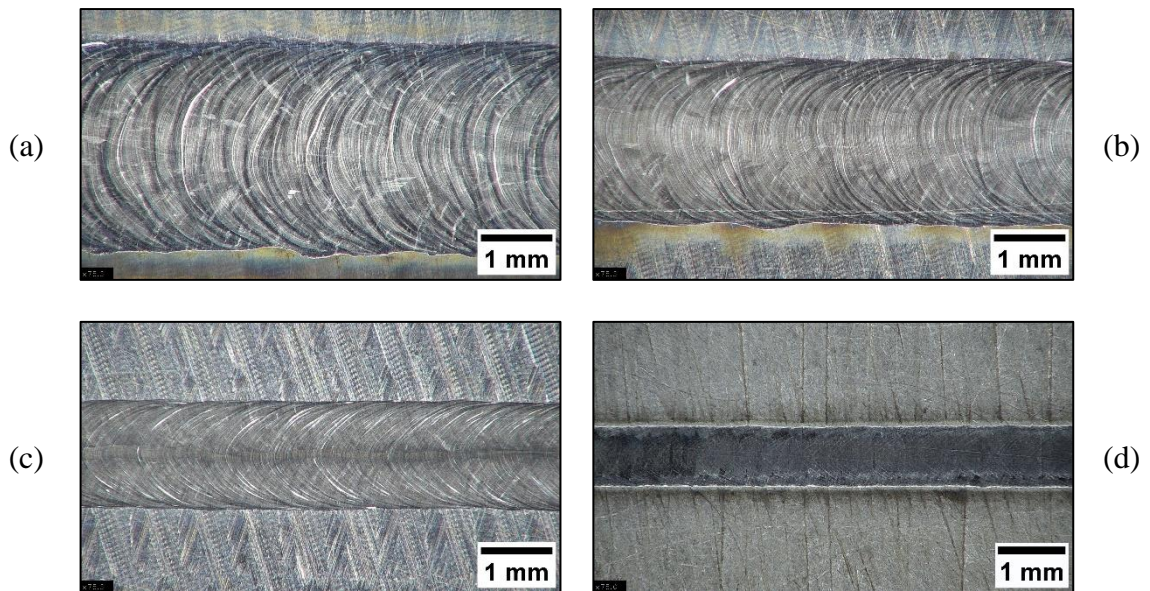


*Figure D.1. 304L laser weld surfaces at 800 W and travel speeds of 5 mm/s (a), 10 mm/s (b), 25 mm/s (c), and 50 mm/s (d).*

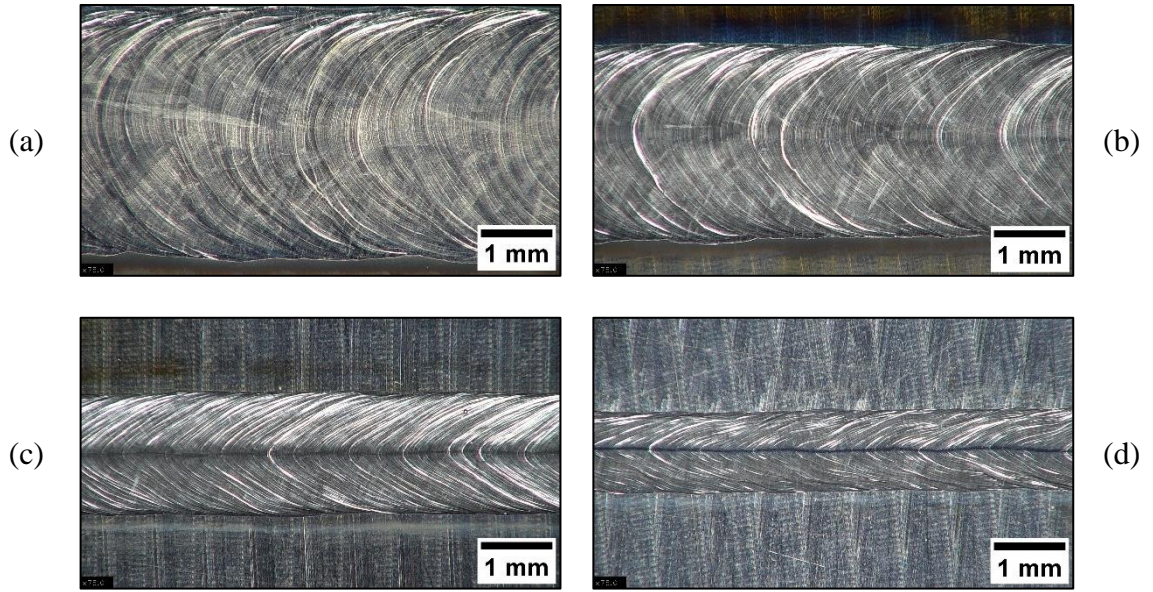


*Figure D.2. 304L laser weld surfaces at 1000 W and travel speeds of 5 mm/s (a), 10 mm/s (b), 25 mm/s (c), and 50 mm/s (d).*

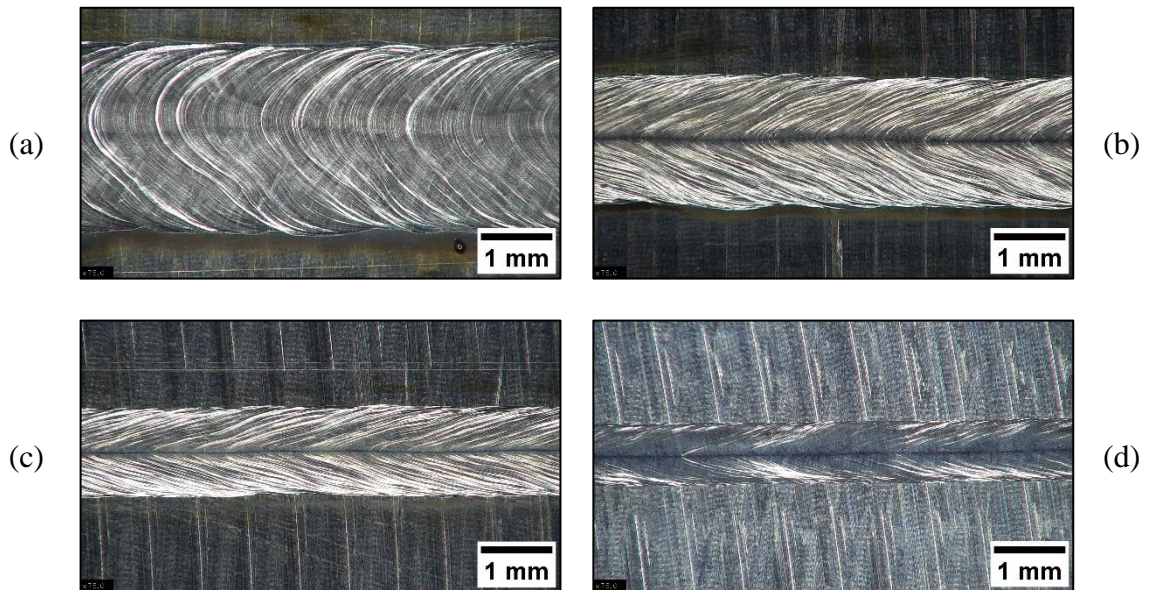


*Figure D.3. 304L laser weld surfaces at 1200 W and travel speeds of 5 mm/s (a), 10 mm/s (b), 25 mm/s (c), and 50 mm/s (d).*

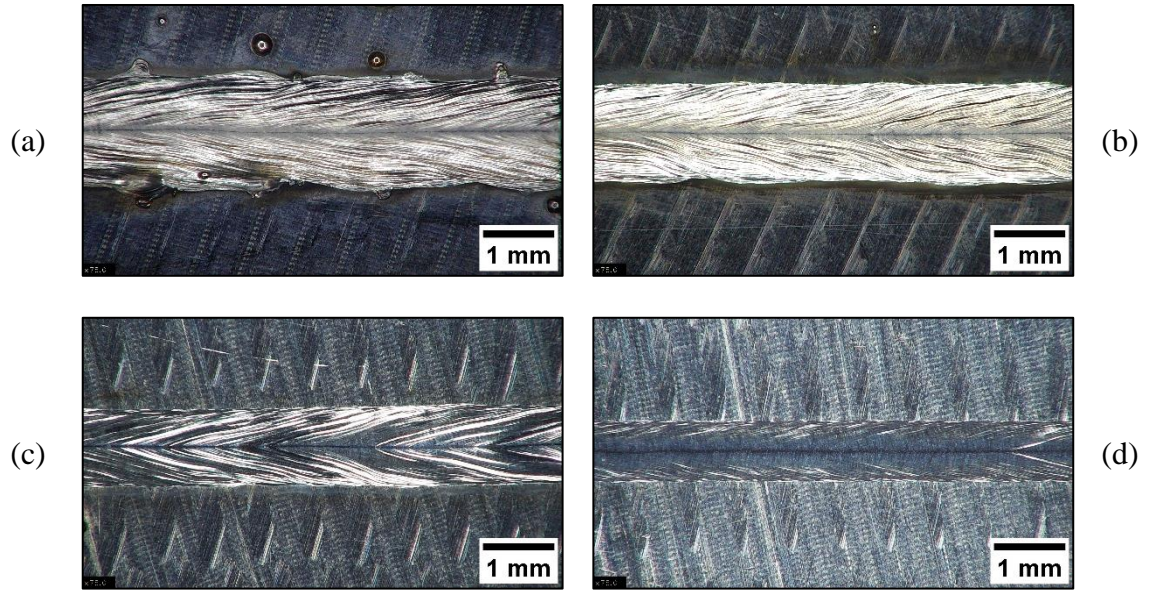


*Figure D.4. 304L laser weld surfaces at 1600 W and travel speeds of 25 mm/s (a), 50 mm/s (b), 100 mm/s (c), and 150 mm/s (d).*

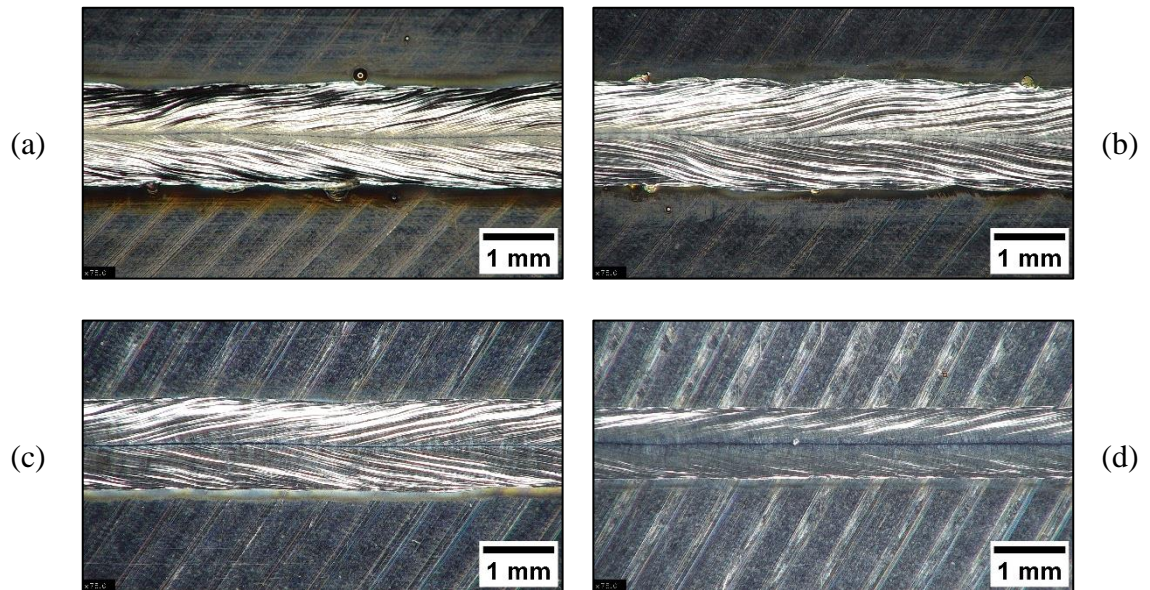


*Figure D.5. 304L laser weld surfaces at 2000 W and travel speeds of 50 mm/s (a), 75 mm/s (b), 100 mm/s (c), and 150 mm/s (d).*

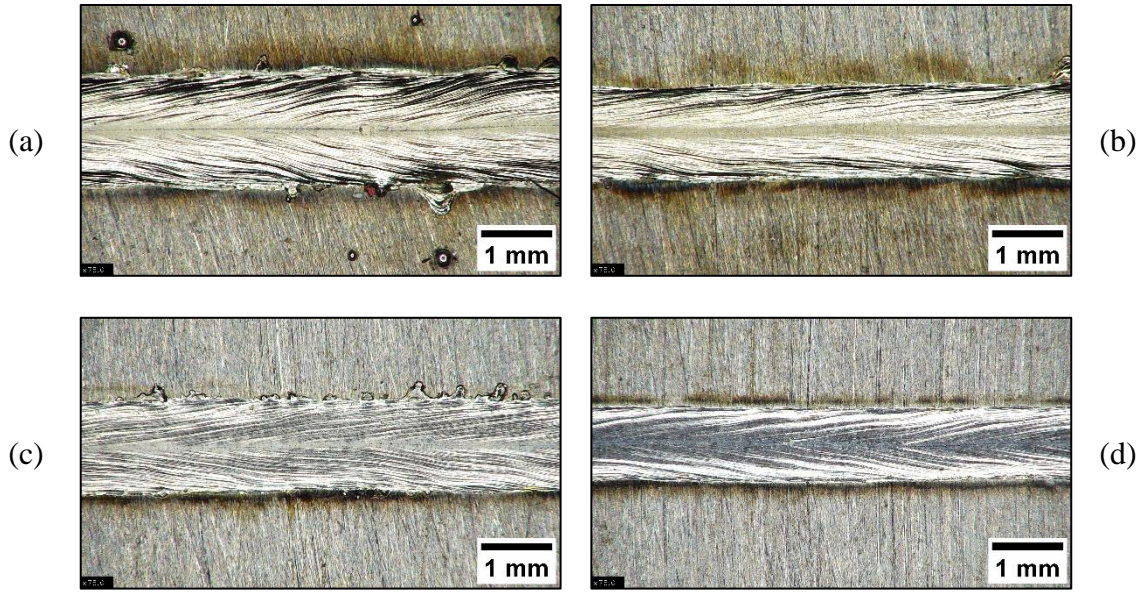


*Figure D.6. 304L laser weld surfaces at 2400 W and travel speeds of 50 mm/s (a), 75 mm/s (b), 100 mm/s (c), and 150 mm/s (d).*

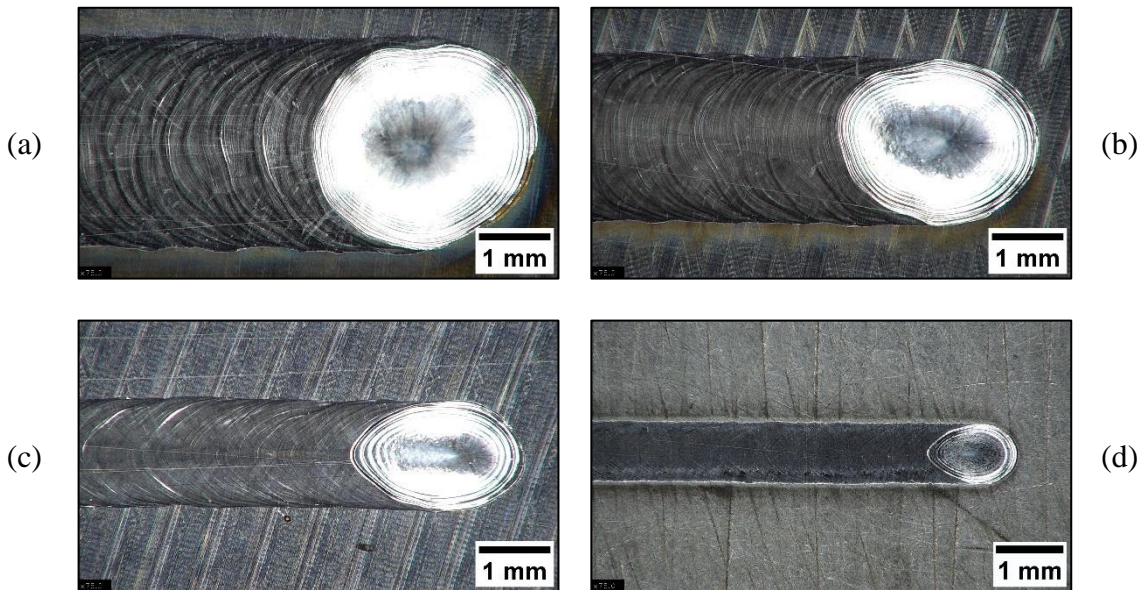


*Figure D.7. 304L laser weld surface ends at 800 W and travel speeds of 5 mm/s (a), 10 mm/s (b), 25 mm/s (c), and 50 mm/s (d).*

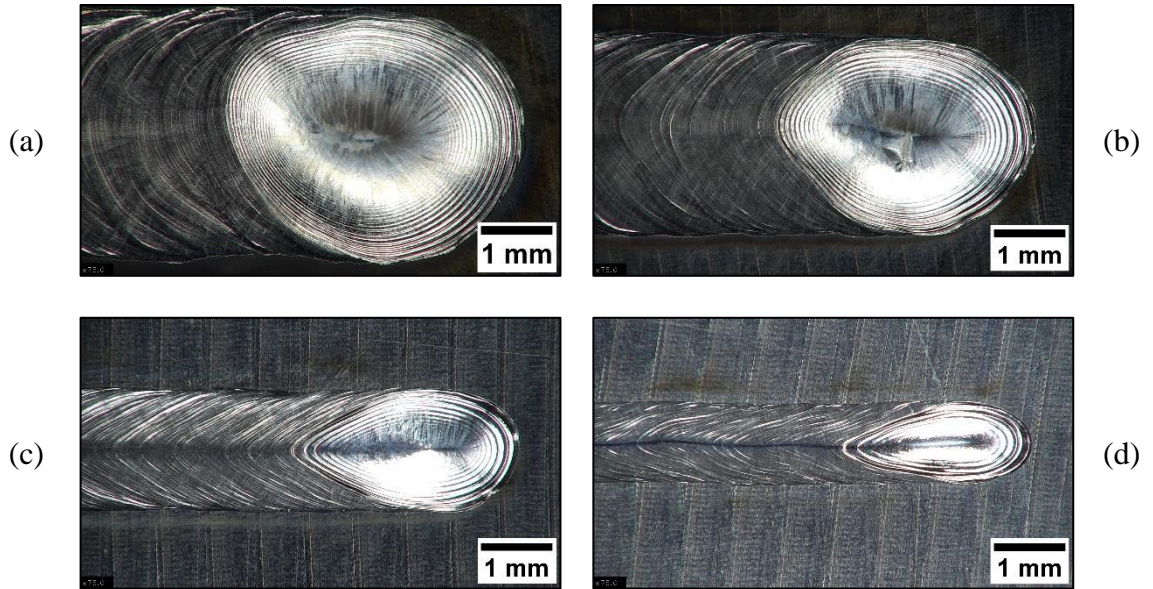


*Figure D.8. 304L laser weld surface ends at 1000 W and travel speeds of 5 mm/s (a), 10 mm/s (b), 25 mm/s (c), and 50 mm/s (d).*

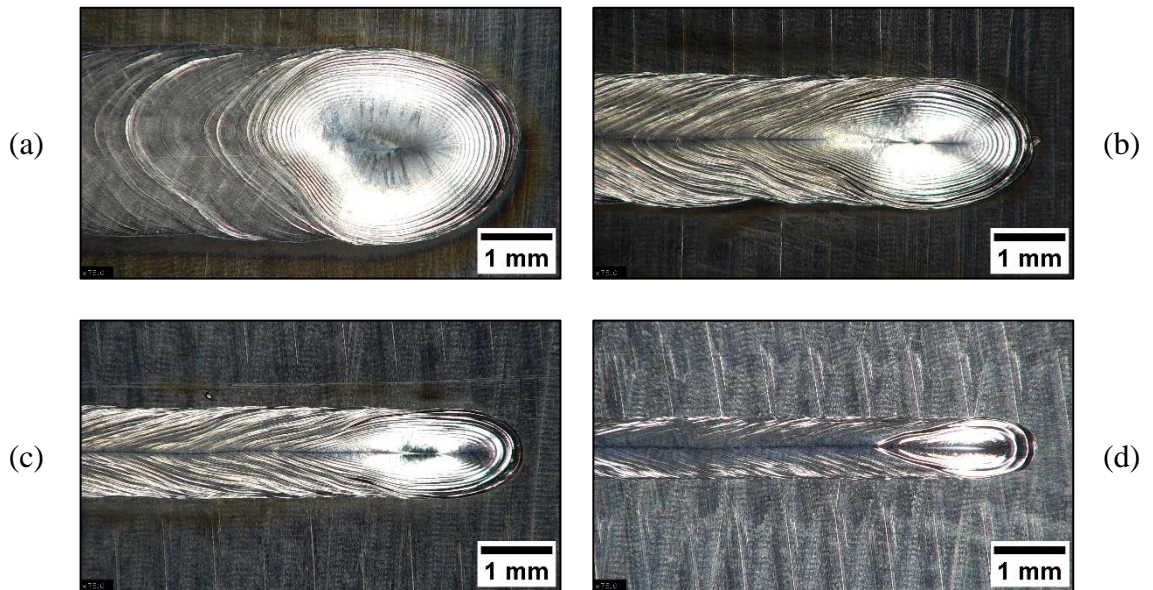


*Figure D.9. 304L laser weld surface ends at 1200 W and travel speeds of 5 mm/s (a), 10 mm/s (b), 25 mm/s (c), and 50 mm/s (d).*

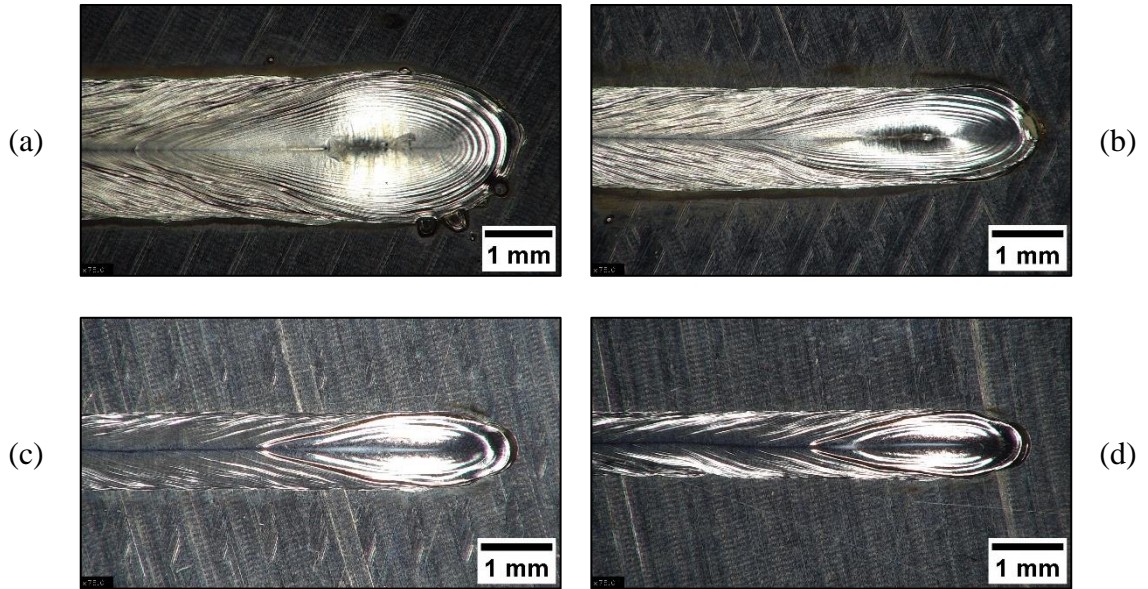


*Figure D.10. 304L laser weld surface ends at 1600 W and travel speeds of 25 mm/s (a), 50 mm/s (b), 100 mm/s (c), and 150 mm/s (d).*

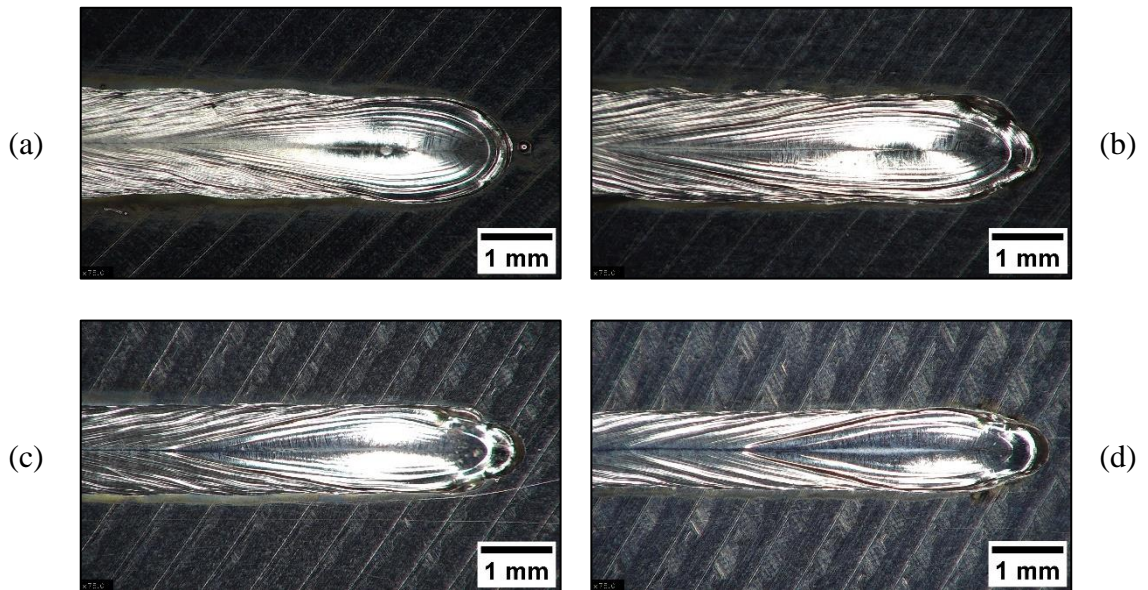


*Figure D.11. 304L laser weld surface ends at 2000 W and travel speeds of 50 mm/s (a), 75 mm/s (b), 100 mm/s (c), and 150 mm/s (d).*

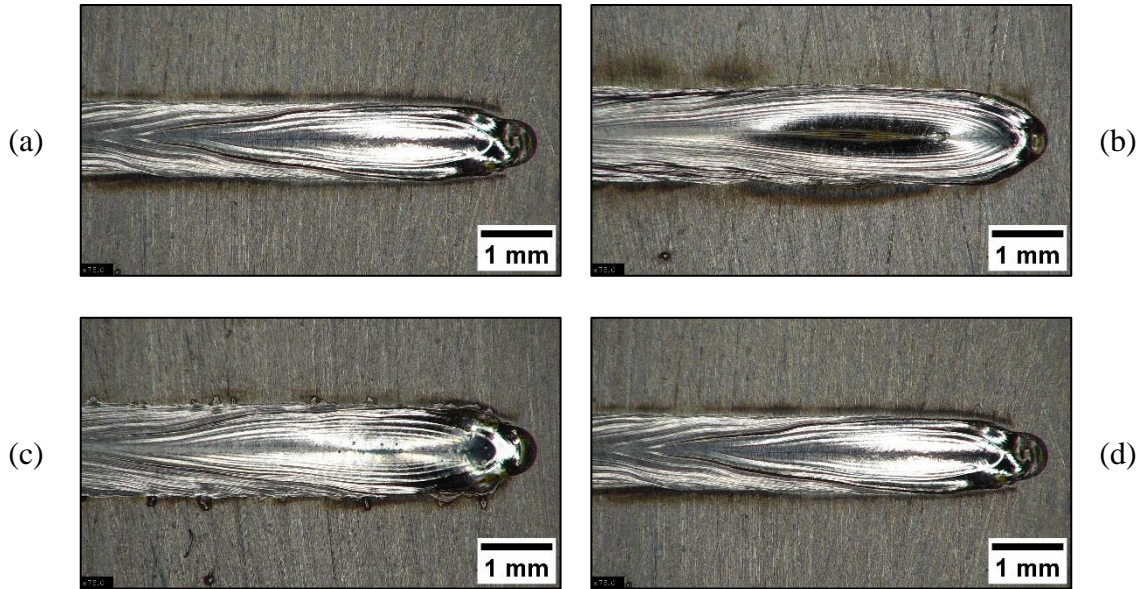


*Figure D.12. 304L laser weld surface ends at 2400 W and travel speeds of 50 mm/s (a), 75 mm/s (b), 100 mm/s (c), and 150 mm/s (d).*

## **D.2 Transverse Sections – 304L**

Transverse cross-sections for most of the 304L laser weld parameters evaluated in this study are provided in Figure D.13-Figure D.18. The powers presented are at 800 W, 1000 W, 1200 W, 1600 W, 2000 W, and 2400 W, respectively. Each figure shows the weld geometries at four travel speeds and traversing from keyhole to conduction mode.

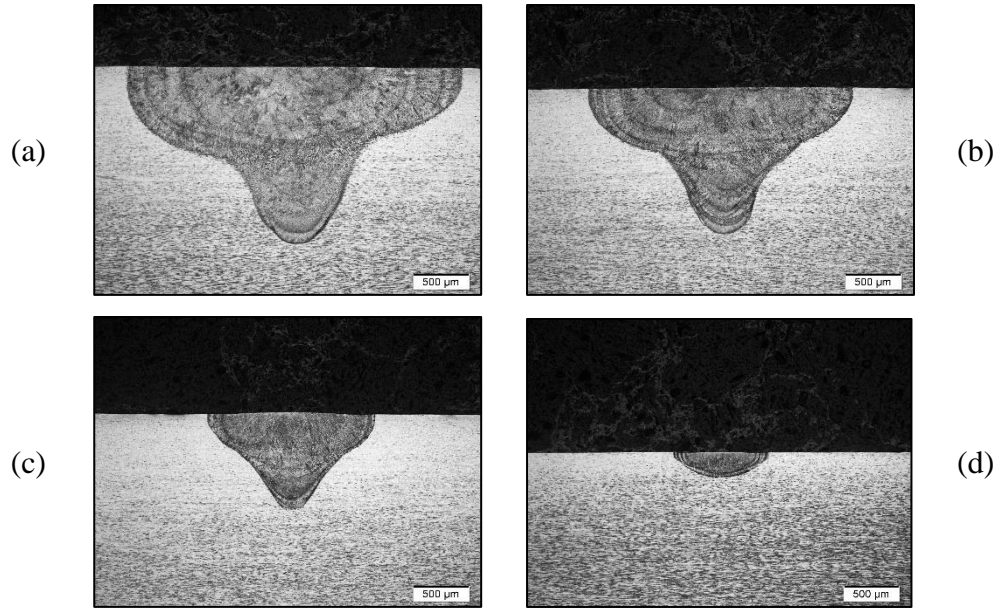


*Figure D.13. 304L laser weld macrosections at 800 W and travel speeds of 5 mm/s (a), 10 mm/s (b), 25 mm/s (c), and 50 mm/s (d).*

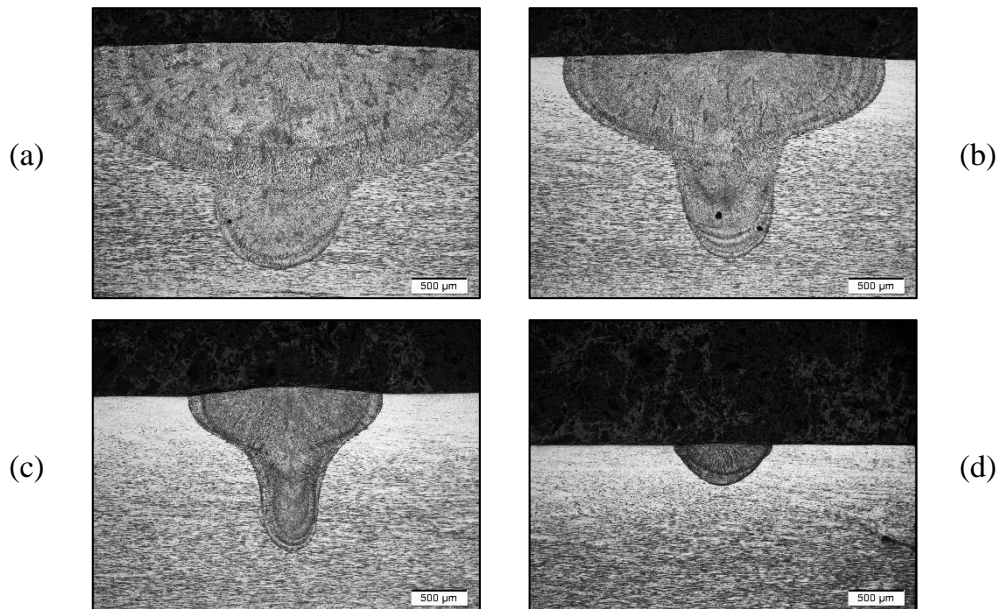


*Figure D.14. 304L laser weld macrosections at 1000 W and travel speeds of 5 mm/s (a), 10 mm/s (b), 25 mm/s (c), and 50 mm/s (d).*

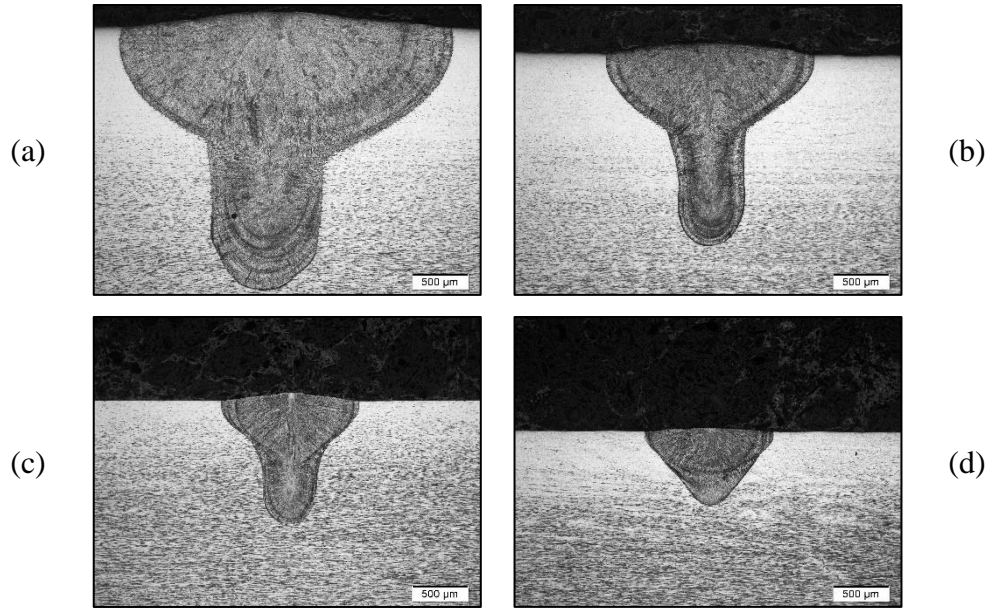


*Figure D.15. 304L laser weld macrosections at 1200 W and travel speeds of 10 mm/s (a), 25 mm/s (b), 50 mm/s (c), and 100 mm/s (d).*

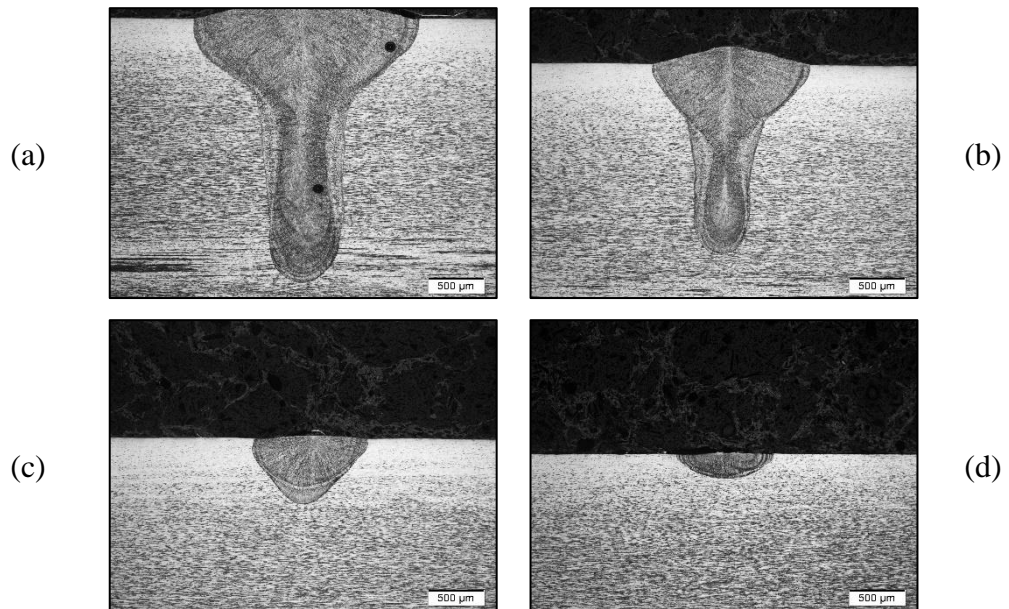


*Figure D.16. 304L laser weld macrosections at 1600 W and travel speeds of 25 mm/s (a), 50 mm/s (b), 100 mm/s (c), and 150 mm/s (d).*

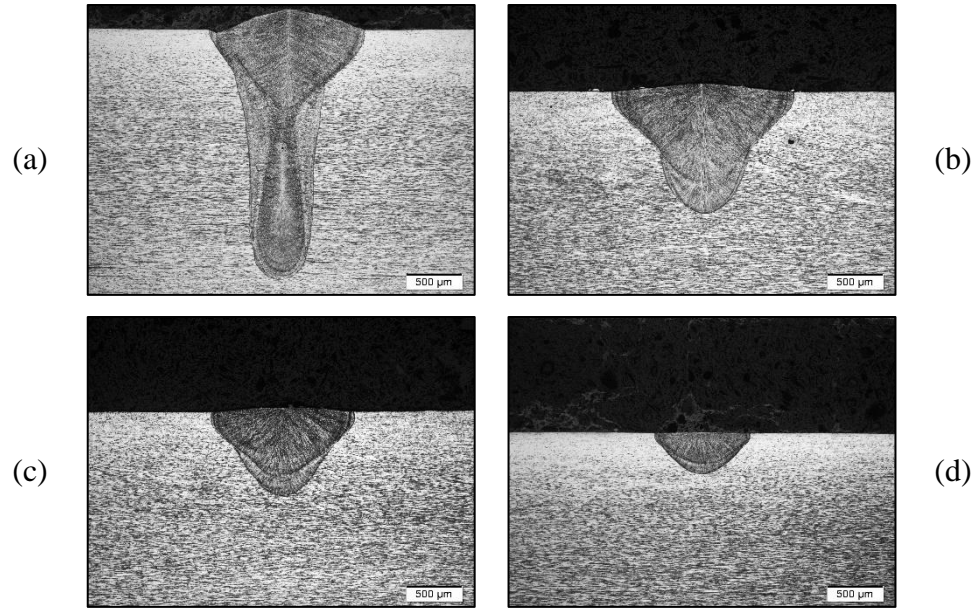


*Figure D.17. 304L laser weld macrosections at 2000 W and travel speeds of 50 mm/s (a), 75 mm/s (b), 100 mm/s (c), and 150 mm/s (d).*

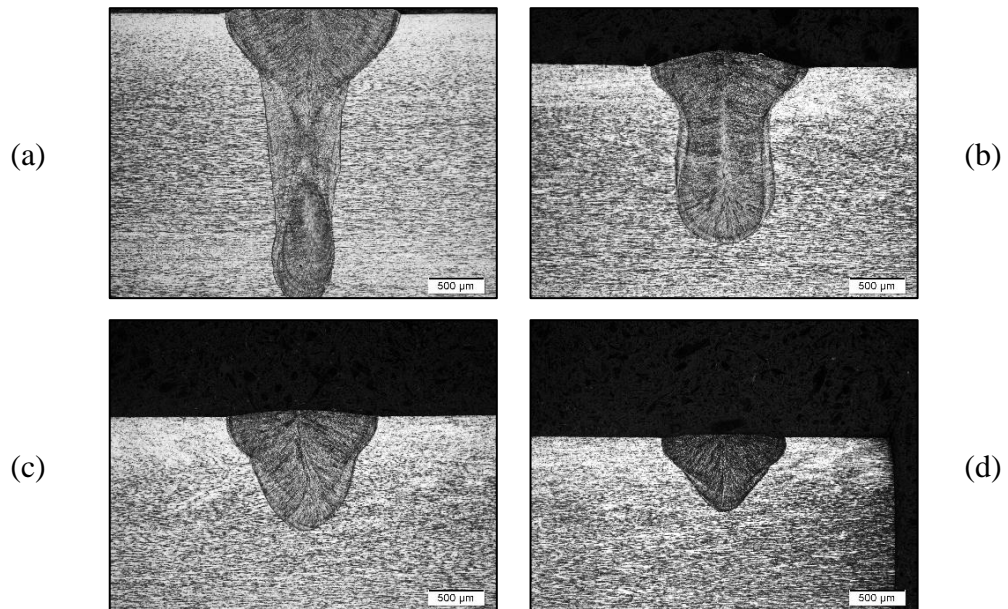


*Figure D.18. 304L laser weld macrosections at 2400 W and travel speeds of 50 mm/s (a), 75 mm/s (b), 100 mm/s (c), and 150 mm/s (d).*

## Appendix E: Weld Geometry Data – 304L

Figure E.1-Figure E.3 contain the measured weld data for 304L SS at all the weld parameters analyzed. The measurements include the penetration, transverse area, weld toe width, centroid width, and FWHM width.

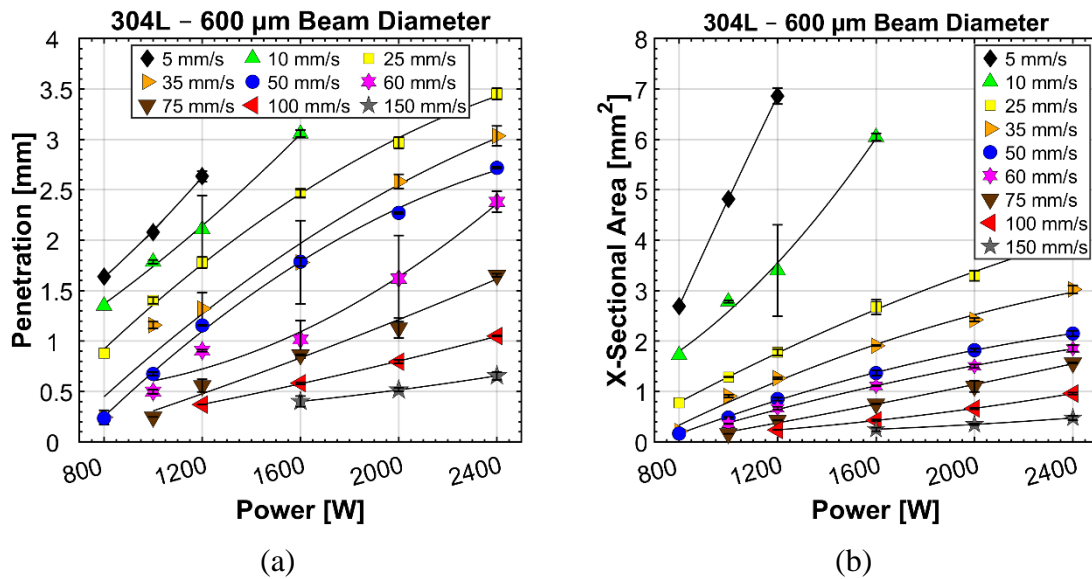


Figure E.1. Penetration (a) and transverse cross-sectional area (b) versus power for 304L. All data except 800 W is from two separate welds.

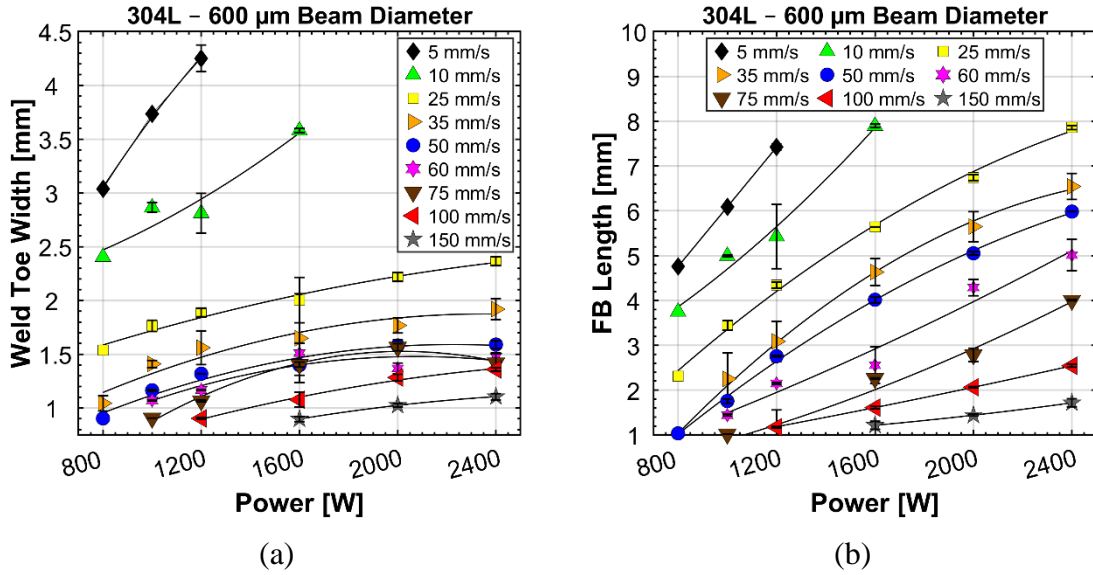


Figure E.2. Weld toe width (a) and fusion boundary length (b) versus power for 304L stainless steel at varying travel speeds. Only data at 800 W is from a single weld.

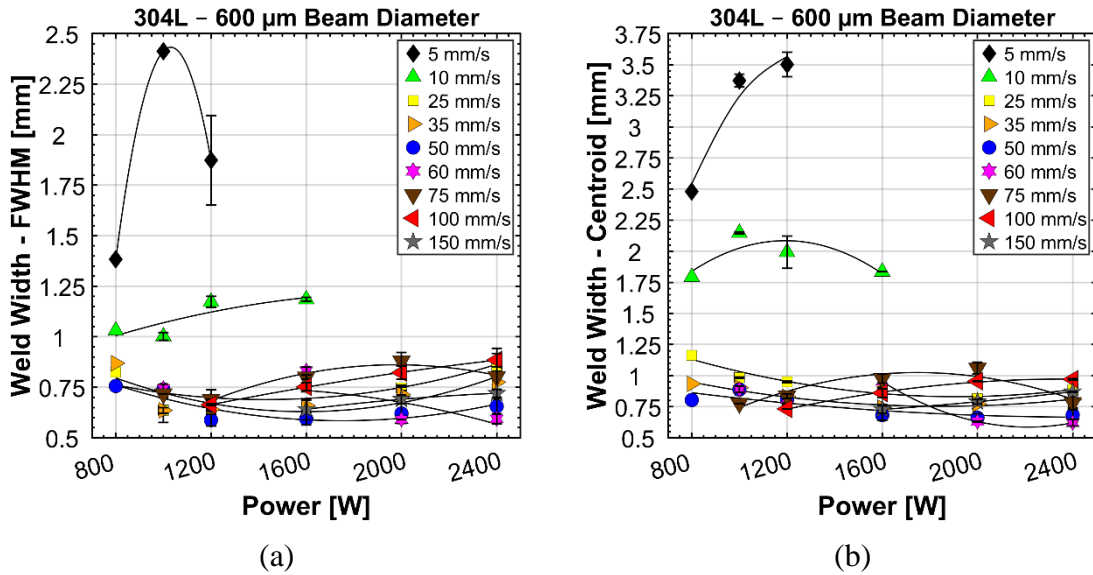


Figure E.3. Weld toe width (a) and fusion boundary length (b) versus power for 304L stainless steel at varying travel speeds. Only data at 800 W is from a single weld.

## Appendix F: Laser Weld Profiles – Ti-6Al-4V

The following subsections contain the surface photographs and transverse section macrographs for the Ti-6Al-4V welds.

### F.1 Weld Surfaces – Ti-6Al-4V

Figure F.1-Figure F.6 show photographs of the weld surfaces at respective powers of 800 W, 1000 W, 1200 W, 1600 W, 2000 W, and 2400 W for Ti-6Al-4V. Four travel speeds at each power are represented. Figure F.7-Figure F.12 show photographs of the weld ends that were used to approximate the weld pool geometries. These were produced by maintaining the beam travel velocity and instantly extinguishing the laser beam.

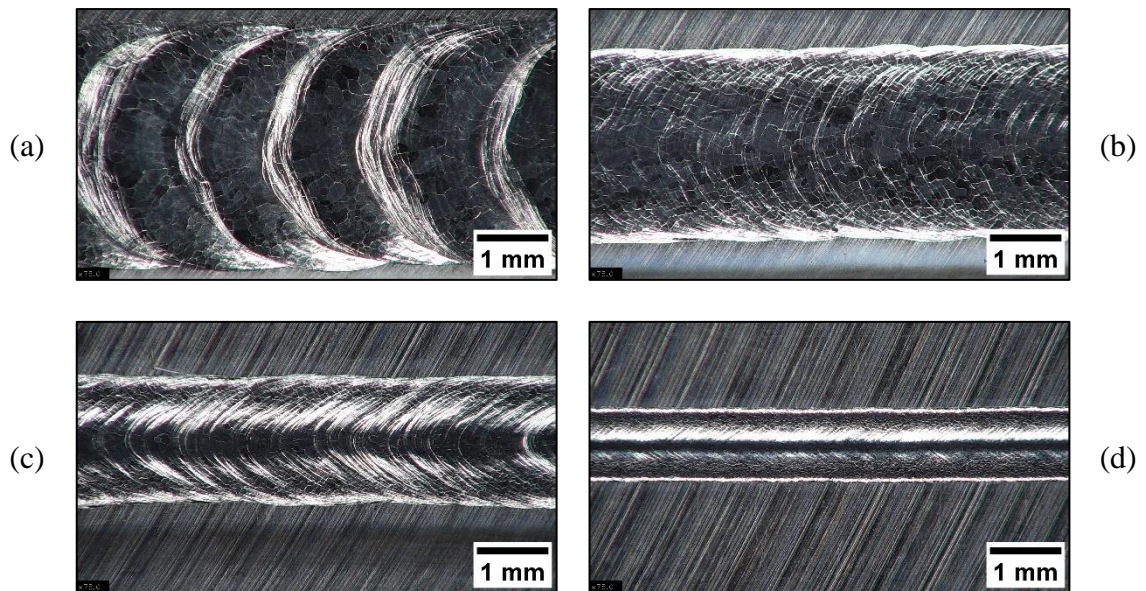


*Figure F.1. Ti-6Al-4V laser weld surfaces at 800 W and travel speeds of 5 mm/s (a), 10 mm/s (b), 25 mm/s (c), and 50 mm/s (d).*

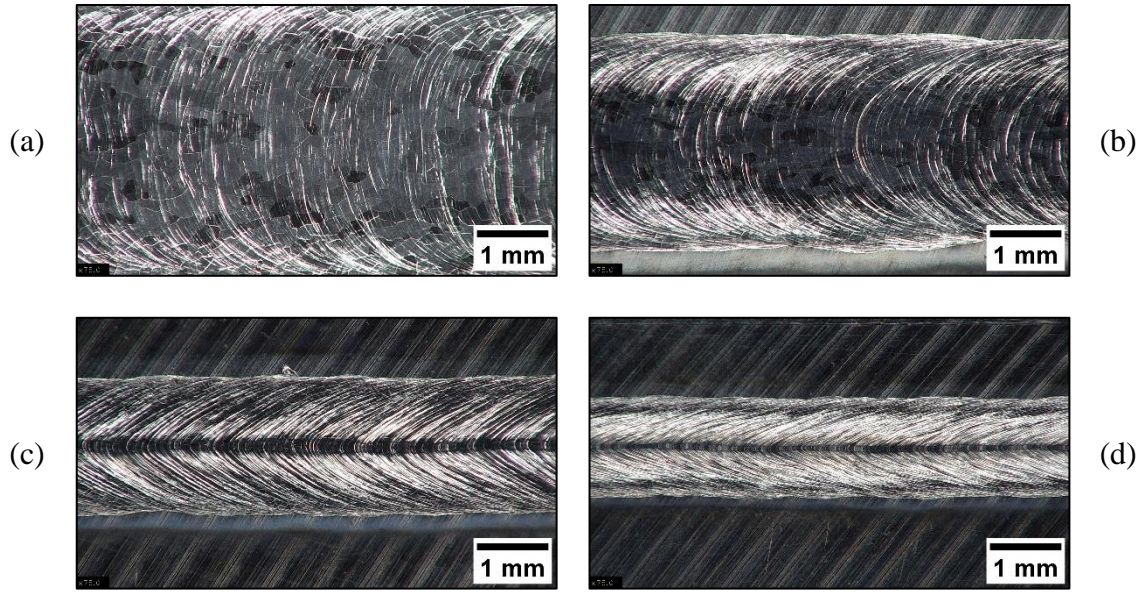


*Figure F.2. Ti-6Al-4V laser weld surfaces at 1000 W and travel speeds of 5 mm/s (a), 10 mm/s (b), 25 mm/s (c), and 50 mm/s (d).*

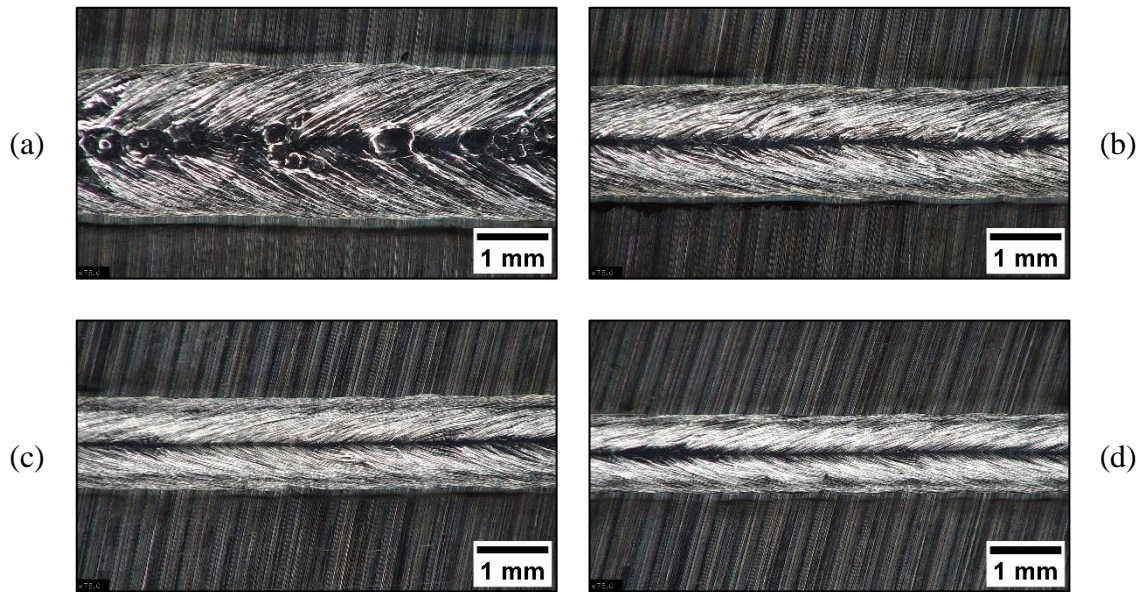


*Figure F.3. Ti-6Al-4V laser weld surfaces at 1200 W and travel speeds of 25 mm/s (a), 50 mm/s (b), 75 mm/s (c), and 100 mm/s (d).*

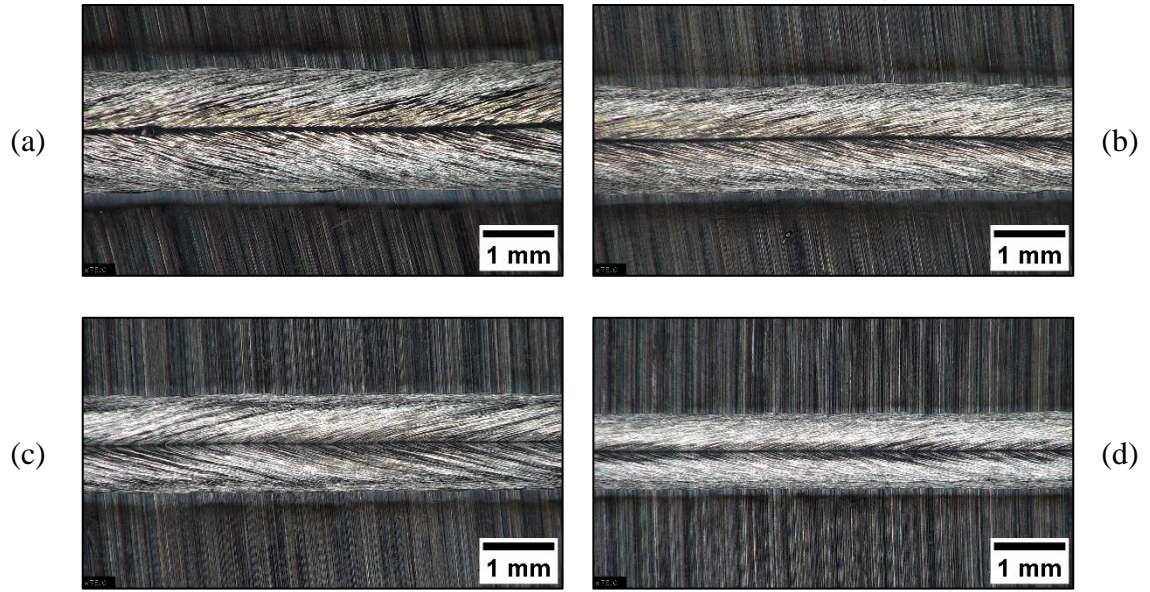


*Figure F.4. Ti-6Al-4V laser weld surfaces at 1600 W and travel speeds of 25 mm/s (a), 50 mm/s (b), 100 mm/s (c), and 150 mm/s (d).*

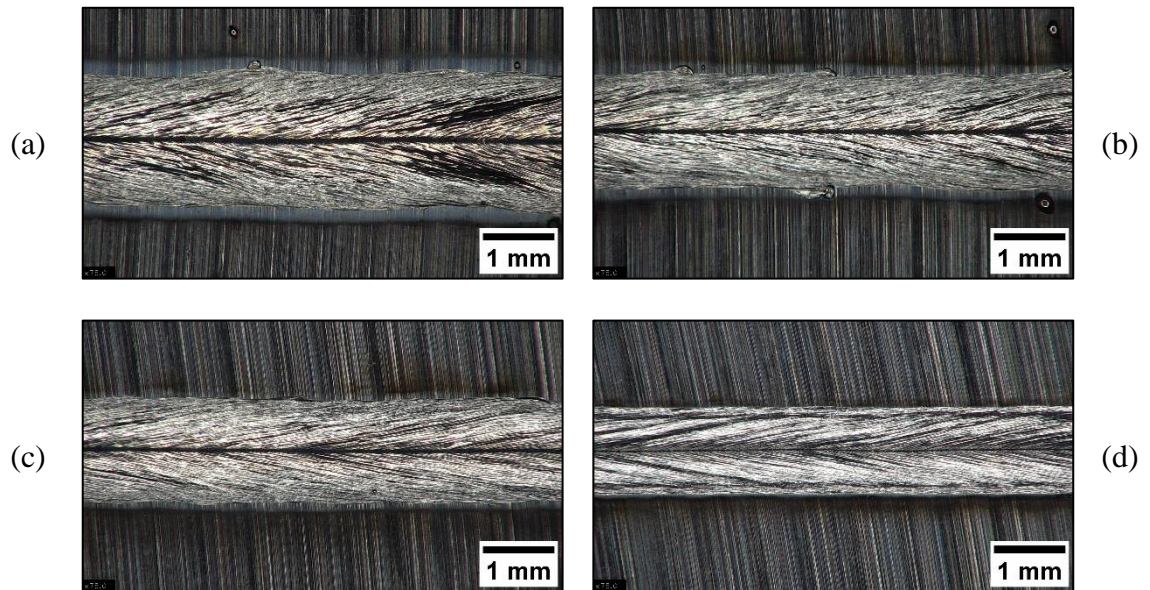


*Figure F.5. Ti-6Al-4V laser weld surfaces at 2000 W and travel speeds of 50 mm/s (a), 75 mm/s (b), 100 mm/s (c), and 150 mm/s (d).*

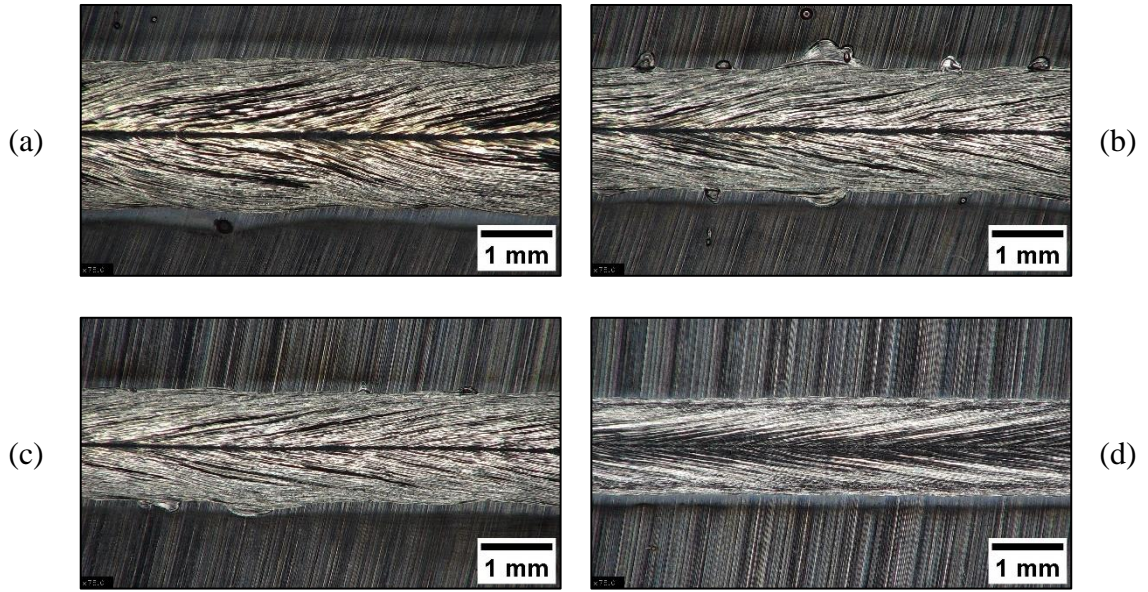


*Figure F.6. Ti-6Al-4V laser weld surfaces at 2400 W and travel speeds of 50 mm/s (a), 75 mm/s (b), 100 mm/s (c), and 150 mm/s (d).*

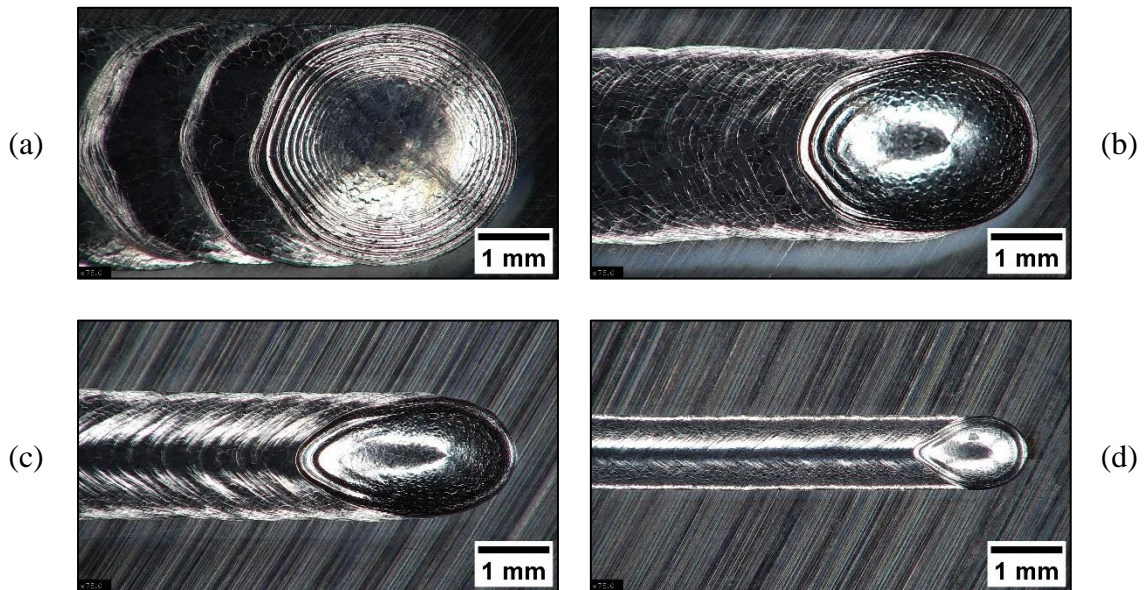


*Figure F.7. Ti-6Al-4V laser weld surface ends at 800 W and travel speeds of 5 mm/s (a), 10 mm/s (b), 25 mm/s (c), and 50 mm/s (d).*

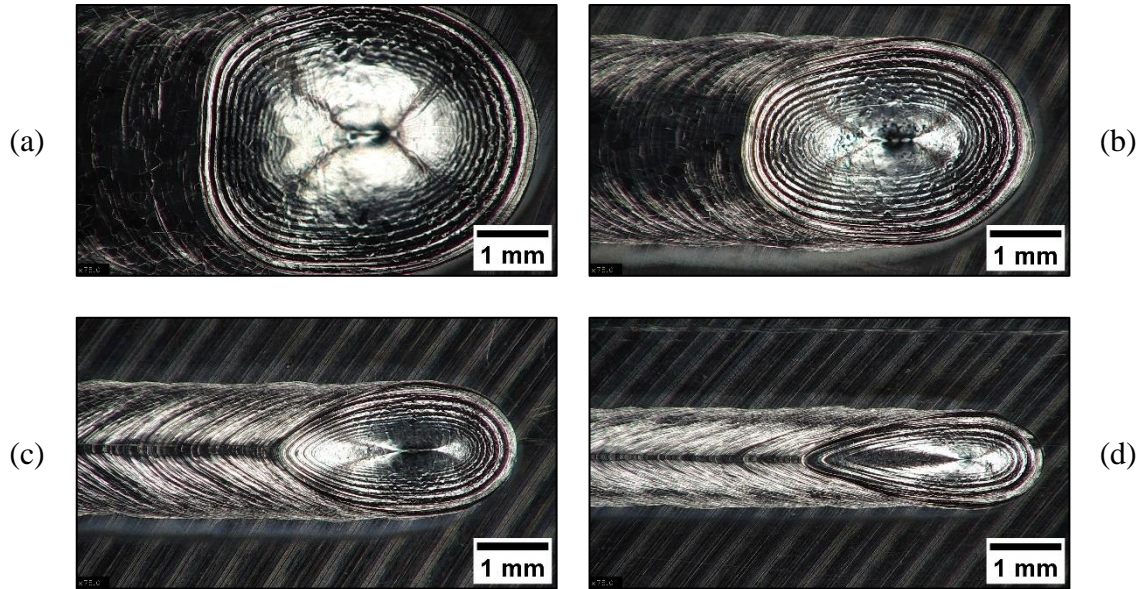


*Figure F.8. Ti-6Al-4V laser weld surface ends at 1000 W and travel speeds of 5 mm/s (a), 10 mm/s (b), 25 mm/s (c), and 50 mm/s (d).*

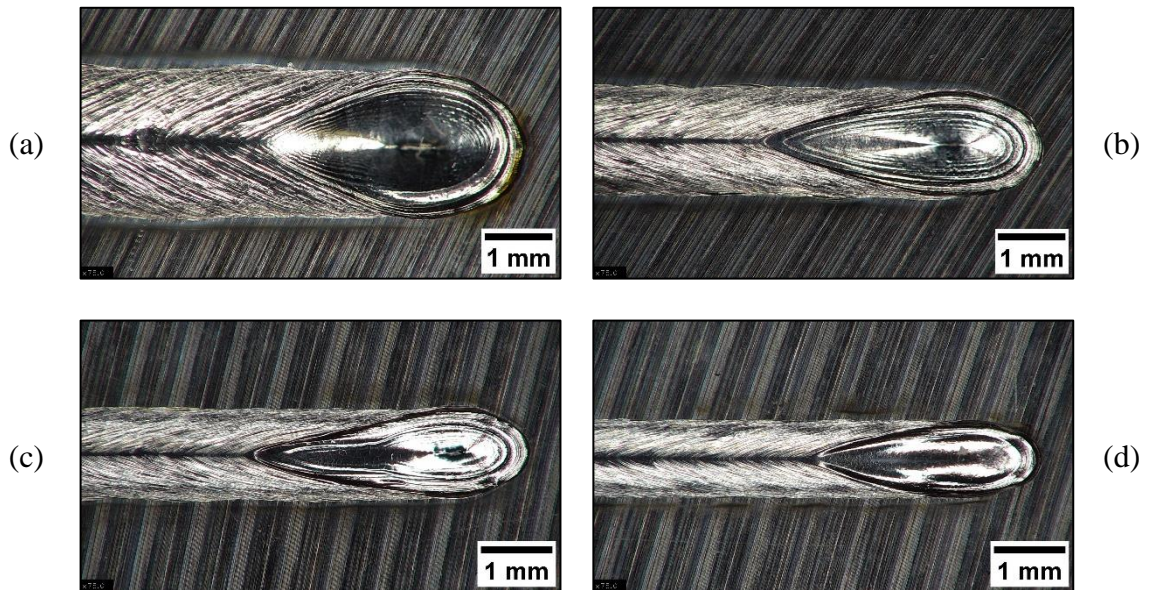


*Figure F.9. Ti-6Al-4V laser weld surface ends at 1200 W and travel speeds of 25 mm/s (a), 50 mm/s (b), 75 mm/s (c), and 100 mm/s (d).*

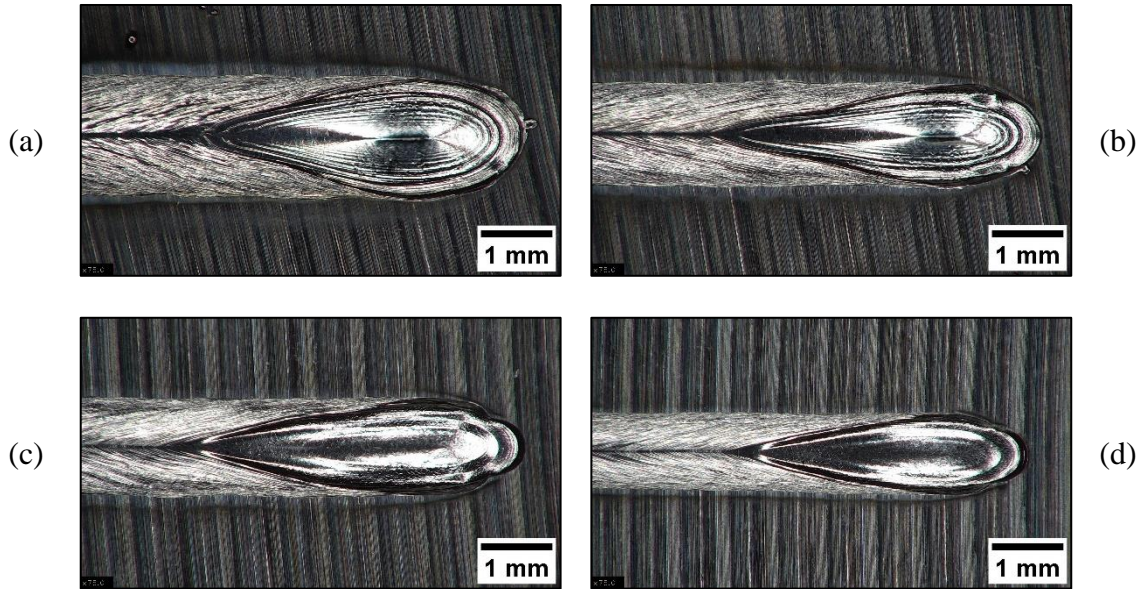


*Figure F.10. Ti-6Al-4V laser weld surface ends at 1600 W and travel speeds of 25 mm/s (a), 50 mm/s (b), 100 mm/s (c), and 150 mm/s (d).*

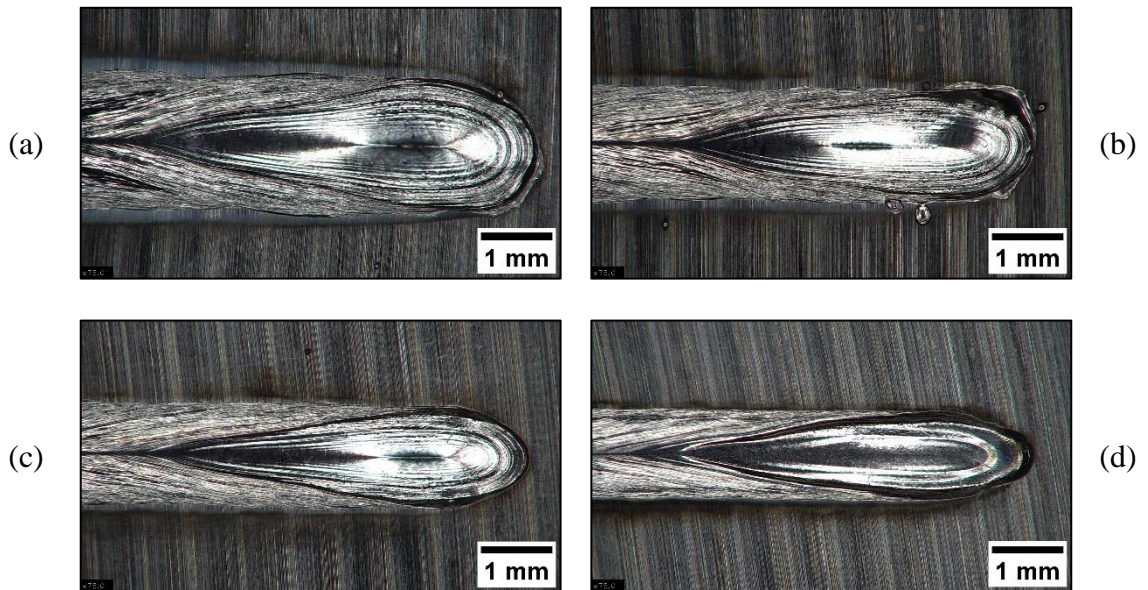


*Figure F.11. Ti-6Al-4V laser weld surface ends at 2000 W and travel speeds of 50 mm/s (a), 75 mm/s (b), 100 mm/s (c), and 150 mm/s (d).*

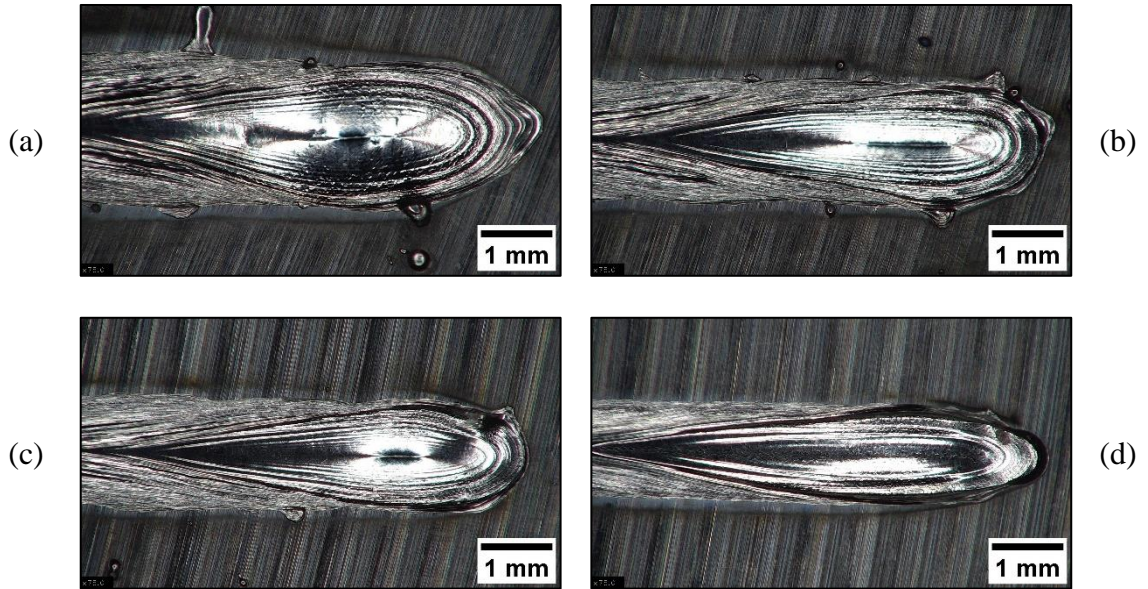


*Figure F.12. Ti-6Al-4V laser weld surface ends at 2400 W and travel speeds of 50 mm/s (a), 75 mm/s (b), 100 mm/s (c), and 150 mm/s (d).*

## **F.2 Transverse Sections – Ti-6Al-4V**

The transverse sections for Ti-6Al-4V laser weld conditions evaluated in this study are provided in Figure F.13-Figure F.18. The powers presented are at 800 W, 1000 W, 1200 W, 1600 W, 2000 W, and 2400 W, respectively. Each figure shows the weld geometries at four travel speeds and traversing from keyhole to conduction mode.

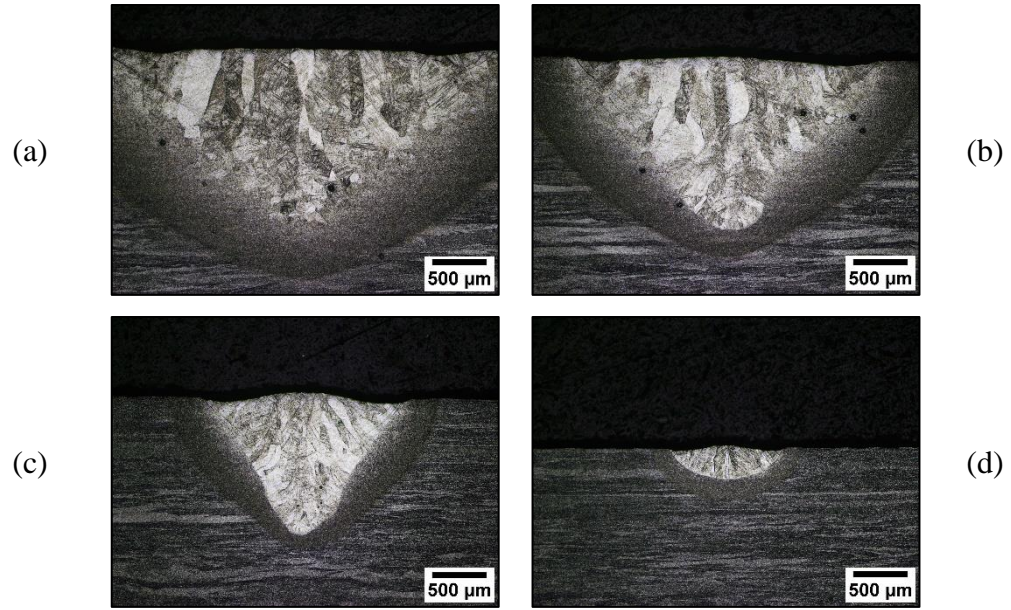


*Figure F.13. Ti-6Al-4V laser weld macrosections at 800 W and travel speeds of 5 mm/s (a), 10 mm/s (b), 25 mm/s (c), and 50 mm/s (d).*

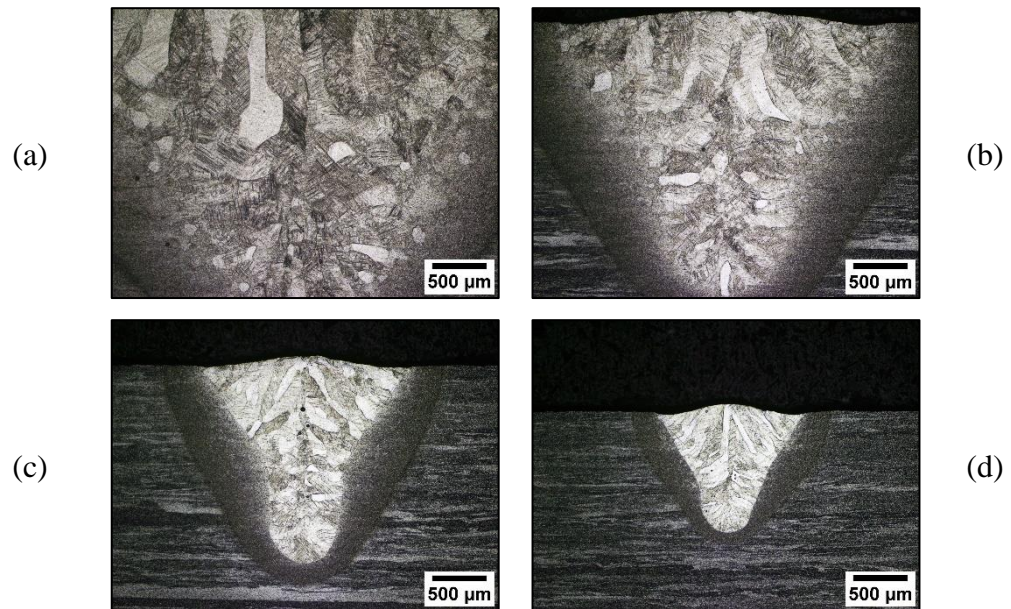


*Figure F.14. Ti-6Al-4V laser weld macrosections at 1000 W and travel speeds of 5 mm/s (a), 10 mm/s (b), 25 mm/s (c), and 50 mm/s (d).*

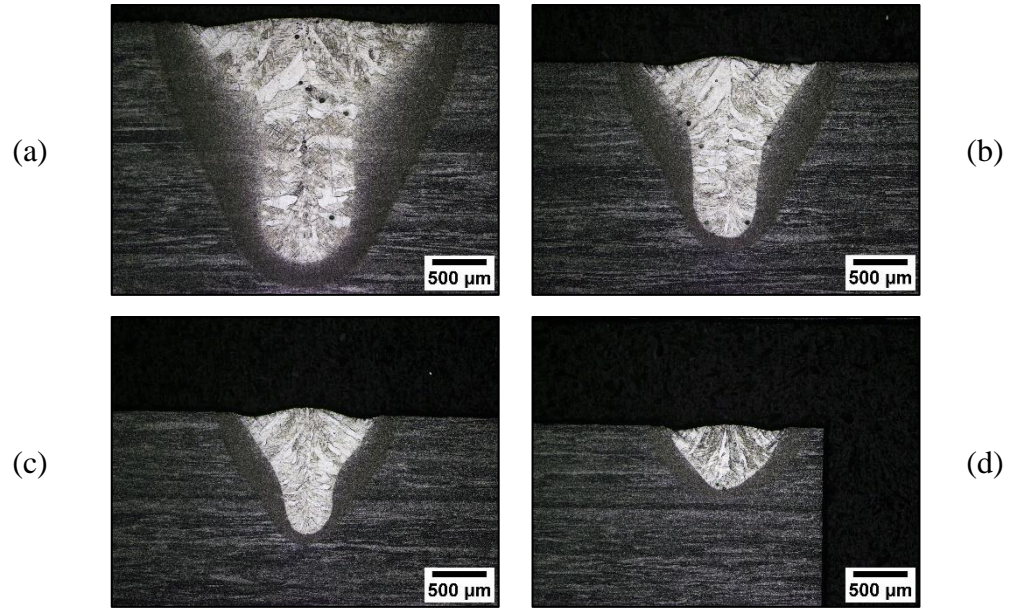


*Figure F.15. Ti-6Al-4V laser weld macrosections at 1200 W and travel speeds of 25 mm/s (a), 50 mm/s (b), 75 mm/s (c), and 100 mm/s (d).*

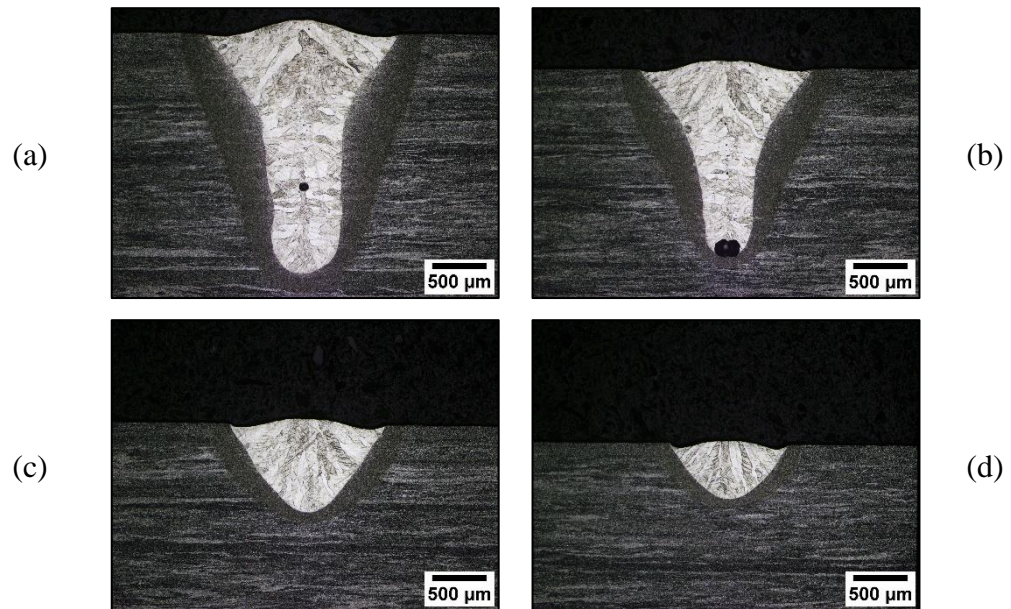


*Figure F.16. Ti-6Al-4V laser weld macrosections at 1600 W and travel speeds of 25 mm/s (a), 50 mm/s (b), 75 mm/s (c), and 100 mm/s (d).*

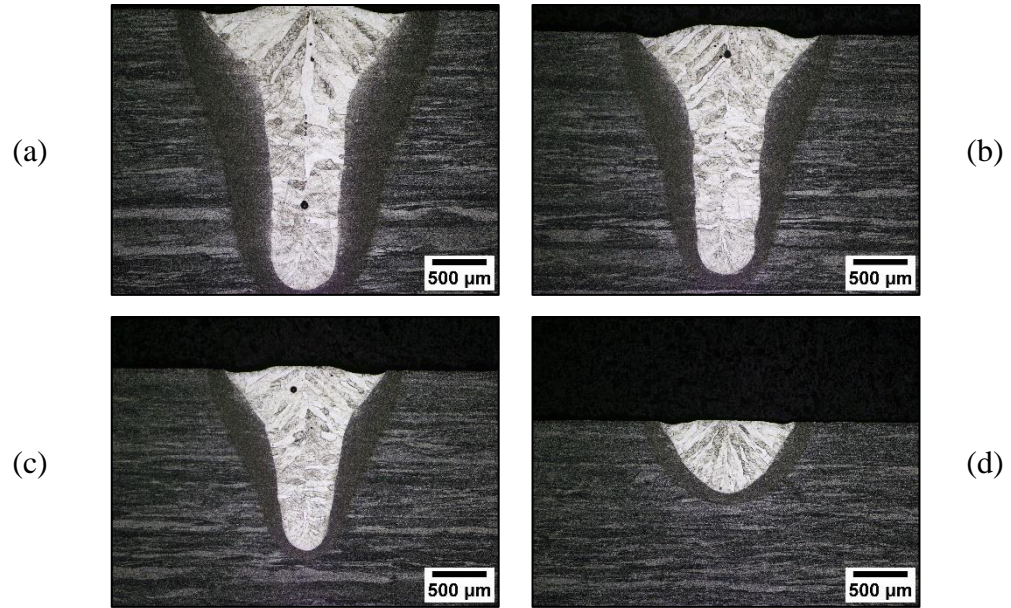


*Figure F.17. Ti-6Al-4V laser weld macrosections at 2000 W and travel speeds of 50 mm/s (a), 75 mm/s (b), 100 mm/s (c), and 150 mm/s (d).*

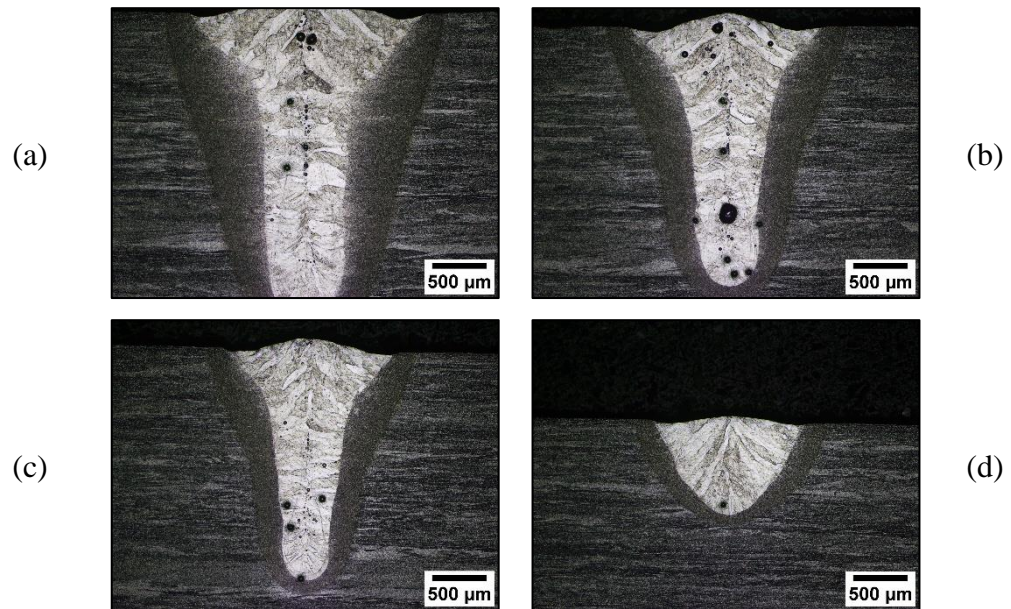


*Figure F.18. Ti-6Al-4V laser weld macrosections at 2400 W and travel speeds of 50 mm/s (a), 75 mm/s (b), 100 mm/s (c), and 150 mm/s (d).*

## Appendix G: Weld Geometry Data – Ti-6Al-4V

The measured cross-sectional data from all the Ti-6Al-4V weld parameters are shown in Figure G.1-Figure G.3. This data was extracted using the MATLAB<sup>®</sup> script provided in Appendix L: from macrophotos of cross-sections including those presented in Appendix F:. The fusion boundary length showed nearly an identical trend compared to the weld penetration. Also, the FWHM measurements and the centroid width measurements showed the same trends, but the centroid widths were consistently larger.

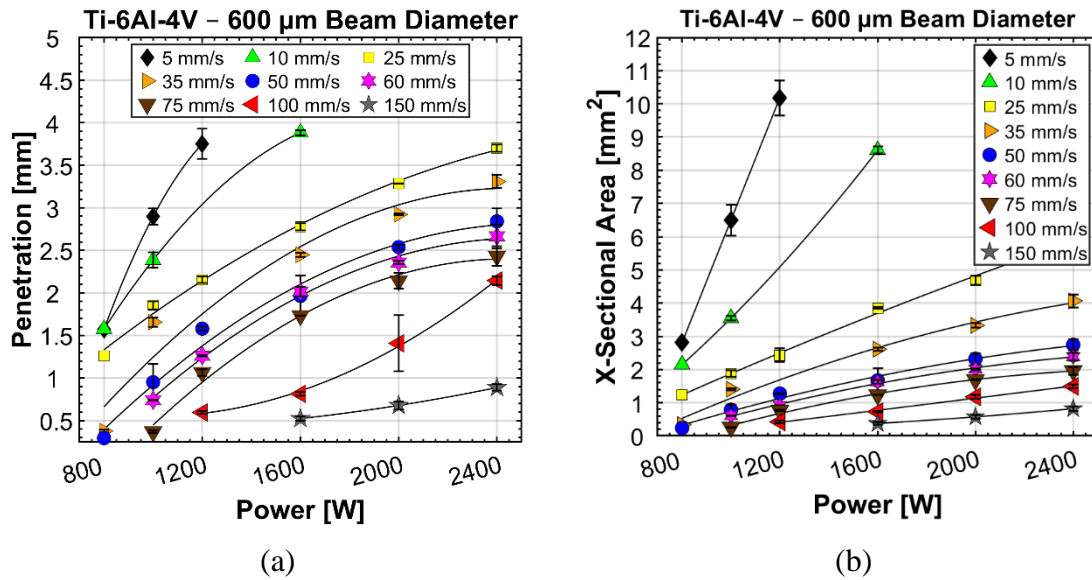


Figure G.1. Penetration (a) and transverse cross-sectional area (b) versus power for Ti-6Al-4V. All data except 800 W is from two separate welds.

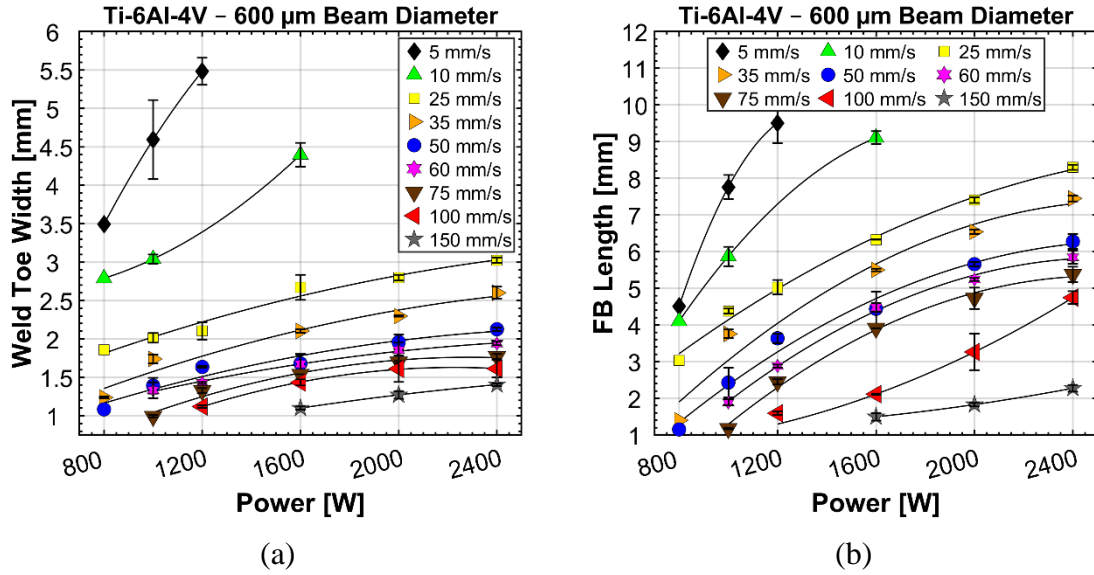


Figure G.2. Weld toe width (a) and fusion boundary length (b) versus power for Ti-6Al-4V. All data except 800 W is from two separate welds.

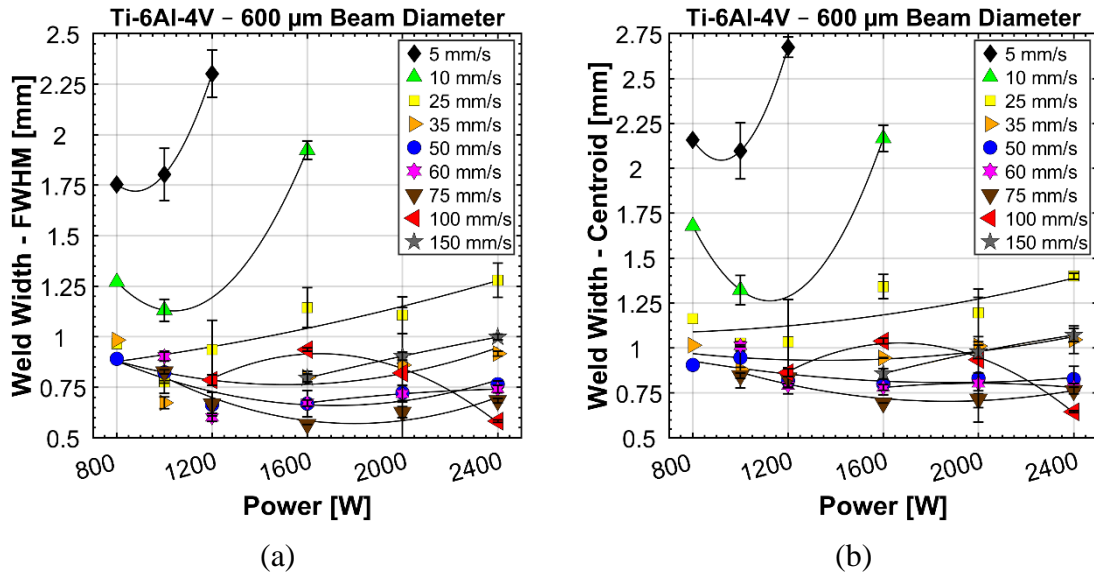


Figure G.3. Full-width-half-maximum (FWHM) weld width (a) and centroid weld width (b) versus power for Ti-6Al-4V. All data except 800 W is from two separate welds.

## Appendix H: Weld Geometry Data – All Stainless Steel Alloys

The data for the SS alloy welds at a constant travel speed of 50 mm/s is plotted in Figure H.1-Figure H.3. For penetration, cross-sectional area, weld toe width, and fusion boundary length, the results remain relatively consistent between each alloy. However, the FWHM and centroid weld widths are drastically different, specifically with the 2205 DSS. At the powers greater than 1600 W, the FWHM and centroid widths for 2205 DSS increased, even compared to the M54 alloy with similar Cr and Ni contents. This showed the influence the high nitrogen ( $\approx 0.15$  wt%) has on widening the vapor cavity and fusion zone in high aspect ratio welds.

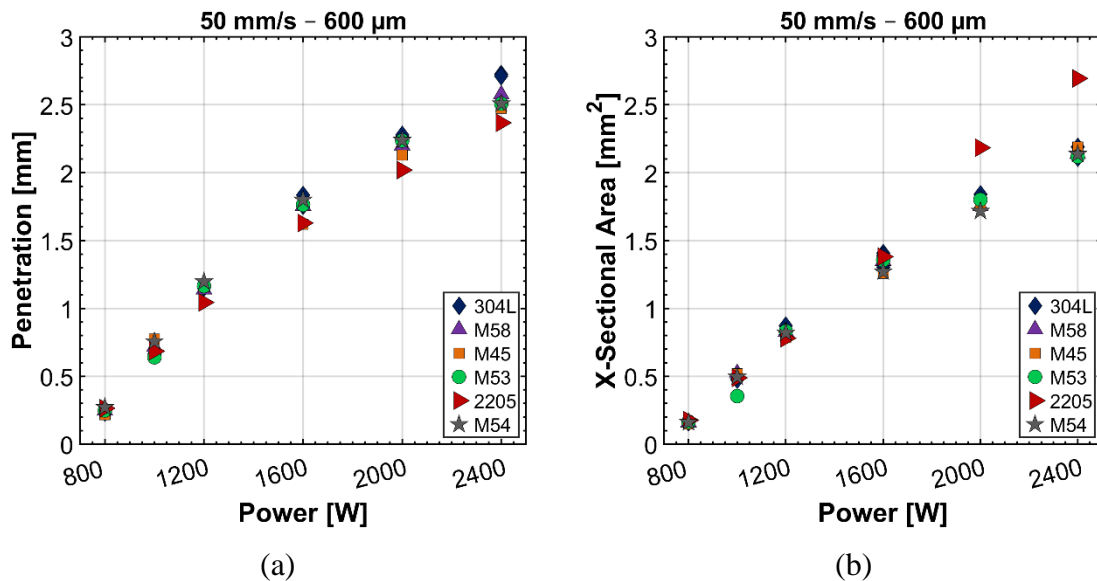
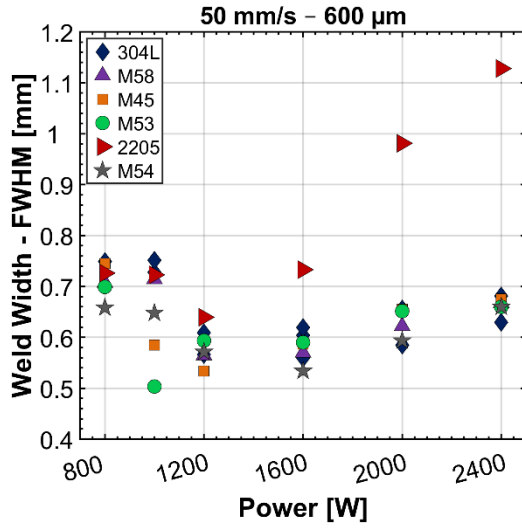
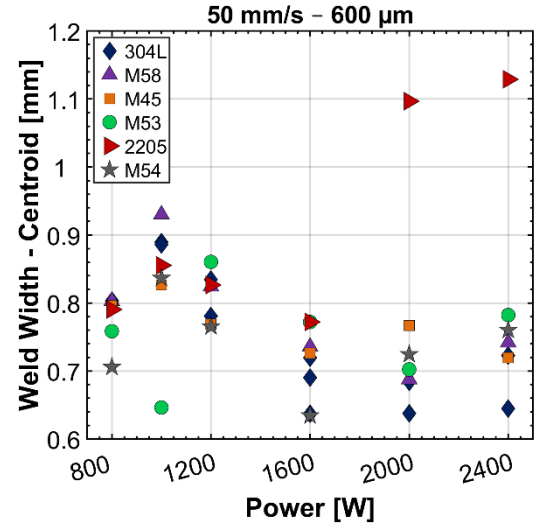


Figure H.1. Penetration (a) and cross-sectional area (b) versus power at 50 mm/s for all SS alloys.

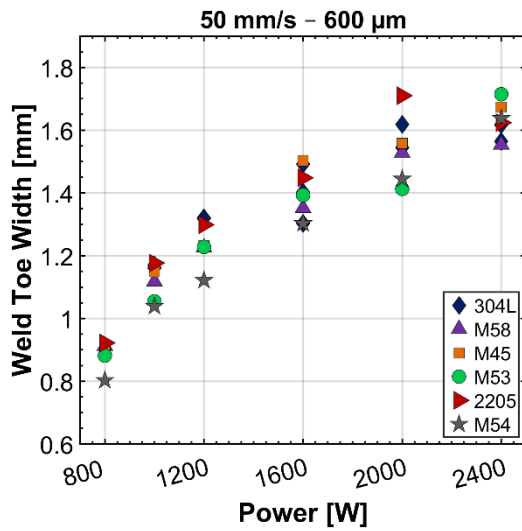


(a)

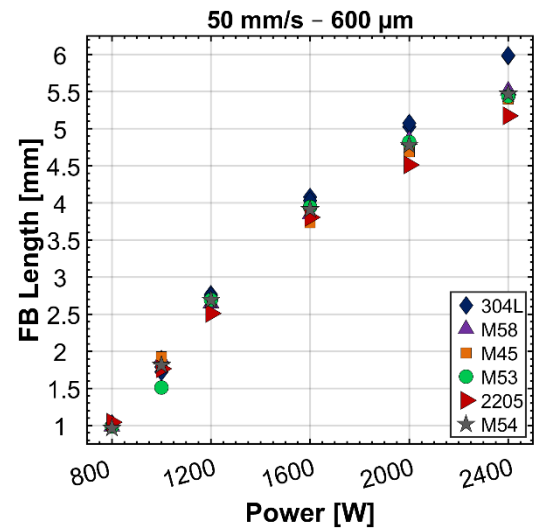


(b)

Figure H.2. Full-width-half-maximum (FWHM) weld width (a) and weld centroid width (b) versus power at 50 mm/s for all SS alloys.



(a)



(b)

Figure H.3. Weld toe width (a) and fusion boundary length (b) versus power at 50 mm/s for all SS alloys.

## Appendix I: Neural Network GUI and Results

Figure I.1 shows the developed graphical user interface for easily performing weld feature prediction with the data extracted from the developed neural networks. All the data measured in the results section was modeled through individual models and is displayed after the user makes a material, power, and travel speed selection. The beam diameter, beam angle, and shielding gas are not changeable but included to eventually become populated with data. A button is also included to toggle the experimental data onto the predicted penetration versus travel speed. However, experimental data only exists for certain weld parameters within the model. If the experimental data is not available, the user is notified within the plot. Figure I.2-Figure I.7 show the NN results and experimental data for penetration (Figure I.2 and Figure I.3), weld toe width (Figure I.4 and Figure I.5), and weld centroid width (Figure I.6 and Figure I.7).

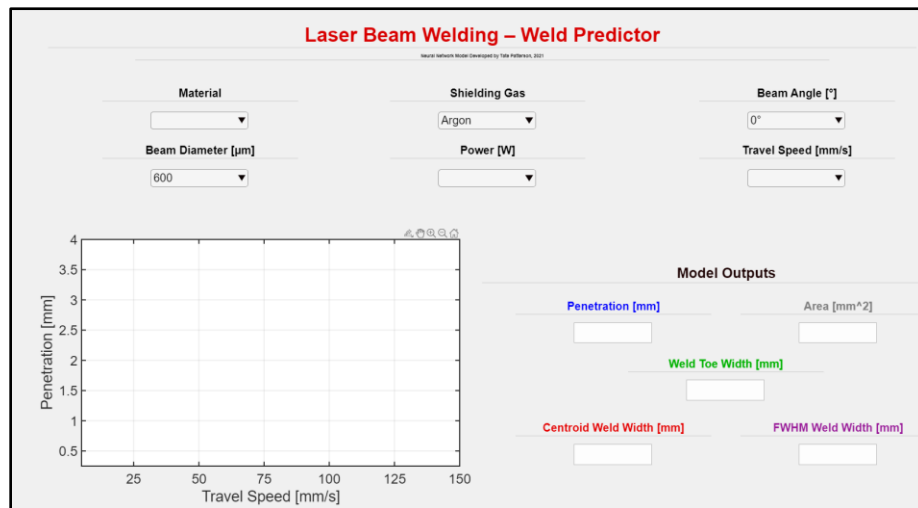
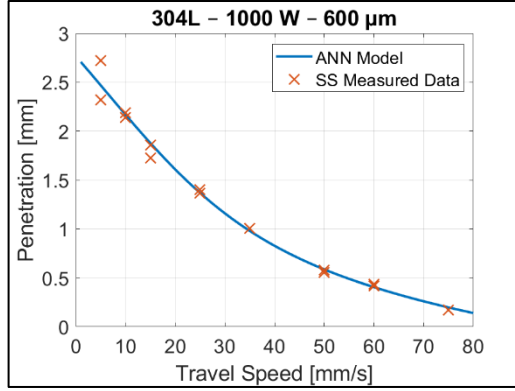
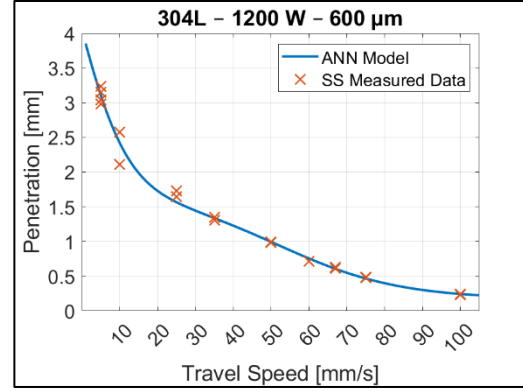


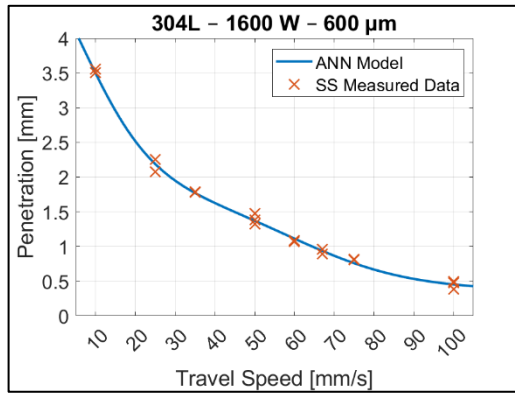
Figure I.1. Graphical user interface for the NN algorithm.



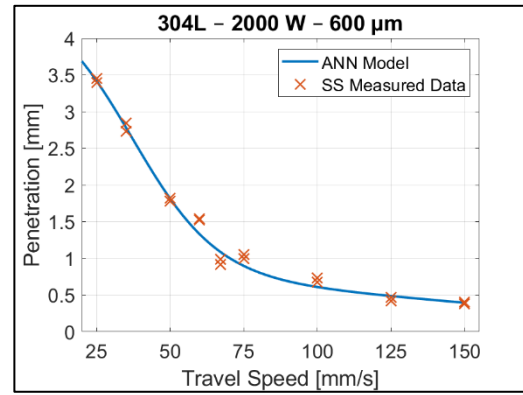
(a)



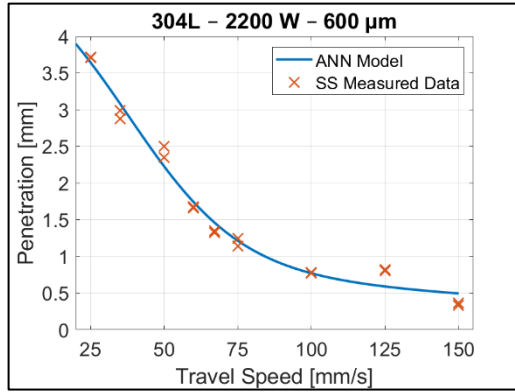
(b)



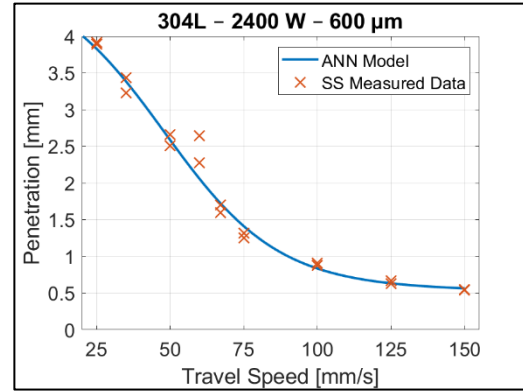
(c)



(d)

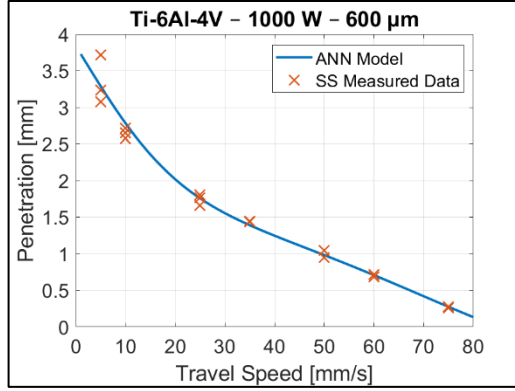


(e)

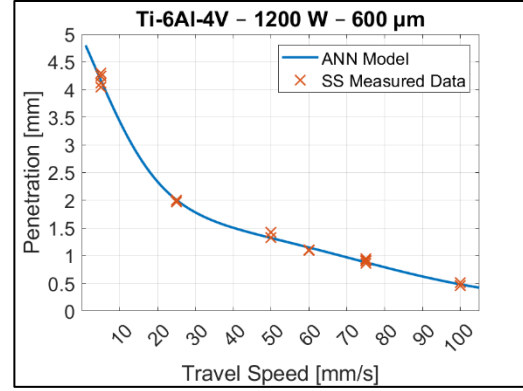


(f)

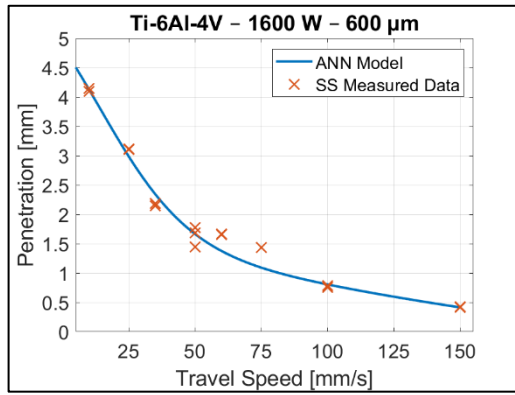
Figure I.2. ANN algorithm predicted penetration results for 304L SS at 1000 W (a), 1200 W (b), 1600 W (c), 2000 W (d), 2200 W (e), and 2400 W (f).



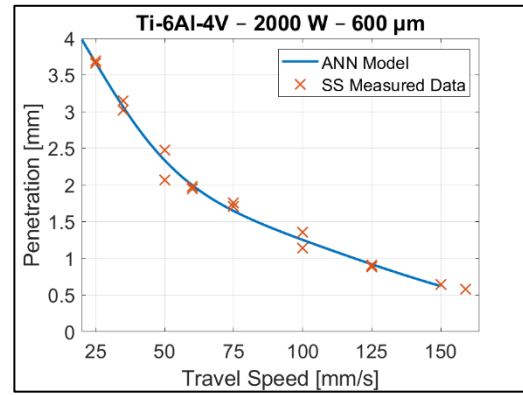
(a)



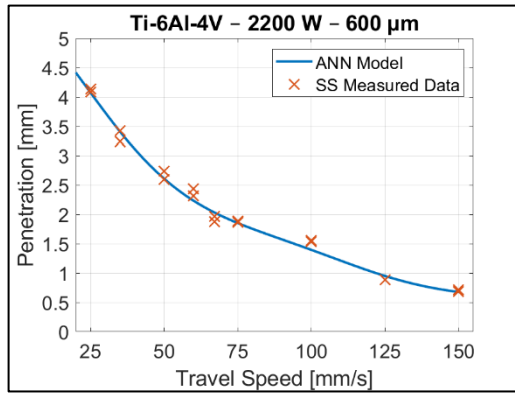
(b)



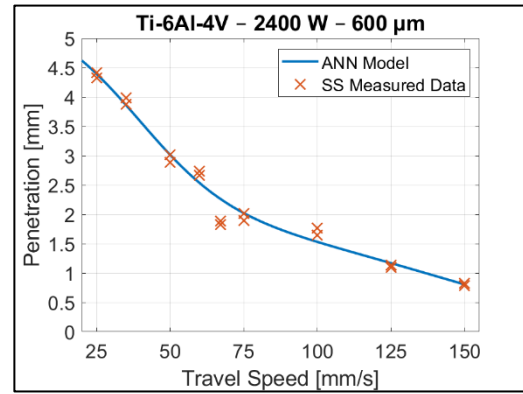
(c)



(d)

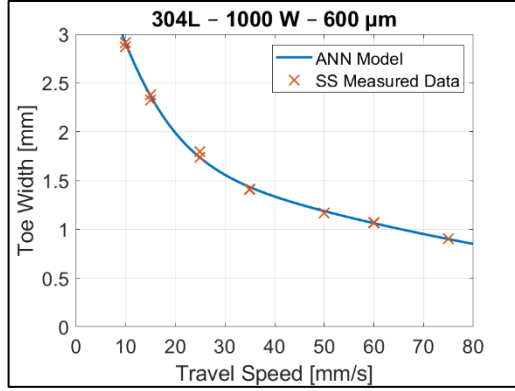


(e)

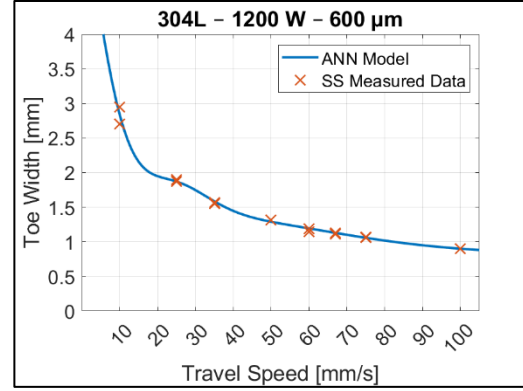


(f)

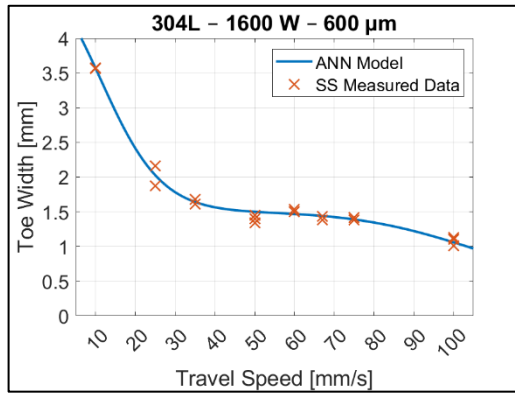
Figure I.3. ANN algorithm predicted penetration results for Ti-6Al-4V at 1000 W (a), 1200 W (b), 1600 W (c), 2000 W (d), 2200 W (e), and 2400 W (f).



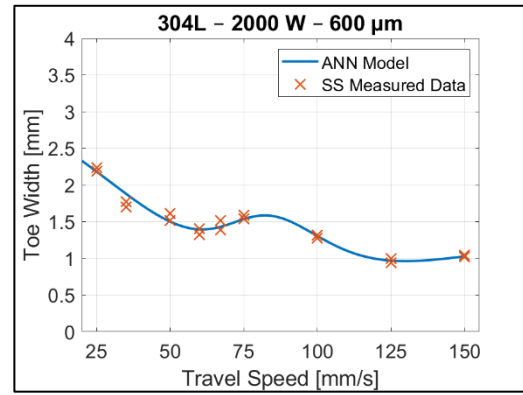
(a)



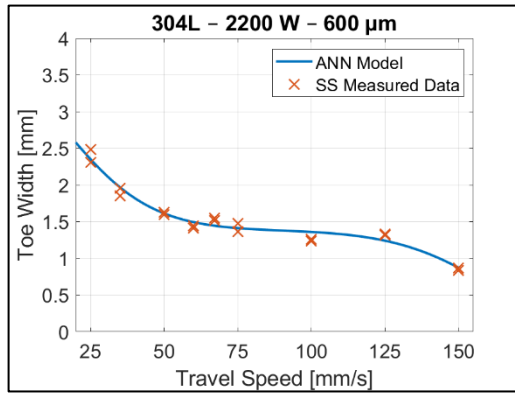
(b)



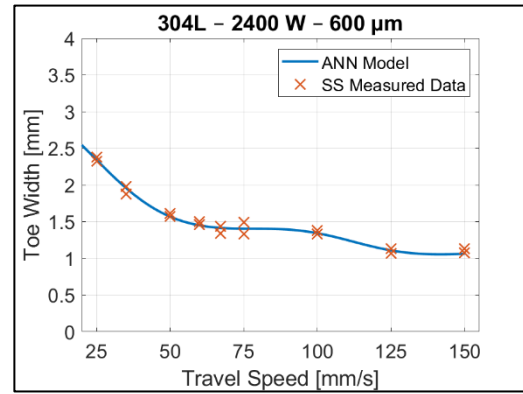
(c)



(d)

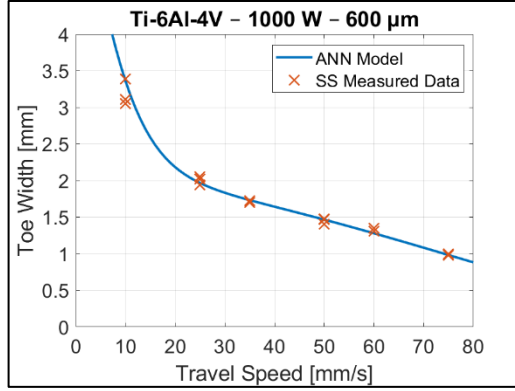


(e)

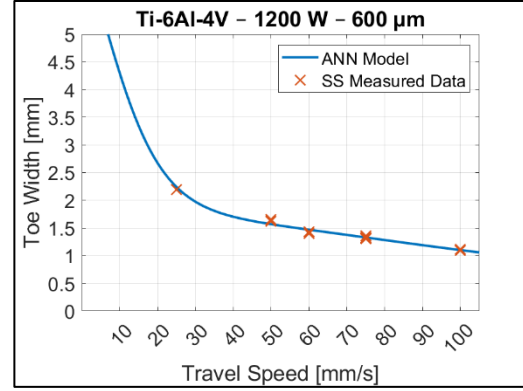


(f)

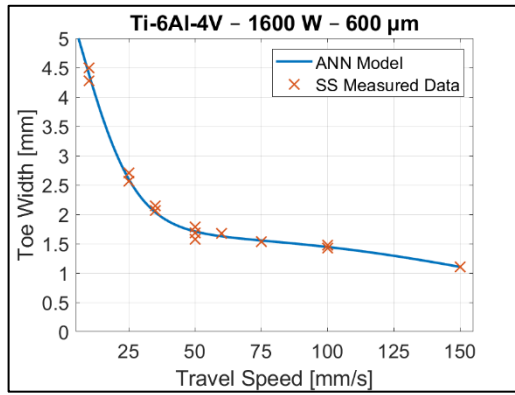
Figure I.4. ANN algorithm predicted toe width results for 304L SS at 1000 W (a), 1200 W (b), 1600 W (c), 2000 W (d), 2200 W (e), and 2400 W (f).



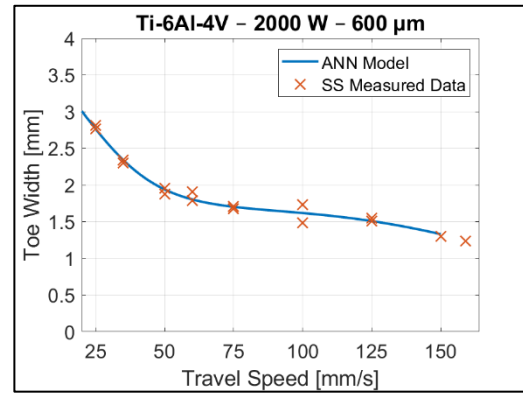
(a)



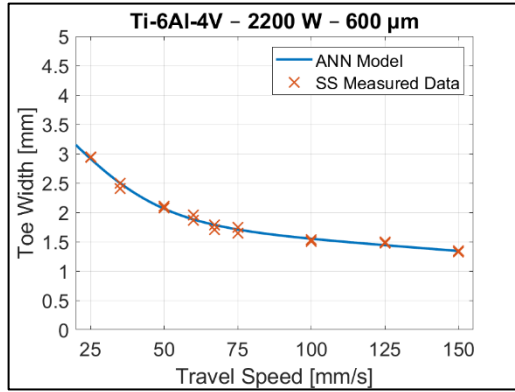
(b)



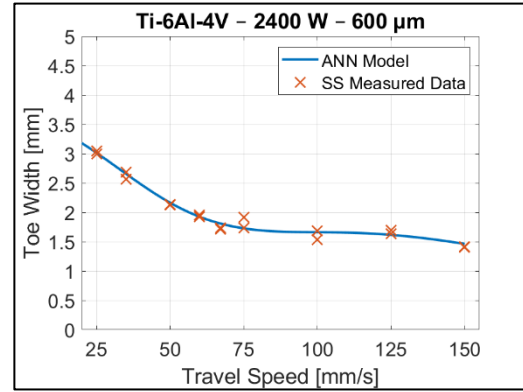
(c)



(d)

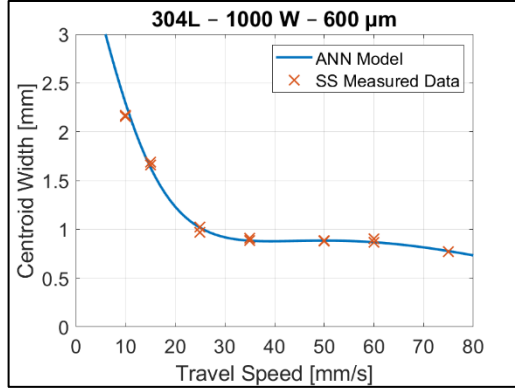


(e)

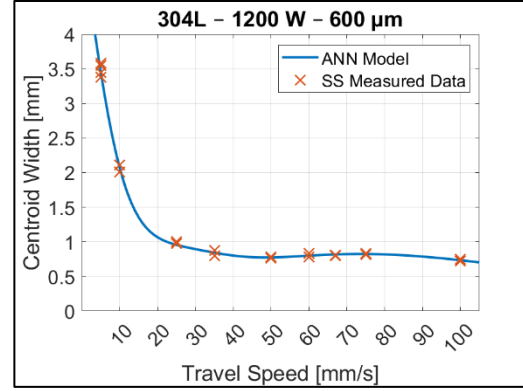


(f)

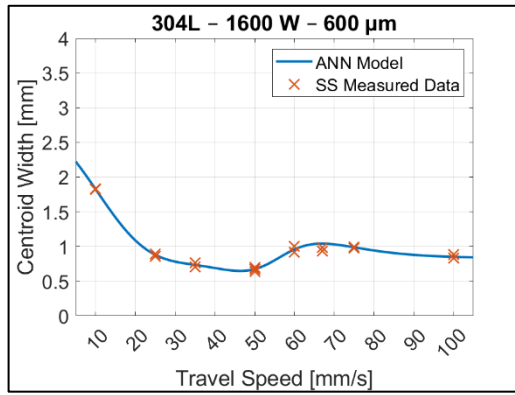
Figure I.5. ANN algorithm predicted toe width results for Ti-6Al-4V at 1000 W (a), 1200 W (b), 1600 W (c), 2000 W (d), 2200 W (e), and 2400 W (f).



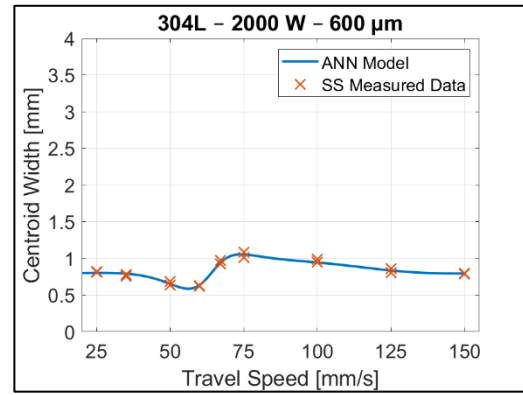
(a)



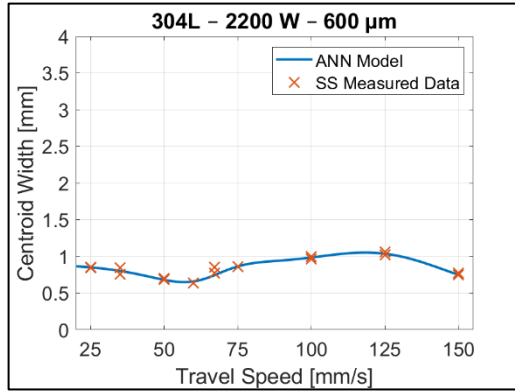
(b)



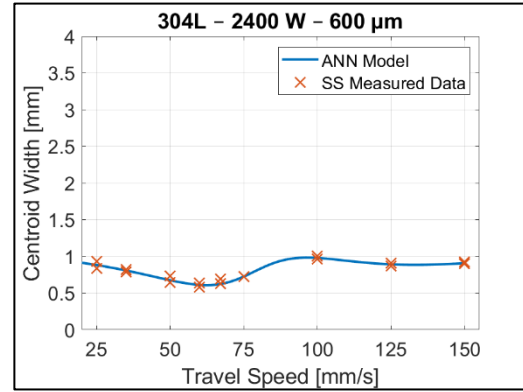
(c)



(d)

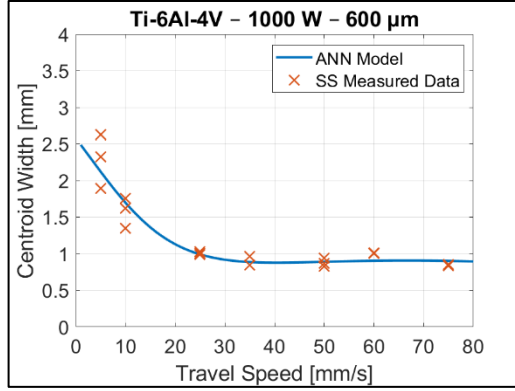


(e)

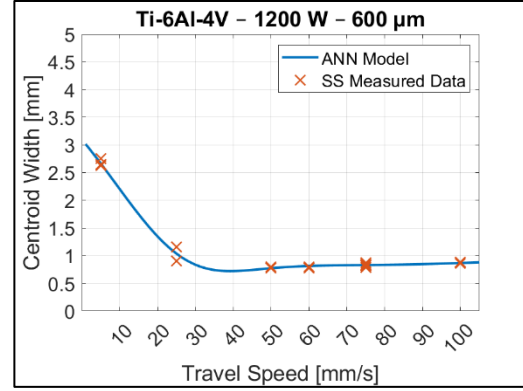


(f)

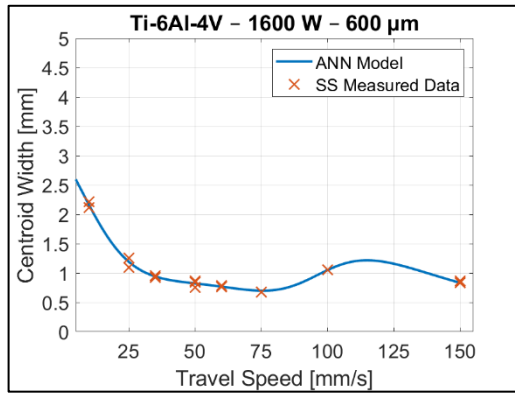
Figure I.6. ANN algorithm predicted centroid width results for 304L SS at 1000 W (a), 1200 W (b), 1600 W (c), 2000 W (d), 2200 W (e), and 2400 W (f).



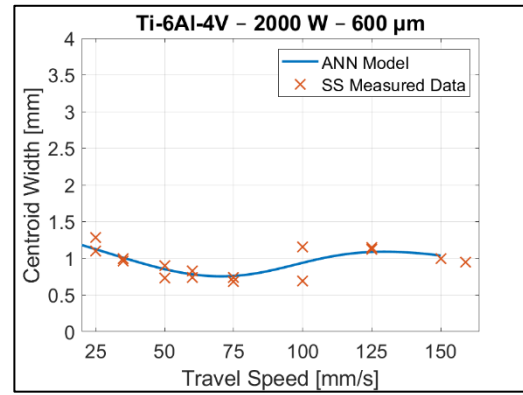
(a)



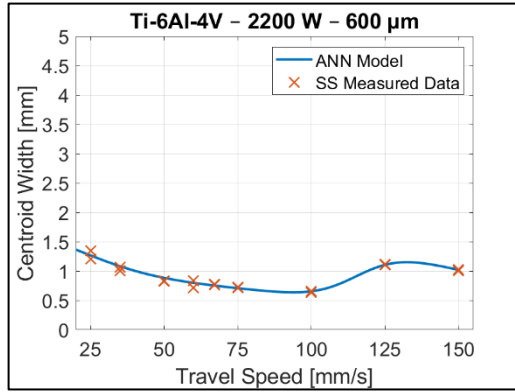
(b)



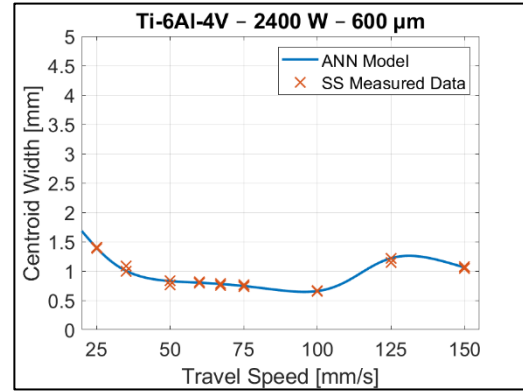
(c)



(d)



(e)



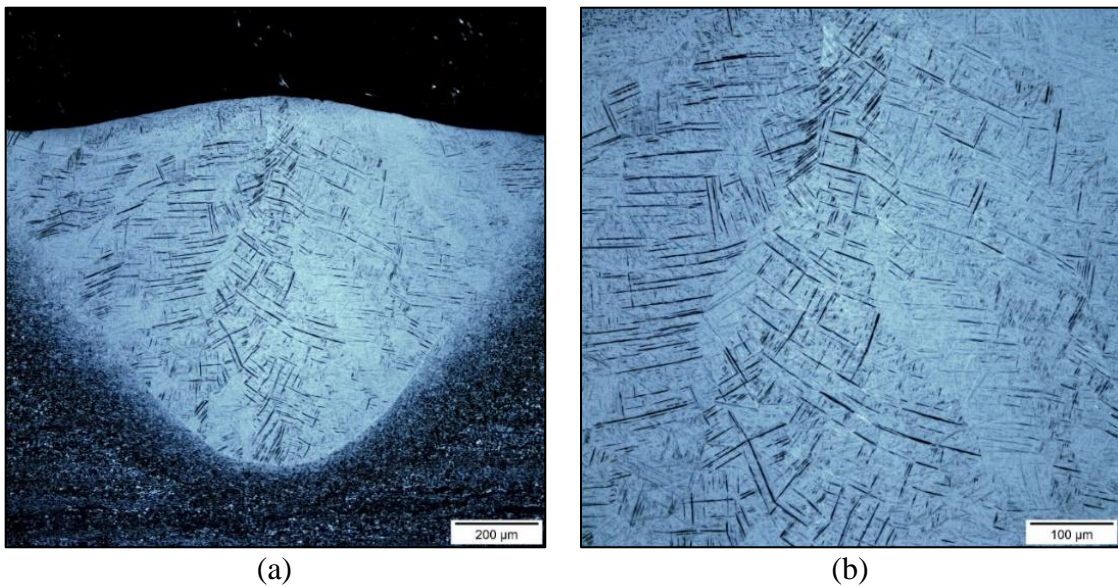
(f)

Figure I.7. ANN algorithm predicted centroid width results for Ti-6Al-4V at 1000 W (a), 1200 W (b), 1600 W (c), 2000 W (d), and 2400 W (e).

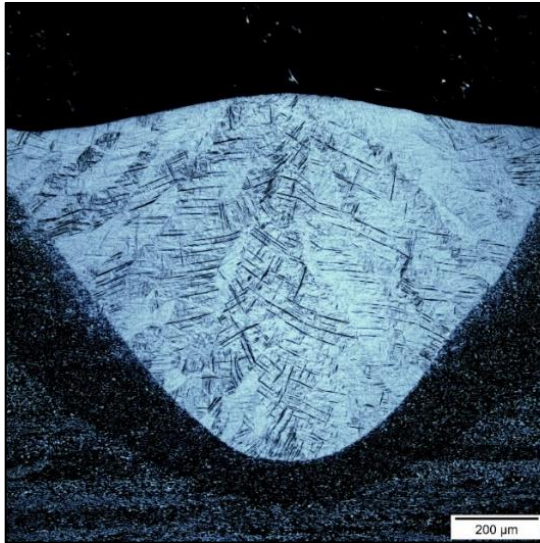
## Appendix J: Ti-6Al-4V Prior Beta Grain Boundary Delineation Analysis

### J.1 Etchant Attempts

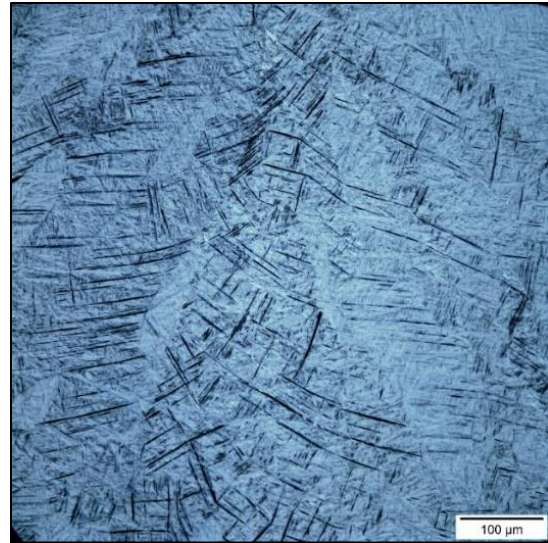
Figure J.1-Figure J.18 show the results for the chemical etching attempts to reveal prior beta grain boundaries using light optical microscopy. Unless specifically noted, all micrographs are captured using brightfield illumination and DIC.



*Figure J.1. Ti-6Al-4V LB weld etched with Kroll's (2 mL HF, 4 mL HNO<sub>3</sub>, 94 mL H<sub>2</sub>O). Immersed for  $\approx$ 20 seconds: a) 100X, b) 200X.*

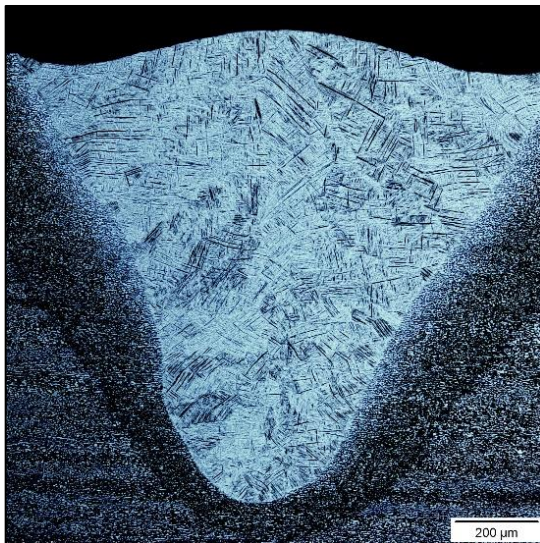


(a)

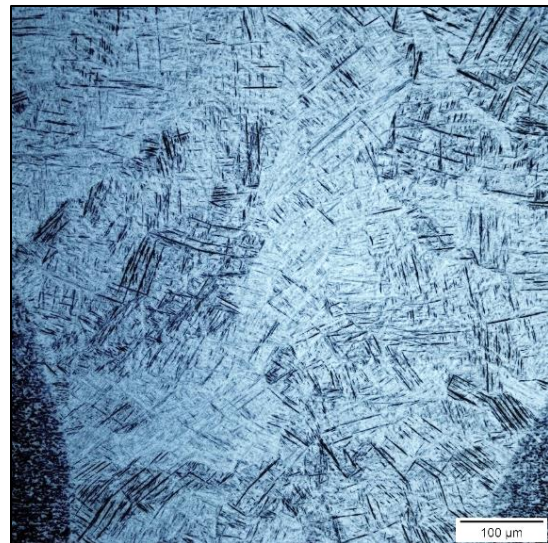


(b)

*Figure J.2. Ti-6Al-4V LB weld etched with Kroll's Etch (2 mL HF, 4 mL HNO<sub>3</sub>, 94 mL H<sub>2</sub>O). Immersed for ≈2 minutes: a) 100X, b) 200X.*



(a)



(b)

*Figure J.3. Ti-6Al-4V LB weld etched with Keller's (2 mL HF, 3mL HCl, 5 mL HNO<sub>3</sub>, 190 mL H<sub>2</sub>O). Immersed for ≈1 minute: a) 100X, b) 200X.*

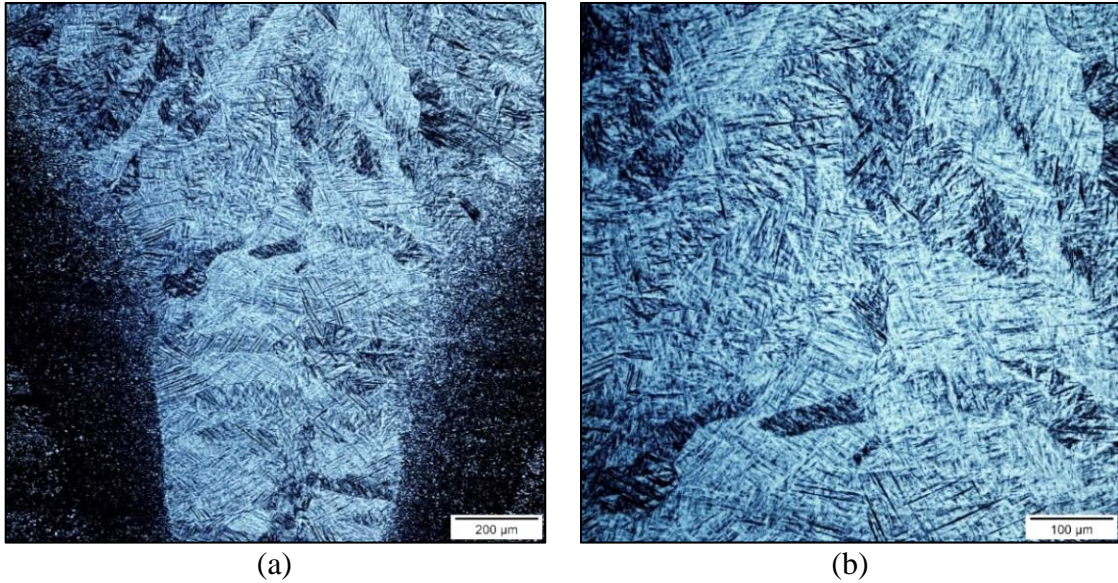


*Figure J.4. Ti-6Al-4V LB weld etched with Keller's Etch (2 mL HF, 3mL HCl, 5 mL HNO<sub>3</sub>, 190 mL H<sub>2</sub>O). Immersed for ≈2 minutes: a) 100X, b) 200X.*

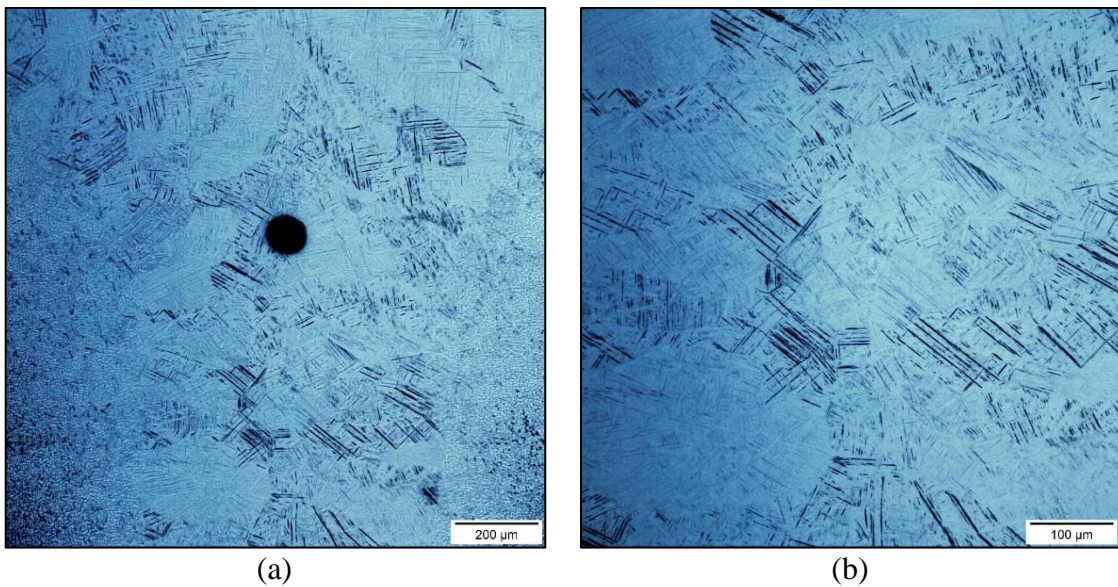


*Figure J.5. Ti-6Al-4V LB weld etched with 2 mL HF – 10 mL 30% H<sub>2</sub>O<sub>2</sub> – 88 mL H<sub>2</sub>O. Immersed for ≈20 seconds: a) 100X, b) 200X.*

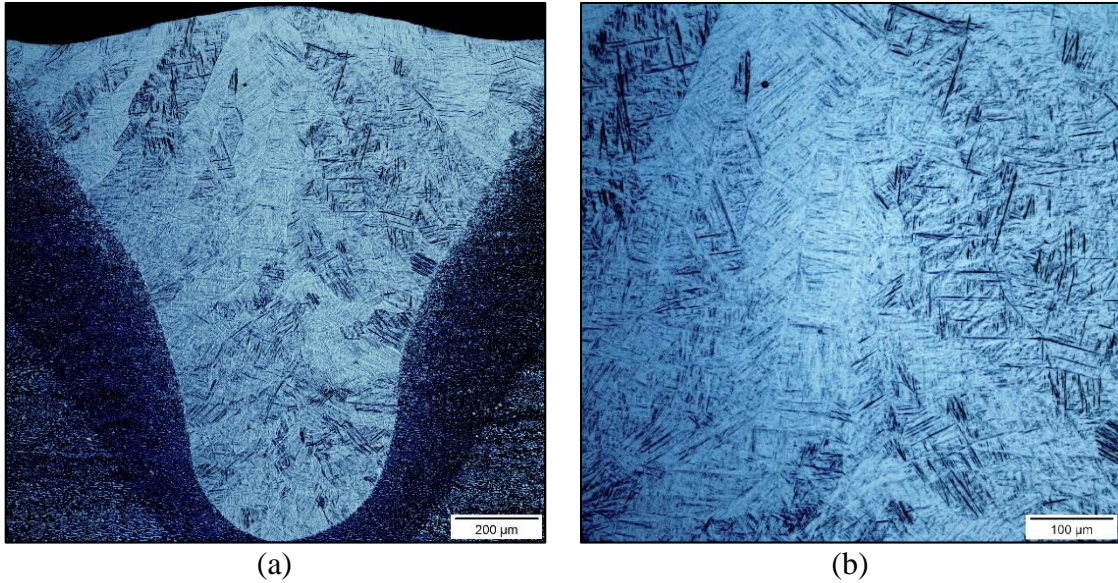


*Figure J.6. Ti-6Al-4V LB weld etched with 2 mL HF – 10 mL 30% H<sub>2</sub>O<sub>2</sub> – 88 mL H<sub>2</sub>O. Immersed for ≈2 minutes: a) 100 X, b) 200X.*

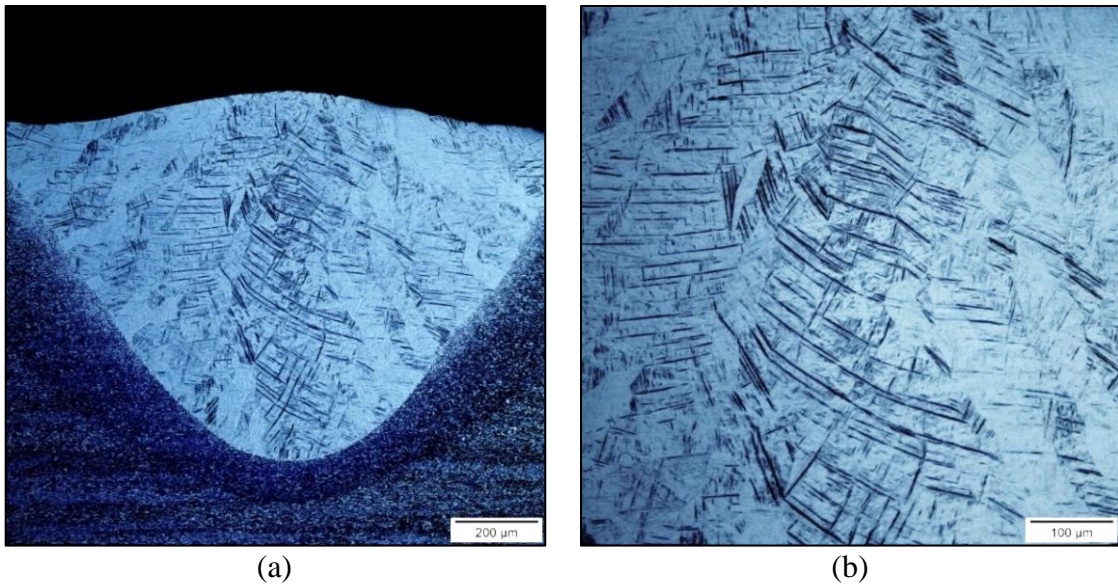


*Figure J.7. Ti-6Al-4V LB weld etched with 2 mL HF – 10 mL 30% H<sub>2</sub>O<sub>2</sub> – 10 mL HCl – 88 mL H<sub>2</sub>O. Immersed for ≈2 minutes: a) 100X, b) 200X.*

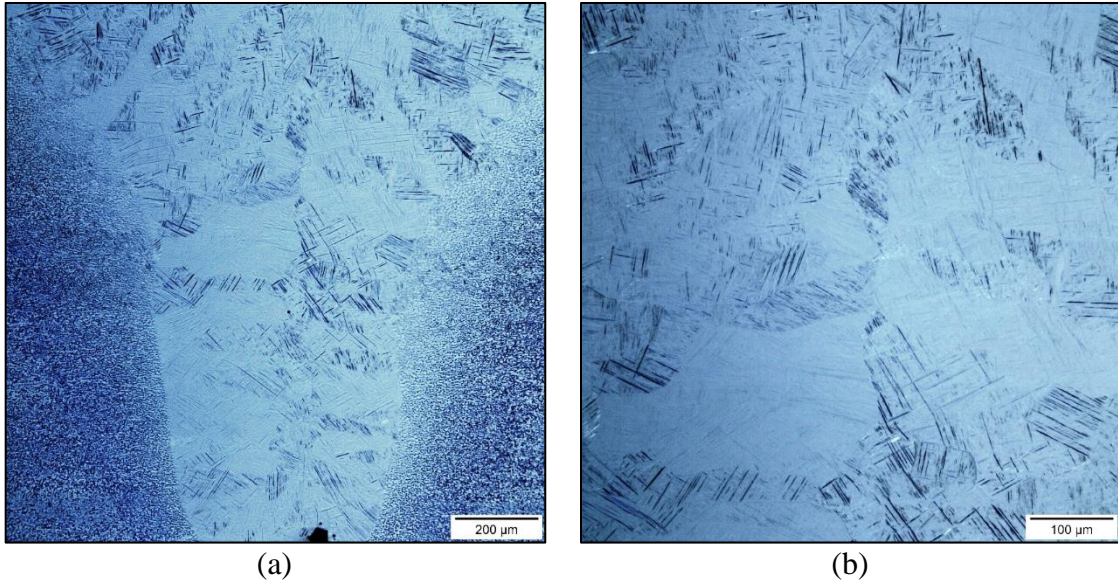


*Figure J.8. Ti-6Al-4V LB weld etched with 3 mL HF – 30 mL HNO<sub>3</sub> – 10 mL HCl – 88 mL H<sub>2</sub>O. Immersed for ≈20 seconds: a) 100X, b) 200X.*

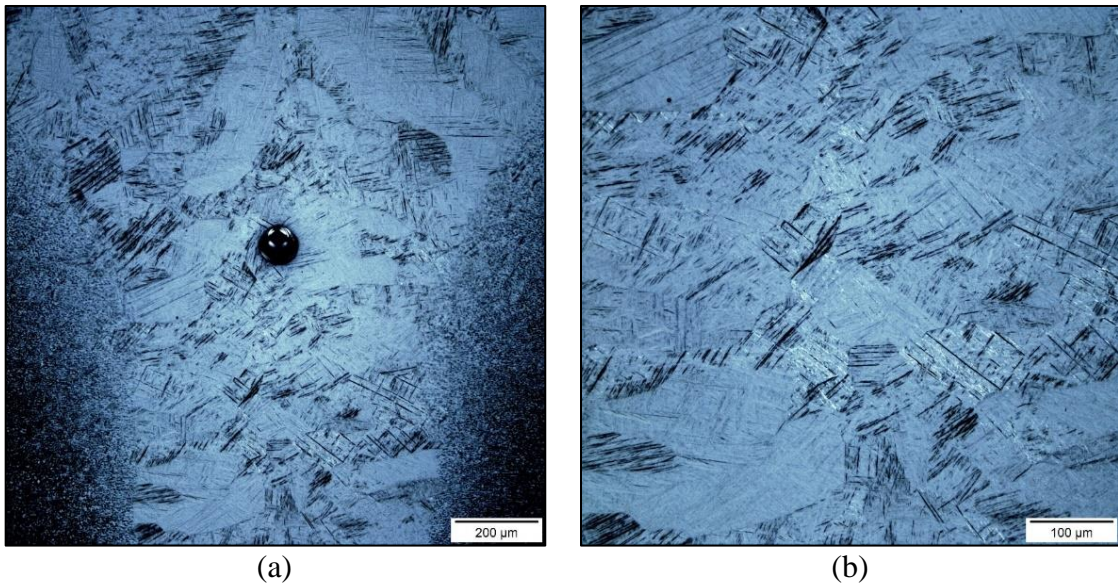


*Figure J.9. Ti-6Al-4V LB weld etched with 10 mL HF – 15 mL HNO<sub>3</sub> – 75 mL H<sub>2</sub>O. Immersed for ≈20 seconds: a) 100X, b) 200X.*

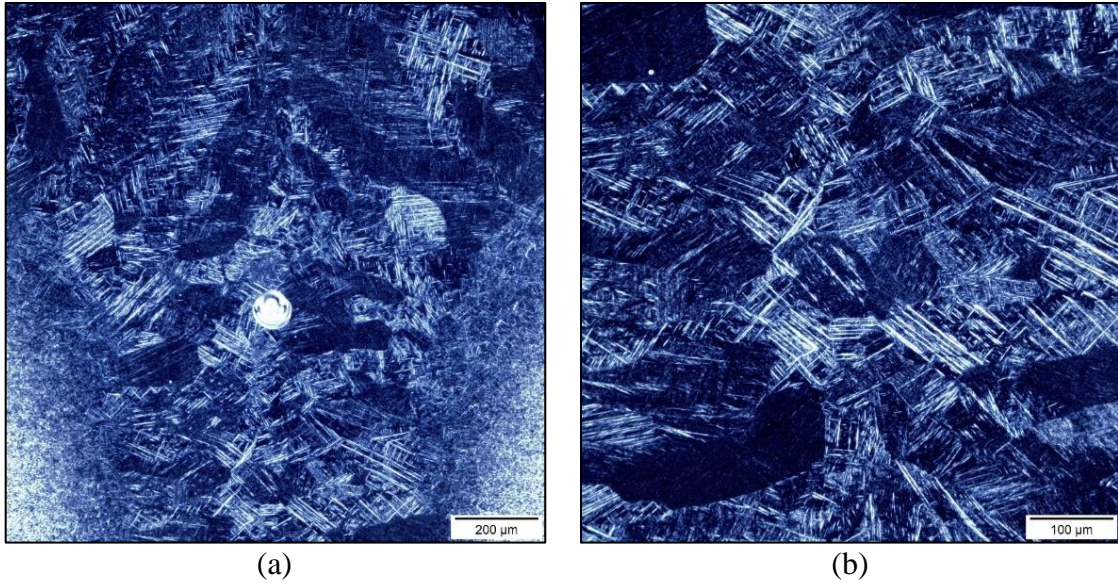


*Figure J.10. Ti-6Al-4V LB weld etched with 10 mL HF – 15 mL HNO<sub>3</sub> – 75 mL H<sub>2</sub>O. Immersed for ≈20 seconds. Darkfield photomicrographs: a) 100X, b) 200X.*

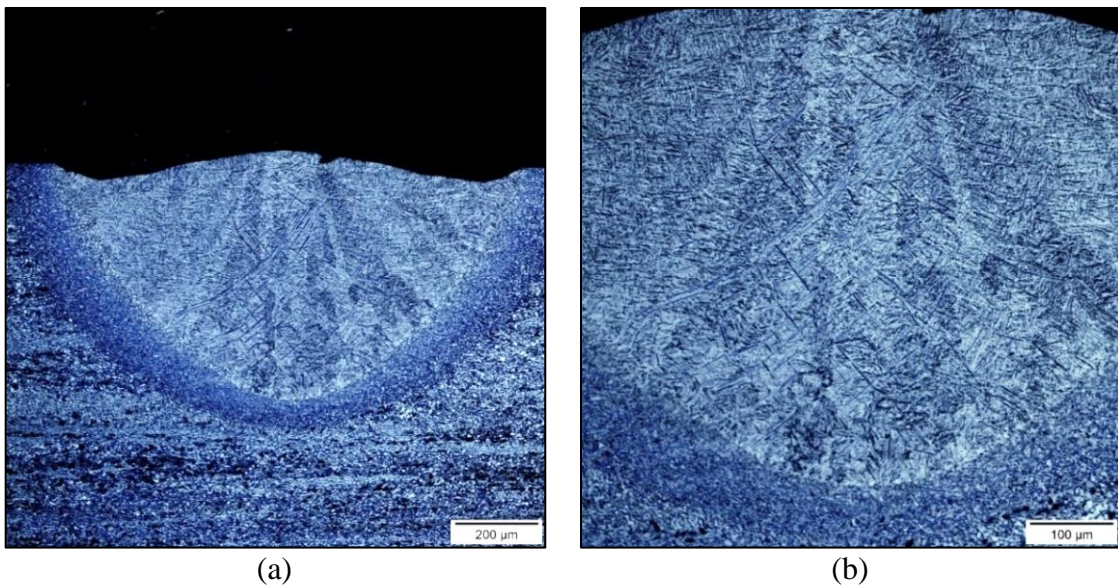


*Figure J.11. Ti-6Al-4V LB weld etched with 2 mL HF – 50 mL HCl – 48 mL H<sub>2</sub>O. Immersed for ≈20 seconds: a) 100X, b) 200X.*

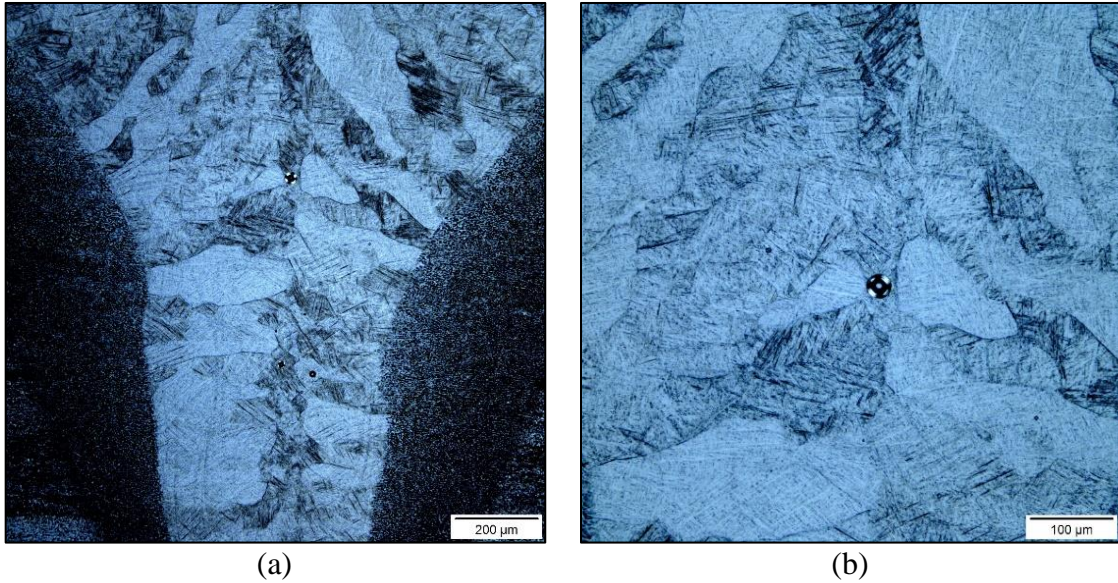


*Figure J.12. Ti-6Al-4V LB weld etched with 10 mL HF – 40 mL HCl – 50 mL H<sub>2</sub>O. Immersed for  $\approx 1$  minute: a) 100X, b) 200X.*

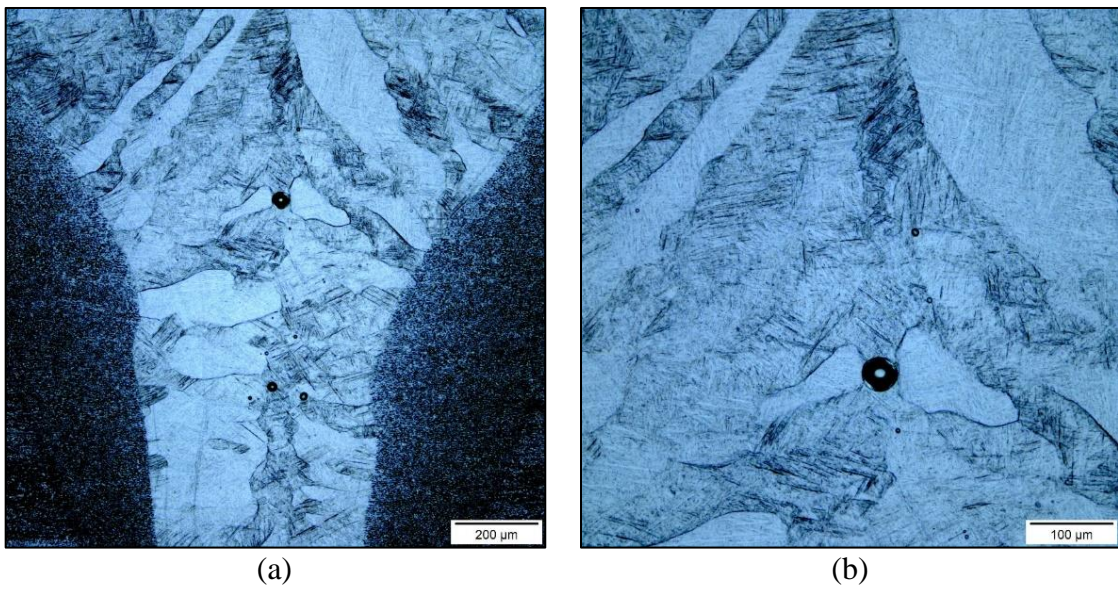


*Figure J.13. Ti-6Al-4V LB weld etched with 20 mL HF – 40 mL HCl – 50 mL H<sub>2</sub>O. Immersed for  $\approx 1$  minute: a) 100X, b) 200X.*

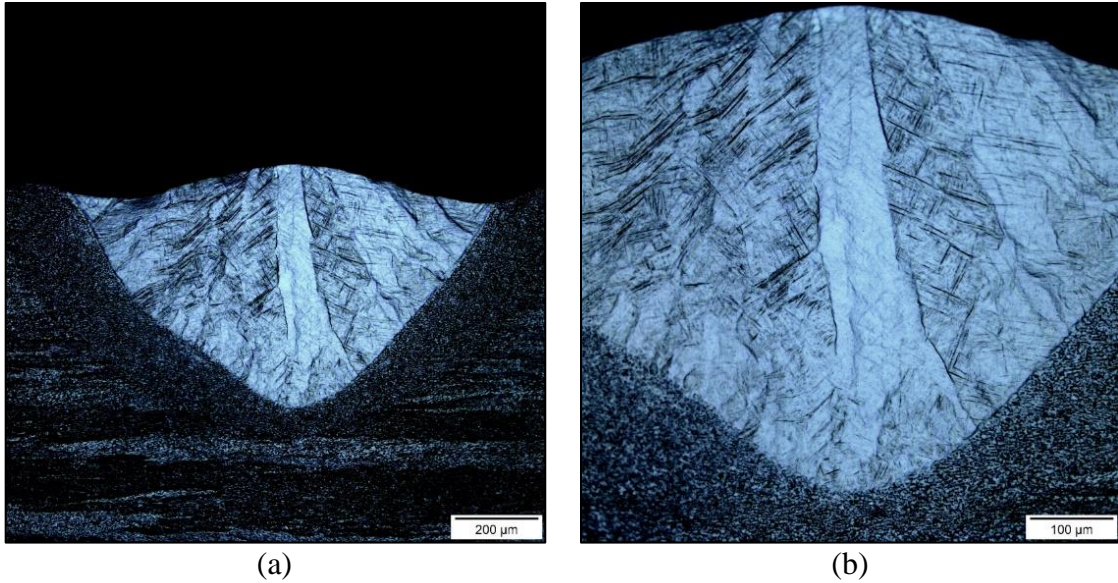


*Figure J.14. Ti-6Al-4V LB weld etched with 20 mL HF – 40 mL HCl – 40 mL H<sub>2</sub>O. Immersed for  $\approx$ 5 minutes: a) 100X, b) 200X.*

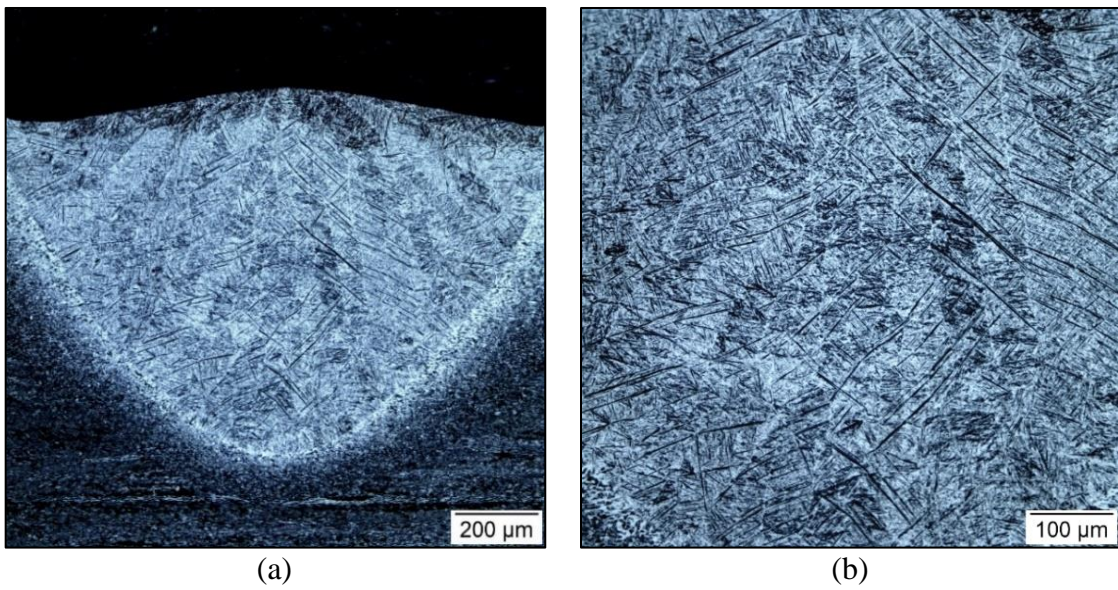


*Figure J.15. Ti-6Al-4V LB weld etched with 50 mL 10% oxalic – 2 mL HF – 48 mL H<sub>2</sub>O. Immersed for  $\approx$ 20 seconds: a) 100X, b) 200X.*

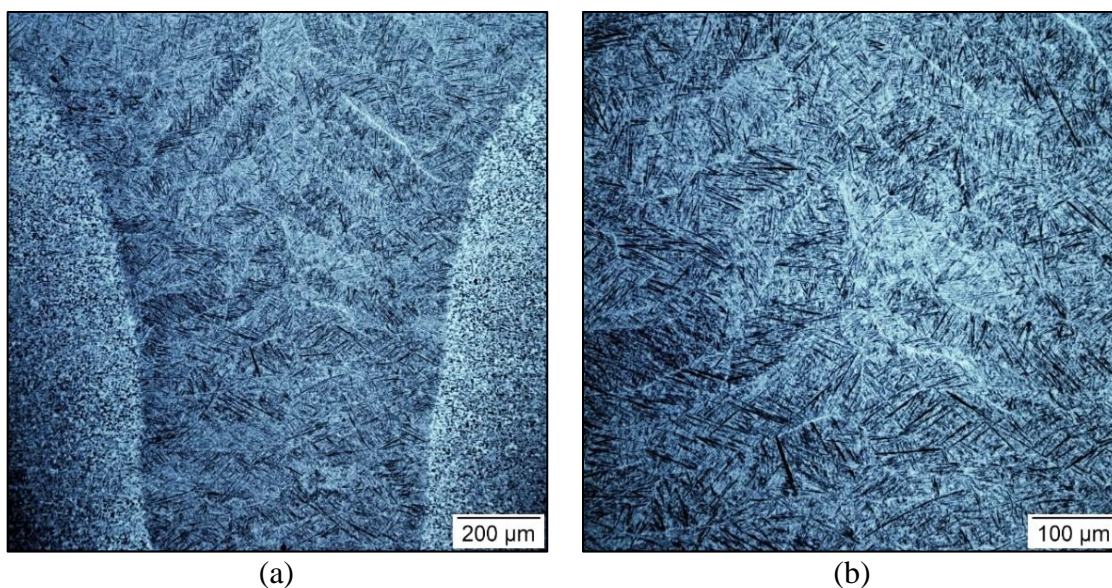


*Figure J.16. Ti-6Al-4V LB weld etched with 30 mL glycerin – 10 mL HF – 10 mL HNO<sub>3</sub>. Swabbed for  $\approx 20$  seconds: a) 100X, b) 200X.*

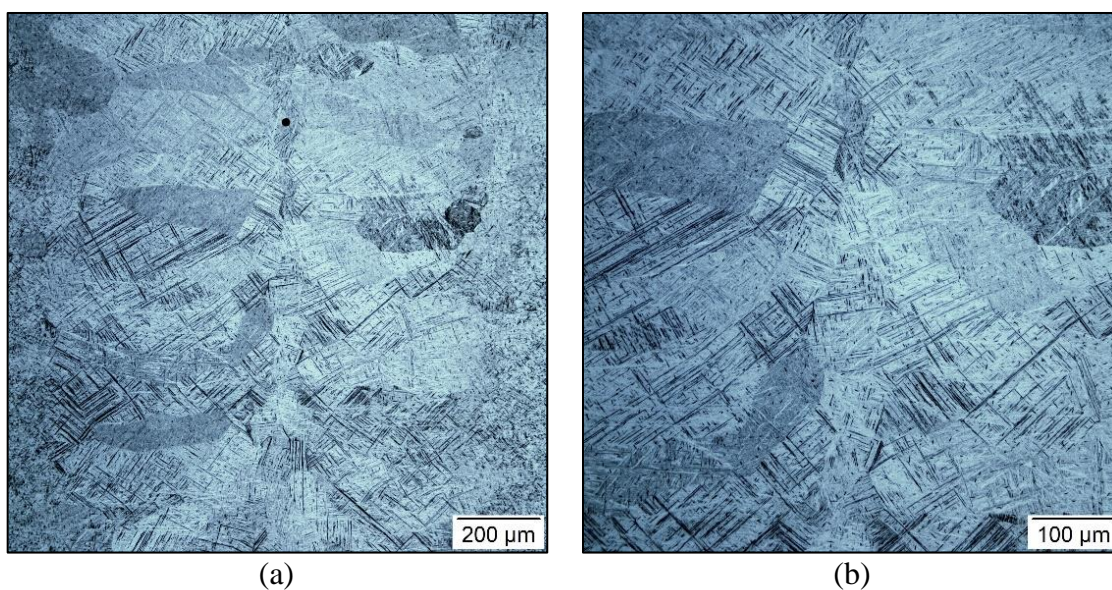


*Figure J.17. Ti-6Al-4V LB weld etched with boiling 4 mL HCl – 1 mL H<sub>2</sub>SO<sub>4</sub> – 95 mL H<sub>2</sub>O. Immersed for  $\approx 2$  minutes: a) 100X, b) 200X.*

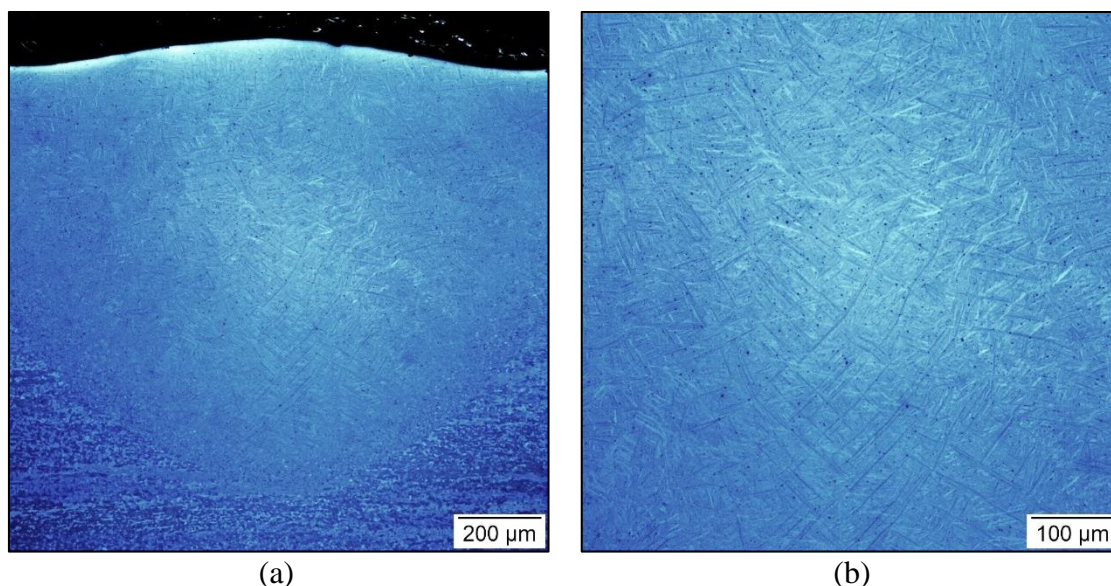


*Figure J.18. Ti-6Al-4V LB weld etched with boiling 50 mL 10% oxalic – 50 mL 40% KHO. Immersed for  $\approx 1$  minute: a) 100X, b) 200X.*

## **J.2 Heat Treatment Attempts**

Figure J.19-Figure J.24 show the initial attempts to preferentially nucleate beta at the PBGBs. The hope was that the PBGB would form a network of beta and become more distinguishable. These tests were performed by encasing small ( $\approx 5 \times 5 \times 2.5 \text{ mm}^3$ ) weld sections in a quartz tube to prevent oxidation and placing room temperature samples in a furnace preheated to  $900^\circ\text{C}$  for 1, 5, and 10 minutes. All samples were air-cooled (while encased in quartz) after soaking for each duration. The longer etch times seemed to reveal greater contrast of the PBGs. As with the as-welded condition, this is assumed to be caused by longer chemical attack providing greater surface relief and topography that is accentuated with the use of DIC LOM.

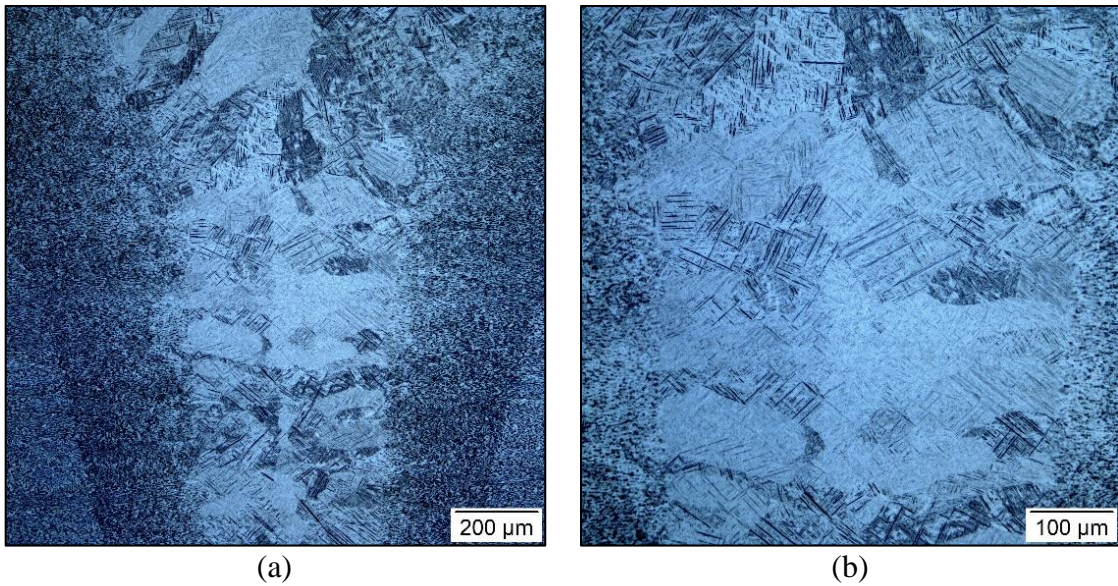


*Figure J.19. Ti-6Al-4V LB weld heat treated by placing in 900°C furnace for 1 minute and free cooled. Kroll's etch. Immersed for ≈20 seconds: a) 100X, b) 200X*

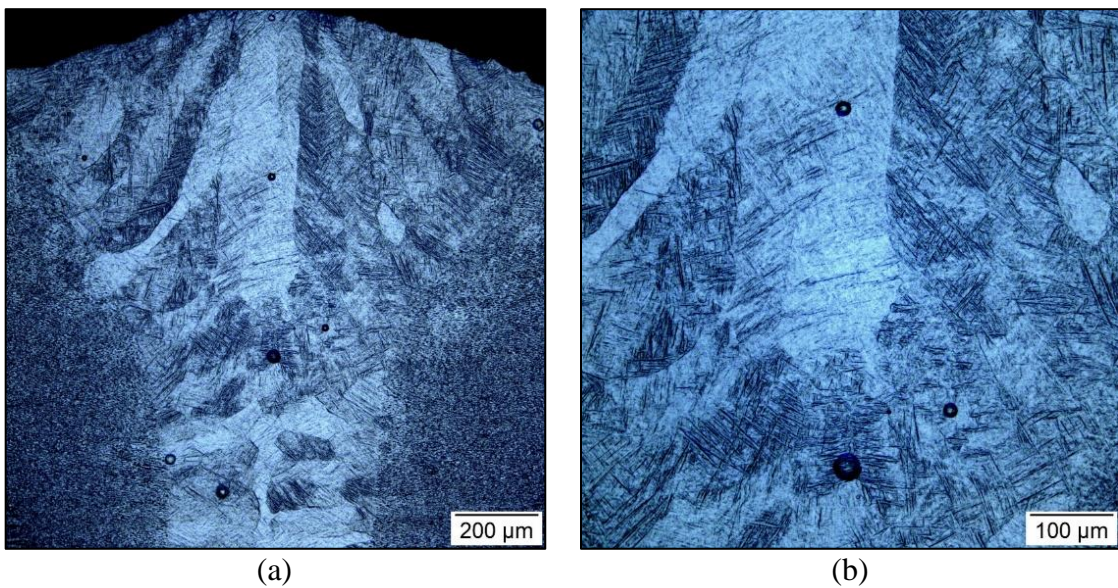


*Figure J.20. Ti-6Al-4V LB weld heat treated by placing in 900°C furnace for 1 minute and free cooled. Kroll's etch. Immersed for ≈1 minute: a) 100X, b) 200X*

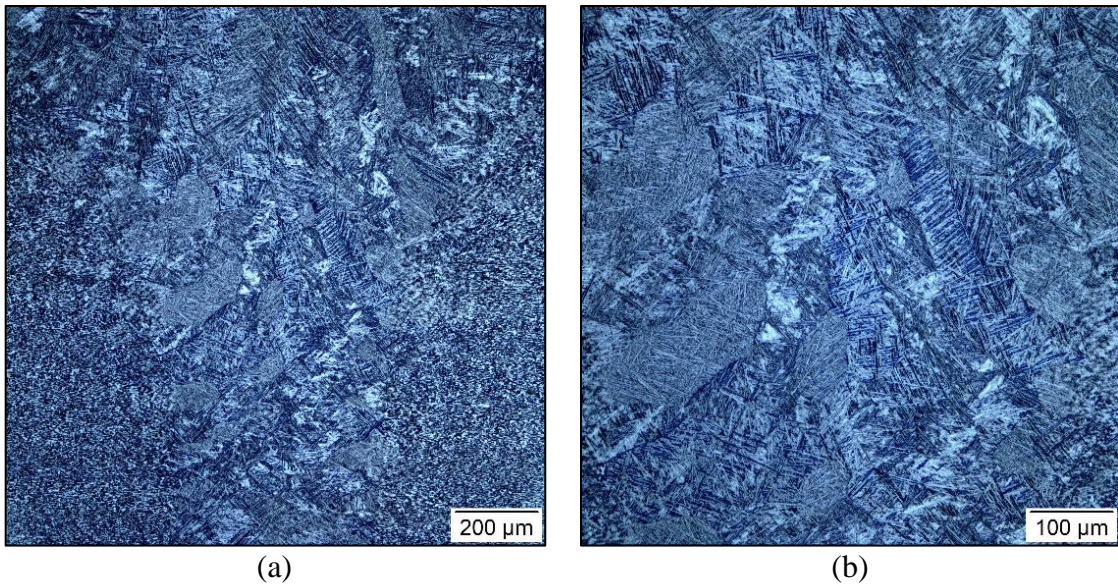


*Figure J.21. Ti-6Al-4V LB weld heat treated by placing in 900°C furnace for 5 minutes and free cooled. Kroll's etch. Immersed for  $\approx 20$  seconds: a) 100X, b) 200X*

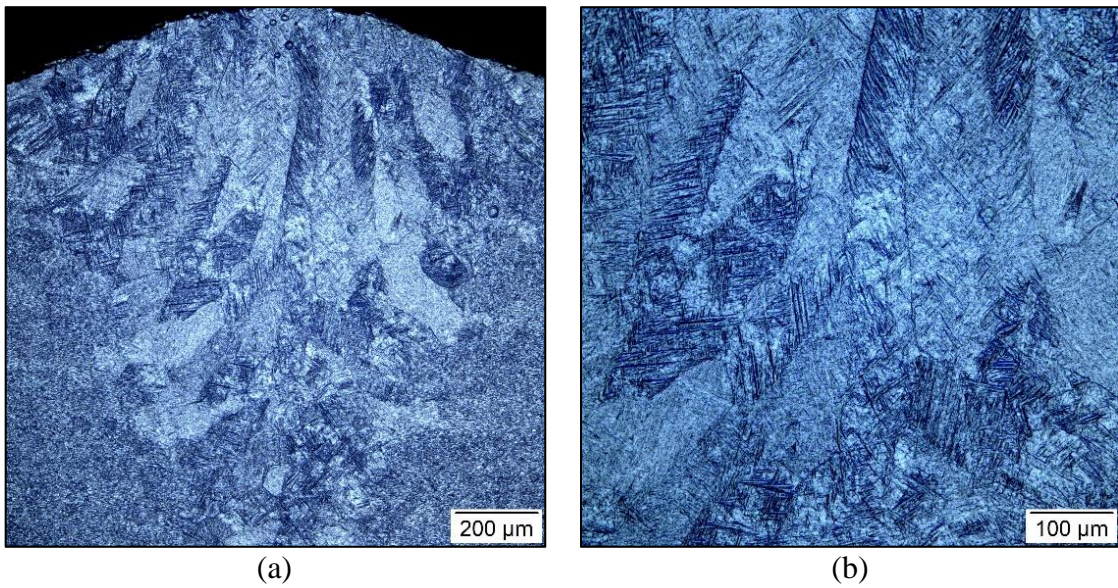


*Figure J.22. Ti-6Al-4V LB weld heat treated by placing in 900°C furnace for 5 minutes and free cooled. Kroll's etch. Immersed for  $\approx 1$  minute: a) 100X, b) 200X*

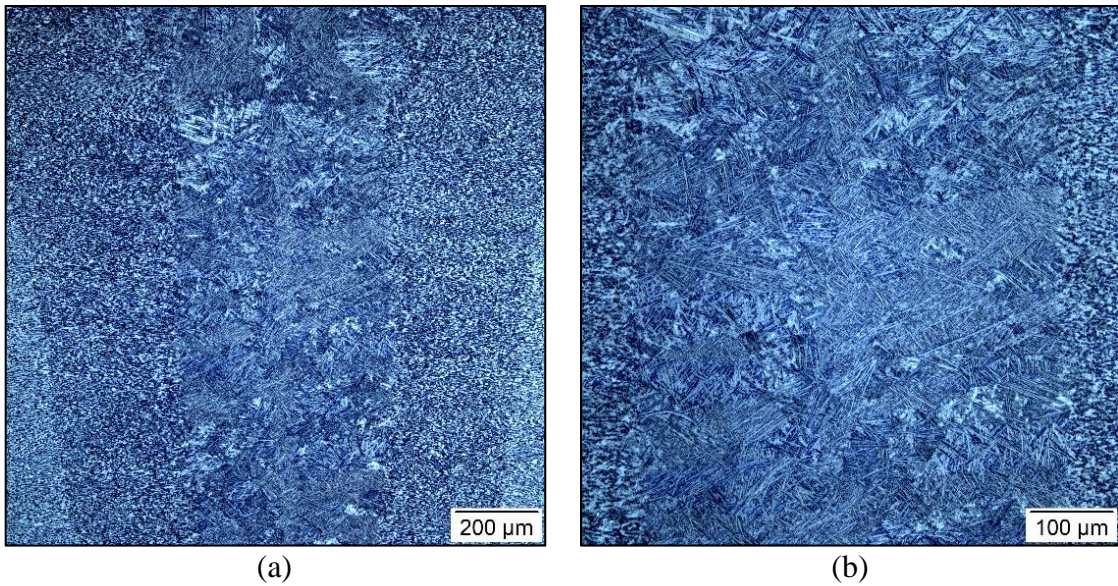


Figure J.23. Ti-6Al-4V LB weld heat treated by placing in 900°C furnace for 10 minutes and free cooled. Kroll's etch. Immersed for ≈20 seconds: a) 100X, b) 200X

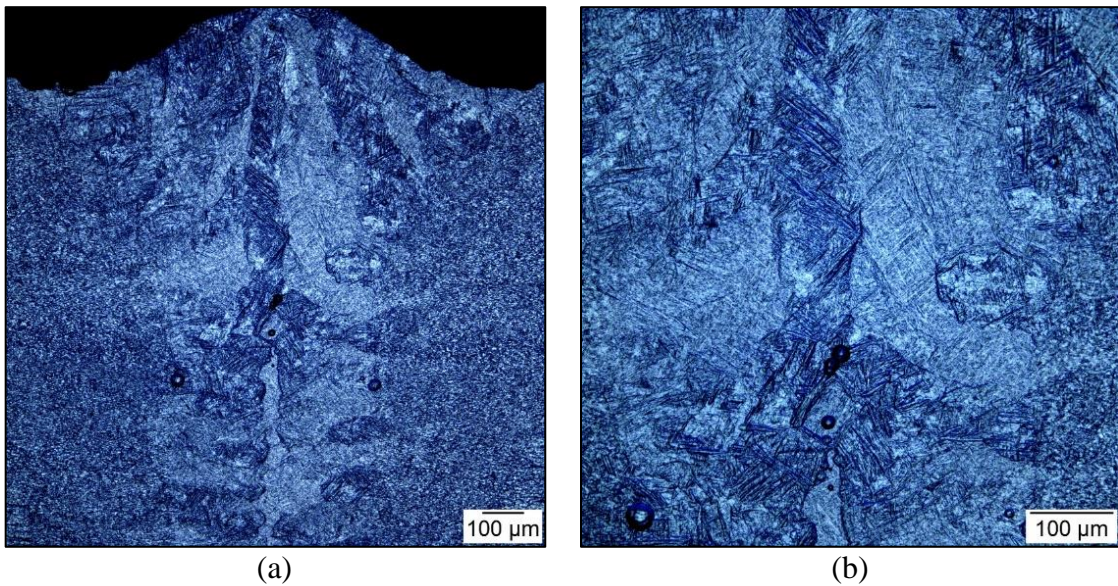
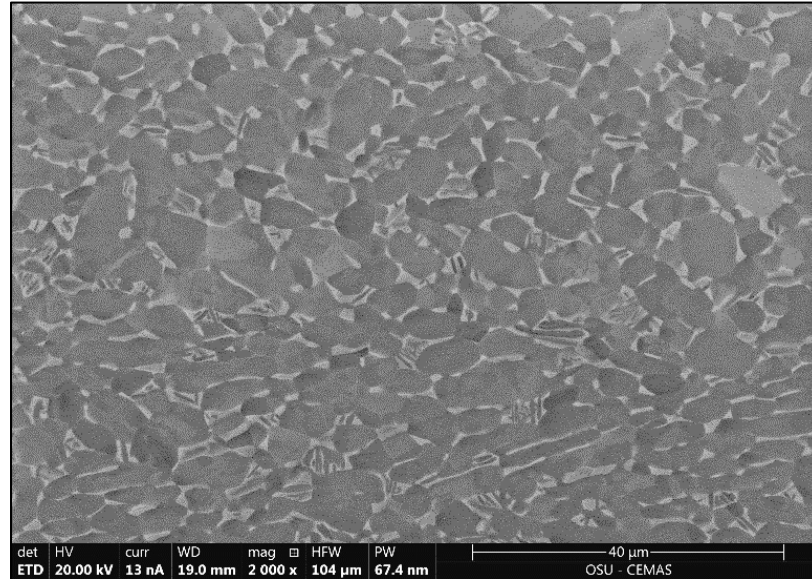


Figure J.24. Ti-6Al-4V LB weld heat treated by placing in 900°C furnace for 10 minutes and free cooled. Kroll's etch. Immersed for ≈1 minute: a) 100X, b) 200X

### J.3 SEM Analysis

Figure J.25 shows an SEM image of the Ti-6Al-4V base material microstructure captured using the ETD detector with BSE and SE electron detection.



*Figure J.25. Ti-6Al-4V base metal microstructure. The larger alpha grains appear dark, and the beta grains appear light.*

### J.4 Elevated Temperature EBSD

The following results show the iterative analysis when attempting to nucleate beta in the eSEM using the heating stage. This *in situ* heating experiment was a feasibility analysis to determine if it was possible to nucleate beta along prior beta grain boundaries. Figure J.26 shows the initial EBSD scan at room temperature (20°C). These scans were subjected to the same post-processing algorithms as previously presented in Section 5.3.2.

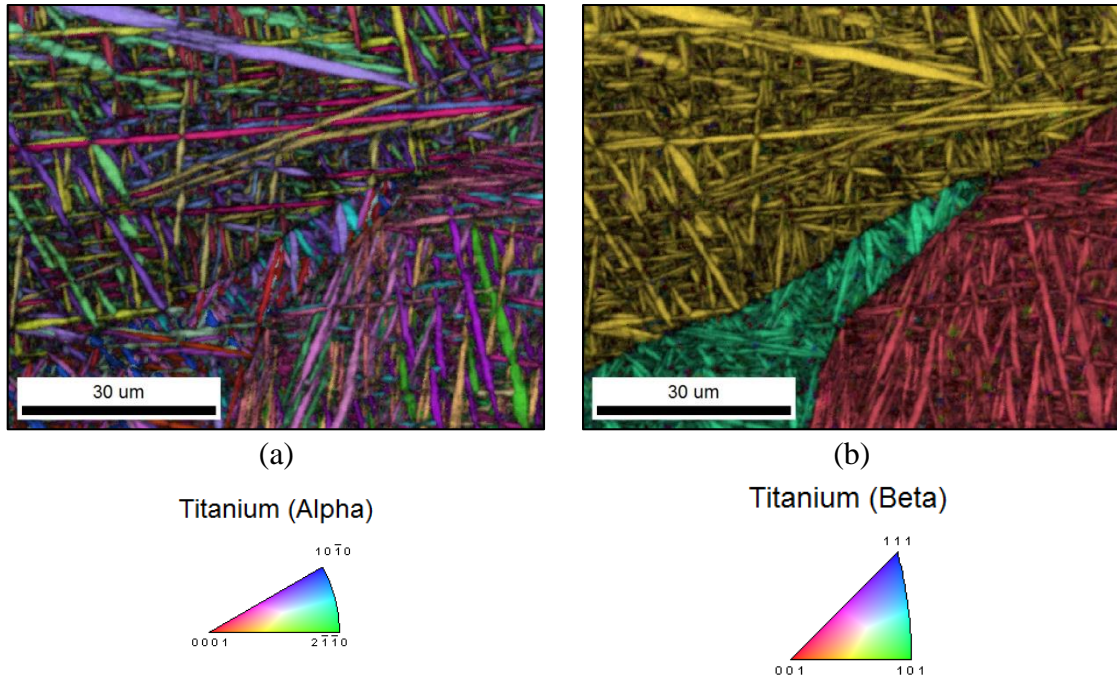


*Figure J.26. Ti-6Al-4V laser weld fusion zone at 1600 W and 50 mm/s. EBSD scan performed at 20°C: a) IPF + IQ map and b) IPF + IQ map of reconstructed parent grains.*

The left image (Figure J.26a) shows the IPF map overlaid on the IQ map of the as-welded structure. This consisted of  $\alpha'$  and was captured in a region containing distinct PBGBs. The right image (Figure J.26b) shows the results of the reconstructed parent or beta grains.

Figure J.27 shows the results of the same location after heating to 900°C at 50°C/min and holding for EBSD analysis. Although the image is slightly shifted, no microstructural change was shown between the room temperature and the 900°C EBSD scan. While holding the sample at 900°C, another EBSD scan was captured towards the root of a keyhole weld. The location of this scan is shown by the box in Figure J.28a. The EBSD

scan was recorded at 900°C after the hold time was  $\approx 20$  min. This is shown in Figure J.28b. Also, Figure J.28b does not show a difference between the room temperature EBSD map and the EBSD map captured just after heating to 900°C.

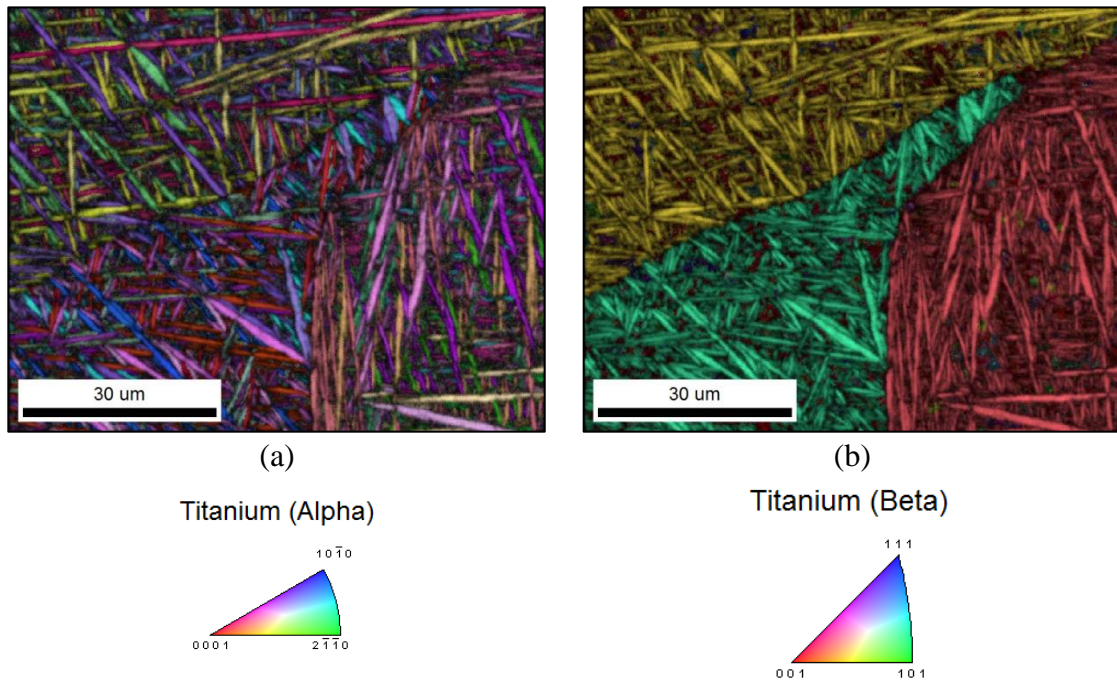


*Figure J.27. Ti-6Al-4V laser weld FZ at 1600 W and 50 mm/s. EBSD scan performed at 900°C: a) IPF + IQ map and b) IPF + IQ map of reconstructed parent grains.*

One issue with this analysis may have been caused by the sample surface not heating to 900°C as set in the eSEM and measured by the heating stage. The heating mechanism requires conductive heating through the sample specimen, which was 2 mm in thickness. Therefore, it was postulated that the sample surface is not at the same temperature. These results may be skewed relative to the set/reported of the heating stage. However, the ETD image captured with only secondary electrons (SE) shows dissolution of the high

temperature heat affected zone and growth of beta phase (dark) that was not observable at room temperature.

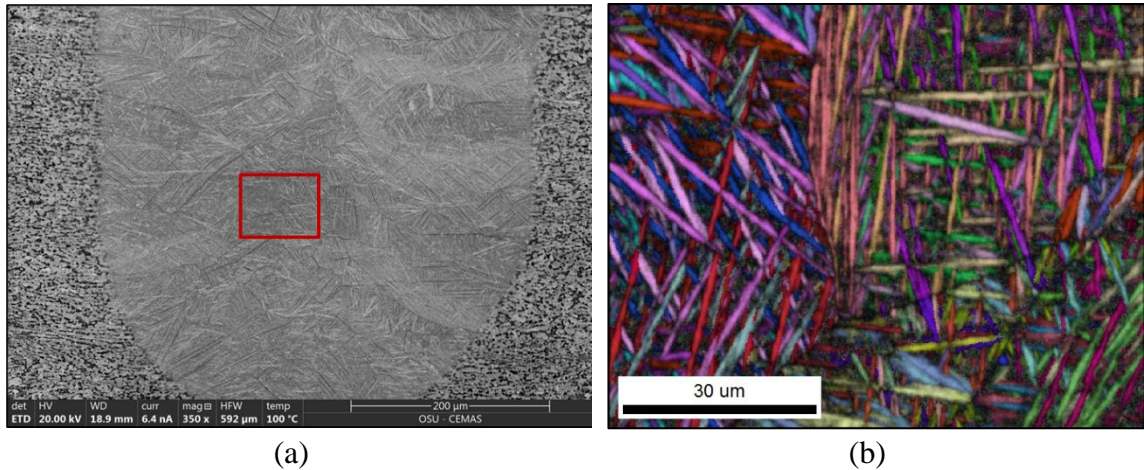


*Figure J.28. Ti-6Al-4V laser weld metal at 1600 W and 50 mm/s. EBSD scan performed at 900°C: a) Image from ETD detector using SE imaging mode after cooling from 900°C, b) IPF + IQ map and c) IPF + IQ map of reconstructed parent grains.*

### J.5 Pure Titanium Laser Weld PBGB Analysis

For comparison to the Ti-6Al-4V microstructures, laser welds were produced on a pure titanium alloy. Results for some of the microstructures are shown in Figure J.29 and Figure J.30. The structures in pure titanium are believed to be entirely alpha phase, and the PBGBs are more difficult to distinguish as compared to Ti-6Al-4V. Therefore, it is assumed that increasing beta or BCC stabilizing elements may result in delineation of PBGBs using chemical etching and optical microscopy.

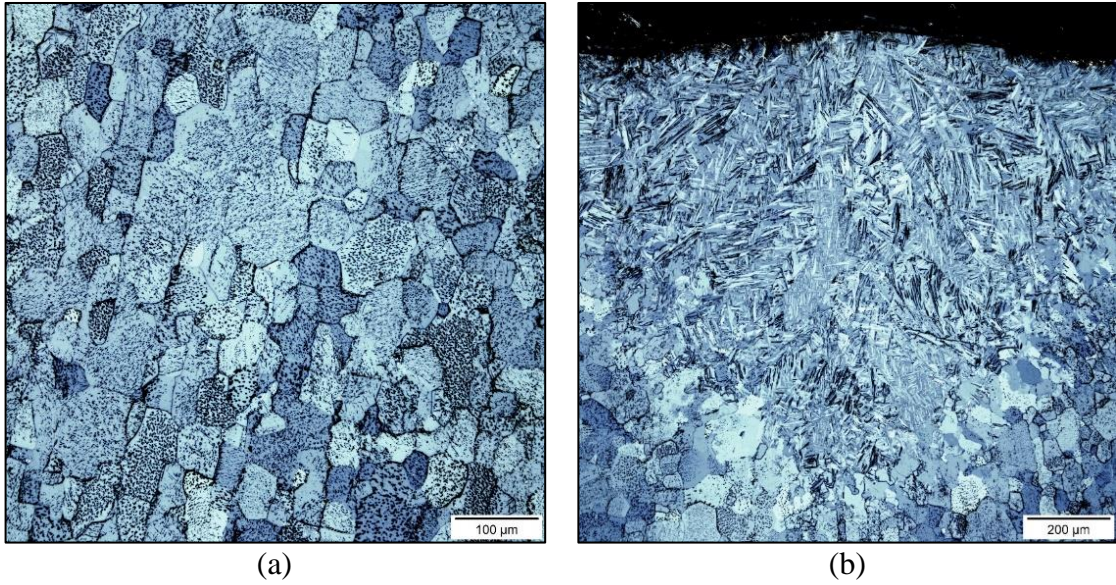


Figure J.29. Pure titanium base material (a). Commercially pure titanium laser weld (b). Kroll's etch. Immersed for  $\approx 10$  seconds: a) 200X, b) 100X.

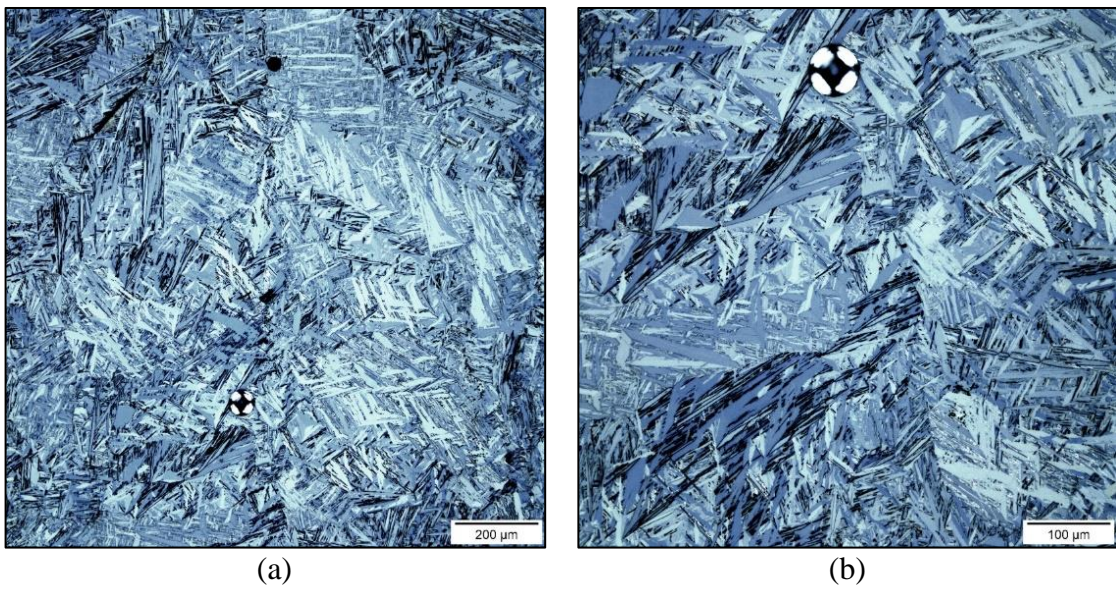


Figure J.30. Pure titanium laser weld microstructure. Kroll's etch. Immersed for  $\approx 10$  seconds: a) 100X, b) 200X.

## Appendix K: MATLAB® Script – Laser Beam Diagnostics

### K.1 Beam Diameter Analysis Script

```
%% D2M/D86 Beam Diameter Analysis
% This code was originally developed to analyze the data output
by Primes
% FocusMonitor and software and evolved into data plotting and
% visualization

% Computations include the D2M calculation and D86 calculation
based on the
% raw ADC values extracted from the PRIMES device/software
% The D2M computation attempts to maintain to ISO 11146-1

% Created by Tate Patterson
% 13 April 2020

%% Modifications since creation
% modified on 1 Sept. 2020
    % includes another user defined function to visualize and
save
    % images in a 2D
% modified on 24 March 2021
    % updated the colorbar scale
% modified on 1 April to rotate the matrix of intensity values
    % to align the axis of the Primes instrument with the axis of
    % OSU's Motoman robot

%%
clc; clear all; close all;

%%
% Enter height of scan!!! Not in Excel file!!!
totalScanHeight = 25; % [mm]

k = 0;
% powerNum = 800;
for powerNum = [800:200:2400]

k = k+1;
fileName = sprintf('%dW.xlsx',powerNum);

% must save the Primes output data as a '.xlsx' file
```

```

[num, txt, raw] = xlsread(fileName); % extract the beam data

% Use user defined function to get the variable locations and
values
[planeLoc,Power,nullPoint, nullRow, nullCol, Amp, xTotal
,yTotal,...
    pixelX, pixelY, rowLength, planeSpacing, XwinRow, XwinCol,...
    YwinRow, YwinCol, XpixRow, XpixCol, YpixRow, YpixCol,...
    AmpRow, AmpCol] = scanInfoLoc(num,txt,raw,totalScanHeight);

%% Iterate through all planes in the scan
% update each variable associated with the scanned Plane

planeNum = 0; % create a plane number and initialize a Plane
counter

j = 0;
for iterations = 1:length(planeLoc(1:end))
j = j + 1;

planeNum = planeNum + 1; % plane number to analyze

% index the location for the first z-height aka spreadsheet
"Plane 0"
z = planeSpacing(planeNum);

% get the window size value
xTotal = num(planeLoc(planeNum),XwinCol(planeNum)+1);
yTotal = num(planeLoc(planeNum),YwinCol(planeNum)+1);

% get the number of pixels used
pixelX = num(planeLoc(planeNum),XpixCol(planeNum)+1);
pixelY = num(planeLoc(planeNum),YpixCol(planeNum)+1);

% find the Amplification value recorded in the spreadsheet
Amp = num(planeLoc(planeNum), AmpCol(planeNum)+1);

% find the null point value recorded in the spreadsheet
nullPoint = num(planeLoc(planeNum),nullCol(planeNum)+1);

% enable every plane to be extracted from the spreadsheet format
if planeNum < length(planeLoc)
    % find the row length of the plane
    rowLength = (planeLoc(planeNum+1)-2) - (planeLoc(planeNum));

```

```

    % get the necessary row and column Intensity values from the
    Plane
    I = num(planeLoc(planeNum) + 1 : planeLoc(planeNum+1)-2, :);

else % use the raw data file to extract the last plane data
    % find the row length of the plane
    rowLength = length(row(:,1)) - planeLoc(planeNum);
    % get the necessary row and column Intensity values from the
    Plane
    I = num(planeLoc(planeNum) + 1 : length(row(:,1)), :);
end

I_raw = I; % maintain unaltered data values

%% Rotate matrix of intensity values
% rotate matrix to align the axis of the Primes instrument with
% the axis of the robot. Primes: +x=right, +y=up. Robot: +x=up,
+y=left
I = rot90(I); % rotate intensity data matrix counterclockwise 90
degrees

%%
% perform "background subtraction" based on the Primes "Null
Point Value"
I = I - round(nullPoint);
I( I <= 0 ) = 0; % set all values below zero to zero

%% Develop the x-y grid for plotting and computation
x = linspace(0,xTotal,rowLength); % create the x-axis points
y = linspace(0,yTotal,rowLength); % create the y-axis points

%% Compute the second moment (D2M) beam diameter from a user
defined funct.

[xAdj, yAdj, calcXCenter, calcYCenter, sumI, sumEx, sumEy,...
Ex, Ey, sqdSum, D2M] = secMomCalc(x,y,I);

%% Compute the 86% energy (D86) beam diameter

[xAdj, yAdj, calcXCenter, calcYCenter, sumI, sumEx, sumEy,...
Ex, Ey, centerX, centerY, radius, D86] = d86Calc(x,y,I);

```

```

%% Determine the power density of individual pixels for plotting

[powerMatrix,PD] = PD_funct(xTotal,yTotal,pixelX,pixelY,I,Power);

%%
% save the D2M data into a vector for each Primes scanned Plane
D2Mvec(planeNum,1) = D2M;
% save the D86 data into a vector for each Primes scanned Plane
D86vec(planeNum,1) = D86;
sumI_vec(planeNum,1) = sumI;
sumEx_vec(planeNum,1) = sumEx;
sumEy_vec(planeNum,1) = sumEy;
calcXCenter_vec(planeNum,1) = calcXCenter;
calcYCenter_vec(planeNum,1) = calcYCenter;
sqdSum_vec(planeNum,1) = sqdSum;
nullPt_vec(planeNum,1) = nullPoint;

%% output info to screen
fprintf('D2M = %0.4f mm \r',D2M);
fprintf('D86 = %0.4f mm \r',D86);

planeText = sprintf('Plane %d', planeNum);
disp(planeText);
D2M_vec(j) = D2M;
D86_vec(j) = D86;

%% Plotting single plane in 2D using raw data
[titleString] =
PD_Plot2D_Primes(xAdj,yAdj,PD,Power,fileName,planeNum,D86,D2M);

%% Plotting single plane in 3D using power density
[titleString] =
PD_Plot3D_Primes(xAdj,yAdj,PD,Power,fileName,planeNum,D86,D2M);

end
end

```

## K.2 Spreadsheet Location Extraction Function

```
function [planeLoc, Power, nullPoint, nullRow, nullCol, Amp, ...
    xTotal, yTotal, pixelX, pixelY, rowLength, planeSpacing, ...
    XwinRow, XwinCol, YwinRow, YwinCol, ...
    XpixRow, XpixCol, YpixRow, YpixCol, AmpRow, AmpCol] ...
    = scanInfoLoc(num, txt, raw, totalScanHeight)

% Find spreadsheet variables
% This section gets all the data saved into the spreadsheet and
% the locations for that data by searching for the text within the
% spreadsheet

% index the string 'Plane' locations in the first column of
% PRIMES raw data
planeLoc = find(contains(txt, 'Plane'));

planeSpacing = linspace(0, totalScanHeight, length(planeLoc));

% find the power value recorded in the spreadsheet
[PowerRow, PowerCol] = find(contains(txt, 'Power'));
Power = num(planeLoc(1), PowerCol(1)+1);

% find the null point value recorded in the spreadsheet
[nullRow, nullCol] = find(contains(txt, 'Null Point'));
nullPoint = num(planeLoc(1), nullCol(1)+1);

% find the Amplification value recorded in the spreadsheet
[AmpRow, AmpCol] = find(contains(txt, 'Amplification'));
Amp = num(planeLoc(1), AmpCol(1)+1);

% find the location of the 'Size of Window X' text in the
% spreadsheet
[XwinRow, XwinCol] = find(contains(txt, 'Size of window X'));
% find the location of the 'Size of Window Y' text in the
% spreadsheet
[YwinRow, YwinCol] = find(contains(txt, 'Size of window Y'));

% get the window size value one column to the right of the text
xTotal = num(planeLoc, XwinCol(1)+1);
yTotal = num(planeLoc, YwinCol(1)+1);

% find the location of the 'Pixels X' text in the spreadsheet
[XpixRow, XpixCol] = find(contains(txt, 'Pixels X'));
[YpixRow, YpixCol] = find(contains(txt, 'Pixels Y'));
```

```
% get the number of pixels used
pixelX = num(planeLoc(1),XpixCol(1)+1);
pixelY = num(planeLoc(1),YpixCol(1)+1);

% find the row length of the first plane
rowLength = (planeLoc(2)-2) - (planeLoc(1));

end
```

### K.3 Power Density Calculation Function

```
function [powerMatrix,PD] =  
PD_funct(xTotal,yTotal,pixelX,pixelY,I,Power)  
% Determine the power density of individual pixels for plotting  
  
% compute the "area" of each scan location  
pixelArea = (xTotal/pixelX)*(yTotal/pixelY);  
  
% sum all matrix intensity values to relate total ADC values to  
total power  
sigSum = sum(sum(I));  
  
% compute the overall intensity to power ratio [W/ADC]  
powerIntRatio = Power/sigSum;  
  
powerMatrix = I.*powerIntRatio;  
  
% compute power density and convert to kW/mm^2  
PD = powerMatrix./pixelArea/1000;  
  
End
```

## K.4 Second Moment Calculation Function

```
function [xAdj, yAdj, calcXCenter, calcYCenter, sumI, sumEx,
sumEy,...
    Ex, Ey, sqdSum, D2M] = secMomCalc(x,y,I);

% Computation of the second moment beam diameter (D2M) from the
"raw"
% intensity profile
% modified Sept. 7 2020 to include sqdSum as output variable

    % create nested for loops to iterate through x and y position
variables
    % in the matrix
    for j = 1:length(y);
        for i = 1:length(x);

            % extract single value at each position in the
intensity matrix
            % for computation
            I1 = I(j,i);

            Elx = I1*x(i); % compute the X first moment values
            Ely = I1*y(j);

            Ex(j,i) = Elx; % store the X first moment values into
a matrix
            Ey(j,i) = Ely; % store the Y first moment values into
a matrix

        end
    end

    sumI = sum(sum(I)); % power or sum of the raw Gaussian
intensity data
    sumEx = sum(sum(Ex)); % sum of the first moment Gaussian data
for X
    sumEy = sum(sum(Ey)); % sum of the first moment Gaussian data
for Y

    calcXCenter = sumEx/sumI;
    calcYCenter = sumEy/sumI;

    % adjust the x position from the determined centroid
    xAdj = x - calcXCenter;
    % adjust the y position from the determined centroid
```

```

yAdj = y - calcYCenter;

% second moment computation
for n = 1:length(yAdj); % y-axis

    for m = 1:length(xAdj); % x-axis
        % compute 2nd moment based on the centroid adjustment
        momCalc = I(n,m)*((xAdj(m))^2+(yAdj(n))^2);
        secMom(n,m) = momCalc; % build the 2nd moment data
matrix
    end

end

sqdSum = sum(sum(secMom)); % squared sum of 2nd moment matrix

% D2M calculation
D2M = 2*sqrt(2)*sqrt(sqdSum/sumI);

End

```

## K.5 D86 Calculation

```
function [xAdj, yAdj, calcXCenter, calcYCenter, sumI, sumEx,
sumEy, Ex,...
    Ey, centerX, centerY, radius, D86] = d86Calc(x,y,I)
% Computes the D86 or 86% beam diameter based on 86% of the
energy from the
% centroid of the intensity distribution

%% Determines the centroid locations
% create nested for loops to iterate through x and y position
variables
    % in the matrix
    for j = 1:length(y);
        for i = 1:length(x);

            % extract single value at each position in the
intensity matrix
            % for computation
            I1 = I(j,i);

            Elx = I1*x(i); % compute the X first moment values
            Ely = I1*y(j);

            Ex(j,i) = Elx; % store the X first moment values into
a matrix
            Ey(j,i) = Ely; % store the Y first moment values into
a matrix

        end
    end

    sumI = sum(sum(I)); % power or sum of the raw Gaussian
intensity data
    sumEx = sum(sum(Ex)); % sum of the first moment Gaussian data
for X
    sumEy = sum(sum(Ey)); % sum of the first moment Gaussian data
for Y

    calcXCenter = sumEx/sumI;
    calcYCenter = sumEy/sumI;

    % adjust the x position from the determined centroid
xAdj = x - calcXCenter;
    % adjust the y position from the determined centroid
yAdj = y - calcYCenter;
```

```

%% D86 calculation from the centroid adjusted intensity matrix
% Start at the center of the centroid adjusted axis and iterate
outward in
% increasing circles while summing the intensity values within
the circle
% until 86% of the total intensity is found

    % find the circle centers. This is the centroid of the
distribution.
    % find the center of the centroid adjusted x axis values
centerX = length(xAdj)/2;
    % find the center of the centroid adjusted y axis values
centerY = length(yAdj)/2;

    % find the total power in the intensity array
totalPower = sum(sum(I));
radius = 0; % initialize the radius variable
I86 = 0; % initialize the 86% power variable
count = 0;

while I86 < 0.865

    radius = radius+1;

    [columnsInImage rowsInImage] = meshgrid(1:length(xAdj),
1:length(xAdj));

    % create a matrix of zeros and ones to multiply the
intensity matrix
    circlePixels = (rowsInImage - centerY).^2 + ...
        (columnsInImage - centerX).^2 <= radius.^2;

    % find the sum of the intensity values within the circle
radius
    intensitySumAtRadius = I.*circlePixels;

    % find the sum of the matrix values
    I86sum = sum(sum(intensitySumAtRadius));

    I86 = I86sum/totalPower;

end

D86x = xAdj(centerX + radius)*2;

```

```
D86y = yAdj(centerY + radius)*2;  
  
% average D86 value from x and y directions  
D86 = (D86x + D86y)/2;  
  
end
```

## K.6 Intensity Distribution Plot – 2D

```
function [titleString] = PD_Plot2D_Primes(xAdj,yAdj,PD,Power,...
    fileName,planeNum,D86,D2M)
% Create a figure and plot showing a colorscale 3D intensity
distribution
% using the raw data intensity profile

% modified on 1 April 2021 to swap the axes of the measurement
device to
% match those of the welding robot. Only changed on the visual
output

D2M = round(D2M,3)*1000; % D2M beam diameter [ $\mu\text{m}$ ]
minPD = min(min(PD));
maxPD = max(max(PD));

figure % create a figure window

% plot the adjusted centroid values with intensity data
p = surf(xAdj,yAdj,PD); hold on;
set(p,'edgecolor','none')

c = colorbar('Location','eastoutside'); % set colorbar location
c.Label.String = 'Power Density [ $\text{kW}/\text{mm}^2$ '];
c.Label.FontSize = 14; % change the font size of the colorbar
title
c.Label.Color = 'k'; % set label color to black
colormap('jet') % select predefined MATLAB colormap

%% labelling the
% label x axis and set font size
xlabel('X [mm]','FontSize',12,'Color','k');
% label y axis and set font size
ylabel('Y [mm]','FontSize',12,'Color','k');
zlabel('PD [ $\text{kW}/\text{mm}^2$ '],'FontSize',12,'Color','k');

set(gcf,'color','w'); % set background of figure to white
plt.XAxis.Color = 'k'; % color the x-axis black
plt.YAxis.Color = 'k'; % color the y-axis black
set(gca,'FontSize',12,'LineWidth',2); % set font size and line
width

xlim([-0.5 0.5]); % set x-axis limits
ylim([-0.5 0.5]); % set y-axis limits
zlim([0 ceil(max(max(PD)))]); % set z-axis limits
```

```

set(c, 'ylim', [0 ceil(max(max(PD)))]) % set the colorbar limits

%Set the x-axis ticks
set(gca, 'XTick', [-0.4:0.2:0.4]);
%Set the y-axis ticks
set(gca, 'YTick', [-0.4:0.2:0.4]);

planeNumString = planeNum + 1;
planeNumString = num2str(planeNum);

% title plot with the beam power from the file name
%     titleString = strcat(num2str(Power), ' W', ' - Plane', ...
%         '{ }', num2str(planeNumString));
titleString = strcat(num2str(Power), ' W', '{ ' }, '-', '{ '
'}, 'Plane', '{ ' }, ...
    num2str(planeNum), '{ ' }, '-', '{ ' }, 'D2M =', '{ ' }, ...
    num2str(D2M), '{ ' }, 'μm');
title(titleString);

% Change the plot view that is displayed by default
view(-180,90)

%% save the figure each time into a folder within the current
directory

% create a new folder in the current directory for storing MATLAB
plots
mkdir 2DPlots-MATLAB

saveString = strcat(num2str(Power), 'W-Plane', planeNumString, '_PD-
2DXY');

% save each figure into the new folder as a tif file
saveas(gcf, [pwd '\2DPlots-MATLAB\', saveString, '.tif']);

end

```

## K.7 Intensity Distribution Plot – 3D

```
function [titleString] = PD_Plot3D_Primes(xAdj,yAdj,PD,Power,...
    fileName,planeNum,D86,D2M)

% Create a figure and plot showing a colorscale 3D intensity
distribution
% using the raw data intensity profile

D2M = round(D2M,3)*1000; % D2M beam diameter [ $\mu\text{m}$ ]
minPD = min(min(PD));
maxPD = max(max(PD));

figure % create a figure window

% plot the adjusted centroid values with intensity data
p = surf(xAdj,yAdj,PD); hold on;
set(p,'edgecolor','none')

c = colorbar('Location','eastoutside'); % set colorbar location
c.Label.String = 'Power Density [ $\text{kW}/\text{mm}^2$ ]';
c.Label.FontSize = 14; % change the font size of the colorbar
title
c.Label.Color = 'k'; % set label color to black
colormap('jet') % select predefined MATLAB colormap

% use built in MATLAB remainder function that divides input by 2
remainder = rem(ceil(maxPD),2);

% label x axis and set font size
xlabel('X [mm]','FontSize',12,'Color','k');
% label y axis and set font size
ylabel('Y [mm]','FontSize',12,'Color','k');
zlabel('PD [ $\text{kW}/\text{mm}^2$ ]','FontSize',12,'Color','k');

set(gcf,'color','w'); % set background of figure to white
plt.XAxis.Color = 'k'; % color the x-axis black
plt.YAxis.Color = 'k'; % color the y-axis black
set(gca,'FontSize',12,'LineWidth',2); % set font size and line
width

xlim([-0.5 0.5]); % set x-axis limits
ylim([-0.5 0.5]); % set y-axis limits
zlim([0 ceil(max(max(PD)))]); % set z-axis limits
set(c,'ylim',[0 ceil(max(max(PD)))]) % set the colorbar limits
```

```

%Set the x-axis ticks
set(gca,'XTick',[-0.4:0.2:0.4]);
%Set the y-axis ticks
set(gca,'YTick',[-0.4:0.2:0.4]);
%Set the z-axis ticks
ztick = linspace(0,ceil(max(max(PD))),6);
set(gca,'ZTick',round(ztick,1));

planeNumString = planeNum + 1;
planeNumString = num2str(planeNum);

% title plot with the beam power from the file name
%     titleString = strcat(num2str(Power),' W', ' - Plane',...
%         '{ }', num2str(planeNumString));
titleString = strcat(num2str(Power),' W',{ ' '},'-',{ '
'},'Plane',{ ' '},...
    num2str(planeNum),{' '},'-',{ ' '},'D2M =',{ ' '},...
    num2str(D2M),{' '},'\mu m');
title(titleString);

% Change the plot view
view([145,20])

%% save the figure each time into a folder within the current
directory

% create a new folder in the current directory for storing MATLAB
plots
mkdir 3DPlots-MATLAB

saveString = strcat(num2str(Power),'W-Plane',planeNumString,'_PD-
3D');

% save each figure into the new folder as a tif file
saveas(gcf,[pwd '\3DPlots-MATLAB\',saveString,'.tif']);

end

```

## K.8 Beam Caustic Plots

```
% Plot the PRIMES data that is exported to a .xls file
% Created by Tate Patterson
% 8 January 2020

%% Modifications since creation
% updated on 31 January 2020 to contain a for loop of each
measured plane
% updated on 10 February 2020 to subtract background data from
planes
% modified on 1 April to rotate the matrix of intensity values
% to align the axis of the Primes instrument with the axis of
% OSU's Motoman robot

%%
% must save the data as a '.xlsx' file
clc; clear all; close all;

%%
for fileName = [800:200:2400]
    fileName = num2str(fileName);
    fileName = strcat(fileName, 'W', '.xlsx');

    [num, txt, raw] = xlsread(fileName);

    % index the string 'Plane' locations in the first column
    % of Primes raw data
    planeLoc = find(contains(txt, 'Plane'));

    % enter height of scan!!! Not in excel file!!!
    totalScanHeight = 25; % [mm]
    planeSpacing = linspace(0, totalScanHeight,
length(planeLoc));

    % find the power value recorded in the spreadsheet
    [PowerRow, PowerCol] = find(contains(txt, 'Power'));
    Power = num(planeLoc(1), PowerCol(1)+1);

    % find the null point value recorded in the spreadsheet
    [nullRow, nullCol] = find(contains(txt, 'Null Point'));
    nullPoint = num(planeLoc(1), nullCol(1)+1);

    % find the Amplification value recorded in the spreadsheet
    [AmpRow, AmpCol] = find(contains(txt, 'Amplification'));
    Amp = num(planeLoc(1), AmpCol(1)+1);
```

```

    % find the location of the 'Size of Window X' text in the
    spreadsheet
    [XwinRow, XwinCol] = find(contains(txt, 'Size of window X'));
    [YwinRow, YwinCol] = find(contains(txt, 'Size of window Y'));

    % get the window size values
    xTotal = num(planeLoc, XwinCol(1)+1);
    yTotal = num(planeLoc, YwinCol(1)+1);
    xTotal = max(xTotal); minSizeOfX = min(xTotal);
    yTotal = max(yTotal); minSizeOfY = min(yTotal);

    sizeOfWindowX1 = num(planeLoc(1), XwinCol(1)+1);
    sizeOfWindowY1 = num(planeLoc(1), YwinCol(1)+1);

    % find the location of the 'Pixels X' text in the spreadsheet
    [XpixRow, XpixCol] = find(contains(txt, 'Pixels X'));
    [YpixRow, YpixCol] = find(contains(txt, 'Pixels Y'));
    % get the number of pixels used
    pixelX = num(planeLoc(1), XpixCol(1)+1);
    pixelY = num(planeLoc(1), YpixCol(1)+1);

    % find the row length of the first plane
    rowLength = (planeLoc(2)-2) - (planeLoc(1));

    % get the necessary rows and all columns from Plane 1
    plane1 = num(planeLoc(1) + 1 : planeLoc(2)-2, :);

    gridWidth1 = linspace(0, sizeOfWindowX1, rowLength);
    gridHeight1 = linspace(0, sizeOfWindowY1, rowLength);

    %%
    figure
    % maximize the size of the figure
    set(gcf, 'Units', 'Normalized', 'OuterPosition', [0 0 0.5
1]);

    i = 0; % set counter equal to zero
    z = 0; % set an arbitrary z height
    % iterate the length of each Plane after the first Plane
    for iterations = 1:length(planeLoc(1:end))
        i = i + 1; % counter
        z = planeSpacing(i);
        % get the window size value
        xTotal = num(planeLoc(i), XwinCol(i)+1);
        yTotal = num(planeLoc(i), YwinCol(i)+1);

```

```

% get the number of pixels used
pixelX = num(planeLoc(i),XpixCol(i)+1);
pixelY = num(planeLoc(i),YpixCol(i)+1);

% find the Amplification value recorded in spreadsheet
Amp = num(planeLoc(i), AmpCol(i)+1);

% find the null point value recorded in the spreadsheet
nullPoint = num(planeLoc(i),nullCol(i)+1);

if i < length(planeLoc)
    % find the row length of the first plane
    rowLength = (planeLoc(i+1)-2) - (planeLoc(i));
    % get the necessary rows and all columns from Plane
    I = num(planeLoc(i) + 1 : planeLoc(i+1)-2, :);

else
    rowLength = length(row(:,1)) - planeLoc(i);
    I = num(planeLoc(i) + 1 : length(row(:,1)), :);

end

gridWidth = linspace(0, xTotal, rowLength)-xTotal/2;
gridHeight = linspace(0, yTotal, rowLength)-yTotal/2;

I_raw = I; % maintain unaltered data values

%% Rotate matrix of intensity values
% rotate matrix to align axis of Primes instrument with
% the axis of the robot.
% Primes: +x=right, +y=up. Robot: +x=up, +y=left
% rotate data matrix counterclockwise 90 degrees
I = rot90(I);

% perform "background subtraction" based on the Primes
% "Null Point Value"
I = I - round(nullPoint);
I( I <= 0 ) = 0; % set all values below zero to zero

% normalize each plot based on amplitude
linearAmp = 10^(Amp/10);

%      I = linearAmp*I; % reamplify everything the same

```

```

%%
% compute the "area" of each scan location
pixelArea = (xTotal/pixelX)*(yTotal/pixelY);

% sum all the matrix intensity values to relate the total
% ADC values to total power
sigSum = sum(sum(I));

% compute the overall intensity to power ratio [W/ADC]
powerIntRatio = Power/sigSum;

powerMatrix = I.*powerIntRatio;

% compute power density and convert to kW/mm^2
PD = powerMatrix./pixelArea/1000;

% get min/max power density value from matrix
minPD = min(min(PD));
maxPD = max(max(PD));

maxADC = max(max(I));
maxPD_vect(i) = maxPD;
maxADC_vect(i) = maxADC;

%% % perform a background subtraction
% find minimum value in matrix planeNorm for plotting
min_planeNorm = min(min(PD));

% set all low level values in Plane matrix to zero for
% better visualization in the plot
PD(PD <= 0.1) = 0;
PD(PD == 0) = NaN;

k = z.*(ones(length(gridWidth), length(gridHeight)));
h = surf(gridWidth, gridHeight, k, PD);
set(h, 'edgecolor', 'none')
colormap('jet');
zlim([0 ceil(max(max(PD)))]); % set z-axis limits
hold on;

ampVect(i) = Amp;

intensityMax(i) = max(max(PD));
intensityMin(i) = min(min(PD));
end

```

```

%% Change plot visualizations
% title plot based on Power Value, set font size
str = sprintf('%0d W', Power);
% label x axis and set font size
xlabel('X [mm]', 'FontSize', 11, 'Color', 'k');
% label y axis and set font size
ylabel('Y [mm]', 'FontSize', 11, 'Color', 'k');
% label z axis and set font size
zlabel('Z [mm] - Beam Axis', 'FontSize', 11, 'Color', 'k');
set(gcf, 'color', 'w');
plt.XAxis.Color = 'k';
plt.YAxis.Color = 'k';
% set the font size of the x and y axis
set(gca, 'FontSize', 20, 'LineWidth', 1.5)
zlim([0 totalScanHeight])
set(gca, 'XTick', [-1:0.5:1]); % x-axis tick labels
set(gca, 'YTick', [-1:0.5:1]); % y-axis tick labels
set(gca, 'ZTick', [0:1.5:totalScanHeight]); % z-axis
xlim([-1 1])
ylim([-1 1])

%% Create colorbar
% add a colorbar showing the variation in intensity
c = colorbar;
% set the colorbar limits
set(c, 'ylim', [0 ceil(max(intensityMax))])
% create string to label colorbar
loadLabel = sprintf('Power Density [kW/mm^2]');
% Label the colorbar with a title on right side of colorbar
c.Label.String = loadLabel;
c.Label.FontSize = 20; % change colorbar title font size
c.Label.Color = 'k';
% set font size and line width
set(gca, 'FontSize', 18, 'LineWidth', 2);
title(str, 'FontSize', 30, 'Interpreter', 'none');

%% Plot title
% title plot with the beam power from the file name
titleString = strcat(num2str(Power), ' W');
title(titleString);

%% Animated rotation
% view(3) %sets the default 3-D view, AZ = -37.5, EL = 30.
% rotate the 3D plot for visualization
% for angle = 0:1:270

```

```

%     view([0 + angle,8])
%     pause(0.1)
% end

%% Set the 3D plot view
view([165, 11])

%% Saving
% save figure each time into folder within current directory
% create new folder in current directory for storing plots
mkdir 3DCausticPlots-MATLAB

saveString = strcat(num2str(Power),'W','-3DCaustic');

% save each figure into the new folder as a tif file
saveas(gcf,[pwd '\3DCausticPlots-
MATLAB\',saveString, '.tif']);

end

```

## Appendix L: MATLAB® Script – Transverse Cross-Section Analysis

```
%% Measure features from a transverse cross-section of the fusion
zone
% for a laser beam weld micrographs

%% Created by Tate Patterson
% 29 July 2019
% updated 30 September 2019 (WeldMeasurementTool)
% labeled the FWHM and 1/e2 fusion zone widths on figure
% latest version as of 30 Dec. 2019 (WeldMeasurementTool_V1b)
% updated to display measured data to the figure window
% updated on 4 Jan. 2020 to measure boundary lengths and
% display more info to the figure window
% modified on 17 Jan. 2020 to include the file name on the
% figure and
% reposition all the output values to the right of the figure
% updated text size on 25 September 2020
% highly modified on 4 Oct. 2021 to allow user selection,
% save data to an Excel file, and
% save black and white images of cross-sections

clc; clear all; close all;

% use uigetfile to select all the images to be measured
[allFileNames] = uigetfile({'*.jpg','jpg Files (*.jpg)';...
    '*.JPG','JPG Files (*.JPG)';...
    '*.jpeg','jpeg Files (*.jpeg)';...
    '*.JPEG','JPEG Files (*.JPEG)';...
    '*.img','img Files (*.img)';...
    '*.IMG','IMG Files (*.IMG)';...
    '*.tif','tif Files (*.tif)';...
    '*.TIF','TIF Files (*.TIF)';...
    '*.tiff','tiff Files (*.tiff)';...
    '*.TIFF','TIFF Files (*.TIFF)'},'Multiselect', 'on');

% get the length of files to measure
[numRows, numCols] = size(cellstr(allFileNames));
measNum = numCols;

for i = 1:measNum

    % fileName = 'IPG_Weld_M1P2C1_A_200X.jpg';
    % allow for user selection of micrograph file
    if measNum == 1
```

```

        fileName = allFileNames;
        trueImage = imread(fileName);
    else
        fileName = allFileNames(1,i);
        fileName = fileName{1,:};
        trueImage = imread(fileName);
    end

    disp(fileName) % display the filename for labeling
    %% check if an image is black and white (binary)
    % if not, convert an image to black and white
    % and save the B&W image

    % check if the image is RGB
    if length(unique(trueImage)) > 255;
        grayScaleImage = rgb2gray(trueImage);
        binaryImage = im2bw(grayScaleImage);
    else
        grayScaleImage = trueImage;
        binaryImage = im2bw(grayScaleImage);
    end

    % display the binary image
    fig = figure; imshow(binaryImage);
    % maximize the size of the image
    pause(0.00001);
    frame_h = get(handle(gcf), 'JavaFrame');
    set(frame_h, 'Maximized', 1);
    figPos = get(fig, 'Position')

    % display the filename on fig. for labeling
    text(0.01,0.03,fileName,'units','normalized',...
        'color','r','FontSize',20,'Interpreter','none',...
        'backgroundcolor','w','edgecolor','k')

    title('Enter in Scale Bar Length!','FontSize',15)

    % set the image scale based on the scale bar [mm]
    prompt = {'Enter the Scale Bar Length in  $\mu\text{m}$ :'};
    dlgtitle = 'Scale';
    dims = [1];
    definput = {'500'};
    answer = inputdlg(prompt,dlgtitle,dims,definput);
    % get the user input
    scaleLength = str2num(answer{1});
    scaleLength = scaleLength/1000 % Convert to millimeters

```

```

%% Get scale bar information
% select location to starting looking for
% the scale bar using the mouse
% on the displayed binary image
disp('Select a location beneath the scale bar. ');
disp('Do not select the scale bar text! ');
title('Do not select scale bar text or within text!',...
      'FontSize',15)

% cross hairs to select location
[x_loc,y_loc] = ginput(1);

x_loc = round(x_loc);
y_loc = round(y_loc);

j = 0;
val = 1;
while val
    j = j+1;
    val = binaryImage(y_loc-j, x_loc);
end
y_loc_bottom = y_loc-j;

j = 0;
while ~val
    j = j+1;
    val = binaryImage(y_loc_bottom-j,x_loc);
end

y_loc_top = y_loc_bottom-j;

% center of black line
yPos = round((y_loc_bottom + y_loc_top)/2);

val = 0;
j = 0;
while ~val
    j = j+1;
    val = binaryImage(yPos, x_loc + j);
end
x_right = x_loc + j - 1;

val = 0;
j = 0;
while ~val

```

```

        j = j+1;
        val = binaryImage(yPos, x_loc - j);
    end
    x_left = x_loc - j + 1;

    scalePixelLength = abs(x_right-x_left) % [mm]

    lengthPerPixel = scaleLength/scalePixelLength % [mm]
    lengthPerPixel_Microns = lengthPerPixel*1000 % [um]

    hold on
    plot(x_left,yPos,'rx','MarkerSize',20); hold on;...
        plot(x_right,yPos,'rx','MarkerSize',20);
    pause(0.001)

    %% Computing the area of the fusion zone through
    % selecting the region of interest (aka fusion zone outline)
    % double click to finish once closing the area

    % display the binary image
    imshow(trueImage);

    title('Trace the Entire Fusion Zone','FontSize',15)

    [maskedImage, xROI, yROI] = roipoly(trueImage);

    hold on;
    plot(xROI, yROI, 'r.', 'MarkerSize', 15);

    hold on;
    a = [1:length(xROI)-1]'; b = num2str(a); dist = cellstr(b);

    % displacement so the text does not overlay the data points
    dx = 10; dy = 10;
    text(xROI(1:end-1) + dx, yROI(1:end-1) + dy,...
        dist,'FontSize',15,'Color','r');

    % Allow user to define the weld toe points from "roipoly"
    % leftToePos=input('What is left weld toe point number: ');
    % rightToePos=input('What is right weld toe point number: ');
    % Use a dialog box for user input
    %     prompt = {'Enter the Left Weld Toe Point #:'};
    %     dlgtitle = 'Left Weld Toe';
    %     dims = [1];
    %     definput = {'1'};

```

```

%     answer = inputdlg(prompt,dlgtitle,dims,definput);
%     leftToePos = str2num(answer{1}); % get the user input
%     prompt = {'Enter the Right Weld Toe Point #'};
%     dlgtitle = 'Left Weld Toe';
%     dims = [1];
%     definput = {' '};
%     answer = inputdlg(prompt,dlgtitle,dims,definput);
%     rightToePos = str2num(answer{1}); % get the user input
%
%     % index the weld toe positions
%     xLeftToePos = xROI(leftToePos,1);
%     xRightToePos = xROI(rightToePos,1);
%     yLeftToePos = yROI(leftToePos,1);
%     yRightToePos = yROI(rightToePos,1);
%
%     % Determine the weld toe width from selected points
%     toeWidth = sqrt((abs(xLeftToePos-xRightToePos))^2 +...
%         (abs(yLeftToePos-yRightToePos))^2);
%     toeWidth = lengthPerPixel*toeWidth;

%% Scale bar creation
% create a scale bar from the original image on
% the black and white image
scaledBWimage = maskedImage;
rowStart = yPos;
thickness = 20;
colStart = x_left;
colStop = x_right;
replaceVec = ones(1, scalePixelLength);
scaledBWimage(rowStart-thickness:rowStart,colStart:colStop) =
1;

fig2 = figure; imshow(scaledBWimage)
% maximize the size of the image
pause(0.00001);
frame_h2 = get(handle(gcf),'JavaFrame');
set(frame_h,'Maximized',1);
figPos = get(fig,'Position');

% Save the binary image file
% get the user input for user dialog
dlgPrompt = {'Enter Material ID: ', ...
    'Enter the power [W]: ',...
    'Enter the travel speed [mm/s]: ',...
    'Enter the beam diameter [um]: ',...
    'Enter weld ID: '};

```

```

dlgName = 'Filename';
dims = [2];
% create dialog window
dlgResponse = inputdlg(dlgPrompt, dlgName, dims);
fileNameCell = strcat(dlgResponse(1,1), '_', ...
    dlgResponse(2,1), 'W_', dlgResponse(3,1), 'mmPs_', ...
    dlgResponse(4,1), 'um_', dlgResponse(5,1), ...
    '_scale', num2str(scaleLength*1000), 'um');
filename = fileNameCell{1,:};

% save the figure each time into a folder within the current
% directory create a new folder in the current directory
% for storing Matlab plots
directoryName = ('FZ_BW-ImageFiles');

% if the directory does not exist, make it
if not(isfolder(directoryName))
% make directory named by directoryName
    mkdir(directoryName)
end

currentFolder = pwd; % return path to the current folder
saveName = strcat('\', filename, '.tif');
saveDir = strcat(currentFolder, '\', directoryName);
imageName = strcat(currentFolder, '\', directoryName, saveName);

j = isfile(imageName);
while j == 1 % check if the file exists
    % File exists.
    dlgTitle = 'Overwrite?';
    dlgQuestion = 'Do you wish to overwrite the image file?';
    choice = questdlg(dlgQuestion, dlgTitle, 'Yes', 'No',
        'Yes');
    % compare strings to see if 'Yes'
    strComp = strcmp(choice, 'Yes')

    if strComp == 1
        % exit if statement and do not satisfy while loop
        j = 0;
    else
        % get the user input for user dialog
        dlgPrompt = {'Enter Material ID: ', ...
            'Enter the power [W]: ', ...
            'Enter the travel speed [mm/s]: ', ...
            'Enter the beam diameter [um]: ', ...
            'Enter weld ID: '};

```

```

        dlgName = 'Filename';
        dims = [2];
        % create dialog window
        dlgResponse = inputdlg(dlgPrompt, dlgName, dims);
        fileNameCell = strcat(dlgResponse(1,1), '_', ...

        dlgResponse(2,1), 'W_', dlgResponse(3,1), 'mmPs_', ...
            dlgResponse(4,1), 'um_', dlgResponse(5,1), ...
            '_scale', num2str(scaleLength*1000), 'um')
        filename = fileNameCell{1,:};
        saveName = strcat('\', filename, '.tif');
        saveDir = strcat(currentFolder, '\', directoryName);
        imageName = strcat(currentFolder, '\', ...
            directoryName, saveName);
        j = isfile(imageName);
    end
end

imwrite(scaledBWimage, imageName);
close(fig2)

%% Compute area of the black and white pixels in image
% nnz computes the number of nonzero matrix elements
areaWhite = nnz(maskedImage);
% find the total number of elements (N) in the image
numberOfElements = numel(maskedImage);
areaBlack = numberOfElements - areaWhite;

fusionZoneFraction = areaBlack/numberOfElements;
% sprintf('Percentage Ferrite: %f', fusionZoneFraction)

% get the number of pixels in height and width of image
[heightInPixels, widthInPixels] = size(maskedImage);

% get the dimensions (width, height, area) of image [mm]
totalImageWidth = lengthPerPixel*heightInPixels;
totalImageHeight = lengthPerPixel*widthInPixels;
totalImageArea = totalImageWidth*totalImageHeight;

clc; % clear the window
areaOfFZ = (lengthPerPixel^2)*areaWhite;

%% Determine the weld width at the FZ centroid
% Determine the centroid of the fusion zone
% by the user in the previous section

```

```

% Use the built in Matlab function "regionprops"
% to determine the centroid location and store values
cen = regionprops(maskedImage, 'centroid');

% 'cat' concatenates the values to a single array
centroid = cat(1, cen.Centroid);

% Use the centroid location and iterate outward
% to determine where the pixels go from white (1)
% to black (0). Save location to determine the
% width/hieght

x_loc = centroid(1,1);
y_loc = centroid(1,2);

x_loc = round(x_loc);
y_loc = round(y_loc);

% move only in the x-direction to determine the width
val = 1; % value of white pixels in image
j = 0; % counter
while val
    j = j+1;
    val = maskedImage(y_loc, x_loc + j);
end
x_right = x_loc + j - 1;

% value of white pixels in image
val = 1; % value of white pixels in image
j = 0; % counter
while val
    j = j+1;
    val = maskedImage(y_loc, x_loc - j);
end
x_left = x_loc - j + 1;

weldCentroidWidth = abs(x_right-x_left)*lengthPerPixel;

% display the two regions measuring the centroid
% width and display the text next to the right marker
hold on
plot(x_left, y_loc, 'ro', 'MarkerSize', 12, 'LineWidth', 2);
hold on;
plot(x_right, y_loc, 'ro', 'MarkerSize', 12, 'LineWidth', 2);
title('Traced Fusion Zone and Measured Values/Locations', ...
    'FontSize', 15)

```

```

% txt = 'Centroid Width';
% text(x_right + x_right/10,y_loc,txt,'FontSize',15,...
% 'Color',[1 0 0],...
% 'HorizontalAlignment','left')
% hold on

%% Determine weld width at half maximum of the FZ
% This section determines the maximum and minimum
% extrema locations from
% the fusion zone cross-section and computes the
% difference between the
% two. Then it uses those points to search to
% the left and right to
% determine the width at half maximum or
% full width - half maximum (FWHM)

% 'Extrema' outputs an 8x2 matrix with each row
% consisting of x-y coordinates of [top-left,
% top-right, right-top, right-bottom,
% bottom-right, bottom-left, left-bottom, left-top].
% For instance, top-left and left-top may be identical

s = regionprops(maskedImage,'extrema');

% 'cat' concatenates the values to a single array
extremaPoints = cat(1,s.Extrema);

% define Extrema points
topLeftExtremeX = extremaPoints(1,1);
topLeftExtremeY = extremaPoints(1,2);
topRightExtremeX = extremaPoints(2,1);
topRightExtremeY = extremaPoints(2,2);
rightTopExtremeX = extremaPoints(3,1);
rightTopExtremeY = extremaPoints(3,2);
rightBottomExtremeX = extremaPoints(4,1);
rightBottomExtremeY = extremaPoints(4,2);
bottomRightExtremeX = extremaPoints(5,1);
bottomRightExtremeY = extremaPoints(5,2);
bottomLeftExtremeX = extremaPoints(6,1);
bottomLeftExtremeY = extremaPoints(6,2);
leftBottomExtremeX = extremaPoints(7,1);
leftBottomExtremeY = extremaPoints(7,2);
leftTopExtremeX = extremaPoints(8,1);
leftTopExtremeY = extremaPoints(8,2);

% find which point is the highest from Matlab function

```

```

% "regionprops" and "extrema"
if topLeftExtremeY > topRightExtremeY
    highestPoint = topLeftExtremeY;
else highestPoint = topRightExtremeY;
end
highestPoint = round(highestPoint);

% find which point is the lowest from Matlab function
% "regionprops" and "extrema"
if bottomRightExtremeY < bottomLeftExtremeY
    lowestPoint = bottomRightExtremeY;
else lowestPoint = bottomLeftExtremeY;
end
lowestPoint = round(lowestPoint);

% find the height in pixels
height = abs(highestPoint-lowestPoint);
fwhm = height/2; % find the FWHM pixel value

% Use FWHM pixel value to start searching left
% and right for the widths
% Use the centroid x-location as a default starting location
x_loc = centroid(1,1);
x_loc = round(x_loc);
y_loc = round(fwhm + highestPoint);

% move only in the x-direction to determine the width
val = 1; % value of white pixels in image
j = 0; % counter
while val
    j = j+1;
    val = maskedImage(y_loc, x_loc + j);
end
x_right = x_loc + j - 1;

% value of white pixels in image
val = 1; % value of white pixels in image
j = 0; % counter
while val
    j = j+1;
    val = maskedImage(y_loc, x_loc - j);
end
x_left = x_loc - j + 1;

weldWidthFWHM = abs(x_right-x_left)*lengthPerPixel;

```

```

% display the two regions measuring the FWHM
% width and display the text
% next to the left marker
hold on
plot(x_left,y_loc,'b^','MarkerSize',12,'LineWidth',2);
hold on;
plot(x_right,y_loc,'b^','MarkerSize',12,'LineWidth',2);

%% Determine toe positions, width, and top surface length

% find all non zero value locations
[rowsNonZero, colsNonZero] = find(maskedImage);

nonZeroPos = [rowsNonZero, colsNonZero];

for ii = 1:length(nonZeroPos)

    cLeft = sqrt(nonZeroPos(ii,2)^2 +...
        nonZeroPos(ii,1)^2);

    cRight = sqrt(nonZeroPos(ii,1)^2 +...
        (widthInPixels - nonZeroPos(ii,2))^2);

    cLeftVec(ii,:) = cLeft;
    cRightVec(ii,:) = cRight;
end

% top left weld toe location
% find distance for each nonzero point to top left
% corner of image (0,0)
leftMinLoc = find(cLeftVec == min(cLeftVec));

leftRowLoc = rowsNonZero(leftMinLoc);
leftColLoc = colsNonZero(leftMinLoc);

leftWeldToe = [leftColLoc, leftRowLoc];

% find distance for each nonzero point to top right
% corner of image (rows,cols)
rightMinLoc = find(cRightVec == min(cRightVec));

rightRowLoc = rowsNonZero(rightMinLoc);
rightColLoc = colsNonZero(rightMinLoc);

```

```

rightWeldToe = [rightColLoc, rightRowLoc];

% find the top surface locations
% iterate through the length of the columns
for n = 1:widthInPixels
    colVal = maskedImage(:,n);
    if sum(colVal) > 0
        colValLoc = find(colVal > 0);
        topPos = min(colValLoc);
        rowNum = topPos;
        colNum = n;
    else
        topPos = 0;
        rowNum = 0;
        colNum = n;
    end
    topPosVec(n) = topPos;
    rowNumVec(n) = rowNum;
    colNumVec(n) = colNum;
end

locations = find(rowNumVec > 1);
leftColLoc = locations(1,1);
rightColLoc = locations(1,end);
leftRowLoc = topPosVec(leftColLoc);
rightRowLoc = topPosVec(rightColLoc);

numSurfPixels = length(find(topPosVec > 1));
toeWidth = numSurfPixels*lengthPerPixel;

hold on
% plot circles at the selected weld toe locations
plot(leftWeldToe(1,1),leftWeldToe(1,2),...
    'gx','MarkerSize',15,'LineWidth',2); hold on;
plot(rightWeldToe(1,1),rightWeldToe(1,2),...
    'gx','MarkerSize',15,'LineWidth',2);

% determine surface length by iterating through pixel values
for nn = 1:length(topPosVec)-1
    if topPosVec(nn) ~= 0
        dist = sqrt((topPosVec(nn)-topPosVec(nn+1))^2 + 1);
    else
        dist = 0;
    end
end

```

```

        distVec(nn) = dist;
end
lengthOfSurf = sum(distVec)*lengthPerPixel;

%% Determine FZ penetration from top surface of plate
% Use the output from the built in Matlab
% function "regionprops" to extract
% the needed information

% average y positions to get a location to search for
% the weld toes, this gets the approximate
% plate surface location
yToePosAvg = mean(round(leftWeldToe(1,1)),...
    round(leftWeldToe(1,2)));

% find the deepest point of penetration using
% the already determined lowest
% point from the 'Extrema' values
penetration = lengthPerPixel*abs(yToePosAvg - lowestPoint);

%% Determine the perimeter of the fusion boundary
% Use the built in matlab function "regionprops" to
% extract the data from
% the traced fusion boundary user measurement
perimeter = regionprops(maskedImage,'Perimeter');
perimeter = cat(1,perimeter.Perimeter);
perimeterOfFZ = perimeter*lengthPerPixel;

%% Label the plot with the measured values
% get the variables that are measured and plot them on
% the figure window
% make all variables left aligned realtive to the figure
% round all variables to three decimal places and set
% font size and color
fusionBoundaryLength = perimeterOfFZ-lengthOfSurf;
hold on
y_labelPos = heightInPixels + 10;
x_labelPosR = widthInPixels + 25;
fontsize = 12; % size of measured data font on figure
text(x_labelPosR, y_labelPos/16,['Depth of Penetration = ',...
    num2str(round(penetration,3)), ' mm'],'FontSize',...
    fontsize,'Color',[0 0 0])
text(x_labelPosR, y_labelPos*(3/16),['Weld Toe Width = ',...
    num2str(round(toeWidth,3)), ' mm'],'FontSize',...

```

```

        fontsize, 'Color', [0 1 0])
text(x_labelPosR, y_labelPos*(5/16), ['Centroid Width = ', ...
    num2str(round(weldCentroidWidth,3)), ' mm'], 'FontSize', ...
    fontsize, 'Color', [1 0 0])
text(x_labelPosR, y_labelPos*(7/16), ['FWHM Width = ', ...
    num2str(round(weldWidthFWHM,3)), ' mm'], ...
    'FontSize', fontsize, ...
    'Color', [0 0 1])
text(x_labelPosR, y_labelPos*(9/16), ['X-Sec FZ Area = ', ...
    num2str(round(areaOfFZ,3)), '
    mm^2'], 'FontSize', fontsize, ...
    'Color', [0 0 0])
text(x_labelPosR, y_labelPos*(11/16), ['FZ Boundary Length =
    ', ...
    num2str(round(fusionBoundaryLength,3)), ' mm'], ...
    'FontSize', ...
    fontsize, 'Color', [1 0.25 0])

text(x_labelPosR, y_labelPos*(13/16), ['Total FZ Perimeter =
    ', ...
    num2str(round(perimeterOfFZ,3)), ' mm'], 'FontSize', ...
    fontsize, 'Color', [0 0.5 0.1])

text(x_labelPosR, y_labelPos*(15/16), ['Weld Surface Length =
    ', ...
    num2str(round(lengthOfSurf,3)), ' mm'], 'FontSize', ...
    fontsize, 'Color', [1 0.25 0.5])

%% Output data to table

% material label from inputs
materialLabel = string(dlgResponse{1,:});
% power label from inputs [W]
powerLabel = str2num(string(dlgResponse{2,:}));
% travel speed label from inputs [mm/s]
tsLabel = str2num(string(dlgResponse{3,:}));
% beam diameter label from inputs [um]
bdLabel = str2num(string(dlgResponse{4,:}));
% weld ID label from inputs
weldIDlabel = string(dlgResponse{5,:});

T = table(materialLabel, weldIDlabel, powerLabel, ...
    tsLabel, bdLabel, ...
    penetration, toeWidth, weldCentroidWidth, ...
    weldWidthFWHM, ...

```

```

        areaOfFZ, fusionBoundaryLength,...
        perimeterOfFZ, lengthOfSurf);
disp(T)
disp('All tabulated values have units based on millimeters')

if i == 1 % get input for creating spreadsheet document
    filenameInput = inputdlg('Input Excel File Name');
    filenameStr = [filenameInput{:}];
    spreadSheetName = strcat(filenameStr, '.xlsx');
    writetable(T, spreadSheetName, 'WriteMode', 'append')

else

    writetable(T, spreadSheetName, 'WriteMode', 'append')

end

end
%%
load handel
sound(y, Fs)

```

## Appendix M: MATLAB® Script – Weld Surface Solidification Angle

```
%% Weld surface solidification analysis
% Measure the surface solidification angles to approximate the
% solidification rate

% Created by Tate Patterson
% Version 1 created 4 Jan. 2020

clear all; close all; clc;

% allow for user selection of micrograph file
fileName = uigetfile({'*.jpg','jpg Files (*.jpg)';...
    '*.JPG','JPG Files (*.JPG)';...
    '*.jpeg','jpeg Files (*.jpeg)';...
    '*.JPEG','JPEG Files (*.JPEG)';...
    '*.img','img Files (*.img)';...
    '*.IMG','IMG Files (*.IMG)';...
    '*.tif','tif Files (*.tif)';...
    '*.TIF','TIF Files (*.TIF)';...
    '*.tiff','tiff Files (*.tiff)';...
    '*.TIFF','TIFF Files (*.TIFF)' });

trueImage = imread(fileName);
figure; imshow(trueImage);
set(gcf, 'Units', 'Normalized', 'OuterPosition', [0 0 1 1]);

% utilize roipoly angle measurement tool

% line = getline;
% point1x = line(1,1); point1y = line(1,2);
% point2x = line(2,1); point2y = line(2,2);
% point3x = line(3,1); point3y = line(3,2);
%
% adjacentLength = sqrt((abs(point1x-point2x))^2)
% oppositeLength = sqrt((abs(point1y-point3y))^2)

rect = getrect;

xmin = rect(1);
ymin = rect(2);
width = rect(3);
height = rect(4);

%%
```

```

% calculate the angle, this is in radians
weldPoolAngle = atan(height/width); % measured pool angle [rad]
% solidification angle [rad]
solidificationAngle = pi/2-weldPoolAngle;
% fprintf('Weld Pool Angle = %0.1f° \r\r',weldPoolAngle*180/pi)
fprintf('Solidification Angle = %0.1f°
\r\r',solidificationAngle*180/pi)

% compute the solidification rate with an input travel speed
% TS = input('Input the travel speed in mm/sec: ');
TS = 100;

solidificationRate = TS*cos(solidificationAngle);
fprintf('Solidification Rate = %0.1f mm/sec
\r\r',solidificationRate)

% text(1220, 0.4, str3,'FontSize',25);
% str = {'Solidification Rate = '};
text(0, 500, ['Solidification Angle = ',...

num2str(solidificationAngle*180/pi,'%0.1f'),'°'],'FontSize',25);
% ['FZ Boundary Length =
',num2str(round(fusionBoundaryLength,3)),...
%' mm'],'FontSize',15,'Color',[1 0.25 0])

```

## Appendix N: MATLAB® Script – ICI Surface Fitting Algorithm

```
% Surface Fitting Algorithm for 3D ICI Data
% Point data must be extracted from text file from LDD 700 system
% Created by Tate Patterson
% August 2021

clc; clear; close all;

yOffset = 0; % measured y offset [μm]
plateSurf = 3000; % ICI Reference Plane Position

% keyholeOffset = -4; % measured keyhole offset [μm]
% file = uigetfile;

power = 1000; % define the power for the data collected
ts = 5; % define the travel speed for the data collected

powerStr = num2str(power); % create string from defined power
variable
tsStr = num2str(ts); % create string from defined ts variable
% create a string to title a plot
titleString = strcat('304L -', {' '}, powerStr, ' W - ', {' '}, ...
    tsStr, ' mm/s - 600 μm');
% create a string for saving figure and titling plot
saveString = strcat('304L_', powerStr, 'W_', tsStr, 'mmPs_600um');
fileString = strcat('M2P1C2-K-', powerStr, 'W-', tsStr, 'mmPs.txt');

data = importdata(fileString); % import defined data file

% extract columns of data and convert to millimeters
xVec = (data(:,1))/1000;
yVec = (data(:,2) + yOffset)/1000;
zVec = (data(:,3)-plateSurf)/1000;

% user defined function to create matrices with input data file
[xMat, yMat, zMat] = matCreation(xVec, yVec, zVec);

figure % create figure of raw data
plot3(xMat, yMat, zMat, 'o'); xlabel('X Distance [mm]');
ylabel('Y Distance [mm]'); zlabel('Depth [mm]');
title('Original Data')
axis equal

% shift values down from the top of plate to zero and remove all
```

```

% erroneous values just below zero
surfLoc = find(zVec > -0.2);
avgZSurf = mean(zVec(surfLoc));

% find the maximum value of the surf to shift all data to a zero
% position this eliminates the offset of data
maxZ = avgZSurf;
zVec = (zVec-maxZ); %
zVec(zVec>-0.3) = 0; % set all values greater than -# to zero

% user defined function to create matrices with the input data
file
[xMat, yMat, zMat] = matCreation(xVec, yVec, zVec);

figure % create 3D scatter plot of raw data
plot3(xMat,yMat,zMat,'o'); xlabel('X Distance [mm]');
ylabel('Y Distance [mm]'); zlabel('Depth [mm]');
title('Zeroed')
axis equal

% define the plot width and length for later use
plotWidth = max(max(xMat)); plotLength = max(max(yMat));
movMeanVal = 5; % define moving average values

%% Matrix Reduction
% Combine the nearest vectors of data to increase number of data
% points for performing a curve fit. This is performed by taking
% minimum value of each if multiple values exist in cells in the
% same row

zMatSize = size(zMat); % find matrix size
zMatSizeRows = zMatSize(1,1); % get rows of z matrix
zMatSizeCols = zMatSize(1,2); % get columns of z matrix

centerY = round(zMatSizeRows/2); % find center of rows
widthVal = 10; % define a column width to combine

% create a for loop to iterate through z matrix m number of times
% relative to the number of vectors being combined by 'widthVal'
for m = 1:zMatSizeRows/widthVal

    colMaxX = widthVal*m; % find the high column location
    colMinX = widthVal*m-widthVal+1; % find low column location

    % extract columns with width defined by 'widthVal'
    xMatRed = xMat(:,colMinX:colMaxX);

```

```

yMatRed = yMat(:,colMinX:colMaxX);
zMatRed = zMat(:,colMinX:colMaxX);

for rowX = 1:zMatSizeRows

    % find where no "NaN" value exists in the z vector
    nan_extract = find(~isnan(zMatRed(rowX,:)));

    % extract all values in column dimension for given row
    avgZ = mean(zMatRed(rowX,[nan_extract]));
    avgX = mean(xMatRed(rowX,[nan_extract]));
    avgY = mean(yMatRed(rowX,[nan_extract]));

    % build out matrices of data height and position data
    zAvgVec(rowX,:) = avgZ;
    xAvgVec(rowX,:) = avgX;
    yAvgVec(rowX,:) = avgY;

end

% extract the column vector data
zCol = zAvgVec(:,1);
xCol = xAvgVec(:,1);
yCol = yAvgVec(:,1);

% get all real values (not NaN)
xRealVec = xCol(~isnan(zCol));
yRealVec = yCol(~isnan(zCol));
zRealVec = zCol(~isnan(zCol));

% check if there is more than 1 real value for 'fit' function
if sum(~isnan(zRealVec)) > 1

    % use built in MATLAB function 'fit' to fit a linear
    % interpolation equation to the data points
    fitZ = fit(xRealVec, zRealVec, 'linearinterp');

    % create a vector of values for fitting
    xFitVec = linspace(-plotWidth,plotLength,...
        zMatSizeRows/widthVal);
    yFitVec = linspace(-plotWidth,plotLength,...
        zMatSizeRows/widthVal)';

    % use fit equation to create a vector
    zFitDataX = fitZ(xFitVec);

```

```

% check to confirm there are non-zero values in vector
if sum(abs(zFitDataX)) > 0

    % find peak values to better fit the data
    [peakVal, peakLoc] = findpeaks(-1*zFitDataX);

    % check to make sure there are three values to fit
    if length(peakVal) >= 3

        % find locations between min and max fit points
        minPeakLoc = min(peakLoc);
        maxPeakLoc = max(peakLoc);
        locsToFit = min(peakLoc):max(peakLoc);

        % build vector of points from z data vector
        oldFitPts = zFitDataX(locsToFit);

        % fit a linear interpolation equation across data
        fitPeak =
        fit(xFitVec(peakLoc)', peakVal, 'linearinterp');

        % construct a vector for evaluation across the
        % minimum and maximum points
        xx = linspace(xFitVec(minPeakLoc), ...
            xFitVec(maxPeakLoc), length(locsToFit));

        % evaluate the fit equation
        fitPeakData = -fitPeak(xx);

        % replace the original data with the new fit data
        % from peak analysis
        zFitDataX(locsToFit) = fitPeakData;
        zFitDataX = movmean(zFitDataX, movMeanVal);
    end
end
% build matrices of processed data
zFitMatX(:, m) = zFitDataX;
% exclude height data >0 produced by the 'fit' function
zFitMatX(zFitMatX < min(min(zMat))) = 0;
xFitMatX(:, m) = xFitVec;
yFitMatX(m, :) = yFitVec;
end
end

%% Iterate through opposite dimension (rows) to refit the data

```

```

zMatSizeY = size(zMat); % find matrix size
zMatSizeRows = zMatSizeY(1,1); % get rows of z matrix
zMatSizeCols = zMatSizeY(1,2); % get columns of z matrix

centerX = round(zMatSizeCols/2); % find center of columns

% create a for loop to iterate through z matrix n number of times
% relative to the number of vectors being combined by 'widthVal'
for n = 1:zMatSizeRows/widthVal

    rowMaxY = widthVal*n; % find the high row location
    rowMinY = (widthVal*n-widthVal)+1; % find low row location

    % extract columns with width defined by 'widthVal'
    xMatRedY = zMat(rowMinY:rowMaxY,:);
    yMatRedY = yMat(rowMinY:rowMaxY,:);
    zMatRedY = zMat(rowMinY:rowMaxY,:);

    for colY = 1:zMatSizeRows

        % find where no "NaN" value exists in the z vector
        nan_extract = find(~isnan(zMatRedY(:,colY)));

        % get averages of values in row dimension for columns
        avgZy = mean(zMatRedY([nan_extract],colY));
        avgXy = mean(xMatRedY([nan_extract],colY));
        avgYy = mean(yMatRedY([nan_extract],colY));

        % build matrices of data height and position data
        zAvgVecY(colY,:) = avgZy;
        xAvgVecY(colY,:) = avgXy;
        yAvgVecY(colY,:) = avgYy;

    end

    % extract the column vector data
    zColy = zAvgVecY(:,1);
    xColy = xAvgVecY(:,1);
    yColy = yAvgVecY(:,1);

    % get all real values (not NaN)
    xRealVecY = xColy(~isnan(zColy));
    yRealVecY = yColy(~isnan(zColy));
    zRealVecY = zColy(~isnan(zColy));

```

```

% check if there is more than 1 real value for 'fit' function
if sum(~isnan(zRealVecY)) > 1

    % use built in MATLAB function 'fit' to fit a linear
    % interpolation equation to the data points
    fitZ = fit(yRealVecY, zRealVecY, 'linearinterp');

    % create a vector of values for fitting
    xFitVecY = linspace(-
plotWidth,plotLength,zMatSizeRows/widthVal);
    yFitVecY = linspace(-
plotWidth,plotLength,zMatSizeRows/widthVal)';

    % use fit equation to create a vector
    zFitDataY = fitZ(yFitVecY);

    % check to confirm there are non-zero values in vector
    if sum(abs(zFitDataY)) > 0

        % find peak values to better fit the data
        [peakValY, peakLocY] = findpeaks(-1*zFitDataY);

        % check to make sure there are three values to fit
        if length(peakValY) >= 3

            % find locations between min and max fit points
            minPeakLocY = min(peakLocY);
            maxPeakLocY = max(peakLocY);
            locsToFitY = min(peakLocY):max(peakLocY);

            % build vector of points from z data vector
            oldFitPtsY = zFitDataY(locsToFitY);

            % fit a linear interpolation equation across data
            fitPeakY = fit(yFitVecY(peakLocY),peakValY,...
'linearinterp');

            % construct a vector for evaluation across the
            % minimum and maximum points
            xxy = linspace(yFitVecY(minPeakLocY),...
                xFitVecY(maxPeakLocY),length(locsToFitY));

            % evaluate the fit equation
            fitPeakDataY = -fitPeakY(xxy);

            % replace the original data with the

```

```

        % new fit data from peak analysis
        zFitDataY(locsToFitY) = fitPeakDataY;
        zFitDataY = movmean(zFitDataY,movMeanVal);
    end
end

    % build matrices of processed data
    zFitMatY(:,n) = zFitDataY;
    % exclude height data >0 produced by the 'fit' function
    zFitMatY(zFitMatY < min(min(zMat))) = 0;
    xFitMatY(:,n) = xFitVecY;
    yFitMatY(n,:) = yFitVecY;

end
end

% figure
% plot3(xFitMatY,yFitMatY,zFitMatY,'-'); hold on; axis equal
% xlabel('X Distance [mm]'); ylabel('Y Distance [mm]');
% zlabel('Depth [mm]');
% title('Test Matrix')
% hold on;
% plot3(xMat,yMat,zMat,'o'); xlabel('X Distance [mm]');
% ylabel('Depth [mm]');
% axis equal

%% Offset removal caused by averaging truncation

yFitMatSize = size(yFitMatY); % find size of previous matrix

% find the dataNum number of maximum original data points and
average
dataNum = 20;
meanZmin = mean(mink(min(zMat),dataNum));
minFitVal = min(min(zFitMatY)); % find most negative (min) fit
value

% iterate through cells in matrix to check and add difference
% between the greatest depth and average of dataNum average
for iii = 1:yFitMatSize(1,1) % iterate through matrix rows
    for jjj = 1:yFitMatSize(1,2) % iterate through matrix columns
        if zFitMatY(iii,jjj) < 0 % if value is neg., add mean
            zFinalVal = zFitMatY(iii,jjj) + (meanZmin-minFitVal);
        else
            % if not, keep the value the same
            zFinalVal = zFitMatY(iii,jjj);
        end
    end
end

```

```

        end
        % reconstruct matrix with new values
        zFinal(iii,jjj) = zFinalVal;
    end
end

%% Average both dimension fitting values in the X direction

avgMatZ = (zFitMatX + zFitMatY')./2;

% figure
% plot3(xFitMatX,yFitMatX,avgMatZ,'-'); hold on; axis equal
% xlabel('X Distance [mm]'); ylabel('Y Distance [mm]');
% zlabel('Depth [mm]');
% title('Average Matrix')

% figure
% surf(xFitMatX,yFitMatX,avgMatZ,'EdgeColor','none'); hold on;
% xlabel('X Distance [mm]'); ylabel('Y Distance [mm]');
% zlabel('Depth [mm]');
% shading interp
% axis equal

%% Iterate through compressed data to find peak values in x-
dimension

zAvgAvgX = avgMatZ; % redefine a z-data matrix variable to modify
numIterations = 5; % set number of iterations to run for loop

for i = 1:numIterations % loop multiple times to find all peaks

    sizeAvgZ = size(zAvgAvgX); % get the size of the matrix

    for j = 1:sizeAvgZ(1,1) % iterate from 1 to number of rows

        % extract columns of data in z-data matrix
        avgAvgZVec = zAvgAvgX(:,j);
        avgXvec = xFitMatX(:,j);
        avgYvec = yFitMatX(:,j);

        % check to confirm there are non-zero values in vector
        if sum(abs(avgAvgZVec)) > 0

            % find peak values to better fit the data
            [avgPeakVal, avgPeakLoc] = findpeaks(-1*avgAvgZVec);

```

```

    % check to make sure there are three values to fit
    if length(avgPeakVal) >= 3

        % find locations between min and max fit points
        minPeakLoc = min(avgPeakLoc);
        maxPeakLoc = max(avgPeakLoc);
        locsToFit = min(avgPeakLoc):max(avgPeakLoc);

        % build vector of points from z data vector
        oldFitPts = avgAvgZVec(locsToFit);

        % fit a linear interpolation equation across data
        fitPeak = fit(avgXvec(avgPeakLoc), ...
            avgPeakVal, 'linearinterp');

        % construct a vector for evaluation across the
        % minimum and maximum points
        x_avg = linspace(avgXvec(minPeakLoc), ...
            avgXvec(maxPeakLoc), length(locsToFit));

        % evaluate the fit equation
        fitPeakData = -fitPeak(x_avg);

        % replace the original data with the
        % new fit data from peak analysis
        avgAvgZVec(locsToFit) = fitPeakData;
        avgAvgZVec = movmean(avgAvgZVec, movMeanVal);
    end
end
% build matrices
zAvgAvgX(:,j) = avgAvgZVec;
zAvgAvgX(zAvgAvgX < min(min(zMat))) = 0;
xAvgAvg(:,j) = avgXvec;
yAvgAvg(j,:) = avgYvec;
end
end

figure % create figure to plot results
surf(xAvgAvg, yAvgAvg, zAvgAvgX); hold on; axis equal
xlabel('X Distance [mm]'); ylabel('Y Distance [mm]');
zlabel('Depth [mm]');
title('X Average Average Matrix')

%% Iterate through compressed data to find peak values in y-
dimension

```

```

zAvgAvgY = zAvgAvgX; % initialize a new z-data matrix

for ii = 1:numIterations % loop as in x-direction loop

    sizeAvgZy = size(zAvgAvgY); % get the size of the matrix

    % iterate from 1 to number of columns
    for jj = 1:sizeAvgZy(1,2)

        % extract columns of data in z-data matrix
        avgAvgZVecY = zAvgAvgY(jj,:);
        avgXvec = xFitMatX(jj,:);
        avgYvec = yFitMatX(jj,:);

        % check to confirm there are non-zero values in vector
        if sum(abs(avgAvgZVecY)) > 0

            % find peak values to better fit the data
            [avgPeakVal, avgPeakLoc] = findpeaks(-1*avgAvgZVecY);

            % check to make sure there are three values to fit
            if length(avgPeakVal) >= 3

                % find locations between min and max fit points
                minPeakLoc = min(avgPeakLoc);
                maxPeakLoc = max(avgPeakLoc);
                locsToFit = min(avgPeakLoc):max(avgPeakLoc);

                % build vector of points from z data vector
                oldFitPts = avgAvgZVecY(locsToFit);

                % fit a linear interpolation equation across data
                fitPeak = fit(avgYvec(avgPeakLoc)',...
                    avgPeakVal','linearinterp');

                % construct vector for evaluation of min and max
                y_avg = linspace(avgYvec(minPeakLoc),...
                    avgYvec(maxPeakLoc),length(locsToFit));

                % evaluate the fit equation
                fitPeakData = -fitPeak(y_avg);

                % replace the original data with the
                % new fit data from peak analysis
                avgAvgZVecY(locsToFit) = fitPeakData;
                avgAvgZVecY = movmean(avgAvgZVecY,movMeanVal);
            end
        end
    end
end

```

```

        end
    end

    % build matrices
    zAvgAvgY(jj,:) = avgAvgZVecY;
    zAvgAvgY(zAvgAvgY < min(min(zMat))) = 0;
    xAvgAvgY(jj,:) = avgXvec;
    yAvgAvgY(jj,:) = avgYvec;
end
end

figure % create figure and plot results
surf(xAvgAvgY,yAvgAvgY,zAvgAvgY); hold on;
xlabel('X Distance [mm]'); ylabel('Y Distance [mm]');
zlabel('Depth [mm]');
title('Y Average Average Matrix')
axis equal % set the axis equal scales
shading interp % smooth color transitions

%% Adjust fitted surface to bottom of averaged data

xFinal = xAvgAvgY;
yFinal = yAvgAvgY;
zFinal = zAvgAvgY;

figure % create figure for 'surf' plot of data
surf(xFinal,yFinal,zFinal); hold on; axis equal
xlabel('X Distance [mm]'); ylabel('Y Distance [mm]');
zlabel('Depth [mm]');
title('Final Fit')
shading interp % smooth color transitions
hold on;

% plot a scatter plot of 3D data overlaid with 'surf' plot
plot3(xMat,yMat,zMat,'o');
xlabel('X Distance [mm]'); ylabel('Y Distance [mm]');
zlabel('Depth [mm]');
title('Zeroed')
axis equal % set the axis equal scales

%% Compute measurement values from the fitted surface

% set x, y, and z inputs for user defined functions
x = xFinal;
y = yFinal;
z = zFinal;

```

```

% call user defined function 'keyholeMeasurements' to compute
volume, second moment beam diameter (D2M), 86% beam diameter
(D86), and full-width-half-maximum beam (fwhm) beam diameter
[volume, D2M, D86, fwhm] = keyholeMeasurements(x, y ,z);

%% Plotting for visualization purposes

% set a consistent or (fixed) plot height
zDepth = 2; % min(min(zFinal));

% call user defined function 'ICI_3D_SurfFitView' for plotting
ICI_3D_SurfFitView(xFinal,yFinal,zFinal,titleString,saveString,zD
epth);

```

## N.1 Keyhole Measurement Function

```
function [volume, D2M, D86, fwhm, depth] = keyholeMeasurements(x,
y, z)
% Volume Calculation from 3D data
% Take input matrix with x, y and z being matrices (x and y must
% be from a 'meshgrid' or matrix) and compute the
% volume encompassed by surface, the second moment beam
% diameter(D2M), 86% beam diameter (D86), and full width half
% maximum beam diameter (FWHM). Units input will determine the
% units output.

%% Get size of depth matrix from input data
sizeZ = size(z);
sizeZx = sizeZ(1,1);
sizeZy = sizeZ(1,2);

%% Set data as needed for computation
x = x(:,1); % set x data vector
y = y(1,:); % set y data vector
z = z;

%% find the maximum depth of the fit data
depth = min(min(z));
display(depth); % display depth value

%% Volume analysis
% utilize the built in MATLAB function 'trapz'

volume = trapz(y,trapz(x,z,2),1); % volume approximation in
[mm^3]

display(volume) % display volume value

%% D86 analysis
% compute 86% beam diameter (D86) of fitted keyhole data using
% a user defined function 'd86Calc_Keyhole'

[xAdj, yAdj, calcXCenter, calcYCenter, sum_z, sum_E_zx, sum_E_zy,
Ex,...
Ey, centerX, centerY, r86, D86] = d86Calc_Keyhole(x,y,z);

display(D86) % display D86 value

%% D2M analysis
% compute the second moment beam diameter (D2M) of the fitted
```

```

% keyhole data using a user defined function 'secMomCalc_Keyhole'

[xAdj, yAdj, calcXCenter, calcYCenter, sum_z, sum_E_zx,
sum_E_zy,...
    Ex, Ey, sqdSum, D2M] = secMomCalc_Keyhole(x,y,z);

display(D2M)

%% FWHM height calculation
% find the vapor capillary width at half the maximum depth
[fw hm] = fwhm_Calc(x, y, z);

display(fwhm) % display fwhm value

%% Sanity check for volume measurement
% cylinder volume for checking integral approximation
cyl_vol = depth*pi*(D86/2)^2; % V_cyl = pi*r86^2*height

end

```

## N.2 D86 Keyhole Diameter Calculation

```
function [xAdj, yAdj, calcXCenter, calcYCenter, sum_z,...
    sum_E_zx, sum_E_zy, Ex, Ey, centerX, centerY, r86, D86]...
    = d86Calc_Keyhole(x,y,z)
% Computes D86 or 86% beam diameter based on 86% of the energy
% from the centroid of the intensity distribution

%% Determine the centroid locations
% create nested for loops to iterate through x and y variables

for j = 1:length(y)
    for i = 1:length(x)

        % extract each value in the depth matrix
        z1 = z(j,i);

        E_zx = z1*x(i); % compute the X first moment values
        E_zy = z1*y(j); % compute the Y first moment values

        % store the X first moment values into matrix
        Ex(j,i) = E_zx;
        % store the Y first moment values into matrix
        Ey(j,i) = E_zy;

    end
end

sum_z = sum(sum(z)); % power or sum of the raw depth data
sum_E_zx = sum(sum(Ex)); % sum of first moment depth for X
sum_E_zy = sum(sum(Ey)); % sum of first moment depth for Y

calcXCenter = sum_E_zx/sum_z;
calcYCenter = sum_E_zy/sum_z;

% adjust the x position from the determined centroid
xAdj = x - calcXCenter;
% adjust the y position from the determined centroid
yAdj = y - calcYCenter;

%% D86 calculation from the centroid adjusted depth matrix
% Start at center of centroid adjusted axis and iterate outward
% in increasing circles while summing intensity values within
% circle until 86% of the total intensity (depth) is found
```

```

% find the circle centers or centroid of distribution
% find the center of centroid adjusted x axis values
centerX = length(xAdj)/2;
% find the center of centroid adjusted y axis values
centerY = length(yAdj)/2;

% find the total power in the intensity array
totalPower = sum(sum(z));
r86 = 0; % initialize the radius variable
depth_86 = 0; %initialize the 86% depth variable

% loop while the depth_86 variable is less than 86%
while depth_86 < 0.865

    r86 = r86+1;

    [columnsInImage, rowsInImage] =
meshgrid(1:length(xAdj),...
    1:length(yAdj));

    % create zeros and ones matrices to multiply depth matrix
    circlePixels = (rowsInImage - centerY).^2 + ...
        (columnsInImage - centerX).^2 <= r86.^2;

    % find sum of depth values within the circle radius
    intensitySumAtRadius = z.*circlePixels;

    % find the sum of the matrix values
    I86sum = sum(sum(intensitySumAtRadius));

    depth_86 = I86sum/totalPower;

end

D86x = xAdj(round(centerX + r86))*2;
D86y = yAdj(round(centerY + r86))*2;

% average D86 value from x and y directions
D86 = (D86x + D86y)/2;

end

```

### N.3 Keyhole D2M Diameter Calculation

```
function [xAdj, yAdj, calcXCenter, calcYCenter, sum_z,...
    sum_E_zx, sum_E_zy, Ex, Ey, sqdSum, D2M] =
    secMomCalc_Keyhole(x,y,z)

%%
% Computation of the second moment keyhole diameter (D2M) from
% surface fit data intensity profile

% create nested for loops to iterate through x and y position
Variables in the matrix
for j = 1:length(y)
    for i = 1:length(x)

        % extract single value at each position in intensity
        % matrix for computation
        z1 = z(j,i);

        E_zx = z1*x(i); % compute the X first moment values
        E_Zy = z1*y(j); % compute the Y first moment values

        Ex(j,i) = E_zx; % store X first moment values
        Ey(j,i) = E_Zy; % store Y first moment values

    end
end

sum_z = sum(sum(z)); % sum all data in the matrix
sum_E_zx = sum(sum(Ex)); % sum of the first moment data for X
sum_E_zy = sum(sum(Ey)); % sum of the first moment data for Y

% determine centroid location in X
calcXCenter = sum_E_zx/sum_z;
% determine centroid location in Y
calcYCenter = sum_E_zy/sum_z;

% adjust the x position from the determined centroid
xAdj = x - calcXCenter;

% adjust the y position from the determined centroid
yAdj = y - calcYCenter;

% second moment computation
for n = 1:length(yAdj) % iterate through y-axis
```

```

for m = 1:length(xAdj) % iterate through x-axis

    % compute 2nd moment based on centroid adjustment
    momCalc = z(n,m)*((xAdj(m))^2+(yAdj(n))^2);

    secMom(n,m) = momCalc; % build 2nd moment data matrix
end

end

sqdSum = sum(sum(secMom)); % squared sum of 2nd moment matrix

% D2M calculation
D2M = 2*sqrt(2)*sqrt(sqdSum/sum_z);

End

```

## N.4 Keyhole FWHM Diameter Calculation

```
function [fwhm] = fwhm_Calc(x, y, z)
% Compute full width half maximum (FWHM) diameter of the fit data
% from ICI imaging
% Takes x, y, and z inputs as matrix with x and y as a meshgrid
%%
% find maximum depth or most negative (min) of the ICI fit data
abs_Depth = abs(min(min(z)));

% turn x and y data into vectors only for calculations
x = x(:,1);
y = y(1,:);

% find the full width half maximum height of input data
fwhm_height = abs_Depth/2;

%% FWHM height distance search based on fwhm_height

rowsZ = size(z); % get the size of the z matrix
rowsZ = rowsZ(1,1); % get the number of rows size

distVecX = []; % preallocate a distance matrix

for rows = 1:rowsZ % iterate from 1 to number of rows

    zRowVec = z(rows,:); % extract row vector data

    % iterate through length of row vector
    for cols = 1:length(zRowVec)

        % get absolute value of fwhm height minus each z value
        fwhm_LocSearchX = abs(abs(zRowVec) - fwhm_height);

        % get the two minimum values after subtraction
        % (checking which is closer to zero)
        minValX = mink(fwhm_LocSearchX,4);

        % create conditional statement to make sure values are
        % greater than zero
        if minValX(1,1) == fwhm_height || minValX(1,2) ==
fwhm_height
            distanceX = 0;
        else

            % get the two minimum locations
```

```

        loc1 = find(fwhm_LocSearchX == minValX(1,1));
        loc1 = loc1(1,end);
        loc2 = find(fwhm_LocSearchX == minValX(1,2));
        loc2 = loc2(1,1);

        xVal_1 = x(loc1); % get first x location value
        xVal_2 = x(loc2); % get second x location value

        % get x values out of location matrix
        distanceX = abs(xVal_1 - xVal_2);

    end

    % build vector of values out of each row
    distVecX(rows) = distanceX;

end

end

maxDistX = max(distVecX); % get the maximum of all row vectors
[mm]

%% Repeat distance search through the columns rather than rows

% get the number of columns from the input matrix
colsZ = size(z); colsZ = colsZ(1,2);

distVecY = []; % preallocate a distance vector

for cols = 1:colsZ % iterate from 1 to number of columns

    zColVec = z(:,cols); % extract column vector data

    % iterate through length of column vector
    for rows = 1:length(zColVec)

        % get absolute value of fwhm height minus each z value
        fwhm_LocSearchY = abs(abs(zColVec)-fwhm_height);

        % get the two minimum values after subtraction
        % (checking which is closer to zero)
        minValY = mink(fwhm_LocSearchY,4);

        % create conditional statement to make sure values are
        % greater than zero

```

```

        if minValY(1,1) == fwhm_height || minValY(2,1) ==
fwhm_height
            distanceY = 0;
        else

            % get the two minimum locations
            loc1y = find(fwhm_LocSearchY == minValY(1,1));
            loc1y = loc1y(1,end);
            loc2y = find(fwhm_LocSearchY == minValY(2,1));
            loc2y = loc2y(1,1);

            yVal_1 = y(loc1y); % get first y location value
            yVal_2 = y(loc2y); % get second y location value

            % get y values out of location matrix
            distanceY = abs(yVal_1 - yVal_2);

        end

        % build vector of values out of each column
        distVecY(cols) = distanceY;

    end
end

maxDistY = max(distVecY); % get the maximum of all column vectors
[mm]

%% Average the x and y values to compute FWHM diameter

fwhm = (maxDistX + maxDistY)/2;

end

```

## N.5 Keyhole Surface Visualization Script

```
function [] = ICI_3D_SurfFitView(xFinal,yFinal,zFinal,...
    titleString,saveString,zDepth)
%% ICI surface fit data plotting

% create a figure window with a maximized view
figure('units','normalized','outerposition',[0.2 0.05 0.48 0.93])

% extract values from inputs
x = xFinal;
y = yFinal;
z = zFinal;

plotWidth = 0.7; % define the plot width and length
plotLength = 0.7;

zDepth = round(min(min(z)),1);

% create the plot on figure
p = surf(xFinal,yFinal,zFinal,'EdgeColor','none'); hold on;
% p =
scatter3(xFinal(:),yFinal(:),zFinal(:),[],zFinal(:),'filled');
caxis([round(zDepth) 0]); % define the colormap/colorbar range
colormap(flipud(jet)); % select predefined MATLAB colormap and
flip colors
cbar = colorbar('Ticks',[round(zDepth):0.25:0]); % set colorbar
location;
cbar.Label.String = 'Keyhole Depth [mm]'; % label colorbar

ax = gca; % get current axes values
ax.Position = ax.Position;
% set colorbar position closer to plot
pos = get(cbar,'Position');
set(cbar,'Position',pos+[-0.055,0,0,0]);

xlh = xlabel('X [mm]'); % label the axes
ylh = ylabel('Y [mm]');
zlh = zlabel('Z [mm]');

% reposition axes labels
xlh.Position(1) = 0.2;
xlh.Position(2) = -0.5;
ylh.Position(2) = 0.5;
xlh.Position(3) = round(zDepth) - 0.3;
ylh.Position(3) = round(zDepth) - 0.3;
```

```

axis equal % make the axis proportional

xlim([-plotWidth,plotLength]); % set x-axis limits
ylim([-plotWidth,plotLength]); % set y-axis limits
zlim([round(zDepth) 0]) % set z-axis limits

% Set the x-axis ticks
set(gca,'XTick',[-0.6:0.2:0.6]);
% Set the y-axis ticks
set(gca,'YTick',[-0.6:0.2:0.6]);
% Set the z-axis ticks
set(gca,'ZTick',[round(zDepth):0.25:0])

set(gcf,'color','w'); % set background of figure to white
plt.XAxis.Color = 'k'; % color the x-axis black
plt.YAxis.Color = 'k'; % color the y-axis black

% set font size and line width
set(gca,'FontSize',24,'LineWidth',2);

% Set the view of the 3D beam caustic
view([-30, 20])
title(titleString); % title figure

end

```

## Appendix O: MATLAB® Script – Neural Network

### O.1 Graphical User Interface Script

```
% Neural Network Graphical User Interface
% Created by Tate Patterson
% October 2021

function neuralNetGUI
%% first get the experimental data used to train NN for 304L
% combine neural network output files to single, sorted matrix
% use user defined function 'datacomb';
expData304L = load('expDataMat304L.mat');
expData304L = expData304L.expDataMat304L;

% get all power from original data [W]
powerExp304L = expData304L(:,1);
% get travel speed data from original data [W]
tsExp304L = expData304L(:,2);
% get penetration data from original data [W]
penExp304L = expData304L(:,4);

% get the unique power values to extract data for a given power
unqExpPower304L = unique(powerExp304L);

% get neural network computed data
allDataStruct304L = load('allDataMat304L.mat');
allDataMat304L = allDataStruct304L.allDataMat304L;
allPower304L = allDataMat304L(:,1);
allTS304L = allDataMat304L(:,2);
allPen304L = allDataMat304L(:,3);
allArea304L = allDataMat304L(:,4);
allToe304L = allDataMat304L(:,5);
allCent304L = allDataMat304L(:,6);
allFWHM304L = allDataMat304L(:,7);

% find where the penetration is zero and set the widths to zero
locZero = find(allArea304L <= 0.1 | allPen304L < 0);
allPen304L(locZero) = 0;
allArea304L(locZero) = 0;
allToe304L(locZero) = 0;
allCent304L(locZero) = 0;
allCent304L(locZero) = 0;
allFWHM304L(locZero) = 0;
```

```

unq_AllDataPower304L = unique(allPower304L);

for ii = 1:length(unq_AllDataPower304L)
    pStrings = string(unq_AllDataPower304L(ii));
    powerLabels304L(ii,:) = pStrings;
end

% create a blank label at beginning
powerLabels304L = [' '; powerLabels304L];
tsLabelVec304L = string(5:5:150)';
tsLabels304L = [' '; tsLabelVec304L];

%% first get the experimental data used to train NN
expDataTi64 = load('expDataMatTi64.mat');
expDataTi64 = expDataTi64.expDataMatTi64;

% get all power from original data [W]
powerExpTi64 = expDataTi64(:,1);
% get travel speed data from original data [W]
tsExpTi64 = expDataTi64(:,2);
% get penetration data from original data [W]
penExpTi64 = expDataTi64(:,4);

% get the unique power values to extract data for a given power
unqExpPowerTi64 = unique(powerExpTi64);

% get neural network computed data Ti64
allDataStructTi64 = load('allDataMatTi64.mat');
allDataMatTi64 = allDataStructTi64.allDataMatTi64;
allPowerTi64 = allDataMatTi64(:,1);
allTSTi64 = allDataMatTi64(:,2);
allPenTi64 = allDataMatTi64(:,3);
allAreaTi64 = allDataMatTi64(:,4);
allToeTi64 = allDataMatTi64(:,5);
allCentTi64 = allDataMatTi64(:,6);
allFWHMTi64 = allDataMatTi64(:,7);

% find where the penetration is zero and set the widths to zero
locZero = find(allAreaTi64 <= 0.1 | allPenTi64 < 0);
allPenTi64(locZero) = 0;
allAreaTi64(locZero) = 0;
allToeTi64(locZero) = 0;
allCentTi64(locZero) = 0;
allCentTi64(locZero) = 0;
allFWHMTi64(locZero) = 0;

```

```

unq_AllDataPowerTi64 = unique(allPowerTi64);

for ii = 1:length(unq_AllDataPowerTi64)
    pStrings = string(unq_AllDataPowerTi64(ii));
    powerLabelsTi64(ii,:) = pStrings;
end

% create a blank label at beginning
% powerLabelsTi64 = [' '; powerLabelsTi64];
% tsLabelVecTi64 = string(5:5:150)';
% tsLabelsTi64 = [' '; tsLabelVecTi64];

%% create a function to output the plot based on user selection

% fig = uifigure('WindowState','maximized','Resize','off');
fig = uifigure('Position',[100 100 1200 800]);

fig.Resize = 'off';
fig.PosPix = fig.Position;

fig.Units = 'normalized';
fig.Name = 'Laser Beam Welding - Weld Predictor';

% create subpanels for labeling selections
titlePanel = uipanel('Parent',fig,...
    'Title','Laser Beam Welding - Weld Predictor',...
    'units','normalized','BorderType','none',...
    'TitlePosition','centertop','FontSize',35,...
    'FontWeight','bold',...
    'ForegroundColor',[0.85 0 0],'Position',[0.1 0.82 .8 .14]);

% create subpanels for labeling selections
titleSubPanel = uipanel('Parent',titlePanel,...
    'Title',...
    'Neural Network Model Developed by Tate Patterson, 2021',...
    'units','normalized','BorderType','none',...
    'TitlePosition','centertop','FontSize',10,...
    'FontWeight','bold',...
    'ForegroundColor',[0 0 0],'Position',[0.1 0.5 0.8 .25]);

% create plot axes for plotting penetration versus travel speed
ax = uiaxes('Parent',fig,...
    'units','normalized','Position',[0.025 0.1 0.5 0.5]);

% define the initial plot axes
plotTitle = powerLabels304L(1,1);

```

```

ax.Title.String = strcat(plotTitle);
ax.Title.FontSize = 20;
ax.FontSize = 22;
ax.XLabel.String = 'Travel Speed [mm/s]';
ax.XLabel.FontSize = 20;
ax.YLabel.String = 'Penetration [mm]';
ax.YLabel.FontSize = 20;
grid(ax,'on');
ax.Box = 'on';
ax.GridColor = [150/256, 150/256, 150/256];
ax.XLim = [5 150];
ax.XTick = (0:25:150);
ax.YLim = [0.25 4];
ax.YTick = (0:0.5:4);
ax.LineWidth = 1.5;

x_pred = [];
pen_pred = [];

plot(ax,x_pred,pen_pred);
plotTitle = ' ';
ax.Title.String = plotTitle;
plotTitleMat = plotTitle;

%% %%%%%%%%%%%%%%%%%%%%%%%%%%%%%%%%%%%%%%%%%%%%%%%%%%%%%%%%%%%%%%%%%%%%%%%%%
% Subpanels
% create subpanels for labeling selections
sp_mat = uipanel('Parent',fig,'Title','Material',...
    'units','normalized','BorderType','none',...
    'TitlePosition','centertop','FontSize',20,...
    'FontWeight','bold',...
    'ForegroundColor',[0 0 0],'Position',[0.15 0.73 .18 .1]);
% 'BorderType','none',

% create subpanels for labeling selections
sp_shield = uipanel('Parent',fig,'Title','Shielding Gas',...
    'units','normalized','BorderType','none',...
    'TitlePosition','centertop','FontSize',20,...
    'FontWeight','bold',...
    'ForegroundColor',[0 0 0],'Position',[0.415 0.73 .18 .1]);

% create subpanels for labeling selections
sp_Angle = uipanel('Parent',fig,'Title','Beam Angle [°]',...
    'units','normalized','BorderType','none',...
    'TitlePosition','centertop','FontSize',20,...
    'FontWeight','bold',...

```

```

    'ForegroundColor',[0 0 0],'Position',[0.7 0.73 .18 .1]);

% create subpanels for labeling selections
sp_diam = uipanel('Parent',fig,'Title','Beam Diameter [ $\mu$ m]',...
    'units','normalized','BorderType','none',...
    'TitlePosition','centertop','FontSize',20,...
    'FontWeight','bold',...
    'ForegroundColor',[0 0 0],'Position',[0.15 0.63 .18 .1]);

% create subpanels for labeling selections
sp_power = uipanel('Parent',fig,'Title','Power [W]',...
    'units','normalized','BorderType','none',...
    'TitlePosition','centertop','FontSize',20,...
    'FontWeight','bold',...
    'ForegroundColor',[0 0 0],'Position',[0.415 0.63 .18 .1]);

% create subpanels for labeling selections
sp_ts = uipanel('Parent',fig,'Title','Travel Speed [mm/s]',...
    'units','normalized','BorderType','none',...
    'TitlePosition','centertop','FontSize',20,...
    'FontWeight','bold',...
    'ForegroundColor',[0 0 0],'Position',[0.7 0.63 .18 .1]);

%% %%%%%%%%%%%%%%%%%%%%%%%%%%%%%%%%%%%%%%%%%%%%%%%%%%%%%%%%%%%
% create subpanels for text outputs
% create subpanels for labeling selections

outputText_sp = uipanel('Parent',fig,...
    'units','normalized',...
    'Title','Model Outputs',...
    'BorderType','none',...
    'TitlePosition','centertop','FontSize',25,...
    'FontWeight','bold',...
    'ForegroundColor',[0.1 0 0],'Position',[0.57 0.2 .38 .4]);

% spPos = outputText_sp.Position;
% spPosPix = outputText_sp.Position.*figPosPix

% create penetration output label
penLabel = uipanel('Parent',fig,'Title',...
    'Penetration [mm]',...
    'BorderType','none',...
    'TitlePosition','centertop','FontSize',20,...
    'FontWeight','bold',...
    'ForegroundColor',[0 0 1],...
    'units','normalized','Position',...

```

```

[0.55 0.45 0.2 0.08]);

penTextPosPix = penLabel.Position;

penText = uitablearea(penLabel,'Editable','off',...
    'Position',[75 2 100 30],...
    'Value',' ',...
    'HorizontalAlignment','center','FontSize',20,...
    'FontColor',[0 0 1],...
    'ValueChangedFcn',@(penText,event) textEntered(...
penText, ts_dd, power_dd, allTS304L, allPower304L));

% create penetration output label
areaLabel = uipanel('Parent',fig,'Title','Area [mm^2]',...
    'BorderType','none',...
    'TitlePosition','centertop','FontSize',20,...
    'FontWeight','bold',...
    'ForegroundColor',[0.5 0.5 0.5],...
    'units','normalized','Position',...
[0.77 0.45 0.2 0.08]);

% areaTextPos = areaLabel.Position;
% areaTextPosPix = areaLabel.Position.*figPosPix;

areaText = uitablearea(areaLabel,'Editable','off',...
    'Position',[75 2 100 30],'Value',' ',...
    'HorizontalAlignment','center','FontSize',20,...
    'FontColor',[0.5 0.5 0.5],...
    'ValueChangedFcn',@(areaText,event) textEntered(...
areaText, ts_dd, power_dd, allTS304L, allPower304L));

% create weld toe width output label
toeLabel = uipanel('Parent',fig,...
    'Title','Weld Toe Width [mm]',...
    'BorderType','none',...
    'TitlePosition','centertop','FontSize',20,...
    'FontWeight','bold',...
    'ForegroundColor',[0 0.7 0],...
    'units','normalized','Position',...
[0.625 0.335 0.25 0.08]);

% toeTextPos = toeLabel.Position;
% toeTextPosPix = toeLabel.Position.*figPosPix;

toeWidthText = uitablearea(toeLabel,'Editable','off',...

```

```

        'Position',[100 2 100 30], 'Value',' ',...
        'HorizontalAlignment','center','FontSize',20,...
        'FontColor',[0 0.7 0],...
        'ValueChangedFcn',@(toeWidthText,event) textEntered(...
toeWidthText, ts_dd, power_dd, allTS304L, allPower304L));

% create centroid output label
cenLabel = uipanel('Parent',fig,'Title',...
    'Centroid Weld Width [mm]',...
    'BorderType','none',...
    'TitlePosition','centertop','FontSize',20,...
    'FontWeight','bold',...
    'ForegroundColor',[0.9 0 0],...
    'units','normalized','Position',...
    [0.625 0.225 0.25 0.08]);

% cenTextPos = cenLabel.Position;
% cenTextPosPix = cenLabel.Position.*figPosPix;

centWidthText = uitextarea(cenLabel,'Editable','off',...
    'Position',[100 2 100 30], 'Value',' ',...
    'HorizontalAlignment','center','FontSize',20,...
    'FontColor',[0.9 0 0],...
    'ValueChangedFcn',@(centWidthText,event) textEntered(...
centWidthText, ts_dd, power_dd, allTS304L, allPower304L));

% create penetration output label
fwhmLabel = uipanel('Parent',fig,'Title',...
    'FWHM Weld Width [mm]',...
    'BorderType','none',...
    'TitlePosition','centertop','FontSize',20,...
    'FontWeight','bold',...
    'ForegroundColor',[0.6 0.1 0.6],...
    'units','normalized','Position',...
    [0.625 0.11 0.25 0.08]);

% fwhmTextPos = fwhmLabel.Position;
% fwhmTextPosPix = fwhmLabel.Position.*figPosPix;

fwhmText = uitextarea(fwhmLabel,'Editable','off',...
    'Position',[100 2 100 30], 'Value',' ',...
    'HorizontalAlignment','center','FontSize',20,...
    'FontColor',[0.6 0.1 0.6],...
    'ValueChangedFcn',@(fwhmText,event) textEntered(fwhmText,...
ts_dd, power_dd, allTS304L, allPower304L));

```

```

%% %%%%%%%%%%%%%%%%%%%%%%%%%%%%%%%%%%%%%%%%%%%%%%%%%%%%%%%%%%%%%%%%%%%%%%%%%%
%% create user interface drop downs
% matDDpos = sp_mat.Position;
matPosPix = round(sp_mat.Position.*figPosPix);

material_dd = uideropdown(sp_mat,...
    'FontSize',20,'Position',...
    [40 20 140 25],...
    'Items',{' ','304L Stainless Steel','Ti-6Al-4V'},...
    'ValueChangedFcn',...
    @(material_dd,event) selection(material_dd, penText,...
    areaText, toeWidthText,...
    centWidthText, fwhmText, ax));

% shieldDDpos = sp_shield.Position;
shieldPosPix = sp_shield.Position.*figPosPix;

shielding_dd = uideropdown(sp_shield,...
    'Position',...
    [40 20 140 25],...
    'FontSize',20,...
    'Items',{'Argon'},...
    'ValueChangedFcn',...
    @(shielding_dd,event) shieldingSelection(shielding_dd));

% angleDDpos = sp_Angle.Position;
anglePosPix = sp_Angle.Position.*figPosPix;

beamAngle_dd = uideropdown(sp_Angle,...
    'Position',...
    [40 20 140 25],...
    'FontSize',20,...
    'Items',{'0°'},...
    'ValueChangedFcn',...
    @(beamAngle_dd,event) beamAngleSelection(...
    beamAngle_dd, plotTitle));

% diamDDpos = sp_diam.Position;
diamPosPix = sp_diam.Position.*figPosPix;

beamDiam_dd = uideropdown(sp_diam,...
    'Position',...
    [40 20 140 25],...
    'FontSize',20,...
    'Items',{'600'},...

```

```

        'ValueChangedFcn',...
        @(beamDiam_dd,event) beamDiamSelection(...
        beamDiam_dd, plotTitle));

% powerDDpos = sp_power.Position;
powerPosPix = sp_power.Position.*figPosPix;

power_dd = uidropdown(sp_power,...
    'Position',...
    [40 20 140 25],...
    'FontSize',20,...
    'Items',powerLabels304L,...
    'ValueChangedFcn',...
    @(power_dd,event) powerSelection(allPower304L, allTS304L,...
    allPen304L, allArea304L,...
    allPowerTi64, allTSTi64, allPenTi64, allAreaTi64,...
    allToe304L, allCent304L, allFWHM304L,...
    allToeTi64, allCentTi64, allFWHMTi64,...
    power_dd, material_dd, ax,...
    penText, areaText, toeWidthText,...
    centWidthText, fwhmText));

% tsDDpos = sp_ts.Position;
tsPosPix = sp_ts.Position.*figPosPix;

ts_dd = uidropdown(sp_ts,...
    'Position',...
    [40 20 140 25],...
    'FontSize',20,...
    'Items',tsLabels304L,...
    'ValueChangedFcn',...
    @(ts_dd,event) ts_selection(ts_dd, penText, areaText,...
    toeWidthText, centWidthText, fwhmText,...
    allPower304L, allTS304L, allPen304L, allArea304L,...
    allPowerTi64, allTSTi64, allPenTi64, allAreaTi64,...
    allToe304L, allCent304L, allFWHM304L,...
    allToeTi64, allCentTi64, allFWHMTi64,...
    power_dd, material_dd));

%%%%%%%%%%%%%%%%%%%%%%%%%%%%%%%%%%%%%%%%%%%%%%%%%%%%%%%%%%%%%%%%%%%%%%%%
% Create a toggle button to toggle the original data on/off
toggleButtonGroup = uibuttongroup(fig,...
    'units','normalized','Position',[0.14 0.03 .3 .05],...
    'BorderType','none');

% togglePos = ax.Position;

```

```

togglePosPix = ax.Position.*figPosPix;

dataButton = uibutton(toggleButtonGroup,...
    'Position', [72 2 200 30],...
    'Text', 'Show Experimental Data',...
    'FontSize', 16,...
    'ButtonPushedFcn',...
    @(dataButton, event) plotButtonPushed(material_dd,
power_dd,...
    powerExp304L, unqExpPower304L, tsExp304L, penExp304L,...
    powerExpTi64, unqExpPowerTi64, tsExpTi64, penExpTi64, ax));

%% Callbacks
%%%%%%%%%%%%%%%%%%%%%%%%%%%%%%%%%%%%%%%%%%%%%%%%%%%%%%%%%%%%%%%%%%%%%%%%%%%%%%
% Create material value change callback
function selection(~, penText, areaText, toeWidthText,...
    centWidthText, fwhmText, ax)

    % reset the model output text values and drop downs
    penText.Value = ' ';
    areaText.Value = ' ';
    toeWidthText.Value = ' ';
    centWidthText.Value = ' ';
    fwhmText.Value = ' ';

    pen_pred = 0.75;
    x_pred = 10;
    plot(ax, x_pred, pen_pred, 'w');

    plotTitle = ' ';
    ax.Title.String = plotTitle;

    hold(ax, 'off')
    legend(ax, 'off')

    power_dd.Value = power_dd.Items(1);
    ts_dd.Value = ts_dd.Items(1);

end

% Create power selection callback:
function powerSelection(allPower304L, allTS304L,...
    allPen304L, allArea304L,...
    allPowerTi64, allTSTi64, allPenTi64, allAreaTi64,...
    allToe304L, allCent304L, allFWHM304L,...

```

```

allToeTi64, allCentTi64, allFWHMTi64,...
power_dd, material_dd, ax,...
penText, areaText, toeWidthText,...
centWidthText, fwhmText)

materialVal = material_dd.Value;

switch materialVal

    case '304L Stainless Steel'

        powerVal304L = power_dd.Value;
        power304L = str2double(powerVal304L);

        tsVal304L = ts_dd.Value;
        ts304L = str2double(tsVal304L);

        % Recompute Model Outpus once power is changed
        loc304L = find(ceil(allTS304L) == ts304L...
            & allPower304L == power304L);
        pen304L = allPen304L(loc304L);
        area304L = allArea304L(loc304L);
        toeWidth304L = allToe304L(loc304L);
        centWidth304L = allCent304L(loc304L);
        fwhm304L = allFWHM304L(loc304L);

        penText.Value = sprintf('%.1f',pen304L);
        areaText.Value = sprintf('%.1f',area304L);
        toeWidthText.Value =
            sprintf('%.1f',toeWidth304L);
        centWidthText.Value = sprintf('%.1f',
            centWidth304L);
        fwhmText.Value = sprintf('%.1f', fwhm304L);

        plotTitleMat = materialVal;
        plotTitlePower304L = strcat(powerVal304L, ' W');
        ax.Title.String = strcat(plotTitleMat, ':',...
            '{ }',...
            plotTitlePower304L, ' - 600', '{ }', 'μm');

        hold(ax, 'off')
        legend(ax, 'off')

    if power304L > 0
        loc = find(allPower304L == power304L);

```

```

        pen_pred = allPen304L(loc);
        x_pred = allTS304L(loc);
        p1 = plot(ax, x_pred, pen_pred);
        p1.LineWidth = 2;
else
    pen_pred = 0.75;
    x_pred = 10;
    plot(ax, x_pred, pen_pred, 'w');

    plotTitle = ' ';
    ax.Title.String = plotTitle;
    legend(ax, 'off')

    % reset the model output text values
    penText.Value = ' ';
    areaText.Value = ' ';
    toeWidthText.Value = ' ';
    centWidthText.Value = ' ';
    fwhmText.Value = ' ';

end

case 'Ti-6Al-4V'

    powerValTi64 = power_dd.Value;
    powerTi64 = str2double(powerValTi64);

    tsValTi64 = ts_dd.Value;
    tsTi64 = str2double(tsValTi64);

    locTi64 = find(ceil(allTSTi64) == tsTi64...
        & allPowerTi64 == powerTi64);
    penTi64 = allPenTi64(locTi64);
    areaTi64 = allAreaTi64(locTi64);
    toeWidthTi64 = allToeTi64(locTi64);
    centWidthTi64 = allCentTi64(locTi64);
    fwhmTi64 = allFWHMTi64(locTi64);

    penText.Value = sprintf('%.1f', penTi64);
    areaText.Value = sprintf('%.1f', areaTi64);
    toeWidthText.Value = sprintf('%.1f',
        toeWidthTi64);
    centWidthText.Value = sprintf('%.1f',
        centWidthTi64);
    fwhmText.Value = sprintf('%.1f', fwhmTi64);

```

```

plotTitleMat = materialVal;
plotTitlePowerTi64 = strcat(powerValTi64, ' W');
ax.Title.String = strcat(plotTitleMat, ...
    ':', '{ }', ...
    plotTitlePowerTi64, ' - 600', '{ }', 'μm');

hold(ax, 'off')
legend(ax, 'off')

if powerTi64 > 0
    loc = find(allPowerTi64 == powerTi64);
    pen_pred = allPenTi64(loc);
    x_pred = allTSTi64(loc);
    p1 = plot(ax, x_pred, pen_pred);
    p1.LineWidth = 2;
else
    pen_pred = 0.75;
    x_pred = 10;
    plot(ax, x_pred, pen_pred, 'w');

    plotTitle = ' ';
    ax.Title.String = plotTitle;
    legend(ax, 'off')

    % reset the model output text values
    penText.Value = ' ';
    areaText.Value = ' ';
    toeWidthText.Value = ' ';
    centWidthText.Value = ' ';
    fwhmText.Value = ' ';

end

case ' '

    pen_pred = 0.75;
    x_pred = 10;
    plot(ax, x_pred, pen_pred, 'w');

    plotTitle = ' ';
    ax.Title.String = plotTitle;
    legend(ax, 'off')

    % reset the model output text values
    penText.Value = ' ';
    areaText.Value = ' ';

```

```

        toeWidthText.Value = ' ';
        centWidthText.Value = ' ';
        fwhmText.Value = ' ';

    end

end

% Create shielding selection callback:
function shieldingSelection(~)
    %         shielding_val = shielding_dd.Value;
end

% Create beam diameter selection callback:
function beamDiamSelection(~)
    %         db_val = beamDiam_dd.Value;
end

% create the toggle button callback for experimental data
function plotButtonPushed(material_dd, power_dd,...
    powerExp304L, unqExpPower304L,...
    tsExp304L, penExp304L,...
    powerExpTi64, unqExpPowerTi64, tsExpTi64,...
    penExpTi64, ax)

    matVal = material_dd.Value;

    switch matVal

        case '304L Stainless Steel'

            powerNum304L = str2double(power_dd.Value);

            if ~isempty(powerNum304L)

                loc = find(unqExpPower304L == powerNum304L);

                if loc > 0

                    % find the power locations
                    valLoc304L = find(powerExp304L...
                        == powerNum304L);
                    % original data extraction
                    % travel speed [mm/s]

```

```

ts_exp304L = tsExp304L(valLoc304L);
% penetration [mm]
pen_exp304L = penExp304L(valLoc304L);
% beam diameter [mm]
% db_exp = sortedMat(valLoc,3);
% area of fusion zone [mm^2]
% area_exp = sortedMat(valLoc,5);
% toe width [mm]
% toeWidth_exp = sortedMat(valLoc,6);
% centroid weld width [mm]
% centWidth_exp = sortedMat(valLoc,8);
% FWHM weld width [mm]
% fwhm_exp = sortedMat(valLoc,7);

hold(ax, 'on')
p2 = plot(ax, ts_exp304L,...
    pen_exp304L, 'x',...
    'Color',[0.85,0,0],'MarkerSize',14);
p2.LineWidth = 2;
legend(ax,'NN Data',...
    'Experimental Data',...
    'Location','northeast');
hold(ax, 'off')

powerVal304L = power_dd.Value;
power304L = str2double(powerVal304L);

tsVal304L = ts_dd.Value;
ts304L = str2double(tsVal304L);

loc304L = find(ceil(allTS304L) ==...
    ts304L...
    & allPower304L == power304L);
pen304L = allPen304L(loc304L);
area304L = allArea304L(loc304L);
toeWidth304L = allToe304L(loc304L);
centWidth304L = allCent304L(loc304L);
fwhm304L = allFWHM304L(loc304L);

penText.Value = sprintf('%.1f',pen304L);
areaText.Value =
sprintf('%.1f',area304L);
toeWidthText.Value = sprintf('%.1f',...
    toeWidth304L);
centWidthText.Value = sprintf('%.1f',...
    centWidth304L);

```

```

                                fwhmText.Value =
sprintf('%0.1f',fwhm304L);

                                else
                                text(ax,42,3.7,...
                                    'Experimental Data Does Not
Exist',...
                                    'FontSize',16,'color','r',...
                                    'FontWeight','bold')
                                end

                                else
                                pen_pred = 0.75;
                                x_pred = 10;
                                plot(ax, x_pred, pen_pred, 'w');
                                plotTitle = ' ';
                                ax.Title.String = plotTitle;
                                end

                                case 'Ti-6Al-4V'

                                powerNumTi64 = str2double(power_dd.Value);

                                if ~isempty(powerNumTi64)

                                loc = find(unqExpPowerTi64 == powerNumTi64);

                                if loc > 0

                                % find the power locations
                                valLocTi64 = find(powerExpTi64 ==...
                                    powerNumTi64);
                                % original data extraction
                                % travel speed [mm/s]
                                ts_expTi64 = tsExpTi64(valLocTi64);
                                % penetration [mm]
                                pen_expTi64 = penExpTi64(valLocTi64);
                                % beam diameter [mm]
                                % db_exp = sortedMat(valLoc,3);
                                % area of fusion zone [mm^2]
                                % area_exp = sortedMat(valLoc,5);
                                % toe width [mm]
                                % toeWidth_exp = sortedMat(valLoc,6);
                                % centroid weld width [mm]
                                % centWidth_exp = sortedMat(valLoc,8);
                                % FWHM weld width [mm]

```

```

        % fwhm_exp = sortedMat(valLoc,7);

        hold(ax, 'on')
        p2 = plot(ax, ts_expTi64, pen_expTi64,...
            'x',...
            'Color',[0.85,0,0], 'MarkerSize',14);
        p2.LineWidth = 2;
        legend(ax, 'NN Data',...
            'Experimental Data',...
            'Location','northeast');
        hold(ax, 'off')
    else
        text(ax,42,3.7,...
            'Experimental Data Does Not Exist',...
            'FontSize',16, 'color','r',...
            'FontWeight','bold')
    end

else
    pen_pred = 0.75;
    x_pred = 10;
    plot(ax, x_pred, pen_pred, 'w');
    plotTitle = ' ';
    ax.Title.String = plotTitle;
end

otherwise

    pen_pred = 0.75;
    x_pred = 10;
    plot(ax, x_pred, pen_pred, 'w');
    plotTitle = ' ';
    ax.Title.String = plotTitle;
end

end

end

% travel speed dropdown callback function
function ts_selection(ts_dd, penText, areaText,
    toeWidthText,...
    centWidthText, fwhmText,...
    allPower304L, allTS304L, allPen304L, allArea304L,...
    allPowerTi64, allTSTi64, allPenTi64, allAreaTi64,...
    allToe304L, allCent304L, allFWHM304L,...
    allToeTi64, allCentTi64, allFWHMTi64,...

```

```

        power_dd, material_dd)

ddVal = material_dd.Value;

switch ddVal

    case '304L Stainless Steel'

        if ts_dd.Value ~= ' '

            powerVal304L = power_dd.Value;
            power304L = str2double(powerVal304L);

            tsVal304L = ts_dd.Value;
            ts304L = str2double(tsVal304L);

            loc304L = find(ceil(allTS304L) == ts304L...
                & allPower304L == power304L);
            pen304L = allPen304L(loc304L);
            area304L = allArea304L(loc304L);
            toeWidth304L = allToe304L(loc304L);
            centWidth304L = allCent304L(loc304L);
            fwhm304L = allFWHM304L(loc304L);

            penText.Value = sprintf('%.1f',pen304L);
            areaText.Value = sprintf('%.1f',area304L);
            toeWidthText.Value =
sprintf('%.1f',toeWidth304L);
            centWidthText.Value = sprintf('%.1f',...
                centWidth304L);
            fwhmText.Value = sprintf('%.1f',fwhm304L);

        else

            penText.Value = ' ';
            areaText.Value = ' ';
            toeWidthText.Value = ' ';
            centWidthText.Value = ' ';
            fwhmText.Value = ' ';

        end

    case 'Ti-6Al-4V'

        if ts_dd.Value ~= ' '

```

```

powerValTi64 = power_dd.Value;
powerTi64 = str2double(powerValTi64);

tsValTi64 = ts_dd.Value;
tsTi64 = str2double(tsValTi64);

locTi64 = find(ceil(allTSTi64) == tsTi64...
    & allPowerTi64 == powerTi64);
penTi64 = allPenTi64(locTi64);
areaTi64 = allAreaTi64(locTi64);
toeWidthTi64 = allToeTi64(locTi64);
centWidthTi64 = allCentTi64(locTi64);
fwhmTi64 = allFWHMTi64(locTi64);

penText.Value = sprintf('%.1f',penTi64);
areaText.Value = sprintf('%.1f',areaTi64);
toeWidthText.Value = sprintf('%.1f',...
    toeWidthTi64);
centWidthText.Value = sprintf('%.1f',...
    centWidthTi64);
fwhmText.Value = sprintf('%.1f',fwhmTi64);

else
    penText.Value = ' ';
    areaText.Value = ' ';
    toeWidthText.Value = ' ';
    centWidthText.Value = ' ';
    fwhmText.Value = ' ';

end

otherwise

    penText.Value = ' ';
    areaText.Value = ' ';
    toeWidthText.Value = ' ';
    centWidthText.Value = ' ';
    fwhmText.Value = ' ';

end

end

end

end

```

## O.2 Neural Network Training Script

```
% Artificial Neural Network from Processed Image File Data
% Created by Tate Patterson

clc; clear; close all;

% ask if user would re-extract the "raw" data or image files
% if new data was added and needs to be trained
dlgTitle    = 'Data Extract?';
dlgQuestion = 'Do you wish to extract the data files for
analysis?';
choice = questdlg(dlgQuestion,dlgTitle,'Yes','No', 'Yes');
% compare strings to see if 'Yes'
strComp = strcmp(choice,'Yes');

if strComp == 1
    % user defined function 'NN_DataExtract' to extract
    % the binary image files from each folder
    NN_DataExtract();

end

%% Call function to get data from image files
% ask if user would like to retrain the data
dlgTitle    = 'Train?';
dlgQuestion = 'Do you wish to train the 304L NN models?';
choice = questdlg(dlgQuestion,dlgTitle,'Yes','No', 'Yes');
% compare strings to see if 'Yes'
strComp = strcmp(choice,'Yes');

if strComp == 1

    % call artificial neural network function for penetration
    [x_predPen, penPred, perfPen] = ANN_Penetration_304L();

    % call artificial neural network function for toe width
    [x_predToe, toePred, perfToe] = ANN_ToeWidth_304L();

    % call artificial neural network function for fwhm width
    [x_predFWHM, fwhmPred, perfFWHM] = ANN_FWHMWidth_304L();

    % call artificial neural network function for centroid
    [x_predCent, centPred, perfCent] = ANN_CentWidth_304L();

    % call artificial neural network function for toe width
```

```

[x_predArea, areaPred, perfArea] = ANN_Area_304L();

%% combine model data with user defined function 'dataCombo'
% this data is the neural network data for each power
% with linear interpolation of the NN data for powers
% that do not have experimental values
dataCombo()

end

%% Call function to get data from image files
% ask if user would like to retrain the data
dlgTitle      = 'Train?';
dlgQuestion = 'Do you wish to train the Ti-6Al-4V NN models?';
choice = questdlg(dlgQuestion,dlgTitle,'Yes','No', 'Yes');
% compare strings to see if 'Yes'
strComp = strcmp(choice,'Yes');

if strComp == 1
    % exit if statement and do not satisfy while loop
    % call function to get data from image files
    %      [nnDataMat] = NN_DataExtract();

    % call artificial neural network function for penetration
    [x_predPen, penPred, perfPen] = ANN_Penetration_Ti64();

    % call artificial neural network function for toe width
    [x_predToe, toePred, perfToe] = ANN_ToeWidth_Ti64();

    % call artificial neural network function for fwhm width
    [x_predFWHM, fwhmPred, perfFWHM] = ANN_FWHMWidth_Ti64();

    % call artificial neural network function for centroid
    [x_predCent, centPred, perfCent] = ANN_CentWidth_Ti64();

    % call artificial neural network function for teo width
    [x_predArea, areaPred, perfArea] = ANN_Area_Ti64();

    %% combine model data with user defined function 'dataCombo'
    % this data is the neural network data for each power
    % with linear interpolation of the NN data for powers
    % that do not have experimental values
    dataCombo()

end

```

### O.3 Fusion Cross-Section Calculation Function

```
function [penetration, areaOfFZ, toeWidth,...
    weldWidthFWHM, weldCentroidWidth,...
    perimeterOfFZ, fusionBoundaryLength,...
    expDataVec] = fzCalcs(shiftImage,...
    lengthPerPixel)

% Compute cross-sectional informatin from the feature values
maskedImage = shiftImage;

%% Determine the perimeter of the fusion boundary
% Use the built in MATLAB function "regionprops" to
% extract the data from
% traced fusion boundary user measurement
perimeter = regionprops(maskedImage, 'Perimeter');
perimeter = cat(1, perimeter.Perimeter);
perimeterOfFZ = perimeter*lengthPerPixel;

%% Compute area of the black and white pixels in image
% nnz computes the number of nonzero matrix elements
areaWhite = nnz(maskedImage);
% Find the total number of elements (N) in the image
numberOfElements = numel(maskedImage);
areaBlack = numberOfElements - areaWhite;

fusionZoneFraction = areaBlack/numberOfElements;

% Get the number of pixels in height and width of image
[heightInPixels, widthInPixels] = size(maskedImage);

% Get the dimensions (width, height, area) of image [mm]
totalImageWidth = lengthPerPixel*heightInPixels;
totalImageHeight = lengthPerPixel*widthInPixels;
totalImageArea = totalImageWidth*totalImageHeight;

clc; % clear the window
areaOfFZ = (lengthPerPixel^2)*areaWhite;

%% Determine the weld width at the FZ centroid
% Determine the centroid of the fusion zone
% by the user in the previous section

% Use the built in MATLAB function "regionprops"
% to determine the centroid location and store values
cen = regionprops(maskedImage, 'centroid');
```

```

% 'cat' concatenates the values to a single array
centroid = cat(1, cen.Centroid);

% Use the centroid location and iterate outward
% to determine where the pixels go from white (1)
% to black (0). Save location to determine the
% width/hieght

x_loc = centroid(1,1);
y_loc = centroid(1,2);

x_loc = round(x_loc);
y_loc = round(y_loc);

% Move only in the x-direction to determine the width
val = 1; % value of white pixels in image
j = 0; % counter
while val
    j = j+1;
    val = maskedImage(y_loc, x_loc + j);
end
x_right = x_loc + j - 1;

% Value of white pixels in image
val = 1; % value of white pixels in image
j = 0; % counter
while val
    j = j+1;
    val = maskedImage(y_loc, x_loc - j);
end
x_left = x_loc - j + 1;

weldCentroidWidth = abs(x_right-x_left)*lengthPerPixel;

%% Determine weld width at half maximum of the FZ
% This section determines the maximum and minimum
% extrema locations from
% the fusion zone cross-section and computes the
% difference between the
% two. Then it uses those points to search to
% the left and right to
% determine the width at half maximum or
% full width - half maximum (FWHM)

% 'Extrema' outputs an 8x2 matrix with each row

```

```

% consisting of x-y coordinates of [top-left,
% top-right, right-top, right-bottom,
% bottom-right, bottom-left, left-bottom, left-top].
% For instance, top-left and left-top may be identical

s = regionprops(maskedImage, 'extrema');

% 'cat' concatenates the values to a single array
extremaPoints = cat(1,s.Extrema);

% define Extrema points
topLeftExtremeX = extremaPoints(1,1);
topLeftExtremeY = extremaPoints(1,2);
topRightExtremeX = extremaPoints(2,1);
topRightExtremeY = extremaPoints(2,2);
rightTopExtremeX = extremaPoints(3,1);
rightTopExtremeY = extremaPoints(3,2);
rightBottomExtremeX = extremaPoints(4,1);
rightBottomExtremeY = extremaPoints(4,2);
bottomRightExtremeX = extremaPoints(5,1);
bottomRightExtremeY = extremaPoints(5,2);
bottomLeftExtremeX = extremaPoints(6,1);
bottomLeftExtremeY = extremaPoints(6,2);
leftBottomExtremeX = extremaPoints(7,1);
leftBottomExtremeY = extremaPoints(7,2);
leftTopExtremeX = extremaPoints(8,1);
leftTopExtremeY = extremaPoints(8,2);

% Find which point is the highest from MATLAB function
% "regionprops" and "extrema"
if topLeftExtremeY > topRightExtremeY
    highestPoint = topLeftExtremeY;
else highestPoint = topRightExtremeY;
end
highestPoint = round(highestPoint);

% Find which point is the lowest from MATLAB function
% "regionprops" and "extrema"
if bottomRightExtremeY < bottomLeftExtremeY
    lowestPoint = bottomRightExtremeY;
else lowestPoint = bottomLeftExtremeY;
end
lowestPoint = round(lowestPoint);

% find the height in pixels
height = abs(highestPoint-lowestPoint);

```

```

fwhm = height/2; % find the FWHM pixel value

% Use FWHM pixel value to start searching left
% and right for the widths
% Use the centroid x-location as a default starting location
x_loc = centroid(1,1);
x_loc = round(x_loc);
y_loc = round(fwhm + highestPoint);

% move only in the x-direction to determine the width
val = 1; % value of white pixels in image
j = 0; % counter
while val
    j = j+1;
    val = maskedImage(y_loc, x_loc + j);
end
x_right = x_loc + j - 1;

% value of white pixels in image
val = 1; % value of white pixels in image
j = 0; % counter
while val
    j = j+1;
    val = maskedImage(y_loc, x_loc - j);
end
x_left = x_loc - j + 1;

weldWidthFWHM = abs(x_right-x_left)*lengthPerPixel;

%% Determine weld toe positions, width, and top surface length
% Iterate through the length of the columns and
% find the top surface locations
for n = 1:widthInPixels
    colVal = maskedImage(:,n);
    if sum(colVal) > 0
        colValLoc = find(colVal > 0);
        topPos = min(colValLoc);
        rowNum = topPos;
        colNum = n;
    else
        topPos = 0;
        rowNum = 0;
        colNum = n;
    end
    topPosVec(n) = topPos;
    rowNumVec(n) = rowNum;
end

```

```

        colNumVec(n) = colNum;
    end

    locations = find(rowNumVec > 1);
    leftColLoc = locations(1,1);
    rightColLoc = locations(1,end);
    leftRowLoc = topPosVec(leftColLoc);
    rightRowLoc = topPosVec(rightColLoc);

    leftWeldToe = [leftColLoc, leftRowLoc];
    rightWeldToe = [rightColLoc, rightRowLoc];

    numSurfPixels = length(find(topPosVec > 1));
    toeWidth = numSurfPixels*lengthPerPixel;

    % Determine the surface length by iterating through pixel values
    for nn = 1:length(topPosVec)-1

        if topPosVec(nn) ~= 0
            dist = sqrt((topPosVec(nn)-topPosVec(nn+1))^2 + 1);
        else
            dist = 0;
        end
        distVec(nn) = dist;
    end
    lengthOfSurf = sum(distVec)*lengthPerPixel;

    %% Determine FZ penetration from top surface of plate
    % Use the output from the built in MATLAB
    % function "regionprops" to extract
    % the needed information

    % Average y positions to get a location to search for
    % the weld toes, this gets the approximate
    %plate surface location
    yToePosAvg = mean(round(leftWeldToe(1,1)),...
        round(leftWeldToe(1,2)));

    % Find the deepest point of penetration using
    % the already determined lowest
    % point from the 'Extrema' values
    penetration = lengthPerPixel*abs(yToePosAvg - lowestPoint);

    %% Determine the perimeter of the fusion boundary

    % Use built in MATLAB function "regionprops" to extract data from

```

```

% the binary image file
perimeter = regionprops(maskedImage, 'Perimeter');
perimeter = cat(1,perimeter.Perimeter);
perimeterOfFZ = perimeter*lengthPerPixel;

fusionBoundaryLength = perimeterOfFZ-lengthOfSurf;

y_labelPos = heightInPixels + 10;
x_labelPosR = widthInPixels + 25;
fontsize = 12; % size of measured data font on figure

expDataVec = [penetration, areaOfFZ, toeWidth,...
              weldWidthFWHM, weldCentroidWidth,...
              perimeterOfFZ, fusionBoundaryLength];

end

```

## O.4 Feedforward Artificial Neural Network Function

```
function [x_pred, penPred, perf] = ANN_Penetration_304L()

%% Neural Network Code
% April 2021
% Created by Tate Patterson

expDataStruct = load('expDataMat304L.mat');
expDataMat = expDataStruct.expDataMat304L;

% Sort the data from low to high for training and plotting
sortedMat = sortrows(expDataMat,[1 2],'ascend');

power = sortedMat(:,1); % power [W]

% All the unique power values to extract data for given power
unqPower = unique(power);
% predefine an empty output data matrix
NN_OutputDataMat = [];

for k = 1:length(unqPower)

    % Find where the power values are all the same
    valLoc = find(power == unqPower(k));

    powerVec = sortedMat(valLoc,1); % power [W]
    % get the power value for later use
    powerVal = powerVec(1,1);
    ts = sortedMat(valLoc,2); % travel speed [mm/s]
    % check for number of unique travel speed
    % data points for training
    tsDataLength = length(unique(ts));
    pen = sortedMat(valLoc,4); % penetration [mm]
    db = sortedMat(valLoc,3); % beam diameter [mm]
    area = sortedMat(valLoc,5); % area of fusion zone [mm^2]
    toeWidth = sortedMat(valLoc,6); % toe width [mm]
    % centroid weld width [mm]
    centWidth = sortedMat(valLoc,8);
    % full width half maximum weld width [mm]
    fwhm = sortedMat(valLoc,7);

    %% Define values and train the ANN
    dataLength = length(pen);

    % Check for sufficient number of data points before
```

```

% creating a model
if tsDataLength > 3

    x = ts';
    t = pen';

    % Define and train artificial neural network (ANN)
    % allow for user to select different numbers of neurons
    hiddenLayerSize = 2; % define number of neurons

    % Create neural network with training performed
    % through Bayseian regularization
    net = fitnet(hiddenLayerSize,'trainbr');
    net = train(net,x,t);
    y = net(x);
    % Compute the model performance
    perf(k) = perform(net,y,t);

    folder = pwd; % select current folder to save in
    % Create a file name with location
    baseFileName = sprintf(...
        '304L_NN_PenModel_%sW.mat', num2str(powerVal));
    fullMatFileName = fullfile(folder, baseFileName);
    % save the network to location with specified filename
    save(fullMatFileName);

    %% Plot results
    x_pred = linspace(1,150,150);
    penPred = net(x_pred);

    % Create a matrix of trained data
    trainedOutputData = [powerVal*ones(length(x_pred),1),...
        x_pred', penPred'];

    figure
    plot(x_pred,penPred,'-','LineWidth',2); hold on;
    xlabel('Travel Speed [mm/s'],'FontSize',16)
    ylabel('Penetration [mm]','FontSize',16)

    plot(ts,pen,'x','MarkerSize',12,'LineWidth',1.2);
    hold on;
    xlim([min(ts)-5, max(ts)+5])
    ylim([0, ceil(max(pen))])

    if max(ts) < 100
        xticks(linspace(min(ts),max(ts),10));

```

```

elseif max(ts) < 150
    xticks(10:10:100);
else
    xticks(25:25:150);
end
yticks(0:0.5:ceil(max(pen)));

titleString = strcat(num2str(unqPower(k)), ' W');
title(titleString, 'FontSize', 22)
legend('ANN Model', 'SS Measured Data', ...
    'FontSize', 14)
set(gca, 'FontSize', 16); grid on;

% Create the output data matrix
NN_OutputDataMat = [NN_OutputDataMat; trainedOutputData];

else
    powerVec(k)
    string = strcat('There is not enough data to train ', ...
        num2str(power(k)), ' W!');
    error(string)

end

end

%% %%%%%%%%%%%%%%%%%%%%%%%%%%%%%%%%%%%%%%%%%%%%%%%%%%%%%%%%%%%%%%%
% Create more data from neural network output through
% linear interpolation of the predicted NN values

penPredMat = []; % initialize variable matrices
tsPredMat = [];

% Get the trained network file names
for ii = 1:length(unqPower)
    % find the trained network files
    networkName = strcat('304L_NN_PenModel_', ...
        num2str(unqPower(ii)), 'W', '.mat');
    trainedNetworks(:, ii) = convertCharsToStrings(...
        networkName);
    % Eventually want to check if model exists

    % Create vector of travel speed values to use in the models
    x_pred = linspace(1, 150, 150);
    nn_str = convertCharsToStrings(networkName);
    trainedNet = load(nn_str);

```

```

    pen_pred = trainedNet.net(x_pred);
    penPredMat = [penPredMat, pen_pred'];
    tsPredMat = [tsPredMat, x_pred'];
end

% Perform linear interpolation to get powers in between
% the powers analyzed experimentally

% Manually create vector of power to interpolate
powerIntps = [1100, 1300, 1400, 1500, 1700,...
    1800, 1900, 2100, 2300];

% Initialize interpolated penetration, power, and
% travel speed matrices
penInterpMat = [];
powerInterMat = [];
tsInterMat = [];
interpDataMat = [];

for ii = 1:length(powerIntps)

    % Get the original power values greater than and less than
    % interpolated powers that want to be used
    loc = find(powerIntps(ii) > unqPower);
    lowPower = unqPower(max(loc));
    highPower = unqPower(max(loc)+1);

    % Compute the interpolated penetration
    penInterpVec = (penPredMat(:,max(loc)+1)-...
        penPredMat(:,max(loc)))*...
        (powerIntps(ii)-lowPower)/(highPower-lowPower)+...
        penPredMat(:,max(loc));

    powerInterpVec = powerIntps(ii)*ones(...
        length(penInterpVec),1);
    tsInterpVec = tsPredMat(:,1);

    % Create the matrix of data
    penInterpMat(:,ii) = penInterpVec;

    interpDataMat = [interpDataMat;...
        [powerInterpVec, tsInterpVec, penInterpVec]];

end

allDataMat = [NN_OutputDataMat; interpDataMat];

```

```
allPenDataMat304L = sortrows(allDataMat,[1 2],'ascend');  
save('allPenDataMat304L.mat', 'allPenDataMat304L')  
end
```

## O.5 Neural Network Data Combination Function

```
% Load all data matrices into the same matrix and save
% the data out to a new matrix
function dataCombo()

%% Load the 304L data
% Penetration data
allPenDataStruct = load('allPenDataMat304L.mat');
allPenDataMat = allPenDataStruct.allPenDataMat304L;

% Fusion zone area data
allAreaDataStruct = load('allAreaDataMat304L.mat');
allAreaDataMat = allAreaDataStruct.allAreaDataMat304L;

% Weld toe width data
allToeDataStruct = load('allToeDataMat304L.mat');
allToeDataMat = allToeDataStruct.allToeDataMat304L;

% Centroid width data
allCentDataStruct = load('allCentDataMat304L.mat');
allCentDataMat = allCentDataStruct.allCentDataMat304L;

% fwhm weld width data
allFWHMDataStruct = load('allFWHMDataMat304L.mat');
allFWHMDataMat = allFWHMDataStruct.allFWHMDataMat304L;

% Combine the data files into single matrix
allData = [allPenDataMat(:,1), allPenDataMat(:,2), ...
           allPenDataMat(:,3), allAreaDataMat(:,3),
           allToeDataMat(:,3), ...
           allCentDataMat(:,3), allFWHMDataMat(:,3)];

allDataMat304L = sortrows(allData,[1 2],'ascend');
save('allDataMat304L.mat', 'allDataMat304L')

%% Load the Ti64 data
% Penetration data
allPenDataStruct = load('allPenDataMatTi64.mat');
allPenDataMat = allPenDataStruct.allPenDataMatTi64;

% Fusion zone area data
allAreaDataStruct = load('allAreaDataMatTi64.mat');
allAreaDataMat = allAreaDataStruct.allAreaDataMatTi64;

% Weld toe width data
```

```

allToeDataStruct = load('allToeDataMatTi64.mat');
allToeDataMat = allToeDataStruct.allToeDataMatTi64;

% Centroid width data
allCentDataStruct = load('allCentDataMatTi64.mat');
allCentDataMat = allCentDataStruct.allCentDataMatTi64;

% fwhm weld width data
allFWHMDataStruct = load('allFWHMDataMatTi64.mat');
allFWHMDataMat = allFWHMDataStruct.allFWHMDataMatTi64;

% Combine the data files into single matrix
allData = [allPenDataMat(:,1), allPenDataMat(:,2), ...
           allPenDataMat(:,3), allAreaDataMat(:,3),
           allToeDataMat(:,3), ...
           allCentDataMat(:,3), allFWHMDataMat(:,3)];

allDataMatTi64 = sortrows(allData, [1 2], 'ascend');

save('allDataMatTi64.mat', 'allDataMatTi64')

```

## Appendix P: Gas Tungsten Arc Weld Micrographs

For a visual comparison between LBW and an arc welding process, GTA welds were produced on the SS alloys investigated. The linear heat inputs were identical by using 100 A and 10 V for 1000 W and a 5 mm/s travel speed. The optical micrographs for the comparable LB welds and GTA welds are shown in Figure P.1-Figure P.3.

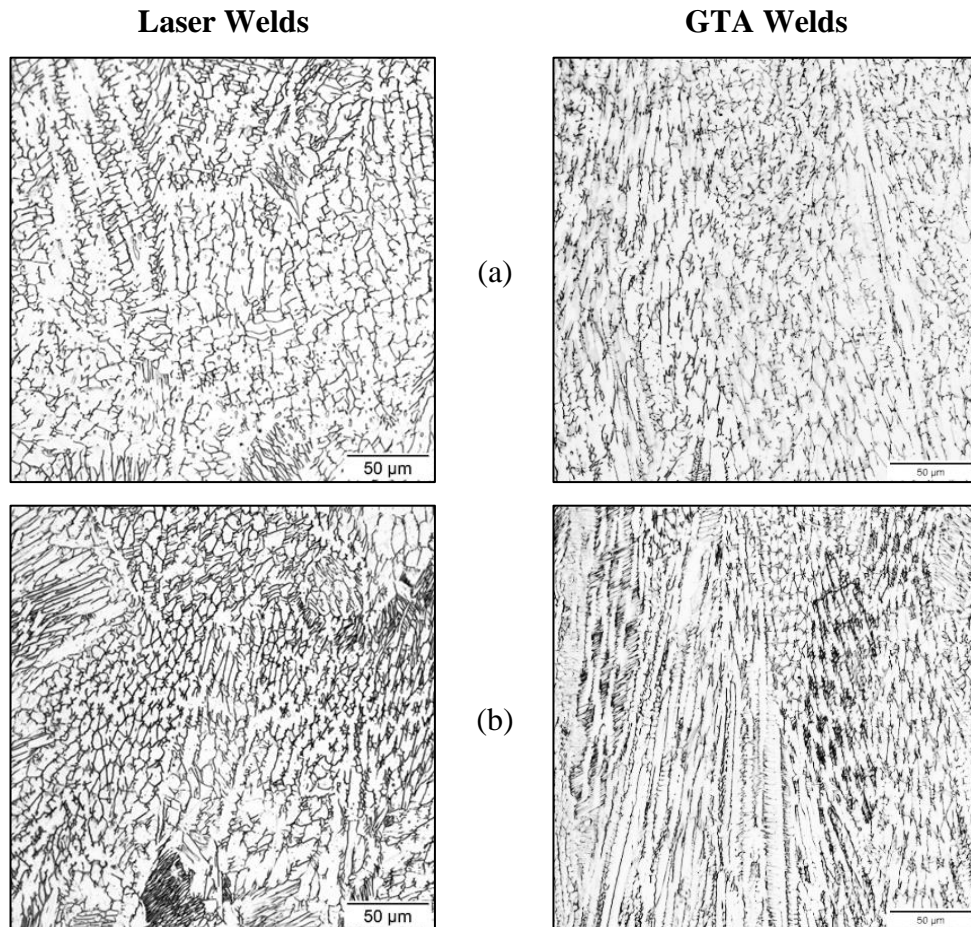
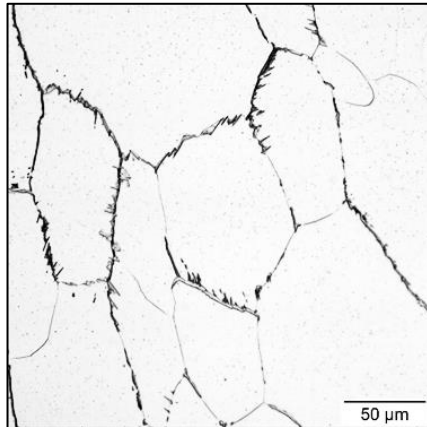
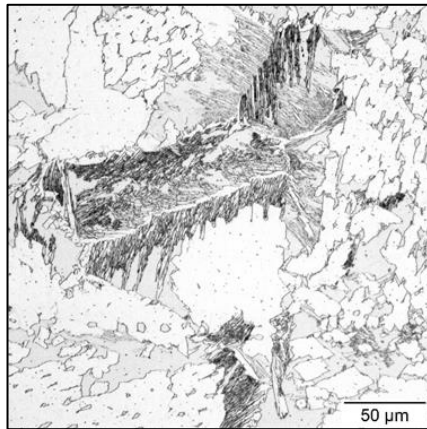
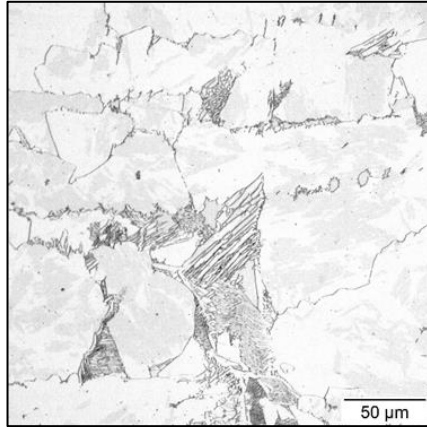


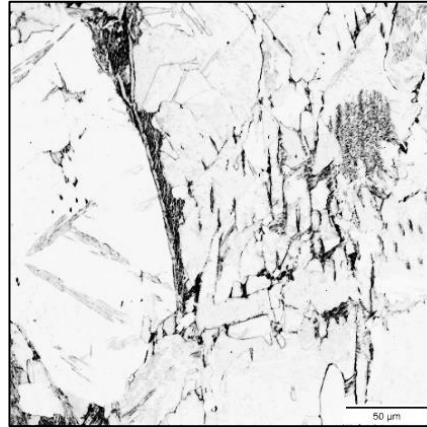
*Figure P.1. Laser (left) and gas tungsten arc weld (right) comparison micrographs at 1000 W of power and a 5 mm/s travel speed: 304L (a) and M58 (b).*

### Laser Welds

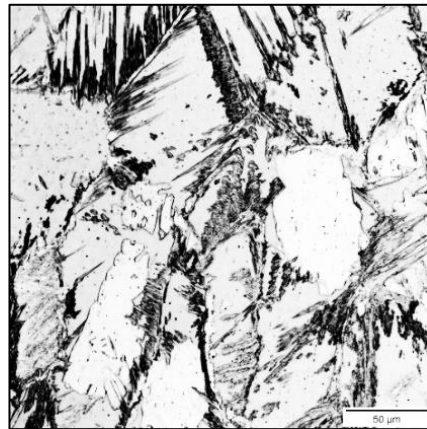


### GTA Welds

(a)



(b)



(c)

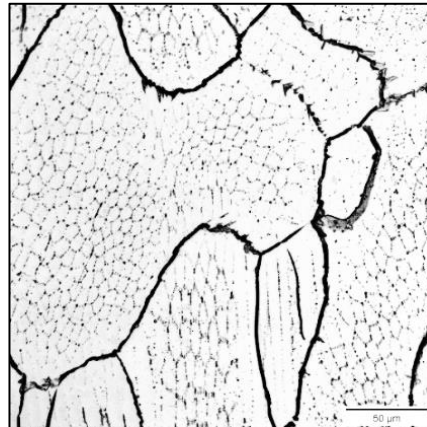
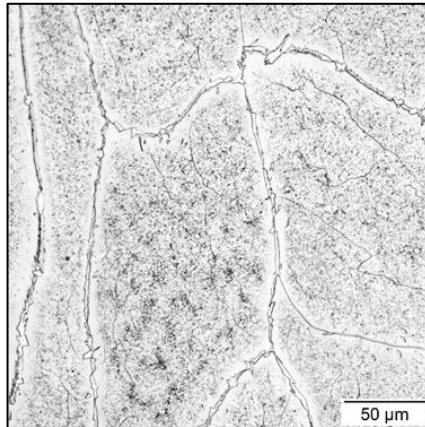


*Figure P.2. Laser (left) and gas tungsten arc weld (right) comparison micrographs at 1000 W of power and a 5 mm/s travel speed: M45 (a), M53 (b), and M54 (c).*

**Laser Weld**



**GTA Weld**

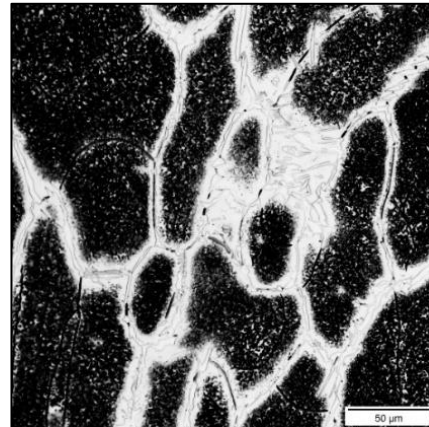


*Figure P.3. Laser (left) and gas tungsten arc weld (right) comparison micrographs at 1000 W of power and a 5 mm/s travel speed for 2205 DSS.*